

Mineral Resource Reviews

Pär Weihed *Editor*

3D, 4D and Predictive Modelling of Major Mineral Belts in Europe



 Springer

Mineral Resource Reviews

Series editor

John Slack, Reston, VA, USA

More information about this series at <http://www.springer.com/series/11683>

Pär Weihed
Editor

3D, 4D and Predictive Modelling of Major Mineral Belts in Europe



 Springer

Editor

Pär Weihed
Division of Geosciences and Environmental
Engineering, Centre of Advanced Mining
and Metallurgy
Luleå University of Technology
Luleå
Sweden

ISSN 2365-0559 ISSN 2365-0567 (electronic)
Mineral Resource Reviews
ISBN 978-3-319-17427-3 ISBN 978-3-319-17428-0 (eBook)
DOI 10.1007/978-3-319-17428-0

Library of Congress Control Number: 2015941135

Springer Cham Heidelberg New York Dordrecht London

© Springer International Publishing Switzerland 2015

This work is subject to copyright. All rights are reserved by the Publisher, whether the whole or part of the material is concerned, specifically the rights of translation, reprinting, reuse of illustrations, recitation, broadcasting, reproduction on microfilms or in any other physical way, and transmission or information storage and retrieval, electronic adaptation, computer software, or by similar or dissimilar methodology now known or hereafter developed.

The use of general descriptive names, registered names, trademarks, service marks, etc. in this publication does not imply, even in the absence of a specific statement, that such names are exempt from the relevant protective laws and regulations and therefore free for general use.

The publisher, the authors and the editors are safe to assume that the advice and information in this book are believed to be true and accurate at the date of publication. Neither the publisher nor the authors or the editors give a warranty, express or implied, with respect to the material contained herein or for any errors or omissions that may have been made.

Printed on acid-free paper

Springer International Publishing AG Switzerland is part of Springer Science+Business Media
(www.springer.com)

This book is dedicated to late Prof. Gabor Gaál, the coordinator of the Promine project. Gabor passed away during the very final stages of the Promine project in June 2013, at the age of 74. Without Gabor the Promine project, and hence, this book would not have been realized. Gabor, a structural geologist and economic geologist by profession, early in his life realized the importance of three-dimensional understanding of geological features. In his career in Finland, with among others the Geological Survey of Finland, he advocated 3D interpretations and predictive metallogeny as key elements in understanding ore deposits. His personality can be summarized as “everything is possible if you believe in it”. This view also made Gabor the obvious coordinator of a multidisciplinary project like Promine, bringing hundreds of scientists and engineers from academia, research institutes and industry together to form and execute the project Promine that won the best FP7 project award at the Industrial Technologies 2014 Conference. An obituary is provided as a preface to this book.

On behalf of Promine colleagues, thank you for keeping the spirits high through the project Gabor!

Obituary



Gabor Gaál (28 October 1938–16 June 2013)

Professor and geologist, Gabor (Gabriel) Gaál, ProMine coordinator, died in his hometown Budapest after a short but severe illness on 16 June 2013.

A passport holder of three countries (Hungary, Austria and Finland), Gabor Gaál was one of Finland's most international and respected geologists. He carried out his scientific work, which he loved, almost until his death at the service of the Geological Survey of Finland (GTK).

Gaál's life and career were exceptional and multifaceted. He was born on 28 October 1938, in Nyitra, Hungary, which is now a part of Slovakia. As a young man, Gabor took part in the Hungarian uprising in 1956 and was exiled in Austria with his identical twin brother, Tibor.

He graduated from high school in Innsbruck in 1957 and started in the same year his studies on geology at Vienna University, where he received his PhD in 1963. Geology was a natural choice to Gabor, since, as a very young boy, he was interested in and charmed by the world of science and palaeontology.

After graduating from the university, Gaál worked in northeast India at the Singhbhum copper zone. In 1965, he moved to North Karelia to work in Outokumpu Ltd. on base metals exploration. The transition almost directly from Vienna to Outokumpu was not without culture shock, but due to his good nature he adapted well to totally new conditions.

In Outokumpu, Gabor became acquainted with his much beloved wife Eine. They have two children: Gabriela and Miklos.

Gabor worked in Northern Finland Ore Geology Council where he supervised 14 ore geology projects. The first indications of new gold deposits in the area were found in these projects.

Gaál was an assistant professor at the Department of Geology at the University of Helsinki from 1978 to 1983. He also worked at the University of Bahia, Brazil; at the University of Western Australia, Perth; and at the University of Oulu.

Gaál's inspirational teaching style and memorable geology field courses remain forever in the minds of many geologists. In the field, he made very often a delicious goulash by the campfire and told fascinating stories of his travels and experiences.

Gaál was a GTK employee from 1983 to 1991. Europe's political turmoil at the beginning of the 1990s made him return to his native country to lead and to modernize the Hungarian Geological Research Institute.

Gaál returned to Finland in 1998. He served as a GTK research director until his retirement in 2003. However, he returned once again to GTK in 2009 as the scientific coordinator of the EU-funded ProMine project, which was of great success. In 2007, he received the Eskola medal of the Geological Society of Finland, which is the highest honour in the field of geology in Finland. In 2010, he was acknowledged with the third Fennoscandian Exploration and Mining Special Award for his outstanding lifetime contributions to Fennoscandian economic geology.

Gabor Gaál's studies fundamentally changed the perceptions of the Fennoscandian Shield and the importance of shield tectonics in ore formation.

Gabor was an unforgettable, heartfelt person. In international projects, his exceptional innovativeness, diverse geological skills and social intelligence came into their own. He made many friends easily right from the Brussels conference rooms to the African savannas. He was well-versed in four languages. He always found more opportunities than obstacles.

As a colleague and friend, he was supportive, always willing to help and to share his knowledge. In difficult situations at work or outside it, he gave full support to his friends unconditionally.

He was laid to rest on 11 July 2013, in Gaál's family grave at Farkasréti Cemetery near his home in Budapest. Farkasréti is the last resting place for many famous Hungarian artists and scientists. Sadly, another great scientist rests there now.

Juha Kaija

The author is Gabor Gaál's friend and co-worker

Acknowledgments

This book is the final output based on the efforts taken by many authors. Besides all the authors, a number of people have been involved, who deserve special acknowledgment. The ProMine project manager Juha Kaija, GTK, Finland, led the team with a never-failing patience and without him the project would not have won the prize for best FP7 project at the industrial technologies conference in 2014. The project officer Milan Grohol from the EU Commission deserves special thanks for stringent guidance and for pushing us forward. Also, the scientific advisor Paul Blewin deserves a thank you for playing devil's advocate to make us think out of the box.

The individual chapters have been reviewed by a number of people who also should be acknowledged. They are Gus Gun (BGS), Martiya Sadeghi (SGU), Sisi Zlatanova (TU Delft), Ernst Schetselaar (NRCan), Alireza Malehmir (Uppsala Uni.), Guillaume Caumon (Uni. Lorraine), Florian Wellman (CSIRO), Adam Piestrzynski (AGH Uni.), Vesa Nykänen (GTK), Laurent Ailleres (Monash Uni.), Cecilio Quesada (IGME, Spain), Tobias Bauer (Luleå Tech. Uni.) and Maria Economou-Eliopoulos (Uni. Athens).

Contents

1	Introduction	1
	Pär Weihed	
 Part I Principles of Database Structure, 3 Dimensional and 4 Dimensional Modelling		
2	ProMine Mineral Databases: New Tools to Assess Primary and Secondary Mineral Resources in Europe	9
	Daniel Cassard, Guillaume Bertrand, Mario Billa, Jean-Jacques Serrano, Bruno Tourlière, Jean-Michel Angel and Gabor Gaál	
3	GST: A Network Based Datastore for Geoscience Data and Geomodels and Its Implementation—ProMine’s Contribution Towards Interoperability	59
	Paul Gabriel, Jan Gietzel, Ha Hai Le and Helmut Schaeben	
4	3D and 4D Geomodelling Applied to Mineral Resources Exploration—An Introduction	73
	J.J. Royer, P. Mejia, G. Caumon and P. Collon	
 Part II The Fennoscandian Shield		
5	The Skellefte District	93
	Tobias E. Bauer, Pietari Skyttä, Tobias Hermansson, Mahdiah Dehghannejad and Saman Tavakoli	
6	The Vihanti-Pyhäsalmi Area	123
	Eevaliisa Laine, Jouni Luukas, Timo Mäki, Jukka Kousa, Aimo Ruotsalainen, Ilkka Suppala, Marcello Imaña, Suvi Heinonen and Tuulia Häkkinen	

Part III The Fore-Sudetic Basin

- 7 New Aspects of Copper Deposits at the Base of the Zechstein in Central Europe** 147
J. Hartsch
- 8 4D Geomodelling A Tool for Exploration—The Kupferschiefer in The Lubin Region, Poland** 163
P. Mejia, J.J. Royer, J.G. Fraboulet and A. Zielińska

Part IV The Iberian Pyrite Belt and Ossa Morena Zone

- 9 Introduction and Geological Setting of the Iberian Pyrite Belt** 191
C. Inverno, A. Díez-Montes, C. Rosa, J. García-Crespo, J. Matos, J.L. García-Lobón, J. Carvalho, F. Bellido, J.M. Castello-Branco, C. Ayala, M.J. Batista, F. Rubio, I. Granado, F. Tornos, J.T. Oliveira, C. Rey, Vítor Araújo, T. Sánchez-García, Z. Pereira, P. Represas, A.R. Solá and P. Sousa
- 10 Modelling of the *Río Tinto* Area** 209
Alejandro Díez-Montes, Jesús García-Crespo, Concepción Ayala, José Luis García-Lobón, Teresa Sánchez-García, Carmen Rey-Moral, Félix Bellido, Félix Rubio, J.F. Mediato and Fernando Tornos
- 11 Modelling of the Neves Corvo Area** 231
C. Inverno, C. Rosa, J. Matos, J. Carvalho, J.M. Castello-Branco, M.J. Batista, I. Granado, J.T. Oliveira, V. Araújo, Z. Pereira, P. Represas, A.R. Solá and P. Sousa
- 12 Modelling of the Cala area (Ossa-Morena Zone)** 263
Teresa Sánchez-García, Félix Bellido, José Mediato, Jose Luis García-Lobón, Jesús García-Crespo, Concepción Ayala, Carmen Rey-Moral, Félix Rubio, Alejandro Díez-Montes, Santiago Martín-Alfageme, Fernando Tornos and César Martínez

Part V The Hellenic Belt

- 13 3D- and 4D-Modelling of the Hellenic Belt, Greece.** 299
N. Arvanitidis, C. Michael, C. Christidis, G. Perantonis, V. Bakalis and D. Ballas

Pär Weihed

Abstract

This book is the result of 3- and 4-D modelling as part of the EU FP7 Promine project, which for the first time in Europe addressed the issue of pan-European 3- and 4 D geological models as a basis for mineral exploration and extraction under cover. The models that have been established cover four major mineral belts in Europe: Skellefte-Vihanti-Pyhäsalmi in Fennoscandia, Forsudetic monocline in Poland-Germany, the Iberian Pyrite Belt and the Ozaa Morena zone in Spain-Portugal and the Hellenic belt of northern Greece. The basic principle for the modelling is to combine geological information from the surface, drill cores/holes, underground exposures with geophysical data, both airborne, ground and drill hole measurements. In most cases all existing and acquired data were imported and visualized in the gOcad software package. For some belts also uncertainty models are presented. 4-Dmodelling added the time aspect to the 3-Dmodels and aimed at visualizing the geological evolution of the district. 3-D predictivity maps are also presented using some different principles for the predictive models. We show in this book that it is possible to build robust 3-D models of major mineral belts in Europe and by using different approaches it is also possible to carry out 4-D modelling to help exploration industry with better targeting. The 3-D predictive models for the mineral belts clearly show the potential of undiscovered resources in various parts of Europe. The results from the modelling in the Promine project is a proof of concept, and we hope that this book serves as an inspiration for future, more full scale, projects that could be developed to contribute to a sustainable supply of metals to the society.

This book is the result of the 3- and 4-dimensional modelling work package (WP2) of the Promine FP7 project that for the first time in Europe addressed the issue of pan-European three and four dimensional geological models as

P. Weihed (✉)
Luleå University of Technology, SE-971 87, Luleå,
Sweden
e-mail: par.weihed@ltu.se

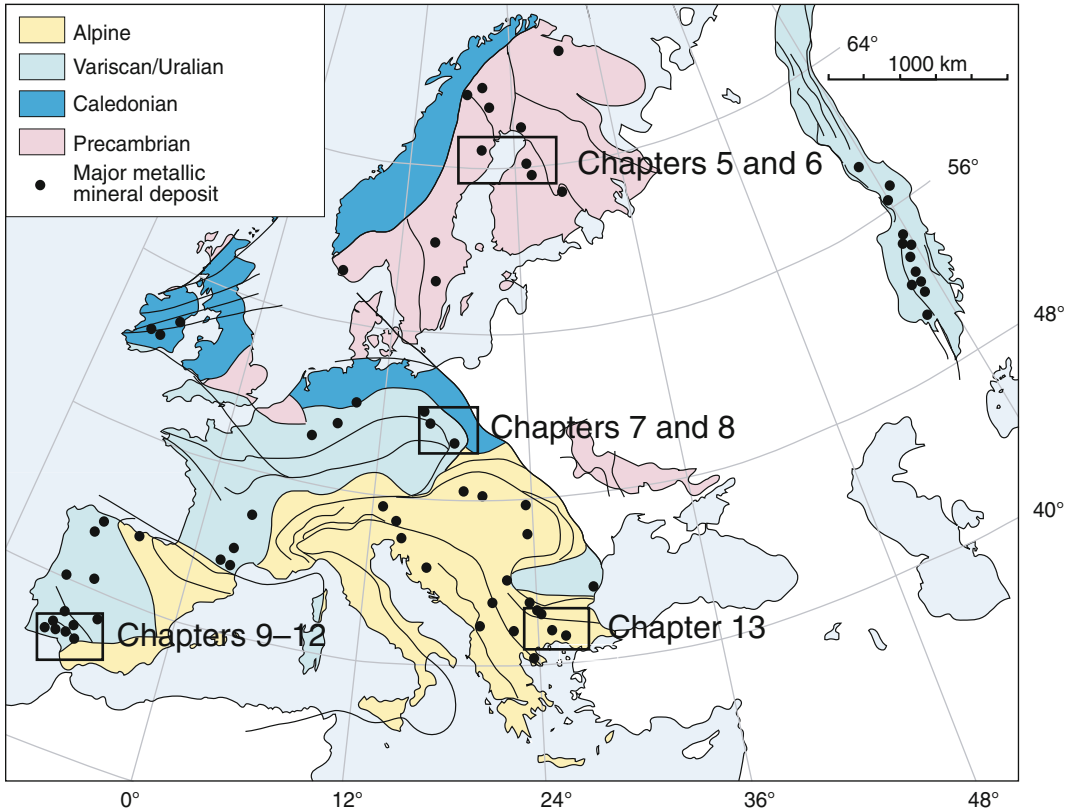


Fig. 1 Geographical location of the modelled mineral belts. Major deposits selection from the Promine database

a basis for mineral exploration and extraction under cover. The work package was developed to address the geological modelling, not only in deposit scale, but also in semi-regional (near mine) and regional (mineral belts) scales. The models that have been established covers four major mineral belts in Europe: Skellefte-Vihanti-Pyhäsalmi in Fennoscandia, Forsudetic monocline in Poland-Germany, the Iberian Pyrite Belt and the Ozza Morena zone in Spain-Portugal and the Hellenic belt of northern Greece (Fig. 1.1).

The work flow in the project was as follows:

1. Establish a common database structure for 3D geological data
2. Build 3D models based on the database structure
3. From the 3D models combined with the understanding of the geological evolution (time) develop 4D models for the different belts
4. Based on the 3- and 4-dimensional models derive predictive models in 3-4D for the mineral belts.

The database structure for the 3D data was developed by TU BAF. This also constituted the first deliverable of the work package and the concept also led to a spin off company now developed by former students from TU BAF. ProMine adopted the data model for a 3D Geoscience Information System GISTriX compiled previously by the Geoscience Mathematics and Informatics Group of TU BAF. GISTriX is a fully-fledged information management system for 3D geoscience data and geo-models with spatial and non-spatial query functionality necessary to analyze and interpret 3D data and models. It has a plug-in for the 3D modelling software “gOcad 2.0” which was the primary modelling software of ProMine, and is able to

combine logical operators with topological, geometrical and non-spatial queries. Its 3D GIS architecture combines a modelling system with 3D GIS functions, data management using XML database server and spatial query computation supported by an application server.

The three-dimensional modelling had the aim to build three-dimensional geological models of the crust down to mineable depth, typically upper 2000 m, in the involved mineral belts in Europa. The modelling was carried out primarily in the gOcad software. Modelling was also done in other software i.e. GEMCOM Surpac. The concept of compiling the 3D models were different in the different mineral belts mainly due to different geology, different availability of geophysical data, different spatial resolution of data and different access to data. The basic principle for the modelling was to combine geological information from the surface, drill cores/holes, underground exposures with geophysical data, both airborne, ground and drill hole measurements. By using this data in an integrated manner, surfaces (faults, geological boundaries, shear zones etc.) and volumes (rock units, alteration zones, mineralization etc.) could be constructed in three dimensions.

Normally all existing and acquired data were imported and visualized in the gOcad software package. To simplify modelling workflows the regional scale modelling volume was split up into several semi-regional scale sub-projects. For each sub-project available data was imported in form of maps and cross-sections into gOcad. In the models drill holes can be visualised as lines with attached lithological information. Structural measurements can be displayed with real 3D orientation. The regional models have been developed also by simplifying the geological parameters to enhance the “readability” of the models. For some belts we also developed uncertainty models. As an example for the final 3D-model of the Skellefte district uncertainty values from one to four for the relevant regions on the 3D-objects have been assigned and colour-coded. The assigned uncertainty values represent: (1) Observed in field, mine or drill-core; (2) Interpreted from geophysical data;

(3) Interpreted from structural data or extrapolated from geophysical data, and (4) Inferred/unknown.

Subsequent 4D-modelling added the time aspect to the 3D-models and aimed at visualizing the geological history in the district and as a support for ore targeting. Four-dimensional modelling was carried out utilizing the MOVE software package in the Skellefte district. The 4D-model shows schematically the formation of listric and related transfer faults, the formation of volcanic and sedimentary rocks and VMS deposits during crustal extension. Furthermore, the subsequent deformation of rocks and transposition of ore bodies and the effect of different block-rotations, subsequent erosion and deformation between the neighbouring fault-bound compartments and the tectonic transposition of the ore bodies were illustrated. A different approach, due to geological conditions, was used for the Forsudetic monocline. Here the 3D model was restored and decompacted using the surface Kine3d gOcad plug-in. Temperatures, pressures, hydro-fracturing probabilities, oil and gas maturation during the burying history had then been reconstructed using the PetroMode 1D software.

Three-dimensional predictivity maps were the final deliverable of the work package. We used some different principles for the predictive models. In the Skellefte district, in order to visualize the predictivity for VMS deposits, values from one to five were assigned on the relevant regions of the model, based on the correlation between distribution and shape of VMS deposits, and regional deformation patterns. Another interesting approach was used for the Kupferschiefer area and expansion to a pan-European potential map of reserves in copper and base metals associated to Kupferschiefer in Central Europe. This predictive model was built using geological, structural and geo-variable descriptive predictors. Several predictive methods were compared including the Support Vector Machine (SVM) and the Logistic Regression Method (LRM). The SVM gives the best results. It is a supervised learning algorithm developed in statistical learning theory for classification. It searches an optimal hyper-plane in the multivariable space for separating groups.

It comprises an initial phase on training dataset (here deposit from non-deposit classes), followed by a predictive phase. The free R package `e1071` was coupled to `gOcad` using a `gOcad` Python plug-in for this purpose.

The results from the three- and four-dimensional modelling in Promine are very promising. We have shown that it is possible to build robust three-dimensional models of major mineral belts and by using different approaches it is also possible to carry out four-dimensional modelling to help exploration industry with better targeting. The three-dimensional predictive models for the mineral belts clearly show the potential of undiscovered resources in the various parts of Europe. Thus, the Promine project, with respect to the aim of WP2 to improve the knowledge base and resource base for major as well as minor commodities, was fulfilled. The results from the modelling in the Promine project is a proof of concept, and serves as a baseline study for future, more full scale, pan-European projects that could be developed in the future.

In this book we present the results from the Promine project for the four mineral belts. In PART I “Principles of database structure, 3 dimensional and 4 dimensional modelling” we try to explain the rationale behind building a pan-European database on mineral deposits, how we worked with 3 dimensional and 4 dimensional modelling and also introduce the concepts and nomenclature so that the following chapters are more easy to follow.

Chapter 2 in PART I by Cassard et al. describes the ProMine mineral databases which provide a new tool to assess primary and secondary mineral resources in Europe. In this chapter a Pan-EU GIS data management and visualization system for natural and man-made mineral endowment is presented. The chapter further discusses the implementation of a Pan-EU predictive resource assessment, and thus provides a renewed picture of European mineral potential. A new method using metals associations describes by-product commodities in formerly known deposits.

In Chap. 3 of PART I we introduce a way to handle 3 dimensional data via a network-based

datastore. Gabriel et al. in this chapter describe how a web portal was developed in order to display and to deliver data through the internet. This portal is based on OGC principles related to open architecture and interoperability.

In Chap. 4 of PART I Royer et al. describe the general principles behind 3D and 4D geomodelling applied to mineral resources. The authors explain the state of the art concerning 3D geomodelling defined as a computer method for modelling and visualizing geological structures in three spatial dimensions. When adding time, 4D modelling allows reproducing the dynamic evolution of geological structures, and reconstructing the past deformation history of geological formations. They define this as a relatively new field in geoscience and a lot of development has occurred over the last 15 years as powerful computers have become available and affordable for a larger community of earth scientists.

In the following PARTS II–V we introduce case studies of modelling performed in major mineral belts across Europe. The PART II Chaps. 5–6 describes the modelling of the major minerals belts in the Precambrian geological units of the Fennoscandian Shield constituting a large part of the Nordic countries and NW Russia. The Fennoscandian Shield is currently the most active mining and exploration area in Europe and contains major iron, base and precious metal deposits. The Skellefte district and the Vihanti-Pyhäsalmi area are modelled in this book. PART III Chaps. 7–8 deals with modelling of the Forsudetic basin in Poland and eastern Germany. This basin contains some of the largest copper deposits in Europe and is a major global producer of silver. In PART IV Chaps. 9–12 are devoted to the Iberian Pyrite Belt in Spain and Portugal and the Ossa Morena Zone in Spain. The Iberian Pyrite Belt arguably contains the largest accumulations of massive sulphides on earth and is a major producer of base metals. Finally PART V Chap. 13, rich in illustrations, describes modelling of the Hellenic belt in northern Greece.

For the Fennoscandian Shield, Chap. 5 introduces the concept of 3 and 4 dimensional modelling of the Skellefte district (Bauer et al.), a Palaeoproterozoic VMS belt situated in northern

Sweden. This chapter describes modelling at different scales from deposit to regional scale and is based on a combination of geological and geophysical investigations. The chapter also explains the importance of uncertainty and prospectivity models as part of the modelling efforts. The 4D-modelling adds the time aspect to the 3D-models and helps gaining confidence about the 3D-models. In Chap. 6 Laine et al. model the Vihanti-Pyhäsalmi district located at the border zone between the Archaean craton in the northeast and the Palaeoproterozoic Svecofennian domain in central Finland. Also, this belt is dominated by VMS deposits. Here, in addition to the 3D modelling, structural geological inference was used to build 3D geological models visualizing the main deformational stages in the past. Geophysical 2D and 3D inversion were used to assist the 3D geological modelling. As a result new zones with exploration potential were identified.

In PART III the Forsudetic basin is investigated in two chapters. Chap. 7 (Hartsch) deals with new aspects of copper deposits of Kupferschiefer type in eastern Germany and Poland. Hartsch provides new aspects on the genetic development of the copper deposit at the base of the Zechstein Formation in the area. This information was then used for 3D and 4D modelling of the Forsudetic Copper Belt in Chap. 8 (Mejia et al.). These authors use the Lubin region (southwestern Poland) for modelling the geological formations in 3- and 4-dimensions in order to better understand the distribution of the Cu-Ag mineralization. The 4D restoring-decompacting modelling described in the chapter allowed the authors to reconstruct the burial, deformation and natural hydro-fracturing history of intra-basin sediment-hosted ore deposits.

The PART IV of this book deals with one of the major mineral belts, not only in Europe but globally, namely the Iberian Pyrite Belt (IPB) and one chapter also describes the Ossa Morena Zone, a mineral belt adjacent to the Iberian Pyrite Belt. In Chap. 9 the geology and tectonic evolution of the Iberian Pyrite Belt is explained by Inverno et al. Here, the authors conclude that the 250 × 20–70 km Iberian Pyrite Belt (IPB) hosts

the largest concentration of massive sulphide deposits worldwide. The Volcanic Sedimentary Complex (VSC), of late Famennian to mid-late Viséan age, is host to world class VMS deposits spatially associated to dacites and rhyolites, corresponding to effusive/explosive lava-cryptodome-pumice cone volcanoes. In Chap. 10 modelling of the largest VMS deposits in the world, Río Tinto, is described by Díez-Montes et al. The Río Tinto area is located in the South Portuguese Zone, in the eastern part of the Iberian Pyrite Belt. Here the volcanic sedimentary complex (VSC) is overthrust in the central part of the syncline forming the Rio Tinto anticline outcrop (an antiformal stack). To achieve a 3D model, compilation was done including new geological mapping and structural interpretations, petrological and petrophysical sampling, drill hole logging, and geophysical data interpretation. The obtained 3D model shows the relationships between several lithologies, tectonic surfaces and mineralization zones, and is an example of reconstruction of complex geological units. The subsequent Chap. 11 authored by Inverno et al. describes the 3D modelling of another of the major VMS deposits in the Iberian Pyrite Belt, the Neves Corvo deposit in SE Portugal. Here 3D, 4D and predictive geological modelling were applied to the 100 × 25 km large Neves Corvo area. Six NE-SW deep 2D reflection seismic profiles between the Neves Corvo mine and the Spanish border allowed to extend a 3D-model of the Neves Corvo main thrust throughout the eastern part of the area. The 4D model established a clear age sequence of mineralization types. The 3D predictive model, constructed for the Neves Corvo mine, delineates, not only the known Neves Corvo orebodies, but also other possible extensions. Chapter 12 of PART IV deals with a different geological unit, the Ossa Morena Zone (Sánchez-García et al.), and more closely the Cala area, a region 400 km² in size that comprises several mines and prospects hosted by Palaeozoic rocks. The Cala area is located in the southern segment of the Iberian Massif that forms the pre-Mesozoic basement in most of the Iberian Peninsula. This study is focused on Variscan plutons that were emplaced into Late Proterozoic

and Paleozoic sediments and associated iron oxide replacement and skarn in the Cala mine and the Ni-(Cu-PGE) deposit in the Aguablanca mafic to ultramafic intrusion. 3D regional and local geological models are presented. The 3D geological models give a new insight into the Cala and Aguablanca Variscan plutons concerning depth geometry, volume of mineralization and geological environment, not previously known. Finally a predictive model was constructed where it is concluded that further occurrences of magnetite deposits related to replacement or skarn formation and possible uranium enrichment would be expected in the area.

In the final PART V and Chap. 13 Arvanitidis et al. give a richly illustrated update on modelling

of the Hellenic belt in northern Greece. Here available geological, geophysical and geochemical data were used to construct 3- and 4-dimensional models of the most important deposits located in the Hellenic belt. The 3D and 4D geological models were produced for major epithermal gold deposits in the Rhodope zone (Perama and Aghios Demetrios) and the main sulphide mineral deposits (Olympias, Madem Lakkos/Mavres Petres and Skouries) in the Serbomacedonian zone, northern Greece. The 3D models were constructed in three different scales; deposit, semi-regional and regional. The 4D models demonstrate the main stages of the development of epithermal gold and polymetallic replacement deposits.

Part I

**Principles of Database Structure,
3 Dimensional and 4 Dimensional
Modelling**

ProMine Mineral Databases: New Tools to Assess Primary and Secondary Mineral Resources in Europe

Daniel Cassard, Guillaume Bertrand, Mario Billa,
Jean-Jacques Serrano, Bruno Tourlière,
Jean-Michel Angel and Gabor Gaál

Abstract

A major objective of the ProMine project was to develop a Pan-EU GIS data management and visualization system for natural and man-made mineral endowment and the implementation of a Pan-EU predictive resource assessment, and thus to provide a renewed picture of European metallogeny. To reach this objective, ProMine work package 1 produced pan-European databases of primary and secondary mineral resources, the ProMine Mineral Deposit (MD) and Anthropogenic Concentration (AC) databases. The present version of the MD database contains 12,979 records (mines, deposits, occurrences or showings) and covers 34 European countries. The total number of records of the AC database is 3408. As an exhaustive inventory of mineral wastes in Europe was far beyond the scope of the project, ProMine focused on major anthropogenic concentrations (i.e. mining and ore processing wastes) and on the most interesting in terms of volume/tonnage and content (e.g. possible presence of critical metals). After briefly presenting the databases—their structure, the way they were fed and their content—the present chapter focuses on how they can allow (i) geological approaches such as the spatial and temporal distributions of commodities and/or deposit types (and, in turn, the identification of metallogenic epochs), as well as (ii) statistics calculation on the main commodities and metallogenic types present in Europe and their contribution to the EU mineral budget. In addition, it is shown that the thorough and homogeneous data contained in the MD database also allows calculation of mineral potential and predictive maps

Gabor Gaál: Deceased.

D. Cassard (✉) · G. Bertrand · M. Billa ·
B. Tourlière · J.-M. Angel
GeoResources Division, BRGM, French Geological
Survey, 3 Avenue Claude Guillemin, BP 36009,
45060 Orléans Cedex 2, France
e-mail: d.cassard@brgm.fr

J.-J. Serrano
Information Systems Division, BRGM, French
Geological Survey, 3 Avenue Claude Guillemin, BP
36009, 45060 Orléans Cedex 2, France

G. Gaál
Southern Finland Office, GTK, Geological Survey of
Finland, Betonimiehenkuja 4, 02151 Espoo, Finland

at European scale. Given the limited number of parameters—present in a homogeneous way—which can be used when working at continental scale, different methods of calculation have been adapted: for the calculation of potential, kernel density and weighting have been used, and for predictivity mapping, besides the use of the well-known Weight-of-Evidence (based on lithostratigraphy) for main commodities present in an ore deposit, a new method using metals associations has been set up for by-product commodities in formerly known deposits. Working at European scale, one should however keep in mind that such studies cannot be used for targeting. The aim is more realistically to precise or to redefine ‘district’ contours and in the best case to enhance ‘some less obvious’ areas. In order to display and to deliver data through the Internet, a web portal was developed. The ProMine web portal architecture is based, especially for metadata and web services, on OGC [Open Geospatial Consortium (<http://www.opengeospatial.org/>)] principles related to open architecture and interoperability. A mapping between the data stored in the ProMine databases and standard data models like GeoSciML for geological information and EarthResourceML for mineral deposits, mines and mining wastes has been implemented to deliver the data according to these international standards.

2.1 Introduction

ProMine was a European Union (EU) co-funded project, of which the main objective was to stimulate the extractive industry to deliver new products to the manufacturing industry. The purpose of the geological parts of the project was to deliver interactive GIS tools and 3D and 4D models of deposits and mineralized belts. These would in turn contribute to define new reserves of minerals—with a special focus on strategic ones—in the European Union, so that the extractive industries can quantify and exploit in the future, and which could be the source of raw materials for the manufacturing industries. The main objectives of developing the GIS tool were: (i) to develop a geographic information system of primary and secondary mineral resources covering all European countries, (ii) to produce derived predictive resource assessments, and (iii) to deliver this data through an on-line data management and visualization system. The purpose of this was to provide a new picture of European metallogeny, replacing the most recent continental synthesis that was published by UNESCO (1984) over 20 years ago.

Three main targets were identified, implementing the latest developments in metallogeny and database management:

- Evaluation of EU mineral resources, including new strategic and ‘green’¹ (Hocquard and Deschamps 2008) commodities such as, for instance, Co, Ga, Ge, In, Nb, Ta, PGE and REE
- Evaluation of secondary (industrial) minerals and resources in combination with metalliferous ores
- Evaluation of potentially valuable mining and metallurgical residues

These data acquisition activities and their dedicated databases allowed a homogeneous multi-layer information system to be developed and delivered. This covered the whole European territory and included not only the mineral

¹High-tech metals are engaged in the major theme sets of “climatic change”, at the level of “renewable energies” and reducing emission of “greenhouse gases”. The CO₂ battle is involving a growing number of these “minor” (often by-products) metals which, in this case, can be qualified as ecological “green metals”.

deposit and mining wastes layers, but also geological, structural and geophysical layers. The work on developing the GIS tool benefited from work already undertaken by BRGM, like the ‘Geology’ layer at 1:1,500,000 scale and the ‘Mineral deposit’ database which served as a basis for the project, reusing parts of the database architecture, the hierarchical lexicons, and records already entered for different BRGM projects such as ‘GIS Central and South-eastern Europe’ (Cassard et al. 2004), ‘GIS Mines France’ (Cassard and Lambert 2007), ‘GIS Karelia’ (Tkachev et al. 2008) and various regional syntheses.

The completion of the inventory, i.e. entering all missing deposits in a consistent way, ensuring that the level of knowledge and of representation is similar throughout Europe, and that the mineral endowment of belts on which WP2 focused was particularly well described—was mainly undertaken by the national geological surveys involved in ProMine. The GIS so built provides a well-founded representation of EU’s mineral potential and allows the development of a predictive approach to EU’s mineral resources endowment. This was accomplished by combining the various thematic layers and by studying their spatial relationships using statistical and geostatistical methods under expert supervision.

However, working at a continental scale presents certain important constraints. The pan-EU 1:1,500,000 scale geological map used results from a process of generalization and homogenization applied to a set of digital country maps generally edited at a larger scale (1:500,000 to 1:1,000,000 scale). The accuracy of such a digital document (e.g. faults and geological formation boundaries representation and location) cannot be perfect and may cause substantial errors in derived maps of mineral potential. In the same way, due to the great number of mineral deposits taken into account, some descriptions are incomplete and some important parameters may be missing. Consequently the calculation of mineral potential derived from them and presented here should be considered as indicative.

The aim of this chapter is not to revisit European metallogeny in detail, instead our

intention is to show, through selected examples, that the pan-EU MD database when properly queried, can answer to several types of questions related to mineral resources, notably their quantity, their spatial and temporal distribution, and the location of new exploration targets (Cassard et al. 2012; Gaál et al. 2012, Arvanitidis et al. 2012).

2.2 The Mineral Deposit (MD) Database

2.2.1 Overview of the MD Database Structure

The MD database stores all the information related to mineral deposits in Europe. Each deposit is described in about 40 fields distributed in 8 folders (Table 2.1): (1) General information, including status, owner, location; (2) Deposit information, including deposit type and morphology; (3) Information on mineralization and host rocks, including age of mineralization and host rock, mineralogy of the ore, gangue and hydrothermal alteration, host rock formation name and lithology; (4) Economic information, including the exploitation type, and, per commodity, ore type, former production, reserves, and resources with associated grades; automatic calculation of the potential,² per commodity; (5) High-tech metals with, per commodity, the characterization of high-tech metals hosts (mineralogy, grade, abundance) and link with the Anthropogenic Concentration (AC) database; (6) Comments (free text); (7) Iconography, including photographs, sketch maps, cross-sections, etc. and (8) Bibliography, i.e. main geological and economic references related to the deposit.

Most fields that contain text values (i.e. non numerical) are lexicon guided, in order to improve the efficiency of future data processing. Lexicons are either simple (list of values), dynamic (list to which new values can be added) or hierarchical (tree-like list with father/son

²Tonnage of commodity (metric tons of metal) in the ore body, based on its grade and the tonnage of ore.

Table 2.1 Organization of the ProMine Mineral Deposit (MD) database (to be exploited by different data queries and extractions)

<p>1. General Information</p> <p>Lexicon guided fields</p> <ul style="list-style-type: none"> • Status: detailed information on mine, deposit, occurrence, showing • Country: link to list of countries <p>Free text fields</p> <ul style="list-style-type: none"> • Mining company (owner); Mining District • Longitude (xx.xxx° and xx°xx'xx"), Latitude (xx.xxx° and xx°xx'xx") (WGS 84) • Ore deposit name(s): multi-entry field to list all possible names of the same deposit • Free comment field • Author + date of entry, Controller + date of control • Links to other databases and numbering in these databases • URL + source of the mine site (if any)
<p>2. Deposit information</p> <p>Lexicon guided fields</p> <ul style="list-style-type: none"> • Deposit type(s): multi-entry field of deposit type hierarchical listing • Main morphology and Deposit morphologies: multi-entry field of deposit morphology hierarchical listing <p>Free text fields</p> <ul style="list-style-type: none"> • Azimuth, dip, length, width, down dip information associated with ore morphology
<p>3. Information on mineralization + host rocks</p> <p>Lexicon guided fields</p> <ul style="list-style-type: none"> • Mineralization stratigraphic age (upper and lower limit) • Ore mineralogy, Gangue mineralogy, Hydrothermal alteration: multi-entry fields • Host rock lithologies: multi-entry field and Host rock stratigraphic age (upper and lower limit) <p>Free text fields</p> <ul style="list-style-type: none"> • Mineralization absolute age, Host rock absolute age (with error + dating method from lexicon) • Host rock formation name
<p>4. Economic information</p> <p>Lexicon guided fields</p> <ul style="list-style-type: none"> • Exploitation type(s): multi-entry field • Main commodity • Multi-commodity window: per commodity: <ul style="list-style-type: none"> – ore type; production and grade units – former production, grade of former production, duration of former production – reserve, type of reserve (proven, probable, measured, ...), grade of reserve, year of estimate, classification code used – resource, type of resource (proven, probable, measured, ...), grade of resource, year of estimate, classification code used – automatic calculation of i) former production, ii) reserves, iii) resources and iv) deposit size class
<p>5. High-Tech Metals</p> <p>Lexicon guided fields</p> <p>Per commodity</p> <ul style="list-style-type: none"> • Characterization of high-tech metals hosts (mineralogy, grade, abundance) <p>Possibility to create a link with the Anthropogenic Concentration (AC) database</p>
<p>6. Comments</p> <ul style="list-style-type: none"> • General comments on geology, General comments on economy, Mine site infrastructure
<p>7. Iconography</p> <ul style="list-style-type: none"> • Illustrations (photographies, schemas, cross-sections, etc.) related to the deposit
<p>8. Bibliography</p> <ul style="list-style-type: none"> • Geological reference(s), Economic reference(s)

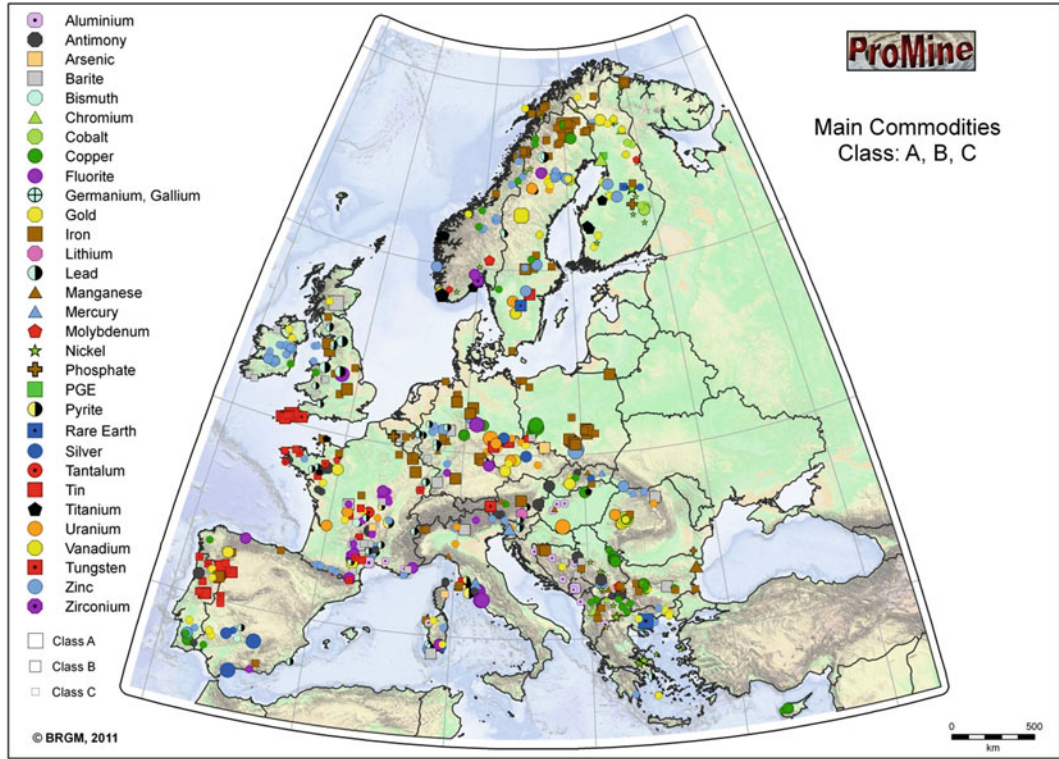


Fig. 2.1 Main deposits of the ProMine MD database, coded for their size (class A–C) and main contained commodity

relationships allowing storage of information according to its level of accuracy).

2.2.2 Overview of the MD Database Content

The total number of records in the MD database is 12,979. Records are either showings, occurrences or mineral and ore deposits. The geographic distribution of records is, to a certain degree, heterogeneous as it reflects the availability and quality of knowledge of primary resources within EU member states. Figure 2.1 shows the spatial distribution of deposits contained in the ProMine MD database, coded according to the main commodity they contain.

Table 2.2 presents elementary statistics on the MD database. Although the aim of the ProMine databases was to compile information as thoroughly as possible, some fields for some deposits have been left blank for several reasons

(e.g. no information available, highly doubtful information or classified information). As a consequence, the present study is not exhaustive and the numbers of cumulated tonnages (or ‘European endowment’) given in Table 2.2 should be considered as rough estimates rather than as precise values. As economic information is not always available, and assuming that all encoding errors that could generate overestimations have been properly eliminated, the calculated endowment figures provided should be regarded as lower end estimations. Nevertheless, aggregated tonnages for the EU are provided in Table 2.2 for 37 important commodities (lead and zinc were grouped and considered as a single commodity). These tonnages are compared to the estimated world mine production (IndexMundi³

³IndexMundi is a platform containing various data concerning selected attributes and characteristics of countries, including detailed statistics on commodities compiled from multiple sources (<http://www.indexmundi.com/en/commodities/minerals/>).

Table 2.2 Statistics on the main commodities in EU and their tonnage (endowment: resources + reserves + past production)

Type	Commodity	Criticality (EU list)	Class A		Class B		Class C		Class D		Σ Tonnage (classes A to D)	World mine production, in tons of commodity (2010, Index Mundi estimate)	Equivalent number of years of world production
			No. of deposits	Σ Tonnage	No. of deposits	Σ Tonnage	No. of deposits	Σ Tonnage	No. of deposits	Σ Tonnage			
Precious metals	Ag		5	185,444.4	17	72,933.7	44	42,102.5	94	21,581.1	322,061.7	23,100	13.9
	Au		1	700.2	17	2,826.2	86	2,563.7	164	628.8	6,718.9	2,560	2.6
	PGMs	yes			1	523.6			2	5.7	529.3	466	1.1
Base metals	Al				2	2.94E+08	13	5.45E+08	18	81,156,000	9.2E+08	41,200,000	22.3
	Cu		3	55,826,080	26	65,278,601	68	21,181,016	219	7,591,200	1.5E+08	16,000,000	9.4
	PbZn		3	51,290,000	63	120,717,118	297	64,552,035	425	12,979,515	249,538,668	16,140,000	15.5
	Sn		2	3,266,000	14	1,405,268	22	112,764	18	6,554.6	4,790,587	265,000	18.1
Iron and ferro-alloy metals	Cu	yes			3	504.4	34	342,744.4	52	35,811.2	882,955.6	89,500	9.9
	Cr		1	39,500,000	5	46,530,000	4	11,051,694	7	3,233,300	1,00E+08	23,700,000	4.2
	Fe		2	2.42E+09	28	7.96E+09	101	3.1E+09	198	6.76E+08	1.42E+10	1,280,000,000	11.1
	Mn		1	1.16E+08	1	10,750,000	14	53,206,990	31	8,391,079	1.89E+08	14,200,000	13.3
	Mo				5	843,148.6	11	223,339	9	23,117	1,089,605	242,000	4.5
	Nb				1	750	1	25.2	1	3,496	778,696	62,900	12.4
	Ni	yes	3	9,115,000	4	2,823,900	36	3,699,562	61	489,138.5	16,127,601	1,620,000	10.0
	V		1	2,005,733	3	984,252.8	16	767,224.8	19	182,321.5	3,939,532	61,200	64.4
	W	yes			4	374,438.4	21	260,367	21	38,315.2	673,120.6	68,800	9.8
	Be	yes			1	6,664	2	2,257	2	158.5	9,079.5	5,080	1.8
Speciality and rare metals	Bi				2	6,115	2	900			7,015	16,000	0.4
	Cd		1	13.6	2	5.22	6	7,938	5	1,534	28,292	22,800	1.2
	Ga	yes			1	90	1	30	1	3	123	260	0.5
	Ge	yes	1	800	1	174	2	58	3	39	1,071	N/A	N/A
	Hf		1	28,628.9							28,628.9	N/A	N/A
	Hg		2	216			7	15,061	3	551.5	231,612.5	2,250	102.9
	In	yes	2	5,387			1	50	2	15.5	5,452.5	659	8.3
	Li		1	1,280,000	1	215	2	116	4	67,012.8	1,678,013	23,500	71.4
	Rb		1	19.5					1	1.8	19,501.8	N/A	N/A
	Re						1	60	1	43	103	47.2	2.2
	REE	yes	1	5,675,013	1	446,85	2	110,426	1	8,447	6,240,736	123,000	50.7
	Sh	yes			8	366,341	36	271,177.4	11	13,163	650,681.4	167,000	3.9
	Se						1	433.4	1	52.5	485.9	1,980	0.2
Ta	yes			2	39.25	1	1,95	3	790.3	41,990.3	682	61.6	
Ti		1	73,440,000	18	1.27E+08	15	11,116,382	9	743,855	2.12E+08	2,210,000	95.9	
Zr		1	1,588,800	5	1,503,200			2	11,381	3,103,381	1,250,000	2.5	
Minerals for chemical use	Brt		4	49,362,400	17	37,159,000	32	14,652,350	20	1,971,813	1.03E+08	7,850,000	13.1
	Fl	yes	6	52,621,000	10	20,061,620	21	9,722,000	29	3,330,705	85,735,325	7,180,000	11.9
	Mg	yes	1	2.1E+08	2	39,215,439	10	29,072,080	10	3,593,800	2.82E+08	755,000	373.5
Speciality and other industrial rocks and	Graphite	yes	1	12,300,000	2	2,677,500	6	1,493,200	5	181,88	16,652,580	925,000	18.0

Classes A, B, C and D refer to the ProMine MD database 'REFERENCE_SUBSTANCE' lexicon (see Appendix 1)

estimates for year 2010) and converted to the equivalent number of years of world production. These estimates of total available tonnages clearly identify important endowments for some commodities within the EU. For example, the endowments of vanadium, mercury, lithium, rare earth elements, tantalum, titanium and magnesium are equivalent to 64.4, 102.9, 71.4, 50.7, 61.6, 95.9 and 373.5 years of world mine production at current levels, respectively. Among these commodities, several (rare earth elements, tantalum and magnesium) belong to the list of 14 critical mineral raw materials for EU published by the European Commission (2010, 2011) following the Raw Material Initiative (European Parliament 2008). Other commodities which are also economically important for the European Union have significant endowments that amount to a decade or more of the world mine production (e.g. cobalt, nickel, tungsten, indium, fluorite and graphite). In addition to these estimates, the ProMine project published a preliminary map of the distribution of the 14 critical raw materials, as

defined by the European Commission 2010. This was updated after completion of the project (Fig. 2.2). This map represents a significant advance in improving our knowledge of the mineral resources in the European Union.

2.2.3 Stratigraphic Distribution of Mineral Occurrences

The MD database stores information on the ages—both stratigraphic and radiometric—of ores and their host rocks. 3750 records contain information on the age of mineralization. To study the temporal distribution of deposits, records have been sorted into 16 stratigraphic divisions (periods for Phanerozoic and eras for Precambrian). 2445 deposits were unambiguously assigned to a unique selected stratigraphic division, with the remainder being too poorly documented to be accurately categorised. For example, records were not used where the mineralization age was given as Cenozoic,

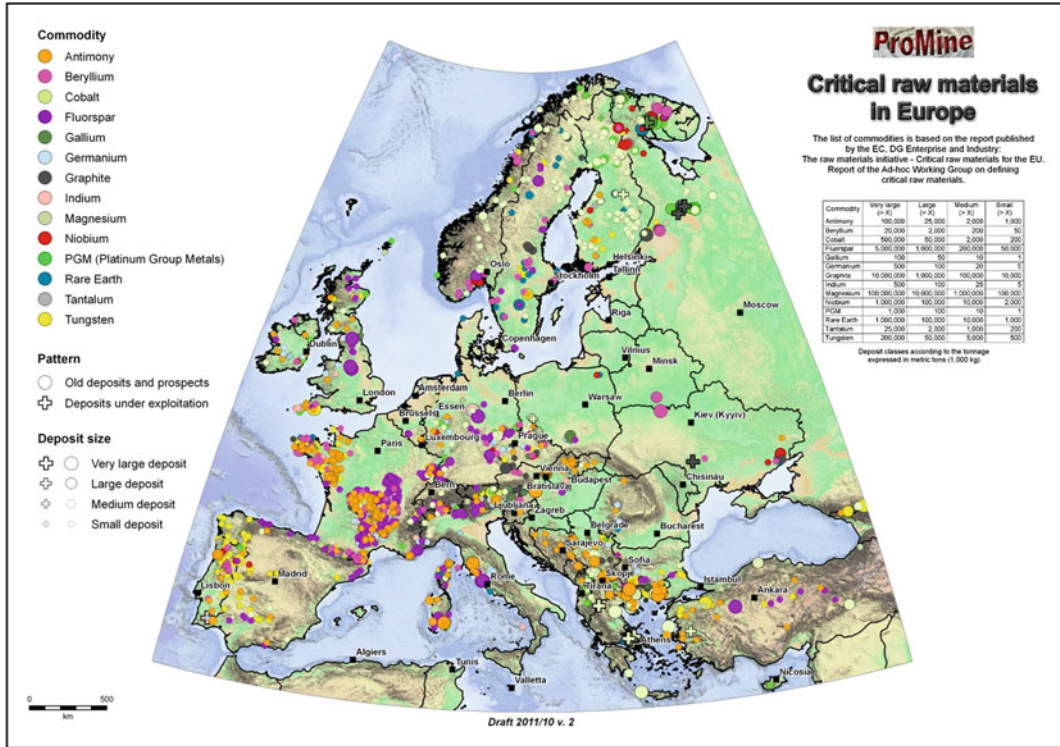


Fig. 2.2 Map of critical raw materials in Europe based on the ProMine MD database and the list of 14 critical commodities identified by the European Commission

Mesozoic, Palaeozoic or Precambrian. This dataset was then sorted by commodity or deposit type to assess the various mineralizing periods that occurred in Europe. As an example, Fig. 2.3 shows the temporal distribution (age of mineralization) of the deposits containing a selection of 6 commodities (aluminum, gold, copper, fluorite, nickel and zinc).

Aluminum is exclusively related to Mesozoic and Cenozoic bauxite mineralizing processes, and particularly to Cretaceous bauxites in southern Europe (Petrascheck 1989) such as the Durancian isthmus in southern France. Mineralizing processes of similar age are also found in lateritic nickel deposits related to the alteration of nickel-bearing silicates in ultramafic ophiolitic formations.

Gold mineralization occurred during several periods of the geological history of Europe. The Neoproterozoic is marked by orogenic-type gold-bearing mineralization related to

greenstone belts of the Ilomantsi region in eastern Finland (Vaasjoki et al. 1993). They are however of limited importance (Eilu et al. 2012) compared to major gold districts in Australia or Canada (Goldfarb et al. 2001).

The main frequency peak is related to the Palaeoproterozoic of the Fennoscandian Shield, and more precisely to the upper part of Palaeoproterozoic, from 1.9 to 1.8 Ga (Svecokarelian orogeny). This period is marked by polyphase convergence including subduction, island arc magmatism, oblique subduction, basin closure, arc and micro-continent collision and accretion of different terranes. Gold mineralization can be associated with early systems mostly of VMS, porphyry and epithermal types, or with the younger orogenic type (Weiheid et al. 2008; Eilu and Weiheid 2005).

The Lower Palaeozoic is marked by a peak centred on the Ordovician, which essentially corresponds to gold-bearing VMS in the

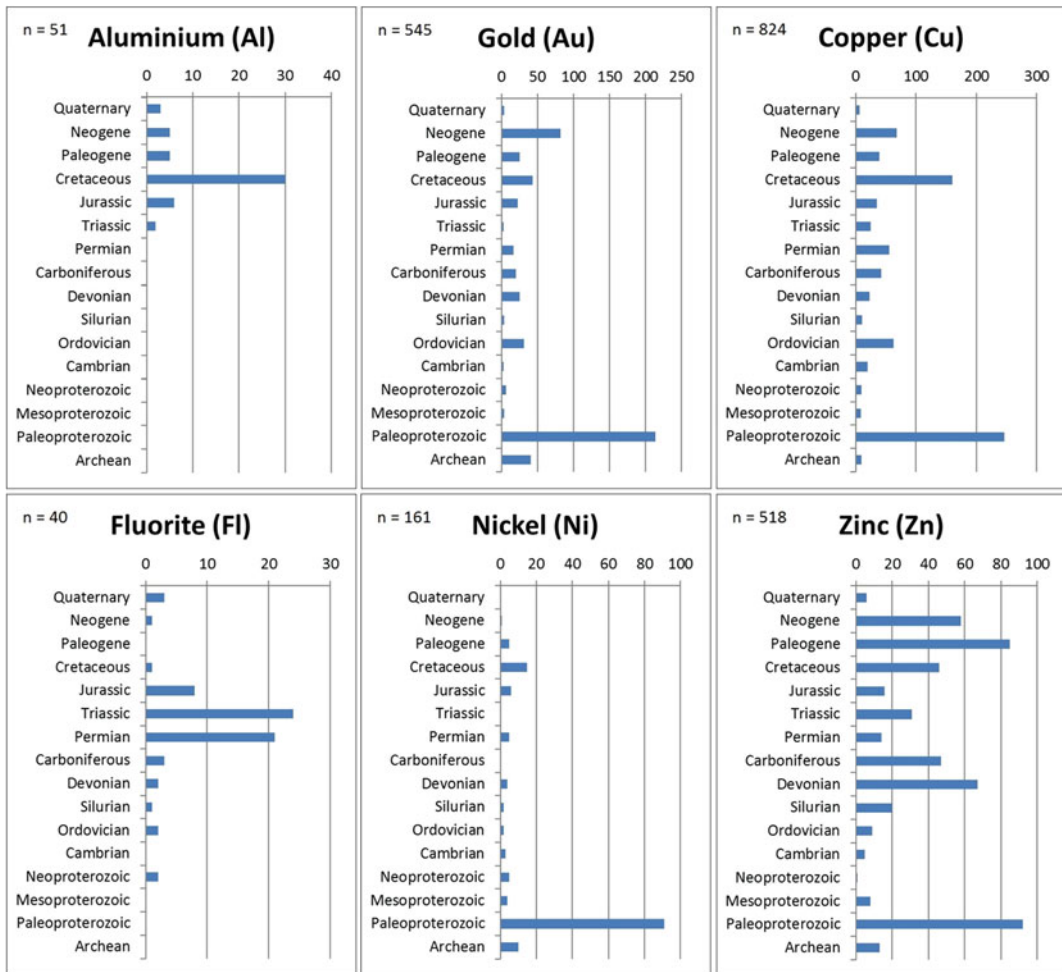


Fig. 2.3 Temporal distribution of selected commodities (n is the number of deposits containing the commodity), per stratigraphic period/era

Caledonian domain of Scandinavia. They are also associated with a more widespread mineralization event in Great Britain and Portugal.

The Upper Palaeozoic is the main gold mineralizing period in the Hercynian. A first episode (Upper Devonian and early Lower Carboniferous) is related to massive sulphides of, for instance, the southern Iberian province (Spain and Portugal) or the Châteaulin basin (France). The second episode is of orogenic type (Bouchot et al. 2005), in relation to the late evolution of the Hercynian orogen (Late Carboniferous and Early Permian).

Younger gold peaks are related to the evolution of Southern Europe along the Tethyan margin in the Balkan-Carpathian domain. Two

main periods can be identified: the first one, of Upper Cretaceous age, corresponds to porphyry-type mineralization (Cu and Au), and the second one, of Cenozoic age with a Miocene maximum, is essentially related to epithermal type mineralization.

The temporal distribution of Copper mineralization shows some similarities with that of gold. Three major periods can be identified, with different types of deposits and geodynamic context.

The Fennoscandian domain is characterized by both mineralization related to mafic or ultramafic complexes (Cu, Ni, PGEs), formed mainly during the Lower Palaeoproterozoic (Weihed et al. 2005), and later mineralization related

to the Svecokarelian orogeny (Upper Palaeoproterozoic), with mostly volcanogenic massive sulphides (e.g. Outokumpu, Skellefte district; Weihed and Eilu 2005), porphyry and/or IOCG type deposits (e.g. Aitik). The Ordovician of the Caledonian domain in Scandinavia is marked by copper mineralization that formed early with respect to the collision period (Grenne et al. 1999).

The Upper Palaeozoic is an important period for copper mineralization with several episodes associated with various types of deposits. In the Devonian and lowermost Carboniferous, large massive sulphide bodies are emplaced in the southern Iberian province (Leistel et al. 1998). Some of these are very rich in copper, such as Neves Corvo in Portugal. The Carboniferous is associated with numerous copper-bearing polymetallic veins but their economic potential is limited. On the other hand, the Permian hosts the world class Kupferschiefer mineralization in southern Poland and Germany (Hitzman et al. 2010).

The Cretaceous peak is related to both the copper-bearing massive sulphides in Cyprus, and the Cu- and Au-bearing porphyry-type mineralization of the Balkan-Carpathian domain (Jankovic 1997; Lips et al. 2004). In the Tertiary, especially in the Miocene, important Au- and Cu-bearing epithermal mineralization is developed in the Balkan-Carpathian region (Heinrich and Neubauer 2002).

Fluorine mineralisation is commonly associated with barite. It is associated with a main episode related to the evolution of post-Hercynian basin domains in the Triassic (and Permo-Triassic) periods, and the evolution of the European southern margin in the Jurassic (e.g. Lias of the Cevennes border in France). An additional recent episode is related to the Plio-Quaternary volcanism in Latium (Rome region in Italy).

Less important fluorine stratabound mineralization also exists in the Neoproterozoic of Scandinavia and the Cambro-Ordovician of the Pyrenees (France). Numerous Late Hercynian veins (Upper Carboniferous and Permian) also host fluorine.

Nickel mineralisation in Europe occurred during two main periods: (i) the Palaeoproterozoic with nickel sulphide mineralization associated with copper, cobalt and occasionally platinum-group elements, and (ii) the uppermost Mesozoic (Upper Cretaceous and beginning of Tertiary) with nickel-bearing laterite mineralization resulting from the alteration of olivine in ophiolites during intense tropical weathering processes.

Economic nickel sulphide mineralisation (with subordinate Cu and PGEs) is almost exclusively located in the Fennoscandian Shield that is a province of major importance for this type of mineralization. The Neoproterozoic komatiites in greenstones belts host some Ni-Cu sulphides deposits of minor importance (e.g. Vaara, Finland).

After the Archaean magmatic and tectono-metamorphic evolution, Fennoscandia underwent a long period of rifting (Weihed et al. 2005). During the Early Palaeoproterozoic (Siderian and Rhyacian) several phases of rifting occurred, probably related to magmatic plume activity, with which several deposits are associated. These include: (i) the Kemi mafic-ultramafic layered complex (Finland) formed during the Siderian, (ii) the Kevitsa deposit (Finland) formed during the Rhyacian, and (iii) the Vammala deposit formed during the Orosirian Svecofennian orogeny. At the beginning of the Palaeozoic, rifting of the Norwegian Caledonian domain was accompanied by the emplacement of mafic-ultramafic complexes associated with Cu-Ni mineralization of minor importance.

The Agua Blanca deposit in Spain formed during the Lower Carboniferous (~340 Ma; Romeo et al. 2006), at an early stage of Hercynian orogeny. It is one of the few Ni-Cu sulphide deposits related to mafic-ultramafic formations outside the Fennoscandian domain (Martínez et al. 2005).

Zinc mineralization also shows a complex temporal distribution with, essentially, (i) massive sulphides and SEDEX (Sedimentary Exhalative) in the Palaeoproterozoic, (ii) MVT along the margins of southern European basins in the Palaeoproterozoic, and (iii) replacement deposits

along the border of porphyry and epithermal deposits of the Balkan-Carpathian domain in Tertiary formations.

The Palaeoproterozoic of Fennoscandia hosts VMS deposits of Rhyacian to Orosirian age (Weiheid and Eilu 2005), such as those in the districts of Skellefte (Sweden), Vihanti-Pyhäsalmi (Finland) and Bergslagen (Sweden). The transition between the Upper Devonian and the Lower Carboniferous is a major period for the formation of zinc deposits, essentially the VMS deposits of the Southern Iberian Province (and to a lesser degree in the Châteaulin basin and Brévenne series in France), the SEDEX of the Pyrenees and the SEDEX deposits and carbonate-hosted deposits of Ireland. Late Hercynian veins are marked by the frequent occurrence of zinc, but are of limited importance. Triassic and Jurassic formations hold Mississippi Valley type “carbonate-hosted” deposits emplaced along the margin of Mesozoic basins and forming sub-continuous alignments from north-western Spain through the Cévénole border (France) and the Alpine margin to the Balkan. In the Balkan-Carpathian domain Upper Cretaceous to the Neogene recurrent zinc mineralisation appears as a secondary commodity in porphyry and epithermal deposits. Zinc is dominant in the skarn-type deposits at the boundary between carbonate and high temperature magmatic and hydrothermal intrusions (e.g. Trepča, Miocene age).

2.3 The Anthropogenic Concentration (AC) Database

2.3.1 Overview of the AC Database Structure

The ProMine AC database stores all the information on anthropogenic concentrations related to the mining and metallurgical industries such as mine wastes and unprocessed products (e.g. run-of-mine ore, unprocessed ore stockpiles, mine waste dumps, barren overburden), ore processing wastes (e.g. cobbing wastes, wash

tailings, flotation tailings, leach residues, magnetic-separation tailings) and treatment wastes (e.g. smelter wastes, flue dusts, roasting residues, chemical treatment wastes, leach tailings, ashes, cocking plant residues, etc.) Each site is described in about 35 fields distributed in 6 folders (Table 2.3): (1) General information, including status, owner, location and the list of processes that have been implemented on the site; from this folder a link with the MD database can be created, allowing identification of the deposit (s) that fed the site; (2) Information on wastes and products including the type of storage, the type of waste, the mineralogy, estimation of volume/tonnage, the type of commodity available and the grade, with automatic calculation of the potential⁴ per commodity, at site scale and the type of environmental impact; (3) The environmental aspects, with per environmental impact, the type of environmental pathways and receptors, the type of water treatment and the description of the type of restoration used. The other three folders—Comments, Iconography and Bibliography—are identical to those of the MD database.

2.3.2 Overview of the AC Database Content

The total number of records of the AC database is 3408. Their spatial distribution and content of critical commodities, according to the list of 14 critical raw material established by the European Commission (2010), is presented in Fig. 2.4. There is a significant variability in the number of records from different countries in the AC database. Some countries like Spain, and to a lesser extent France, are over-represented. This is probably due to the fact that these two countries have already (at least partly) synthesized information related to their wastes for national programmes or completed international projects (e.g. the 5th EU-FP project DECHMINUE—Thomassin et al. 2001).

⁴Tonnage of commodity (metric tons of metal) in the anthropogenic concentration, based on its grade and the tonnage of waste.

Table 2.3 Organization of the ProMine Anthropogenic Concentration (AC) database (to be exploited by different data queries and extractions)

<p>1. General Information</p> <p>Lexicon guided fields</p> <ul style="list-style-type: none"> • Status: information on mining site or plant (mill, smelter, active, inactive, ...) • Country: link to list of countries • Implemented processing(s): information on ore processing <p>Free text fields</p> <ul style="list-style-type: none"> • Owner(s) • District/province • Longitude (xx.xxx° and xx°xx'xx"), Latitude (xx.xxx° and xx°xx'xx") (WGS 84) • Mining site /plant name(s): multi-entry field to list all possible names of the same mining site /plant • Author + date of entry, Controller + date of control • URL + source of the mine site /plant (if any) • Links to other databases and numbering in these databases <p>Possibility to create a link with the MD database: 'Comes from' deposit(s): Name(s) of deposit(s) related to ore processed. Note that the site record has to be created first, and then entered in the Mineral Deposit (MD) database</p>
<p>2. Wastes and products</p> <p>Lexicon guided fields</p> <ul style="list-style-type: none"> • Multi-storage/waste window: per type of storage and type of waste: <ul style="list-style-type: none"> – Waste or product storage: type of storage used for wastes or products – Type of waste or product: description of wastes and products; hierarchical listing Mineralogy: waste or product mineralogy Class: category class information on waste or product Commodity(ies): type of commodity(ies) available in wastes or products <ul style="list-style-type: none"> • Unit: unit of commodity grade • Manual calculation of estimated resource per commodity Impacts: type of environmental impacts with area affected by pollution and volume of water affected (linked to)
<p>3. Environmental aspects</p> <p>Free text fields</p> <ul style="list-style-type: none"> • Surface area (m²), volume (m³), and tonnage (t) of a type of waste or product • Density retained for calculation • Grades (min, max, average), date, accuracy of estimation (%) • Area affected by pollution (km²) • Volume of water affected (m³) • Comments on impacts (free text) • Automatic calculation of potential resource, per commodity, at the site scale (synthesis)
<p>3. Environmental aspects (new window with impact recapitulation—linked under 2. Waste and products/Impacts)</p> <p>Lexicon guided fields</p> <ul style="list-style-type: none"> • Per environmental impact: <ul style="list-style-type: none"> – Pathways: type of environmental pathways – Receptors: type of environmental receptors – Water treatment: management and treatment processes and structures of water – Restoration: description of restoration used
<p>4. Comments</p> <ul style="list-style-type: none"> • General comments on environmental issues, plant infrastructure (free text)
<p>5. Iconography</p> <ul style="list-style-type: none"> • Illustrations (photographies, schemas, maps, etc.) related to the site
<p>6. Bibliography</p> <ul style="list-style-type: none"> • Reference(s)

Similarly, the completeness of the data is highly variable between countries. This can be accounted for by a lack of information, restricted access to

information and by the availability of information dealing only with specific aspects. Examination of the content of the AC database indicates that the

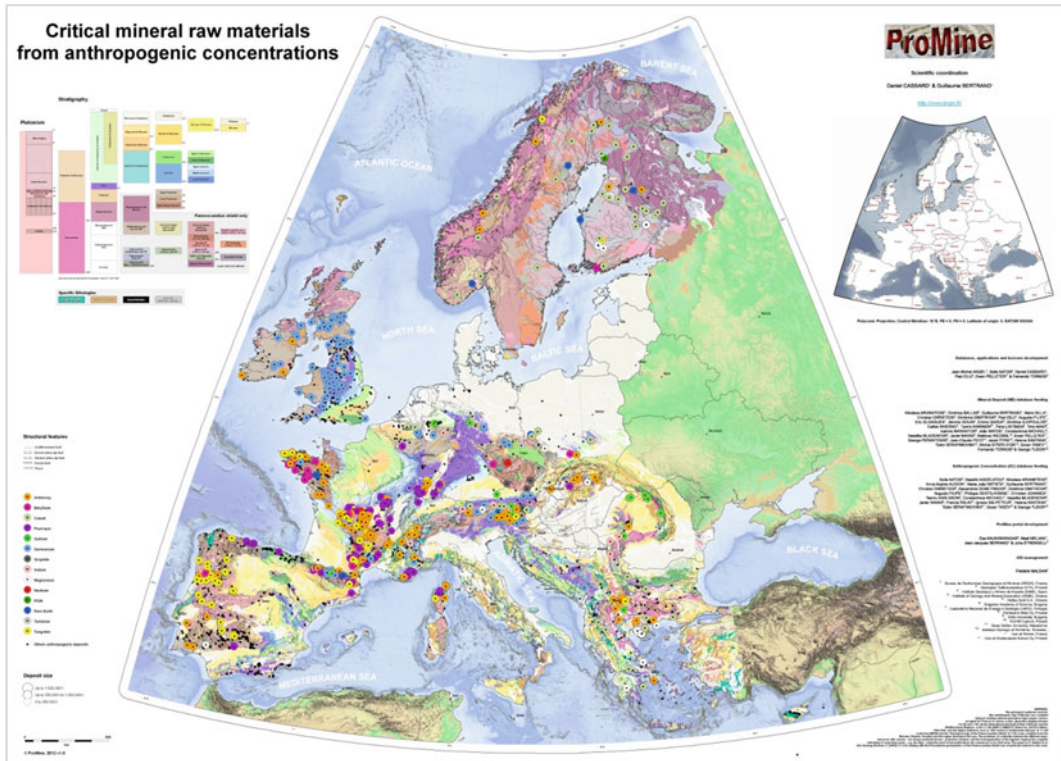


Fig. 2.4 ProMine AC database: spatial distribution of anthropogenic sites with a special attention to sites containing critical mineral raw materials

assessment of anthropogenic concentrations is not a simple task. Nevertheless, compared to the results of previous projects (e.g. DECHMINUE), ProMine has made a significant advance in terms of the number and quality of the records compiled, and has laid the foundation of an infrastructure which is INSPIRE compliant (cf. Sect. 2.6 “Data dissemination and web portal”) and which can be used in future projects related to mining wastes.

The ProMine project focused on the largest anthropogenic concentrations and on those of greatest interest in terms of volume/tonnage and content (i.e. possible presence of critical commodities). The aim was to have an inventory, as complete as possible, of concentrations which could be processed for the recovery of strategic/high-tech/critical commodities, and to avoid overlap between the ProMine project and the work done by the member states under the

Mining Wastes Directive. The ProMine approach targeted those sites with the greatest potential for the recovery of strategic commodities, with particular emphasis on establishing links with the primary concentration(s). It was beyond the scope of ProMine to compile a comprehensive inventory of wastes throughout Europe. Such a very detailed and systematic inventory was done by Member States in the frame of the Mining Wastes Directives (notably, the directives 2006/12/EC and 2008/98/EC, European Parliament 2006, 2008). This inventory, though, was more focused on environmental impact than on the characterization of secondary resources and, as such, does not overlap with the work done in ProMine.

The definition of the size of wastes (surface occupied, volume or tonnage) and the grade of the contained commodities was a common problem. In many cases, it was impossible to fill

Table 2.4 Statistics on critical mineral raw materials from anthropogenic concentrations

Commodity	Total no. of sites	Number of sites with calculated potential	Σ potential (t)
Be	36	9	41
Co	131	62	39.656
Ga	59	28	8.82
Ge	157	18	408
In	36	7	4.273
Mg	42	27	17,147,091
Nb	18	8	379
Pt	5	1	0.6
REE	13	5	13.755
Sb	198	37	78.299
W	124	23	15.137

these fields in the AC database because of the lack of data. As a result the information collected in the ProMine AC database is essentially qualitative, rather than quantitative, and does not permit the calculation of aggregated resource potential or its spatial distribution. On the other hand, the inventory compiled for the Mining Wastes directive brought useful data on volume and tonnage of wastes in European countries. Although the schedules of the MWD activities and of ProMine did not allow complete integration of the available data, an important future development would be to merge the information from both sources in order to improve the overall quality of the data on secondary resources in Europe.

Despite the data shortcomings, the aggregated potential from a limited number of sites for critical commodities has been calculated and is presented in Table 2.4. It is important to stress that these values are indicative and provide minimum estimates of the potential tonnages available in selected European wastes. It should be noted that these estimates are much lower than those calculated as potentially available from

primary resources derived from the MD database (Table 2.2).

2.4 Mineral Potential Mapping

The goal of this section is to identify areas of high mineral resource potential, solely based on the distribution and size of known mineralization, and using spatial extension of ‘carrier’ (and thus favourable) lithologies. In the present work, potential is understood as being the endowment, i.e. the sum of cumulated past production, reserves and resources.

2.4.1 Methodology

Potential maps presented here show the spatial density of known deposits, sorted by metallogenetic families and weighted on their size. 16 deposit ‘families’ or groups were identified by the ProMine consortium and extracted from the MD database (Table 2.5). From each of these

Table 2.5 Statistics on the main metallogenic types found in EU and their tonnage (endowment) for their three main commodities (by order of decreasing frequency within the deposit type)

Metallogenic type Type number	Metallogenic type Name	Number of deposits	Ratio of commodities with documented potential (%)	Commodity 1		Commodity 2		Commodity 3	
				Name	Total tonnage	Name	Total tonnage	Name	Total tonnage
1	Alkaline and peralkaline intrusions	30	34.1	U	95,892	REE	718,948	Nb	778,963
2	Epithermal	512	27.9	Au	2051	Ag	19,199	Pb	2,694,389
3	Igneous felsic	890	17.8	U	113,888	Sn	1,284,825	W	300,861
4	Igneous intermediate	131	35.6	Cu	41,168,901	Au	1939	Ag	18,406
5	Igneous replacement	390	42.6	Zn	14,384,048	Pb	21,141,522	Fe	244,433,280
6	IOCG	67	78.4	Fe	2,538,790,905	Cu	567,297	Mn	1,107,910
7	Mafic intrusion	45	72.0	Ti	171,207,562	V	373,052	Fe	325,582,230
8	Mafic or UltraMafic	641	47.5	Cu	2,625,595	Ni	2,682,432	Co	124,389
9	Orogenic gold	514	20.8	Au	1309	Cu	399,129	Ag	6,892
10	Pegmatites	349	7.3	Li	307,713	Feld	4,266,023	Be	680
11	Carbonate-hosted	641	19.6	Zn	34,832,297	Pb	9,404,228	Fe	427,871,659
12	Sandstone- and shale-hosted	322	31.3	U	438,927	Cu	92,663,587	Pb	2,119,515
13	Sedimentary deposits	630	35.9	Fe	8,501,259,818	Mn	14,752,044	Ni	3,531,669
14	VMS	820	54.6	Cu	27,240,890	Zn	79,963,991	Ag	59,925
15	Residual deposits	588	24.3	Al	933,038,160	Fe	239,478,322	Ni	6,227,977
16	Base metals veins	1947	21.7	Pb	17,859,114	Fl	36,033,304	Br	31,647,820

Tonnage (endowment) is expressed in metric tons. Total number of deposits: 8994, representing 69.3 % of the database (12,979 deposits). Other deposits are either of undefined metallogenic type (insufficient information for establishing the type), or belong to the 'Rocks and Industrial Minerals' group, or to the 'Energy Commodities' (e.g. coal, oil and gas. ...) group or to minor types

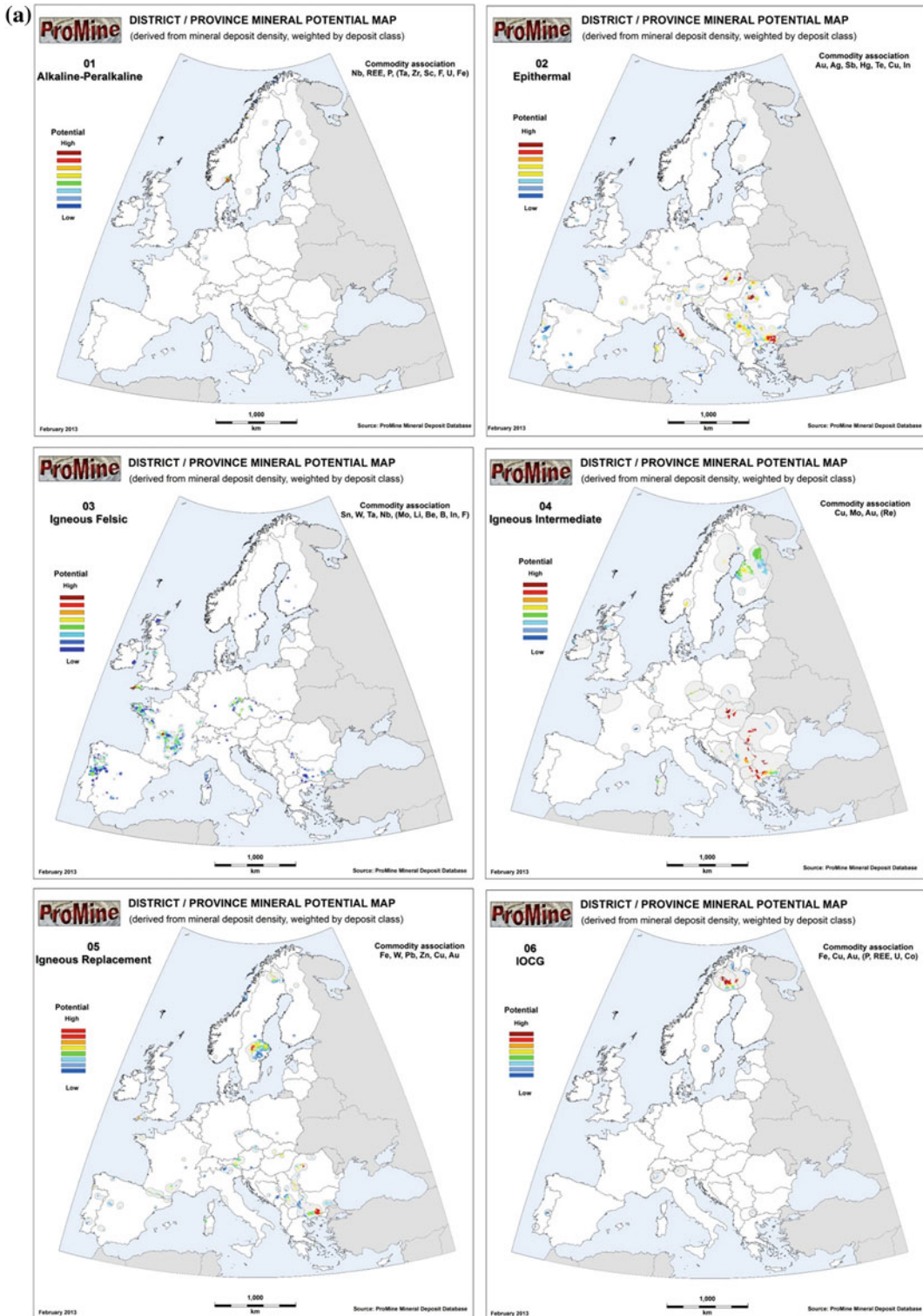


Fig. 2.5 a Map of mineral potential for commodity associations 1–6. b Map of mineral potential for commodity associations 7–12. c Map of mineral potential for commodity associations 13–16

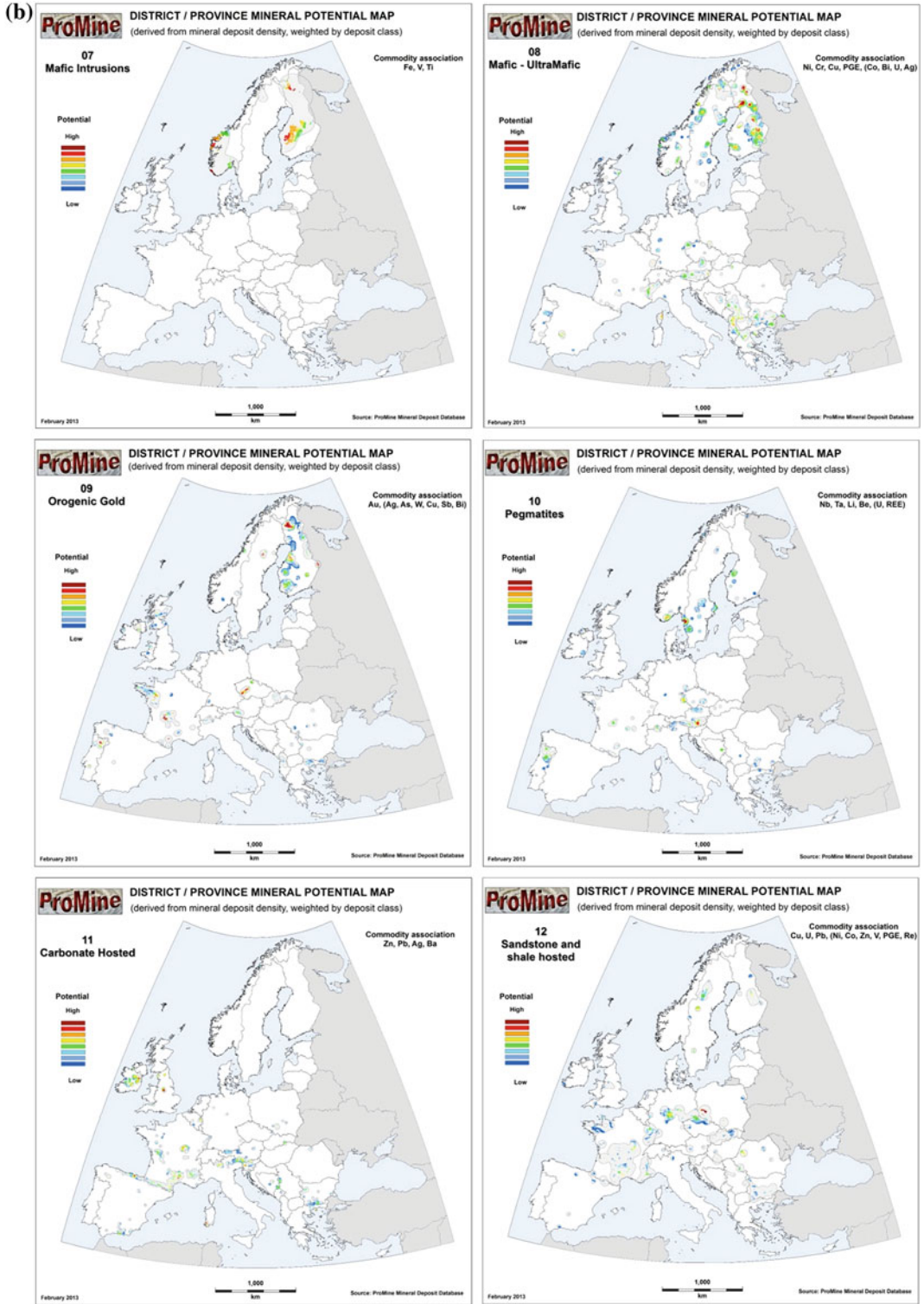


Fig. 2.5 (continued)

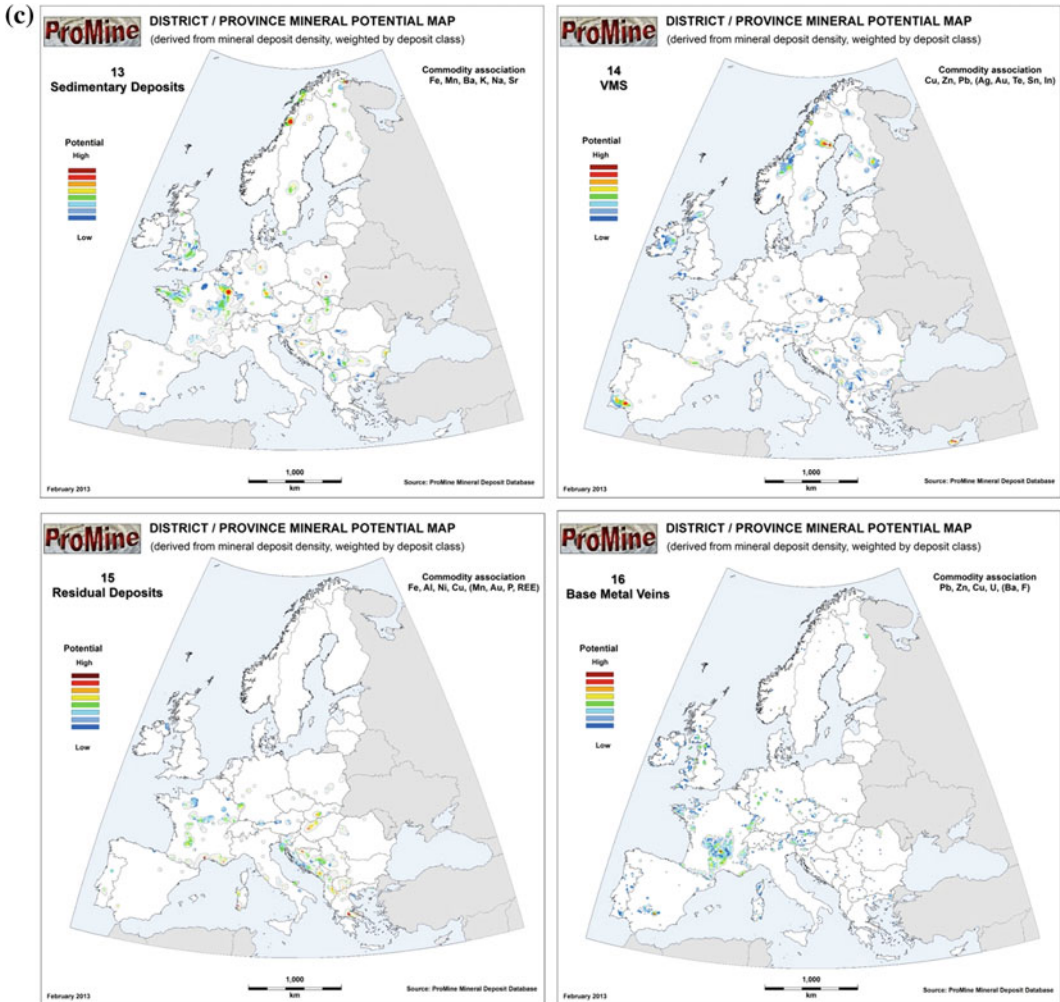


Fig. 2.5 (continued)

16 populations of deposits, a single map of mineral potential was calculated.

The methodology used to calculate these maps combine (1) a statistical study of the spatial distribution of deposits (kernel density⁵ in a first stage), (2) geological constrains, by selecting lithology polygons containing deposits of the selected population (i.e. favourable lithologies) and (3) the introduction, as a weight, of the size (class of the main commodity) of the deposits

(weight of 1 for showings and occurrences, 4 for small deposits, 9 for medium deposits, 16 for large deposits and 25 for very large deposits). The calculation made here—contrary to predictive mapping—does not involve probabilities. The weight used here is a single portrayal enhancer based on commodities classes (see Appendix 1) and whose five values have been graphically defined, the strict respect of magnitude of threshold values having led to hardly readable maps (over-representation of larger districts and disappearance of low potential districts). Grids so obtained are then combined in a potential map that images the weighted density

⁵Kernel density is a method to calculate the density of point (or line) features (deposits in our case) per unit area using a kernel function to fit a smoothly tapered surface to each point (or line).

of deposits in favourable lithologies. 16 potential maps were thus produced (Fig. 2.5a–c) to get a representation of the mineral potential of the 16 selected metallogenic types (Table 2.5). The importance of this methodical approach is that it could be used whatever the type and the density of deposits over large areas and yields consistent results at continental scale. The mineral potential maps are presented and discussed below. They show how the continental scale distribution of known mineralization derived from the ProMine MD database is consistent with the regional geological and tectonic context. This confirms the reliability of the database, and its scientific value for further studies.

2.4.2 Enhanced Mineral Potential Maps by Metallogenic Associations

The metallogenic associations considered herein are based on the 16 families identified by the ProMine consortium to describe the various European mineralization.

Group 01: Alkaline and peralkaline intrusions (Fig. 2.5a)

Theoretical commodity association: Nb, REE, P, (Ta, Zr, Sc, F, U, Fe)

The largest part of the Alkaline group (i.e. alkaline rocks and carbonatites) and its associated mineralization is located within the Fennoscandian Shield (Woolley and Kjarsgaard 2008; Woodard 2010). It includes geographically scattered deposits that were emplaced during various periods: (i) the Palaeoproterozoic (Katajakangas, Siilinjärvi), (ii) the Mesoproterozoic (Norra Kärr), (iii) Neoproterozoic (Søve and Alnö 580 Ma) and (iv) the Upper Palaeozoic (Sokli and Sæteråsen, Upper Devonian carbonate and Permian trachyte, respectively).

In other parts of Europe, less important mineral deposits are present, such as Laacher See and Kaiserstuhl in Germany (related to the volcanism in the Rhine graben), Loch Borrallan in Great Britain, or Svidviya syenites in Bulgaria.

Group 02: Epithermal and volcanic systems (Fig. 2.5a)

Theoretical commodity association: Au, Ag, Sb, Hg, Te, Cu, In

Minor epithermal and volcanic group potential can be found in the Fennoscandian Shield and western Europe Hercynian domain. On the other hand, the potential is much higher along the Tethyan suture, in south-eastern Europe, especially between Slovakia and Greece. This high potential province extends eastwards to Turkey and the Caucasus region (Georgia, Armenia, and Azerbaijan).

The westernmost typical epithermal deposits are associated with Miocene magmatism related to the opening and evolution of the western Mediterranean sea. They are represented by, for instance, the small Rodalquilar ore deposit in Spain (Arribas et al. 1995) and the north-western Sardinia mineral deposits (e.g. Calabona). The Latium district, in Italy, is the first group of some importance. It includes mineral deposits related to Plio-Quaternary volcanism, such as a fluorite-bearing ore deposit group (Pianciano) and a mercury- and/or antimony-bearing group (Monte Amiata and Tafone, respectively).

To the east, the various epithermal and porphyry districts (Cassard et al. 2004) of Upper Cretaceous (Lips et al. 2004) to Mio-Pliocene age (Neubauer et al. 2005) in the Carpathian-Balkan region are well known and form a semi-continuous belt which includes Kremnica in Slovakia, Telkibanya in Hungary, Baia Mare and Apuseni Mountains in Romania, Bor in Serbia, Assarel in Bulgaria and the eastern Rhodopes (Madan group in Bulgaria and Perama in Greece). Farther south, in the Balkan domain, epithermal type mineral deposits are more scattered. Of particular note is the Trepča district, in Kosovo, that combines carbonate-related and epithermal types.

Group 03: Igneous felsic (Fig. 2.5a)

Theoretical commodity association: Sn, W, Ta, Nb, (Mo, Li, Be, B, In, F)

The distribution of igneous felsic deposits and potential is mostly related to Hercynian granites

and their associated ores (W–Sn, U and Mo mineralization, with Cu, Zn and Pb associated sulphur; Bouchot et al. 2000).

The major domains where these deposits are located fit with late-orogenic Hercynian leucogranites (Williamson et al. 1996). Five such domains follow the Hercynian arc (Ledru et al. 1994; Matte 1994; Franke et al. 2005) in Galicia-Portugal (W dominant), British Cornwall, French Brittany (Sn dominant) and French Massif Central, and western Bohemian Massif (Erzgebirge). They show a large variety of occurrences, especially intrusion-related peripheral polymetallic veins and uranium ore deposits (Marignac and Cuney 1999).

Outside these major districts are additional more scattered deposits in other Hercynian domains (e.g. Vosges and Black Forest, the Pyrenees, Corsica, Sardinia), Rhodopes (Bulgaria), the Caledonian belt (Great Britain and Norway) and the Scandinavian Precambrian domain.

Group 04: Igneous intermediate (Fig. 2.5a)

Theoretical commodity association: Cu, Mo, Au, (Re)

Igneous intermediate mineralization (i.e. porphyry type, Singer et al. 2008; Cooke et al. 2005) is typically related to the evolution of the western Tethyan suture in the late Cretaceous and Cenozoic, especially in Eastern Europe where there is high potential for additional deposits.

In Eastern Europe, the Upper Cretaceous in the Tethyan margin, contains large porphyry-type districts (Lips et al. 2004), of which most were subsequently reactivated and are associated with epithermal-type ores. The most important are Kremnica in Slovakia, Telkibanya in Hungary, the Apuseni Mountains in Romania, Bor in Serbia, Assarel in Bulgaria and Bucim in Macedonia.

Other domains also host porphyry-type mineralization, of older age, although their classification as belonging to this deposit type is still debated. In the Fennoscandian Shield, several Cu-(Au)- or Cu–Mo-bearing Palaeoproterozoic

deposits are described as porphyry style. The most important are Aitik (Cu–Au) and Tallberg (Cu–Au, Skellefte district), both in Sweden, and Kopsa (Au–Cu) related to a tonalite stock in the Hitura belt (in Finland).

In relation to the Caledonian volcanism, there are a few smaller porphyry-type deposits of Lower Palaeozoic age in Great Britain, such as Coed y Brenin (Wales) and Black Stockarton Moor (Scotland).

Hercynian magmatism in the Upper Palaeozoic is associated, especially in France, with Cu–Mo–W porphyry deposits, although their geodynamic context is poorly described (e.g. Beauvain, Mo; Sibert, Cu; Auxelles-le-Haut, W).

There are also porphyry Mo mineral of various ages in Europe. The most important of these is probably Nortli in Norway (Sandstad et al. 2012), a group of deposits related to Permian intrusions in the Oslo rift.

Group 05: Igneous replacement or skarn (Fig. 2.5a)

Theoretical commodity association: Fe, W, Pb, Zn, Cu, Au

Igneous replacement or skarn deposits (Einaudi et al. 1981) occur where carbonate rocks are cut by younger intrusions. In Europe, they are distributed in three major domains: (i) the Precambrian Fennoscandian Shield, (ii) the Hercynian domain in southern Europe, and (iii) the Cenozoic Carpathian-Balkan domain.

The Fennoscandian Shield contains iron deposits in greenstones of the Lappland Palaeoproterozoic domain (e.g. Puoltsa, Sautusvaara and Stora Sahavaara in Sweden, Kolari district in Finland). These deposits are related to ‘magnetite-enriched formations and Ca–Mg calc-silicates’, spatially associated with BIFs or Kiruna type IOCG. Recent studies in the Kolari area in Finland (i.e. Laurinoja and Kuervitikko Rautuvaara) show that metasomatized replacements are preferentially IOCG type facies rather than typical ‘intrusion-related skarn deposits’. In the Bergslagen district in Central Sweden skarn mineralization is hosted by Palaeoproterozoic marbles intruded by post-tectonic granites

(~1.8 Ga). Examples of such deposits include the Yxsjöberg (Hallberg et al. 2012) “scheelite-skarn deposit”, skarn iron lenses and skarn iron-sulphides lenses of Stollberg (Fe–Pb–Zn–Mn (Ag)), and sulphide skarn of Garpenberg (Zn). The Arendal (Klodeborg) iron deposit in Norway comprises magnetite skarn in Mesoproterozoic sequences (~1.2–1.5 Ga) cut by younger intrusions (~0.9–1 Ga), and the Knaben deposit (same age) is located in gneisses, paragneisses and amphibolites.

In the southern part of the Hercynian domain, well developed Palaeozoic (Cambrian and Devonian, essentially) carbonate layers and Hercynian (Upper Carboniferous, ~310 Ma) magmatism allowed the development of tungsten- (and/or magnetite-) bearing skarns in the Pyrenees, the southern Massif Central, in Sardinia and in the Alps. The northern parts of the Hercynian arc display only minor occurrences, essentially because of the lack of Palaeozoic carbonate units.

In the Balkan-Carpathian domain, numerous carbonates, essentially of Mesozoic age, and Upper Cretaceous-Cenozoic magmatic episodes allowed development of numerous replacement deposits in the vicinity of epithermal and porphyry domains. Important examples include Kremšica, Baia Mare, Bor, Madan and Trepča.

Minor deposits of this group can also be found in the western Mediterranean, related to Tertiary and Quaternary magmatic episodes in Spain, Sardinia (e.g. Calabona skarn associated with a dacitic porphyry copper) and close to Elba.

Group 06: IOCG (Fig. 2.5a)

Theoretical commodity association: Fe, Cu, Au, (P, REE, U, Co)

This type of mineralization can be found essentially in two Palaeoproterozoic districts in the Fennoscandian Shield (Weihed 2001). The most important is Kiruna (northern Sweden), which is a type locality for IOCG, and the other one is Bergslagen (central Sweden). These districts contain large world-class iron deposits, with a typical magnetite-apatite paragenesis and sodium alteration. These districts also contain copper sulphide deposits that are interpreted as

VMS (Viscaria) or porphyry (Aitik; Wanhainen et al. 2005).

More limited IOCG style deposits are also known in other parts of Europe. Some Fe (Fe–Cu) IOCG style deposits are identified in the Ossa Morena Zone in southwestern Iberia. They are mesozonal albitite-related magnetite deposits and are interpreted (Tornos et al. 2005) as being related to either residual melts of rift-related juvenile magmas (Cambrian) or anatexis of earlier mineralization during high T/low P metamorphism along major shear zones of Variscan age.

Group 07: Mafic intrusion (Fig. 2.5b)

Theoretical commodity association: Fe, Ti, V

This type of deposit is clearly associated with Precambrian rocks in the Fennoscandian Shield, with groups varying in age from one district to another.

In Finland, these deposits are of Palaeoproterozoic age and are related to mafic complexes, in the Karelian domain, that were emplaced during several episodes of rifting triggered by mantle plume activity. To the north, deposits of chromite, vanadium, titanium, platinum-group elements are located along the boundary of the Archaean domain. They are related to stratified mafic complexes of Siderian age (~2.44–2.5 Ga). The Mustavaara deposit (Eilu et al. 2012) displays a typical stratified sequence composed of (from bottom to top) a marginal zone, then layers of pyroxene-gabbro, anorthosite-gabbro, magnetite-gabbro, and anorthosite-gabbro again.

Younger Palaeoproterozoic deposits, such as Otanmäki (Fe–Ti–V) of Rhyacian age (2060 Ma, Talvitie and Paarma 1980) and the Kauhajarvi gabbro complex (1874 Ma, Kärkkäinen and Appelqvist 1999) occur farther south in Finland.

Farther west in the Fennoscandian Shield, deposits of this type are essentially of Sveconorwegian age (Late Mesoproterozoic–Early Neoproterozoic). They could be equivalent to the Greenvillian Ti–V anorthosites in Canada. The main deposit is Tellness, in the Rogaland province of Norway (the major plutonism took place

between 932 and 920 Ma, 50–60 Ma after the last major regional deformation; Schärer et al. 1996). Bamble and Arendal, and probably Selvag, are also of late Sveconorwegian age (~990 Ma).

In Norway, some deposits were emplaced during late Palaeoproterozoic-early Mesoproterozoic, such as Raudsand (or Rødsand), in the Møre province (1.7 Ga) and some in the Lofoten (1.9 Ga). Similar Precambrian deposits that was later affected by the Caledonian orogeny can also be found, such as at Bergen (Norway) and Routevare (Sweden). They are related to Precambrian anorthosites (~1.78–1.76 Ga, Rehnström 2003). In Norway, the Kodal deposit (P–Fe–Ti) is related to Permian magmatism in the Oslo graben. This deposit however also shows alkaline characteristics (basalts and jacupirangites).

In Poland, the Suwalski (or Krzemianka) Fe–Ti–V deposit (Morgan et al. 2000) is related to an anorthosite-norite Mesoproterozoic (~1.5 Ga) intrusion and is similar to deposits in the Fennoscandian Shield. It is located in the deep Precambrian basement, at approximately 1000 m depth.

Group 08: Mafic-Ultramafic (Fig. 2.5b)

Theoretical commodity association: Ni, Cr, Cu, PGE, (Co, Bi, U, Ag)

Major deposits of this type are located in the Fennoscandian Shield mainly in the Karelian area. They are related to the main rifting pulse and plume activity of the early Palaeoproterozoic (Weihed et al. 2005). These deposits are located in Finland (i) in the Kemi district (Kemi, Cr; Sompujarvi, Pt; Siika-Kama, Pd and Suhanko, Pd); (ii) in Kevitsa (Ni) and Koitelainen (Cr), (iii) in the Uutela district (talc), (iv) in Hitura (Ni), Kotolahti (Ni) and Laukunkangas (Ni), and (v) farther south in Vammala (Ni) and Petolahti (Ni).

Other deposits (Sandstad et al. 2012) can be found in the Sveconorwegian domain (~1000–900 Ma). They are related to Ni–Cu sulphur-bearing deformed noritic intrusions in Rana, Flat and Ertelien (Norway). They were

probably emplaced during an early rifting stage of the Sveconorwegian orogeny (equivalent to Grenvillian in Canada).

Several deposits in Norway are related to the Scandinavian Caledonian domain. These include: (i) Altermark (talc) in Norway, (ii) the nickel district of Stekenjokk (Njeretjakke), with Cu–Ni sulphur (and PGE + Au enrichment in Stormyrplutten and Lillefjellklumpen) in Lower Ordovician basalts and gabbros, and (iii) the Rana deposit (Cu–Ni sulphur) related to a mafic-ultramafic intrusion.

This type of deposit is uncommon in Palaeozoic rocks. One exception is the Cu–Ni sulphur deposit of Aguablanca (Tornos et al. 2005) located in a mafic breccia pipe intrusion (of Lower Carboniferous age) fed by a mid-crust mafic-ultramafic stock. It contains pyrrhotite, pentlandite and chalcopyrite formed from the crystallization of an immiscible sulphide-rich liquid.

In the ‘ultramafic’ type, other deposits which should be included are: (i) the Amaden mercury deposit, which formed from the activity of a Silurian mantle plume (Higuera et al. 2005; Jebrak et al. 2002) although the host-rock is sedimentary to volcano-sedimentary and (ii) the ‘five elements’ vein deposits (Bi, Co, Ni, Ag, U), such as Jachymov in Czech Republic, which have a mafic to ultramafic signature.

Finally, in the Balkan domain and in Greece, various deposits in the Mesozoic ophiolites are associated with ultramafic bodies (talc, magnetite, lateritic nickel, chromite lenses).

Group 09: Orogenic gold (Fig. 2.5b)

Theoretical commodity association: Au, (Ag, As, W, Cu, Sb, Bi)

The distribution of deposits of this type (Groves et al. 1998) is relatively straightforward as it is characterized by a single main commodity and a well-constrained type of mineralization. Major known gold-bearing districts belong to two groups:

- Palaeoproterozoic orogenic deposits (Eilu et al. 2003; Eilu and Weihed 2005) in the Fennoscandian Shield;

- Hercynian gold-bearing districts (Bouchot et al. 1997, 2005) related to late Hercynian (~300 Ma) deformation belts, especially the deposits in the northern Iberian Peninsula, the French Massif Central and the Bohemian Massif.

Additional more scattered deposits can be found in other Hercynian domains (e.g. Salsigne in southern France, Lescuyer et al. 1993), the Caledonian domain (Great Britain and Norway) and the Balkan-Carpathian domain.

Group 10: Pegmatite (Fig. 2.5b)

Theoretical commodity association: Nb, Ta, Sn, Li, Be, (U, REE)

This group is related to the igneous group as it represents its peripheral and shallow expression (Cerný and Ercit 2005). This explains the very similar distribution of deposits of both groups.

In the Fennoscandian Shield, pegmatite deposits are related to Palaeoproterozoic (Svecokarelian) magmatism in southern Sweden and Finland, and Sveconorwegian (end of Mesoproterozoic) magmatism to the southwest of the shield (Sweden, Norway).

In the Variscan zone, most deposits are related to the late-Variscan magmatism, especially in the tungsten and/or tin provinces, i.e. (i) in north-western Iberian Peninsula (Hesperids domain, Portugal, Spain), (ii) in Cornwall, (iii) in Brittany, (iv) in the northern part of the French Massif Central, and (v) in the eastern Alps (Austria). Beside these major groups, additional pegmatite deposits can be found in most other Palaeozoic ranges (e.g. the Pyrenees, Corsica, Vosges Mountains and Bohemian Massif).

Group 11: Carbonate-hosted (Fig. 2.5b)

Theoretical commodity association: Zn, Pb, Ag, Ba

This group includes not only deposits characterized by carbonated host rocks but also and essentially MVT (Mississippi Valley Type) deposits. Numerous Pb–Zn (Ba–F) deposits are located along the boundary between Hercynian basement and the Mesozoic transgression

(Muechez et al. 2005). They are hosted by Palaeozoic, Triassic or Liassic limestones. In northern Europe, deposits are located in two areas:

- In Great Britain (F–Ba–Zn–Pb) where they are hosted by Palaeozoic basement and related to Triassic transgression in Derbyshire and northern Pennines;
- In upper Silesian district (southern Poland) where they are hosted by Triassic limestones with a multiphase reworking of mineralization that includes intense weathering and karstification during the Tertiary.

The most extensive belt of carbonate-hosted deposits is located in southern Europe from Galicia, in Spain, to the Central Alps (with possible extension into eastern Europe and Greece). It combines (i) Palaeozoic mineralization hosted by Cambro-Ordovician (Eastern Pyrenees, French Montagne Noire, Iglesias in Sardinia) and Devonian carbonates (Central Pyrenees), (ii) mineralization related to Triassic transgression, and (iii) Mesozoic reactivation of this belt during normal faulting and rifting along the alpine Tethyan margin. Major deposits in this belt are, from west to east, Caravia (Trias), Rubiales (Cambrian) Reocin (Aptian), Pierrefitte (Ordovician, Devonian), Escarro (Cambrian-Ordovician), Les Malines (Trias), Croix de Pallières, Menglon, La Plagne, Gorno (Permian-Trias) Salafossa (Trias), Idrija (Hg in Trias), Mezica (Slovenia, in Trias). Farther east, in Greece and the Balkan, various deposits combine carbonated host rock and replacements processes (e.g. Sedmochislenitzi, Madan in Bulgaria; Olympias-Kassandra, Laurium in Greece).

A specific case is the Navan district (Ireland), which is related to exhalative zinc deposits (type 14), but hosted by Carboniferous limestones (Anderson et al. 1998; Ashton 2005).

Group 12: Sandstone and shales hosted (Fig. 2.5b)

Theoretical commodity association: Cu, U, Pb, (Ni, Co, Zn, V, PGE, Re)

This type includes the major copper mineralization in the Kupferschiefer Permian sediments

(Oszczepalski and Blundell 2005; Hitzman et al. 2010). This type of mineralization mainly occurs in southern Poland (Lubin district), but also in Germany (Mansfeld, Richelsdorf, Spremberg). It also includes the Palaeoproterozoic metamorphosed black shales of Talvivaara in Finland (Ni, Co, Cu). These deposits were the subject of specific studies in the ProMine project aimed at testing ore bioleaching processes.

This type also includes uranium deposits hosted in sandstones and schists of various ages. The main of potential are related to (i) uranium deposits of Tåsjö, Myrviken and Ranstad (alum shales) in relation with Cambro-Ordovician schists and sandstones (Sweden); (ii) Late Hercynian (Permian) deposits (e.g. Lodève half-graben in France, and Bulgaria), (iii) Cretaceous limestones (Cenomanian) in the Hamr-Liberec district (Czech Republic), and (iv) the Coutras Eocene sandstones (France).

In addition to these typical Cu- or U-bearing mineralization, numerous Pb, Ba and/or F mineral deposits are hosted in sandstones in a transgressional context (e.g. Triassic), along the margin of Hercynian basement.

Group 13: Sedimentary deposits (Fig. 2.5c)

Theoretical commodity association: Fe, Mn, Ba, K, Na, Sr

The distribution of deposits from this type is essentially controlled by iron sedimentary deposits. They include Scandinavian BIFs and Jurassic oolitic iron deposits in England (e.g. Northampton), France (e.g. Lorraine), Germany (e.g. lower Saxony), Belgium (e.g. Campine), Poland (e.g. Silesia), etc.

This type also includes less common Palaeozoic deposits (e.g. Carboniferous in Great Britain, Cambrian and Ordovician in France and Iberian Peninsula).

The only important non-ferrous sedimentary group comprises Oligocene manganese deposits in the Obrochishte district (Bulgaria), near the Black Sea.

Group 14: VMS (Volcanogenic massive sulphide deposits) (Fig. 2.5c)

Theoretical commodity association: Cu, Zn, Pb, (Ag, Au, Te, Sn, In)

The distribution of deposits of this type clearly highlights the major known VMS type provinces:

- The Palaeoproterozoic districts of Skellefte and Bergslagen, in Sweden, and Vihanti-Pyhäsalmi and Outokumpu, in Finland (Weihered and Eilu 2005)
- The Upper Palaeozoic (Devonian, Carboniferous) district of the southern Iberian province (e.g. Rio Tinto in Spain, Neves Corvo in Portugal) in Spain and Portugal (Leistel et al. 1998)
- The Upper Cretaceous VMS district in Cyprus (Skouriotissa, Mavrovouni, Limni), related to the Troodos ophiolite complex (Jowitt 2008)

In addition to these three major mineralized provinces, there are several other smaller deposits:

In Scandinavia, copper-rich stratiform sulphides formed in the Palaeozoic along the Caledonian domain. They could be VMS deposits of various types (e.g. Rösros VMS in back arc setting, Tverrfjellet and Joma VMS of Besshi type, Sulitjelma VMS of Cyprus type). These mineral deposits seem to extend southward into the Dalradian Caledonian domain of Scotland (e.g. Ben Collum, Auchtertyre).

Other VMS mineralization, of Devonian-Carboniferous age, can be found in the European Hercynian domain. In France (Châteaulin basin, Saint-Georges-sur-Loire and Chessy), several volcanic related deposits have ages similar to those in the southern Iberian Province (Upper Devonian and Tournaisian). Their tonnages, however, are much smaller. In other parts of the Hercynian domain, massive sulphide deposits are preferentially of SEDEX type (e.g. Rammelsberg and Meggen in

Germany, Rhinish-Hercynian domain; Large and Walcher 1999; Schneider 2005). In the Navan district (Ireland), they are hosted in a Carboniferous foreland sedimentary basin.

In addition, there are also numerous mineral deposits or groups of mineral deposits (with various commodities) where the classification is still debated. This is the case, in particular, for iron deposits in the Alps and the Balkan-Carpathian domain that were classified as SEDEX. They could in fact be replacement deposits (e.g. Ljubija and Omarska in Bosnia and Herzegovina, Erzberg in Austria). Mercury and copper deposits (e.g. Idrija in Slovenia, Munella in Albania), classified as SEDEX could also be epithermal.

Group 15: Residual Deposits (Fig. 2.5c)

Theoretical commodity association: Fe, Al, Ni, Cu, (Mn, Au, P, REE)

This type of deposit shows a significant geographic control and is found essentially in southern Europe. The main types of deposits are bauxites, lateritic nickel, residual concentration in carbonated ores (Mn, Fe a.o.), or gossan-type concentration from sulphides ore (Cu, Au a.o.).

Bauxites develop in emerged domains, in relation to the alteration (essentially from Upper Cretaceous to Palaeogene) of an older carbonate basement (essentially Triassic to Lower Cretaceous). They result from the palaeogeographic and climatic evolution of the Tethyan margin during this period. The main bauxitic domains are to the west, the northern Pyrenean and Provence domains (Villevayac, les Baux) and to the east, the Balkan domain (e.g. Niksic in Montenegro, Mostar in Bosnia and Herzegovina, and the Giona-Parnassus district in Greece) and Hungary (Fenyőfő, Nyirád district).

In ophiolitic series of the Balkan domain, some nickel lateritic mineral deposits formed as a result of the alteration of silica. Examples of such deposits are Citakovo-Glavica in Serbia, Rzanovo in Macedonia, Evia (or Madu di Limni) and Aghios Ioannis (or Larimna) in Greece.

Nickel residual deposits (e.g. Szklary en Poland) also formed from older Variscan ophiolitic mafic or ultramafic rocks.

Some deposits have residual concentrations significantly enriched, relative to primary ores. Examples include: Mn (e.g. Urkút in Hungary), Fe (Ljubija in Bosnia), Zn (Iglesiente district in Sardinia), Cu and/or Au (e.g. Las Cruces, southern Iberian Province; Rudno and Banska, porphyry and epithermal provinces of Slovakia; Rouez in France, etc.)

Group 16: Polymetallic veins (Fig. 2.5c)

Theoretical commodity association: Pb, Zn, Cu, U, (Ba, F)

Underground extraction in mineralized veins is the oldest mining industry in Europe. It extends in time from the Middle Ages to the twentieth century, with the geographic distribution of mined deposits controlled not only by mining criteria but also by culture and history. This mining activity mainly took place in the Hercynian domain, from the Bohemian Massif (Czech Republic) to France. Potential mapping of these deposits shows a heterogeneous distribution with an over-representation of France relative to its neighbouring countries (compare for instance the Vosges and Black Forest Mountains on both sides of the Rhine graben).

These polymetallic vein deposits are related to the Hercynian orogeny (e.g. Bouchot et al. 2005). The main vein-types are (i) Pb–Zn–Cu–Ag veins extracted since the Middle Ages essentially for silver (famous districts, such as the Erzgebirge, the Vosges Mountains, the Black Forest), (ii) antimony veins in the Brioude-Massiac district (France), (iii) peripheral tin and tungsten veins near felsic intrusions (e.g. Portugal, France and Cornwall), (iv) fluorite and barite low temperature veins along the border of the Hercynian domain (e.g. France).

There are also uranium veins in two Hercynian domains (French Massif Central and Czech Bohemian Massif). The high frequency of such

uranium deposits in some countries (e.g. France, L'Escarprière district; Czech Republic, Pibram district) partly results from intense prospection work carried out to support specific government policies at various times.

2.5 Mineral Predictive Mapping

Methodologies used for the calculation of mineral predictive maps are numerous (see review in Carranza 2011) and vary depending on a range of factors, for instance, and this is particularly true for 'strategic' commodities, whether the targeted commodity is a main element in the deposit or a by-product. Up to now, the majority of predictive studies have dealt with only a few elements which are the main commodities in the deposits and/or which belong to the main paragenesis. Examples include copper and gold in porphyries (Bougrain et al. 2003; Billa et al. 2004; Roy et al. 2006), gold and silver in epithermal deposits (Carranza 2009a), orogenic gold deposits (Knox-Robinson and Groves 1997; Bierlein et al. 2006; Nykänen et al. 2008), iron oxide copper gold deposits (IOCG—Nykänen 2008) or gold placers (Cassard et al. 2008) and, more recently, uranium (Kreuzer et al. 2010). However, the ProMine project paid particular attention to strategic and critical commodities, especially to the 14 critical raw materials identified by the European Commission (2010), which may or may not be the main commodity within a given deposit.

In practice, these strategic or critical raw materials are either major constituents of the ore minerals that are actually mined (e.g. tungsten, antimony, fluorite, tin) or commodities which are by-products from mining of major metals (e.g. germanium, indium, gallium, tantalum). As a consequence, the predictive methods used have to be adapted to take account of both possibilities. In this study we used, for the first case, a geographic prediction method (Weight of Evidence, or WofE) and, for the second case, a database querying method, which has been specifically developed for the ProMine project.

The WofE method was applied to identify areas favourable for tin, tungsten, antimony, fluorite, copper and a selection of lead-zinc carbonate-hosted deposits. The same data processing was used for all these commodities. The database querying method was applied to explore the relationships between descriptive fields of the database (i.e. what best characterizes the deposits that contain the targeted commodity), and to predict those deposits, of the 13,000 in the database, possibly containing cobalt, gallium, germanium, indium and tantalum. One should note that, in the latter case, it implies that this method identifies and ranks deposits in the database that might be regarded as potential sources of the targeted by-product commodity, but does not map the favourability around these sites.

2.5.1 Predictive Mapping of Favourable Host Rocks for Main Commodities Using the Weight of Evidence (WofE) Method

2.5.1.1 Methodology for the Weight of Evidence Method

The WofE method is a probability-based approach (Bonham-Carter et al. 1989; Bonham-Carter 1994) that uses Bayes' rule to combine evidence with an assumption of conditional independence. This method requires, on a specific area, a set of training points (mineral occurrences) and a coverage of polygons (geological map). Where sufficient data are available, it can be applied to estimate the relative importance of evidence by statistical means. Calculating the WofE on a geological map, covering several geological formations, is similar to using a multi-class evidential theme. The calculation of WofE characterizes each formation by three numerical values: $W+$, $W-$ and C (see Bonham-Carter (1994) and Kemp et al. (2001) for details of these calculations). The positive and negative weights ($W+$ and $W-$) provide a measure of the spatial association between the

training points (in this case the mineral deposits of the particular target type) and the evidential theme (in this case, the lithostratigraphy polygons). A weight is calculated for each class of the evidential theme:

In these equations:

- D is the number of unit cells containing a prospect or deposit (training point);
- B is the number of unit cells containing a given formation b;
- $P(B | D)$ is the probability of occurrence of formation b, given the condition of being on a deposit;
- $P(B | \bar{D})$ is the probability of occurrence of formation b, given the condition of not being on a deposit;
- $P(\bar{B} | D)$ is the probability of non-occurrence of formation b, given the condition of being on a deposit;
- $P(\bar{B} | \bar{D})$ is the probability of non-occurrence of formation b, given the condition of not being on a deposit.

The absolute value of a weight indicates whether a criterion is slightly significant ($0 < W < 0.5$), significant ($0.5 < W < 1$), very significant ($1 < W < 2$), or discriminant ($W > 2$). The contrast, C, which is the difference between the weights ($C = W+ - W-$), is an overall measure of spatial association between the training points and the evidential theme, combining the effects of the two weights.

The spatial analysis was performed on the training points and lithostratigraphy layers, using the Arc-SDM (Spatial Data Modeller) extension (Kemp et al. 2001), developed for ESRI®'s ArcView 9.x / Spatial Analyst. The same process was used for all targeted commodities (i.e. tungsten, antimony, fluorite and tin, copper and a selection of Pb–Zn carbonate hosted deposits). Weights were calculated separately for deposits (i.e. class A, B, C, D, E) and showings (i.e. class N/A) in the database. Results were added as follows: (Weight of deposits) + 0.5 (Weight of showings).

In conclusion, WofE modelling has been performed on one evidential theme, the lithostratigraphy which has been carefully homogenized when preparing the 1:1,500,000 ProMine geological background map. Other available ‘layers’—e.g. structural (resulting from generalization), geophysical etc.—are not enough accurate at this scale, and their use would have brought no real improvements, but possible artefacts. In general, the results confirm the interest of already known areas. New areas/sectors of possible interest resulting from this study generally make sense in terms of geological context. They will, however, need to be confirmed in the future by field work.

2.5.1.2 Predictive Mapping of Favourable Host Rocks for Selected Main Commodities

Tungsten

280 deposits containing tungsten were used: 41 deposits in which W is the main commodity, and 239 showings (i.e. occurrences with W minerals present, but without any resource indication). Among them, the dominant deposit types are igneous felsic (56 %) and igneous replacement (23 %). The dominant associated commodity is tin (e.g. Cornwall, UK; Moon 2010).

Most results are located within the Palaeozoic domain (Fig. 2.6a) of Iberia (e.g. Panasqueira in Portugal, Noronha et al. 1991; Los Santos in Spain, Sánchez et al. 2009), the French Pyrenees (e.g. Salau, Costabonne, in Autran et al. 1980), the French Massif Central (Leucamp-La Châteigneraie district, Lerouge and Bouchot 2005), the Austrian Alps (Mittersill-Felbertal; Raith and Stein 2006) and the Bohemian Massif (e.g. Erzgebirge Sn–W Zinnwald district; Webster et al. 2004). In the Fennoscandian Shield, some results are related to the Archaean and Palaeoproterozoic metavolcanic greenstones cut by granitic intrusions (e.g. the Yxsjöberg W–Mo skarn deposit; Romer and Öhlander 1994; Hallberg et al. 2012). Favourable results are found mostly in: (i) sandstones and shales with Lower Palaeozoic carbonate

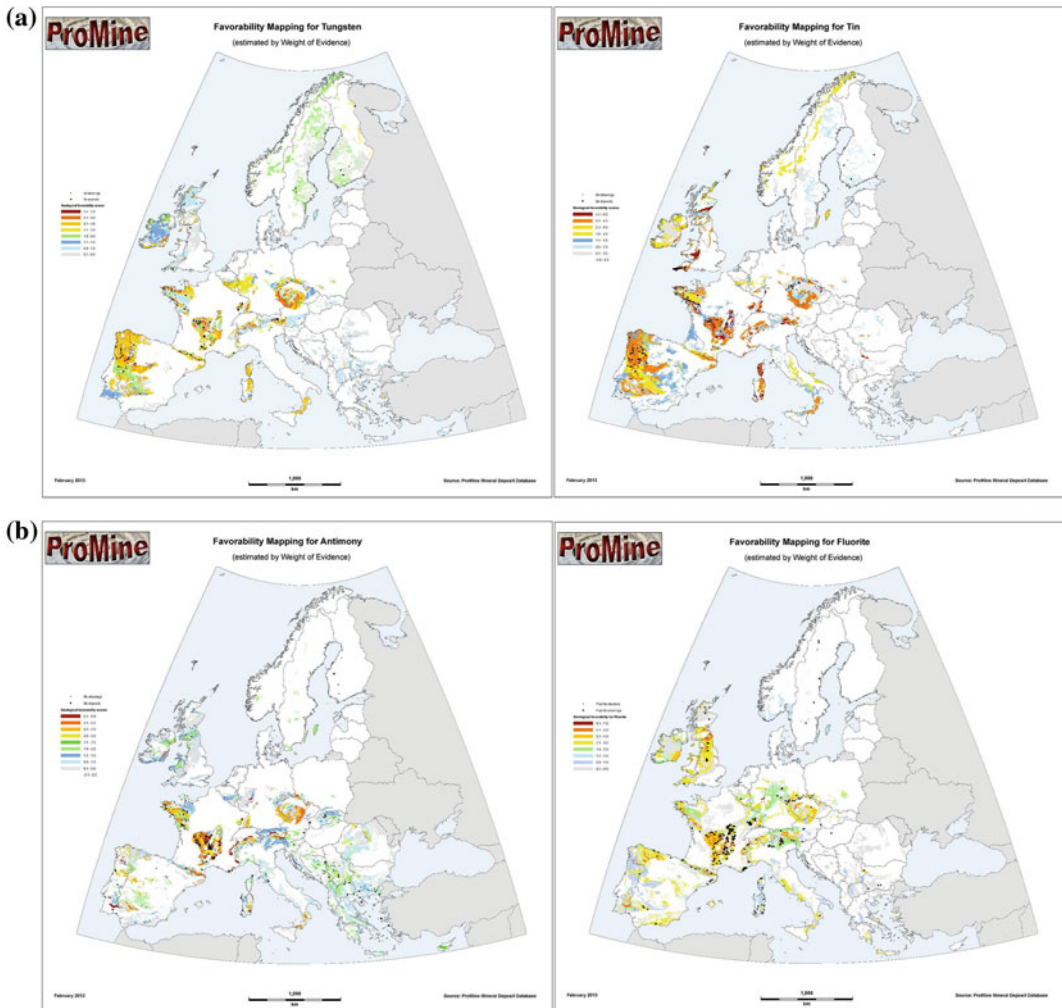


Fig. 2.6 a Maps of favourability, estimated with the weight of evidence method, for tungsten (*left*) and tin (*right*). **b** Maps of favourability, estimated with the weight of evidence method, for antimony (*left*) and fluorite

(*right*). **c** Maps of favourability, estimated with the weight of evidence method, for zinc in carbonate hosted deposits (*left*) and copper (*right*)

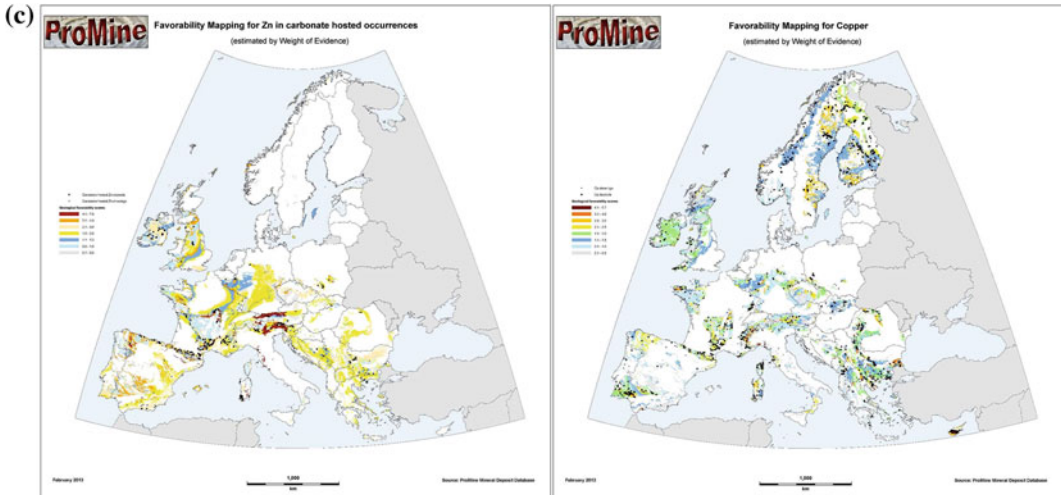


Fig. 2.6 (continued)

intercalations (Infra Cambrian, Cambrian and Ordovician), and (ii) Devonian sedimentary series with intercalated carbonates or Carboniferous granitic intrusions.

The map of favourable areas obtained with the WofE method, along with the density of known W-bearing deposits, allows favourable domains to be delineated in areas where no or few occurrences are known, such as the eastern Bohemian Massif, the Black Forest and the southern Iberian Peninsula.

Tin

252 deposits containing tin were used: 67 deposits in which Sn is the main commodity, and 185 showings (i.e. occurrences with Sn minerals present but without any resource indication). Among them, the dominant deposit types are igneous felsic (72.5 %) and pegmatite (9.5 %). The dominant associated commodity is W, along with, in smaller proportions, As, In, Zn and Mo.

The results highlight the importance of Upper Palaeozoic Hercynian intrusions (Fig. 2.6a), especially the late Upper Carboniferous leucogranites (~300 Ma). The Palaeozoic host rocks of these granites also appear favourable, especially Lower Palaeozoic sandstone-rich series. In the Fennoscandian Shield most favourable areas are located in the Palaeoproterozoic Svecokarelian (~1.9 Ga) volcano-sedimentary

belts and in the Neoproterozoic sandstones and metagreywackes of the Caledonian belt.

Besides the usual tin provinces (e.g. Cornwall, UK, north-western Iberian Peninsula, French Brittany; Derre 1982; Plimer 1987), the results highlight several favourable areas, such as the north-western French Massif Central, Calabria, the eastern Bohemian Massif and several Neovariscan Carpathian massifs.

Antimony

342 deposits containing antimony were used: 109 deposits in which Sb is the main commodity, and 233 showings (i.e. occurrences with Sb minerals present but without any resource indication). Among them, the dominant deposit types are base metals veins (55.05 %), epithermal (17.8 %), orogenic gold (8.78 %) and, with a much lower importance (<5 %), carbonate hosted deposits and VMS. The dominant associated commodities are Au and As, along with, in smaller proportions, the (Pb, Zn, Cu, Ag) group and Hg in epithermal parageneses.

The main areas of favourability are located in the French Hercynian domain [Massif Central and southern Brittany, respectively the Brioude-Massiac district (Bril 1982), and the Vendée district (Bailly et al. 2000)] and correspond to late orogenic veins (~300 Ma) on Palaeozoic basement (Fig. 2.6b). The dominant

host rocks are Lower Palaeozoic clastic metasediments and Upper Palaeozoic (including Devonian-Carboniferous) volcanics. Another area favourable for Sb is the Carpatho-Balkan region, in relation to Mesozoic and Cenozoic rocks (including volcanic). In summary the result allow Sb favourability to be defined in several areas of the Palaeozoic (e.g. Wales, the Alps, eastern Bohemia) and Balkan-Carpathian domains.

Fluorite

407 deposits containing fluorite were used: 113 deposits in which fluorite is the main commodity, and 294 showings (i.e. occurrences with fluorite mineralogy but without any resource indication). Among them, the dominant deposit types are base metals veins (70 %), carbonate-hosted (16.6 %) and igneous felsic (6.65 %). Fluorite is rarely present in other deposit types. The dominant associated commodities are Ba, Pb and Zn, and to a smaller degree Cu.

Fluorite mineralisation was emplaced during several periods. It is associated with plutonism and volcanism of various ages (Fig. 2.6b). This association with volcanic facies is a characteristic feature of fluorite mineralization. Two major periods of mineralization can be identified: (i) early Palaeozoic stratabound deposits (Infra-cambrian to Ordovician; e.g. Escarro in French Pyrenees) and (ii) the transitional period between Upper Hercynian (igneous, veins; e.g. Le Burg-Montroc in Montagne Noire, France) and Lower Mesozoic (veins, carbonate-hosted deposits; e.g. Pierre-Perthuis, France).

One should note also the fluorite associated with Quaternary volcanism in Latium (Barbieri et al. 1977). Scandinavian deposits are very scattered within huge domains and therefore are not conspicuous on the map.

Most favourable areas identified with the WofE method contain known fluorite occurrences. The predictive role of the map is therefore limited, allowing only the identification of scattered smaller domains (e.g. Calabria and Sicilia in Italy, Galicia and Aragon in Spain, northern England).

Carbonate-Hosted Zinc

In this case the problem is slightly different as the goal is not directly to seek the critical commodity, but to identify deposits that may contain germanium (i.e. zinc-bearing carbonate-hosted deposits). However, the methodology applied remains the same.

Commodity association corresponds to a usual paragenesis [i.e. Zn, Pb, Ag, Ba, (Cu, Ga)], and includes germanium in 7 % of selected deposits.

641 carbonate-hosted deposits containing zinc were used: 186 deposits in which Zn is the main commodity, and 455 showings (i.e. occurrences with Zn mineralogy but without any resource indication).

The results show clusters of deposits (Fig. 2.6c) related to carbonate series of Cambro-Ordovician (e.g. Iglesias in Sardinia) and Devonian (e.g. French Pyrenees) ages, and series along the boundary between the Hercynian basement and the Mesozoic cover, especially the Liassic and Triassic formations (e.g. the Cevennes border in southern France).

The results also highlight domains where Zn-bearing carbonate-hosted deposits are known. They also extend favourable areas into contact zones between basement and sedimentary cover where no mineralization is known. This is the case, for instance, in the north-western French Massif Central, the Liassic margin of Normandy and the northern Hercynian domain in Germany.

Copper

Cu is a common commodity in the ProMine MD database: in the selected dataset, 22 % of deposits contain copper. 1777 deposits containing copper were used: 722 deposits in which Cu is the main commodity, and 1055 showings (i.e. occurrences with Cu mineralogy but without any resource indication). Only five deposit types, however, are enriched with copper (igneous intermediate, VMS, mafic-ultramafic, sandstone- and shale-hosted and IOCG).

Geological formations favourable to copper are quite numerous and include essentially sedimentary and volcanic rocks (Fig. 2.6c). Ages are

also widespread, with (i) Palaeoproterozoic VMS, mafic-ultramafic type and IOCG in Scandinavia, (ii) Lower Palaeozoic Caledonian VMS and veins, (iii) Upper Palaeozoic VMS in the southern Iberian province and French Brittany, and (iv) Permian sandstone-hosted deposits and Cenozoic igneous intermediate porphyry deposits in the Balkan-Carpathian region.

The distribution of favourable areas clearly highlights the major known copper districts. In addition, because of the large dataset used (1777 deposits), a considerable amount of detail is present in the results and show favourable areas where copper mineralization has not been recognised, especially in the Balkan-Carpathian region.

2.5.2 Predictive Mapping for By-Product Commodities Using the Database Querying Method

2.5.2.1 Methodology

The objective here was not to discover new deposits but to evaluate known deposits for a new targeted commodity. When searching for ‘high-tech’ commodities, which most of the time are by-products, searching for a specific type of deposit (e.g. Cu–Mo porphyries for Re, or Pb–Zn deposits for Ge) does not help because it can contain, or not, the searched by-product. For several reasons (e.g. commodity not searched or not analysed), ore deposits mined in ancient times may have an unknown potential. Sampling the dumps and the tailings and then performing analyses could be a very costly task due to the generally complex structure of the mining wastes. Hence, the idea of a predictive method to assess the favourability for by-products of other commodities from deposits in the ProMine MD database. This was done by ranking deposits of the appropriate types in the database according to their similarity to deposits known to contain the targeted commodity. Interestingly, this

non-spatial method, when applied to a number of deposits sufficiently important, may result, using a simple parameter of transformation (here the “enrichment ratio”, see below), in the definition of favourable areas for the searched by-product.

After identifying the most favourable deposit types, those enriched in the target commodity, commodity associations were investigated in all deposits containing the target commodity in order to identify the most favourable polymetallic associations (or signatures). These signatures were then searched for, and the results ranked, in all other deposits to identify those favourable for the target commodity. The following steps describe the methodology in more detail:

Step 1: The frequency of the target commodity is evaluated by deposit type. This is then compared to the whole database and an “enrichment ratio” (ER) is calculated as follows:

$$ER = (\text{frequency of targeted commodity in the deposit type}) / (\text{frequency of the targeted commodity in all deposit types})$$

(ER > 1 for enriched types, ER = 1 for neutral types and ER < 1 for depleted types)

The ER is used to identify those deposit types most favourable for the target commodity.

Step 2: In all deposits that contain the targeted commodity and for each favourable deposit type, a list of associated commodities and their frequency is calculated. For a given commodity, the result is a table of characteristic polymetallic association, or “signature”, associated with the presence of the target commodity in each favourable deposit type. This characteristic polymetallic signature is then searched for in all deposits of a given type.

Step 3: The deposits in the database are ranked relative to the polymetallic signature of the deposit type they belong to. The ranking is the sum, for all commodities in the polymetallic association, of the product of a

Boolean value (i.e. “commodity is present” = 1 and “commodity is not present” = 0) and the frequency of the commodity in the signature. This formula is applied to all deposits in the database that belong to enriched types ($ER > 0$) in order to measure their level of similarity to deposits containing the target commodity. The result is a score given to all ranked deposits, with higher values corresponding to greater similarity to deposits containing the target commodity. Deposits with a high score are more likely to contain the target commodity and should be investigated as a priority.

The results of ranking by deposit type can be displayed on a map using a rank-based symbology or iso-contouring. More globally, to display in a single map (and compare) results for a target commodity found in several types, the rank of each deposit is weighted by the ER (see step 1) of the type it belongs to. The results can then be mapped as density, in order to show the geographic distribution of favourability for the target commodity.

2.5.2.2 Predictive Maps for Selected Secondary or by-Product Commodities

Germanium

To measure the influence of deposit type on the presence of germanium (Höll et al. 2007), the enrichment ratio (ER) was calculated for each deposit type where germanium is present. This ratio is the frequency of germanium in the deposit type relative to the frequency of germanium in the whole database. Amongst the 7614 deposits that belong to one of the 16 commodity associations (or deposit types) defined by ProMine, 111 contain germanium. Germanium is preferentially enriched (i.e. high ER) in the following 4 deposit types (Table 2.6): carbonate-hosted ($ER = 3.35$), VMS ($ER = 1.78$), epithermal ($ER = 1.50$) and base metals veins ($ER = 1.14$). These 4 types include 79 % of the 111 deposits. The remaining 21 % are distributed in other types with lower enrichment ratios. The “base metals veins” type is only slightly enriched probably because it includes some parageneses (U, F, Co ...) that are not favourable to the presence of germanium.

Table 2.6 Enrichment ratios (ER) of deposit types containing germanium

Metallogenic type	No. of occurrences	Enrichment ratio (ER)
Base metals veins	31	1.14
Carbonate-hosted	28	3.35
Epithermal	10	1.50
VMS	19	1.78
Igneous felsic	8	0.69
Igneous intermediate	1	0.59
Igneous replacement	5	0.98
Orogenic gold	1	0.20
Residual deposits	1	0.13
Sandstone and Shale-hosted	5	1.09
Sedimentary deposits	2	0.24

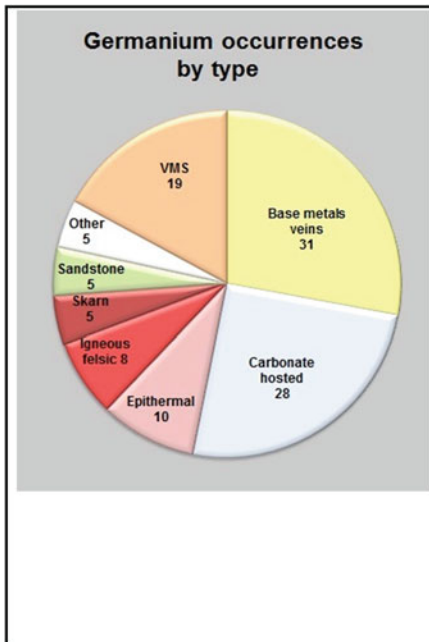


Table 2.7 Polymetallic signature of germanium-bearing deposits, by deposit type

Commodity	Global %	Base metals veins	Carbonate-hosted	Epithermal	VMS	Igneous felsic	Igneous replacement.	Shales- and sandstones-hosted
Zn	74	87	79	40	89	75	40	0
Pb	68	74	71	30	68	75	80	60
Ag	58	68	43	70	37	100	60	60
Cd	40	48	32	20	32	63	60	40
Cu	33	19	25	80	26	50	40	60
Ga	25	32	18	10	37	0	60	20
In	17	16	7	30	16	38	40	0
Au	15	3	4	70	11	13	40	40
Ba	12	13	14	20	11	13	0	0
As	11	13	11	30	0	13	0	20
Sb	10	6	7	30	5	13	40	0
Bi	9	6	4	10	5	13	60	20
Fe	8	0	7	10	16	0	40	0
Sn	7	10	0	0	5	38	0	0
Tl	7	3	4	10	0	13	40	20
Ni	6	3	7	10	5	0	20	0
Te	6	0	4	20	0	0	40	20
Co	5	3	4	0	11	0	0	20
U	5	6	0	0	0	25	20	0
F	4	10	4	0	0	0	0	0
Hg	4	0	7	20	0	0	0	0
Se	4	0	0	10	5	0	40	0

Considering only the deposits that contain germanium, the frequency of other associated commodities is calculated for each enriched type (Table 2.7). The results show, by deposit type, the commodities that are preferentially associated with germanium, or the characteristic polymetallic association. For instance, zinc, the most frequently occurring element, occurs in 87 % of base metals veins deposits that contain germanium, while Pb and Ag occur in 74 and 68 % respectively of these deposits. In epithermal deposits containing germanium, the polymetallic associations are quite different with Cu in 80 % of the deposits, but Zn in only 40 %. In this way a characteristic polymetallic signature associated with each favourable deposit type is established. This signature was then searched for in all deposits of a given type.

For each deposit in each identified favourable type, a rank was calculated in order to measure the level of similarity with deposits of the type that contain the targeted commodity (see step 3 here above). For instance, for germanium in base metals veins deposits, the ranking is calculated as follows:

$$\text{Rank for base metals veins deposits} = ((0.87 * [1 \text{ if Zn}; 0 \text{ if not}]) + (0.74 * [1 \text{ if Pb}; 0 \text{ if not}]) + (0.68 * [1 \text{ if Ag}; 0 \text{ if not}]) + (0.48 * [1 \text{ if Cd}; 0 \text{ if not}]) + (0.19 * [1 \text{ if Cu}; 0 \text{ if not}]) + (0.32 * [1 \text{ if Ga}; 0 \text{ if not}]) + (0.16 * [1 \text{ if In}_-; 0 \text{ if not}]) + (0.03 * [1 \text{ if Au}; 0 \text{ if not}]) + (0.13 * [1 \text{ if Ba}; 0 \text{ if not}]) + (0.13 * [1 \text{ if As}_-; 0 \text{ if not}]) + (0.06 * [1 \text{ if Sb}; 0 \text{ if not}]) + (0.06 * [1 \text{ if Bi}; 0 \text{ if not}]))$$

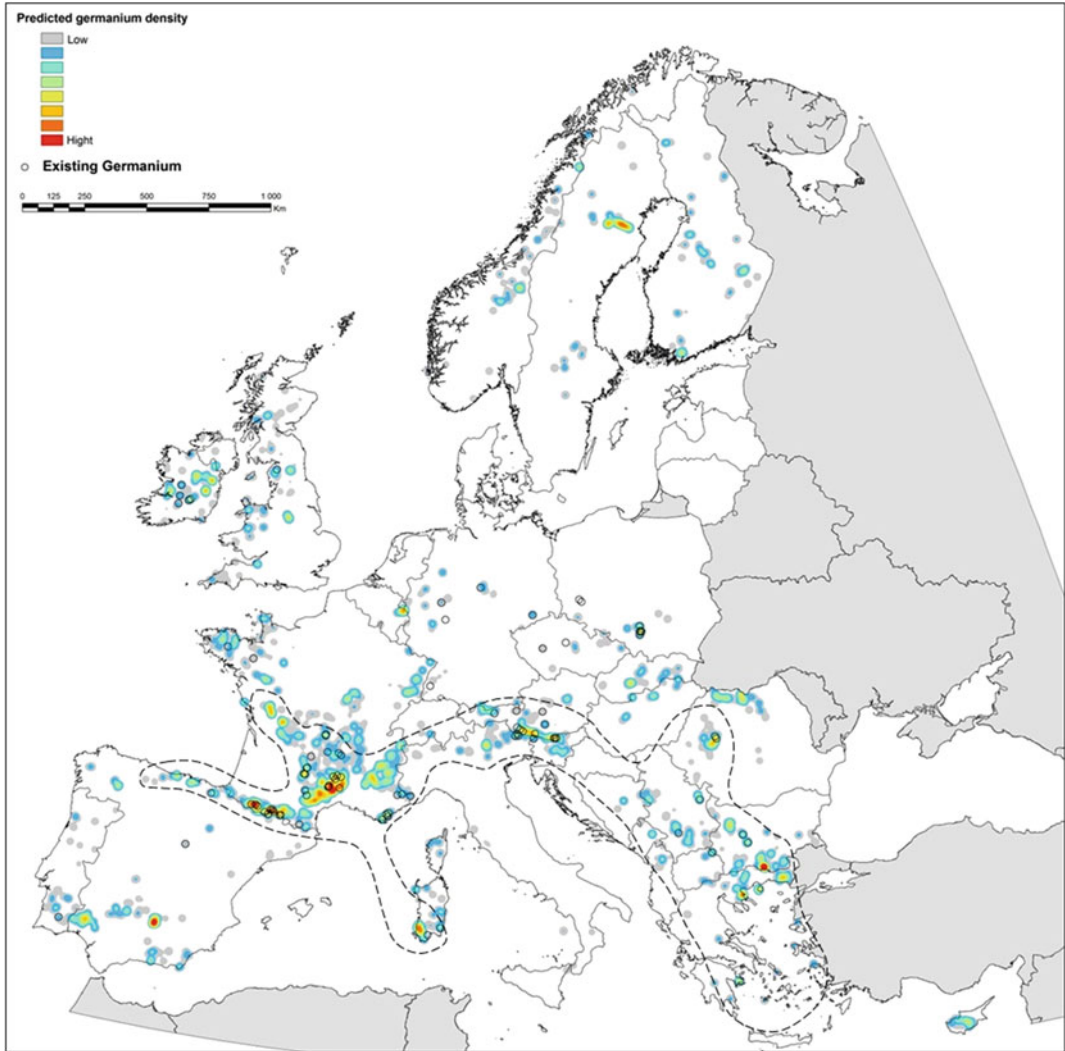


Fig. 2.7 Predictive map for germanium, obtained with the database querying method

The results for each favourable deposit type highlight those deposits that are most similar to those known to contain germanium and, consequently, have the highest probability of containing germanium. Then, to map and compare ranks of deposits from the different types, the ranking scores are weighted with the enrichment ratios (ER), as follows:

Global ranking = $(1.14 * [1 \text{ if base metals veins; } 0 \text{ if not}]) + (3.35 * [1 \text{ if carbonate-hosted; } 0 \text{ if not}]) + (1.58 * [1 \text{ if$

$\text{epithermal; } 0 \text{ if not}]) + (1.78 * [1 \text{ if VMS; } 0 \text{ if not}])$

The results are then mapped as density, in order to show the geographic distribution of areas favourable for germanium. The resulting map (Fig. 2.7) highlights a germanium province in southern Europe with various types of mineralization emplaced in the Lower Palaeozoic (Cambro-Ordovician), the Mesozoic (in relation to carbonates of the Tethyan margin), and the Upper Cretaceous-Cenozoic (porphyries and

epithermal deposits). This temporal extension may be related to the palaeogeographic domain (Gondwana margin undergoing fragmentation during Cambro-Ordovician), distinct from the European terranes and where pre-concentrations had possibly occurred. Some areas, such as massive sulphides domains, also show relatively high favourability and should be investigated in more detail.

Gallium

Only 39 deposits in the ProMine MD database contain gallium. Five deposit types are significantly enriched in gallium (Table 2.8): igneous replacement (ER = 2.80), VMS (ER = 2.13), carbonate-hosted (ER = 2.04), epithermal (ER = 1.71) and base metals veins (ER = 1.26).

The similarity between polymetallic signatures (Zn, Pb, Ag, Cd) and enriched deposit types (base metal veins, carbonate-hosted, epithermal, VMS) for gallium (Table 2.9) and germanium (Table 2.7) is notable. Also, gallium-bearing deposits are commonly enriched in germanium (74 %) although the opposite is not necessarily true (25 %). It is also notable that in the “magmatic” deposit types (epithermal and igneous replace-

ment) indium is often enriched along with Bi, Au, Sb and Te that are not present in other types.

After weighting of ranks by the enrichment ratio (ER) ((1.26 *base metals veins) + (2.04 *carbonate-hosted) + (1.71 *epithermal) + (2.13 *VMS) + (2.80 *igneous replacement)) the resulting map (Fig. 2.8) is very similar to germanium. However, the skarn domains are better depicted (e.g. Bergslagen district in central Sweden, the Pyrenees in France) as are the skarns and epithermal deposits in the eastern Europe districts (e.g. Moldova Nova in Romania, Majdanpek in Serbia, Trepča in Kosovo, Skouries in Greece).

Indium

Only 96 deposits in the ProMine MD database contain indium. Five deposit types are significantly enriched in indium (Table 2.10): igneous felsic (ER = 3.89), igneous intermediate (ER = 2.71), igneous replacement (ER = 2.5), epithermal (ER = 1.56) and VMS (ER = 1.3). Unlike germanium, indium (Schwarz-Schampera and Herzig 2002) is preferentially associated with “magmatic” deposit types (igneous and epithermals). Despite the fact that indium is

Table 2.8 Enrichment ratios (ER) of deposit types containing gallium

Metallogenic type	No. of occurrences	Enrichment ratio (ER)
Base metals veins	12	1.26
Carbonate-hosted	6	2.04
Epithermal	4	1.71
VMS	8	2.13
Igneous replacement (Skarn)	5	2.80
Pegmatite	1	0.63
Residual deposits	2	0.74
SandStone-and Shale-hosted	1	0.68

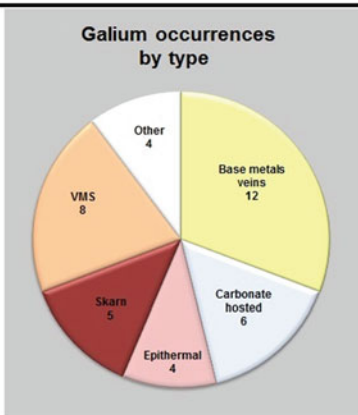


Table 2.9 Polymetallic signature of gallium-bearing deposits, by deposit type

Commodity	Global %	Base metals veins	Carbonate-hosted	Epithermal	Igneous replacement	VMS
Zn	83	83	50	100	80	100
Ge	74	83	83	25	60	88
Pb	74	67	67	100	100	63
Cd	69	67	33	100	100	63
Ag	63	75	17	100	100	38
Cu	26	25	33	25	40	13
In	26	8	0	75	80	13
Bi	23	0	17	50	80	13
Au	17	0	0	50	60	13
Sb	14	8	0	25	40	13
Te	11	0	17	25	40	0
As	9	17	17	0	0	0
Co	9	8	17	0	0	13
Ni	6	8	17	0	0	0
Ba	3	0	0	0	0	13
F	3	8	0	0	0	0
Mo	3	0	17	0	0	0
Sn	3	0	0	25	0	0
U	3	0	0	25	0	0
Y	3	0	0	25	0	0

found in 15 base metal vein deposits, this type is not favourable (ER = 0.64).

Polymetallic associations (Table 2.11) show that indium is typically associated with Cu and Sn, as well as Zn, Pb and Ag. Indium-bearing epithermal deposits are not associated with Sn enrichment, but are characterised by Ge and Ga in their polymetallic association. Presence of other commodities (e.g. W, Sb, Mo, Au) seem to be more controlled by the deposit type than the presence of indium.

As indium seems to be independent of other critical commodities, its distribution should be different. Indeed, the results (Fig. 2.9) for indium are very different to those of germanium and gallium. They highlight a vast domain (indium belt) that includes the tin province of Cornwall, UK, and Brittany, the north-western French Massif Central, the Vosges Mountains, the Erzgebirge in the Bohemian Massif and the

north-western Iberian Peninsula. The results also show Cu- (and sometimes Sn-) rich VMS provinces such as Cyprus, the southern Iberian Peninsula, the Skellefte (Sweden), Vihanti-Pyhäsalmi and Outokumpu (Finland) districts, and Cu porphyry and epithermal domains in the Balkan-Carpathian region.

Tantalum

Only 93 deposits in the ProMine MD database contain tantalum. Three deposit types are significantly enriched in tantalum (Table 2.12): pegmatites (ER = 18.3), alkaline and peralkaline intrusions (ER = 12.21) and igneous felsic (ER = 1.95). Tantalum is most commonly associated with pegmatites (74 %) and their associated magmatic sources (alkaline-peralkaline and felsic magmatism). These associations are consistent with the incompatible behaviour of tantalum (Audion and Piantone 2012) that results

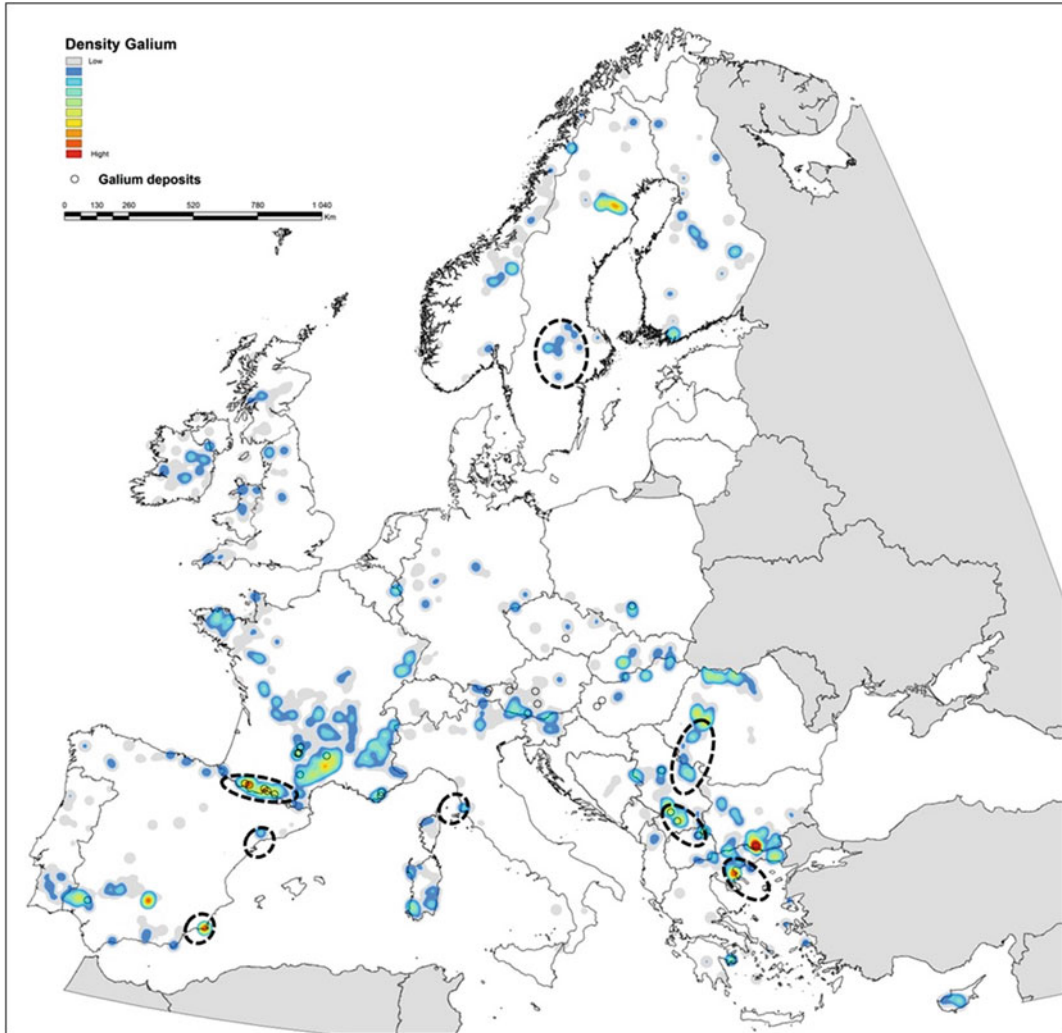


Fig. 2.8 Predictive map for gallium, obtained with the database querying method

in its concentration in highly differentiated residual magmas, in particular in pegmatites.

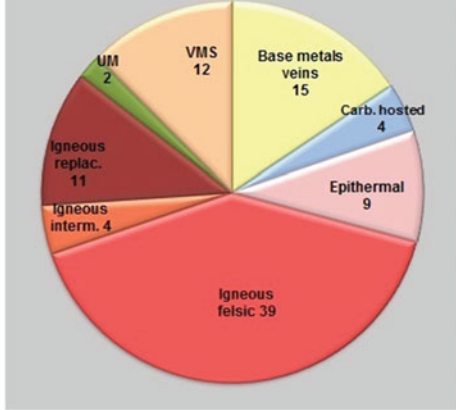
Tantalum-enriched deposits are characterized by a polymetallic signature (Table 2.13) with Be, Nb, REE and Li common in pegmatites. This signature also includes various other incompatible elements often associated with highly differentiated magmas (e.g. Beauvoir granite, in France, Cuney et al. 1992) such as Sn, U and Th. The presence of scandium, despite its low level, is unexpected and is difficult to explain.

The distribution of favourability for tantalum (Fig. 2.10) is similar to potential maps for the pegmatite deposits, the main Ta-bearing ore type. This distribution shows two main domains: (1) the Hercynian arc, related to crustal leucogranites magmatism, and (2) the southern Fennoscandian Shield, in the Sveconorwegian domain, and its associated magmatism.

Cobalt

A relatively large number of deposits, 239, in the ProMine MD database contain cobalt. Three

Table 2.10 Enrichment ratios (ER) of deposit types containing indium

Indium occurrences by type	Metallogenic type	No. of occurrences	Enrichment ratio (ER)
	Epithermal	9	1.56
	Igneous felsic	39	3.89
	Igneous intermediate	4	2.71
	Igneous replacement	11	2.5
	VMS	12	1.3
	Base metals veins	15	0.64
	Carbonate-hosted	4	0.55
	Mafic or UltraMafic	2	0.28

deposit types are significantly enriched in cobalt (Table 2.14): mafic/ultramafic (ER = 6.06), VMS (ER = 1.61) and residual deposits (ER = 1.10). The metallogeny of cobalt confirms that it is preferentially found in deposits related to mafic and ultramafic rocks and VMS. Less frequently, it can be present in residual deposits developed above ophiolitic basements and in some polymetallic veins. Cobalt can also occur in other deposit types, but generally without significant concentration. Cobalt is frequently associated with Cu and Ni, along with Zn, Au and Ag in VMS, or Cr and Mn in residual deposits (Table 2.15).

The most significant region (Fig. 2.11) is the Fennoscandian Shield, with important mineralization related to mafic and ultramafic complexes emplaced during the Palaeoproterozoic and the early stages of the Caledonian orogeny. In other regions of Europe, the favourability is more scattered and is related to mineralization of various types in the Cenozoic ophiolitic domain (especially lateritic nickel mineralization) to Bi–Co–Ni–Ag–U “five elements” veins (e.g. Bohemian Massif), and to VMS-type Cu mineralization, especially in Cyprus massive sulphides.

2.6 Data Dissemination and Web Portal

To disseminate ProMine data and results, an information system was developed. It is based on open and distributed architecture principles and the use of standards. The goal was not only to publish maps and data on a web portal, but also to allow these maps and data to be reused by other projects to make them interoperable. This requirement is in line with the European Directive INSPIRE⁶ (Infrastructure for Spatial Information in Europe) which has specified rules to share information for 34 data themes, one of them being Mineral Resources. The INSPIRE principles can be summarized:

- the data and the layers must be described by their metadata (according to a standard) registered into a catalogue,

⁶Directive 2007/2/EC of the European Parliament and of the Council of 14 March 2007 establishing an Infrastructure for Spatial Information in the European Community (INSPIRE) <http://inspire.jrc.ec.europa.eu>.

Table 2.11 Polymetallic signature of indium-bearing deposits, by deposit type

Commodity	Global %	Igneous felsic	Igneous intermediate	Igneous replacement	Epithermal	VMS
Cu	56	49	75	64	78	83
Zn	66	56	25	91	44	67
Sn	46	74	75	36	0	17
Ag	46	26	50	64	78	50
Pb	47	21	25	73	44	58
Au	23	3	25	36	89	58
W	22	38	50	18	0	0
Cd	17	5	0	45	33	17
As	18	26	25	9	0	8
Mo	7	8	50	9	0	0
Li	6	10	50	0	0	0
Sb	9	3	25	27	11	8
Bi	15	8	0	36	11	25
U	16	15	25	9	11	0
Ge	19	8	0	18	33	25
Ga	9	0	0	36	33	8
Ba	10	3	25	9	0	8
Mn	5	3	25	9	0	8
F	8	3	25	9	0	0
Se	4	0	0	18	11	8
Tl	6	3	0	18	11	0
Co	4	3	0	0	0	8
Ni	4	3	0	0	0	8

- a view service must be setup to deliver the maps,
- an access (or download) service must be setup to provide the data,
- the data must be delivered according to a common, standard data model.

During the ProMine project, the following components were developed according to these principles:

- metadata have been provided for datasets and maps according to the ISO metadata standard (ISO 19115) and the INSPIRE profile (subset of the ISO standard);
- view services have been set up, compliant with the Web Map Service standard (WMS, specified by ISO and OGC, and selected for INSPIRE);
- an access service has been setup to deliver data according to the Web Feature Service (WFS, specified by ISO and OGC, and selected for INSPIRE);
- the Web Feature Service delivers data according to a standard data model, Earth-ResourceML (<http://www.earthresourceml.org>) developed by the IUGS/CGI (International Union of Geological Sciences / Commission for Geoscience Information, <http://www.cgi-iugs.org/>). To describe the geological aspects of mineral resources, the standard GeoSciML (<http://www.geosciml.org/>, also developed by the IUGS/CGI) has been used.

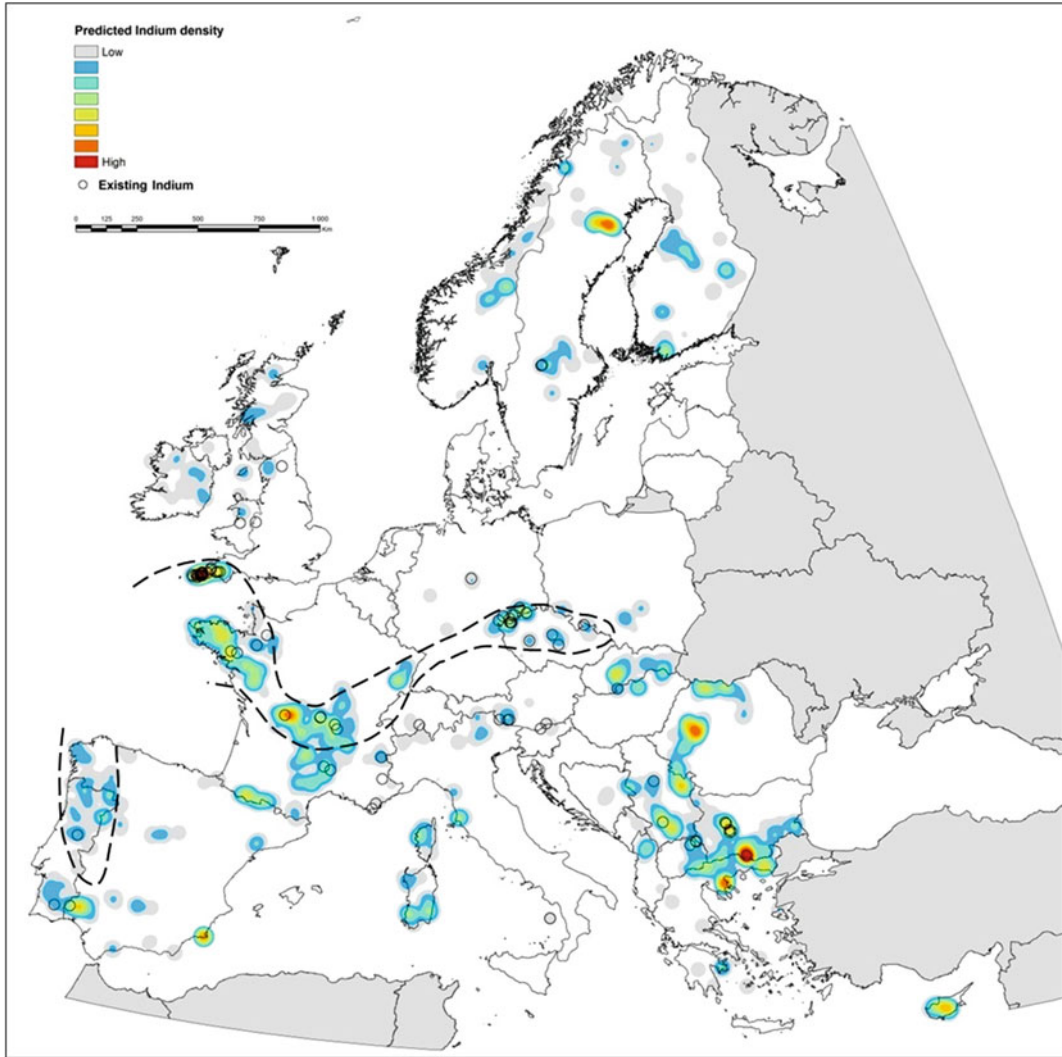


Fig. 2.9 Predictive map for indium, obtained with the database querying method, showing an “Indium belt” to the north of the Hercynian domain

All these elements are accessible from the ProMine internet portal (<http://ptrarc.gtk.fi/promine>) developed by GTK (Geological Survey of Finland). In addition, the clear separation between the ProMine portal and the web services make the maps reusable by other portals or applications. For example, the maps displaying the mineral deposits in the ProMine portal can be also displayed in the OneGeology portal (<http://onegeology.brgm.fr/>), using the ProMine WMS URL in the OneGeology portal.

It is important to note that for the ProMine databases to be fully compliant with INSPIRE and the distributed architecture principles, the data should have been managed and delivered by each data provider, and the European map should have been built by integrating all national maps. The INSPIRE principle related to this option states that the data should be managed at the “best” level, which is often the data provider. ProMine decided to implement a unique database for the following reasons:

Table 2.12 Enrichment ratios (ER) of deposit types containing tantalum

Metallogenic type	No. of occurrences	Enrichment ratio (ER)
Alkaline to Peralkaline intrusions	4	12.21
Igneous felsic	20	1.95
Igneous replacement	1	0.23

The pie chart shows the distribution of tantalum occurrences by metallogenic type. Pegmatites account for 69 occurrences (approximately 75%), Igneous felsic for 19 occurrences (approximately 21%), and Alkaline to peralkaline for 4 occurrences (approximately 4%).

Table 2.13 Polymetallic signature of tantalum-bearing deposits, by deposit type

Commodity	Global %	Pegmatites	Alkaline and peralkaline	Igneous felsic	Igneous replacement
Be	44	46	50	37	0
Nb	44	42	75	47	0
REE	42	45	100	21	0
Li	34	30	50	47	0
Sn	31	23	0	68	0
U	26	19	75	42	0
Y	25	29	25	11	0
W	9	4	0	26	0
Sc	6	7	0	5	0
Th	4	4	25	0	0
Cs	3	3	0	5	0
Cu	3	0	0	11	100
Bi	2	3	0	0	0
Mo	2	1	0	5	0
F	1	1	0	0	0

- Not all the data providers were ProMine partners, so restricting data collection to ProMine partners would not have produced full European coverage;
- Not all partners had the capacity to setup web services according to OGC/INSPIRE rules to deliver their data compliant with the standard.

Nevertheless, the system is based on the use of standards and is able to manage more than one WMS. A possible next step for ProMine would be to split the central databases into a number of separate databases (one for each provider, i.e. by Geological Survey) and to ask the providers to setup a WMS and a WFS (the same as already

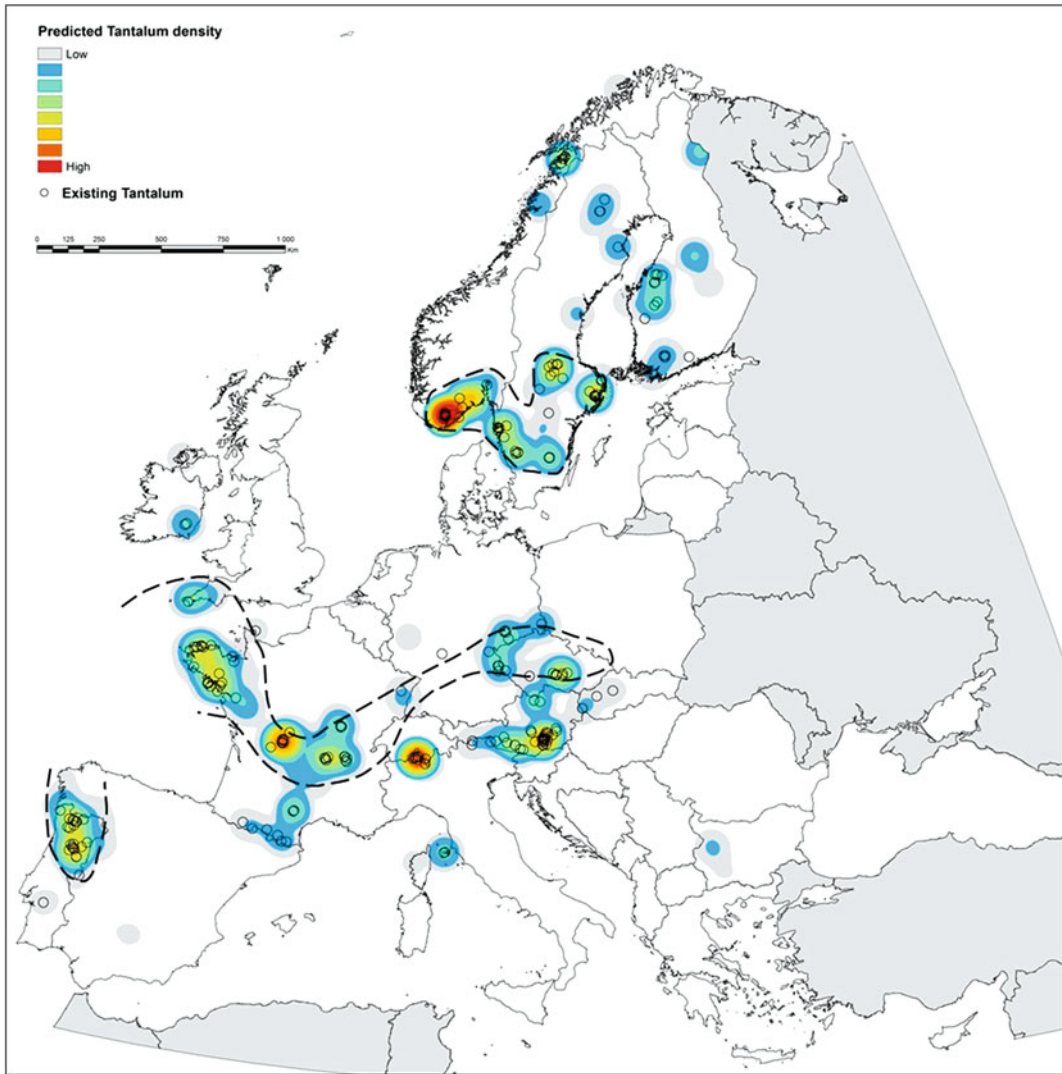


Fig. 2.10 Predictive map for tantalum, obtained with the database querying method

exists for ProMine, which would be facilitated by the use of open source software for the services).

By using real data the ProMine project has contributed to the improvement of the EarthResourceML standard and the INSPIRE rules to describe mineral resources, in terms of:

- Data model: the ProMine input is about Mining Waste, Mining Waste Measure and Exploration activity;
- Code-lists: many code-lists/vocabularies for EarthResourceML and INSPIRE have been improved from inputs by the ProMine project;
- Portrayal rules: no symbols were adopted in EarthResourceML and INSPIRE; ProMine has defined a set of symbols to display mineral deposits, mineral occurrences and anthropogenic concentrations which provide a starting point for the EarthResourceML working group.

Table 2.14 Enrichment ratios (ER) of deposit types containing cobalt

Metallogenic type	No. of occurrences	Enrichment ratio (ER)
VMS	37	1.61
Residual deposits	18	1.10
SandStone-and Shale-hosted	8	0.89
Base metals veins	39	0.67
Orogenic gold	6	0.56
Sedimentary deposits	7	0.39
Igneous felsic	6	0.24

Cobalt occurrences by type	
Mafic or ultramafic	109
Base metal veins	39
Other	36
VMS	37
Residual	18

Table 2.15 Polymetallic signature of cobalt-bearing deposits, by deposit type

Commodity	Global %	Mafic ultra mafic	VMS	Residual deposits	Base metals veins
Cu	0.87	0.86	0.84	0.11	0.90
Ni	0.83	0.94	0.49	0.94	0.38
Ag	0.19	0.09	0.46	0.06	0.28
Au	0.22	0.08	0.49	0.11	0.17
Zn	0.20	0.08	0.68	0.11	0.15
PGE	0.10	0.15	0.00	0.06	0.00
Pb	0.09	0.01	0.30	0.06	0.05
As	0.08	0.04	0.11	0.28	0.05
Cr	0.08	0.04	0.00	0.50	0.00
Mn	0.05	0.00	0.03	0.44	0.00
U	0.06	0.07	0.00	0.00	0.15
Bi	0.05	0.06	0.05	0.00	0.03
V	0.02	0.03	0.00	0.06	0.00
Ge	0.01	0.00	0.05	0.00	0.03
Sb	0.01	0.00	0.03	0.06	0.00

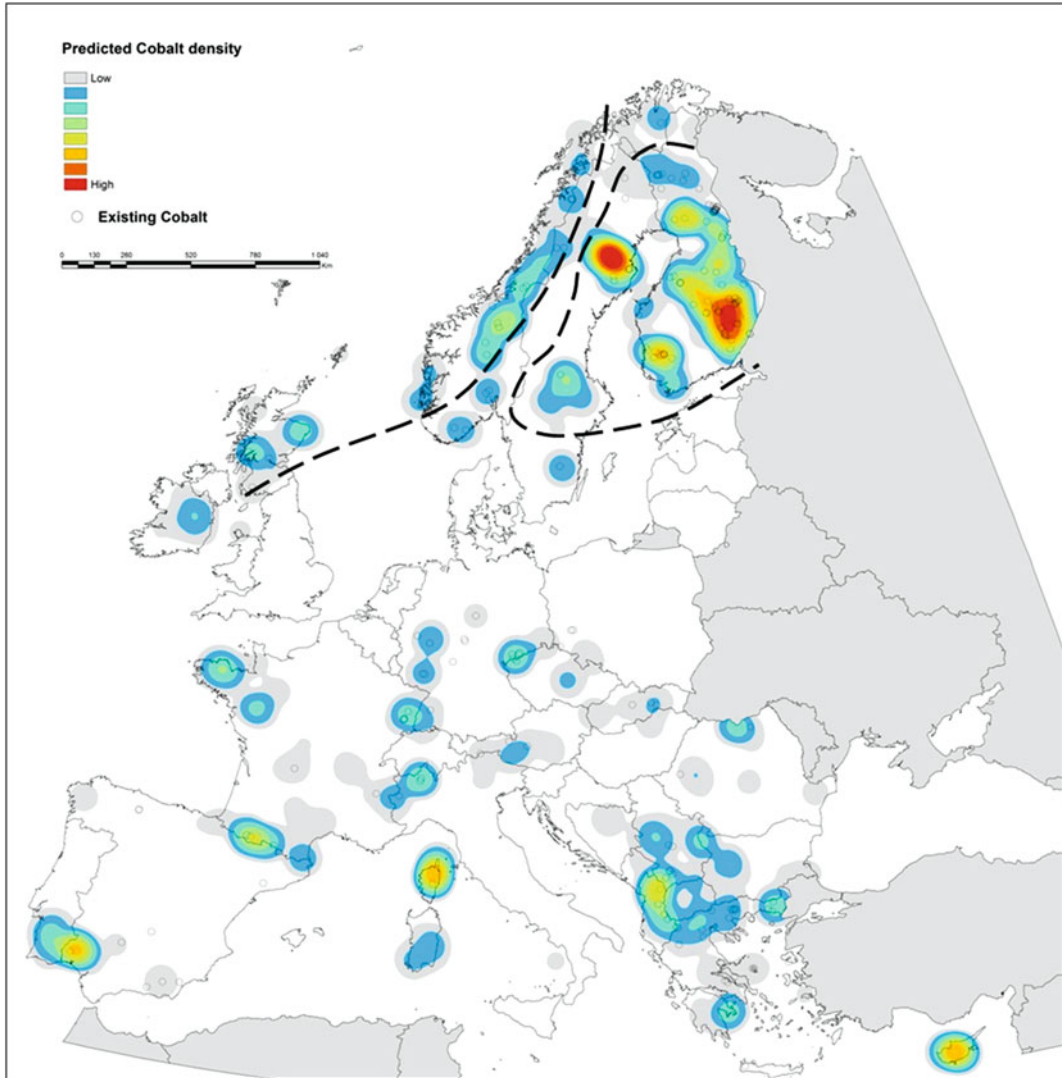


Fig. 2.11 Predictive map for cobalt, obtained with the database querying method

2.7 Conclusions

The ProMine databases described here are a significant deliverable from the ProMine project and a crucial step toward a better assessment of primary and secondary resources in Europe. This will strengthen the extractive industry and help secure the European supply of mineral resources, including critical and ‘green’ commodities. The MD database provides a new consistent and

detailed dataset, containing a considerable amount of information that allows mineral resource potential and predictive assessment studies to be carried out. Preliminary assessments at the continental scale have been presented, but many other workers will be able to benefit from the ProMine MD dataset in the future for various purposes and at a variety of scales. The AC database is the first continental-scale dataset on mining and mineral processing wastes in Europe. It will need to be improved, by completing

tonnages and grades data for instance, but already constitutes a crucial step towards a better assessment of secondary mineral resources in Europe.

Another significant output of ProMine WPI is the development of a methodology that allows calculation of predictive maps for critical commodities. Classical methods (reviews in Carranza 2009b, 2011) are generally restricted to predicting major metallogenic types and their associated main commodities. Typical examples are gold-rich porphyries, Au-Ag epithermal deposits, etc. (see Billa et al. 2004 and Roy et al. 2006). The problem with critical commodities (e.g. Ge, Ga) is that they are rarely the main commodities in a deposit. They are most commonly found in the ores of a related commodity the presence or absence of which cannot be used to predict the possible presence of a deposit of the critical material. For instance, Cu–Mo porphyries may or may not contain Re. The presence of Mo is a prerequisite, but alone this is not sufficient. Similarly, Zn deposits may or may not contain Ge. The method developed for ProMine is strongly dependent on the quality of the descriptions entered in the database (description of all commodities contained in a deposit and of the mineralogy), their accuracy, their reliability and their completeness. The statistical approach adopted allows better characterization of the ‘rules’ governing the presence or the absence of the targeted commodity. By comparing exploited deposits for which the targeted commodity has never been investigated to those where it has been identified, the definition of possible new targets and prospective districts can be made.

The ProMine databases, together with the added-value layers derived from them (mineral potential and predictive maps) are publicly delivered through an internet web portal and web services. This ProMine portal complies with the most recent directives in terms of data

visualization and delivery. It also provides a core knowledge base that will be very useful for new EU-FP7 and Horizon 2020 projects (e.g. EURARE, Minerals4EU).

Acknowledgments The authors wish to thank all WPI ProMine partners for their fruitful collaboration and contributions: Soile Aatos (GTK, Finland), Vassiliki Aggelatou (IGME, Greece), Nikolaos Arvanitidis (IGME, Greece; now at SGU, Sweden), Anne-Sophie Audion (BRGM, France), Dimitrios Ballas (Hellas Gold S.A., Greece), Christos Christidis (IGME, Greece), Alexandros Demetriadis (IGME, Greece), Dimitrina Dimitrova (Bulgarian Academy of Sciences, Bulgaria), Pasi Eilu (GTK, Finland), Augusto Filipe (LNEG, Portugal), Emmy Gazea (Hellas Gold S.A., Greece), Philippe Gentilhomme (BRGM, France), Eric Gloaguen (BRGM, France), Jérôme Gouin (BRGM, France), Dimitrios Iliopoulos (IGME, Greece), Carlos Inverno (LNEG, Portugal), Christian Joannes (BRGM, France), Maria João Batista (LNEG, Portugal), Tuomo Karinen (GTK, Finland; now at Mustavaaran Kaivos Oy, Finland), Teemu Karlsson (GTK, Finland), Esa Kauniskangas (GTK, Finland), Panu Lintinen (GTK, Finland), Timo Mäki (Pyhäsalmi Mine Oy, Finland), Frédéric Maldan (BRGM, France), Ioannis Marantos (IGME, Greece), Santiago Martín Alfageme (IGME, Spain), João Matos (LNEG, Portugal), Maël Meliani (BRGM, France), Constantinos Michael (IGME, Greece), Wojciech Mizera (KGHM Cuprum, Poland), Vassilka Mladenova (Sofia University, Bulgaria), Javier Navas (IGME, Spain), Mateusz Niedbal (KGHM Cuprum, Poland), Ewan Pelleter (BRGM, France; now at IFREMER, France), George Perantonis (Hellas Gold S.A., Greece), Jean-Claude Picot (BRGM, France), Jacek Pyra (KGHM Cuprum, Poland), Francis Ralay (BRGM, France), Ignace Salpeteur (BRGM, France), Helena Santana (LNEG, Portugal), Todor Serafimovski (Goce Delčev University, FYROM), Juha Strengell (GTK, Finland), Michal Strzelecki (KGHM Cuprum, Poland), Goran Tasev (Goce Delčev University, FYROM), François Tertre (BRGM, France), Fernando Tornos (IGME, Spain) and George Tudor (Institutul Geologic al României, Romania). The authors also want to kindly thank ProMine’s Project Leader Juha KAJA (GTK, Finland) for his constant support. Detailed reviews by Gus GUNN and Martiya SADEGHI are kindly acknowledged and have substantially contributed to improve the initial manuscript. The ProMine project was funded by the European Community’s Seventh Framework Programme (FP7/2007-2013) under grant agreement no. 228559.

Appendix 1

Class Threshold Values for Selected Commodities

Commodity	Description	Class threshold values (in metric tons)			
		Super-large deposits (class A)	Large deposits (class B)	Medium deposits (class C)	Small deposits (class D)
Ag	Silver (metal)	10,000	2,500	500	100
Al	Aluminum (Bauxite ore)	1,000,000,000	100,000,000	10,000,000	1,000,000
Au	Gold (metal)	500	100	10	1
Be	Beryllium (BeO)	20,000	2,000	200	50
Bi	Bismuth (metal)	20,000	2,000	200	2
Brt	Barite (BaSO ₄)	5,000,000	1,000,000	200,000	50,000
Cd	Cadmium (metal)	10,000	2,000	500	100
Co	Cobalt (metal)	500,000	50,000	2,000	200
Cr	Chrome (Cr ₂ O ₃)	25,000,000	5,000,000	1,000,000	200,000
Cu	Copper (metal)	10,000,000	1,000,000	100,000	10,000
Fe	Iron (metal)	1,000,000,000	100,000,000	10,000,000	1,000,000
Fl	Fluorite (CaF ₂)	5,000,000	1,000,000	200,000	50,000
Ga	Gallium (metal)	100	50	10	1
Ge	Germanium (metal)	500	100	20	5
Gr	Graphite (substance)	10,000,000	1,000,000	100,000	10,000
Hf	Hafnium (metal)	10,000	1,000	100	10
Hg	Mercury (metal)	50,000	5,000	500	100
In	Indium (metal)	500	100	25	5
Li	Lithium (Li ₂ O)	1,000,000	100,000	50,000	5,000
Mg	Magnesium, magnesite (MgCO ₃)	100,000,000	10,000,000	1,000,000	100,000
Mn	Manganese (metal)	100,000,000	10,000,000	1,000,000	100,000
Mo	Molybdenum (metal)	500,000	100,000	5,000	1,000
Nb	Niobium–columbium (Nb ₂ O ₅)	1,000,000	100,000	10,000	2,000
Ni	Nickel (metal)	2,000,000	500,000	20,000	2,000
PbZn	Lead + Zinc (metal)	10,000,000	1,000,000	100,000	10,000
Pltd	Platinoids, group (metal)	1,000	100	10	1
Rb	Rubidium (Rb ₂ O)	1,000	100	10	1
Re	Rhenium (metal)	5,000	500	50	5
REE	Rare Earths (RE ₂ O ₃)	1,000,000	100,000	10,000	1,000
Sb	Antimony (metal)	100,000	25,000	2,000	1,000
Se	Selenium (substance)	5,000	1,000	250	50
Sn	Tin (metal)	200,000	25,000	1,000	100
Ta	Tantalum (Ta ₂ O ₅)	25,000	2,000	1,000	200

(continued)

Commodity	Description	Class threshold values (in metric tons)			
		Super-large deposits (class A)	Large deposits (class B)	Medium deposits (class C)	Small deposits (class D)
Ti	Titanium, general (TiO ₂)	20,000,000	2,000,000	200,000	20,000
V	Vanadium (metal)	2,000,000	200,000	20,000	2,000
W	Wolfram (WO ₃)	200,000	50,000	5,000	500
Zr	Zirconium (ZrO ₂)	1,000,000	100,000	10,000	1,000

References

- Anderson I.K., Ashton J.H., Boyce A.J., Fallick A.E., Russell M.J. (1998). Ore Depositional processes in the Navan Zn–Pb deposit, Ireland. *Economic Geology*, 93, 535–563.
- Arribas A., Cunningham C.G., Rytuba J.J., Rye R.O., Kelly W.C., Podwysoccki M.H., McKee E.H., Tosdal R. M., (1995). Geology, geochronology, fluid inclusions, and isotope geochemistry of the Rodalquilar gold alunite deposit, Spain. *Economic Geology*, 90, p. 795–822
- Arvanitidis N.D., Michael C., Christidis C., Cassard D., Perantonis G., Bertrand G., Kaja J., Ballas D. and Bakalis V. (2012). GIS-Based datasets of mineral deposits and man-made resources as valuable exploration tools for discovering potential ore deposits in Greece. 7th EUROGEO, Bologna, June 12th–15th 2012, Proceedings, 551–552.
- Ashton J. (2005). The Navan carbonate-hosted Zn–Pb deposit, Ireland: Lat. 53°39' N, Long. 6°41' W. In: Special Issue on Geodynamics and Ore Deposit Evolution in Europe (D. Blundell, N. Arndt, P.R. Cobbold and C. Heinrich Eds.). *Ore Geology Reviews*, 27, 270.
- Audion A.S., Piantone P. (2012). Panorama 2011 du marché du tantale. Final report. BRGM/RP-61343-FR, pp. 91. <http://www.mineralinfo.fr/panoramas.html>.
- Autran A., Derré C., Fonteilles M., Guy B., Soler P., Toulhoat P. (1980). Genèse des skarns à tungstène dans les Pyrénées. In Johan Z. (Coordinator), *Minéralisations liées aux granitoïdes*. Mémoire du BRGM, 99, 193–319.
- Bailly L., Bouchot V., Bény C., Milesi J.-P. (2000). Fluid inclusion study of stibnite using infrared microscopy: an example from the Brouzils antimony deposit (Vendée, Armorican Massif, France). *Economic Geology*, 95 (1), 221–226.
- Barbieri M., Masi U., Tolomeo L. (1977). Geochemical evidence on the origin of the epithermal fluorite deposit at Monte Delle Fate near Cerveteri (Latium, Central Italy). *Mineralium Deposita*, 12, 393–398.
- Bierlein F.P., Murphy F.C., Weinberg R.F., Lees T. (2006). Distribution of orogenic gold deposits in relation to fault zones and gravity gradients: targeting tools applied to the Eastern Goldfields, Yilgarn Craton, Western Australia. *Mineralium Deposita*, 41, 107–126.
- Billa M., Cassard D., Lips A.L.W., Bouchot V., Tourlière B., Stein G. and Guillou-Frotier L. (2004). Predicting gold-rich epithermal and porphyry systems in the central Andes with a continental-scale metallogenic GIS. *Ore Geology Reviews*, 25, 39–67.
- Bonham-Carter G.F. (1994). Geographic information systems for geoscientists. Modelling with GIS Computer Methods in the Geosciences, vol. 13. Pergamon, New York, 398 pp.
- Bonham-Carter G.F., Agterberg F.P., Wright D.F. (1989). Weights of evidence modeling: a new approach to mapping mineral potential. In: Agterberg F.P., Bonham-Carter G.F. (Eds.), *Statistical Applications in Earth Sciences*, Geological Survey of Canada, 89 (9), 171–183.
- Bouchot V., Ledru P., Lerouge C., Lescuyer J.-L., Milesi J.-P. (2005). Late Variscan mineralizing systems related to orogenic processes: The French Massif Central. In: Special Issue on Geodynamics and Ore Deposit Evolution in Europe (D. Blundell, N. Arndt, P.R. Cobbold and C. Heinrich Eds.). *Ore Geology Reviews*, 27, 169–197.
- Bouchot V., Milesi J.-P., Ledru P. (2000). Crustal-scale hydrothermal palaeofield and related Au, Sb, W orogenic deposits at 310–305 Ma (French Massif Central, Variscan Belt). *SGA News*, 10, 6–12.
- Bouchot V., Milesi J.-P., Lescuyer J.-L., Ledru P. (1997). Les minéralisations aurifères de la France dans leur cadre géologique autour de 300 Ma. *Chronique de la Recherche Minière*, 528, 13–62.
- Bougrain L., Gonzalez M., Bouchot V., Cassard D., Lips A.L.W., Alexandre F., Stein G. (2003). Knowledge recovery for continental-scale mineral exploration by neural networks. *Natural Resources Research*, 12 (3), 173–181.
- Bril H. (1982). Fluid inclusions study of Sn–W–Au, Sb– and Pb–Zn mineralizations from the Brioude-Massiac district (French Massif Central). *Mineralogy and Petrology*, 30, 1–16.
- Carranza E.J.M. (2009a). Controls on mineral deposit occurrence inferred from analysis of their spatial pattern and spatial association with geological features. *Ore Geology Reviews*, 35, 383–400.

- Carranza E.J.M. (2009b). Geochemical anomaly and mineral prospectivity mapping in GIS. *Handbook of Exploration and Environmental Geochemistry*, Vol. 11, M. Hale (Series Editor), Elsevier, 351 pp.
- Carranza E.J.M. (2011). Geocomputation of mineral exploration targets. *Computers & Geosciences* 37, 1907–1916.
- Cassard D., Bertrand G., Maldan F., Gaál G., Juha K., Aatos S., Angel J.M., Arvanitidis N., Ballas D., Billa M., Christidis C., Dimitrova D., Eilu P., Filipe A., Grazea E., Inverno C., Kauniskangas E., Maki T., Matos J., Meliani M., Michael C., Mladenova V., Navas J., Niedbal M., Perantonis G., Pyra J., Santana H., Serafimovski T., Serrano J.J., Strengel J., Tasev G., Tornos F., Tudor G. (2012). ProMine pan-European Mineral Deposit database: a new dataset for assessing primary mineral resources in Europe. *Mineral Resources Potential Maps : a Tool for Discovering Future Deposits*. 12th-14th March 2012, Nancy, France
- Cassard D., Billa M., Lambert A., Picot J.-C., Husson Y., Lasserre J.-L., Delor C. (2008). Gold predictivity mapping in French Guiana using an expert-guided data-driven approach based on a regional-scale GIS. *Ore Geology Reviews*, 34, 471-500.
- Cassard D., Lambert A. (2007). Le SIG Mines France : <http://sigminesfrance.brgm.fr/>
- Cassard D., Lips A.L.W., Leistel J.-M., Itard Y., Debeglia-Marchand N., Guillou-Frottier L., Spakman W., Stein G., Husson Y. (2004). Understanding and assessing European mineral resources – a new approach using GIS Central Europe. *Schweizerische Mineralogische und Petrographische Mitteilungen*, 84, 3-24.
- Černý P., Ercit T.S. (2005). Classification of granitic pegmatites. *Canadian Mineralogist*, 43, 2005–2026.
- Cooke D.R., Hollings P., Walshe J.L. (2005). Giant porphyry deposits: characteristics, distribution and tectonic controls. *Economic Geology*, 100, 801-818.
- Cuney M., Marignac C., Weisbrod A. (1992). The Beauvoir Topaze-Lepidolite Albite granite (Massif-Central, France): the disseminated magmatic Sn-Li-Ta-Nb-Be mineralization. *Economic Geology*, 87, 1766-1794.
- Derre C. (1982). Caractéristiques de la distribution des gisements d'étain et de tungstène dans l'Ouest de l'Europe. *Mineralium Deposita*, 17, 55 – 77.
- Eilu P., Weihed P. (2005). Fennoscandian Shield – Orogenic gold deposits, *Ore Geology Reviews*, 27, 326-327.
- Eilu P., Ahtola, T., Äikäs, O., Halkoaho, T., Heikura, P., Hulkki, H., Iljina, M., Juopperi, H., Karinen, T., Kärkkäinen, N., Konnunaho, J., Kontinen, A., Kontoniemi, O., Korkiakoski, E., Korsakova, M., Kuivasaari, T., Kyläköski, M., Makkonen, H., Niiranen, T., Nikander, J., Nykänen, V., Perdahl, J.-A., Pohjolainen, E., Räsänen, J., Sorjonen-Ward, P., Tiainen, M., Tontti, M., Torppa, A. & Västi, K. 2012. Metallogenic areas in Finland. In *Mineral deposits and metallogeny of Fennoscandia* (P. Eilu Ed.), Geological Survey of Finland, Special Paper 53, 207–342.
- Eilu P., Sorjonen-Ward P., Nurmi P., Niiranen T. (2003). A review of gold mineralization styles in Finland. *Economic Geology*, 98, 1329-1353.
- Einaudi M.T., Meinert L.D., Newberry R.J. (1981). Skarn Deposits. In: B.J. Skinner (Ed.) *Seventy-fifth Anniversary Volume, 1906-1980*, *Economic Geology*, 317-391.
- European Commission (2010). Critical raw materials for the EU, Report of the ad-hoc working group on defining critical raw materials. European Commission, Raw Materials Supply Group, 30 July 2010, 85 pp.
- European Commission (2011). Communication from the Commission to the European Parliament, the Council, the European Economic and Social Committee and the Committee of the Regions – Tackling the challenges in commodity markets and on raw material. COM (2011) 25 final.
- European Parliament (2006). DIRECTIVE 2006/12/EC OF THE EUROPEAN PARLIAMENT AND OF THE COUNCIL of 5 April 2006 on waste (<http://eur-lex.europa.eu/LexUriServ/LexUriServ.do?uri=OJ:L:2006:114:0009:0021:en:PDF>)
- European Parliament (2008). DIRECTIVE 2008/98/EC OF THE EUROPEAN PARLIAMENT AND OF THE COUNCIL of 19 November 2008 on waste and repealing certain Directives. (<http://eur-lex.europa.eu/LexUriServ/LexUriServ.do?uri=OJ:L:2008:312:0003:0030:en:PDF>)
- Franke W., Matte P., Tait J. (2005). Europe: Variscan orogeny. *Encyclopedia of Geology*, vol. 2, Elsevier, Oxford, 75–85.
- Gaál G., Cassard D., Bertrand G., Schaeben H., Royer J.J., Weihed P., Skyttä P. and Bauer T. (2012). Pan European Mineral Resource Assessment: The ProMine Project', 34th Session of the International Geological Congress (IGC). Brisbane, Australia, 5-10 August. Abstract on CD-ROM.
- Goldfarb R.J., Groves D.I., Gardoll S. (2001). Orogenic gold and geologic time: A global synthesis. *Ore Geology Reviews*, 18, 1-75.
- Grenne T., Ihlen P.M., Vokes F.M. (1999). Scandinavian Caledonide metallogeny in a plate tectonic perspective. *Mineralium Deposita*, 34, 422–471.
- Groves D.I., Goldfarb R.J., Gebre-Mariam M., Hagemann S. G., Robert F. (1998). Orogenic gold deposits: A proposed classification in the context of their crustal distribution and relationship to other gold deposit types. *Ore Geology Reviews*, 13, 7-27.
- Hallberg A., Bergman T., Gonzalez J., Larsson D., Morris G. A., Perdahl J. A., Ripa M., Niiranen T., Eilu P. (2012). Metallogenic areas in Sweden. In *Mineral deposits and metallogeny of Fennoscandia* (P. Eilu Ed.), Geological Survey of Finland, Special Paper 53, 139–206.
- Heinrich C. A., Neubauer F. (2002). Cu–Au–Pb–Zn–Ag metallogeny of the Alpine–Balkan–Carpathian–Dinaride geodynamic province. *Mineralium Deposita*, 37, 533–540.

- Higuera P., Munha J., Oyarzun R., Tassinari C.G., Ruiz I.R. (2005). First lead isotopic data for cinnabar in the Almadén district (Spain): implications for the genesis of the mercury deposits. *Mineralium Deposita*, 40, 115–122.
- Hitzman M.W., Selley D., Bull S. (2010). Formation of sedimentary rock-Hosted stratiform copper deposits through Earth history. *Economic Geology*, 105, 627–639.
- Hocquard C., Deschamps Y. (2008). Strategic metals, high-tech metals, environmentally “green metals”: a convergence. IGC 33rd, Oslo, August 6-14, 2008. Abstracts on CD-ROM.
- Höll R., Kling M., Schroll E. (2007). Metallogensis of germanium - A review. *Ore Geology Reviews*, 30, 145–180.
- Jankovic S. (1997). The Carpatho-Balkanides and adjacent area: a sector of the Tethyan Eurasian metallogenic belt. *Mineralium Deposita*, 32, 426–433.
- Jebra M., Higuera P., Marcoux E., Lorenzo S. (2002). Geology and geochemistry of high-grade, volcanic rock-hosted, mercury mineralization in the Nuevo Entredicho deposit, Almaden, Spain. *Mineralium Deposita*, 37, 421–432.
- Jowitt S. M. (2008). Field, petrological and geochemical constraints on the release of base metals into hydrothermal fluids in Cyprus-type Volcanogenic Massive Sulphide (VMS) systems: an investigation of the Spilia-Kannavia epidosite zone, Troodos ophiolite, Cyprus. PhD Thesis, University of Leicester, 268 pp.
- Kärkkäinen N., Appelqvist H. (1999). Genesis of a low-grade apatite-ilmenite-magnetite deposit in the Kauhajärvi gabbro, western Finland. *Mineralium Deposita*, 34, 754–769.
- Kemp L.D., Bonham-Carter G.F., Raines G.L., Looney, C.G. (2001). Arc-SDM: Arcview extension for spatial data modelling using weights of evidence, logistic regression, fuzzy logic and neural network analysis. <http://www.ige.unicamp.br/sdm/>
- Knox-Robinson C.M., Groves D.I. (1997). Gold prospectivity mapping using a Geographic Information System (GIS) with examples from the Yilgarn Block of Western Australia. *Chronique de la Recherche Minière* 529, 127–138.
- Kreuzer O.P., Markwitz V., Porwal A.K., McCuaig T.C. (2010). A continent-wide study of Australia’s uranium potential. Part I: GIS-assisted manual prospectivity analysis. *Ore Geology Reviews*, 38, 334–366.
- Large D., Walcher E. (1999). The Rammelsberg massive sulphide Cu–Zn–Pb–Ba–Deposit, Germany: an example of sediment-hosted, massive sulphide mineralisation. *Mineralium Deposita*, 34, 522–538.
- Ledru P., Costa S., Echtler H. (1994). Structure. In: Keppie, J.D. (Ed.) *Pre-Mesozoic geology in France and related areas. Part III, The Massif Central*, Springer-Verlag, Berlin, 305–323.
- Leistel J.M., Marcoux E., Thieblemont D., Quesada C., Sánchez A., Almodóvar G.R., Pascual E., Sáez R. (1998). The volcanic-hosted massive sulphide deposits of the Iberian Pyrite Belt. Review and preface to the special issue. *Mineralium Deposita*, 33, 2–30.
- Lerouge C., Bouchot V. (2005). Châtaigneraie—example of a late Variscan tungsten district: Southern French Massif Central: Lat. 44°40' N, Long. 2°35' E. In: *Special Issue on Geodynamics and Ore Deposit Evolution in Europe* (D. Blundell, N. Arndt, P.R. Cobbold and C. Heinrich Eds.). *Ore Geology Reviews*, 27, 200–201.
- Lescuyer J.L., Bouchot V., Cassard D., Feybesse J.L., Marcoux E., Moine B., Piantone P., Tegye M., Tollon F. (1993). Le gisement aurifère de Salsigne (Aude, France): une concentration syntectonique tardivariscane dans les sédiments détritiques et carbonatés de la Montagne-Noire. *Chronique de la Recherche Minière*, 512, 3–73.
- Lips A.W., Herrington R.J., Stein G., Kozelj D., Popov K., Wijbrans J.R. (2004). Refined timing of porphyry copper formation in the Serbian and Bulgarian portions of the Cretaceous Carpatho-Balkan Belt. *Economic Geology*, 99, 601–609.
- Marignac C., Cuney M. (1999). Ore deposits of the French Massif Central: insight into the metallogensis of the Variscan collision belt. *Mineralium Deposita*, 34, 472–504.
- Martinez C., Tornos F., Casquet C., Galindo C. (2005). The Aguablanca Ni–(Cu–PGE) deposit, SW Spain, Ossa Morena Zone. *Ore Geology Reviews*, 27, 164–165.
- Matte P. (1994). Accretionary history and crustal evolution of the Variscan belt in Western Europe. *Tectonophysics*, 10, 309–337.
- Moon C.J. (2010). Geochemical exploration in Cornwall and Devon: a review. *Geochemistry: Exploration, Environment, Analysis*, 10, 331–351. AAG/Geological Society of London Ed.
- Morgan J.W., Stein H.J., Hannah J.L., Markey R.J., Wiszniewska J. (2000). Re-Os study of Fe-Ti-V oxide and Fe-Cu-Ni sulphide deposits, Suwalki Anorthosite Massif, northeast Poland. *Mineralium Deposita*, 35, 391–401.
- Muchez P., Heijlen W., Banks D., Blundell D., Boni M., Grandia F. (2005). Extensional tectonics and the timing and formation of basin-hosted deposits in Europe. *Ore Geology Reviews*, 27, 241–267.
- Neubauer F., Lips A., Kouzmanov K., Lexa J., Ivășcanu P. (2005). Subduction, slab detachment and mineralization: The Neogene in the Apuseni Mountains and Carpathians. In: *Special Issue on Geodynamics and Ore Deposit Evolution in Europe* (D. Blundell, N. Arndt, P.R. Cobbold and C. Heinrich Eds.). *Ore Geology Reviews*, 27, 13–44.
- Noronha E., Doria A., Dubessy J. and Charoy B. (1991). Characterization and timing of the different types of fluids present in the barren and ore-veins of the W-Sn deposit of Panasqueira, Central Portugal. *Mineralium Deposita*, 27, 72–79.
- Nykänen V. (2008). Spatial data analysis as a tool for mineral prospectivity mapping. PhD Thesis, Geological Survey of Finland, Espoo, 27 pp., and 6 original articles.

- Nykänen V., Groves D.I., Ojala V.J., Gardoll S.J. (2008). Combined conceptual/empirical prospectivity mapping for orogenic gold in the northern Fennoscandian Shield, Finland. *Australian Journal of Earth Sciences*, 55 (1), 39-59.
- Oszczepalski S., Blundell D. (2005). Kupferschiefer copper deposits of SW Poland: Lubin-Sieroszowice District. *Ore Geology Reviews*, 27, p. 271.
- Petrasccheck W.E. (1989). The genesis of allochthonous karst-type bauxite deposits of southern Europe. *Mineral. Deposita*, 24, 77-81.
- Plimer I.R. (1987). Fundamental parameters for the formation of granite-related tin deposits. *Geologische Rundschau*, 76/1, 23-40.
- Raith J.G., Stein H.J. (2006). Variscan ore formation and metamorphism at the Felbertal scheelite deposit (Austria): constraining tungsten mineralization from Re-Os dating of molybdenite. *Contributions to Mineralogy and Petrology*, 152, 505-521.
- Rehnström E.F. (2003). Geochronology and petrology of the Tielma Magmatic Complex, northern Swedish Caledonides – results and tectonic implications. *Norwegian Journal of Geology*, 83, 243-257.
- Romeo I., Lunar R., Capote R., Quesada C., Dunning G. R., Pina R., Ortega L. (2006). U-Pb age constraints on Variscan magmatism and Ni-Cu-PGE metallogeny in the Ossa-Morena zone (SW Iberia). *Journal of the Geological Society*, 163 (5), 837-846.
- Romer R.L., Öhlander B. (1994). U-Pb age of the Yxsjöberg Tungsten-Skarn deposit, Sweden. *GFF*, 116(3), 161-166.
- Roy R., Cassard D., Cobbold P.R., Rossello E.A., Billa M., Bailly L., Lips A.L.W. (2006). Predictive mapping for copper-gold magmatic-hydrothermal systems in NW Argentina: use of a regional-scale GIS, application of an expert-guided data-driven approach, and comparison with results from a continental-scale GIS. *Ore Geology Reviews*, 29, 260-286.
- Sánchez S.M.T., Benito M.C. M., Pérez, M.L.C. (2009). Mineralogical and physiochemical evolution of the Los Santos scheelite skarn, Salamanca, NW Spain. *Economic Geology*, 104(7), 961-995.
- Sandstad J. S., Bjerkgård T., Boyd R., Ihlen P., Korneliussen A., Nilsson L. P., Often M., Eilu P., Hallberg A. (2012). Metallogenic areas in Norway. In *Mineral deposits and metallogeny of Fennoscandia* (P. Eilu Ed.), Geological Survey of Finland, Special Paper 53, 35–138.
- Schärer U., Wilmar, E., Duchesne J.C. (1996). The short duration and anorogenic character of anorthosite magmatism: U-Pb dating of the Rogaland complex, Norway. *Earth and Planetary Science Letters*, 139, 335–350.
- Schneider J. (2005). SEDEX/VMS deposits in the Rhe-nohercynian Zone, Germany Rammelsberg. *Ore Geology Reviews* 27, p. 268.
- Schwarz-Schampera U., Herzig P.M. (2002). *Indium. Geology, mineralogy and economics*. Springer-Verlag, Berlin, Heidelberg, New York, 276 pp.
- Singer D. A., Berger V. I., Moring B. C. (2008). *Porphyry copper deposits of the world: database and grade and tonnage models*. U.S.G.S. Open-File Report 2008-1155, 45 pp.
- Talvitie J., Paarma H. (1980). Precambrian basic magmatism and the Ti-Fe ore formation in central and northern Finland. *Geological Survey of Finland Bulletin*, 307, 98–107.
- Thomassin J.F., Charbonnier P., Angel J.M., Boudot A., Fauconnier D. (2001). Déchets miniers européens. Notice d'utilisation de la base DECHMINUE, issue des données du rapport "Mining Waste Management" de la DG Environnement. BRGM Report RP-51393-FR, 50 pp.
- Tkachev A., Cassard D., Cherkasov, S., Arbuzova E., Gateau, C., Maldan F., Ivashenko V., Debeglia N., Husson Y., Golubev A., Smolkin V., Leistel J.-M. (2008). Kola-Karelia GIS. Mineral deposits of the eastern part of the Fennoscandian Shield. NavigaSIG CD-ROM v. 1.0, July 2008, Russian-French Metallogenic Laboratory, Moscow. ISBN978-5-9900765-3-2.
- Tornos F., Casquet C., Rodriguez Pevida L., Velasco F. (2005). The iron oxide - (Cu-Au) deposits of SW Iberia: Fregenal-Burguillos-Cala district. *Ore Geology Reviews*, 27, 166-167.
- UNESCO (1984). Explanatory memoir of the metallogenic map of Europe and neighbouring countries, 1:2,500,000. *Earth Sciences*, 17, 560 pp.
- Vaasjoki M., Sorjonen-Ward P., Lavikainen S. (1993). U-Pb age determinations and sulphide Pb-Pb characteristics from the late Archaean Hattu schist belt, Ilomantsi, eastern Finland. *Geological Survey of Finland, Special Paper* 17, 103–131.
- Wanhainen C., Billström, K., Martinsson O., Stein H., Nordin R. (2005). 160 Ma of magmatic/hydrothermal activity in the Gällivare area: Re-Os dating of molybdenite and U-Pb dating of titanite from the Aitik Cu-Au-Ag deposit, northern Sweden. *Mineralium Deposita*, 40, 435–447.
- Webster J., Thomas R., Förster H.-J., Seltmann R., Tappe, C. (2004). Geochemical evolution of halogen-enriched granite magmas and mineralizing fluids of the Zinnwald tin-tungsten mining district, Erzgebirge, Germany. *Mineralium Deposita*, 39, 452-472.
- Weihed P. (2001). A review of Palaeoproterozoic intrusive hosted Cu-Au-Fe-oxide deposits in northern Sweden. In Weihed P. (Ed.): *Economic Geology Research*, 1, 4-32.
- Weihed P., Arndt N., Billström C., Duchesne J.C., Eilu P., Martinsson O., Papunen H., Lahtinen R. (2005). Precambrian geodynamics and ore formation: The Fennoscandian Shield. In: *Special Issue on Geodynamics and Ore Deposit Evolution in Europe* (D. Blundell, N. Arndt, P.R. Cobbold and C. Heinrich Eds.). *Ore Geology Reviews* 27, 273–322.
- Weihed P., Eilu P. (2005). Fennoscandian Shield - Proterozoic VMS deposits. In: *Special Issue on Geodynamics and Ore Deposit Evolution in Europe*

- (D. Blundell, N. Arndt, P.R. Cobbold and C. Heinrich Eds.). *Ore Geology Reviews*, 27, 324–325.
- Weihed P., Eilu P., Larsen R. B., Stendal H., Tontti M. (2008). Metallic mineral deposits in the Nordic countries. *Episodes*, 31 (1), 125-132.
- Williamson B.J., Shaw A., Downes H., Thirlwall M.F. (1996). Geochemical constraints on the genesis of Hercynian two-mica leucogranites from the Massif Central, France. *Chemical Geology*, 127, 25–42.
- Woodard J. (2010). Genesis and Emplacement of Carbonatites and Lamprophyres in the Svecofennian Domain. Academic Dissertation, University of Turku, Finland, 50 pp.
- Woolley A.R., Kjarsgaard B.A. (2008). Carbonatite occurrences of the world: map and database. Geological Survey of Canada, Open File 5796, 28pp.

GST: A Network Based Datastore for Geoscience Data and Geomodels and Its Implementation—ProMine’s Contribution Towards Interoperability

Paul Gabriel, Jan Gietzel, Ha Hai Le
and Helmut Schaben

Abstract

A task of the EU funded project ProMine “Nano-particle products from new mineral resources in Europe” coordinated by the Geological Survey of Finland (GTK) is spatial geomodelling of mineralized belts and development of spatio-temporal geomodels. An essential prerequisite is a genuine data model to manage geoscience data and geoscience models efficiently towards a network based 3D/4D GeoScience Data Base and Geoscience Information System (GSIS) contributing to interoperability of project partners and eventually to a Geodata Infrastructure.

3.1 Introduction and Motivation

GST, spelled out “Geosciences in Space and Time” is our software system to provide interoperability to facilitate geoscientific communication. It is based on a unique flexible data model for (i) geoscience data (“geodata”) comprising geometrical, topological, and geological, geophysical, geochemical, topographical, etc. data, and (ii) geoscience models (“geomodels”) and the geobjects they are built of with some

geomodelling software, e.g. gOcad™, Move™ and many others. Our data model is easy to extend, and the software system is easy to customize to a given environment. To account for legal issues, a central database server shared by cooperating partners to hold all data is not required as long as networking partners refer to the data model.

This paper is meant to document GST’s concept as well as its actual implementation. Our GST system features a 3-tier architecture of client, middleware, and server. It encompasses several components, in particular web and other services, and complies with existing norms or standards and quasi standards as well as widely accepted models like Markup Languages (ML).

P. Gabriel · J. Gietzel · H.H. Le · H. Schaben (✉)
Geomathematics and Geoinformatics, Department
of Geophysics and Geoinformatics,
TU Bergakademie, Freiberg, Germany
e-mail: schaben@tu-freiberg.de

P. Gabriel · J. Gietzel
GiGa Infosystems, Freiberg, Germany

3.1.1 Historical Note

The development of GST is a reflection of a historical evolution. For 200 years geologists

communicated by means of maps, hand drawn and coloured, then printed (Winchester and Morris 2002). The ability to design and read geological maps is a difficult skill to learn. Individual geologists have been aware of this difficulty and seeking for alternatives. A prominent example is Hans Cloos, who worked hard to display the dynamics of geologic processes in his pen-and-ink drawings (Cloos 1947).

In the 1980s, of the last century Geographical Information Systems surfaced and made their way into all geosciences as they provide the IT means (i) to geocode, register, store and manage 2D geological data in database systems and (ii) to design and analyze digital map images. Already at this time it became obvious that hierarchical file systems manage data, but only database systems convey information. Today only a vanishing minority of geologists still use computer aided tools as provided by e.g. CorelDraw to draw maps.

At the same time computer aided geometric design and computer graphics developed quickly and gave rise to the idea of 3D geological-geometrical modelling. Then maps and sections are mere 2D derivatives of 3D digital geomodels. An early report of geomodelling and its potential applications in simulating geological processes is Pflug and Bitzer (1990). For a while, 3D geomodelling with exquisite and expensive software was a privilege of research institutions or big oil and gas companies. About 10 years ago, 3D modelling was introduced in national or state geological surveys and other administrative institutions in Europe as an experimental complement to digital map images. Very soon the complement turned into an alternative for routine tasks and in turn promoted the development of database systems for 3D raw geodata and 3D geomodels and their constituting objects. To use these digital 3D models like 2D digital map images then requires to extend geographic to geoscience information systems. For example, the operation of buffering is much more versatile and involved in 3D than in 2D. Digital 3D geomodels also require new means of visualization. Eventually joint objects of cooperating partners sharing a common Earth model ask for IT means to exchange geodata and geomodels efficiently,

i.e. for components of a geodata infrastructure to facilitate this exchange rather than for countless interfaces. GST is TU Bergakademie Freiberg's and in turn ProMine's contribution to this task.

3.1.2 State of the Art of 3D GIS —Similar Work

In this chapter, similar DBMS or extensions for DBMS are compared with respect to their management of 3D spatial information. There are numerous DBM systems available to manage spatial geodata, e.g. ArcSDE, Oracle Spatial, Spatial Lite, to mention just a few. Most available solutions are capable of storing 2D data (xy-coordinates) only, or managing the third (pseudo) dimension (z-coordinate) as additional information, i.e. as a property, assigned to 2D data. This chapter focuses on DBMS managing truly 3D data.

3.1.2.1 PostGIS

PostGIS is an open source C-extension that adds support for geographical objects to the PostgreSQL object-relational database. Initially focused on 2D geometries, PostGIS itself has been extended to represent 3D geometries since its version 2. It is closely related to the project Geometry Engine Open Source (GEOS), which implements 3D geometries since its version 3. PostGIS supports the Simple Feature Standard (SFS), a representation of geometry data for SQL specifications approved by the Open Geospatial Consortium (OGC; Obe and Hsu 2011). It also supports X3D to be used to visualize geometries in a web application using WebGL (Gabriel 2011). PostGIS comprises several vendor independent formats both in read and write mode featuring the GML format. PostGIS is rather restrictive in that properties can only be assigned to entire geobjects and not to their constituting cells, vertices or simplices.

3.1.2.2 DB4geo

DB4geo is a long term academic development of a spatial extension of the object-oriented java database system db4o. The database system has

been designed to store and manage 3D geobjects, mainly 3D simplicial complexes or “meshes” (Breunig 2001; Breunig et al. 2010).

3.1.2.3 Rasdaman

Raster Data Manager—in short rasdaman—is a database system designed to store and manage raster data highly efficiently, e.g. when processing requests. It implements the SQL based raster query language rasql, which enables querying, e.g. a time series of satellite raster images, and processing them all at once. The system is developed along with the Web Coverage Service (WCS) and implements the raster aspects of this standard (Baumann 2006).

3.2 Data Modelling— Conceptual Model of the Data Store

Our own work draws on previous developments towards a 3D geoscience information system pursued both at TU Bergakademie Freiberg, Germany, and Ecole Nationale Supérieure de Géologie Nancy, France (Apel 2004, 2006), including an early predecessor of a webservice (Frank et al. 2003), and continued by Pouliot et al. (2007).

3.2.1 Data Model

The elements constituting the geometries are stored in a relational schema of primitive data in

the database. Thus it is possible to use integrated functions of the database management system provided by the vendors such as index structures to query data efficiently, or functions of the management system for backups or distribution on clusters.

A simplified part of the data model is displayed in Fig. 3.1. There is one relation for storing the vertices and related characteristics like their coordinates and some identifiers such as to which geometry the particular vertex belongs and what its index is. Some triples of vertices make up triangles which in turn are stored with their shown indexes and with references to their vertices. A *TFace* is usually a collection of connected triangles. Several *TFaces* constitute the final triangular irregular network (TIN). Other geometries like lines or tetrahedral networks are stored analogously. All information regarding the geometry, its spatial reference system and its properties are stored in the relation *proscatalog*. All properties, e.g. color, name, etc., assigned to geometric objects are stored in tables referring to them, (Fig. 3.2). Additional properties can be assigned to the vertices or the elementary cells of an object, e.g. a tetrahedron in a tetrahedral net. Thus it is possible to store any type of property that is supported by the database management system like integers, doubles, blobs etc.

Our data model enables the user to manage complex geometries with a database and relate multidimensional geoscience properties to geometries. Passing the geomodel as stored in the database to applied geologists, these properties

Fig. 3.1 Inheritance of the supported objects types in GST

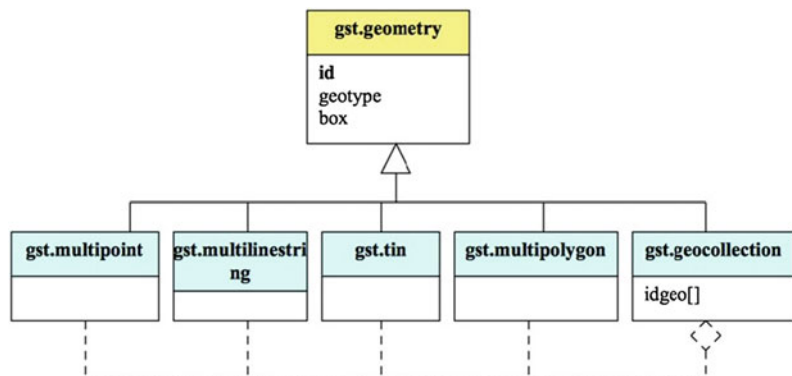
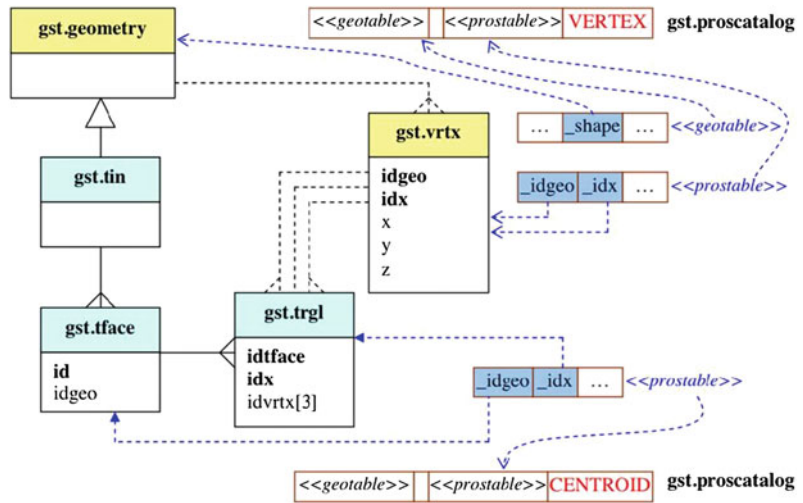


Fig. 3.2 View of the structure of an object stored in GST. Here an exemplary for type TIN



may be instrumental for e.g. potential modelling or transport simulations.

To manage, for instance, a specific structural geomodel consisting of base horizons and faults, the user should initialize classes for each group of objects first. In this example he or she will define a relation to store all base horizons and a second relation to store all faults. Then GST’s function *add_geocolumn* is used to define what kind of geometries represent the geomodel, and how properties relate to the geometries, vertices or cells. These user defined relations are appended as an additional geometry column. This approach allows the combination of any property table with a geometry and thus the 3D geometries can be included into custom semantic data models or standardized models like NADM, GeoSciML, RESQML and others.

3.2.2 Architecture

The data model and the database system combined with a webservice feature a service oriented 3-tier architecture (Fig. 3.3) of clients, middle ware and data server (Pouliot et al. 2007) It encompasses several components, in particular web and other services. It complies with standards, wherever they exist, or widely accepted models like Markup Languages (ML).

A 3-tier architecture meets several requirements. The very first requirement is that the client will just access data which is stored on powerful servers. Another requirement is the need for a possibility to adjust the data visibility to e.g. public users and to serve the data. The first step separates a system into two tiers. By adding another tier the last requirement can be met.

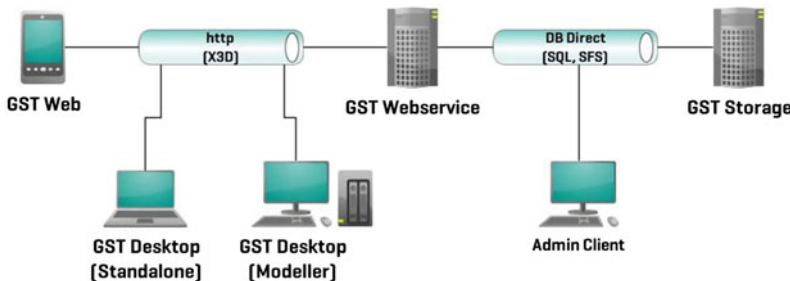


Fig. 3.3 3-tier architecture comprising front end of clients, middle ware of webservices, and back end including server hosting the data base

A GST client implemented in a geomodelling software initially featuring a proprietary format becomes an integral part of it and enables the augmented modelling software to store the model and its constituting objects in a generic format facilitating their exchange. Thus its implementation enables cooperation of several partners using different geomodelling software for a common geomodel based on shared geodata. The communication of geomodels, in particular their actual versions while under construction, is without loss of information due to conversions between proprietary formats.

The GST Web client opens the possibility to visualize the 3D geomodel stored in the generic format independently of the original modelling software or any other specific viewing software. In this way our web client is a response to the growing demand of scientific communication and contributes to the dissemination of achievements in geomodelling through geodata and geomodel portals.

At last, a 3-tier architecture is appropriate to meet security concerns of public administrations like national or state geological surveys.

3.3 Software System of the Data Store

3.3.1 Components—Front End, Middleware, Back End

3.3.1.1 Front End—Clients

The front end includes all possible GST clients as there is a GST Desktop client, a geomodeler plugin client and a Web Application client.

The GST desktop client is a C++ application installed locally on the users' PC and enables him or her to administer the database with respect to GST. The major purpose of this client is to manage a project, in particular to upload and download the involved geometries and their properties. Uploading geometries includes the fundamental conversion of the proprietary format as possibly featured by a geomodelling software

into the "generic" format used by OGC's simple feature standard (SFS). The corresponding properties in initial proprietary format are mapped into object properties if necessary. Thus geometries together with their associated properties now encoded in the generic format are passed to the database.

A geomodeler client is an application integrated into a geomodelling software as a plugin, e.g. for gOcadTM. It allows direct uploading and downloading of the modeled geometries and their properties to and from the database. A plugin to the geomodelling software is required to integrate an appropriate GST client which in turn communicates via SQL with the database. Direct access of the client to the database can be prevented, e.g. for data security reasons, by a web service put in the middle between the client at the front end and the database at the back end.

The GST Web client is an application to visualize a geomodel as stored in the database directly with a web browser. It is based on the web graphics library (WebGL) and Ajax (asynchronous javascript and XML). It visualizes not only the geometries, but also physical properties assigned to them. The web client permits to explore the model interactively, revealing details and relationships between subsurface geobjects and surface characteristics. Obviously, this visualization is independent of any geomodeler software and of any specific viewer software. Thus, it contributes essentially to the dissemination of geoinformation, e.g. to the interested public.

The 3DWebGL Viewer is used to visualize and explore geomodels of the four mineralized belts in ProMine. The visualization is an integral part of the pan-European WebGIS (<http://ptrarc.gtk.fi/ProMine/default.aspx>) providing digital maps indicating location of mines and of actual and potential mineral deposits throughout Europe. The software was kindly provided by the GiGa infosystems.

3.3.1.2 Middleware—Webservices

The webservice of GST is the central of exchange and communication. Installed at a user's institution (A), it enables a user with

another institution (B) to access A's data if B is authorized. The webservice actually secures the database of institution A from direct access as direct accessibility of A's database via the internet is not required. Since a command-line client is used to hide the database type from the webservice, it aids to the versatility of GST's webservice and facilitates its portability to different web application frameworks.

Since the webservice is implemented in PHP, it can be easily extended for OGC services like WFS, WCS, WPS, etc. Extending the webservice allows to integrate data from different sources involving other webservices as well. Connections with other webservices allow to include for instance a shared stratigraphic column encoded in GeoSciML.

The service also deploys the Web Viewer Client which is implemented in JavaScript and will be sent to the user upon request.

3.3.1.3 Back End—Database

The data tier (back end) is provided by a database extension to a relational database management system (RDBMS), which encapsulates functions called stored procedures defined in the database. This extension manages the input and output within several formats like Well-Known-Text (WKT), Well-Known-Binary (WKB), Geography Markup Language (GML), a 3D web format (X3D), and a geological description language for reservoirs (RESQML) (King et al. 2012). These standards have been defined by the Open Geospatial Consortium (OGC), the World Wide Web Consortium (W3C), and by Energetics, a consortium of oil and gas companies, to facilitate the exchange of geodata.

The stored procedures, which are used to transfer data into and out of the database, can be called via the SQL interface. Thus, third party applications are able to use these functions. A request of all geometries from class *faults* might look like

```
Select gst.select_geometry(geometryid, 'SFS')
from faults;
```

The result of this query is a set of records of text with 3 fields, the first representing the geometry in WKT as part of the OGC Simple Feature Standard, the second providing meta data about the geoscience properties, and the third providing the values of the properties assigned to the cells or their vertices.

3.3.2 Issues of Implementation

3.3.2.1 Multi User Access

Storage engines play a central role within a network. Thus they need to be capable to manage simultaneous (as opposed to sequential) multi user access. Functions for this task need to be provided by the database management system to guarantee consistence of the data.

The transaction based system of relational database management systems provides many tools which enable and facilitate the networking on shared resources. Isolation of transactions is one of them. It provides non-blocking access to the data based on versioned views of the data themselves (MVCC) (Meier 2010). Thus, it builds a base for simultaneous access to the data preventing undesirable phenomena such as lost update, dirty read etc. Moreover, the database management system provides functions to lock and unlock data, in particular an access control system (ACS) synchronizing parallel writes on the same memory area (Eisentraut 2003).

Often a 3D modelling session lasts several hours from the commencing request of the actual state of the geomodel to the closing write of its updated state. During such an editing session the model must not be changed by any other modeler to prevent the generation of inconsistencies. To guarantee this kind of consistency GST implements a locking system referred to as “lock, modify and unlock” (LMU). It excludes simultaneous editing by any other party while the model is checked out for editing by the first authorized party. A request of a stored model or a part of it is only authorized if it is not locked by

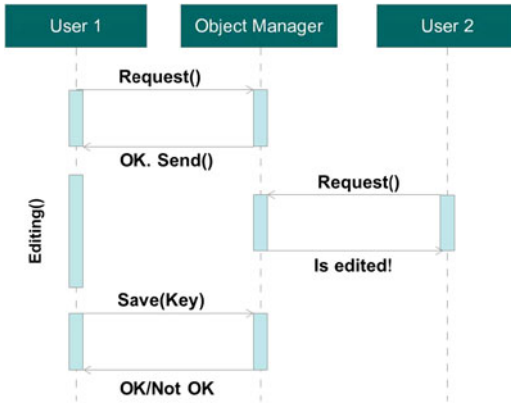


Fig. 3.4 A schematic view of the lock, modify and unlock strategy applied with GST. User A is requesting an object from the object manager for editing. For this period another user B is prohibited to edit the same object

any other user. Then the LMU system provides a key that identifies the user as being authorized to write edits back to the database (Fig. 3.4).

3.3.2.2 Seamless 3D Tiles

There are basically two approaches to “large” models, i.e. to geomodels of large regions the size of provinces of large potential for natural resources or entire states. A complete large model constructed with low spatial resolution may serve for a general overview, but its intersection with a digital elevation model would not meet the expectation of a geological map. Initially individual geomodels of smaller subregions constructed with a high spatial resolution have to be merged to a large model of the entire region. The latter approach is widely used but has several drawbacks especially when the partial models are stored in a file system. An inevitable prerequisite of merging is that the subregions overlap and that there the corresponding geomodels match perfectly. Then editing a partial model usually requires editing all adjacent models as well (Fig. 3.5).

GST applies a complementary approach. A complete model is stored in the database, but the subregions with their margins are generated on demand. Thus subsequent edits can be done much more efficiently. Moreover, GST’s multi user access secures a requested area being edited against writes by other users.

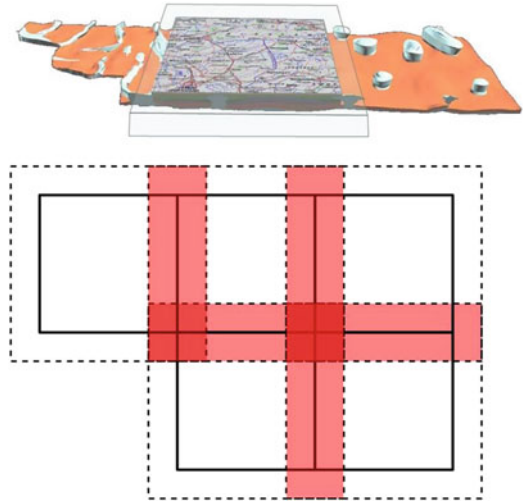


Fig. 3.5 A file based approach would mean to open several files. Edits of one tile require changes in the adjacent tiles, too. Often used overlapping areas require up to 4 times editing in the overlaps (*color transparent red areas*). With GST’s seamless 3D tiles this is prevented by defining dynamic tiles. Figure of the 3D model in the upper image is from LBEG, the state geological survey of Lower Saxony, Germany

Using this approach it is possible to have several users elaborating simultaneously on the same model. The size of the model is not important at all because it just exists within the database. The model itself can be extended at any location or partially substituted with a model of higher spatial resolution in regions of special interest.

In order to generate an overview of the complete model a simplified view is generated on request. An edge collapse operator is applied to address several levels of detail of the model (Hoppe 1997).

3.4 Current Implementations of GST Data Store

A first prototypical implementation was successfully tested at Luleå University of Technology, Sweden, and their gOcadTM model of the Fennoscandian Shield (Skellefte–Pyhäsalmi).

Current implementations apply PostgreSQL or Oracle as database, a server application as



Fig. 3.6 A 3D model of the Skellefte District in the Fennoscandian Shield from Luleå University of Technology, visualized with the web application directly in the web browser (no plugin required, just a regular browser)

middleware software, and gOcadTM or MoveTM as client and front end. With this setting, the GST software has been installed at the State Geological surveys of Bavaria, Baden Württemberg, and Saxony, all Germany, and at the National Geological Survey of Switzerland, and will be routinely used (Fig. 3.6).

The GST system was completed and extended within the frame of the EU project GeoMol “Assessing subsurface potentials of the Alpine Foreland Basins for sustainable planning and use of natural resources” funded by the Alpine Space Programme as a part of the European Territorial Cooperation 2007–2013 (<http://geomol.lfu.bayern.de/geomol/webGUI/>).

3.5 Conclusions and Perspectives

This chapter is a reflection of ProMine’s contribution to efforts to harmonize and standardize geoscience data which are the subject of OneGeology (<http://www.onegeology.org/>), OneGeology Europe (<http://www.onegeology.org/docs/OneGeologyEuropeJacksonApril2011.pdf>), INSPIRE (<http://inspire.jrc.ec.europa.eu/>), and other activities.

In particular, the GST provides a major component of a geodata infrastructure to facilitate exchange of geoscience data and models, i.e.

it is a step towards interoperability of cooperative partners. Eventually it contributes to the dissemination of geoinformation and geoknowledge. The GST data model is easy to extend and generalize, the software system can easily be customized to a given environment and users' need. GST will be further pursued and extended in the future (Le et al. 2013) both by TU Bergakademie Freiberg and by the spin off company GiGa infosystems.

Beyond "ProMine" GST will provide the means of interoperability between partners of the "GeoMol" EU project devoted to "Assessing subsurface potentials of the Alpine Foreland Basins for sustainable planning and use of natural resources". Eventually, GST will provide a unique web based hub for geodata and geomodels.

Acknowledgments The project "Nano-particle products from new mineral resources in Europe—ProMine" was funded by the European Community's Seventh Framework Programme (FP7/2009-2013) under grant agreement no 228559. The authors PG, JG, and HS thankfully acknowledge funding by "ProMine", the author LHH would like to thank the German Academic Exchange Service (DAAD) as for a DAAD-MOET scholarship at TU Bergakademie Freiberg. This publication communicates the authors' view only, exempting the Community from any liability.

Glossary

Ajax Asynchron JavaScript and XML. A JavaScript library allowing asynchronous request operations for web browser applications.

BoreholeML (<http://www.infogeo.de/home/boreholeML?lang=2>) accessed 2013-04-19 has been developed in order to be the comprehensive exchange format for borehole data.

CGI (<http://www.cgi-iugs.org/>) accessed 2013-04-19 The Commission for the Management and Application of Geoscience Information is a Commission of the International Union of Geological Sciences to enable the global exchange of knowledge about geoscience information and systems.

DBMS A Database Management System (DBMS) is a set of computer programs that controls the generation, maintenance, and the use of a database. It allows organizations to place control of database development in the hands of database administrators (DBAs) and other specialists.

db4o (<http://www.db4o.com/>) accessed 2013-04-19 db4objects is the open source object database that enables Java and .NET developers to store and retrieve any application object.

EarthServer (<http://www.earthserver.eu/index.php>) accessed 2013-04-19 EarthServer establishes open access and ad-hoc analytics on extreme-size Earth Science data, based on and extending leading-edge Array Database technology complying with open standards of OGC and W3C. Array database management systems provide database services specifically for raster data.

EGDI-Scope (<http://www.egdi-scope.eu/>) accessed 2013-04-19 Scoping Study for a pan-European Geological Data Infrastructure, CORDIS European R&D Project to "provide the backbone for serving interoperable, pan-European geological data currently held by NGSO, and data from past, ongoing and future European projects".

Energistics (<http://www.energistics.org>) accessed 2013-04-19 Energistics is a global, not-for-profit, membership organization founded to serve as a neutral body to facilitate and manage open data, information and process standards for the upstream oil and gas industry.

EuroGeoSource (<http://www.eurogeosource.eu/>) accessed 2013-04-19 EuroGeoSource is a data portal, which allows access by Internet to the aggregated geographical information on geo-energy (oil, gas, coal etc.) and mineral resources (metallic and non-metallic minerals, industrial minerals and construction materials: gravel, sand, ornamental stone etc.), coming from a wide range of sources in a significant coverage area of Europe (ten countries).

GeoSciML (<http://www.geosciml.org>) accessed 2013-04-19 GeoSciML or Geoscience Markup Language is a GML Application Schema that can be used to transfer information about geology, with an emphasis on the “interpreted geology” that is conventionally portrayed on geologic maps. Its feature-type catalogue includes Geologic Unit, Mapped Feature, Earth Material, Geologic Structure, and specializations of these, as well as Borehole and other observational artefacts.

GIC (<http://www.geology.cz/gic>) accessed 2013-04-19 Geoscience Information Consortium is open to all national Geological Survey Organisations (GSOs) who wish to contribute to the improved understanding of geoscience information systems. Its mission is the exchange of information among GSOs related to the use and management of geoscience information systems in support of the earth sciences internationally.

GIS A geographic information system (GIS), or geographical information system, is any system that captures, stores, analyzes, manages, and presents data that are linked to location. In the simplest terms, GIS is the merging of cartography and database technology.

GML (<http://www.opengeospatial.org/standards/gml>) accessed 2013-04-19 The Geography Markup Language (GML) is the XML grammar defined by the Open Geospatial Consortium (OGC) to express geographical features. GML serves as a modelling language for geographic systems as well as an open interchange format for geographic transactions on the Internet (<http://www.geosciml.org/>).

INSPIRE <http://inspire.jrc.ec.europa.eu/> accessed 2013-04-19 INSPIRE (Infrastructure for Spatial Information in Europe) is a recent initiative launched by the European Commission and developed in collaboration with Member States and accession countries. It aims at making available relevant, harmonised and quality geographic information to support formulation, implementation, monitoring and evaluation of

Community policies with a territorial dimension or impact.

IUGS (<http://www.iugs.org/>) accessed 2013-04-19 The International Union of Geological Sciences (IUGS) is a non-governmental scientific organization to promote and encourage the study of geological problems, especially those of world-wide significance, and to support and facilitate international and interdisciplinary cooperation in the earth sciences.

KML (<http://www.opengeospatial.org/standards/kml/>) accessed 2013-04-14 Keyhole Markup Language is an XML notation for expressing geographic annotation and visualization within Internet-based, two-dimensional maps and three-dimensional Earth browsers. KML was developed for use with Google Earth, which was originally named Keyhole Earth Viewer. It was introduced by Keyhole, Inc, which was acquired by Google in 2004. KML became an international standard of the Open Geospatial Consortium in 2008. (text from http://en.wikipedia.org/wiki/Keyhole_Markup_Language accessed 2013-04-14).

MVCC Multiversion concurrency control (MCC or MVCC), is a concurrency control method commonly used by database management systems to provide concurrent access to the database and in programming languages to implement transactional memory. (text from http://en.wikipedia.org/wiki/Multiversion_concurrency_control accessed 2013-04-14).

NADM (<http://ngmdb.usgs.gov/www-nadm/>) accessed 2013-04-19 The North American Geologic Map Data Model (NADM) Steering Committee – a consortium of American and Canadian geoscientists, database designers, and developers of geologic map information – sponsors and facilitates cooperative development of digital infrastructure for geologic map databases, and it works on behalf of the sponsoring agencies to develop products and ideas that can be adapted as agency standards for geologic map databases.

OGC (<http://www.opengeospatial.org>) accessed 2013-04-19 The Open Geospatial Consortium (OGC), an international voluntary consensus standards organization, originated in 1994. In the OGC, more than 370+ commercial, governmental, nonprofit and research organizations worldwide collaborate in an open consensus process encouraging development and implementation of standards for geospatial content and services, GIS data processing and data sharing.

PostGIS (<http://postgis.refractory.net/>) accessed 2013-04-19 PostGIS is an open source software program that adds support for geographic objects to the PostgreSQL objectrelational database. PostGIS follows the Simple Features for SQL specification from the Open Geospatial Consortium.

Qt (<http://qt.nokia.com>) accessed 2013-04-19 Qt (pronounced “cute”) is a cross-platform application development framework widely used for the development of GUI programs (in which case it is known as a widget toolkit), and also used for developing non-GUI programs such as console tools and servers.

RDBMS A relational database management system (RDBMS) is a database management system (DBMS) that is based on the relational model as introduced by E. F. Codd, of IBM’s San Jose Research Laboratory. Many popular databases currently in use are based on the relational database model. (text from http://en.wikipedia.org/wiki/Relational_database_management_system accessed 2013-04-14)

RESQML (<http://www.energistics.org/reservoir/resqml-standards>) accessed 2013-04-19 RESQML™ (Reservoir Characterization Markup Language) is an industry initiative to provide open, nonproprietary data exchange standards for reservoir characterization, earth and reservoir models. It is meant to become the exchange format for transferring Earth model data between applications in a vendor neutral, open and simple format.

SFS (<http://www.opengeospatial.org/standards/sfa>) accessed 2013-04-19. The OpenGIS®

Simple Features Interface Standard (SFS) provides a well-defined and common way for applications to store and access feature data in relational or object-relational databases, so that the data can be used to support other applications through a common feature model, data store and information access interface. OpenGIS Simple Features are geospatial features described using vector data elements such as points, lines and polygons.

SOA Service-oriented architecture (SOA) is a software design methodology based on structured collections of discrete software modules, known as services, that collectively provide the complete functionality of a large or complex software application. (text from http://en.wikipedia.org/wiki/Service-oriented_architecture accessed 2013-04-14).

SQL Structured Query Language is a special-purpose programming language designed for managing data held in a relational database management systems (RDBMS). (text from <http://en.wikipedia.org/wiki/SQL> accessed 2013-04-14).

W3C (<http://www.w3.org/>) accessed 2013-04-19 The World Wide Web Consortium (W3C) is the main international standards organization for the World Wide Web (abbreviated WWW or W3). (text from http://en.wikipedia.org/wiki/World_Wide_Web_Consortium accessed 2013-04-14).

WCS (<http://www.w3.org/>) accessed 2013-04-19 The World Wide Web Consortium (W3C) is the main international standards organization for the World Wide Web (abbreviated WWW or W3). (text from http://en.wikipedia.org/wiki/World_Wide_Web_Consortium accessed 2013-04-14).

WCS (<http://www.opengeospatial.org/standards/wcs>) accessed 2013-04-19 The Open Geospatial Consortium Web Coverage Service Interface Standard (WCS) defines Web-based retrieval of coverages, that is, digital geospatial information representing space/time-varying phenomena. (text from http://en.wikipedia.org/wiki/Web_Coverage_Service accessed 2013-04-14)

WebGL (Web Graphics Library) is a JavaScript API for rendering interactive 3D graphics and 2D graphics within any compatible web browser without the use of plug-ins. WebGL is integrated completely into all the web standards of the browser allowing GPU accelerated usage of physics and image processing and effects as part of the web page canvas. WebGL elements can be mixed with other HTML elements and composited with other parts of the page or page background. (text from <https://en.wikipedia.org/wiki/WebGL> accessed 2013-04-14).

WFS (<http://www.opengeospatial.org/standards/wfs>) accessed 2013-04-14. The Open Geospatial Consortium Web Feature Service Interface Standard (WFS) provides an interface allowing requests for geographical features across the web using platformindependent calls.

WKT/WKB (<http://www.opengeospatial.org/standards/sfa>) accessed 2013-04-14. Well-known text (WKT) is a text markup language for representing vector geometry objects on a map, spatial reference systems of spatial objects and transformations between spatial reference systems. A binary equivalent, known as well-known binary (WKB) is used to transfer and store the same information on databases, such as PostGIS. The formats are regulated by the Open Geospatial Consortium (OGC) and described in their Simple Feature Access and Coordinate Transformation Service specifications.

XML (Extensible Markup Language) is a set of rules for encoding documents electronically. It is defined in the XML 1.0 Specification produced by the W3C, and several other related specifications, all gratis open standards.

X3D (<http://www.web3d.org/x3d/specifications/>) accessed 2013-04-14 X3D is the ISO standard XML-based file format for representing 3D computer graphics, the successor to the Virtual Reality Modeling Language (VRML). X3D features extensions to VRML (e.g. Humanoid animation, NURBS, GeoVRML etc.), the ability to encode the scene using an XML syntax as well as the Open Inventor-like syntax

of VRML97, or binary formatting, and enhanced application programming interfaces (APIs). (text from <http://en.wikipedia.org/wiki/X3D> accessed 2013-04-14).

References

- Marcus Apel. *A 3d geoscience information system framework*. PhD thesis, TU Bergakademie Freiberg, Germany, and Ecole Nationale Supérieure de Géologie, Nancy, France, 2004.
- Marcus Apel. From 3d geomodelling systems towards 3d geoscience information systems: Data model, query functionality, and data management. *Computers & Geosciences*, 32(2):222–229, 2006. ISSN 0098-3004. URL <http://www.sciencedirect.com/science/article/pii/S0098300405001524>.
- Peter Baumann. Large-scale earth science services: a case for databases. In *Advances in Conceptual Modeling-Theory and Practice*, pages 75–84. Springer, 2006.
- Martin Breunig. *On the way to component-based 3D/4D geoinformation systems*, volume 94. Springer Verlag, 2001.
- Martin Breunig, Björn Schilberg, Andreas Thomsen, Paul Vincent Kuper, Markus Jahn, and Edgar Butwilowski. Db4geo, a 3d/4d geodatabase and its application for the analysis of landslides. In *Geographic Information and Cartography for Risk and Crisis Management*, pages 83–101. Springer, 2010.
- Hans Cloos. *Gespräch mit der Erde*. R. Piper, 1947.
- Peter Eisentraut. *Postgresql—das offizielle handbuch*. Bonn: mitp-Verlag, 3(4.2):3–4, 2003.
- Tobias Frank, Marcus Apel, and Helmut Schaeben. Web integration of gocad using a 3d-xml application server. In *Proceedings of the 23rd Gocad Meeting, Nancy, France, June*, pages 10–11, 2003.
- Paul Gabriel. *Webgl basierte visuelle analyse von 3d geomodellen*. Master's thesis, TU Bergakademie Freiberg, 2011.
- Hugues Hoppe. View-dependent refinement of progressive meshes. In *SIGGRAPH*, pages 189–198, 1997.
- Michael King, Paulo Ballin, Chakib Bennis, David Heath, Allan Hiebert, William McKenzie, Jean-Francois Rainaud, and Jana Schey. Reservoir modeling: From rescue to resqml. *SPE Reservoir Evaluation & Engineering*, 15(2):127–138, 2012.
- Hai Ha Le, Paul Gabriel, Jan Gietzel, and Helmut Schaeben. An object-relational spatiotemporal geoscience data model. *Computers & Geosciences*, 57(0):104–115, 2013. ISSN 0098-3004. URL <http://www.sciencedirect.com/science/article/pii/S0098300413001143>.
- Andreas Meier. *Relationale und postrelationale Datenbanken*. Springer, 2010.

- Regina Obe and Leo Hsu. *PostGIS in Action*. Manning Publications Co., Greenwich, CT, USA, 2011. ISBN 1935182269, 9781935182269.
- Reinhard Pflug and Klaus Bitzer. *Three-dimensional Computer Graphics in Modeling Geologic Structures and Simulating Geologic Processes: Freiburg, October 7-11, 1990: Extended Abstracts*. Geological Institute of Freiburg University, 1990.
- Jacynthe Pouliot, Étienne Desgagné, Thierry Badard, Karine Bédard, and Vincent Thomas. Development of a web geological feature server (wgfs) for sharing and querying of 3d objects. In *Advances in 3D Geoinformation systems -Lecture Notes in Geoinformation and cartography*, pages 115–130. Springer, 2007. ISBN 3-540-72134-7.
- Simon Winchester and MD Morris. The map that changed the world: William smith and the birth of modern geology. *Leadership and Management in Engineering*, 2(2):12–13, 2002.

3D and 4D Geomodelling Applied to Mineral Resources Exploration—An Introduction

4

J.J. Royer, P. Mejia, G. Caumon and P. Collon

Abstract

3D geomodelling, a computer method for modelling and visualizing geological structures in three spatial dimensions, is a common exploration tool used in oil and gas since more than several decades. When adding time, 4D modelling allows reproducing the dynamic evolution of geological structures, and reconstructing the past deformation history of geological formations. 3D geomodelling has been applied to mineral exploration with some success since more than 15 years, but can be considered still challenging for modelling hard rock settings. If very few 4D modelling case studies have been carried out in mineral exploration, it nowadays begins to be applied in structural geology and mineral resources exploration. This paper describes the 3D and 4D geomodelling basic notions, concepts, and methodology when applied to mineral resources assessment and to modelling ore deposits. It draws on the state of the art of 3D and 4D-modelling, describing advanced techniques, limitations and recommendations. The text is illustrated by several 3D GeoModels of mineral belts across Europe, including the Fennoscandian Shield (Finland, Sweden), Hellenic (Greece), Iberian (Spain, Portugal) and Foresuedic (Poland, Germany) belts, all of those case-studies have been performed within the EU FP7 ProMine research project (Part of objectives of the 4 years ProMine project were to integrate the mapping of metal and mineral resources across the European Union, especially in WP1 and WP2). Perspectives and recommendations on applying 3 and 4 geomodelling in mineral resources appraisal are given in the conclusions.

4.1 Introduction

3D and 4D Geomodelling is nowadays applied in mineral resources exploration as an exploration tool by geo-practitioners and geoscientists

J.J. Royer (✉) · P. Mejia · G. Caumon · P. Collon
Université de Lorraine, CNRS-ENSG,
Vandoeuvre-Lès-Nancy, France
e-mail: royer@gOcad.org

involved in better understanding mineral resources appraisal, both at the mining exploitation and at the exploration stages for identifying potential new mineral resources. Data acquired during mining exploration and exploitation is interpreted and processed using computers. Several packages are available on the market for processing 2D and 3D datasets such as GIS and geomodelers (Bonham-Carter 1994; Mallet 2002; Internet Guide to GIS 2009). Among them, the most widely used are: 3D Geomodeler (Geomodeler 2012) from BRGM and Intrepid, gOcad-SKUA from Paradigm (2012) for geological applications, gOcad Mining Suite from Mira Geoscience (2013) for mining, AutoCAD (2012), Irap RMS from Roxar (2009), Isatis from Geovariances (2012), Leapfrog Geo (2013), MicroMine (2012), Microstation (2012), MineSight Implicit Modelling (MSIM) from Mintec (2012), Move3D from Midland Valley (2012), Petrel from Schlumberger (2009), Surfer (2012), Surpac from Gems from Geovia (2013) a subsidiary of Dassault System, and Vulcan3D (Vulcan 2012) from Maptek. These software programs generally address one or more specific modelling applications, but none of them can actually encompass all tasks generally required in an integrated mining study, including: structural and geobody modelling, restoration, geophysical inversion and interpretation, geochemical analysis, resource and reserves estimation, mine planning, mine design and risk and environmental impact mitigation. Such a general-

purpose modelling framework is nonetheless most relevant for geological modelling as observed for instance by McGaughey (2006), Caumon et al. (2005, 2006, 2009, 2013a) and Caumon (2010). Similar challenges have been considered in the Oil and Gas industry which has led to spectacular advances regarding the 3D modelling, geological history reconstruction (referred here as 4D modelling or restoration) and multi-disciplinary integration for better understanding basin history and target reservoir behavior. If the modelling of some ore deposits in igneous formations can be relatively simple, it can become extremely complex when poly-phase structural events are overprinted on inherited mineralization processes, like for ore deposits in regionally metamorphosed rock assemblages. Geological reconstruction and restoration techniques are now quite mature on sedimentary formations, but definitively calls for further research for hard rock settings where fault displacement cannot be easily inferred from topological relationships between geological formations and structures (Fig. 4.1). Basic geomodelling notions and concepts do not depend on the software package used, although some aspects such as geometry, topology, fault networks, geological interfaces etc., depend on the software package and its underlying technology.

This paper introduces geomodelling to geoscientist specialists and stakeholders involved in exploration and exploitation of mineral resources.

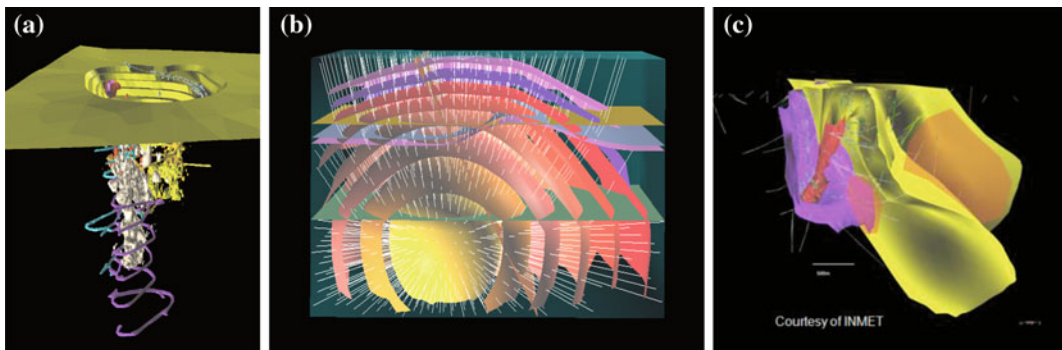


Fig. 4.1 **a** Open-pit mine in Central Massif (France): an underground ore 3D model points out unknown mineralization which extended the mine life by more than 10 years. **b** Iso-value front surfaces representing the

propagation of seismic waves. **c** Complex folding of the Pyhäsalmi VMS deposit (INMET-Finland) reconstructed in 3D

It aims at presenting a comprehensive overview of these new digital earth techniques and provides examples obtained on the gOcad™ software platform, which originated as an academic project in the 90's and is now a Paradigm product. This modelling topic meets the three phases of Knowledge Generation and Innovation technologies (2010), Knowledge Integration and Knowledge Distribution set out in the Communication Strategy and aims to direct, record and analyses the consequences for the future in mineral exploration (Critical raw materials for the EU, 2010).

4.2 Introduction to 3D Geomodelling

Geomodelling is a term coined in the 90's to refer to computer processes used to build 3D models of the real-world using geo-located data (Mallet 2002). These techniques have been extensively used in the geosciences for modelling underground reservoirs, ore bodies, aquifers, and natural hazards (Fig. 4.2). The different basic notions involved in geomodelling will be explained in the following.

4.2.1 Notions of Geometry, Topology and Properties

Modelling deep geological structures is difficult because geologists face a lack of information. The subsurface is generally sampled at irregular locations (borehole, outcrop sampling), and interpreted through maps and cross-sections or indirectly measured with geophysical tools (seismic data, potential fields). As a result, the geometry and the topology (i.e. spatial relationship and connection between geological structures) of the underlying geological objects are unknown: the connections between geological objects must be determined (and may change) during the geomodel building process. Depending on how geologists interpret connection between faults, a given geological structure can be split in many different structural blocks (Fig. 4.3c). Measuring this complexity is a challenging problem for which several authors have suggested some quantitative approaches (Pellerin et al. 2013). This topological uncertainty is a specific difficulty of geomodelling, which is seldomly addressed in classical computer-aided-design (CAD) approaches.

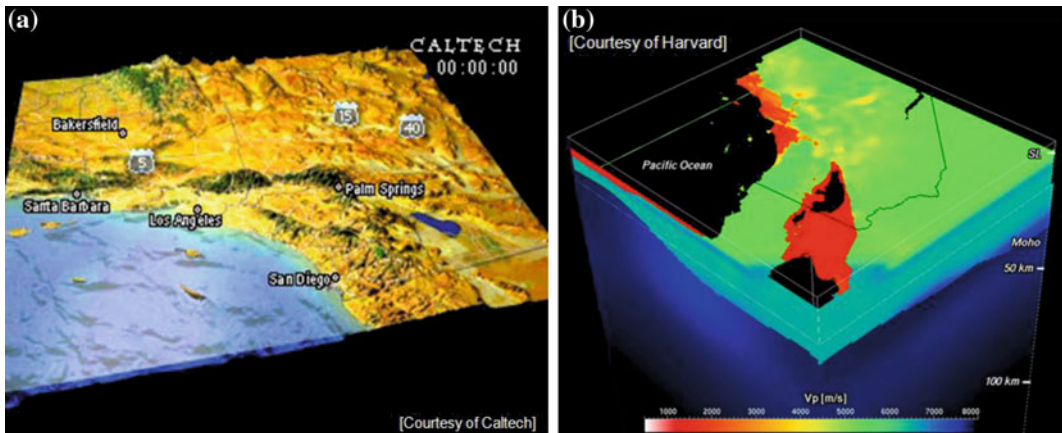


Fig. 4.2 Geological (a) and velocity (b) geo-models built using gOcad of the Los Angeles basin. This model has been used by the SCEC Community Velocity Model—Harvard (CVM-H) for building a velocity model of the

crust and upper mantle structure in southern California for exploration purposes and seismic risk analyses (After Tape et al. 2009; Plesch et al. 2009)



Fig. 4.3 Classical constructive solid geometry and parametric surfaces can be used to model manufactured objects (a) and (b) but are generally not used to represent

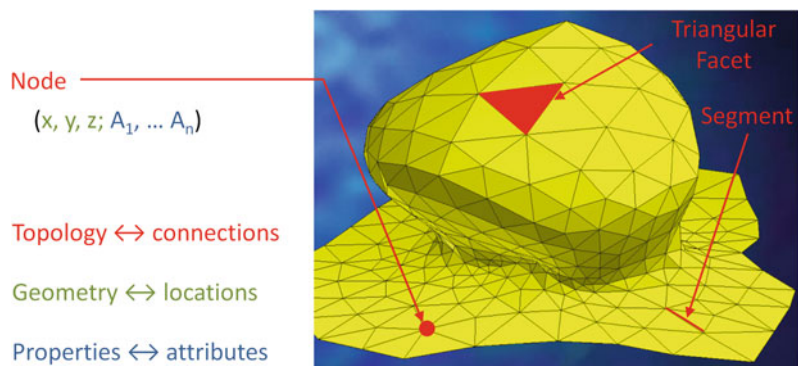
geological structures such as a circular graben (c). 3D models from the Grabcad library (<https://grabcad.com/library>) ((a) and (b)) and from Total/Gocad Consortium (c)

Classical computer aided design methods are based on parametric surfaces such as Bézier, Splines, NURBS, etc. for representing objects (Fig. 4.3a, b). They are easy to use and can fit sample points just accounting for numerical constraints in the parametric representation. They are well suited for representing regular surfaces such as folds (Sprague and de Kemp 2005), but raise difficulties to handle discontinuities induced by faults (Fig. 4.3c). In CAD systems, object shapes (car, plane, and building) are conceived by engineers. In geosciences shapes of geological structures are not known and must be assumed and interpolated in space from partial and scarce information. This makes all the difference between engineering and geoscience, and explains why CAD systems are seldomly used in geoscience applications.

Most geomodelling softwares provide tools for interpolating object shape from drill hole or

outcrop data. Beyond simple 3D digital elevation models, which are hardly applicable outside shallow or unfaulted domains, most geomodelers use a discrete representation of objects made of points set linked by segments (curves) and triangular elements (surfaces) (Fig. 4.4). The final surface is obtained by optimizing the spatial positions of nodes by best fitting sampled points, minimizing surface curvature and honoring other geometrical criteria such as fault contacts, etc. In the gOcad software, this method is referred as Discrete Smooth Interpolation (DSI) (Mallet 2002). This type of method is very flexible and can virtually honor all sorts of complicated geological structures (Fig. 4.5). The resulting models may be used to address several types of problems such as subsurface visualization, modelling of physical problems, resource and reserves estimation, etc. (Fig. 4.6).

Fig. 4.4 Complex geomodels are decomposed into simpler connected elements (triangles, segments, vertices) (courtesy of Mallet 2002)



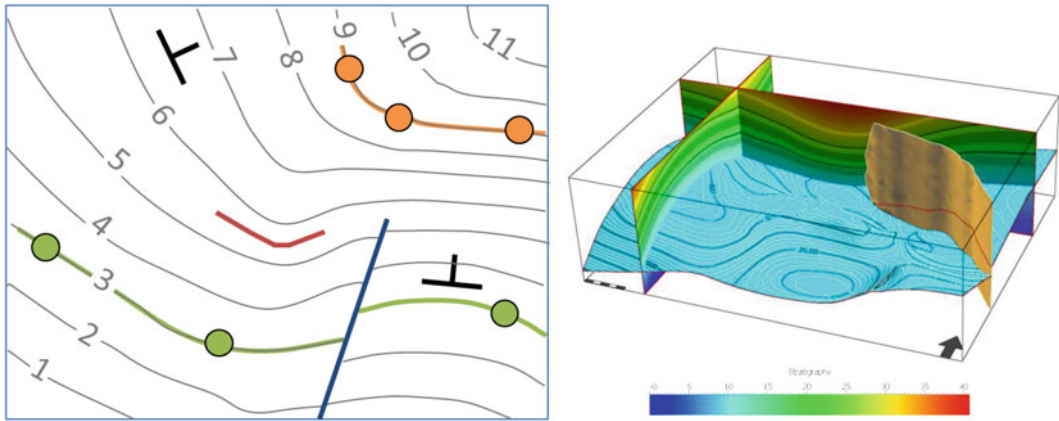


Fig. 4.5 Implicit representation of a conformable stratigraphy. Concepts (*left*) and practice (*right*)

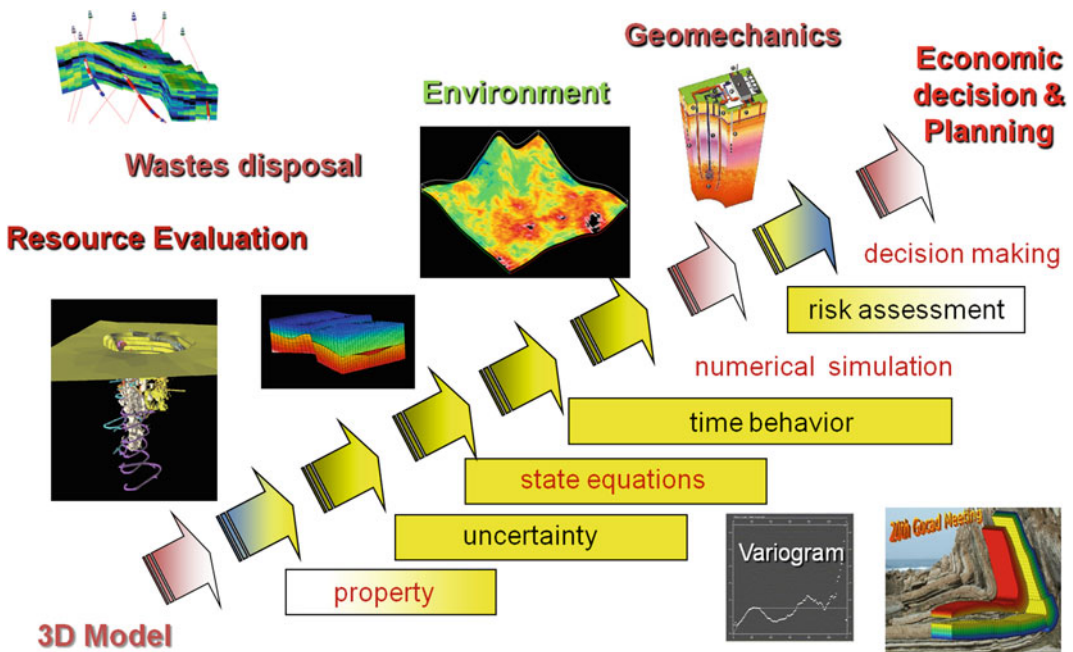


Fig. 4.6 Various steps illustrating a geomodelling workflow

Other technologies are based on an implicit representation of the surfaces. These implicit surfaces are described by specifying locations in 3D through which the surface should pass, eventually defining the local slopes (gradient) and also identifying locations that are interior or exterior to the surface (Turk and O’Brien 2002). A 3D implicit function, generally defined at the nodes of a tetrahedral or hexahedral grid, is

created from these constraints using a variational scattered data interpolation approach, and the iso-surface of this function describes the surface. Several methods have been investigated to build the 3D implicit function, radial function such as in Leapfrog Geo (2013), potential fields in the Geomodeler (2012), discrete representation in gOcad™, a.o.. An example of implicit surface modelling based on a tetrahedral grid is given in

Fig. 4.5. Geostatistical tools or discrete interpolation can be used to run the computations, see discussion in Caumon et al. (2013b). One of the major benefits of these methods is that they can directly represent several conformable surfaces and remove the need for projections from data to surfaces. Therefore, they allow users to build 3D models more efficiently and in a more systematic manner. Implicit surface modelling is now becoming available in commercial software such as 3D Geomodeler, SKUA-gOcad and Leapfrog.

4.2.2 Geomodelling Concepts

“Geomodelling consists of a set of mathematical methods and computer packages used to model the *topology*, *geometry* and *physical properties* of geological objects while taking into account any type of data related to these objects also called ‘Geo-Objects’”(Mallet 2002). Thus, 3D geomodelling is a computer method for modelling and visualizing geological structures in three spatial dimensions.

4.2.2.1 Basic Geometrical Elements of Geomodelling (Micro-Topology)

Philip II, king of Macedon (382–336 BC) applied his famous strategy “*divide and conquer*” to gain

power on the Greek city-states. As many smaller opponents are easier to manage than one large, this strategy can also be applied for mastering complex geo-objects by splitting them into several simpler elements as illustrated in Fig. 4.7. The basic simple elements are:

- *Points*: Sample locations defined by their coordinates X, Y, Z.
- *Curves*: Sets of points linked together by segments. A curve corresponding to a geological object may consist of several connected components, e.g. several contours or map traces (Fig. 4.8).
- *Triangles*: Three points are linked to form an elementary triangle; a set of adjacent triangles form a triangular surface (sometimes termed *TSurf*). As in the case of curves, a geological surface may have several connected components, for instance, when it has been cut by faults or unconformities (Caumon et al. 2009).
- *Tetrahedron*: Four points linked together delineate an elementary volume called a *Tetrahedron*. A set of tetrahedra forms an unstructured grid representing a volume in space. Such tetrahedral meshes are a classical support in the finite element method used to solve partial differential equations governing thermal, hydrodynamic and mechanical processes.

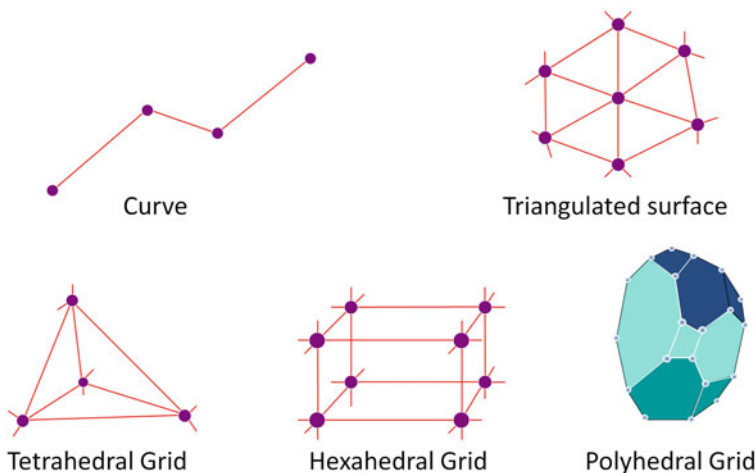


Fig. 4.7 Basic elements used to build discrete geo-objects. The topology is the set of connections or links between nodes

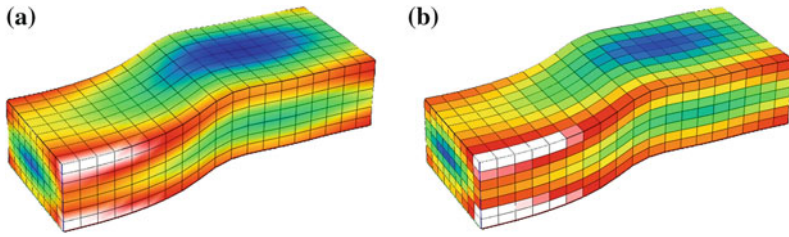


Fig. 4.8 Grid properties are stored at (a) the node location or at (b) the centre of cells

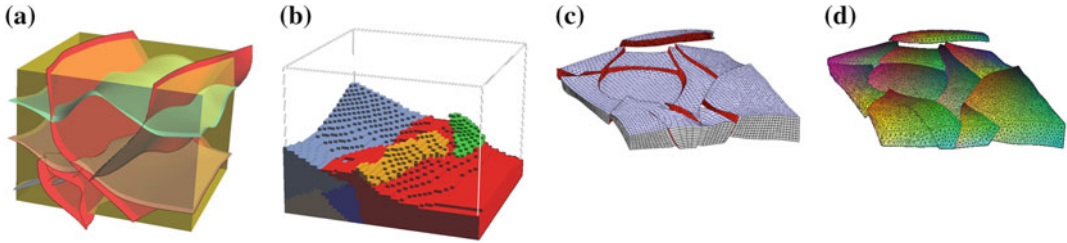


Fig. 4.9 a Surface models. b Regular rectangular grid model (sugar box or Voxel). c Regular deformed cells (SGrid = Stratigraphic Grid). d Tetrahedral cells (unstructured grids)

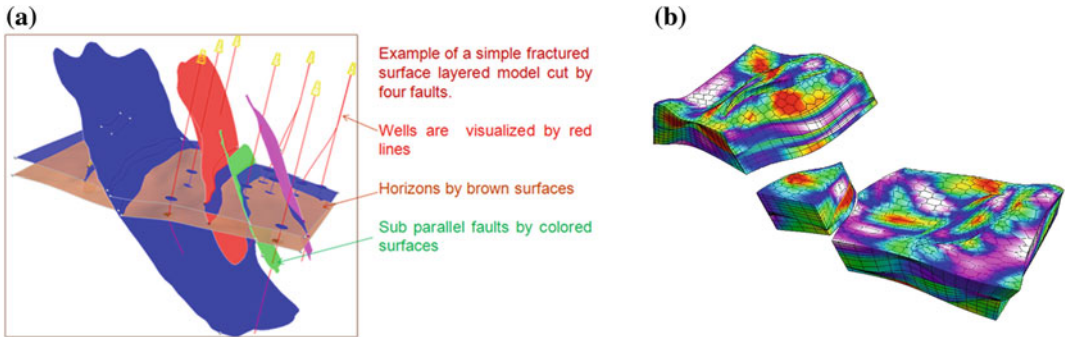


Fig. 4.10 a Faulted Surface Model (left). b Complex corner point polyhedral grids on which a continuous property is painted

- **Rectangular prisms (or Voxels):** A cube may be deformed so as to form an elementary hexahedron cell; when the cells are all identical (same sizes) and adjacent together, they define a regular Cartesian Grid (Fig. 4.9b). Prisms may also be deformed to fit curvilinear stratigraphic formations. These volumetric grids, referred as *SGrid* (Fig. 4.9c), are also commonly used to compute physical phenomena with numerical techniques.
- **Polyhedral cells:** Irregular cells whose juxtaposition forms unstructured grids (Fig. 4.10b).

4.2.2.2 Notion of Topology

The shape defines the geometry of an object that changes when deforming the objects during, for instance, a tectonic event, but there is another important notion used in geomodelling, this is the *topology* of the objects. This notion relates to

the object properties that are preserved under continuous transformations (including *stretching* and *bending*, but not tearing). In simpler terms, topology relates to the *connections and relative layout* between objects. For instance, a faulted surface can be made of several sub-surfaces (Fig. 4.10a) related to each other by other surfaces (the faults). As long as the number and faults connectivity remains constant in this model, the number of fault blocks in the horizon does not change, hence the topology remains constant.

A particular challenge in geomodelling is to efficiently interleave topological and geometrical operations. Geometrical operations imply being able to interpolate the shape (*geometry*) of geological objects from the available information (drill holes, geophysical interpretations, cross-sections, mining gallery, geophysical surveys, etc.). Topological operations basically amount to cutting surfaces or volumes to reflect the effect of faults, erosion, etc. Because such cutting operations are sometimes difficult to revert, it can be useful for flexible model updating purposes to replace topological operations by clipping operations performed by the graphics card. This is commonly done by most packages and is very useful for visualization and model prototyping purposes. However, in most model-related decisions, quantitative modelling is involved (e.g., flow simulations or mechanical computations). In that case, the model topology must generally be strictly honored in the representation and calls for robust topological operators and conformable meshing tools. Few geomodelling packages have this capability because limited computer numerical accuracy calls for delicate computational geometry algorithms.

4.2.2.3 Notion of Properties

Quantitative modelling needs to process qualitative (e.g. rock types, alteration types) and quantitative properties (e.g. grade, thickness). In discrete models, properties or attributes are stored at the node location (Figs. 4.4 and 4.7) or at the centre of cells (Fig. 4.8). The cell-centered technique is the simplest as it represents the property values constant in the elementary cell

(see Fig. 4.8b). On the contrary, when properties are stored at the cell corners, it is necessary to interpolate the attribute within the cell. In general, linear interpolation between nodes is generally used and non-linear variations of the physical parameters are represented through local mesh refinement, leading to a smooth visualization of continuous properties (Fig. 4.10b). Higher-order interpolates could be used in principle, but in practice only when the physical processes are locally highly nonlinear such as in wave propagation.

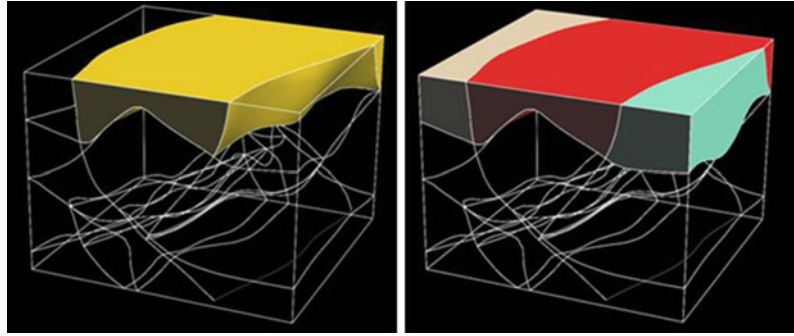
4.2.2.4 Notion of Regions

In geosciences, it is important to be able to manipulate the notion of rock type (or geological facies). More generally, the concept of region is very useful to consider object's subsets for processing and querying tasks. In quantitative geology, regions are often represented by a binary indicator, whereby a point or cell belongs to a region if its indicator value is equal to 1 and outside the region if the indicator is equal to 0. This binary technology is used in gOcad to facilitate spatial queries¹ in its 3D GIS plug-in developed by Apel (2006) and commercialized by Mira Geosciences. GIS does not in general use regions to define queries, they directly apply binary overlay principles when combining spatial objects; however, they are often limited to 2D.

Regions may be defined according to various criteria, which can be *geometric* (above, nearby a surface), or defined using a *property* (grade greater than a cut-off), or using an *indicator* (rock type). Several logical operations are available to manipulate regions (e.g. union, intersection, complimentary). The regions can be *static* when defined once by a condition and stored in a string of bits, or *dynamic* when the region is continuously updated when the model geometry or values change. Figure 4.11 gives example of regions delimited by surfaces on a structured regular grid. This region concept is simple but extraordinary well adapted to geosciences applications. They can be used to build 3D geological maps, an innovative technology existing in research

¹Isatis uses a similar technology.

Fig. 4.11 Geological rock types are represented by regions delimited by surfaces



laboratory (see the BGS website 2014). Some 3D map of England are currently done successfully and offer to the public by the BGS, British Geological Survey, the Geological Survey of Denmark (on cell phone), and at the Canadian Geological Survey. They are using regular triangulated surfaces and grids as well as regions to represent and query 3D geological structures (Fig. 4.12).

4.2.2.5 Representing Volumes

Several volume representations can be used to model 3D objects, see Figs. 4.9 and 4.11 (Caumon et al. 2004):

- *Closed surfaces* for delimitating the boundary of the volume (called *Boundary Representations* or *Sealed Geological Models*) (Figs. 4.9a and 4.13a). Geological surfaces corresponding to different geo-objects, must be glued together to form sealed regions. Ensuring the sealing of

the contacts between the surfaces (i.e. a surface model without “holes”) is one of the main issues when using this representation.

- *Regular rectangular cells*, Sugar box or *Voxel* (Figs. 4.9b and 4.13b). Each cell is within or without the defined regions. This method is easy to use, but the rock types and regions limits are irregular and approximated with stair-steps (aliasing effect). Precision depends on the cell size. Huge grids are generally needed to get acceptable accuracy.
- *Regular deformed cells* (*Sgrid* = stratigraphic grids) (Fig. 4.9c). It derives from the previous regular rectangular cells method, but the grid is deformed according to various layering styles corresponding to different deposition environments (e.g. proportional to a top and bottom horizon, eroded). They are well adapted to model sedimentary structures, or vein type deposits, and have become the standard in the oil and gas industry to

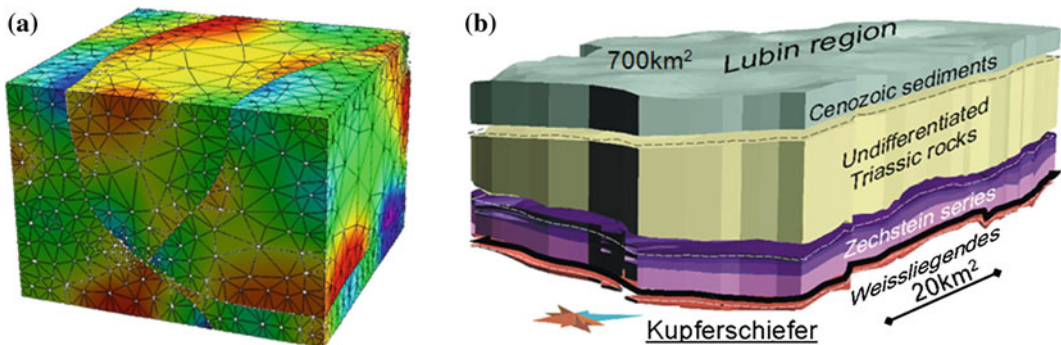


Fig. 4.12 a Unstructured grid made of tetrahedral elements. b 3D geo-model of the Kupferschiefer Foresuedic belt around the Lubin region (Poland), famous for its copper deposits (courtesy of CUPRUM and University de Lorraine)

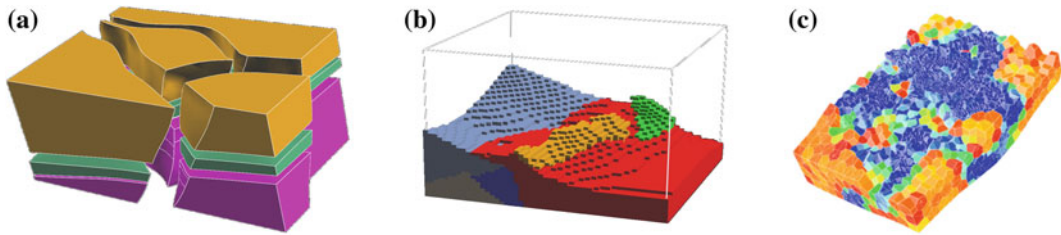


Fig. 4.13 a Boundary model. b Cellular model (Voxel grid). c Hybrid grids



Fig. 4.14 a Conformal hybrid grid consisting of tetrahedra, triangular prisms and pyramids; with b details showing a perfect fitting with the horizons (from Pellerin et al. 2012)

simulate flow in reservoirs. In complex faulted cases, the generation of these grids can be extremely difficult and calls for compromise between geological and numerical accuracy by using stair-step approximations. Over the recent years, improvements in implicit methods have significantly enhanced the robustness of creation of these grids (e.g. Gringarten et al. 2008). Notably, these grids are suitable for local grid refinement, whereby locally high-resolution meshes are embedded into coarser meshes.

- *Tetrahedral cells* of various sizes (*tetrahedral grids* i.e. grids using tetrahedral meshes, also called *unstructured grids*) (Fig. 4.12a). This is the most adapted method to model complex faulted geological objects. The main advantages are that the size cells can be smoothly adapted to honor local complexity. They are extensively used in mechanics and civil engineering because they are suitable to the finite element method. However, fully automatic conforming tetrahedral mesh generation is still a matter of research because of conflicting requirements between accuracy, element shapes and numbers (Fig. 4.14) (Caumon et al. 2005; Pellerin et al. 2012). As a result, tetrahedral meshes are not so commonly used in geosciences.

- *Mixed polyhedra* (hybrid grids) aim at combining the merits of hexahedral and tetrahedral grids in terms of number of elements, numerical properties and geological accuracy. This is an active research area (Pellerin et al. 2012) with important possible consequences in coupled transport, hydraulic, geomechanical and chemical (THMC) models² of geological processes.

Regular block grids are generally used in the mining industry because of their simplicity at the exploitation stages. However, in complex faulted ore bodies, or when the selectivity of mining blocks is an issue at the exploitation stage, regular blocks are not enough accurate and tetrahedral grids should be more adapted (Fig. 4.12a), especially for rock mechanics and civil engineering studies. This remains an issue because most of geostatistical packages are not available on unstructured grids (the same holds for fluid flow modelers in oil and gas exploration). However, ongoing and future progresses in up-scaling and gridding technologies are expected to

²Those models couple the heat transport (T), and the hydraulic (H)/geomechanical (M) behavior as well as chemical processes (C). They are referred in the literature as THMC models.

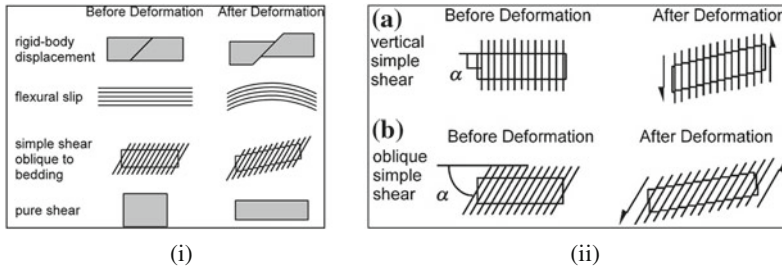


Fig. 4.15 i Various basics restoration kinematic models; ii Simple shear oblique to bedding. a Vertical simple shear. b Oblique simple shear (after Groshong 2006)

make unstructured grids a major element of future earth modelling. In particular, unstructured grids are the most convincing support to accurately model coupled THMC processes through geological time in faulted areas (e.g. Nick and Matthäi 2011).

kinematic models (Groshong 2006) are necessary to reproduce a pertinent geological deformation history or deformation style. Several elementary deformation style models (kinematics models) are usually investigated including: *rigid-body displacement*, *flexural slip*, *simple shear* and *pure shear* (Fig. 4.15).

4.3 Introducing the 4D Modelling

The past two decades have seen a rapid development in structural restoration as a key tool to identify favorable target, source and host rock formations, to reconstruct fluid migration in oil and gas surveys and to predict faults and fracturing in the rock mass.

4.3.1 Restorable and Non-Restorable Models

A restorable model can be unfolded and unformed to its original pre-deformation geometry with a perfect or near-perfect fit of all its segments. Its geometry is internally and topologically consistent. A non-restorable structure is topologically impossible and therefore is geologically not possible (Dahlstrom 1969). Chamberlin (1910) was a pioneer in performing a restoration of geological cross sections using the surface conservation principle (keeping areas constant). Later, this concept has been expanded to constant volumes by Dahlstrom (1969). However, time plays a fundamental role in the restoration method, and

4.3.2 Deformation Modes

The *rigid-body displacement* (or *block rigid deformation*) is the simplest method, which restores the un-deformed shape by translations and rotations of elementary blocks until they fit together.

The *flexural slip* involves slip along bedding planes or along surfaces of foliation keeping the individual strata thickness constant (unless otherwise specified) and the resultant folds being parallel. It preserves the area of the structures to be restored, their lengths and thicknesses in a vertical plane.

If the restored structure is isopach, the preservation of both thickness and length results in area conservation. If the thickness varies, the strict preservation of bed thickness and bed length may lead to area changes (Moretti 2008).

Simple shear is produced by slip on closely spaced parallel planes with no parallel or perpendicular to the slip planes length or thickness changes. Simple shear parallel to bedding is the mechanism of *flexural slip*. Simple shear that is oblique to bedding is a kinematic model that causes *bed length* and *bed thickness changes*. Simple shear methods preserve distances in the

shear direction, but length and thickness are not kept constant, consequently the area is not preserved. *Pure shear* is an area-constant shape change for which the shortening in one direction is exactly balanced by orthogonal extension (Groshong 2006). The *Flexural slip* and *simple shear* methods are available in the restoration module known as KINE3D-2 of the geomechanical software gOcad (Moretti 2008). Both methods have been used in a first approximation for the restoration of the Kupferschiefer case-study (Mejia and Royer 2012; Mejia et al. 2013). Block rigid deformation, simple and pure shear, and geomechanical modelling are implemented both in 3DMove (Midland Valley 2012) and gOcad.

4.3.3 Unfolding and Unfaulting

Removing the effect of folding and faulting generates a different restored geometry depending on the method used. For the simple shear case, the restored area is less than or equal to the original surface, and all geometric elements within the structure are shrunk by the same ratio. The use of this deformation mode for restoring competent beds in compression areas remains highly questionable in 3D and in 2D since the horizon area is not preserved and, when more than one layer is restored, the thicknesses are not preserved (Moretti 2008). Simple shear is commonly used for restoring surfaces of granulated materials,

poorly consolidated sediments, extensive domains affected by listric faults, and in shear zones. By contrast, the flexural slip method preserves the areas and lengths, so its results are sometimes more realistic, depending on if the strain is non-coaxial to the structure. In the Kine3D-2 restoration module, this method uses a global parameterization that preserves the lengths and areas of the horizons if the surface is developable (i.e. a surface that can be flattened onto a plane without distortion) (Mallet 2002). If the surface is not developable (for instance domes, diapirs), the algorithm searches the best solution in a least squares sense. For faulted surfaces, an optimization method that closes the gap where the surface was cut is applied for searching the best fit.

In the case of sediment-hosted ore deposits such as the Kupferschiefer deposits in the Foresudetic basin (Fig. 4.16), the restoration procedure can be used to identify mineralizing fluids pathways and the locations of economic mineral resources. This is usually done using 3D reconstruction and restoration tools considering geometric or geomechanical constraints (Rouby et al. 2000; Durand-Riard et al. 2010, 2011, 2013).

4.3.4 Discussion and Perspectives

Despite the extraordinary developments of geomodelling during the last decades, practical and

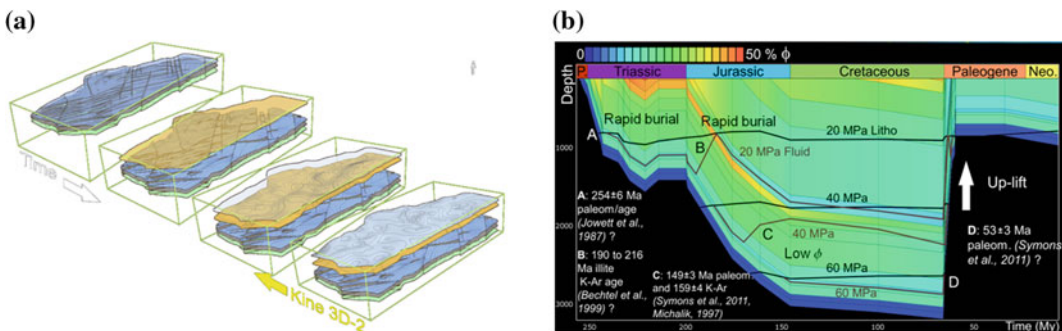


Fig. 4.16 **a** A Kine 3D-2 reconstruction of the burial history of the Kupferschiefer deposits in the Lubin region which is coupled with the pressure, temperature, organic matter maturation and hydraulic fracturing, calculated by

PetroMod. **b** Mineralization events are suggested at 250, 149 and 55 Ma during tectono-regional events observed during the geological history of the basin (After Mejia et al. 2012; Mejia and Royer 2012)

theoretical challenges remain. Standard workflows have been introduced by software companies to streamline geomodelling tasks and increase productivity (e.g. fault framework modelling, ore body modelling, gridding, petrophysical modelling). Robustness has made significant improvements and now makes it possible to improve automation and run multiple scenarios. However, automation can never be perfect and often calls for essential quality control (QC) steps after the main workflow steps. To facilitate model updating and uncertainty management, improvements are clearly needed in geomodelling workflows to further reduce these QC tasks and modelling effort once the initial controls have been made (Caumon et al. 2013b).

Another significant avenue for research is in the management of scales during geomodel construction. The dynamic regional modelling of ore concentration processes relies on large-scale, relatively coarse models, in which small-scale features have been conserved explicitly or homogenized. This calls for considering multiple scales during structural modelling itself, for instance by defining ways to automatically simplify fault networks.

Moreover, whereas geomodelling workflows are well adapted to sedimentary contexts, especially for oil and gas exploration, they still remain limited when applied to hard rock settings including igneous and metamorphic terranes. For the last decade, mineral resource modelling has gained momentum especially among Australian (the Australian Geological Survey offers now 3D mineral exploration maps on line, see AGS 2014) and Canadian (Caumon et al. 2006; Pouliot et al. 2008; Janssens-Coron et al. 2010) geoscientists. More recently, the ProMine project has explored the possibilities of 3D modelling in the European mining community.

4D modelling has been proved to be helpful in many exploration projects in the oil and gas sector in sedimentary rocks. It is still in its early stages when applied in mineral resources exploration in hard rocks. If restoration techniques can be applied with some success for understanding deformation phases of stratiform or sediment

related ore deposits (Mejia et al. 2012, 2013; Mejia and Royer 2012) using similar techniques as those applied in oil and gas, they are still limited for understanding poly-folded hard rock settings and cryptic discontinuities (De Kemp and Jessell 2013). The main unknowns are: (i) measuring the role and extent of the subsequent deformation phases is difficult as only the final stages can be observed; (ii) the history of the deformations is generally subject to high uncertainty; (iii) modelling is subject to underlying hypotheses and results are uncertain and non unique; (iv) hard rock properties, especially for fractured rocks, are difficult to account for in mechanical models, a still active research topic. Nevertheless, 3D and 4D approaches provide significant knowledge and improvements in better understanding the geological background of the mineralization zones. There is a growing interest in many parts of the world, including Europe, in 4D geomodelling to assess mineral potential. Challenges for future developments in the 3D and 4D research geomodelling are: (i) a geological 3D model is never complete. It is continuously developed with the acquisition of new data and new ideas, and automatic procedures would be helpful in up-dating geomodels when new data are acquired; (ii) current 3D and 4D software enables 4D geological structural modelling, and can be used to make more than a single interpretation or model to support a range of alternative interpretations when knowledge of the geologic history is poorly constrained (de Kemp and Jessell 2013). Although, in case of more than two deformation phases, 4D modelling remains very difficult to apply, especially in hard rock settings. New breakthroughs are needed in this field, for instance, by better incorporating mechanical and hydraulic failure aspects in the restoration procedure. Most of current mechanical models are based either on block or elastic deformation behavior. The two aspect must be combined as major faults do not behave according to elasticity theory. Some results on this subject have been published (Laurent et al. 2012a, b).

4.3.5 3D Geomodels as a Mean to Extend the Life of a Mine

At the end of the ProMine project (2012), it is too early to identify examples in which 3D models lead to a major mineral discovery. So, a well-documented case study selected in the French Massif Central is presented here.

A 3D Model of a mine in Massif Central (France) has been built (Fig. 4.17). Before 1990, the mine was considered as a sub-vertical mineralized socket (yellow) exploited in an open-pit (orange). At a given depth of the open-pit, the exploitation of the deeper levels would have required the enlargement of the open pit and the extraction of a huge amount of waste rock. Given the high stripping ratio, it was considered as non-profitable, and the owner company decided to close the exploitation. Before closing, they integrated all the available drill hole assays from more than 1000 drill holes into a unique 3D model on gOcad, and used them to estimate the grade using the Discrete Smooth Interpolation (DSI) method (Mallet 2002).

To their surprise, the DSI method pointed out unknown sub-vertical mineralized sockets confirmed by additional drillings.³ Given the huge in situ tonnage in place (about 6600 t U @ 0.56 % U) and the structure being open at depth, the company decided to sell the deposit to another company instead of closing the mine. This saves jobs and mining activity in the region and extended the life of mine by 10 years (this mine was among the most recent mines to be closed in France). The new company converted open-pit extraction into an underground mine exploited at >400 m depth (Fig. 4.17). This short success story demonstrates that: (i) there could still be mineral resources at depth even in mature mining districts (typically for U, French mines were mined to than 100–200 m depth); (ii) 3D modelling can extend the life of mature mines; (iii) innovative technologies can maintain and create jobs.

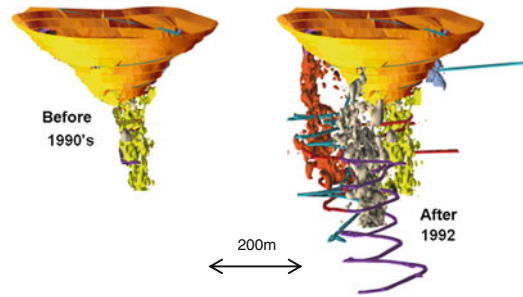


Fig. 4.17 Geomodelling a mine in Massif Central (France). The mine was considered as a sub-vertical mineralized socket (yellow) exploited by open-pit (orange) (left). After integrating all the available drill holes and modelling the mineralized zone, two major mineralized structures (red and grey) were discovered (right). The mine was then exploited underground (galleries in blue and violet) an additional 10 years

4.4 Discussion

Various case studies related to mineral exploration or/and mining using different 3D and 4D geomodelling technologies have been investigated during the ProMine project. They demonstrate that new geomodelling methods and ore potential mapping tools can be used in mineral exploration 3D and 4D geomodelling technologies contribute in improving knowledge and understanding of the mineralized zones and geological setting. In ore exploration, they provide new ideas and methods for helping new discoveries. Since a decade, there is a growing interest in 4D modelling as a tool for investigating future availability of minerals in Europe (ETP SMR 2007). Beside this ideal picture, there is still a lot of hard work to explain the benefit of these new technologies to stakeholders, in order to make them fully accepted by the mining industry and to improve geomodelling technology applied to mineral resources. Improvements can be made on the technological point of view:

- Most of the 3D regional models in mining exploration are based on surface data, drill holes being available at the mine camp scale. It reflects more or less the subsurface geological knowledge at the moment when the model is built, assuming some hypotheses and

³Personal communication from P. Jamet, the mining geologist in charge of the project at this date.

containing a lot of uncertainty in terms of concepts. Of course, 3D models are never complete as they evolve as soon as new data are acquired. It is therefore important that 3D models include metadata describing location of available data, quality of data and assumed hypotheses. It also requires better compilation of available surface and subsurface data sources and interpretations in 3D geodatabases;

- As models evolve through time, it is important to benefit from simple procedures and technologies making data model updating as simple as possible, such as those used in real time geosteering (Pelling et al. 2010) or using tetrahedral mesh such as in real-time updated modelling (Tertois and Mallet 2007). Present workflows are more or less linear making up-dating complicated and time consuming, especially in 4D. More research is needed in this field;
- Data quality is an important issue of geomodelling as well as uncertainty. Advanced modelling and visualization techniques must be investigated to quantify conceptual uncertainty, to visualize colors, textures, sounds and animation (see Viard et al. 2011) and to express uncertainty;
- Mineral resource exploration handles data coming from different sources such as drilling observations or measurements, sampling in galleries, chemical analyses, etc. (referred as *primary data*) or indirect measurements or modelling such as from geophysics (*secondary data*). These data are heterogeneous and need to be integrated on the same platform.

Improvements must be made in European infrastructures related to deep mineral resource exploration in order to benefit from new technologies. Partnerships between mining companies, software providers, public research institutes and geological surveys were made possible during the ProMine project where good talents from different areas and disciplines worked closely together as a team with common interests and not as isolated units. This approach must be strongly sustained and encouraged in the coming years before becoming a market-driven activity.

4.5 Conclusions

It is too early to state that 3D and 4D modelling of the ProMine project has led to a major mineral resources discovery. Nonetheless, we are convinced that it indirectly supported discoveries of new targets, confirming the add-on value of geomodelling to mineral exploration. Publication by industrial partners of discoveries based on 3D models would benefit the whole mining community, justifying a posteriori the initial public investment in the ProMine project. In Canada it is assumed that for one dollar invested from public money in similar 3D exploration programs, two and half dollars are collected indirectly through taxes.⁴ In the case of an ore deposit discovery, the investment is multiplied by hundreds⁵ (depending on the commodities) (Duke 2010, p. 6). European governments and Europe at large benefited by this project which made it possible to improve their mineral resources policy to stimulate future mining activities in Europe.

Acknowledgments The authors would like to express their thanks for the support from the gOcad consortium, the Centre National de Recherche Scientifique CNRS-CRPG, and the Université de Lorraine. This work was performed within the frame of the “Investissements d’avenir” Labex RESSOURCES21 (ANR-10-LABX-21) and partially financed by the ProMine FP7 NMP European Research Project grant agreement no 228559. The opinions expressed in this document are the sole responsibility of the author and do not necessarily reflect those of the involved companies or agencies. The authors acknowledge an anonymous reviewer for his suggestions for improving the initial version of the text.

⁴If a major exploration campaign is undertaken by the Geological Surveys on public funds, revealing new possible targets, mining industries generally invest in drilling programs for evaluating these new targets. This additional exploration works, even in case of no major new ore deposit discovery, generates revenues for the government from taxes paid by the companies when present in the country.

⁵According to Duke (2010), the Mining Association of Canada estimated that, from 2004 to 2008, revenues paid to Canadian governments from mining as royalties, corporate and individual income taxes averaged \$5.5 billion/year. Federal, provincial and territorial geological survey expenditures over the same period to promote exploration averaged \$80 million, or just 1.5 % of revenues.

References

- AGS (2014) – Geological Survey of Australia, <http://www.ga.gov.au/cedda/maps/593>
- Apel M. (2006) - From 3D geomodelling systems towards 3D geosciences information systems: Data model, query functionality, and data management. *Computer & Geosciences*, **32**, 222-229.
- AutoCAD (2012) - <http://usa.autodesk.com/>
- Bonham-Carter G. F (1994) - *Geographic Information Systems for Geoscientists: Modeling with GIS*. Computer Methods in the Geosciences. Pergamon Press, New York, NY, 1994. ISBN0-08-042420-1. 414 p. 10
- BGS (2014) - British Geological Survey website, <http://www.bgs.ac.uk/research/UKGeology/nationalgeologicalmodel/home.html>
- Caumon G., Grosse O. and Mallet J.-L., (2004) - *High resolution geostatistics on coarse unstructured flow grids*. In O. Leuangthong and C. V. Deutsch, editors, Geostatistics Banff, Proc. of the 7th Int. Geostatistics Congress. Kluwer, Dordrecht.
- Caumon G., Levy B., Castanié L., and Paul J.-C. (2005) - Visualization of grids conforming to geological structures: a topological approach. *Computers and Geosciences*, **31**(6), 671–680.
- Caumon G., Ortiz, J. and Rabeau, O. (2006) - A comparative study of three mineral Potential Mapping techniques, Proc. IAMG 2006, XI Int. Cong. Liege, 4p.
- Caumon G., Collon-Drouaillet P., Le Carlier de Veslud C., Viseur S., Sausse J. (2009) - Surface-Based 3D Modeling of Geological Structures. *Mathematical Geosciences*, **41**(8), 927–945.
- Caumon. G (2010) - Towards stochastic time-varying geological modeling: *Mathematical Geosciences* **42** (5), 555–569.
- Caumon G., Laurent G., Pellerin J., Cherpeau N., Lallier F., Merland R. and Bonneau F. (2013a) - *Current bottlenecks in geomodeling workflows and ways forward*. In: Closing the Gap: Advances in Applied Geomodeling for Hydrocarbon Reservoirs: 43–52, Canadian Society of Petroleum Geologists.
- Caumon G., Gray G., Antoine C., and Titeux M. O. (2013b) - Three-dimensional implicit stratigraphic model building from remote sensing data on tetrahedral meshes: theory and application to a regional model of La Popa basin, NE Mexico. *IEEE Transactions on Geoscience and Remote Sensing*, **51**(3), 1613–1621.
- Chamberlin R.T. (1910) - The Appalachian folds of central Pennsylvania. *Journal of Geology*, **18**, 228–251.
- Critical raw materials for the EU* (2010) - Report of the Ad-hoc Working Group on, European Commission, Enterprise and Industry, 85p.
- Dahlstrom C.D.A. (1969) - Balanced cross sections. *Canadian Journal of Earth Sciences*, **6**, 743–757.
- De Kemp E., and Jessell M. (2013) – Challenges in 3D modeling of complex geologic objects. 33th GOCAD Meeting, Nancy, France, September, 11p.
- Duke J.M. (2010) - *Government geosciences to support mineral exploration: public policy rationale and impact*. Prepared for Prospectors and Developers Assoc. of Canada, PDAC Geosciences Committee Report. 72p.
- Durand-Riard P., Caumon G., and Muron P. (2010) - Balanced restoration of geological volumes with relaxed meshing constraints, *Computers & Geosciences*, **36**(4), 441–452.
- Durand-Riard P., Salles L., Ford M., Caumon G. and Pellerin J. (2011) Understanding the evolution of syn-depositional folds: Coupling decompaction and 3D sequential restoration. *Marine and Petroleum Geology*, **28**(8), 1530–1539.
- Durand-Riard P., Guzofski C. A., Caumon G. and Titeux M. O. (2013) - Handling natural complexity in 3D geomechanical restoration, with application to the recent evolution of the outer fold-and-thrust belt, deepwater Niger Delta. *AAPG Bulletin*, **97**(1), 87–102.
- ETP SMR (2007) - *European Technology Platform on Sustainable Mineral Resources Strategic Research Agenda*, (ETP SMR), 70p. http://cordis.europa.eu/technology-platforms/smr_en.html
- Geovariances (2012) – Vendor of Isatis. <http://www.geovariances.com/en/>
- Geomodeler (2012) - Intrepid vendor of 3D geomodeler. URL <http://www.geomodeler.com>
- Geovia (2013) – Virtual planet. <http://www.3ds.com/products/geovia/>
- Gringarten E., Arpat B., Jayr S. and Mallet J.L. (2008) – *New Geologic Grids for Robust Geostatistical Modeling of Hydrocarbon Reservoirs*. GEOSTATS 2008, VIII Int. Geostatistics Congress, Santiago, Chile, Vol. 2, 647–656, Gecamin.
- Groshong R. (2006) - *3-D Structural Geology: A Practical Guide to Quantitative Surface and Subsurface Map Interpretation*. Springer, Heidelberg. 400p.
- Internet Guide to GIS, 2009. URL <http://www.gis.com>
- Janssens-Coron E., Pouliot J., Moulin B., Rivera A. (2010) - An Experimentation of Expert Systems Applied to 3D Geological Models Construction. Developments in 3D Geo-Information Sciences, Lecture Notes in Geoinformation and Cartography, Springer, 71-91
- Knowledge Generation Innovative Technologies (2010) – *A participatory model for knowledge generation and knowledge exchange to support eco-functional intensification*. TPorganics, http://tporganics.eu/upload/IAP/TPOrganics_IAP_InnovativeResearchMethods_draft_15Nov2010.pdf, 12p.
- Laurent G., Caumon G., Jessell M., Royer J.J. (2012a) - A Rigid Element Method for Building Structural Reservoir Models. 13th European Conf. on the Mathematics of Oil Recovery (ECMOR), Biarritz, 10p.
- Laurent G., Caumon g., and Jessell M. (2012b) - Forward Modeling of 3D Geological Structures with Rigid Elements Method, 32th GOCAD Meeting, Nancy, France, September, 11p.
- Leapfrog Geo (2013) - <http://www.leapfrog3d.com/>

- Mallet J.-L. (2002) - *Geomodeling. Applied Geostatistics*. Oxford University Press, New York, NY, 624 p.
- McGaughey J. (2006) - *The Common Earth Model: A Revolution in Mineral Exploration Data Integration*. In: J. Harriss (Ed), *GIS for the Earth Sciences*, SP 44: 567-576, Geological Association of Canada, St John, NL, Canada.
- Mejia P., Royer J.J. and A. Zielińska (2012) - *Late Cretaceous-Early Paleocene up-lift inversion in northern Europe: implications for the Kupferschiefer ore deposit in the Lubin-Sierosowice Mining District, Poland*. ProMine Workshop on Mineral Resources Potential Maps, Nancy, March, France, 8p.
- Mejia P. and Royer J.J. (2012) - *Explicit Surface Restoring-Decompacting Procedure to Estimate the Hydraulic Fracturing: Case of the Kupferschiefer in the Lubin Region, Poland*. 32th GOCAD Meeting, Nancy, France, September, 19p.
- Mejia P., Royer J.J., Fraboulet J.G. and Zielińska A. (2013) - *4D Geomodelling: a Tool for Exploration – Case of the Kupferschiefer in the Lubin Region, Poland*. (this book), 33p.
- MicroStation (2012) - Bentley vendor of MicroStation. URL <http://communities.bentley.com/products/microstation/default.aspx>
- MICROMINE's consulting (2012) - <http://www.micromine.com/>
- Midland Valley (2012) – Vendor of 3D Move. <http://www.mve.com/software/move>
- Mintec (2012) - Vendor of MineSight Implicit Modeling (MSIM) <http://www.minesight.com>
- Mirageosience (2013) – Modeling the Earth. <http://www.mirageosience.com/>
- Moretti I. (2008) - Working in complex areas: New restoration workflow based on quality control, 2D and 3D restorations. *Marine and Petroleum Geology*. **25**, 205–218.
- Nick H.M. and Matthäi S.K. (2011) - Comparison of Three FE-FV Numerical Schemes for Single- and Two-Phase Flow Simulation of Fractured Porous Media. *Transp Porous Med.*, **90**(2), 421–444.
- Paradigm (2012). Vendor of the GOCAD suite. URL <http://www.pdgm.com/>
- Pellerin J., Levy, B. and Caumon G. (2012) - Conformal hybrid meshing of structural models. 32th GOCAD Meeting, Nancy, France, September, 19p.
- Pellerin J., Caumon G., Julio C., Mejia P. And Botella A. (2013) - *Elements for measuring the complexity of 3D structural models; topology and geometry*. 33th GOCAD Meeting, Nancy, France, September, 17p.
- Pelling R., Gilmour D. and Innes R. (2010) - *Real-time geosteering software enhances data sharing, updating to optimize well placement*. Innovating While Drilling, Drilling Contractor magazine, IADC, 2p.
- Plesch, A., C. Tape, J. H. Shaw, and members of the USR working group, 2009, CVM-H 6.0: Inversion integration, the San Joaquin Valley and other advances in the community velocity model, in 2009 Southern California Earthquake Center Annual Meeting, Proceedings and Abstracts, **19**, 260–261.
- Pouliot J., Bénard K., Kirkwood D., Lachance B. (2008) - Reasoning about geological space: Coupling 3D GeoModels and topological queries as an aid to spatial data selection. *Computer & Geosciences*, **34** (5), 529-541.
- Rouby D., Xiao H. and Suppe J. (2000) - 3D restoration of complexly folded and faulted surfaces using multiple unfolding mechanisms. *Amer. Assoc. Petrol. Geol. Bull.* **84**(6), 805–829.
- Roxar (2009) - Irap rms software URL <http://www.roxar.com>
- Schlumberger (2009) - Vendor of Petrel and Eclipse. URL <http://www.slb.com/content/services/software/index.asp?>
- Sprague K. B. and de Kemp E. A. (2005) - Interpretive Tools for 3-D Structural Geological Modeling Part II: Surface Design from Sparse Spatial Data, *GeoInformatica*, **9**(1), 5–32.
- Surfer 9 (2012) - Grapher, Didger, Mapviewer and Strater, Voxler <http://www.ssg-surfer.com/>
- Tape, C., Q. Liu, A. Maggi, and J. Tromp, (2009) - Adjoint tomography of the southern California crust, *Science*, **325**, 988–992.
- Tertois A.L., and Mallet J.L., (2007) - Editing faults within tetrahedral volume models in real time, Geological Society, London, Special Pub., **292**, 89-101.
- Turk G. and O'Brien J.F. (2002) - Modeling with Implicit Surfaces that Interpolate, *ACM Trans. on Graphics*, **21** (4), 855-873
- Viard T., Caumon G. and Levy B. (2011) - Adjacent versus coincident representations of geospatial uncertainty: Which promote better decisions? *Computers and Geosciences*, **37**(4), 511–520.
- Vulcan (2012) – Maptek vendor of Vulcan. URL: <http://www.maptek.com/products/vulcan/>

Part II

The Fennoscandian Shield

Tobias E. Bauer, Pietari Skyttä, Tobias Hermansson,
Mahdieh Dehghannejad and Saman Tavakoli

Abstract

Four-dimensional geological modelling has been conducted in the Palaeoproterozoic Skellefte mining district. 3D-modelling of volcanic-hosted massive sulphide deposits and associated host-rocks has been carried out in multiple scales from deposit to regional scale and is based on a combination of geological and geophysical investigations. A conceptual model founded on unravelling the structural control on sedimentation, volcanism and mineralization and the subsequent deformation patterns, acts as a base for geological modelling. The final 3D-model provides a structural framework in which the mineralizations can be studied by improved understanding of the structural evolution in the mine areas, and by comparing the regional structural patterns versus the form and attitude of ore deposits. Additionally, uncertainty and prospectivity models were constructed showing the distribution of data and the potential of discovering new ore deposits. Subsequent 4D-modelling adds the time aspect to the 3D-models and aims at visualizing and understanding the geological history in the district and as a support for ore targeting. Moreover, adding geological time to the modelling helps gaining confidence about both the conceptual models and the 3D-models. The final 3D- and 4D-models provide a regional three-dimensional context for both industrial and academic activities in the Skellefte district, and aid the understanding of large-scale tectonic processes.

T.E. Bauer (✉) · P. Skyttä · S. Tavakoli
Division of Geosciences and Environmental
Engineering, Luleå University of Technology,
971 87 Luleå, Sweden
e-mail: tobias.bauer@ltu.se

T. Hermansson
Boliden Mines, 936 81 Boliden, Sweden

M. Dehghannejad
Department of Earth Sciences, Uppsala University,
Villavägen 16, 75236 Uppsala, Sweden

5.1 Introduction

5.1.1 Background and Aims

The Skellefte district is located in northern Sweden and is one of Europe's most important mining districts. Mining started in 1924 in Boliden paving

the way for exploration in the Skellefte district. The district hosts approximately 80 volcanogenic massive sulphide deposits, several intrusion related gold (and copper/zinc) deposits, and a few orogenic gold deposits (Kathol and Weihed 2005; Bejgarn et al. 2012). Currently, zinc, copper, lead, arsenic, tellurium and gold are mined by Boliden Mines from the Kristineberg, Renström and Kankberg underground operations and the, Maurliden East and Maurliden West open pit mines. Additionally, gold is mined by Gold Ore Resources Ltd. from the Björkdal deposit.

Exploration commenced in the 1920s and the majority of shallow deposits are believed to be already discovered. Today, most of the ore is mined from between 500 and 1300 m depth, and the ore systems are still open down plunge. For this reason, good control on the 3D-architecture of the uppermost 4 km of the Earth's crust in the Skellefte district is crucial for future exploration.

3D-modelling is based on a combination of geological and geophysical investigations. Detailed studies aim at unravelling the structural control on sedimentation, volcanism and mineralization and the subsequent deformation patterns. The 3D-model provides a structural framework in which the mineralizations can be studied by improved understanding of the structural evolution in the mine areas (e.g. *fault-system geometry, kinematics, nature of the fold structures and strain partitioning*), and by comparing the regional structural patterns versus the form and attitude of ore deposits. Subsequent 4D-modelling adds the time aspect to the 3D-models and aims at visualizing (but also understanding) the geological history in the district and also constitutes a support for ore targeting. Moreover, adding geological time to the modelling helps gaining confidence about both the conceptual models (e.g. by 2D-forward modelling; Bauer et al. 2011) and the 3D-models.

The final 3D- and 4D-models provide a regional three-dimensional context for both industrial and academic activities in the district, and aid the understanding of large-scale tectonic processes. Furthermore, the models represent a visualization tool for decision-makers and for educational purposes, and provide a possibility to

present the often complex geological scenarios in an intuitive way.

5.1.2 Modelled Volumes

Modelling in the Skellefte district has been carried out in three different scales, ranging from regional to semi-regional to deposit scale (Fig. 5.1). The regional scale 3D-model covers the bulk of the Skellefte district and acts as a framework for the smaller-scale sub-projects. Due to the availability of suitable data from the reflection seismic studies, the regional scale 3D-model extends down to approximately 4 km depth. The semi-regional scale model covers the central parts of the Skellefte district and mainly concentrates on the geometry of a sedimentary sub-basin, the so-called Vargfors syncline or Vargfors basin. Due to the good exposure and relatively low strain, detailed structural and facies analyses acted as a base for the construction of a conceptual model. Additional high-resolution geophysical methods constrained the basin geometry and allowed modelling down to approximately 1 km. Deposit scale 3D-models have been produced for 21 VMS deposits throughout the district (Fig. 5.1). The depth extent of each deposit model varies with the size of the individual deposits and ranges from 45 m down to 1.3 km. Both the semi-regional scale and the deposit scale models have been integrated into the regional scale model.

5.2 Geological Background

The Skellefte district comprises Palaeoproterozoic supracrustal and intrusive rocks that formed in a volcanic arc setting and were deformed and metamorphosed during the Svecokarelian orogeny (Allen et al. 1996; Lundström et al. 1997; Mellqvist et al. 1999; Kathol and Weihed 2005). The district lies in-between two major tectonic units (Fig. 5.1): (i) an area with Palaeoproterozoic and reworked Archaean rocks of the Norrbotten craton north of the Skellefte district and (ii) Bothnian Basin metasedimentary rocks to the

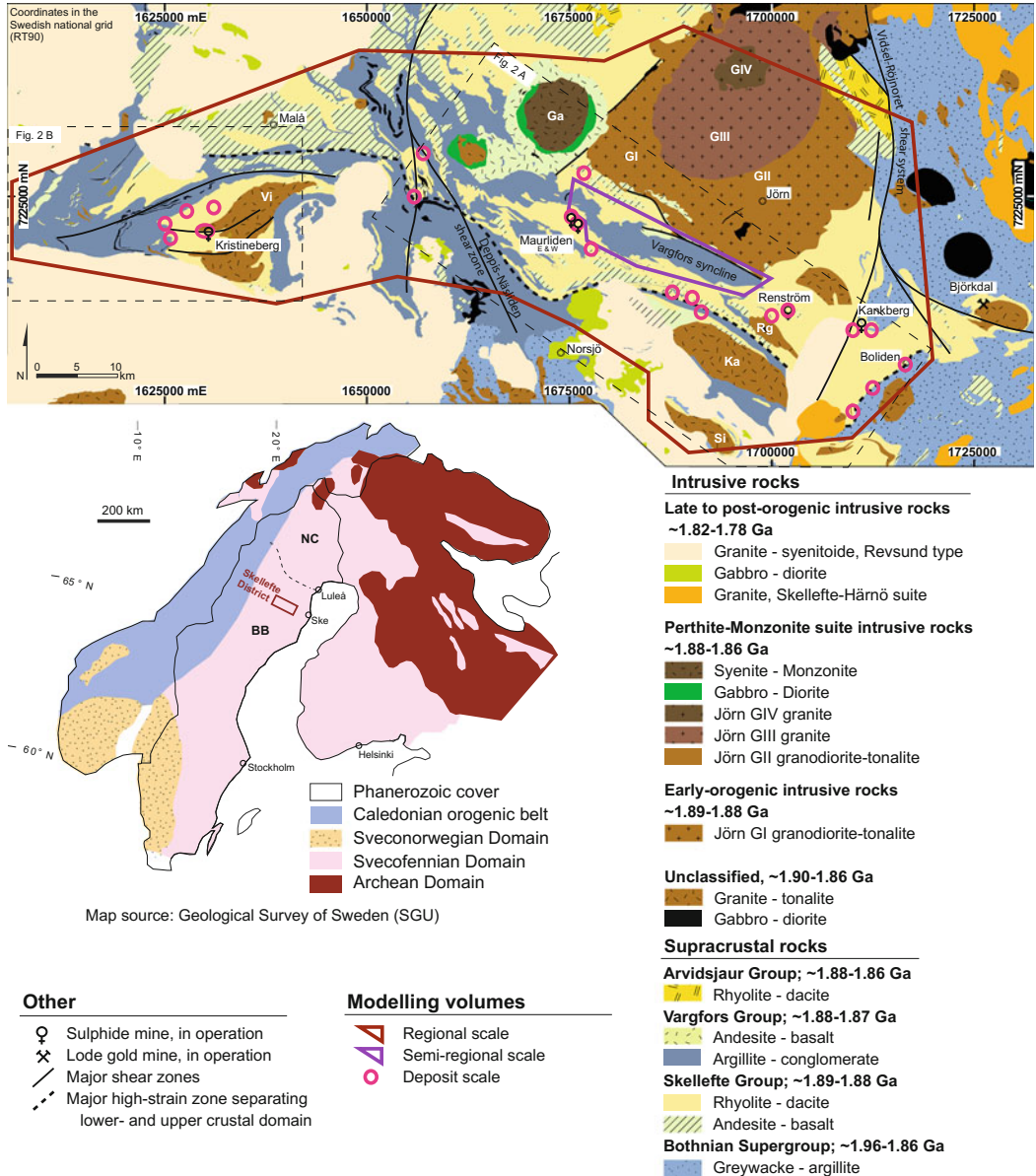


Fig. 5.1 Inset Generalized Fennoscandian Shield geology. Geological domains: BB Bothnian Basin; NC Norrbotten Craton. The dashed line marks the boundary between the rocks with Archean and Proterozoic εNd-signatures (Mellqvist et al. 1999). Geology drawn after Koistinen et al. (2001). **Main map** Geological overview of the Skellefte district, as loosely defined by the

occurrence of the Skellefte Group metavolcanic rocks, and their immediate vicinity. Intrusions: Vi Viterliden, Ga Gallejaur, Rg Rengård, Ka Karstråk, Si Siktråk, Bj Björkdal, GI, GII, GIII, GIV = Jörn type intrusions, phases I–IV, S Stavatråk. Geology after Kathol et al. (2005) and Bergman Weihed (2001)

south and east of the district. Due to the increase of strain and metamorphic grade from north to south, and the change from localized to more

penetrative deformation, the Skellefte district was interpreted as a transitional zone between these two units (Skyttä et al. 2012).

Metasedimentary rocks of the Bothnian Supergroup have been suggested to form the basement to the 1.89–1.88 Ga Skellefte Group volcanic rocks. The latter comprise at least 3 km of volcanic stratigraphy dominated by felsic volcanic and volcanoclastic rocks (Figs. 5.2 and 5.3; Allen et al. 1996; Billström and Weihed 1996; Montelius 2005; Malehmir et al. 2007; Skyttä et al. 2011). The volcanogenic massive sulphide (VMS) deposits formed as sub-seafloor replacement and partly exhalative deposits in volcanoclastic and sedimentary rocks within the uppermost part of Skellefte Group stratigraphy (Allen et al. 1996).

The upper parts of the overlying Vargfors Group (1.88–1.87 Ga) predominantly consist of sedimentary rocks and the stratigraphically lower parts are dominated by laminated mudstones and sandstones. Whereas the latter occur throughout the district, the conglomerates, belonging to the stratigraphically higher parts of the Vargfors

Group, are limited to the Vargfors syncline in the central parts of the Skellefte district (Fig. 5.2; Allen et al. 1996; Kathol and Weihed 2005; Bauer et al. 2011, 2013). Vargfors Group sedimentary rocks at the southern extent of the Skellefte district grade into Bothnian Supergroup rocks whereas the contact has been drawn in an arbitrary manner (Kathol and Weihed 2005).

The oldest intrusive rocks in the Skellefte district are granitoids and intermediate or mafic rocks with an age of 1.89–1.88 Ga, and therefore co-magmatic with the volcanic Skellefte Group (Figs. 5.2 and 5.3). The most prominent intrusions of this phase are the GI-phase of the Jörn intrusive complex and the Viterliden, Rengård, Karstråk and Siktråk intrusions (Wilson et al. 1987; Kathol and Weihed 2005; Gonzales Roldan 2010; Skyttä et al. 2010, 2012; Bejgarn et al. 2012). Younger intrusive rocks that post-date the volcanic activity are represented by the GII to GIV phases of the Jörn intrusive complex and

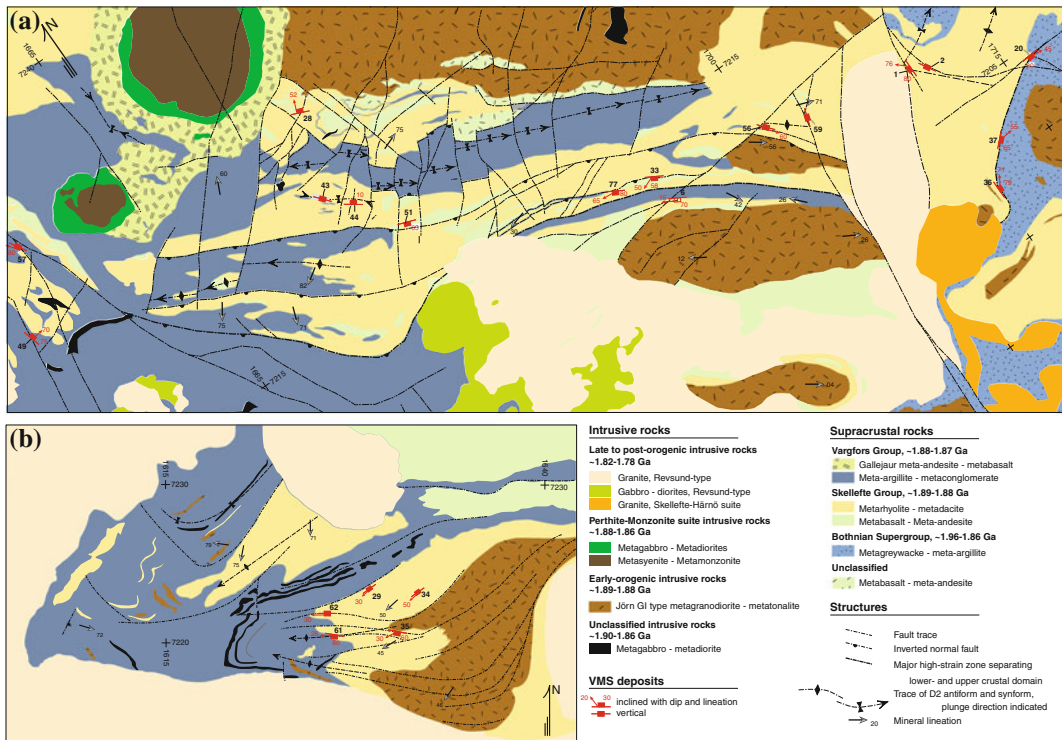


Fig. 5.2 Geological map of the central Skellefte district and Kristineberg area, including the location and orientation of volcanogenic massive sulphide deposits. Modified after Allen et al. (1996), Kathol et al. (2005) and Bauer (2010)

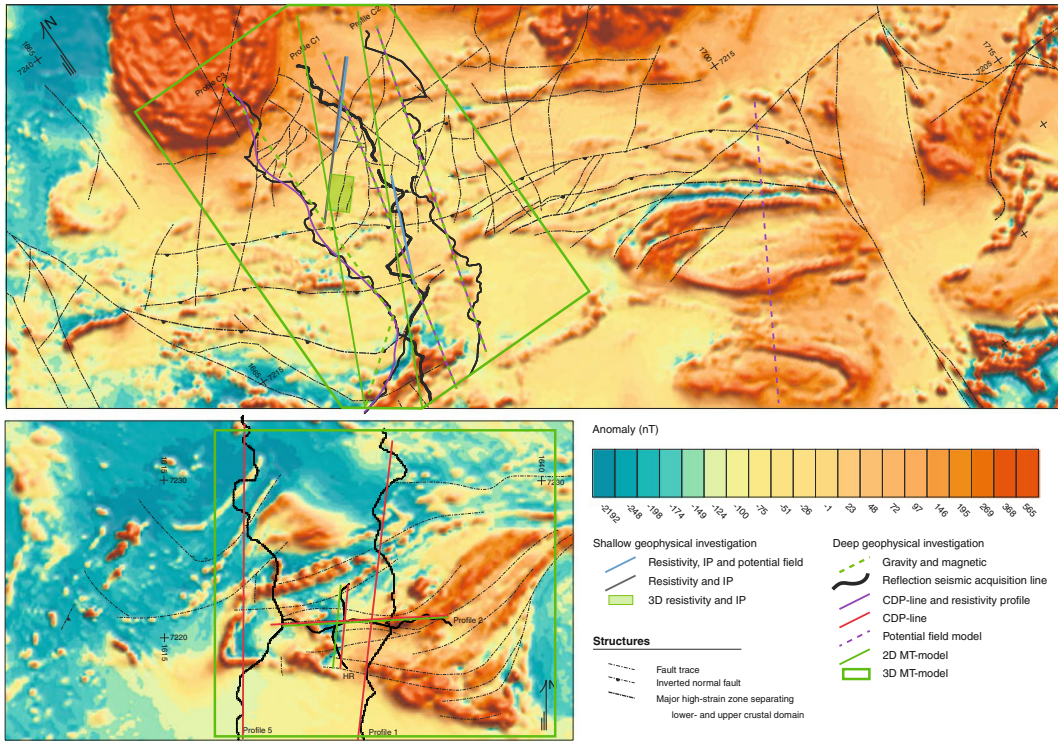


Fig. 5.3 Magnetic anomaly map of the central Skellefte district and Kristineberg area including the location of geophysical investigations and high-strain zones. Modified after Kathol and Weihed (2005) and Bauer (2010)

intrusive rocks of the Perthite-Monzonite suite that formed between 1.88 and 1.86 Ga (Kathol and Weihed 2005; Bejgarn et al. 2012). Late Sveco-karelian rocks ranging from 1.82 to 1.78 Ga are bordering the Skellefte district (Kathol and Weihed 2005).

Structurally, the western part of the Skellefte district (Kristineberg area) is dominated by E-W-striking shear zones (Figs. 5.2 and 5.3; Skyttä et al. 2013). In the central part of the district, these shear zones strike WNW-ESE and are associated with NNE-SSW-striking shear zones. At the southern end of the Skellefte district a major WNW-ESE-striking shear zone (Figs. 5.1, 5.2 and 5.3; Dehghannejad et al. 2012b) separates two crustal domains with characteristic deformational signatures (Skyttä et al. 2012). In the northern domain, Bauer et al. (2011) and Skyttä et al. (2012) showed that these shear zones have a syn-extensional origin and influenced sedimentation in the Vargfors Group. Furthermore, Bauer et al.

(2013, 2014) suggested that these syn-extensional faults acted as fluid conduits for ore-forming hydrothermal fluids.

Subsequent crustal shortening at shallower crustal levels (1.88–1.87 Ga) was oriented SSW-NNE, coaxial in nature, and resulted in inversion of the WNW-ESE syn-extensional faults (Bauer et al. 2011). Furthermore, deformation resulted in the transposition of VMS ore bodies and a penetrative pattern of steep to sub-vertical mineral lineations (Skyttä et al. 2012).

Crustal shortening in the southern domain reflects deformation at deeper crustal levels and is characterized by non-coaxial high-strain deformation, accompanied by lateral stretching and gently plunging mineral lineations, which is suggested to result from NNW transpression at 1.88–1.87 Ga or by later compression at 1.86 Ga (Skyttä et al. 2012).

A later E-W-directed crustal shortening event at 1.82–1.80 Ga (Weihed et al. 2002) resulted in

the re-activation of major \sim N-S-striking high-strain zones (e.g. Deppis-Näsliden shear zone and Vidsel-Röjnoret shear system in Fig. 5.1; Bergman Weihed et al. 1996; Bauer et al. 2011; Skyttä et al. 2012).

5.3 Dataset and Methods Used to Build the 3D Model

5.3.1 Geological and Geophysical in-Data—Character and Acquisition

5.3.1.1 Geological Data

As a base for 3D-modelling, extensive semi-regional and regional scale field mapping (cf. Fig. 5.1) has been carried out, resulting in a total of approximately 1800 observation points, approximately 5700 structural measurements and 293 oriented thin sections. Based on this, a detailed, semi-regional scale structural analysis of the Vargfors syncline has been produced and a conceptual model for basin inversion has been suggested (Bauer et al. 2011). Combining sedimentary facies analysis (Bauer et al. 2013) with regional scale structural analysis and geochronological studies (Skyttä et al. 2012), a regional structural concept for transpression and fault inversion in the central Skellefte district was also developed (Skyttä et al. 2012). This conceptual model was tested and locally validated by observation of sparse drill-cores. For the deposit-scale models abundant near-mine drill core data, level plans and cross-sections were available from Boliden Mines.

5.3.1.2 Geophysical Data

For regional scale modelling, 142 km of seismic reflection lines along six profiles in the Kristineberg area, the central Skellefte district, and northwest of the district provided a framework for identifying major shear zones and lithological contacts down to approximately 5 km (Fig. 5.3; Malehmir et al. 2006, 2007, 2009a, b; Dehghannejad et al. 2010, 2012a, b; Ehsan et al. 2012). 120 broadband

magnetotelluric sites, along six profiles, and a 3D grid were also recorded (Fig. 5.3; Hübner et al. 2009, 2013; García Juanatey et al. 2012). Furthermore, potential field (magnetic and gravity) modelling along three seismic profiles in the central Skellefte district was conducted to a depth of approximately 5 km, aiming to further improve the result from the interpretation of the seismic data (Tavakoli et al. 2012a). Density and magnetic susceptibility data, determined on core samples from selected drill-holes, were used to support geophysical interpretations (Tavakoli et al. 2012a).

Semi-regional scale geophysical studies in the central Skellefte district utilized DC resistivity, induced polarization (IP), and magnetic and gravity data down to approximately 0.5–1 km depth (Fig. 5.3; Tavakoli et al. 2012b). The 2.5D geometries of the three early orogenic intrusions Rengård, Karsträsk and Sikträsk were modelled based on potential field data (Skyttä et al. 2012). In addition, the geometries of the Vargfors syncline and the major contact between the latter and the Skellefte Group rocks were outlined from the semi-regional geophysical interpretations, suggesting a synform boundary. In addition, the contact between different types of Skellefte Group rocks is also understood using the resistivity/IP data. Furthermore, 2D resistivity/IP and 3D resistivity/IP measurements down to approximately 1.5 km depth were utilized to identify geological structures potentially related to VMS deposits (Tavakoli et al. 2015).

5.3.2 Processing of Geological and Geophysical in-Data and Input to Model

5.3.2.1 Structural and Facies Analysis in the Vargfors Syncline

Due to the occurrence of soft-sediment deformation structures in Vargfors Group rocks, stratigraphic variations between fault-bound compartments and their correlation with faults that have varying dip directions and geometries, the concept of syn-extensional sedimentation due to subsidence along growth faults has been

suggested. Furthermore, subsequent basin inversion along the faults, favoured by a rheologically weak carbonate-rich layer at the bottom of the basin, has been inferred from strongly sheared carbonaceous rocks in the lower-most parts of Vargfors stratigraphy (Bauer et al. 2011). Based on the distribution and clast-composition of conglomerates in the upper Vargfors Group stratigraphy, Bauer et al. (2013) suggested a progressive opening of the basin starting from its centre. Complementing the field observations, 2D-forward geological modelling was carried out using 2D MOVE (Midland Valley Exploration Ltd.) in order to test and validate the suggested geometries and, consequently, the concept of basin inversion in the Vargfors syncline (Fig. 5.4; Bauer et al. 2011). The products of the above results were geological maps and cross-sections, which acted as a direct input into the models (Figs. 5.5, 5.6 and 5.7).

5.3.2.2 Reflection Seismic Investigations

Field seismic data from the surveys were processed by pre-stack signal enhancement and subsequent stacking (Dehghannejad et al. 2010, 2012b). Detailed processing of seismic data has been described by Malehmir et al. (2006, 2007, 2009a, b) Dehghannejad et al. (2010, 2012a, b) and Ehsan et al. (2012). Due to the crooked character of the seismic acquisition lines, cross-dip analysis was performed to identify out-of-the-plane reflections (Dehghannejad et al. 2012b and references therein). The migrated seismic sections were then interpreted by correlating seismic reflectors with geological structures visible on the surface or inferred from magnetic maps. By doing this a regional scale structural framework of high-strain zones was obtained.

5.3.2.3 Magnetotellurics

Magnetotelluric measurements were carried out in the areas where reflection seismic data were available (Fig. 5.3) in order to enable a correlation

between those two techniques. A detailed description of the acquisition and processing is presented by García Juanatey (2012).

5.3.2.4 Resistivity/IP and Potential Field

Model Vision Pro™ (Encom Technology) was used to calculate the forward response and inverse density and magnetic susceptibility models. For semi-regional and regional interpretations, magnetic and gravity modelling was conducted in 2.5D, where the modelled body has an infinite length in the strike direction (Tavakoli 2012). The modelled bodies were extended beyond the actual length of the profiles, both along and perpendicular to the direction of the profiles, in order to take the effect of the neighbouring rocks into account. The regional magnetic and gravity fields were calculated covering an area beyond the original profiles using a 2nd order polynomial (Model Vision Pro™, Encom Technology; Tavakoli et al. 2012b). The regional fields were then subtracted from measured data using the polynomial fitting method to achieve residual anomalies, which theoretically are related to the local geological structures. The resistivity/IP interpretations were conducted using several modelling codes such as Res2Dinv, Res3Dinv and Res2Dmod (Loke 2010), DCIP2D and DCIP3D (University of British Columbia-Geophysical Inversion Facility) developed by Oldenburg and Li (1994). For forward modelling of the resistivity data, the initial models were divided into rectangular cells where each cell was assigned a resistivity value. The forward models were then inverted to find the optimum model consistent with other interpretations. For inversion of the 2D resistivity data, a combined Marquardt and Occam approach was used. This type of inversion is suggested to be particularly suitable when targeting thin sheet-like formations, such as ore bodies (Loke 2010). The models were calculated at greater depths where areas of the depth sections with sparse data coverage are also shown in the pseudo-sections. The inversion results were,

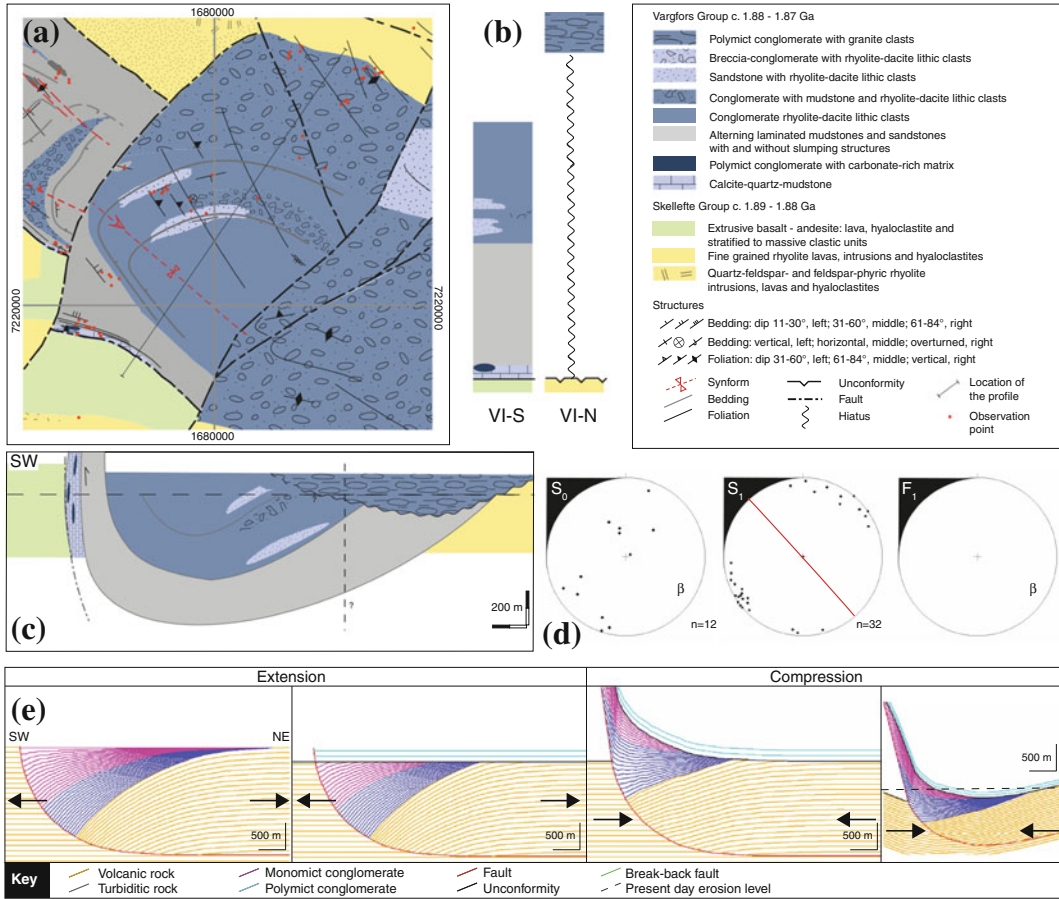


Fig. 5.4 Example from structural and facies analysis in one fault-bound compartment in the Vargfors syncline, central Skellefte district: **a** geological map with detailed structures; **b** stratigraphic column; **c** geological cross-section; **d** lower-hemisphere, equal-area stereographic

projections of bedding planes, foliation planes and fold axis; **e** 2D-forward modelling of syn-extensional sedimentation and subsequent basin inversion. Modified after Bauer et al. (2011)

subsequently, exported to Surfer (Golden software) to create the iso-value contours for presentations of the inverted data (Tavakoli et al. 2015). 3D resistivity/IP data were inverted using the UBC inversion code (DCIP3D). The 3D mesh included 30×30 m cell size for horizontal cells and 15 m in vertical direction. The inverted conductivity model was used for the calculation of sensitivities for the chargeability inversion. The conductivity model was also used to construct a reference model for the

chargeability inversion through an empirical relation (Tavakoli et al. 2015).

5.3.2.5 Regional Scale Structural Analysis

Regional scale structural analysis utilized the results of the smaller scale sub-studies and provided a structural summary of the two key areas, the central Skellefte district and the Kristineberg area. Results of the regional scale structural analysis are summarized in Skyttä

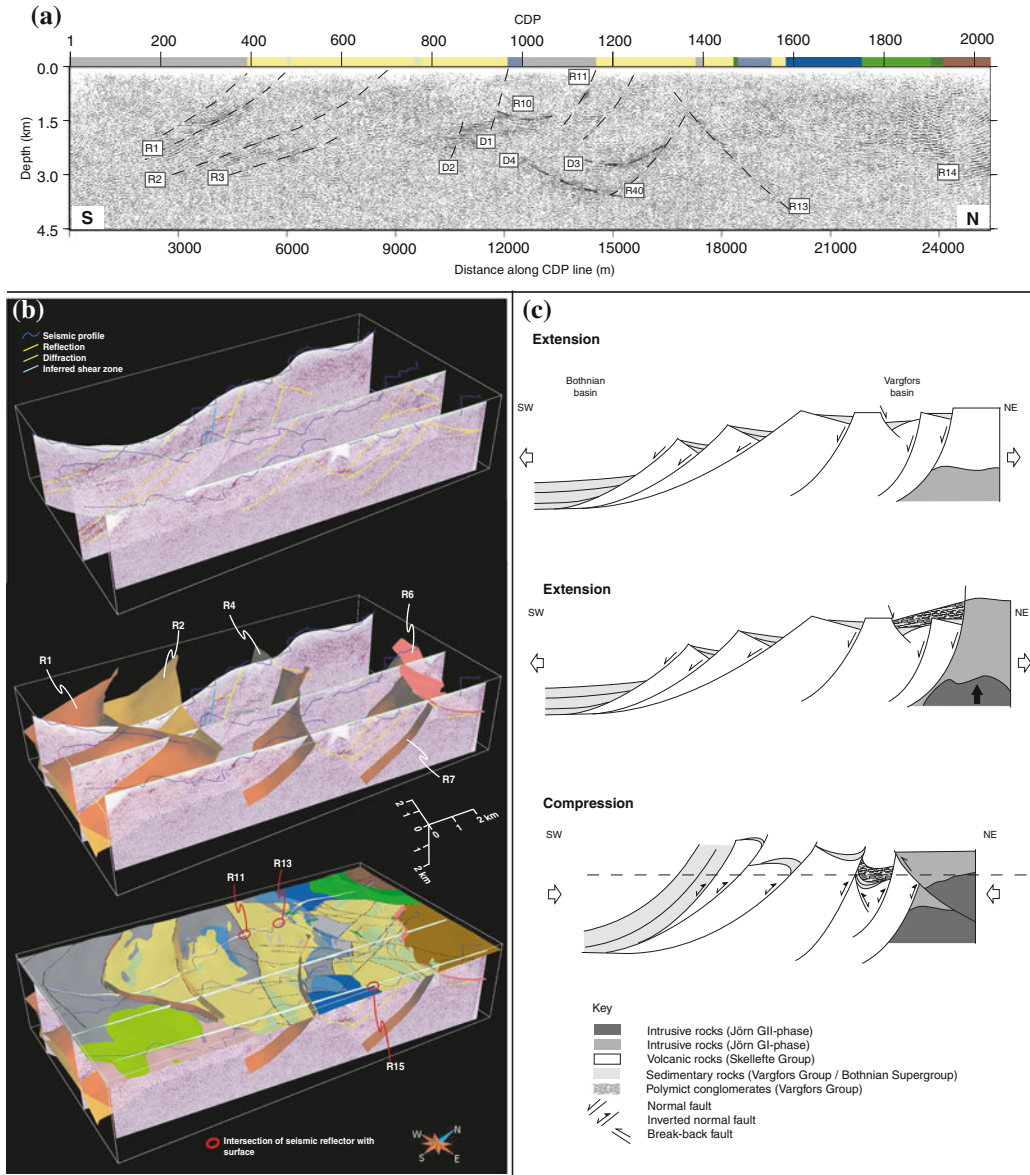


Fig. 5.5 Examples from reflection seismic investigations: **a** interpreted migrated seismic section of Profile C3 in Fig. 5.3a, including surface geology along the acquisition line; **b** 3D views showing interpreted seismic profiles C1, C2 and C3 (cf. Fig. 5.3a), and their

correlation with surface geology; **c** reconstruction of the geological history in the central Skellefte district. Modified after Dehghannejad et al. (2012b) and Bauer et al. (2013)

et al. (2012, 2013). In the central Skellefte district the concept of syn-extensional faulting and subsequent fault inversion, developed in the Vargfors syncline (cf. Bauer et al. 2011), was

applied on a larger scale. Combined with the detailed field work throughout the region, alternative scenarios for the tectonic evolution of the Skellefte district were proposed (Fig. 5.8).

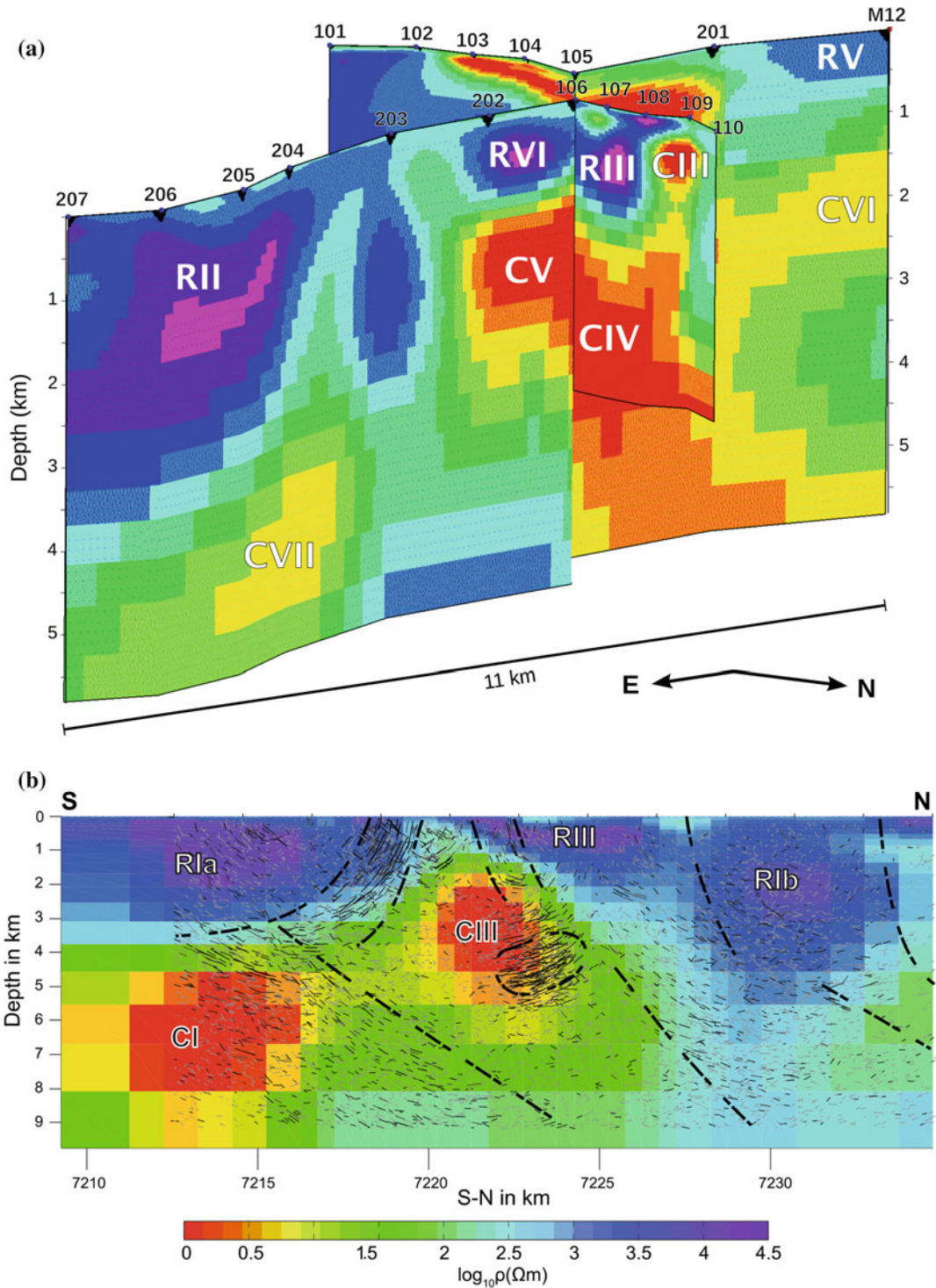


Fig. 5.6 Examples from magnetotelluric investigations in the Skellefte district: **a** two cross-cutting 2D-MT-models in the Kristineberg area (see Fig. 5.3b for location); **b** section through the 3D conductivity model

in the Kristineberg area with migrated line drawings of seismic reflectors from Malehmir et al. (2007). Modified after Hübner et al. (2013)

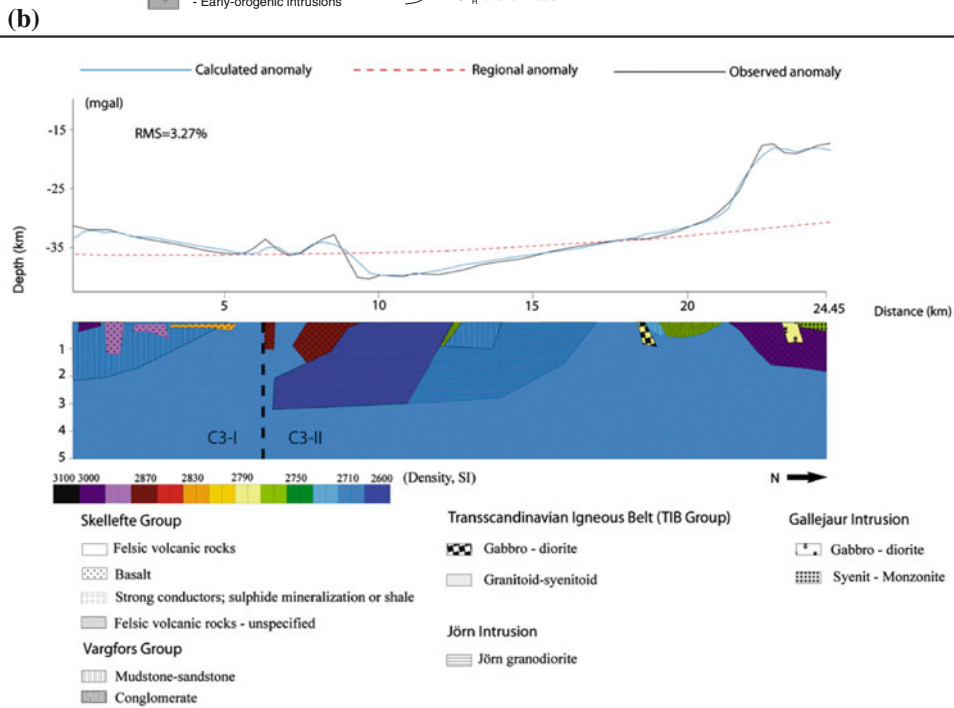
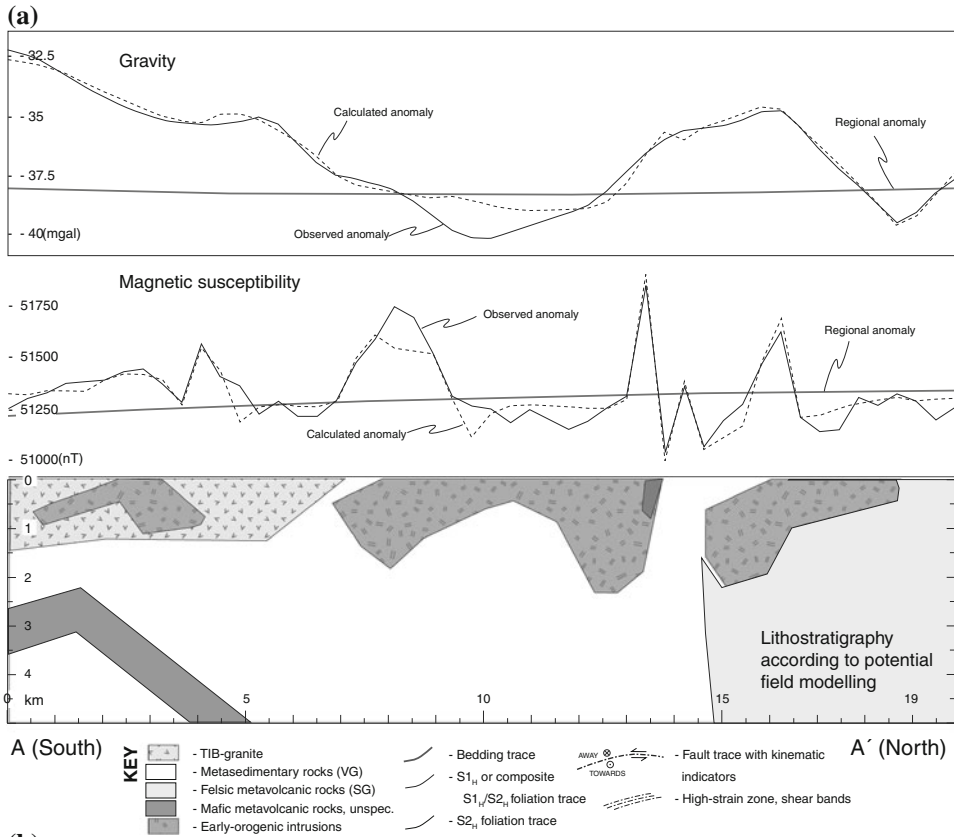


Fig. 5.7 Examples from potential field modelling in the Skellefte district: **a** potential field modelling across the Rengård, Holmträsk and Sikträsk intrusions; **b** gravity

modelling along reflection seismic profile C2 (see Fig. 5.3a for location; cf. Dehghannejad et al. 2012b). Modified after Skyttä et al. (2012) and Tavakoli et al. (2012a)

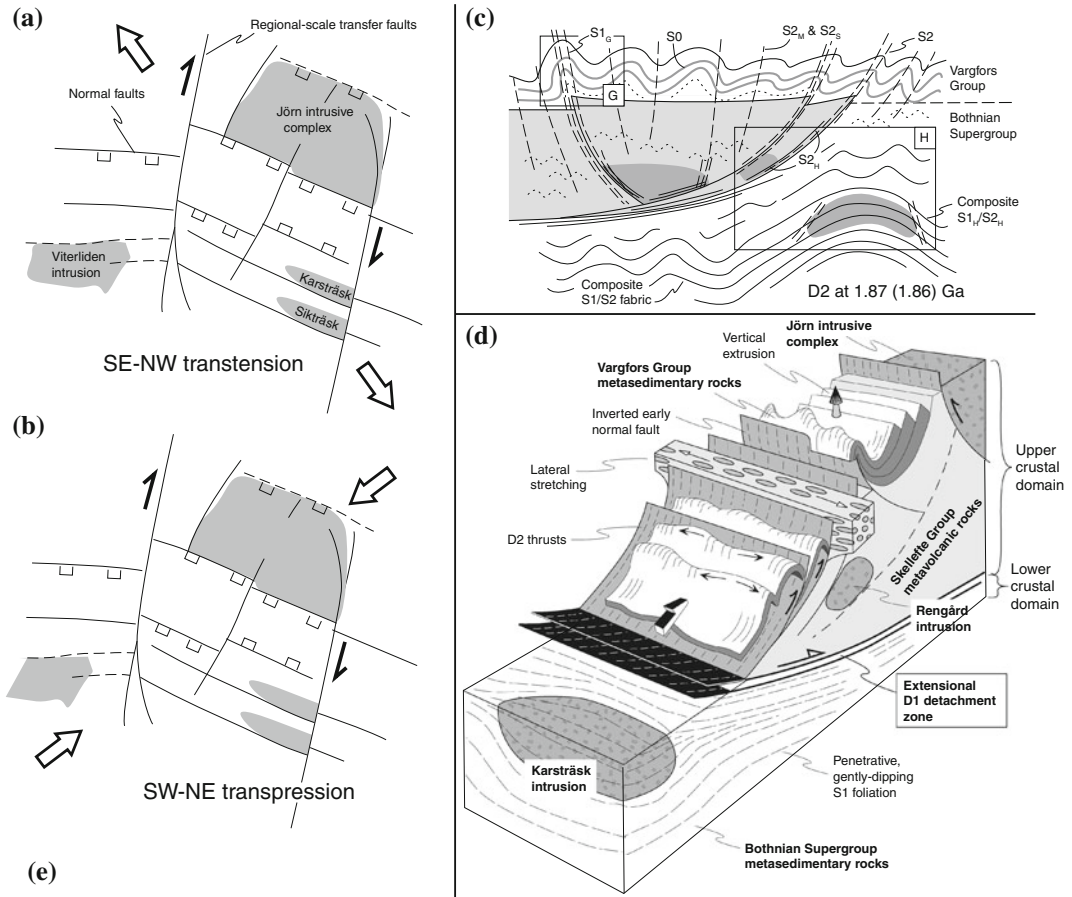


Fig. 5.8 Results from region scale structural analysis: **a** and **b** alternative scenarios for the formation of pull-apart basins in the Skellefte district. **c** schematic presentation over the development of Skellefte district. **d** block diagram illustrating the crustal geometry of the central Skellefte district. **e** Tectonic sketch map over the development of Skellefte district. Modified after Skyttä et al. (2012)

5.3.3 Modelling Methodology

5.3.3.1 Deposit Scale

A total of 21 deposits with adequate amount of available data were modelled in three dimensions. Modelling was performed using the gOcad software platform (Paradigm) utilizing existing mine models provided by Boliden Mines for the Kristineberg, Maurliden W, Rävliiden, Rävliidmyran and Renström W deposits.

Modelling started with importing existing level plans and cross sections from Boliden and Gold Ore Resources based on dense drilling patterns. As the majority of level plans and cross-sections were in paper format, digitization was required. Due to a relatively high degree of details, the outline of the ore bodies on the plans and sections were simplified without modifying their general shape and character (Fig. 5.9). Subsequently, surfaces were built from the produced set of parallel, closed curves. In order to

remove artefacts from surface building, the triangles were beautified utilizing the gOcad command “beautify triangles”.

5.3.3.2 Semi-regional Scale

Semi-regional scale modelling concentrated on the Vargfors syncline in the central Skellefte district (Fig. 5.1). Modelling was based on a combination of abundant structural data and IP/resistivity data. Primarily, the pattern of inverted normal faults and associated transfer faults (cf. Bauer et al. 2011) was modelled. The basin-bounding faults were created from curves digitized on resistivity/IP profiles and consequently interpolated along their map traces. For areas without geophysical data, the re-activated listric faults were modelled based on the results of 2D-forward modelling or by assuming their geometry based on comparison with neighbouring faults. The transfer faults were constructed by vertical interpolation of their map traces down to 500–2000 m.

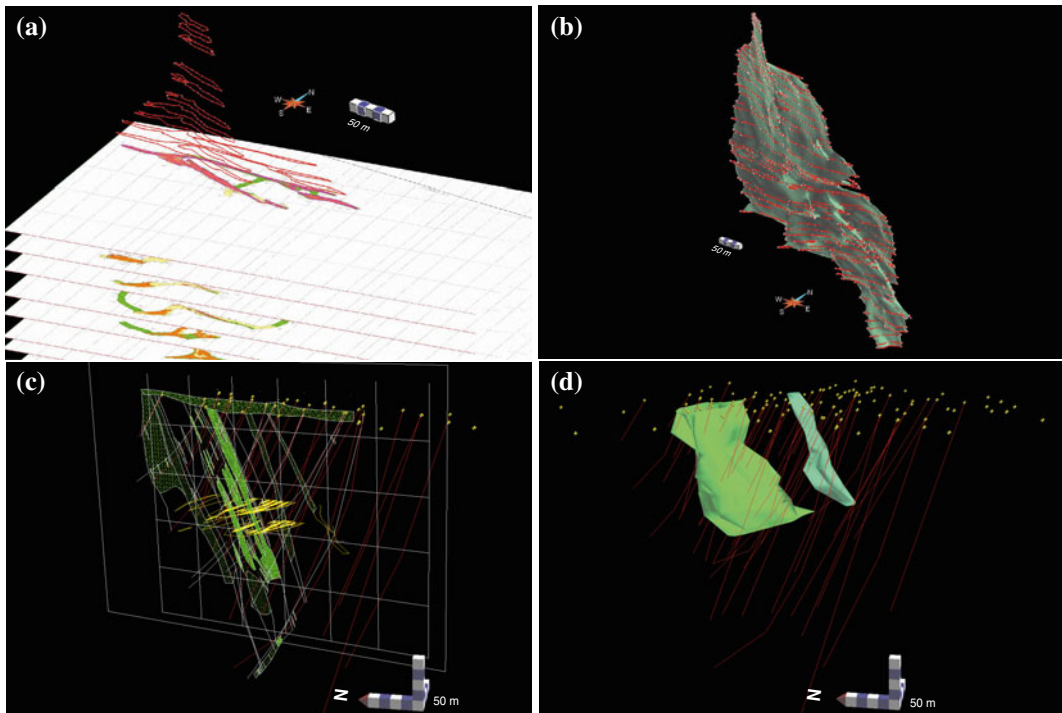


Fig. 5.9 Modelling and simplification of VMS ore bodies: **a** digitalizing of georeferenced paper level plans, **b** modelled surface of the ore body, **c** digitalizing and

simplification of level plans, cross-sections and drill paths, **d** 3D model of an ore body with available drill-holes

Subsequently, the sedimentary strata within each of the fault-bound compartments was modelled in smaller scale sub-projects and later combined into one semi-regional scale model. Structural measurements were visualized in 3D as discs with true strike and dip (Fig. 5.10) and map traces of lithological contacts were digitized onto the geological map. Subsequently, structural measurements were interpolated along the map trace using a distance tolerance of 200 m from the map trace (Fig. 5.10). Parallel

with the corresponding fold axis (measured and/or calculated b-axis) a keel was constructed. Based on the map trace, the interpolated structural measurements and the keel, a frame with several parallel lines was constructed. The geometries of the frames were adjusted manually to fit resistivity/IP profiles and drill-hole data, where available, by dragging/snapping to defined markers. Finally, the frames were converted to absolute surfaces (e.g. De Kemp and Sprague 2003).

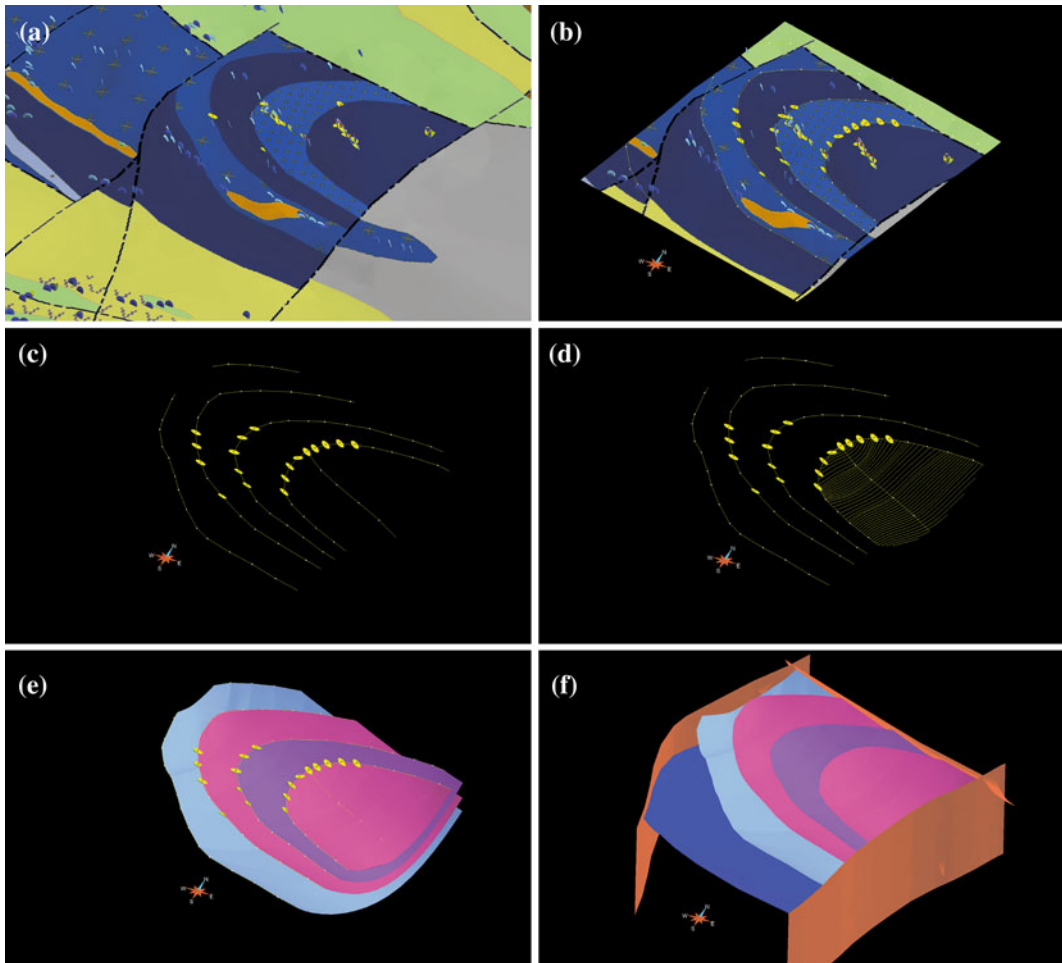


Fig. 5.10 Modelling of a fault-bound compartment in the Vargfors basin using gOcad (Paradigm) and SPARSE (Mira Geoscience): **a** geological map with structural measurements in 3D-orientation, **b** interpolation of structural measurements along the map traces of the geological

contact, **c** construction of a keel parallel to the fold axis, **d** construction of a frame based on the structural measurements, the map trace and the keel, **e** conversion of the frame into surfaces, **f** cutting of surfaces with surrounding faults

5.3.3.3 Regional Scale

Modelling in a regional scale was carried out in several smaller scale sub-projects, and later combined into one regional scale model. First, the regional scale fault pattern was modelled based on the reflection seismic investigations, magnetic and Bouguer anomaly data, and data from geological field mapping. Seismic reflectors were digitized onto the profiles and, where possible, correlated between parallel profiles. For areas without seismic data, geological field data were interpolated downwards, applying the concept of fault inversion established from structural analysis. This method requires a correct conceptual model and has to be clearly marked and communicated. Subsequently, lithological contacts were modelled based on field data and resulting geological cross sections. The modelling methodology was similar to that of the semi-regional scale modelling. The surfaces were constrained by resistivity/IP profiles and MT-data, where available. Furthermore, sparse drill-hole data outside mineralized areas added constraints to the model.

The models produced from deposit and semi-regional scale modelling were subsequently incorporated into the regional scale model. Due to the complexity of ore transposition patterns, the lack of marker horizons in ore-related alteration systems, the complex volcanic successions, and the detail of the smaller scale models, a certain degree of simplification was necessary during incorporation into the regional scale model.

5.3.3.4 Uncertainties

Modelling uncertainties were assigned for the final 3D-model of the Skellefte district in order to visualize the primary data and to serve as a base for interpretations on which 3D-surfaces and bodies were constructed (Fig. 5.11). The assigned uncertainty values represent: (1) observed in field, mine or drill-core; (2) interpreted from geophysical data; (3) interpreted from structural data or extrapolated from

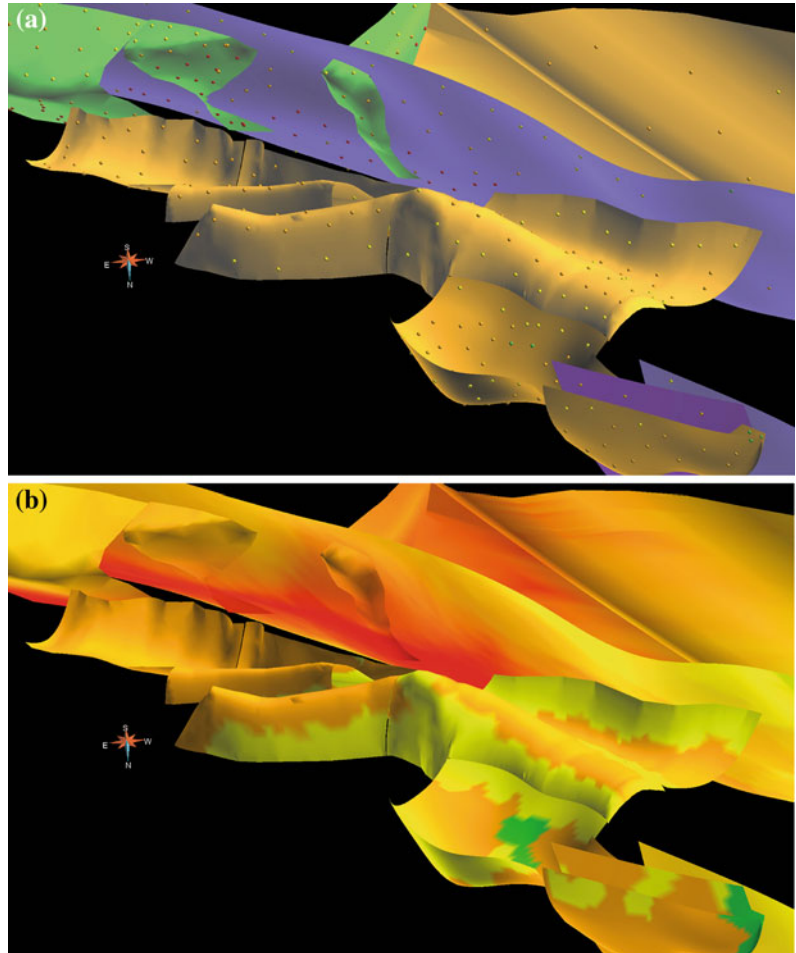
geophysical data, and (4) inferred/unknown. The resulting uncertainty model shows the distribution of primary data, interpolation of structural data, interpretation of geophysical data as well as areas without sufficient data. Uncertainty values from one to four, for the relevant regions on the 3D-objects, have been assigned manually with a spacing ranging from 50 to 500 m depending on the level of detail of the surface. Subsequently, the surfaces were colour-coded by draping and kriging methods (Fig. 5.11).

5.3.4 Potential Resources Assessment

Predictivity values were assigned on the 3D-model of the Skellefte district, showing the structural control on ore formation and transposition. A simplified weight of evidence method (cf. Bonham-Carter et al. 1989; Agterberg et al. 1990) was applied on the model by extracting predictive evidence for a particular deposit type, based on the correlation between distribution and shape of VMS deposits, and regional deformation patterns (Bauer et al. 2014). Subsequently, the evidential themes were combined to predict the mineral potential in the Skellefte district.

In order to visualize the predictivity for VMS deposits, values from one to five were assigned to the relevant regions of the model (Fig. 5.12). The assigned predictivity values represent: (1) very high prospectivity: intersection of two syn-extensional faults and upper Skellefte Group; (2) high prospectivity: intersection of one syn-extensional fault and upper Skellefte Group stratigraphy or intersection of two syn-extensional faults and lower to mid Skellefte Group stratigraphy; (3) elevated prospectivity: intersection of syn-extensional fault and lower to mid Skellefte Group, or solely upper Skellefte Group; (4) medium prospectivity: solely lower-mid Skellefte Group, or solely syn-extensional fault; (5) decreased prospectivity: post-ore stratigraphy or syn-compressional fault.

Fig. 5.11 Uncertainty modelling: **a** Assigning uncertainties manually onto modelled surfaces, **b** colouring of the surfaces and visualization of modelling uncertainties. Uncertainty values represent: *green* Observed in field, mine or drill-core; *yellow* Interpreted from geophysical data; *orange* Interpreted from structural data or extrapolated from geophysical data, and *red* Inferred/unknown



5.4 Description of 3D Geological Models

This section provides an overview of the crustal architecture of the modelled sub-areas, proceeding from the Kristineberg area in the west to the Boliden area in the east. The location of each modelling sub-area is shown in Fig. 5.13.

5.4.1 Kristineberg

The geological 3D model of the Kristineberg area shows a series of E-W-striking high-strain zones that dip both towards north and south (Fig. 5.14). Furthermore, major lithological

contacts are visualized, such as the contact between the Vargfors Group and the underlying Skellefte Group. This contact is folded and fold axes show the, for the Kristineberg typical, “steep-flat-steep” geometry. This geometry is repeated in the ore body of the Kristineberg deposit. Furthermore, 3D-models of the Hornträskviken, Rävliiden and Rävliidmyran ore bodies replicate the orientation of the W-plunging fold axis. The area is surrounded by granitic intrusions.

5.4.2 Storliiden

The model of the Storliiden area illustrates the transitions between flat-lying structures in the

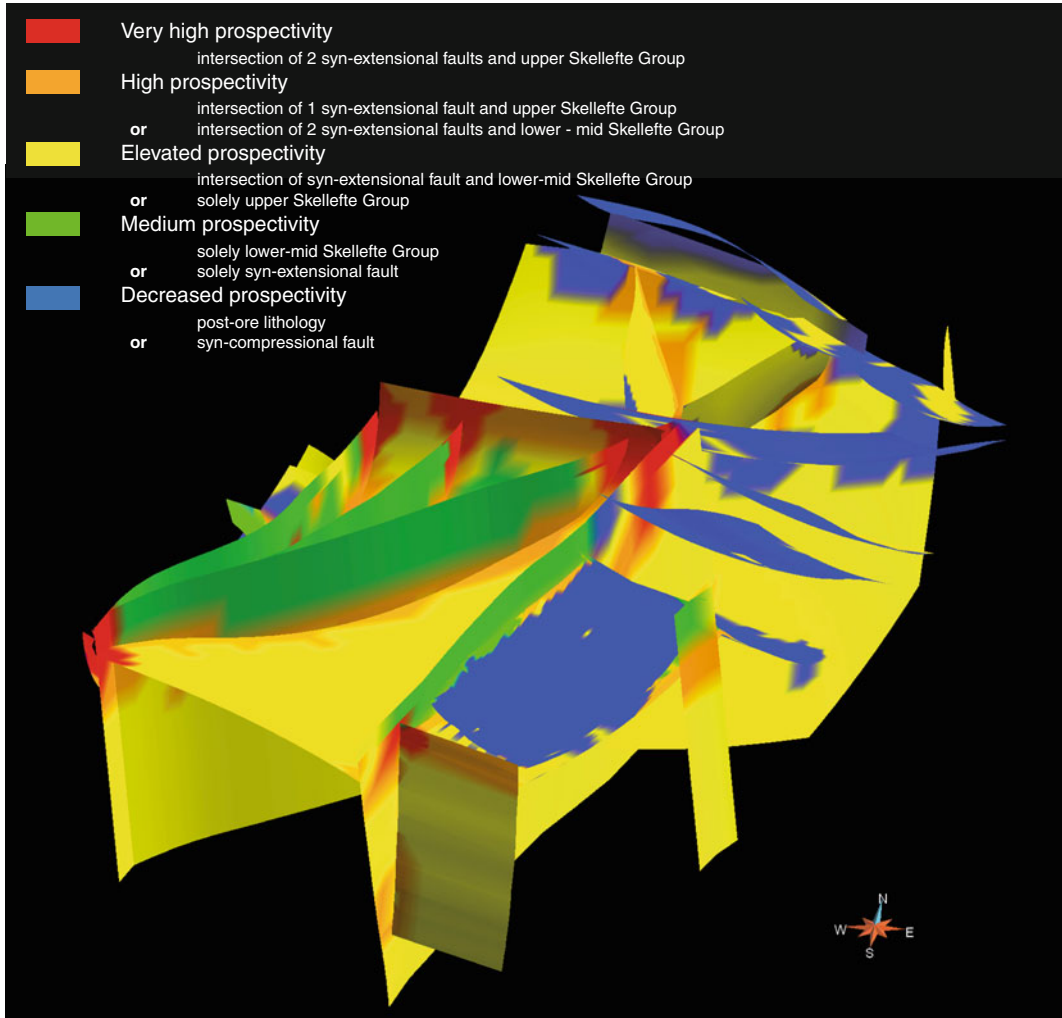


Fig. 5.12 Potential resources assessment modelling

vicinity of the Storliden deposit, steeper ~E-W striking structures towards the Kristineberg area, and the steep westerly dips in the Näsliden sub-area. The felsic late-orogenic intrusion in the southern part of the Storliden area dominates the model (Fig. 5.15), whereas the shape of the intrusion at depth and the shape of the extrapolation above the surface are unknown. Folded metasedimentary rocks and high-strain zones are wrapped around the northern end of the intrusion. At the northern extent of the sub-model, steeply dipping, folded ultramafic sills are the dominating objects.

5.4.3 Deppis-Näsliden Shear Zone

The area occurs between the Storliden, Gallejaur and Maurleden model areas, and illustrates a set of approximately N-S striking high-strain structures, occurring along and in the vicinity of the regional-scale Deppis-Näsliden shear zone. The main components are the W-dipping high-strain zones, the doubly-plunging Finnberget antiform hosting the Näsliden deposit, folded metasedimentary rocks with curvilinear fold axes present to the south of the Näsliden deposit, and the

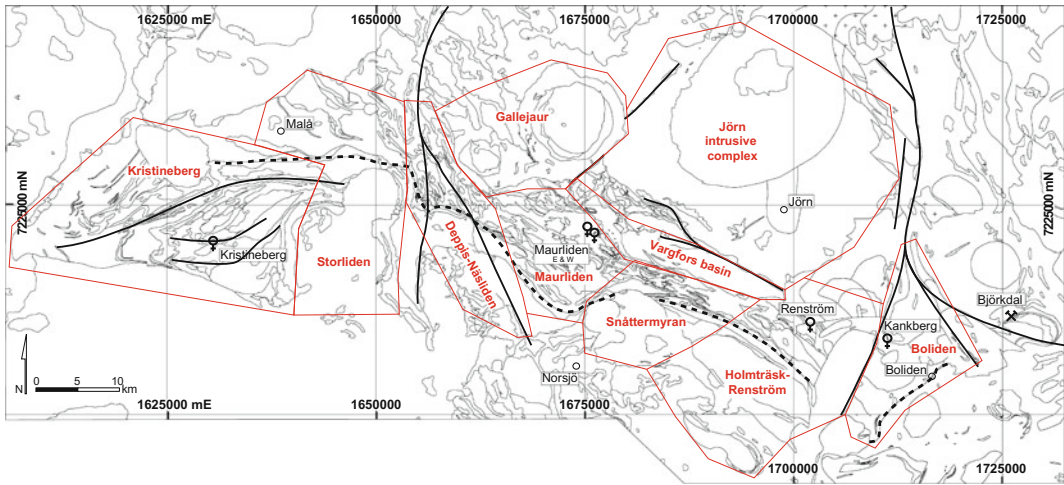


Fig. 5.13 Locations of modelling sub-areas in the Skellefte district

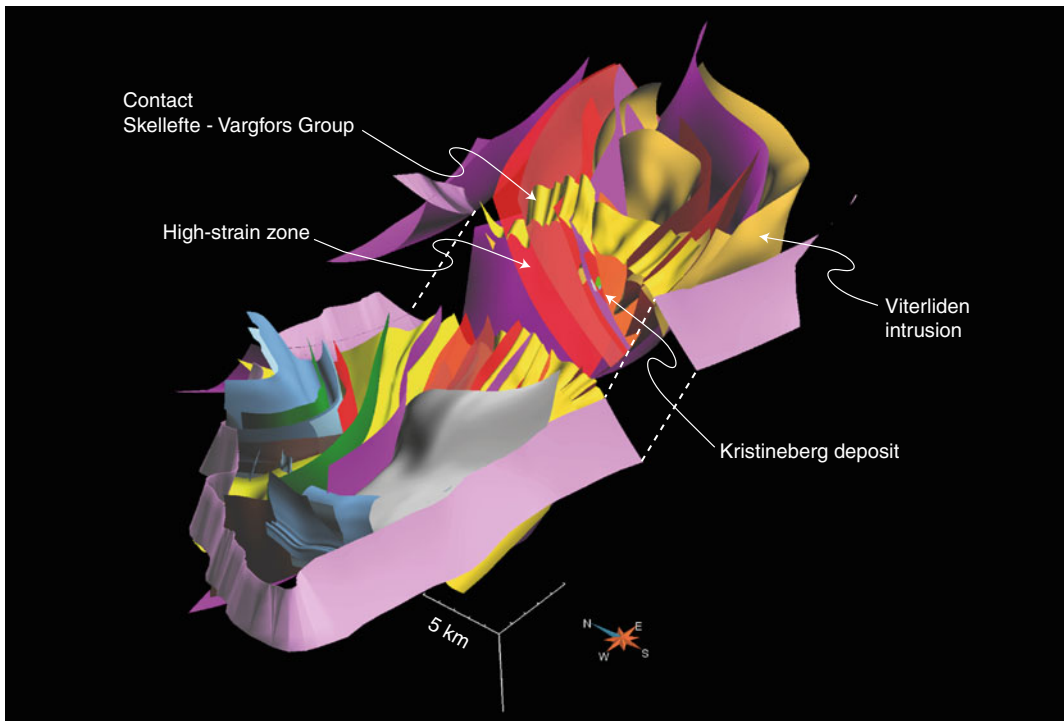


Fig. 5.14 Screenshot from the Kristineberg sub-area model

regional Rakkejaur synform in the eastern part of the area (Fig. 5.16). Deformation and tectonic transposition has been intense between the

Näsliden deposit and the Finnberget antiform (Fig. 5.16), whereas the Finnberget antiform itself is only weakly deformed.

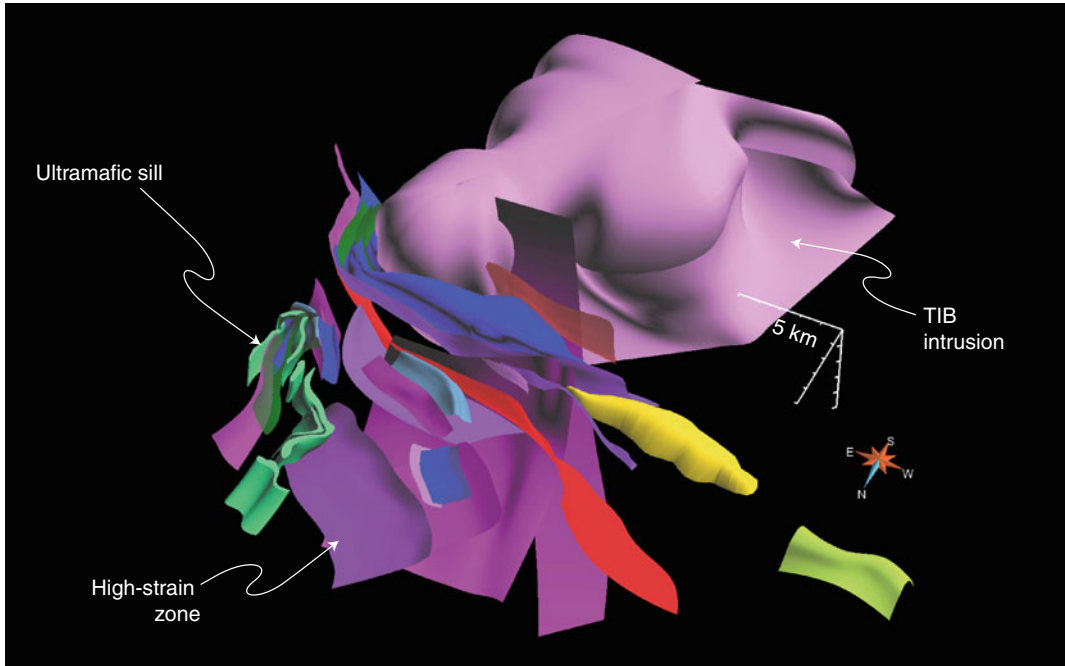


Fig. 5.15 Screenshot from the Storliden sub-area model

5.4.4 Gallejaur

The Gallejaur sub-model is dominated by bowl-shaped intrusive phases of the Gallejaur complex, with a syenitic-monzonitic centre and a gabbroic-dioritic rim (Fig. 5.17). The flat-lying extrusive Gallejaur-type mafic volcanic rocks are surrounding the complex. Furthermore, the model shows the continuation of the Vargfors syncline (Bauer et al. 2011, 2013; Skyttä et al. 2012), which is doubly plunging in the area.

5.4.5 Maurliden Domain

The Maurliden sub-area model shows a distinct set of WNW-ESE-striking, WSW-dipping shear zones (Fig. 5.18) interpreted from seismic reflections (cf. Dehghannejad et al. 2012b) and associated transfer faults (cf. Bauer et al. 2011). In the centre of the sub-area, the contact between

Skellefte Group and Vargfors Group rocks form the NW-plunging Finnsliden antiform. The doubly plunging Maurliden synform, in the northern part of this sub-area, hosts the Maurliden East and West deposits.

5.4.6 Vargfors Syncline

The sub-model of the Vargfors syncline shows a set of WNW-ESE-striking basin-bounding faults and associated NNE-SSW-striking, vertical transfer faults, segmenting the Vargfors syncline in distinct fault bound compartments (I–XII in Fig. 5.19). Surfaces within the syncline represent both the contact between the Skellefte and Vargfors Groups, and the contact between certain Vargfors Group sedimentary facies (cf. Bauer et al. 2013). Fold axes of the synclinal fault-bound compartments plunge WNW in compartments I and II and ESE in compartments IV to XI, respectively.

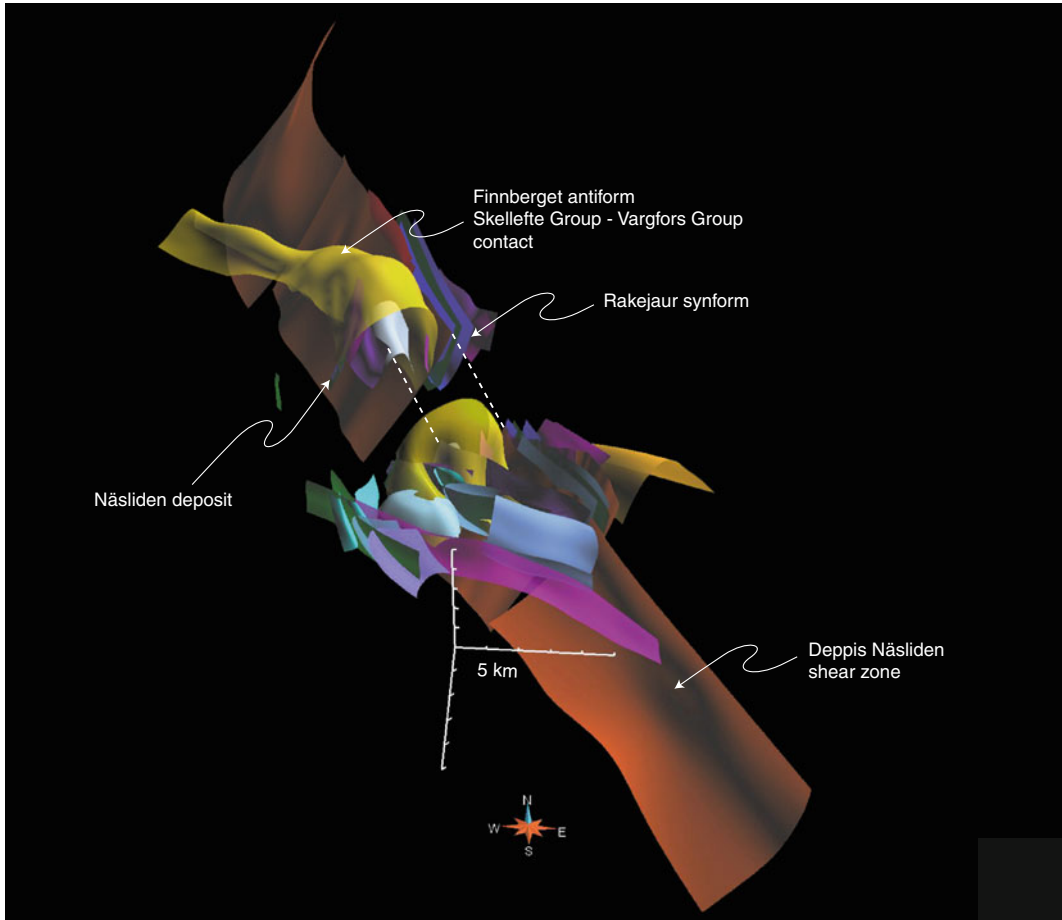


Fig. 5.16 Screenshot from the Deppis-Näsliden sub-area model

5.4.7 Jörn Intrusive Complex

The model covers the GI–GIV phases of the Jörn intrusive complex and the north-dipping high-strain zones with reverse kinematics along the southern contact of the intrusive complex (Fig. 5.20; cf. Bauer et al. 2013). Furthermore, the continuations of high-strain zones from the neighbouring sub-areas into the intrusive complex are visualized. The geometries of the western and eastern contacts of the intrusive complex are weakly constrained, but appear to be fault-bound and, consequently, have been drawn sub-vertical, parallel with the major transfer faults.

5.4.8 Snåttermýran

The architecture of high-strain zones in the Snåttermýran area resembles the geometries of high-strain zones in the Maurliden area. The WNW-ESE-striking, WSW-dipping shear zones represent a continuation from the Maurliden area, and are associated with the Åsen, Kedträsk and Udden deposits (Fig. 5.21). Furthermore, sub-vertical, NNE-SSW-striking transfer faults are a prominent feature in this area. The areas in-between the high-strain zones are characterized by mainly asymmetric folds. The southern border of the area is defined by a post-orogenic granitic intrusion with unknown shape (Fig. 5.22).

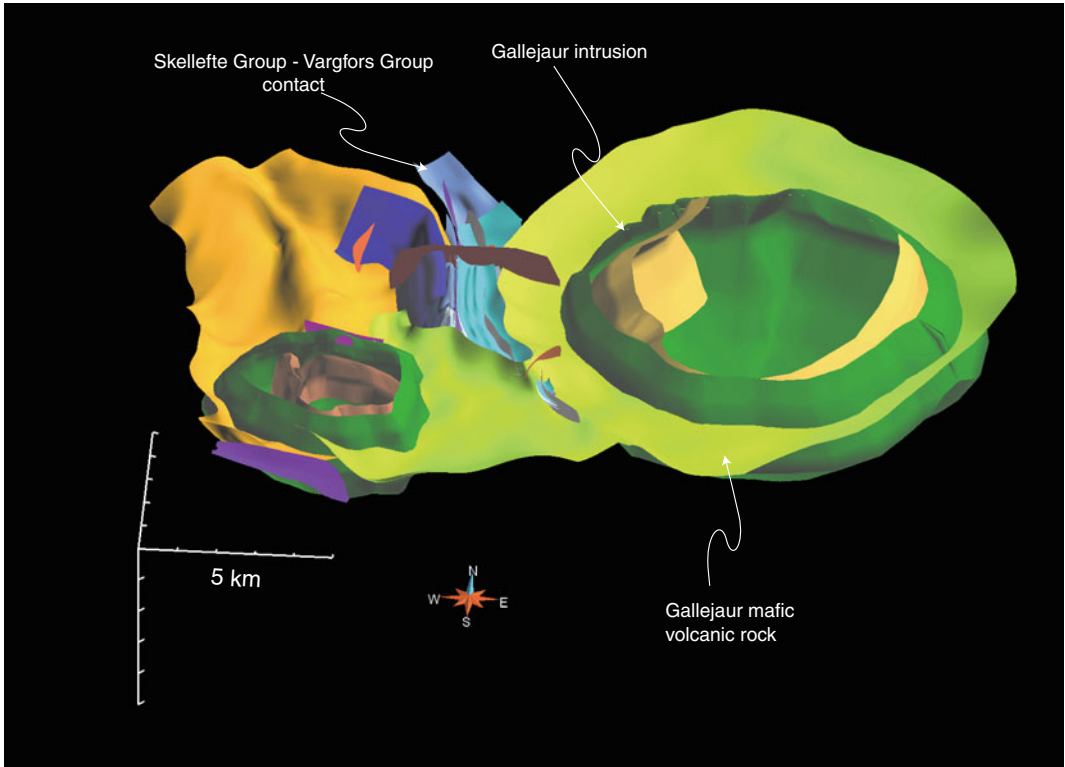


Fig. 5.17 Screenshot from the Gallejaur sub-area model

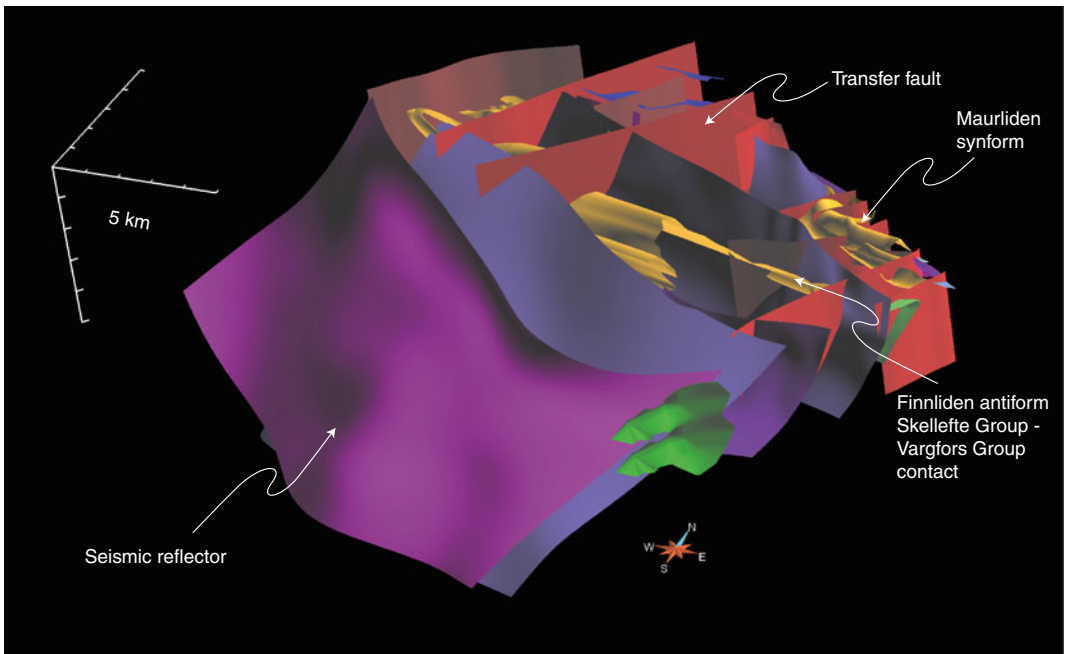


Fig. 5.18 Screenshot from the Maurliden sub-area model

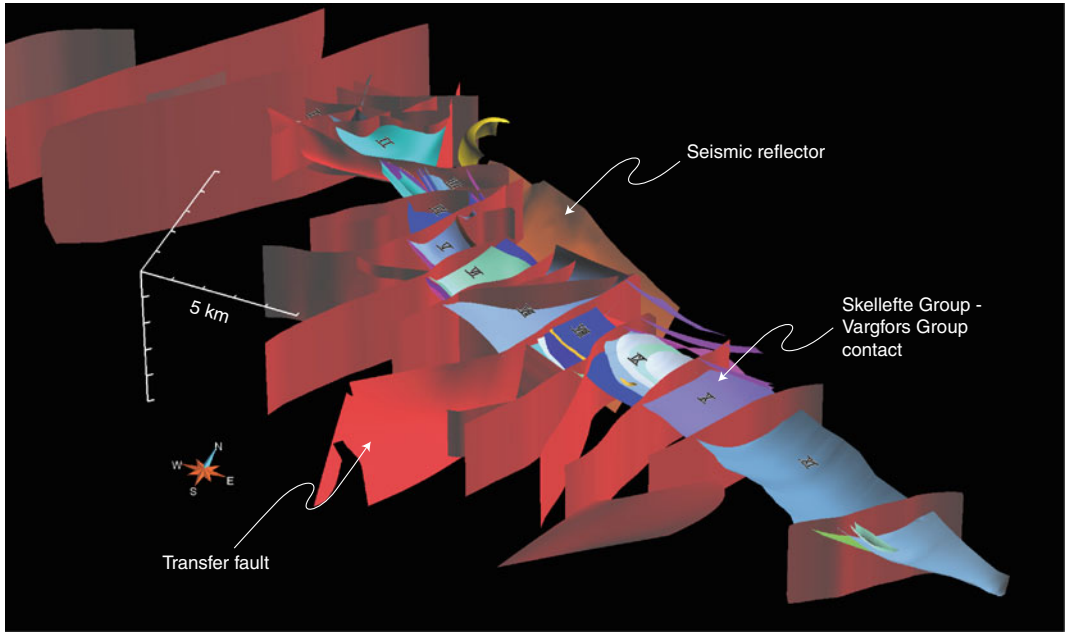


Fig. 5.19 Screenshot from the Vargfors syncline sub-area model

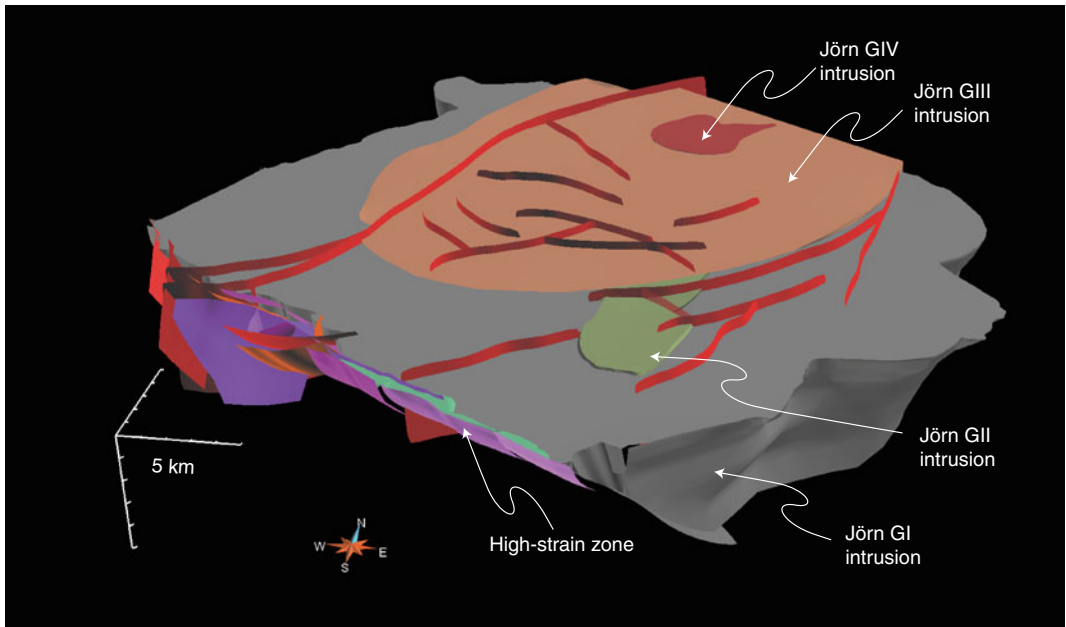


Fig. 5.20 Screenshot from the Jörn intrusive complex sub-area model

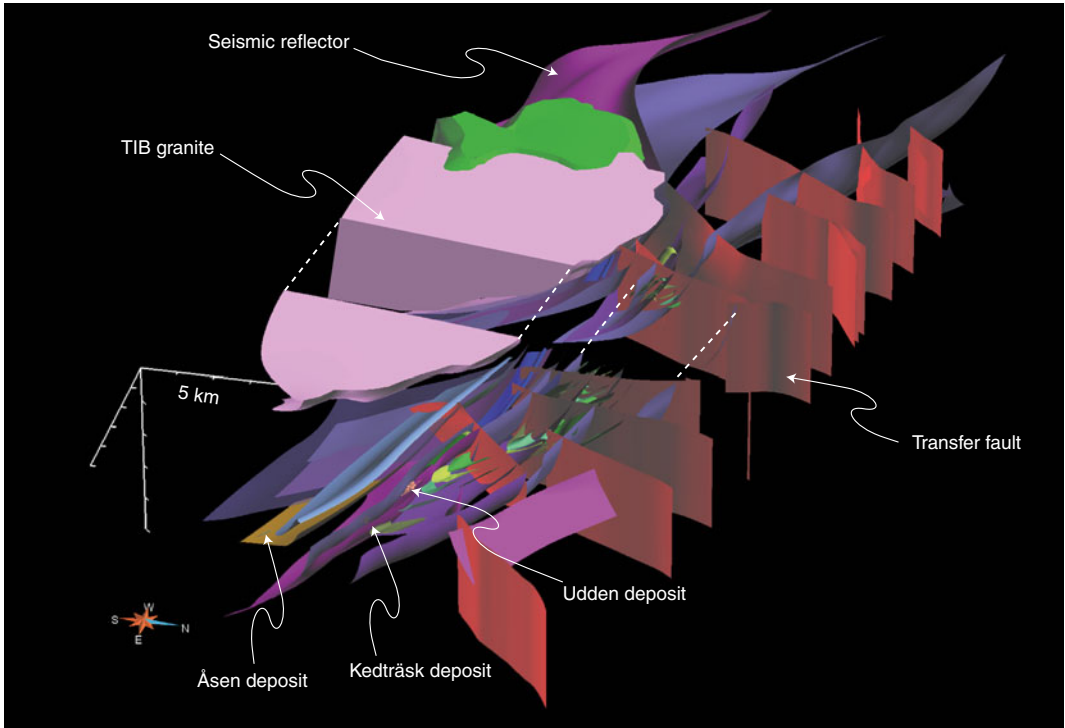


Fig. 5.21 Screenshot from the Snåttermýran sub-area model

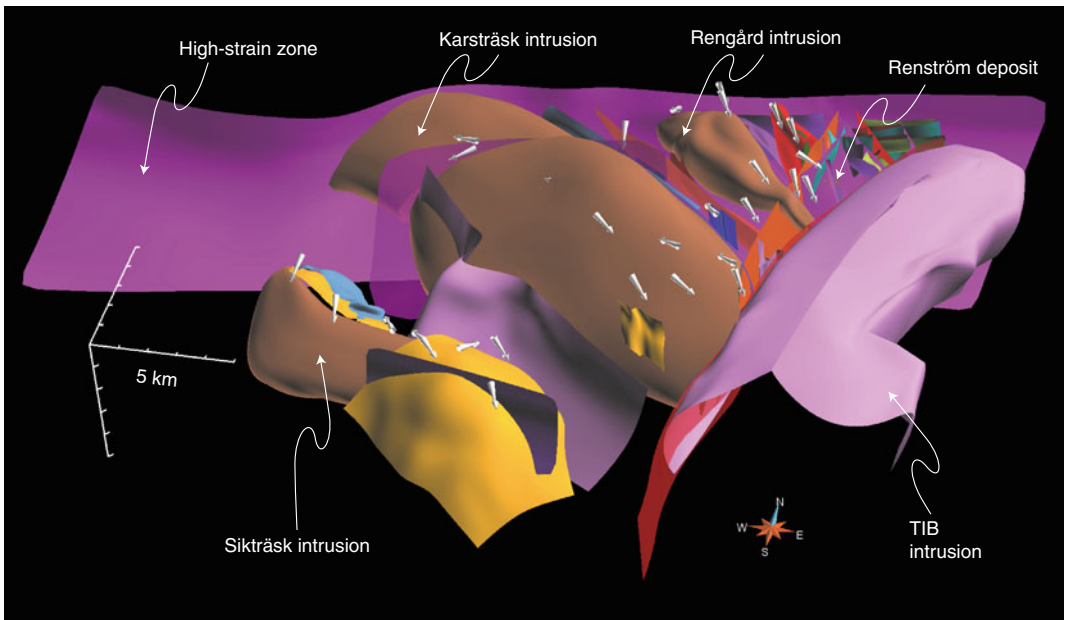


Fig. 5.22 Screenshot from the Holmträsk sub-area model. Arrows display orientation of mineral lineations

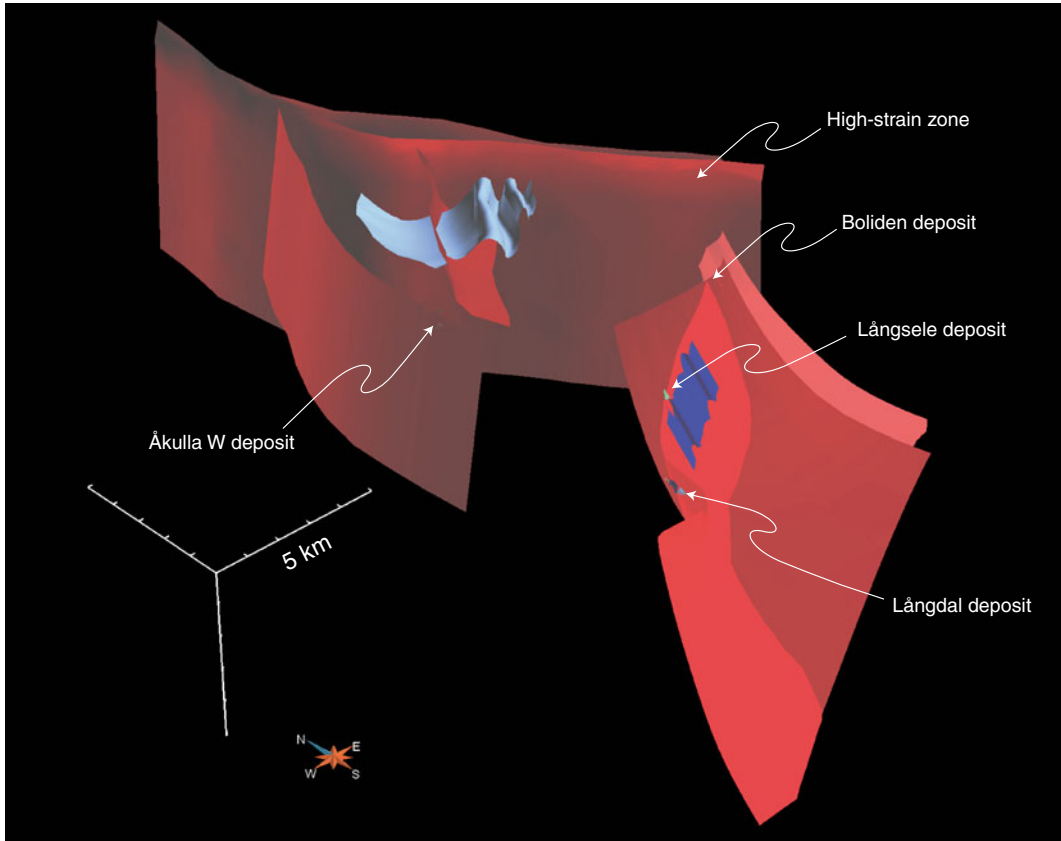


Fig. 5.23 Screenshot from the Boliden sub-area model

5.4.9 Holmträsk-Renström

The model of the Holmträsk-Renström area illustrates the transition from penetratively deformed, dome-shaped intrusions in the south to the rigid Rengård intrusion bound by high-strain zones in the north. The shape of the three parallel intrusions is well constrained by potential field modelling (Skyttä et al. 2012). Lineation arrows in the model exemplify the change in deformation style from north to south. The highly detailed model around the Renström deposit shows the main syncline axial surfaces and the inferred ore horizons folded into synformal shapes. In the south-east, this sub-model is bordered by a

granitic intrusion of unknown shape at depth and extrapolated above the surface.

5.4.10 Boliden

The model of the Boliden area represents the least developed part of the regional geological model. Nevertheless, a pattern of high-strain zones is visualized hosting the Långsele, Långdal, Boliden and Åkulla W deposits (Fig. 5.23). However, the geometries of the high-strain zones are only interpreted from structural observations, and observations in the vicinity of the deposits. They are not constrained by geophysical studies.

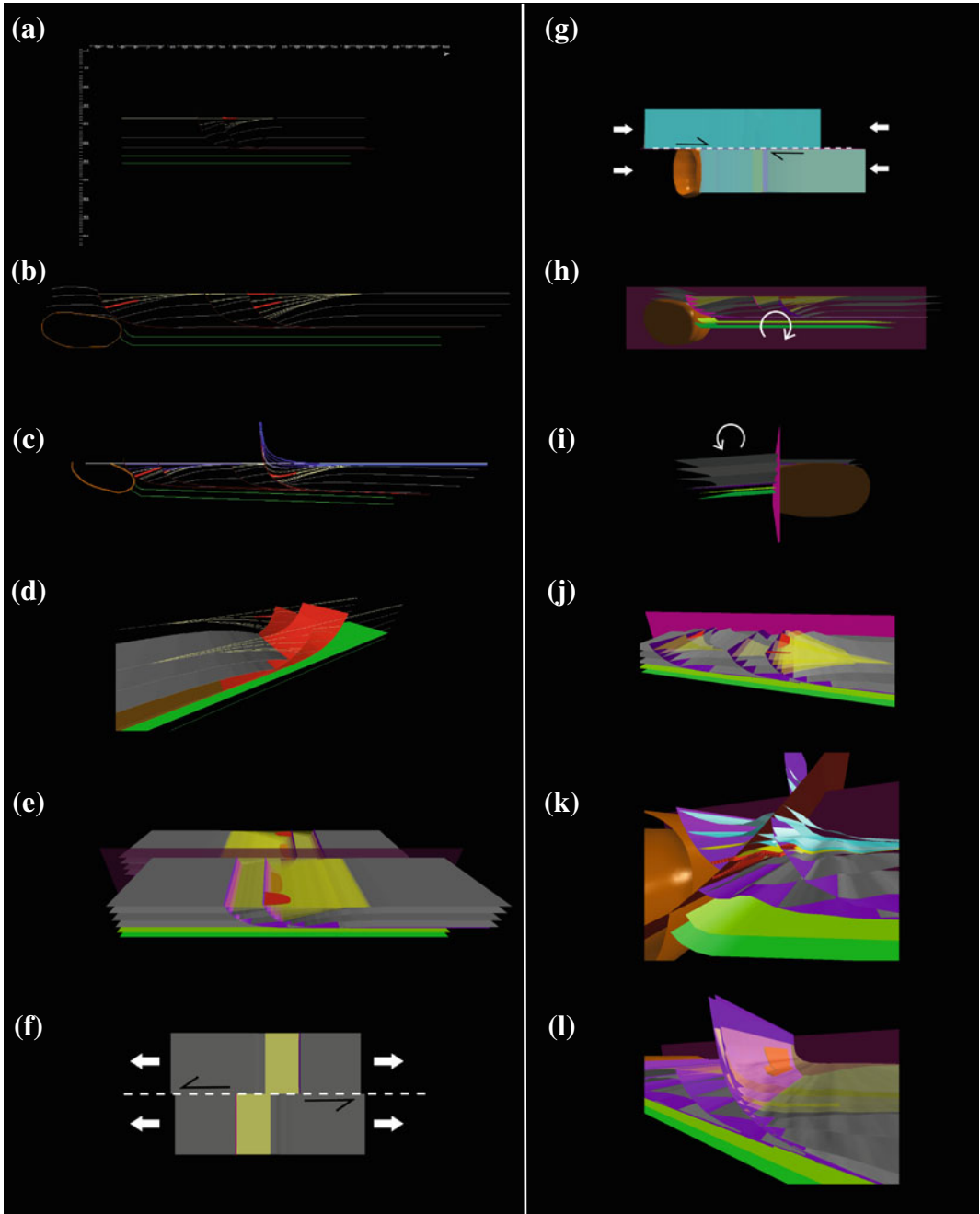


Fig. 5.24 Screenshots illustrating the 4D-modelling workflow using MOVE (Midland Valley Exploration Ltd.): **a–c** Initial 2D modelling, **d** construction of 3D surfaces from a set of parallel 2D-models, **e** two crustal compartments with opposing normal fault dip directions,

f–g strike slip shearing along a transfer fault, **h–i** effects of block rotation, **j–l** different shapes of VMS deposits as an effect of fault inversion, block rotation and erosion. Modified after Skyttä (2012)

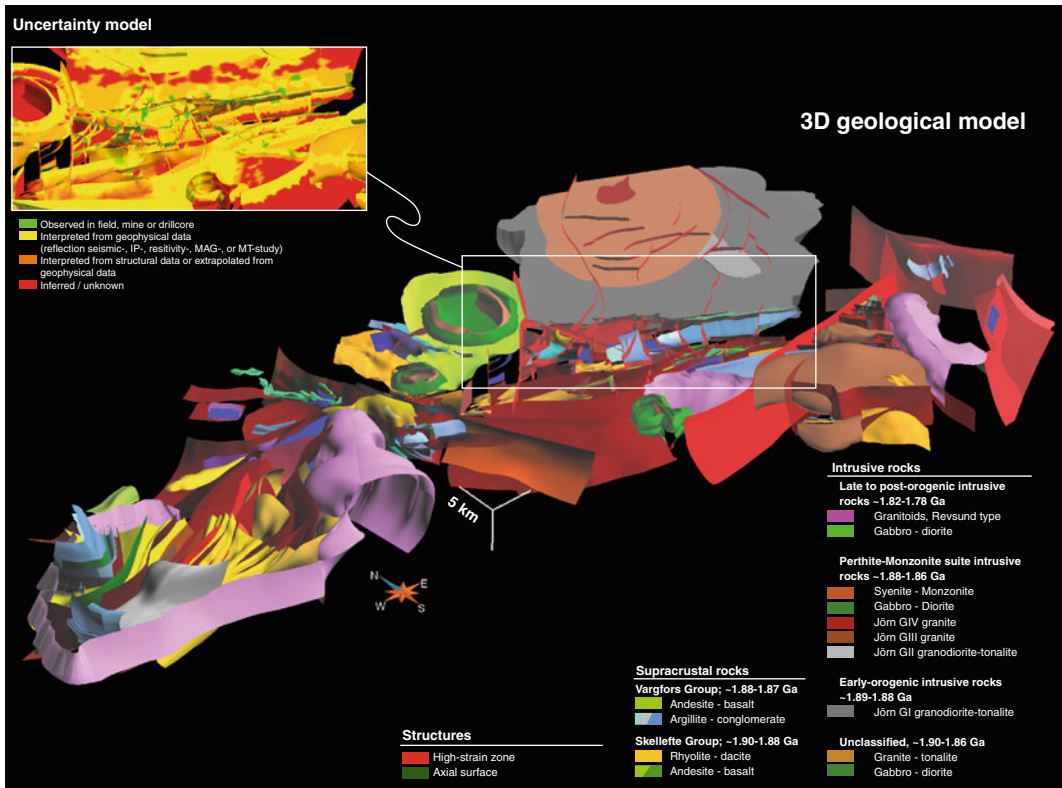


Fig. 5.25 Screenshot from the 3D geological model of the Skellefte district, including part of the uncertainty model (inset)

Additionally, the folded contact between the Skellefte and Vargfors Groups is shown.

5.5 4D-Modelling

The time aspect was added to the 3D-models by 4D-modelling (Skyttä 2012). The aim was to visualize the geological history in the district and to provide support for ore targeting. Four-dimensional modelling was carried out utilizing the MOVE software package (Midland Valley Exploration Ltd.). Modelling started with kinematic 2D-modelling, visualizing the formation of volcanic rocks, associated faulting and subsequent deformation (Fig. 5.24a–c). During 3D-modelling a correlation between the 2D-sections was made (Fig. 5.25d). The different stages of deformation were successively visualized as a

4D-animation (Fig. 5.24e–k). The 4D-model shows schematically the formation of listric and related transfer faults, the formation of volcanic and sedimentary rocks and VMS deposits during crustal extension (Skyttä 2012). Furthermore, the effect of different block-rotations between neighbouring fault-bound compartments, and subsequent erosion and deformation of rocks, and tectonic transposition of ore bodies were illustrated. The final 4D-animation is available as supplementary material in Skyttä (2012).

5.6 Concluding Remarks

The final 3D-model shows the simplified structural framework of the Skellefte district combined with the major lithological contacts and the spatial distribution of VMS deposits. Due to the

complex volcanic successions, extensive hydrothermal alteration, metamorphic overprint and the sparse occurrence of outcrops, no marker horizons could be used for modelling. Moreover, the complex interplay between sedimentation and deformation in Vargfors Group sedimentary rocks, in the Vargfors syncline, complicated the correlation of sedimentary horizons between the fault bound compartments. For these reasons, the contact between the Skellefte and the Vargfors Group plays an important role in the area and represents the dominant lithological feature in the regional scale 3D-model. The complex crustal architecture required some degree of simplification to find a satisfying balance between clarity and detail.

The model represents the current state of knowledge, but has to be judged as a work in progress. Due to continuous investigations and exploration in the district, the model can be constantly refined and/or modified. Potential improvements can be achieved in the vicinity of the deposits by adding more detailed structural data. Furthermore, hydrothermal alteration systems could be modelled in three dimensions to support, for example, near mine exploration activities. The uncertainty model shows the distribution of data and knowledge. In areas with sparse data coverage the model could be substantially improved. Particularly, deep drill hole information would be useful to improve and validate the model.

Acknowledgments The authors want to thank Rodney L. Allen and Hans Årebäck from Boliden Mines. Maria Garcia, Juliane Hübert, Christopher Juhlin, Alireza Malehmir and Ari Tryggvason from the Department of Earth Sciences, Uppsala University are thanked for their contributions. Jenny Ellis from Midland Valley Exploration Ltd. is acknowledged for support with 2D, 3D and 4D modelling. The author acknowledges the use of the Move Software Suite granted by Midland Valley's Academic Software Initiative. Sten-Åke Elming and Pär Weiheid from Luleå University of Technology and Hans Tunehed from Geovista AB are thanked for their collaboration in the project. Dr. Dave Collier is acknowledged for his contribution, ideas and discussions. This work is part of the VINNOVA 4D modelling of the Skellefte district project funded by VINNOVA and the Boliden Group, and the ProMine project partially funded by the European Commission under the 7th Framework Programme.

References

- Agterberg FP, Bonham-Carter GF, Wright DF (1990) Statistical pattern integration for mineral exploration: In: Gaal G, Merriam DF (eds) Computer applications in Resource Estimation: Predictions and Assessment for Metals and Petroleum, Pergamon, Oxford, p. 1–21
- Allen RL, Weiheid P, Svenson S-Å (1996) Setting of Zn-Cu-Au-Ag massive sulphide deposits in the evolution and facies architecture of a 1.9 Ga marine volcanic arc, Skellefte district, Sweden. *Economic Geology* 91:1022
- Bauer TE (2010) Structural and Sedimentological Reconstruction of the Inverted Vargfors Basin – A base for 4D-modelling. Dissertation or Thesis, Luleå University of Technology
- Bauer TE, Skyttä P, Allen RL, Weiheid P (2011) Syn-extensional faulting controlling structural inversion – Insights from the Palaeoproterozoic Vargfors syncline, Skellefte mining district, Sweden. *Precambrian Research* 191:166–183
- Bauer TE, Skyttä P, Allen RL, Weiheid P (2013) Fault-controlled sedimentation in a progressively opening extensional basin: the Palaeoproterozoic Vargfors basin, Skellefte mining district, Sweden. *International Journal of Earth Sciences* 102: 385–400
- Bauer TE, Skyttä P, Hermansson T, Allen RL, Weiheid P (2014) Correlation between distribution and shape of VMS deposits, and regional deformation patterns, Skellefte district, northern Sweden. *Mineralium Deposita*, doi [10.1007/s00126-013-0503-2](https://doi.org/10.1007/s00126-013-0503-2).
- Bejgarn T, Söderlund U, Weiheid P, Årebäck H, Ernst R (2012) Palaeoproterozoic porphyry Cu–Au, intrusion-hosted Au and ultramafic Cu–Ni deposits in the Fennoscandian Shield: Temporal constraints using U–Pb geochronology. *Lithos*, doi:[10.1016/j.lithos.2012.06.015](https://doi.org/10.1016/j.lithos.2012.06.015)
- Bergman Weiheid J (2001) Palaeoproterozoic deformation zones in the Skellefte and Arvidsjaur areas, northern Sweden. Vol. 1, 1999–2000. In: Weiheid P (ed) *Economic geology research*, C 833 edn. Sveriges geologiska undersökning, Uppsala, pp 46–68
- Bergman Weiheid J, Bergstrom U, Billstrom K, Weiheid P (1996) Geology, tectonic setting, and origin of the Paleoproterozoic Boliden Au-Cu-As deposit, Skellefte District, northern Sweden. *Economic Geology* 91:1073–1097
- Billström K, Weiheid P (1996) Age and provenance of host rocks and ores in the Paleoproterozoic Skellefte District, northern Sweden. *Economic Geology* 91:1054–1072
- Bonham-Carter GF, Agterberg FP, Wright DF (1989) Weights of evidence modelling: a new approach to mapping mineral potential. In: Agterberg FP, Bonham-Carter GF (eds) *Statistical Applications in the Earth Sciences*, Geological Survey of Canada, Paper 89-9, p. 171–183

- Dehghannejad M, Juhlin C, Malehmir A, Skyttä P, Weihed P (2010) Reflection seismic imaging of the upper crust in the Kristineberg mining area, northern Sweden. *Journal of Applied Geophysics* 71:125–136
- Dehghannejad M, Malehmir A, Juhlin C, Skyttä P (2012a) 3D constraints and finite-difference modelling of massive sulfide deposits: The Kristineberg seismic lines revisited, northern Sweden. *Geophysics* 77(5): WC69–WC79.
- Dehghannejad M, Bauer TE, Malehmir A, Juhlin C, Weihed P (2012b) Crustal geometry of the central Skellefte district, northern Sweden – constraints from reflection seismic investigations. *Tectonophysics* 524–525:87–99
- De Kemp EA, Sprague KB (2003) Interpretive Tools for 3-D Structural Geological Modeling Part I: Bézier-Based Curves, Ribbons and Grip Frames. *GeoInformatica* 7(1): 55–71.
- Ehsan SA, Malehmir A, Dehghannejad M (2012) Re-processing and interpretation of 2D seismic data from the Kristineberg mining area, northern Sweden. *Journal of Applied Geophysics* 80: 43–55
- García Juanatey MA (2012) Seismics, 2D and 3D Inversion of Magnetotellurics – Jigsaw pieces in understanding the Skellefte Ore District. Dissertation, Uppsala University. 55 pp
- García Juanatey MA, Hübert J, Tryggvason A, Pedersen LB (2012) Imaging the Kristineberg mining area with two perpendicular magnetotelluric profiles in the Skellefte Ore District, northern Sweden. Accepted for publication in *Geophysical prospecting*
- Gonzales Roldan MJ (2010) Mineralogía, petrología y geoquímica de intrusiones sin-volcanicas en el distrito minero de Skellefte, norte de Suecia. Dissertation or Thesis, Universidad de Huelva, Spain
- Hübert J, Malehmir A, Smirnow M, Tryggvason A, Pedersen LB (2009) MT measurements in the western part of the Paleoproterozoic Skellefte Ore District/northern Sweden: A contribution to an integrated 3D geophysical study. *Tectonophysics* 475: 493–502.
- Hübert J, García Juanatey MA, Malehmir A, Tryggvason A, Pedersen LB (2013) Upper crustal resistivity structure of the Kristineberg area, Skellefte district, northern Sweden with 3D magnetotellurics. *Geophysical Journal International* 192: 500–513.
- Kathol B, Weihed P (2005) Description of regional geological and geophysical maps of the Skellefte district and surrounding areas. Geological Survey of Sweden SGU, Uppsala
- Kathol B, Weihed P, Antal Lundin I, Bark G, Bergman Weihed J, Bergström U, Billström K, Björk L, Claesson L, Daniels J, Eliasson T, Frumierie M, Kero L, Kumpulainen RA, Lundström H, Lundström I, Mellqvist C, Petersson J, Skiöld T, Sträng T, Stølen L-K, Söderman J, Triumf C-A, Wikström A, Wikström T, Årebäck H (2005) Regional geological and geophysical maps of the Skellefte District and surrounding areas. Bedrock map. *Geol Survey Sweden Ba 57:1*
- Koistinen T, Stephens MB, Bogatchev V, Nordgulen Ø, Wennerström M, Korhonen J (2001) Geological map of the Fennoscandian Shield, scale 1:2 000 000. Geological Surveys of Finland, Norway and Sweden and the North-West Department of Natural Resources of Russia–223
- Loke MH (2010) Tutorial: 2-D and 3-D electrical imaging surveys. <http://www.geoelectrical.com/downloads.php>.
- Lundström I, Vaasjoki M, Bergström U, Antal I, Strandman F (1997) Radiometric age determinations of plutonic rocks in the Boliden area: the Hobergsleden granite and the Stavaträsk diorite. In: Lundqvist T (ed) Radiometric dating results 3, C 830, 20–30 edn. Sveriges geologiska undersökning, pp 20–30
- Malehmir A, Tryggvason A, Juhlin C, Rodriguez-Tablante J, Weihed P (2006) Seismic imaging and potential field modeling to delineate structures hosting VHMS deposits in the Skellefte Ore District, northern Sweden. *Tectonophysics* 426: 319–334
- Malehmir A, Tryggvason A, Lickorish H, Weihed P (2007) Regional structural profiles in the western part of the Paleoproterozoic Skellefte ore district, northern Sweden. *Precambrian Research* 159: 1–18
- Malehmir A, Thunehed H, Tryggvason A (2009a) The Paleoproterozoic Kristineberg mining area, northern Sweden: Results from integrated 3D geophysical and geologic modelling, and implications for targeting ore deposits. *Geophysics* 74: B9–B22
- Malehmir A, Schmelzbach C, Bongajum E, Bellefleur G, Juhlin C, Tryggvason A (2009b) 3D constraints on a possible deep > 2.5 km massive sulphide mineralization from 2D crooked-line seismic reflection data in the Kristineberg mining area, northern Sweden. *Tectonophysics* 479: 223–240
- Mellqvist C, Öhlander B, Skiöld T, Wikström A (1999) The Archaean-Proterozoic Palaeoboundary in the Luleå area, northern Sweden: Field and isotope geochemical evidence for a sharp terrane boundary. *Precambrian Res* 96:225–243
- Montelius C (2005) The Genetic Relationship between Rhyolitic Volcanism and Zn-Cu-Au Deposits in the Maurliden Volcanic Centre, Skellefte district, Sweden: Volcanic facies, Litho-geochemistry and Geochronology. Dissertation or Thesis, Luleå University of Technology
- Oldenburg DW, Li Y (1994) Inversion of induced polarization data. *Geophysics*, 59: 1327–1341
- Skyttä P (2012) Crustal evolution of an ore district illustrated – 4D-animation of the Skellefte district, Sweden. *Computers and Geosciences*, <http://dx.doi.org/10.1016/j.cageo.2012.05.029>
- Skyttä P, Hermansson T, Elming S, Bauer T (2010) Magnetic fabrics as constraints on the kinematic history of a pre-tectonic granitoid intrusion, Kristineberg, northern Sweden. *J Struct Geol* 32: 1125–1136
- Skyttä P, Hermansson T, Andersson J, Weihed P (2011) New zircon data supporting models of short-lived igneous activity at 1.89 Ga in the western Skellefte District, central Fennoscandian Shield. *Solid Earth* 2: 205–217
- Skyttä P, Bauer TE, Tavakoli S, Hermansson T, Andersson J, Weihed P (2012) Pre-1.87 Ga development of crustal

- domains overprinted by 1.87 Ga transpression in the Palaeoproterozoic Skellefte district, Sweden. *Precambrian Res* 206–207: 109–136
- Skyttä P, Bauer T, Hermansson T, Dehghannejad M, Juhlin C, García M, Hübner J, Weihed P (2013) Structural evolution of the VMS-hosting Kristineberg area, Sweden – constraints from structural analysis and 3-D-modelling. *Solid Earth* 4: 387–404.
- Tavakoli S, Bauer T, Elming S-Å, Thunehed H, Weihed P (2012a) Regional-scale geometry of the central Skellefte district, northern Sweden – results from potential field modelling along three previously acquired seismic profiles. *Journal of Applied Geophysics* 85: 43–58
- Tavakoli S, Elming S-Å, Thunehed H (2012b) Geophysical modelling of the central Skellefte district, Northern Sweden; an integrated model based on the electrical, potential field and petrophysical data. *Applied Geophysics* 82: 84–100
- Tavakoli S, Thunehed H, Bauer T, Elming, S-Å (2015) Targeting VMS ore deposits within 1.5 km upper crust of the central Skellefte District, northern Sweden, using 2D and 3D-resistivity/IP data. *Geophysical Prospecting*.
- Tavakoli S (2012) Geophysical Investigation for 3D Geological Modelling and Ore Exploration in the Skellefte Mining District. Doctoral thesis, Luleå University of Technology. 150 pp
- Weihed P, Billström K, Persson P-O, Bergman Weihed J (2002) Relationship between 1.90–1.85 Ga accretionary processes and 1.82–1.80 Ga oblique subduction at the Karelian craton margin, Fennoscandian Shield. *GFF* 124: 163–180
- Wilson MR, Sehlstedt S, Claesson L-, Smellie JAT, Aftalion M, Joseph Hamilton P, Fallick AE (1987) Jörn: An early proterozoic intrusive complex in a volcanic-arc environment, north Sweden. *Precambrian Res* 36: 201–225

Eevaliisa Laine, Jouni Luukas, Timo Mäki, Jukka Kousa,
Aimo Ruotsalainen, Ilkka Suppala, Marcello Imaña,
Suvi Heinonen and Tuulia Häkkinen

Abstract

The Vihanti-Pyhäsalmi district is located at the border zone between the Archaean craton in the northeast and the Palaeoproterozoic Svecofennian domain in central Finland. It is part of the Savo belt and contains one operating and four past mines and several uneconomic VHMS (Volcanic Hosted Massive Sulphide) deposits. Regional, semi-regional and mine scale 3D models of the Vihanti-Pyhäsalmi area were built in order to understand the formation of the VHMS deposit and accordingly map the ore critical geological formations and structures. In addition to the 3D modelling of the present day geology, structural geological inference was used to build 3D geological models visualizing the main deformational stages in past. The used data and information consisted of geological maps and reports, drill core logs, lithogeochemistry, reflection seismic profiles, potential field measurements and electromagnetic surveys. The geophysical 2D and 3D inversion were used to assist the 3D geological modelling seeking for continuity of the surficial structures especially in areas with only few or no drill core data. As a result, regional and semi-regional 3D models of the Vihanti-Pyhäsalmi area were obtained and new zones with VHMS exploration potential were identified in the vicinity of the Pyhäsalmi mine.

E. Laine (✉) · J. Luukas · J. Kousa ·
A. Ruotsalainen · I. Suppala · S. Heinonen
Geological Survey of Finland, Espoo, Finland
e-mail: eevaliisa.laine@gtk.fi

T. Mäki · M. Imaña · T. Häkkinen
Pyhäsalmi Mine Oy/First Quantum Minerals LTD,
Vancouver, Canada

S. Heinonen
Institute of Seismology, University of Helsinki,
Helsinki, Finland

T. Häkkinen
WSP Finland Ltd, Helsinki, Finland

6.1 Introduction

Volcanic hosted massive sulphide (VHMS) ore deposits in the Vihanti-Pyhäsalmi districts form a linear ore belt on the Metallic Mineral Deposit Map by Eilu et al. (2013). VHMS deposits within this belt were formed in intra-arc extensional settings at c. 1.92 Ga (Lahtinen et al. 2012). The Vihanti-Pyhäsalmi district is located at the border

zone between the Archaean craton in the north-east and the Paleoproterozoic Svecofennian domain in central Finland (Fig. 6.1). It is a part of the so called Savo belt (Nironen et al. 2002; Vaasjoki et al. 2005). This belt is characterized by numerous shear zones and predominant rocks are mica gneisses, which contain volcanic rocks, graphite schists, black schists, and carbonate rocks as interlayers. The Savo belt is the NW part of the Raahe-Ladoga zone also known as the Main Sulphide Ore Belt (Kahma 1973) in Finland or as the Raahe-Ladoga Shear Complex (Kärki et al. 2012).

There is one operating and four closed mines and several uneconomic deposits in the Vihanti-Pyhäsalmi district and mineralizations are typically found in the specific lithological associations. The Pyhäsalmi Zn-Cu deposit is the largest VHMS deposit in Finland. The total reserve, mined out and reserves, are 58.3 Mt @ Cu 0.9 %, Zn 2.4 %, S 37.8 %, Au 0.4 g/t and Ag 14 g/t. Three satellite deposits have been processed in regional modelling of the Vihanti-Pyhäsalmi area. The satellite deposit Mullikkoräme produced 1.15 Mt of ore during 1990–2000. Vihanti mine was in operation 1954–1992 and produced in total 28 Mt ore (1.447 Mt Zn, 131 000 t Cu, 103 000 t Pb, 190 t Ag, 3038 kg Au).

Development of software and increase in computing power has enabled computer based 3D modelling of geologically complicated areas. There are rarely enough data for unambiguous geological models even in the vicinity of the active mines. Successful 3D modelling of the subsurface requires geological inference, interpretation and choice of methodology in order to build a 3D geological model satisfying geological and geophysical data and interpretations. The choice of modelling methodology is obviously driven by available data and modelling scale. Schetselaar (2013) used observations from drill core and outcrops, and numerical grid methodology to model 3D lithofacies architecture of the Flin Flon VHMS ore system in Canada. Hillier et al. (2013) employ strike and dip observations of the geological structures in an algorithm that visualizes geometric trends and structural features in 3D. In the research conducted by

Dehghannejad et al. (2012), Malehmir et al. (2009), Skyttä et al. (2013), seismic reflection profiling has played a major role in defining the crustal architecture and subsurface models of the Skellefte district in Sweden. Saalman and Laine (2014) built 3D geological models of different scales using a variety of information from the Outokumpu area in Finland including geological, aeromagnetic and gravity maps, digital terrain models, and mine cross sections as well as data such as drill core logs combined with observations from underground mine galleries, structural measurements, aeromagnetic data, and seismic surveys.

6.2 Data and 3D Modelling Methods

Because of the high ore potential of Vihanti-Pyhäsalmi belt, Geological Survey of Finland (GTK) and Pyhäsalmi Mine Oy have conducted several geological and geophysical studies in the area and the data were used for 3D modelling (Table 6.1). Modelling was divided in regional, semi-regional and mine scale studies since the amount and resolution of the available data is not uniform throughout the area. GTK has conducted high resolution airborne geophysical surveys resulting in magnetic, electromagnetic and radiometric maps of the whole Finland (e.g. Airo 2005). Gravity maps of Finland are based on regional Bouguer-anomaly data with 5 km station spacing provided by the Finnish Geodetic Institute. These high quality data have played a crucial role in regional and semi-regional modelling of the Vihanti-Pyhäsalmi area. Regional and semi-regional 3D models of the Vihanti-Pyhäsalmi belt are based on the GTK's digital geological map (DigiKP), structural geological analysis (Luukas 1997, 2002), the regionally defined stratigraphic major units and more detailed stratigraphic subdivisions in the Pyhäsalmi area (Puustjärvi 1999), Vihanti area (Nikander et al. 2002, 2005).

During the HIRE-project (High Resolution Reflection Seismics for Ore exploration

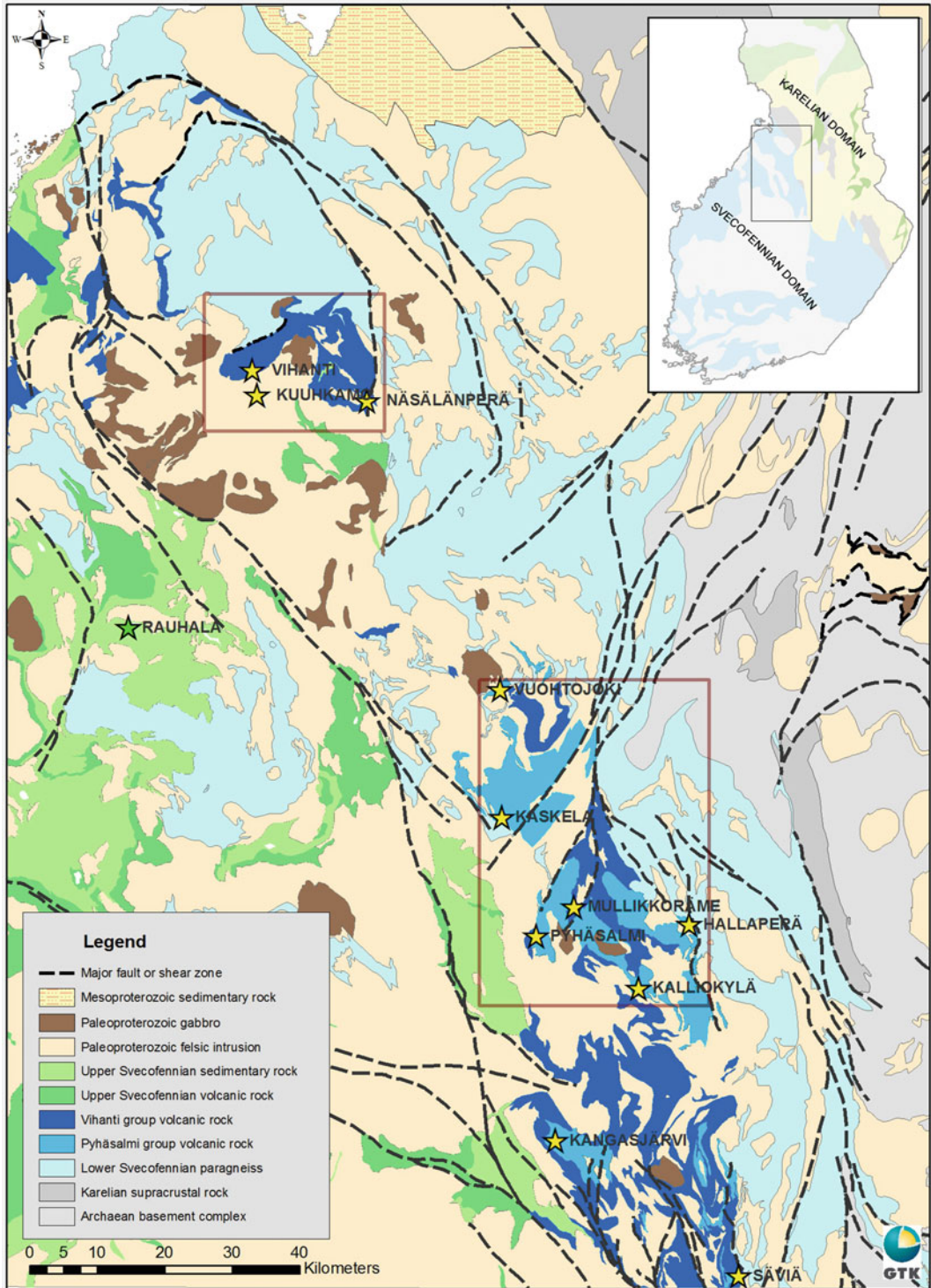


Fig. 6.1 Outlines of the Vihanti and Pyhäsalmi areas for the semiregional 3D modelling (red) and the most important Zn-Cu deposits (stars). The main structural

features are presented by black lines. The base map is modified after Bedrock of Finland—DigiKP

Table 6.1 Data and methods used for 3D models at different scales

3D model	Size	Data	Methods and software
Regional 3D model of the Vihanti-Pyhäsalmi belt	160 km × 50 km × 5 km	Surface lithological polygons from GTK's digital map database (DigiKP), diverse geophysical data	Lithological solid built from digitized strings based on DigiKP and structural geology using Gemcom Surpac
Inversion model of regional gravity data	170 km × 200 km × 7 km	Combined gravity data from Finnish Geodetic Institute and Geological Survey of Finland	UBC-GIF code MAG3D; A Program Library for Forward Modelling and Inversion of Magnetic Data over 3D Structures developed under the consortium research project Joint/Cooperative Inversion of Geophysical and Geological Data, UBC-Geophysical Inversion Facility, Department of Earth and Ocean Sciences, University of British Columbia, Vancouver, British Columbia and model vision
Semi-regional 3D models of the Vihanti area	Areal dimensions from 10 km to 50 km	Surface lithological polygons from GTK's digital map database (DigiKP), diverse geophysical data	Lithological solid built from digitized strings based on DigiKP and structural geology using Gemcom Surpac
Semi-regional 3D model of the Lampinsaari volcanites in contact with granodiorite	9 km × 7 km × 5 km	Surface lithological polygons from GTK's digital map database (DigiKP), seismic sections	Numerical processing and interpretation using Paradigm gOcad and 3D model building from interpreted reflections using Intrepid GeoModeller
Semi-regional inversion model of magnetic data	10 km × 8 km × 5 km	VTEM magnetic data	UBC-GIF code MAG3D, results visualized using Paradigm gOcad
3D model of Pyhäsalmi mine	5 km × 3 km × 2 km?	Lithochemistry, tectonic observations from oriented drillcores, diverse geophysical data	Mira Science SPARSE plugin, Paradigm gOcad and Gemcom Surpac
Vihanti and Kuuhkamo deposit models	<1 km × 1 km × 1 km	Drill hole data and geophysical interpretations	Lithological solids built from digitized strings based on drill hole data, geophysical interpretations and structural geology using Gemcom Surpac

2007–2010), reflection seismic profiles were acquired in the Vihanti, Pyhäsalmi and Mullikoräme areas (Kukkonen et al. 2012). Locations of these seismic profiles are presented in Fig. 6.1. A network of seismic profiles enabled imaging and interpretation of the subsurface reflectivity down to 5 km depth and these seismic data have also shown promising results

regarding deep ore exploration (Kukkonen et al. 2012; Heinonen et al. 2012). In addition, geological maps and seismic data enabled detailed modelling of faults and the 3D geology surrounding the Vihanti deposit. In addition to seismic reflection data, semi-regional 3D models were also constrained by airborne electromagnetic surveys. Airborne electromagnetic methods

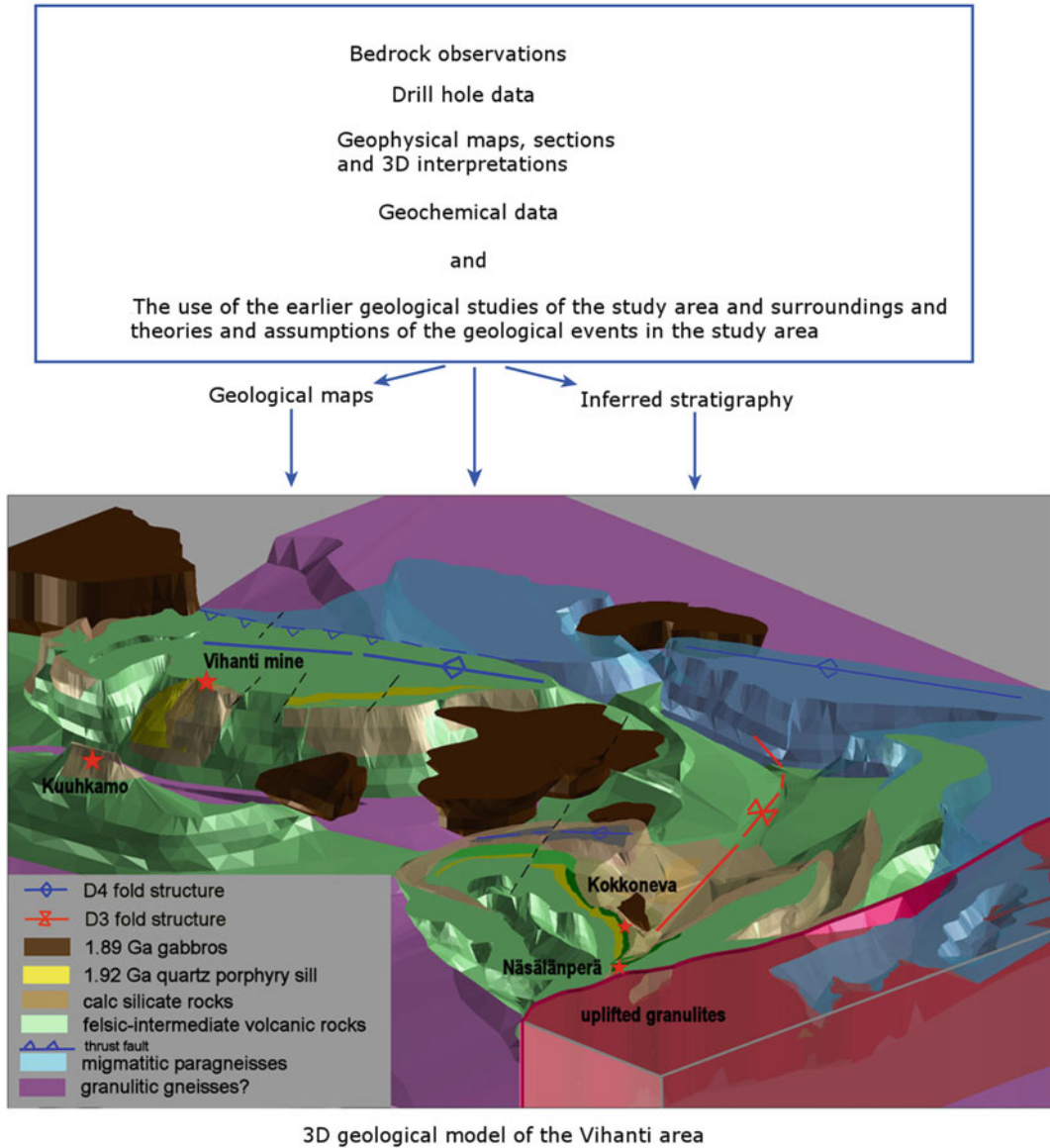


Fig. 6.2 Datasets used in regional and semi-regional modelling and the 3D-model of the Vihanti area shown from the SE. *Red syncline* = Peuraneva syncline, *blue anticlines* represent a second folding stage

(AEM) were used for mapping the electrical properties of the ground, for locating conductors, and for mapping overburden, bedrock geology and structure.

Besides geophysical data and geological field observations, drill hole data were also available for mine-scale 3D modelling of the Pyhäsalmi, Mullikkoräme, Vihanti and Kuuhkamo deposits. In the Vihanti area, there are about 600

exploration holes drilled from the surface but only few of these are deeper than 500 m. In the Pyhäsalmi mine area there are 150 exploration holes (50 km) of which several of the most recent holes are longer than 1500 m. Different geophysical data and drill holes are shown in Figs. 6.2 and 6.3. The mine-scale models give the best information about detailed 3D geology. Interpretation of the structures and stratigraphy at

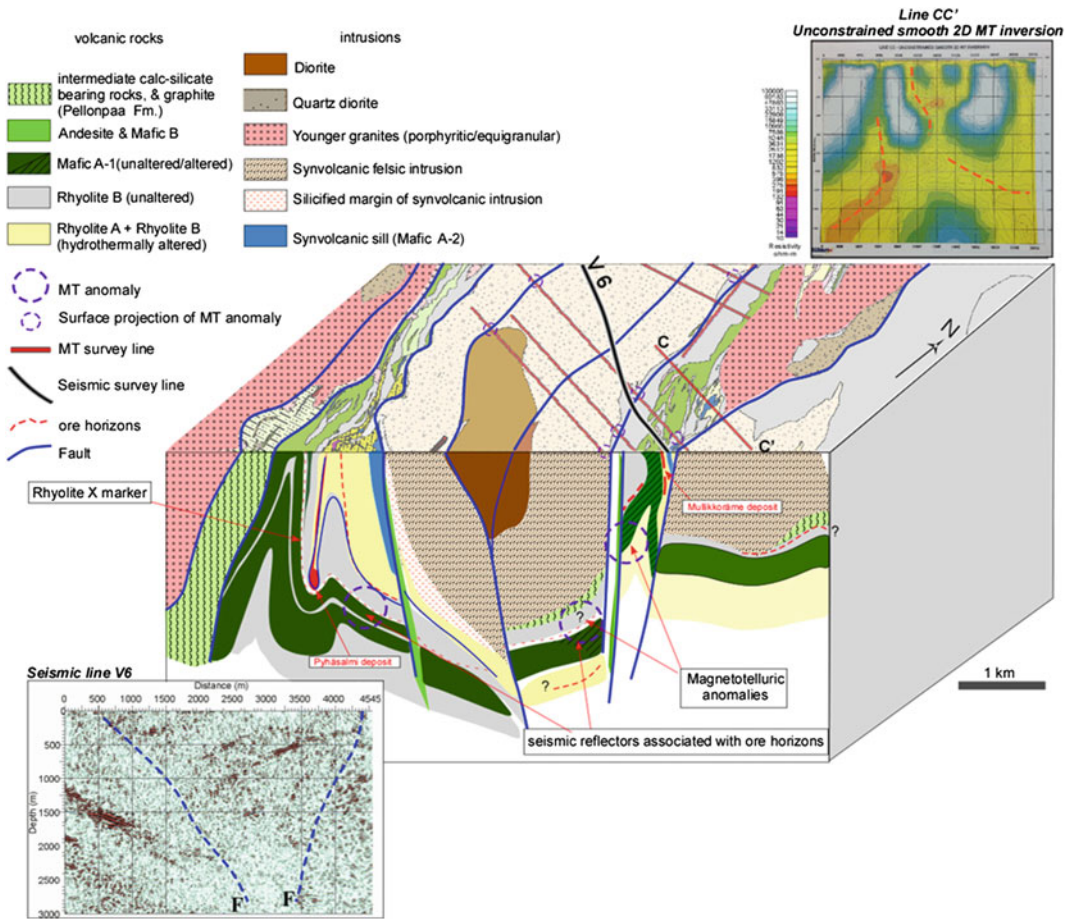


Fig. 6.3 Examples of data used for 3D regional and semi-regional modelling in the Pyhäsalmi mine area

the regional scale also benefit from detailed geological models done in restricted locations. Geochemical analysis was done in several drill holes in the vicinity of the Pyhäsalmi Mine and litho-geochemistry was used for simplifying and classifying rock suites. With this classification a protolith model was developed. There are several oriented drill holes in the Pyhäsalmi area and it was possible to make structural observations from these drill cores. These observations were employed in structural modelling together with high-resolution seismic and Titan-24 methods. Along four acquired Titan-24 profiles, DC (Direct Current) resistivity and IP (Induced Polarization) chargeability was mapped down to depths of 500 m and MT (Magnetotelluric) resistivity as deep as 2000 m. Resistivity and

chargeability contrasts are useful tools to map mineralization, alteration and geological structures.

In the Pyhäsalmi mine, the 3D models were based on the combined application of multidisciplinary techniques that include geophysics, litho-geochemistry and structural geology which were visualized in a three dimensional geological modelling software Paradigm gOcad®. The 3D regional model, Vihanti 3D semi-regional and Vihanti and Kuuhkamo mine scale 3D models were built by using Gemcom Surpac™. In the Pyhäsalmi mine scale model, the Sparse Module of gOcad® Mining Suite was used to construct 3D structural geology models from structural observations on oriented drill cores. In addition, an alternative approach was applied for the 3D

modelling of the area surrounding the Vihanti deposit. Seismic reflectors were interpreted from the HIRE seismic sections and connected into 3D model using an implicit approach (e.g. McInerney et al. 2005) by GeoModeller (Intrepid Geophysics). In addition, gravity and magnetic data were used to estimate spatial distribution of physical properties in 3D using the UBC potential field inversion software (gravity and magnetic inversion codes of University of British Columbia) with gOcad® Mining Suite and ModelVision.

Because of the scarcity of direct bedrock observations and deep seismic soundings, the regional 3D model of the Vihanti-Pyhäsalmi area illustrates the present structural geological view in 3D supported by gravity inversion and potential field data, processed in various ways. During the ProMine project, the structural geological understanding of the study areas was developed in parallel with the 3D modelling process. Complex structural history, high metamorphism and originally heterogeneous volcanic sequence made the 4D modelling of the Vihanti-Pyhäsalmi area challenging. The 4D modelling was done by visualizing different deformational stages of the main tectonic events in 3D starting from magmatism and the sedimentation on the Archaean basement and ending with the present deformed state.

In the Vihanti and Pyhäsalmi areas mineralization is associated with specific lithological units. 3D distribution of petrophysical properties was obtained from geophysical inversion and tested for ore exploration since VHMS host rocks typically are denser and more magnetic than the surrounding country rocks.

6.3 3D Models of the Vihanti-Pyhäsalmi Area

6.3.1 Regional 3D Model

The regional 3D model of the Vihanti-Pyhäsalmi area located in the NW end of the Savo belt (160 × 50 km), consists of Archaean basement

complexes in the east and diverse Palaeoproterozoic rocks in the west. The Mesoproterozoic Muhos formation represents the youngest unit in the area (Fig. 6.4).

The zircon age, Sm–Nd isotope and trace element geochemical data indicate a dominantly crustal, mixed Archaean-Proterozoic source and anatectic origin for the 1.8 Ga granites along the Oulujärvi shear zone (Kontinen et al. 2013). Isotopic data and the seismic data acquired during the Finnish Reflection Experiment (FIRE) during 2001–2005 (Kukkonen and Lahtinen 2006) suggest that Archaean basement extends towards south to the SE–NW trending major shear zones in the Raahe Ladoga zone (Korja et al. 2006). The Karelian supracrustal sequences were deposited on the Archaean basement between 2.3 and 2.1 Ga. During 1.93–1.85 Svecofennian sedimentary and volcanic rocks were deposited to the west of Karelian supracrustal sequences and voluminous intrusions were also emplaced. These Svecofennian formations collided with the Archaean basement (Lahtinen 1994). Finally, Karelian and Svecofennian formations were thrust over the Archaean craton and as a result intense thrust and fold systems were developed within the Archaean border zone. In the later stage of the deformational history, major shear zones like the sinistral Oulujärvi shear zone (OSZ) developed and the older Revonnenva shear zone (ReSZ) and Ruhanperä (RuSZ) shear zone were reactivated (Kousa et al. 1997).

The interpretation of the gravity data (Fig. 6.5) suggests the possibility that the large bedrock boundaries and major shear zones continue towards greater depths. This interpretation is based on regional gravity data (4–6 observation points/km²) and density measurements of rock samples of the investigated area (~5000). The bedrock is poorly exposed and lithological contacts cannot be observed in the field. Analysis of density measurements is crucial for the inversion, and the mean density for all samples was about 2730 kg/m³. First modelling was carried out with the Encon Model Vision using 3D-prisms. Outlines for the sub-outcropping bodies were determined from Bouguer anomaly

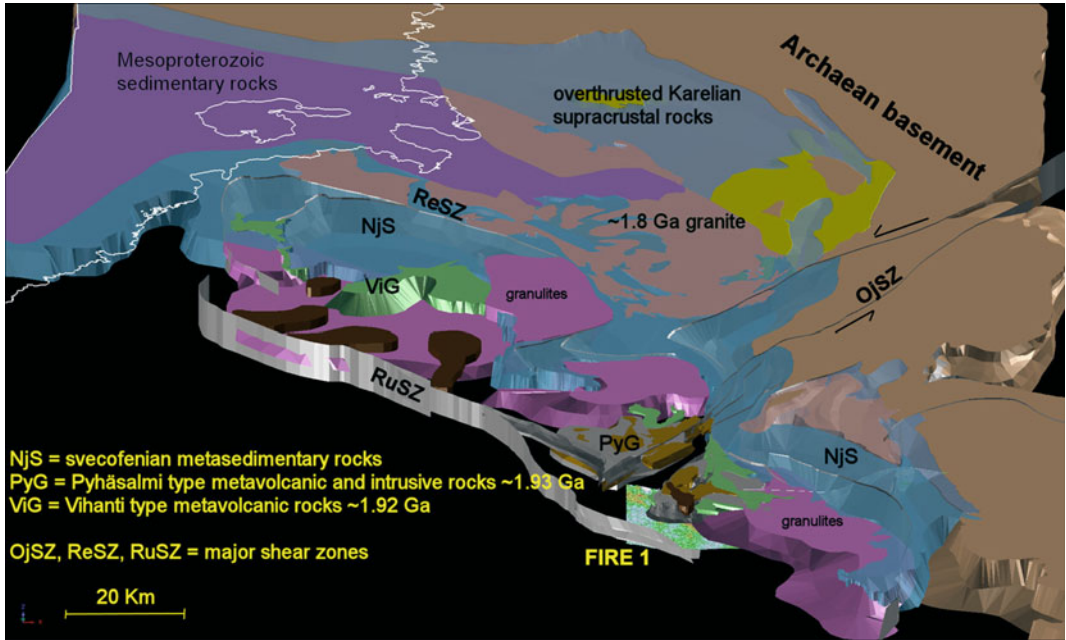


Fig. 6.4 A regional 3D model of the NW part of the Raahel-Ladoga zone

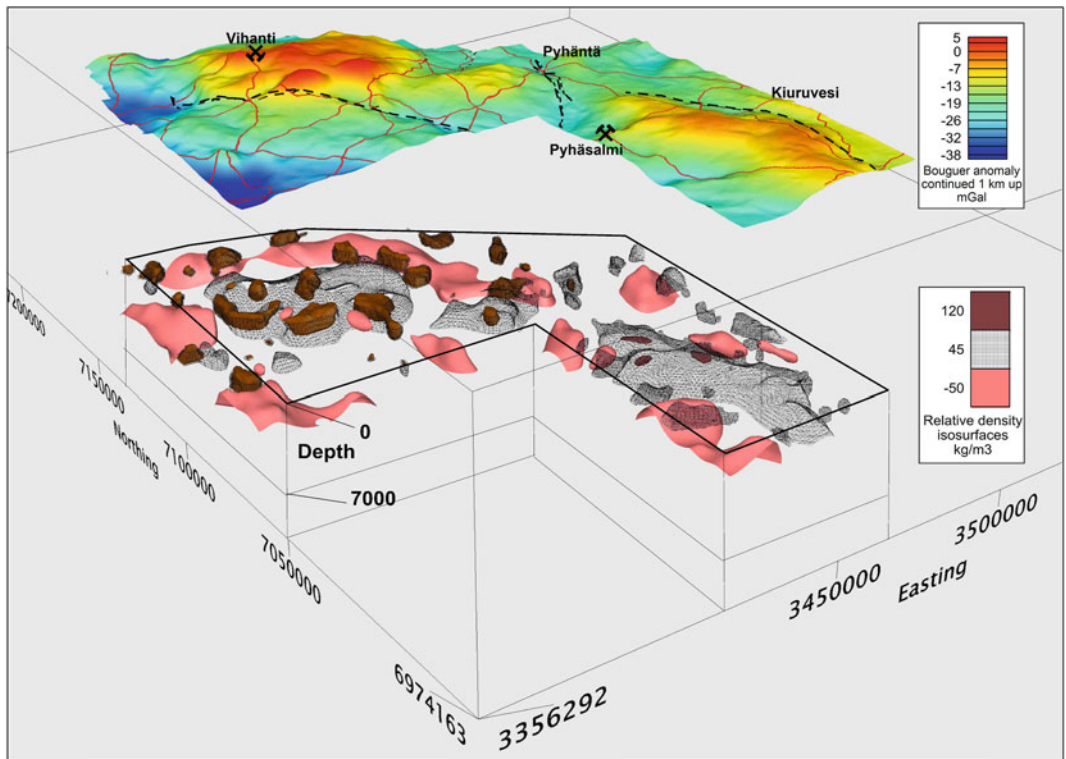


Fig. 6.5 Inversion model of regional gravity data from the Vihanti-Pyhäsalmi area

data and its derivatives at ground surface. Depths and especially the bodies at greater depth were interpreted from gravity data continued to different levels upward. 3D voxel-based inversion (Geosoft Oasis montaj) was done using the prism model as a starting value. Mean densities of major blocks were used to limit the inversion to give a more compact model. As a result the regional model shows gabbros and denser mafic volcanic rocks (brown, mean density 2910 kg/m^3), rocks with lower density (red, mainly granites and mica gneisses, density 2671 kg/m^3) and probably granulitic deeper blocks (grey, density 2780 kg/m^3). In the Vihanti area the top of this denser block is at a depth of about 2 km. Blocks with density near to the regional mean density (2730 kg/m^3) are not shown in Fig. 6.5.

6.3.2 Semi-Regional 3D Model of the Vihanti Area

The semi-regional model of the Vihanti area covers an area of $20 \times 30 \text{ km}$. Lithological bodies were modelled down to 4 km depth. The model consists of 26 lithological solids. The most important rock formations are shown in Fig. 6.2. The main features of the 3D model are: uplifted granulites and pyroxene granites in the east, migmatized mica gneisses in the north, gently folded intermediate to felsic volcanic rocks in the central area and the lowermost granulitic paragneisses unit. Voluminous intrusive rocks in the south and west have not been shown in Fig. 6.2, except small gabbroic bodies.

According to the structural model, the Vihanti deposit is situated on the southern limb of the large anticlinal dome (Fig. 6.7). The Kuuhkamo deposit is situated in the hinge area of a similar fold structure although intrusive rocks cover almost the whole area. The Kokkoneva deposit is located on the western limb and the Näsälänperä deposit at the nose area of the Peuraneva syncline (Fig. 6.2).

The supracrustal units were built according to the stratigraphic subdivision (Fig. 6.2). The lowermost unit of the Vihanti group is

voluminous intermediate to felsic volcanic rock, which forms an anticline in the Vihanti area and a syncline in the Näsälänperä area. A narrow uniform layer of calc-silicate rocks and felsic tuffaceous rocks is rimming these structures. At the Vihanti mine area a layer of intermediate volcanic rocks with minor mafic volcanic rocks were deposited on top of the calc-silicate rocks. Similar voluminous intermediate and mafic volcanic rocks fill the syncline in the Näsälänperä area. In the Vihanti-Vilminko area massive greywackes form the uppermost lithological units. The relationship between these volcanic rocks and the migmatized mica gneisses in the north is not clear but a tectonic contact between them could explain the change of the metamorphic grade. A sequence of volcanic rocks and related sediments (Ylivieska group) were deposited on the Vihanti group at 1.89–1.87 Ga.

Figure 6.6A illustrates the 3D fault model. The location of the vertical faults is based on the DigiKP and simply continued vertically into deeper levels. Verticality has been inferred from the geological observations from the mine (Rouhunkoski 1968, Fig. 6.6b). Seismic sections show the near horizontal layering of the rock units cut by several faults. One main discontinuity surface can be interpreted from several seismic sections and connected to a fault or shear zone dipping about 60° to the northwest. A similar fault dipping towards the southwest has been interpreted earlier from seismic sections (Heinonen et al. 2013). Even though the ores are not controlled by these faults or shear zones, the faults and shear zones have disrupted and displaced them. In ore exploration, these faults should be taken into account and it is important to determine the kinematics of these faults.

6.3.3 3D Models of the Vihanti and Kuuhkamo Areas

In the Vihanti area the major lithostratigraphical units are mostly gently folded and the lithological key horizons can be rather easily followed. Detailed models of the Vihanti and Kuuhkamo deposits show the close association of the ore to

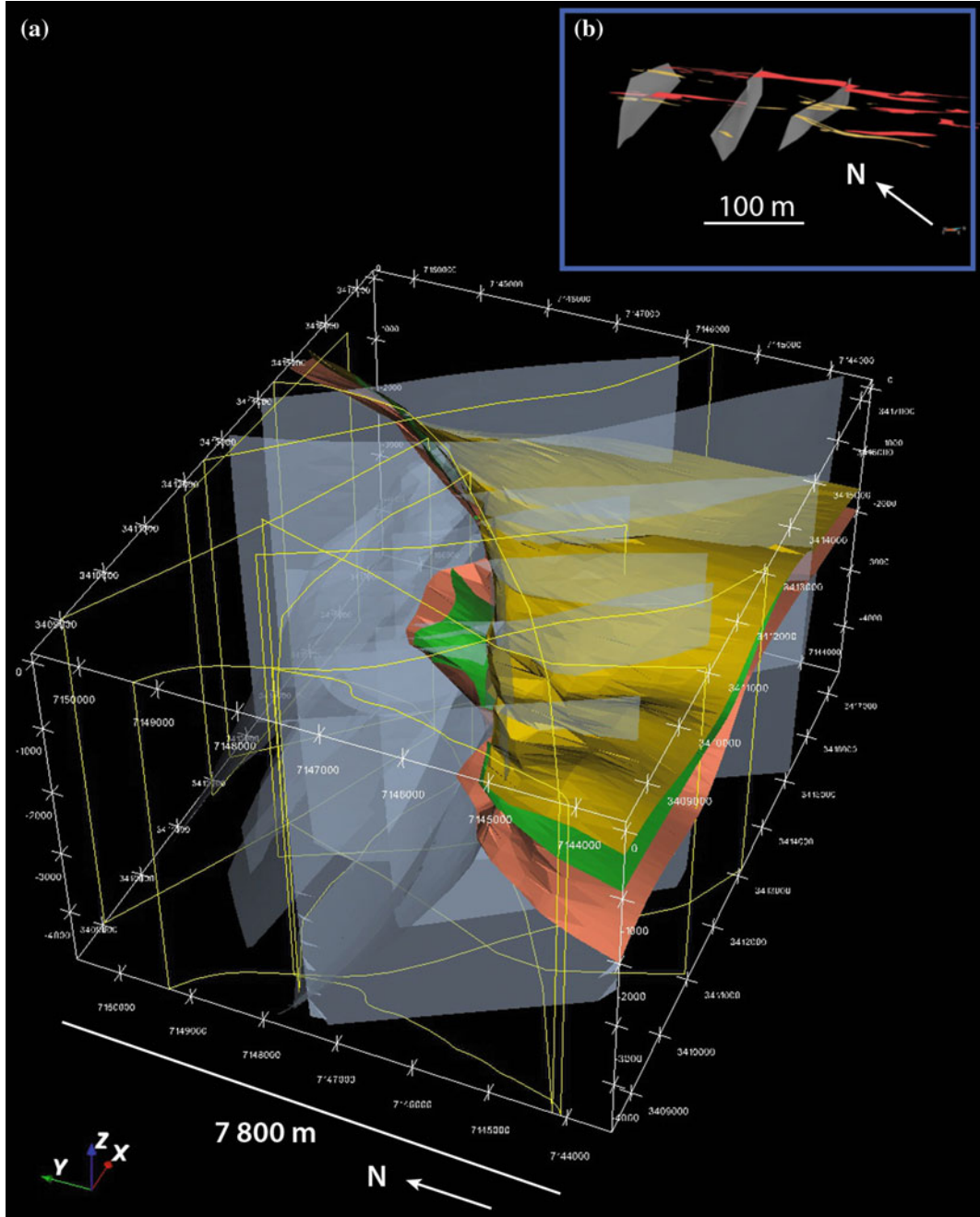


Fig. 6.6 a The 3D fault model of the boundary between the Lampinsaari volcanic rocks and granodiorite in the southeast, faults in grey color and colored surfaces refer to lower contacts of the granodiorite by a light brown color, volcanite by a green color and high reflective layer

including the Lampinsaari ore by a red color; b Zn ore (in red) and pyrite ore (in light brown) and associated faults (in grey) at the levels of 200 and 250 m measured from the surface

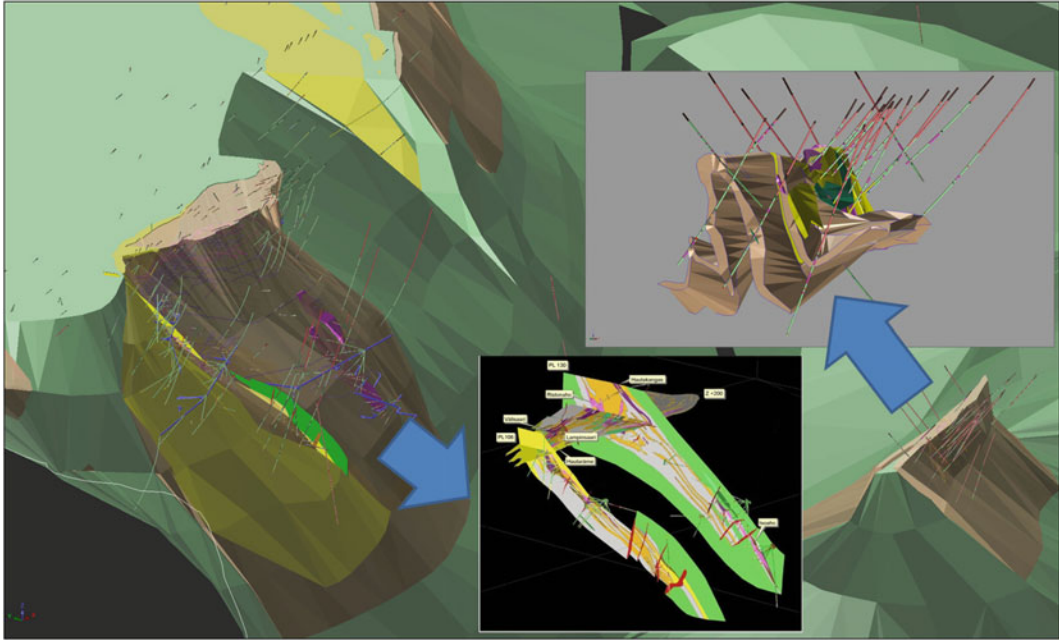


Fig. 6.7 The 3D model of the Vihanti-Kuuhkamo area shown from the west. A detailed model of the Vihanti mine and the Kuuhkamo mineralization shows the close

association of the ore (*lilac*) to the calc-silicate rock (*beige*) and altered quartz feldspar porphyry sill (*yellow*)

the calc-silicate rock and altered quartz feldspar porphyry sill (see Fig. 6.7). The lowermost unit of the volcanic pile is voluminous intermediate to felsic volcanic rocks, which form an anticline in the Vihanti area and a syncline in the Näsälänperä area. A narrow uniform layer of calc-silicate rocks and felsic tuffaceous rocks is rimming these structures. From the seismic sections it is evident that the latest SE-NW faults had a vertical movement also disrupting the ore (Figs. 6.6 and 6.7).

6.3.4 Semi-Regional 3D Model of the Pyhäsalmi Area

The semi-regional model of the Pyhäsalmi area covers an area of 20×35 km in the vicinity of the Archaean-Proterozoic boundary in central Finland. Structurally the area is situated in the southwestern end of the Oulujärvi shear zone

(Kärki et al. 1993), see Fig. 6.8. The main lithological units in the study area are 1.93–1.92 Ga bimodal metavolcanic rocks (Fig. 6.8) and related tonalitic subvolcanic intrusions, which form domal, fold structures. The major part of the Pyhäsalmi type ore deposits are situated in this sequence. Slightly younger intermediate to felsic volcanic rocks with minor calc-silicate and dolomite intercalations (Vihanti group) are deposited on top of Pyhäsalmi type rocks. Structurally these rocks are situated in the synformal basins inside the domal structures. In the later geological evolution, voluminous Svecofennian intrusive rocks, 1.89–1.87 Ga, intruded into the volcanic sequences. The large scale antiform and synform structures as well as homogenous intrusive bodies can be interpreted from the seismic HIRE profiles. Many of the ore deposits in the Pyhäsalmi area are located in the immediate vicinity of the faults related to the Oulujärvi shear zone.

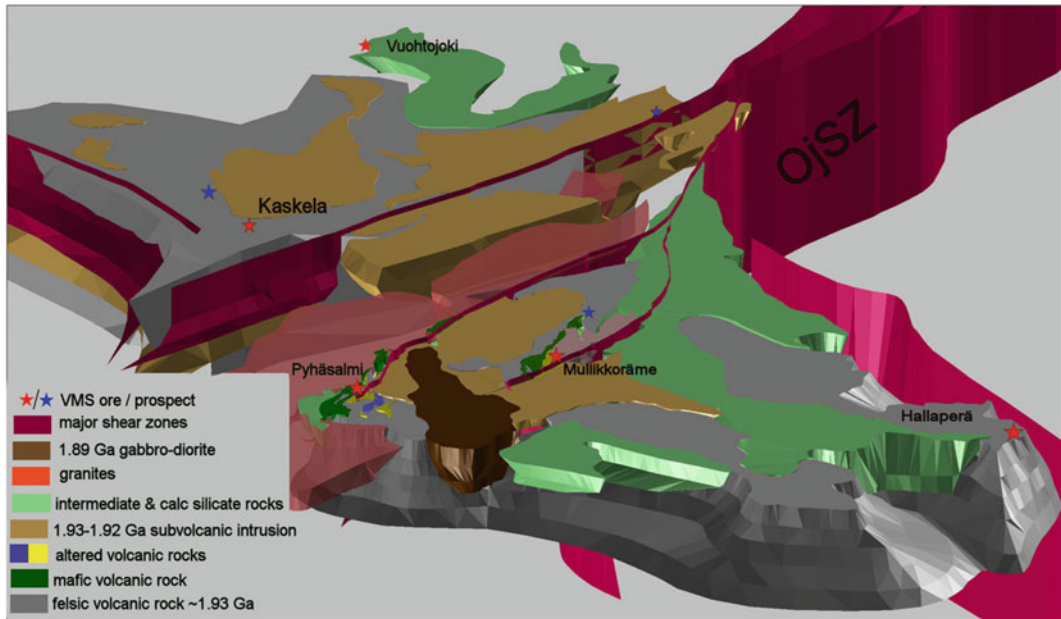


Fig. 6.8 Regional 3D model of the Pyhäsalmi area shown from the SE

6.3.5 3D Model of the Pyhäsalmi Mine Area

The Pyhäsalmi area (Fig. 6.9) is composed of a lowermost unit of felsic mass flows and tuffaceous and pyroclastic rocks with minor mafic intercalations. These give way to mafic massive lavas, pillow lavas, pillow breccias and pyroclastic rocks towards the stratigraphic top. The volcanic rocks are low- to medium-K rhyolites, transitional between calc-alkaline and tholeiitic affinity, and sub-alkaline low- to medium-K tholeiitic basalts and basaltic andesites. The Pyhäsalmi massive Zn-Cu-pyrite deposit is situated in the bimodal volcanic sequence characterised by a voluminous sericite-cordierite-antophyllite alteration zone. The massive ore was originally hosted by altered felsic and mafic volcanic rocks, but the deep parts of the ore body have been separated by shear zones from the upper part. The deep ore is hosted by unaltered felsic and mafic volcanic rocks with sharp and mylonitic contacts (Mäki 1986; Puustjärvi ed 1999; Imanä et al. 2013).

6.4 Structural Evolution of the Vihanti-Pyhäsalmi Area

At the pre-compressional stage, the epicontinental sediments were deposited on the western edge of the Archaean basement block. Palaeoproterozoic 1.93–1.92 Ga volcanism can be interpreted as an early arc complex in the Svecofennian domain, which was separated from the Archaean craton by a sea (Fig. 6.11a). Detailed stratigraphic columns of the Pyhäsalmi and Vihanti groups are presented in Fig. 6.10. The relationship between Karelian sediments and the sediments of the Näläntöjärvi suite is not unambiguous but in this model the latter is interpreted as a Svecofennian unit and it has been considered to be closely associated with the Svecofennian volcanism at Pyhäsalmi and Vihanti areas although with the present configuration they might be separated by a shear zones. In the following, the structural evolution is presented step by step and the main tectonic events are presented in Table 6.2.

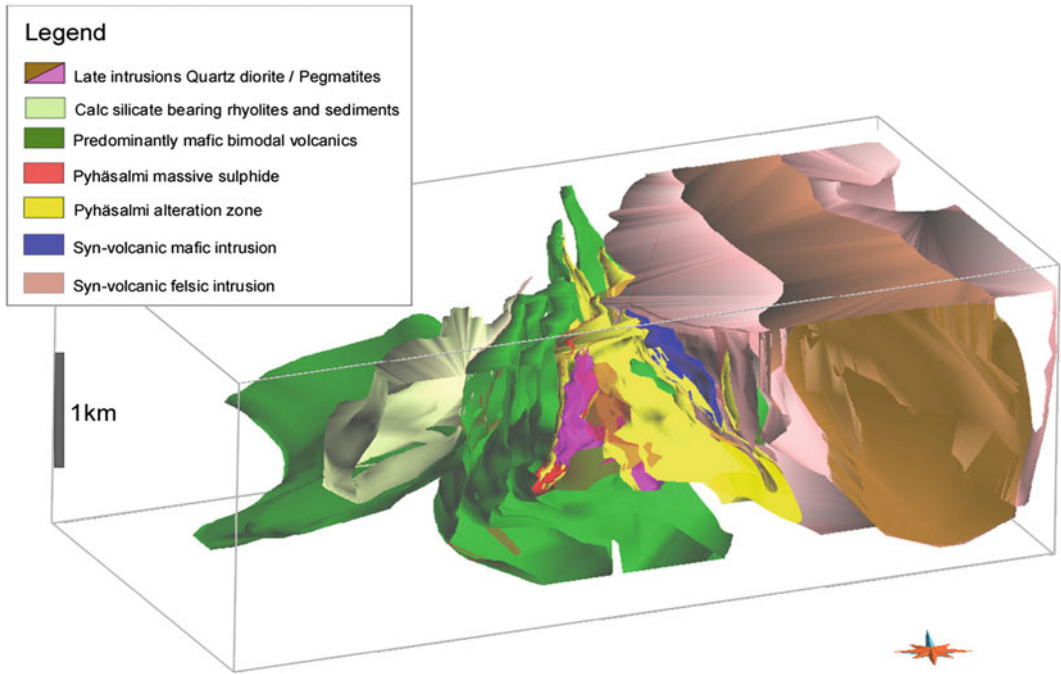


Fig. 6.9 3D geological model of the Pyhäsalmi mine area. Volcanic rocks form steep folds inside of which the Pyhäsalmi ore is trapped. Volcanic stratigraphy continues underneath the granites on the eastern side of the mine

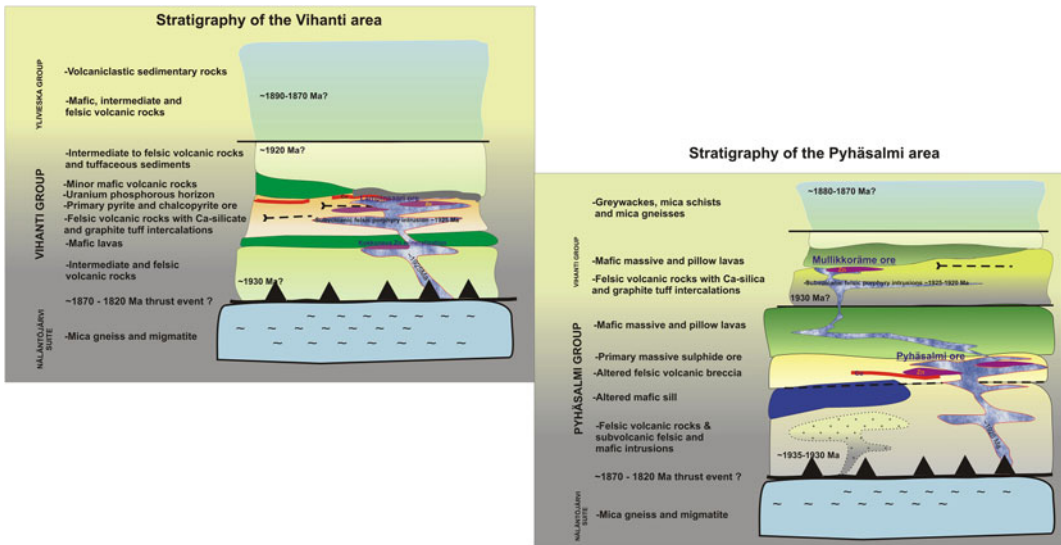


Fig. 6.10 The schematic stratigraphic model of the Vihanti (a) and Pyhäsalmi (b) area illustrating both volcanic and subvolcanic units in relation to ore formation

Table 6.2 Geological evolution of the Vihanti-Pyhäsalmi ore belt

4D	Tectonic events	Magmatism	Ore forming processes
2.3–1.93 Ga	Sedimentation and magmatism on the Archaean basement	<ul style="list-style-type: none"> • 2.06 felsic and mafic volcanism at Siilinjärvi • 2.1 mafic volcanism 	
1.93–1.90 Ga	Lower Svecofennian sedimentation (Näläntjärvi suite NjS) and early arc related volcanism Fig. 6.11a	<ul style="list-style-type: none"> • Mafic volcanism in NjS • 1.93 Ga Pyhäsalmi bimodal volcanism • 1.92 Ga Vihanti volcanism • 1.92 Ga quartz porphyry sill 	Primary VHMS-ore deposition secondary replacement type Zn-Pb-ores
1.91 Ga	D1-D2: thrusting and flat lying folding towards NE Fig. 6.11b		Early thickening and remobilization of the ores
1.89–1.85 Ga	Upper Svecofennian mature arc volcanism and sedimentation in the central Finland	Ylivieska volcanism	Rauhala type ores
1.89–1.85 Ga	Svecofennian and undefined craton margin intrusive rocks Fig. 6.11c	Voluminous synorogenic intrusive rocks (mainly felsic)	Nickel bearing intrusions
1.85 Ga	D3: refolding of the early stage flat lying structures into upright position and peak of metamorphism 1.88 Ga		Refolding and recrystallization of the sulphide ores
<1.85 Ga	D3-shearing along craton margin	Voluminous post-kinematic porphyritic granites	
1.85–1.82 Ga	Extension and uplift of granulite along old shear zones Fig. 6.11d		
1.82–1.79 Ga	D4-shearing along OSZ and RLZ and intrusion of late granites Fig. 6.11e	Late-orogenic granites and pegmatites	Final shearing and remobilization of the ore (Pyhäsalmi area)
	Brittle SE-NW faulting		Late faulting of the ore (Vihanti area)
1.2–1.0 Ga	Deposition of the meso- and neoproterozoic formations		

6.4.1 First Compressional Stage

The earliest Svecofennian tectono-metamorphic stage (1.91 Ga) caused thrusting of the epicontinental sediments towards the east and northeast. As a result these sequences formed parautochthonous-autochthonous nappes on the Archaean basement (Fig. 6.11b). The position of the Näläntjärvi suite (NjS) and the Vihanti-Pyhäsalmi volcanic arc is ambiguous at this stage, but most probably they have been moved eastward and finally collided against the Archaean basement and earlier epicontinental sediment

nappes causing a major thrust zone between these units. This major thrust zone that has reactivated several times during later orogenic movements is known as the Raahe-Ladoga zone.

Continuous SW-NE compression caused tectonic thickening and intense SE-NW trending F3 folding, which refolded the earlier flat lying structures into an upright position along the Raahe-Ladoga zone. Contemporaneous magmatism between 1890–1885 Ma produced a large volume of igneous rocks intruded into the Näläntjärvi suite and the Vihanti Pyhäsalmi volcanic arc (Fig. 6.11c). This process resulted in

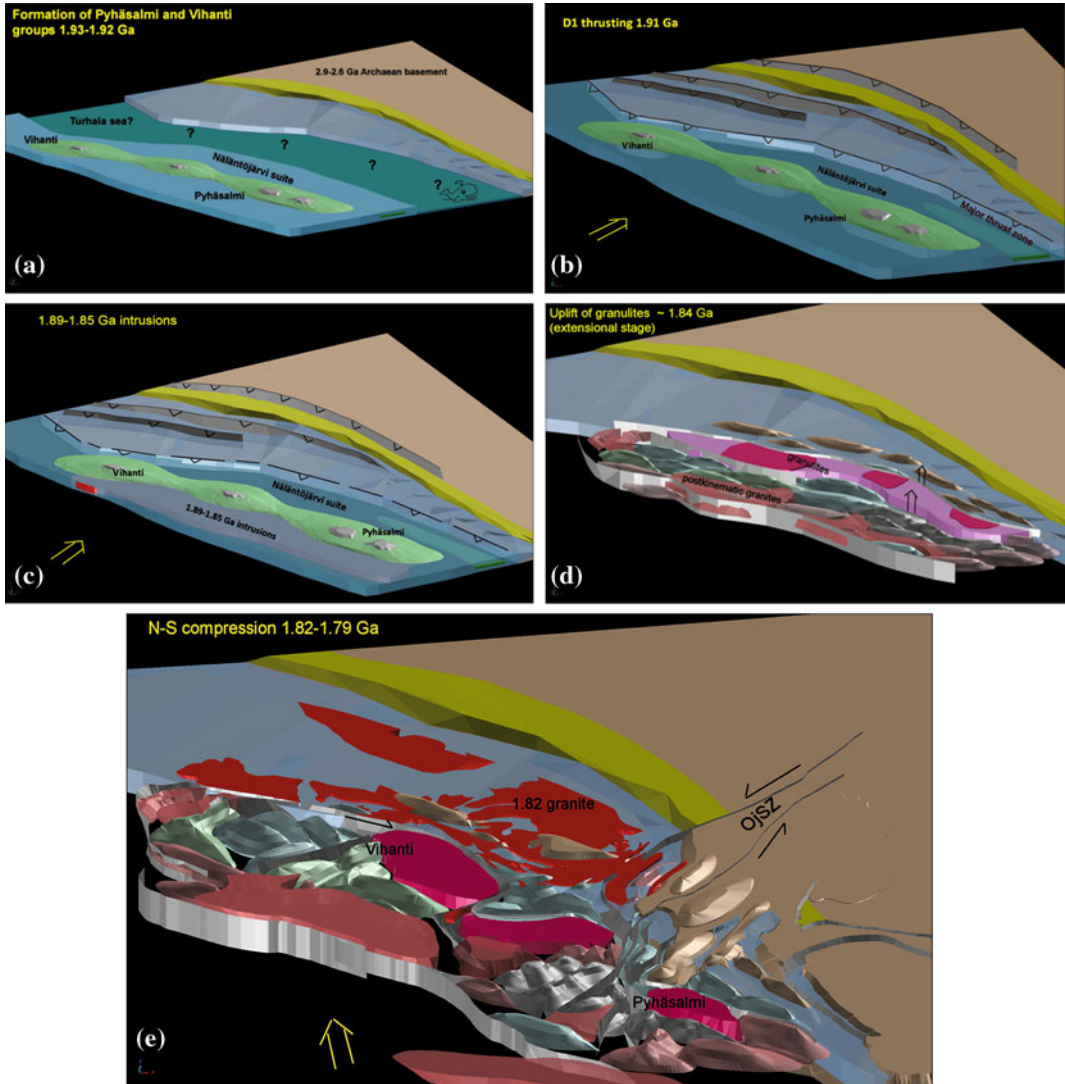


Fig. 6.11 **a** Formation of the 1.93–1.92 Ga early arc volcanism along the Archaean boundary zone; **b** At the early compressional stage the Karelian epicontinental sediments, the Nälantöjärvi suite and the Svecofennian

early arc sequences were collided against the Archaean basement; **c** Voluminous intrusive activity at 1.89–1.85 Ga **d** Extensional stage and uplift of the granulite blocks at 1.84 Ga **e** Second compressional stage at 1.82–1.79 Ga

high temperature, low-pressure metamorphism at 670–800 °C and 5 kb (Korja et al. 1994). At the same time younger Svecofennian volcanism produced a new sequence of volcanic rocks (Ylivieska group) and related sediments farther west. At the present erosion level these units are seen as 10–20 km long and about 5 km wide SE-NW trending fold belts in the airborne geophysical maps.

Large-scale vertical shear zones are developed along the edge of the Archaean basement in the latest stages of D3. Slowly the compression ceases and extensional processes causes uplift of granulite facies metamorphic blocks along the earlier shear zones (Fig. 6.11d). Voluminous porphyritic orthopyroxene-bearing granites were emplaced into the folded sequences at this stage.

6.4.2 Second Compressional Stage (D4)

After the extensional stage a new compressional phase started to deform the earlier structures (Fig. 6.11e). At this stage the earlier SW-NE compression was shifted to N-S. A new set of SW-NE trending large-scale F4 folds refolded earlier F3 folds in the Raahe-Ladoga zone. The D4 stage caused an easily recognizable D3-D4 basin and dome interference structure in the Pyhäsalmi and Vihanti areas. For example, the Lampinsaari mine is situated in the southern limb of such D4 antiformal dome. The most conspicuous structural feature of the D4 stage is the crustal scale sinistral SW-NE trending Oulujärvi shear zone (Kärki et al. 1993), which transected the Archaean craton and the Kainuu schist belt in the east. The horsetail system of the shear zone caused intense shearing in the Pyhäsalmi area resulting in remobilization of the massive sulphide ores. At the same stage also the earlier shear zones along the Archaean craton were reactivated and a large amount of late granites and pegmatites were emplaced close to the major shear zones between 1.82 and 1.79 Ga.

6.4.3 Schematic 4D Evolution of the Pyhäsalmi Deposit

The Pyhäsalmi ore was formed at or close to the seafloor in relation to hydrothermal activity in a bimodal volcanic system. During later stages the ore was affected by multiphase deformation. The earliest structures were subhorizontal thrusts and related sheath folds, which caused thrusting of ore and part of the altered rocks over the originally overlying rocks. At this stage also parts of subvolcanic intrusion were over-thrust on top of volcanic sequences. Later all formations were refolded into an upright position. At the final stage of deformation intense vertical shearing deformed the ore to the present shape. These shear structures might be reactivated original synvolcanic faults. The structural history is demonstrated in Fig. 6.12.

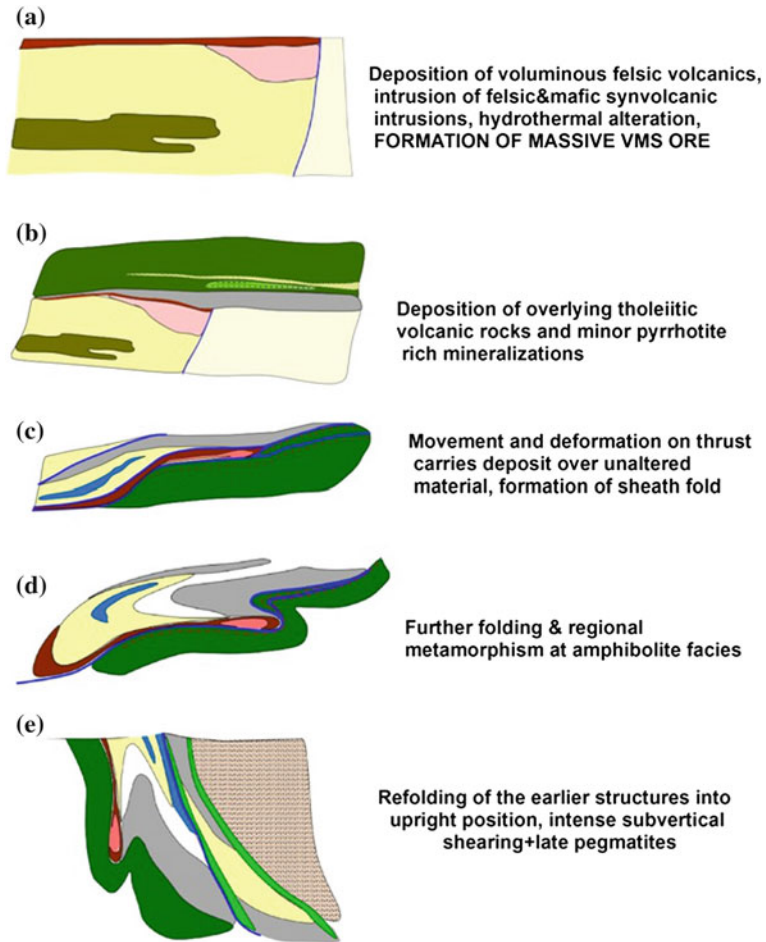
6.5 Potential Resources Assessment

The Zn-Cu zone of the Vihanti-Pyhäsalmi area has been geomathematically evaluated by Tontti et al. (1981) using cluster and characteristic analyses. Data included the chemical composition of the ore, ore mineralogy, petrography of the host and wall rocks, geometry of the deposits, reserves, and geological, aeromagnetic and gravimetric maps. The most significant results were achieved with the aeromagnetic data. The best potential for ore was defined for the SE end of the zone (Pyhäsalmi area. During 1983–1986, a Multi-method Mineral Resource Prediction Project carried out by the Geological Survey of Finland was focused on this area (Gaál 1988; Kuosmanen 1988). Subsequently, the ore potential within the Vihanti-Pyhäsalmi area has been studied by several authors (e.g., Puustjärvi 1999; Ekdahl 1993; Kousa and Luukas 2004; Roberts 2002).

In the Vihanti-Pyhäsalmi area, VHMS-deposits are related to specific rock types and lithological association (Rouhunkoski 1968; Helovuori 1979; Mäki 1986; Puustjärvi 1999; Nikander et al. 2002). This fact could be used in ore exploration and the Vihanti-Pyhäsalmi type VHMS deposits are hosted either in the lower Pyhäsalmi group or the overlying Vihanti group. The role of the co-genetic subvolcanic intrusions seems to be extremely important at both stratigraphic levels (Fig. 6.10).

Traditionally, exploration in the Pyhäsalmi district has been constrained by the depth penetration of conventional geophysical techniques and was focused along zones with outcropping mineralization. This study focused on the test of new exploration tools and methods for detecting and predicting concealed massive sulphide ore bodies at depths greater than 600 m and up to 3000 m below surface. The initial work consisted of identifying petrophysical and chemical characteristics of the host rocks in order build 3D models of the ore horizons. Such models were extended into new and deeper areas by interpreting data obtained from deep penetrating geophysical methods and new drill holes. The modelling

Fig. 6.12 Evolutionary model of the Pyhäsalmi ore deposit



indicates that the Pyhäsalmi and Mullikkoräme areas represent the western and eastern flanks of an open synformal structure. According to the model presented in Fig. 6.3, the prospective rock types are situated below the co-genetic subvolcanic intrusive rocks at the depth of 1500–2500 m. Vertical shear zones deformed and remobilized the sulphide ores into the vertical position. Therefore, exploration potential remains to be tested in the hinge and western flank of the synform (Fig. 6.3 and 6.13) and also along late vertical shear zones where the occurrence of mobilized ores is possible. Potential continuation of the ore horizons at depth near the mine sites is significant between the two deposits. Contrary to the traditional assumption that all structures are near vertical in the district, the new interpretation suggests that a significant

portion of the prospective volcanic stratigraphy is not much deformed and dips gently under a series of sub-volcanic units interpreted as sill complexes.

At the Pyhäsalmi mine area lithogeochemical studies were successful at defining the ore horizons. Structural data obtained from oriented core measurements were an effective tool for the initial 3D delineation of such horizons. The lateral and deep extensions of the ore horizons were identified by the interpretation of data sourced from deep penetrating geophysical surveys (e.g. reflection seismics and magnetotellurics) and exploration drilling. As a result a new mineralized rhyolite horizon that locally contains high tenors of Zn-Pb sulphide mineralization was found and a new idea of multi-stage ore formation was generated.

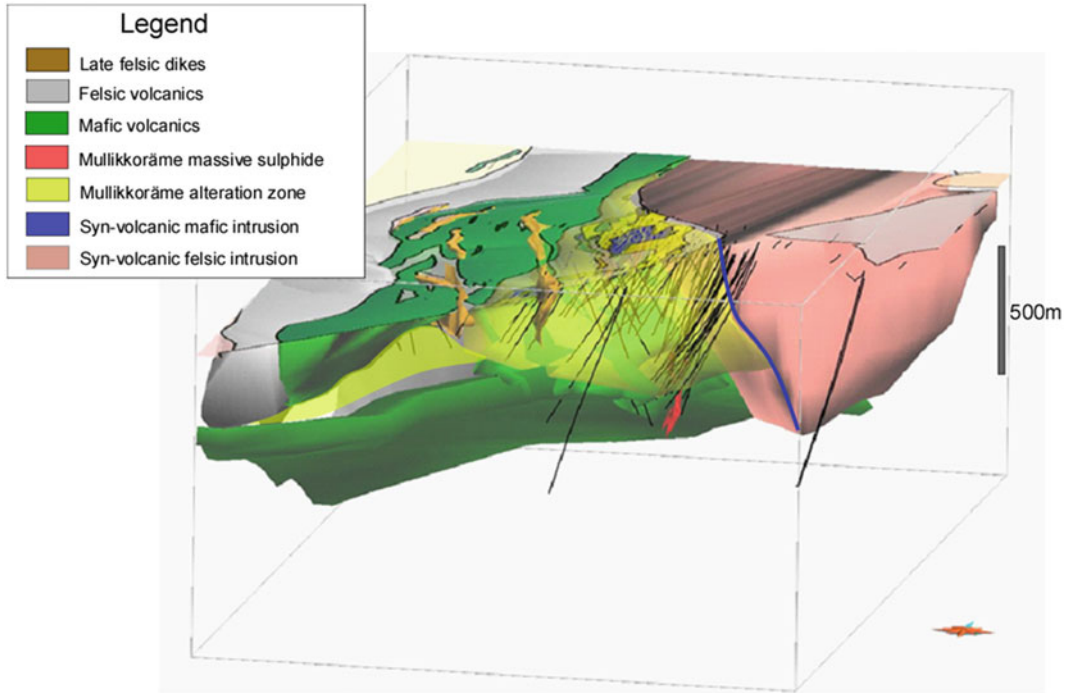


Fig. 6.13 3D geological model of the satellite deposit of Pyhäsalmi; Mullikkoräme

In the Vihanti area the known Zn mineralizations are associated with calc-silicate rocks and graphite tuffs in the thick felsic to intermediate volcanic piles. The key strata are easily recognizable by geophysical means. The co-genetic subvolcanic quartz plagioclase porphyry sills seem to be a critical factor in the ore forming processes. The alteration and replacement processes related to the porphyry were described already by Rouhunkoski (1968).

3D mineral potential mapping was carried out using reflection seismic data and magnetic inversion at near surface. In the Vihanti area, ore-hosting skarn, cordierite gneisses and mafic volcanic rocks have high acoustic impedances and distinct contrast against the surrounding, low acoustic impedance, intermediate tuffites. This suggests that the host rocks of the deposit could be traced in the subsurface with reflection soundings (Kukkonen et al. 2011; Heinonen et al. 2013). In addition, the magnetic anomalies in aeromagnetic maps are associated with the Lampinsaari and Kuuhkamo Zn deposits in the Vihanti area. Figure 6.14 illustrates how the 3D inverted VTEM (a

helicopter borne time domain EM system; Wetherly et al. (2004) magnetic data is associated with the Lampinsaari deposit, felsic porphyritic dykes, calc-silicate rocks and gabbros in the Vihanti area.

6.6 Uncertainty Related to the 3D Geological Models

It is important to realize that 3D models are based only on the surficial data and few drill holes and represent the present idea of the subsurface geology. Thus, geological interpretations and assumptions are crucial because it is impossible to build 3D geological models from sparse observations without this. The challenges with 3D geological modelling of Precambrian bedrock have been described by for example by Laine and Saalman 2012.

One way to present the uncertainty is to show the 3D models together with data locations (e.g. Figure 6.7). The data density and geological

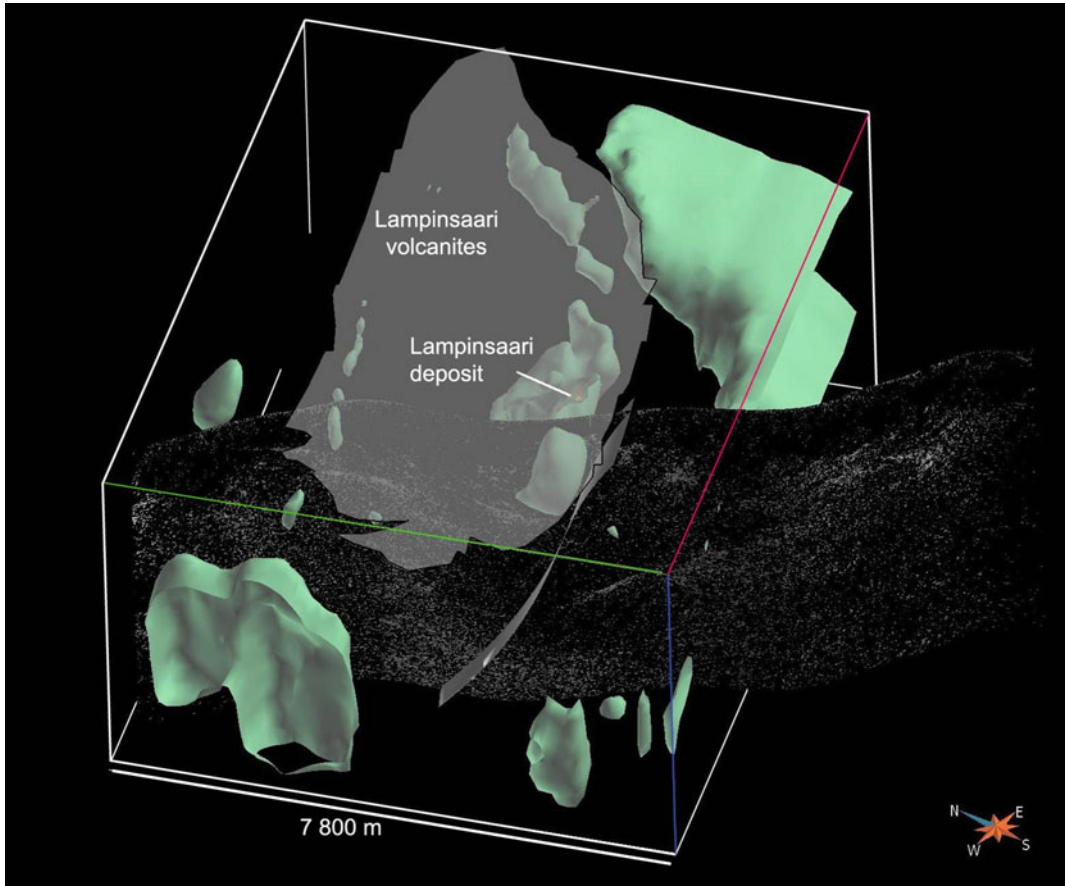


Fig. 6.14 Green surfaces enclose the anomalous magnetic volumes (>0.035 SI) resulting from unconstrained 3D magnetic inversion of the VTEM magnetic data (UBC-GIF code MAG3D, a Program Library for Forward Modelling and Inversion of Magnetic Data over 3D Structures, version developed under the consortium research project Joint/Cooperative Inversion of

Geophysical and Geological Data, UBC-Geophysical Inversion Facility, Department of Earth and Ocean Sciences, University of British Columbia, Vancouver, British Columbia) in the Vihanti area. One seismic HIRE section (Kukkonen et al. 2012) is included and seismic data were processed to show high absolute amplitudes with white colour

heterogeneity can be used as measures for the uncertainty of the 3D geological models. In general, the uncertainty related to 3D geological models in the Vihanti-Pyhäsalmi area is due to several facts:

- Several possible ways to continue or connect structures and lithologies observed in drill cores and at surface exist. In addition, Precambrian lithologies are often discontinuous because of intense folding, shearing and partial melting, especially in the Vihanti-Pyhäsalmi area. Furthermore, in many places the thick overburden prevents direct geological observations of the bedrock.
- Geological observations are already interpretations done on the outcrops or from drill cores, and, thus, may vary according to the skills and opinions of geologists, geological theories of the time, and the purpose and scale of the mapping campaign.
- Faulting and jointing has a pronounced effect on the bedrock structures, especially in the Savo belt, characterized by numerous shear zones and faults, but it is difficult to trace often undulating and variably thick fracture, fault or shear zones to greater depths.
- Uncertainties increases with depths with decreasing amount of drill holes, resolution of

geophysical methods and existence of horizontal geophysical anomalies which we are not able to connect to any geological structure at the surface. In general, the geophysical interpretations especially of gravity and magnetic data are non-unique.

Modern geological 3D modelling approaches make it possible to build 3D models using different geological ideas as a starting point in ore exploration and update the models while when new data is available and new ideas are presented.

6.7 Conclusions

The first regional and semi-regional 3D models of the Pyhäsalmi-Vihanti region were built during the Promine project. They are mainly based on the geological information inferred from densely drilled areas and geophysical maps. The Raahe-Ladoga zone hosts many important VHMS deposits. The 3D geological models proved to be an important tool for exploration because the VHMS deposits in the Vihanti-Pyhäsalmi area display a lithological control. Modelling also showed that ductile and brittle structures control location of the ores. New areas with VHMS potential were identified in the vicinity of the Pyhäsalmi mine using 3D modelling and new geophysical data, especially reflection seismic and electromagnetic surveys together with chemostratigraphic studies. Furthermore, 3D modelling proved to be a useful tool in visualization of the tectonic evolution of the area. The 4D modelling process helped to present the ore forming processes and to develop new exploration strategies in the Vihanti-Pyhäsalmi area.

References

- Airo, M.-L. (ed.), 2005. Aerogeophysics in Finland 1972-2004: Methods, System Characterization and Applications. Geological Survey of Finland, Special paper 39. 197 p.
- Dehghannejad, M., Bauer, T.E., Malehmir, A., Juhlin, C. and Weihed, P., 2012. Crustal geometry of the central Skellefte district, northern Sweden – constraints from reflection seismic investigations. *Tectonophysics* 524–525, p. 87–99.
- Eilu, P., Bergman, T., Bjerkgård, T., Feoktistov, V., Hallberg, A., Korsakova, M., Krasotkin, S., Litvinenko, V., Nurmi, P.A., Often, M., Philippov, N., Sandstrand, J.S. and Voytekhovskiy, Y.L. (comp.) 2013. Metallic Mineral Deposit Map of the Fennoscandian Shield 1:2 000 000. Revised edition. Geological Survey of Finland, Geological Survey of Norway, Geological Survey of Sweden, The Federal Agency of Use of Mineral Resources of the Ministry of Natural Resources of the Russian Federation.
- Ekdahl, E. 1993. Early Proterozoic Karelian and Svecofennian formations and the evolution of the Raahe-Ladoga Ore Zone, based on the Pielavesi area, central Finland. Geological Survey of Finland. Bulletin 373. Espoo: Geologian tutkimuskeskus. 137 p. + 2 app., 2 app. maps.
- Gaal, G. (ed.) 1988. Exploration target selection by integration of geodata using statistical and image processing techniques: an example from central Finland. Geologian tutkimuskeskus. Tutkimusraportti 80. Espoo: Geologian tutkimuskeskus. 156 p.
- Heinonen, S., Imana, M., Snyder, D. B., Kukkonen, I. T., & Heikkinen, P. J. (2012). Seismic reflection profiling of the Pyhäsalmi VHMS-deposit: A complementary approach to the deep base metal exploration in Finland. *Geophysics*, 77(5), WC15-WC23. doi: <http://dx.doi.org/10.1190/GEO2011-0240.1>
- Heinonen, S., Heikkinen, P., Kousa, J., Kukkonen, I.T. and Snyder, D.B. (2013) Enhancing hardrock seismic images: reprocessing of high resolution seismic reflection data from Vihanti, Finland. *Journal of Applied Geophysics* 93, pp. 1-11.
- Helovuori, O. 1979. Geology of the Pyhäsalmi ore deposit, Finland. *Economic Geology* 74 (5), 1084-1101.
- Hillier, M., de Kemp, E., and Schetselaar, E., 2013. 3D form line construction by structural field interpolation (SFI) of geologic strike and dip observations. *Journal of Structural Geology*, 51, 167-179.
- Imaña M., Heinonen S., Mäki T., Häkkinen T., and Luukas, J. 2013. 3D modeling for VMS exploration in the Pyhäsalmi district, Central Finland *in Proceedings of the 12th Biennial SGA Meeting*, 12–15 August 2013, Uppsala, Sweden.
- Kahma, A. 1973. The main metallogenic features in Finland. *Geol. Surv. of Finland, Bull.* 265, 28 p.
- Kärki, A., Laajoki, K. and Luukas, J. 1993. Major Palaeoproterozoic shear zones of the central Fennoscandian Shield. In: *The Baltic Shield. Precambrian Research* 64 (1-4), 207-223.
- Kärki, A., Korja, T., Mahmoud, M., Pirttijärvi, M., Tirronniemi, J., Tuisku, P. and Woodard, J. 2012. Structure of the Raahe - Ladoga Shear Complex. In: *Lithosphere 2012 : Seventh Symposium on the Structure, Composition and Evolution of the Lithosphere in Finland*, Espoo, November 6-8, 2012 : programme and extended abstracts. Institute of

- Seismology. University of Helsinki. Report S-56. Helsinki: Institute of Seismology, 55-58.
- Kontinen, A., Huhma, H., Lahaye, Yann and O'Brien Hugh (2013). New U-Pb zircon age, Sm-Nd isotope and geochemical data on Proterozoic granitic rocks in the area west of the Oulujärvi lake, Central Finland. In: Hölttä, P. (ed., 2013). Current Research: GTK Mineral Potential Workshop, Kuopio, May 2012. Geological Survey of Finland, Report of investigation 198, pp. 70-74.
- Korja, A., Lahtinen, R., Heikkinen, P., Kukkonen, I.T. and FIRE Working Group 2006. A geological interpretation of the upper crust along FIRE 1. In Kukkonen, I.T. and Lahtinen, R. (Eds.), Finnish Reflection Experiment 2001-2005, Geological Survey of Finland, Special paper 43, 45-76. Appendix 1: A geological interpretation of the upper crust along FIRE 1.
- Korja, T., Luosto, U., Korsman, K. and Pajunen, M. 1994. Geophysical and metamorphic features of Paleoproterozoic Svecofennian orogeny and Palaeoproterozoic overprinting on Archaean crust. Geological Survey of Finland, Guide 37, 11–20.
- Kousa, J., and Luukas, J. (eds.) 2004. Bedock and exploration studies in Vihanti area in 1992–2003 (In Finnish). Vihannin ympäristön kallioperä- ja malmitutkimukset vuosina 1992–2003. Geological Survey of Finland (GTK) Project report M10.
- Kousa, J., Luukas, J., Mäki, T., Ekdahl, E., Pelkonen, K., Papunen, H., Isomäki, O-P., Penttilä, V-J. and Nurmi, P. 1997. Geology and mineral deposits of the central Ostrobothnia. In: Research and exploration - where do they meet? 4th Biennial SGA Meeting, August 11-13, 1997, Turku, Finland. Excursion guidebook A2 : volcanic hosted massive sulphide and gold deposits in the Skellefte district, Sweden and western Finland. Geologian tutkimuskeskus. Opas 41. Espoo: Geologian tutkimuskeskus, 43-67.
- Kukkonen, I.T., Heikkinen, P., Heinonen, S., Laitinen, J. and HIRE Working Group 2011. Reflection seismics in exploration for mineral deposits: Initial results from the HIRE project. In: Nenonen, K. and Nurmi, P. (Eds.) 2011, Geoscience for Society 125th Anniversary Volume, Geological Survey of Finland, Special Paper 49, pp. 49-58.
- Kukkonen, I.T., Kosonen E.M., Oinonen, K., Eklund, O., Korja, A., Korja, T., Lahtinen, R., Lunkka, J.P. and Poutanen, M., 2012 (Eds.). Lithosphere 2012 – Seventh Symposium on the Structure, Composition and Evolution of the Lithosphere in Finland. Programme and Extended Abstracts, Espoo, Finland, November 6-8, 2012. Institute of Seismology, University of Helsinki, S-56, 116 pages.
- Kukkonen, I.T. and Lahtinen, R. (Eds.) 2006. Finnish Reflection Experiment FIRE 2001-2005. Geological Survey of Finland, Special Paper 43.
- Kuosmanen, V. (ed.) 1988. Exploration target selection by integration of geodata using statistical and image processing techniques: an example from Central Finland. Part II, (Atlas). Geologian tutkimuskeskus. Tutkimusraportti 84. Espoo: Geologian tutkimuskeskus. 47 p.
- Lahtinen, R., 1994. Crustal evolution of the Svecofennian and Karelian domains during 2.1 - 1.79 Ga, with special emphasis on the geochemistry and origin of 1.93 - 1.91 Ga gneissic tonalites and associated supracrustal rocks in the Rautalampi area, central Finland. Geological Survey of Finland. Bulletin 378. Espoo: Geologian tutkimuskeskus. 128 p.
- Lahtinen, R., Hallberg, A., Korsakova, M., Sandstad, J. S. and Eilu, P. 2012. Main metallogenic events in Fennoscandia: summary. In: Mineral deposits and metallogeny of Fennoscandia. Geological Survey of Finland. Special Paper 53. Espoo: Geological Survey of Finland, 397-401.
- Laine, E. and Saalmann, K. 2012. Problems and challenges of 3D modelling of the Precambrian of Finland. In: Laine, E. (Ed.) 2012, 3D modelling of polydeformed and metamorphosed rocks: the old Outokumpu Cu-Co-Zn mine area as a case study. Geological Survey of Finland, Report of Investigation 195.
- Luukas, J., 1997. Geology and mineral deposits of the central Ostrobothnia. Deformation history. In: Weihed and Mäki (1997) Research and exploration - where do they meet? 4th Biennial SGA Meeting, August 11-13, 1997, Turku, Finland. Excursion guidebook A2 : volcanic hosted massive sulphide and gold deposits in the Skellefte district, Sweden and western Finland. Geologian tutkimuskeskus. Opas 41. Espoo: Geologian tutkimuskeskus, pp. 46-47.
- Luukas, J., 2002. Tutkimusalueen rakennegeologia. In: Nikander, J., Luukas, J., Ruotsalainen, A. and Kousa, J. 2002. Kallioperä- ja malmitutkimukset Vihannin Vilmingon ja Rantsilan Pelkoperän välisellä alueella vuosina 1993-2002. 71 s., 3 liites. Geologian tutkimuskeskus, arkistoraportti, M 19/2434, 3412/2002/1/10, pp 21-24.
- Mäki, T. 1986. Lithochemistry of the Pyhäsalmi zinc-copper-pyrite deposit, Finland. In: Prospecting in areas of glaciated terrain 1986 : papers presented at the seventh international symposium organized by The Institution of Mining and Metallurgy and The Geological Survey of Finland, Kuopio, 1-2 September, 1986. London: The Institution of Mining and Metallurgy, 69-82.
- Malehmir, A., Thunehed, H., Tryggvason, A., 2009. The Paleoproterozoic Kristineberg mining area, northern Sweden: Results from integrated 3D geophysical and geologic modelling, and implications for targeting ore deposits. Geophysics 74, B9 – B22
- McInerney, P., Guillen, A., Courrioux, G., Calcagno, P., Lees, T., 2005. Building 3D geological models directly from data? A new approach applied to Broken Hill, Australia. Digital Mapping Techniques 2005 Workshop in Baton Rouge.
- Nikander, J., Luukas, J., Ruotsalainen, A. and Kousa, J. 2002. Kallioperä- ja malmitutkimukset Vihannin Vilmingon ja Rantsilan Pelkoperän välisellä alueella vuosina 1993-2002. 71 s., 3 liites. Geologian tutkimuskeskus, arkistoraportti, M 19/2434, 3412/2002/1/10.

- Nikander, J., Luukas, J. and Ruotsalainen, A., 2005. Vihannin Lampinsaaren ympäristön ja Kuuhkammon kairaukset karttalehdellä 2434 05 vuosina 2004-2005. Geologian tutkimuskeskus, arkistoraportti, M 19/2434/2005/2/10. 18p.
- Nironen, M., Lahtinen, R. and Koistinen, T., 2002. Suomen geologiset aluenimet-yhtenäisempään nimitykseen! Summary: Subdivision of Finnish bedrock-an attempt to harmonize terminology. *Geologi* 54 (1), pp. 8-14.
- Puustjärvi, H. (ed.) 1999. Pyhäsalmi modeling project. Technical Report. 13. 5. 1997-12. 5. 1999. 251 s., 76 liites. *Geologian tutkimuskeskus, arkistoraportti, M 19/3321/99/1/10*.
- Roberts, M.D., 2002. Architecture, geochemistry and dynamics of Paleoproterozoic seafloor hydrothermal systems preserved in a high-grade metamorphic terrane, Vihanti-Pyhäsalmi district, central Finland. Townsville, Qld: James Cook University of North Queensland. 411 p.
- Rouhunkoski, P., 1968. On the geology and geochemistry of the Vihanti zinc ore deposit, Finland. *Bull. Comm. Géol. Finlande*, Vol. 236, p. 1-121, illus.
- Saalmann, K. and Laine, E. 2014. Structure of the Outokumpu ore district and ophiolite-hosted Cu-Co-Zn-Ni-Ag-Au sulfide deposits revealed from 3D modelling and 2D high-resolution seismic reflection data. *Ore Geology Reviews*, Volume 62, October 2014, pp. 156-180.
- Schetselaar, E., 2013. Mapping the 3D lithofacies architecture of a VMS ore system on a curvilinear-faulted grid: A case study from the Flin Flon mining camp, Canada. *Ore Geology Reviews* 53, p. 261-275.
- Skyttä, P., Bauer, T., Hermansson, T., Dehghannejad, M., Juhlin, C., García, M., Hübert J., and Wehied, P., 2013. Structural evolution of the VMS-hosting Kristineberg area, Sweden – constraints from structural analysis and 3-D-modelling. *Solid Earth*, 4, p. 387-404.
- Tontti, M., Koistinen, E. and Seppänen, H., 1981. Vihannin Zn-Cu-malmivyöhykkeen geomatemattinen arviointi. Summary: Geomathematical evaluation of the Vihanti Zn-Cu ore zone. Geological Survey of Finland, Report of Investigation 54, 58 p.
- Vaasjoki, M., Korsman, K. and Koistinen, T., 2005. Overview. In: Lehtinen, M., Nurmi, P. and Rämö, T. (Eds.), *The Precambrian Geology of Finland - Key to the Evolution of the Fennoscandian Shield*. Elsevier B. V., Amsterdam, pp. 1-18.
- Wetherly, K., Irvine, R. and Morrison, E. 2004. The Geotech VTEM, Time domain helicopter EM system. 74th Ann. Internat. Mtg. Soc. of Expl. Geophys., Extended Abstract, pp. 1217-1220.

Part III
The Fore-Sudetic Basin

New Aspects of Copper Deposits at the Base of the Zechstein in Central Europe

7

J. Hartsch

Abstract

New geological exploration works on Kupferschiefer in the Weißwasser region in Lusatia and published data about the Kupferschiefer mineralisation in the Fore-Sudetic Monocline and other areas of Central Europe provided new aspects concerning the genetic aspects of the copper deposit at the base of the Zechstein Formation. This information was compiled and re-interpreted. The results were used for 3D and 4D modelling works in the Fore-Sudetic Copper Belt. The very specific geological conditions at Weißwasser is characterised by an oxidised facies (Rote Fäule) above and below the copper mineralisation. Based on geochemical investigations, increased gold contents could be identified in the transition zone between the Rote Fäule and the copper facies zone, as reported for other Kupferschiefer deposits. However, in the case of Weißwasser an additional second gold mineralisation could be identified above the copper zone. The copper mineralisation was not limited to the immediate Zechstein base in this area, as could be expected based on the present stage of knowledge, but was also found in the Main Dolomite (Ca₂) of the Staßfurt Cyclothem. Comparing the similar copper contents of the Kupferschiefer ore at Weißwasser, Spremberg-Graustein and Bolesławiec with the deposits in Central Europe, the conclusion can be drawn that in the North-Sudetic Trough the mineralisation intensity is significantly higher than in Central Germany, but similar to the Fore-Sudetic Monocline. The main reason for the huge copper accumulation at the base of Zechstein in Poland and East Germany is due to the high elevation of the Mohorovičić Discontinuity, large NW-SE striking faults, a large area with oxidised rocks (Rote Fäule) and a strong heat flow from the

J. Hartsch (✉)
G.E.O.S. Ingenieurgesellschaft mbH, Freiberg,
Germany
e-mail: j.hartsch@geosfreiberg.de

Upper Mantle at the beginning the Triassic. All areas with rich copper ores (surface densities $> 60 \text{ kg/m}^3$) are found concentrated in a zone of 200 km length and 140 km width. This zone is bound to the NE by the Eger Lineament. Outside of this zone there is less potential for significant deposits of the Kupferschiefer type.

7.1 Introduction

The ProMine project, contained a special sub-project for 3D and 4D modelling of sulphidic base metal deposits, situated at the base of the Zechstein in the Fore-Sudetic Basin. Two study areas were selected for the modelling:

- The North-Sudetic Trough
- The Lubin-Sieroszowice Mining District in the Fore-Sudetic Monocline

This paper will focus on the studies performed in the North-Sudetic Trough (see Fig. 7.1) and will discuss the results based on the knowledge of the Kupferschiefer in Central Europe.

Mineral exploration conducted by KGHM Kupfer AG in Germany from 2008 to 2012 and the investigations performed as part of the ProMine Project provided significant increase in information, which allowed new conclusions about the genesis and structure of the copper deposits at the base of the Zechstein. These deposits are part of the so called Central European Copper Belt (Rentzsch 1981).

Comparison of the results with the geological conditions in the Fore-Sudetic Monocline—the other Study Area—was important for a better understanding of the emplacement of the copper deposits in the North-Sudetic Trough and allowed integrating this area in the regional geological framework.

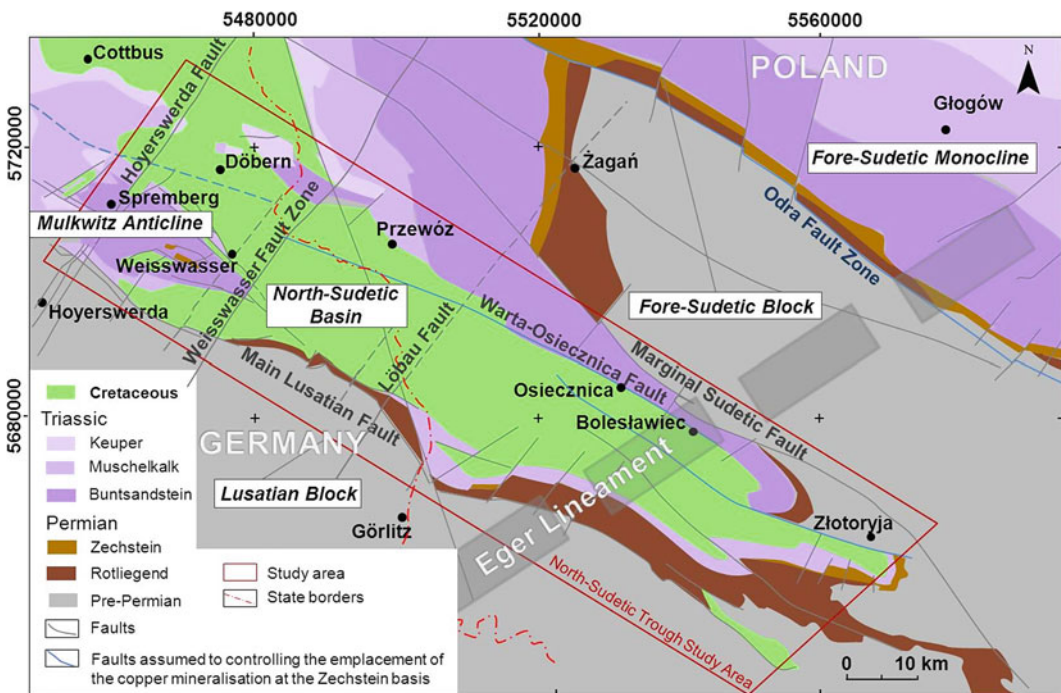


Fig. 7.1 Location of the North-Sudetic Trough study area and main tectonic structures and assumed copper controlling faults (based on Cymerman 2010 and Hielscher and Hartsch 2010)

7.2 Geological History and Conditions

The copper-hosting sediments occur only within the oldest formations of the Zechstein (Upper Permian—P2). Transgression of the Zechstein Sea into the Central European Depression began 258 Ma. and according to Kopp et al. (2008) the sea obtained access to this Rotliegend intra-continental basin probably by a combination of rift-induced subsidence and eustatic rise of the sea level. During the Zechstein marine and lagoon conditions dominated. Several chemogenic sedimentation cycles occurred combined with the development of thick evaporitic series.

The underlying Rotliegend (Lower Permian—P1) is characterised by terrestrial siliciclastic sediments consisting of sandstones, silt- and mudstones. In many places they include conglomeratic sequences. In the North-Sudetic Trough the character of the pebbles and the rock debris suggest a short transport from source to deposition. They consist of volcanic, plutonic, metamorphic and sedimentary rocks. The uppermost unit of the Rotliegend sandstones, the Grauliegend or Weisslied (S1), may reach a thickness of more than 30 m and has been partly reworked and reduced during the transgression of the Zechstein sea (see Borg et al. 2012). In the eastern parts of the North-Sudetic Trough the Weisslied may contain a “Basal Limestone” (Ca0).

The Kupferschiefer (T1) is the lowest formation member at the base of the Zechstein, which developed at a regional scale (Kopp et al. 2008). This black shale, deposited discordantly on the older rocks, shows a sharp facial contact to the underlying formations and can be described lithologically as a clay-marl with a black to black-grey colour. It developed under anoxic marine conditions, is bituminous and contains elevated contents of heavy metals. The thickness of the Kupferschiefer and its marly equivalents varies in the North-Sudetic Trough from a few cm to >2 m and it may even wedge out locally at sand bars.

The Kupferschiefer is overlain by the carbonate rocks of the Zechstein Limestone (Ca1). They consist of limestone/dolomite and

show at their base a clay-rich transition zone of up to several metres in thickness, defined as the Zechstein Marl or Lead Marl (Ca1m). The thickness of the Zechstein Limestone varies from <20 to 150 m with the thickest values reported from the area south of Weißwasser (Franz et al. 1967; Henning et al. 1974).

The younger formations of the Zechstein are dominated by evaporites (mainly anhydrite and partly additional halite). When forming a low to impermeable cap above the Kupferschiefer they could have been one important prerequisite for the later emplacement of rich copper mineralisations in the underlying sequences. The exploration results, reported by Henning et al. (1974) for the Spremberg-Weißwasser region in Lusatia indicate such a relationship.

7.3 Tectonic Conditions

Two WNW-ESE to NW-SE and NE-SW to NNE-SSW striking fault systems occur within the North-Sudetic Trough (Basin) (Fig. 7.1). The fault zones and single faults are most dense close to the NE flank of the Lusatian Block, which is part of the Variscan Bohemian Massif and separated from the adjacent basin by the Main Lusatian Fault.

The Mulkwitz Structure was developed during Saxonian movements. It is located between Spremberg and Weißwasser within the North-Sudetic Trough Study Area and can be described as a horst, resulting from SW-NE compression. Probably it was reactivated during the Alpine orogeny. The term “Mulkwitz Anticline” (anticlinal structure) has been used in the literature (cf. Kopp et al. 2006; Borg et al. 2012), although folding is not characteristic. Overthrusting and repetition of lower Zechstein sediments were observed in borehole 31/59 at its northwest border. Generally, in the area of the Mulkwitz Structure the bedding of the mineralised layers at the base of the Zechstein is more tectonically disturbed and complicated than in other regions. The Mesozoic sequences were intensively eroded due to uplift and Tertiary sediments occur

discordantly on top of the Cretaceous to Triassic formations, partly even on the Zechstein units, e.g. to the SE of the Mulkwitz Village.

A local uplifted block of pre-Permian rocks, 200 km² in size, was identified between the Mulkwitz Structure and the Lusatian Block in the SW (bordered by the Main Lusatian Fault). This significantly reduces the thickness of the Rotliegend and locally this formation is missing and in places the sedimentation of the Kupferschiefer was influenced (Hartsch 2012). This situation explains why the Mulkwitz Structure developed as a horst as this small block of the crystalline basement acted as a local abutment during the compression.

The morphology of the base of the Rotliegend shows only little variation in a NW-SE direction within the Study Area. In contrast, perpendicular to the Main Lusatian Fault, distinct morphological steps occur, not only below the SW flank of the Mulkwitz Structure where the base of the Rotliegend is downthrown more than 100 m, but also below its NE flank, with an additional downthrow of about 150–200 m (see Fig. 7.2).

The NE-SW faults crossing the Mulkwitz Structure have been interpreted by Franz et al. (1967) as synthetic downthrown faults. In the northwest and southeast of the Mulkwitz Structure they form two large NE-SW fault zones of regional character (Fig. 7.3): (1) The Cretaceous

Türkendorf Graben as part of the Hoyerswerda Fault and (2) The Weißwasser Fault Zone.

These structures were repeatedly activated, especially during the lower Zechstein and from the Cretaceous to the Tertiary. In the case of the Türkendorf Graben, Franz et al. (1967) reported a maximum vertical subsidence of more than 600 m. These tectonic zones can be followed to the SW across the Elbe valley to the East Erzgebirge Mountains. Towards NE they seem to extend across the Žary Pericline.

The Weißwasser Fault Zone is characterised in places by Tertiary basalt volcanism bound to fault crossings, e.g. at Uhyst (at the crossing with the Main Lusatian Fault), at Stolpen and at Oberfrauendorf. Similar neo-volcanic activities are typical for another long NE-SW structure, the Löbau Fault Zone (Fig. 7.1). It is defined by Runge (2002) as a zone with increased permeability for heat transfer and fluid transport at 265 ± 15 Ma. Probably, it can be extended to the NE towards Zagan, where the northwest margin of the uplifted Fore-Sudetic Block is located.

A very large structure crossing the North-Sudetic Trough, the Eger Lineament (Fig. 7.1), is an important ENE-WSW striking element in the northern part of the Bohemian Massif. It controlled the extensive mafic volcanism over a distance of more than 300 km during the Tertiary. This volcanic

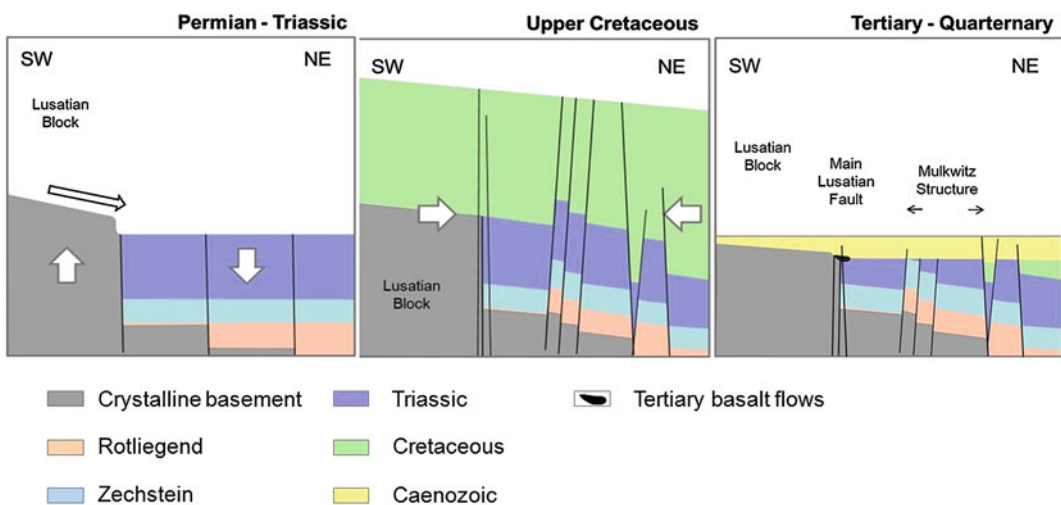


Fig. 7.2 Main geological development phases in the area of the Mulkwitz Structure. Stages at the end of the named periods

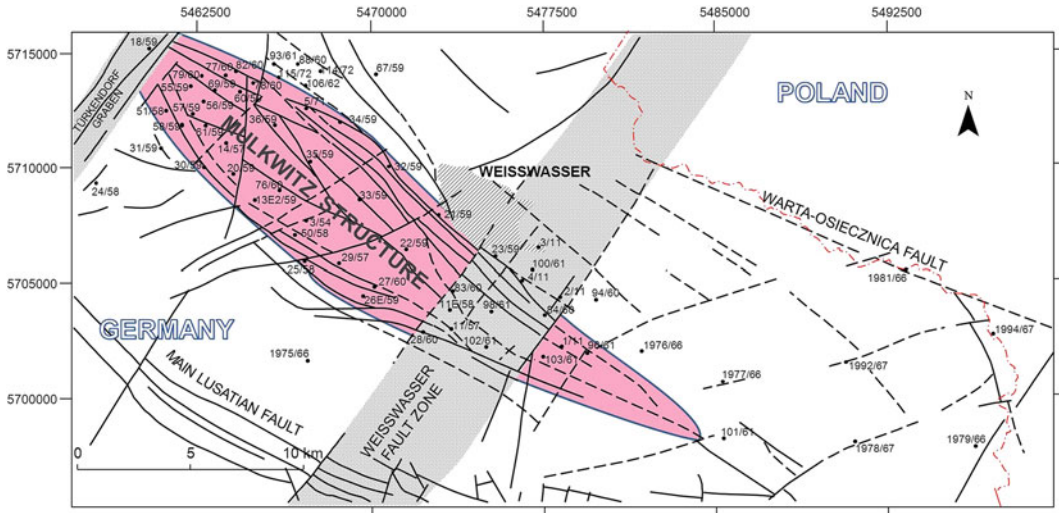


Fig. 7.3 Detailed fault tectonics around the Mulkwitz Structure in the NW part of the North-Sudetic Trough and selected deep boreholes (after Hartsch 2012)

activity was concentrated to the Eger Graben to the north of the Czech Republic. However, further centres of basaltic and phonolithic volcanism exist towards NE at Zittau/Turow, Luban and in the Grodziec Syncline SE of Bolesławiec and north of Legnica, in the Fore-Sudetic Block. The lineament may extend towards the ENE across Lubin. It should be noted that this lineament is located within a broad zone hosting numerous lamprophyric dykes of Variscan age situated between the North-Sudetic Trough and the Fichtelgebirge Mountains in the SW.

The intersection of these fault structures with a NW-SE fault systems seems to be an important structural criteria for the emplacement of copper mineralisations at the base of the Zechstein. Elevated copper concentrations occur close to these intersections at the northeast flank of the Mulkwitz Structure at Spremberg, Graustein and Weißwasser as well as near Bolesławiec, which are all located in the North-Sudetic Trough. The most important copper district of Lubin-Sierszowice is situated at the intersection of the Eger Lineament with the Odra Fault Zone and the Dolsk Fault.

In addition the intersection of the two main fault systems was affected by vertical syn-sedimentary movements at different geological periods. The thicknesses of both Zechstein

and Tertiary sediments vary across such intersections. The intersection of the Weißwasser Fault Zone with the SE end of the Mulkwitz Structure is one typical example.

Within the Polish part of the North-Sudetic Trough, at the basin margins, the Kupferschiefer repeatedly crops out to the surface. Towards NW it is located deeper and is covered by Mesozoic and Cenozoic sediments. In the basin centre the Zechstein basis may reach depths of 2000–2200 m according to seismic measurements. Towards the centre of the Southern Permian Basin the Kupferschiefer is deeper, for example in the North Sea (Haslam 1982), and Schmidt et al. 2000), northeast of the Netherlands (Oszczepalski and Speczik 2011) and in the Fore-Sudetic Monocline where the Kupferschiefer occurs at depths of close to 3000 m.

7.4 Genesis of the Copper Deposits

Distinct types of copper deposits are hosted in the sediments at the base of the Zechstein in Central Europe. They are not only bound to the European Crystalline Zone (Kopp and Bankwitz

2003), but are also characterised by areas of thin crust (see Fig. 7.4). The Mohorovičić Discontinuity is situated at a shallow depth of approximately 28–30 km. It should be emphasized that this position does not correlate with the centres of Tertiary basaltic volcanism in the region. As mentioned, all the copper accumulations at the base of the Zechstein developed preferably at the intersections of NW-SE and SW-NE striking fault zones (cf. Rentzsch and Franzke 1997a).

An other important criterion controlling the emplacement of copper deposits was discussed by Blundell et al. (2001 and 2003). They discussed a huge heat flow anomaly in the early Triassic, identified in the area immediately north of Wrocław (see Fig. 7.4). In addition, they interpreted indications for significantly increased helium contents with an upper mantle signature as evidence for fluid components from the mantle

that transported significant quantities of copper and precious metals and were an essential prerequisite for the development of the copper district in the Fore-Sudetic Monocline.

This heat flow anomaly in the Fore-Sudetic Monocline developed immediately after the Siberian trap volcanism around 250 Ma (Kuzmin et al. 2010). This eruption of millions of cubic kilometres of magma may have destabilised large parts of the earth crust and triggered tectonic movements along fault zones in a large area and also be the reason for the heat plume on the NE-branch of the Eger Lineament activated at that time (Fig. 7.4).

Królikowski (2006) summarized geophysical measurements in Poland. According to him the area of the heat plume is not showing an anomalous magnetic field today. It is located on the intersection of the Eger Lineament with a large

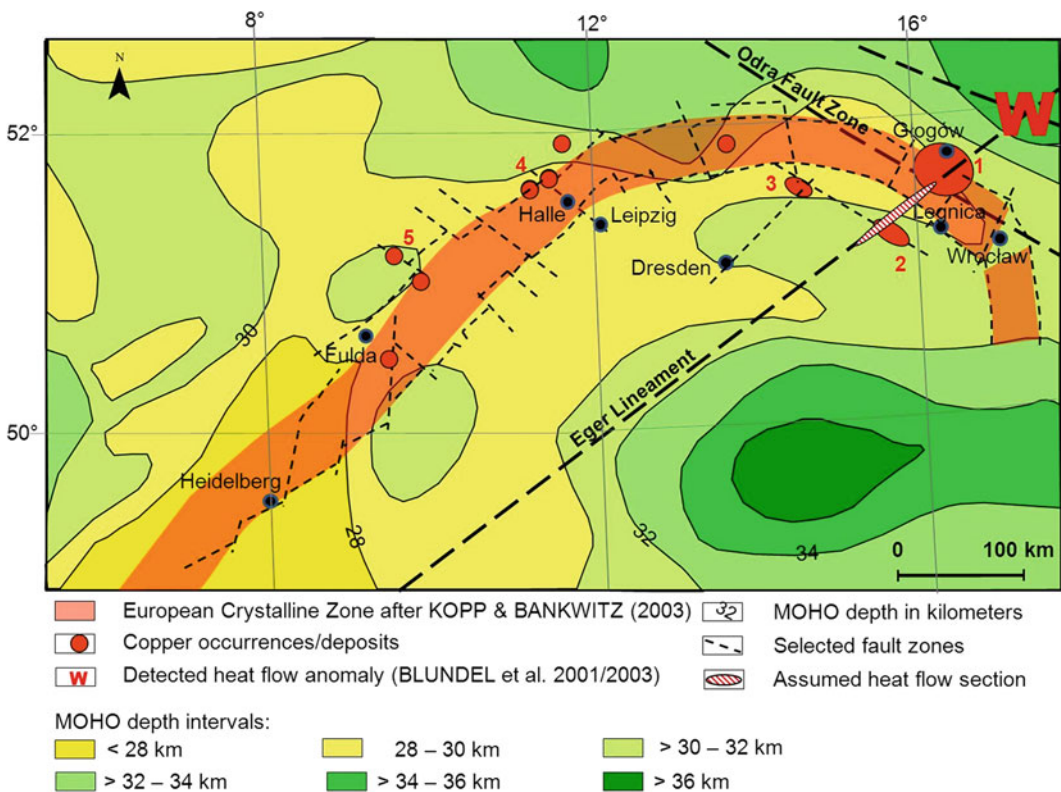


Fig. 7.4 Depth of MOHO (Dèzes and Ziegler 2010). Location of important copper deposits at the base of the Zechstein in Central Europe and heat flow anomalies.

Important Cu deposits and occurrences: 1—Fore-Sudetic Monocline, 2—Bolesławiec, 3—Spremberg-Weißwasser, 4—Sangerhausen-Mansfeld, 5—Richelsdorf

WNW-ESE striking fault (Dolsk Fault) following Silesian High gravimetric crest. The helium anomaly discussed by Blundell et al. (2001 and 2003) can be correlated with this structure. This 200 km long “hot” section on the Eger Lineament (Fig. 7.4) may explain why large fluid systems developed in the eastern part of the so-called Central European Copper Belt.

High density of copper mineralization can only be found in the Fore-Sudetic Monocline and in the North-Sudetic Trough. This region represents a metallogenic district characterised by mean copper surface densities of up to $>90 \text{ kg/m}^2$ according to Oszczepalski and Speczik (2011) and Kopp et al. (2008). In other well-known deposits like Mansfeld-Sangerhausen or Richelsdorf, located in Central Germany, the surface densities do not exceed 40 kg/m^2 , characterizing lower grade mineralisation (Rentzsch and Franzke 1997a). This difference can be interpreted as an indication for reduced heat flow and a less active hydrothermal systems in this region during the formation of the deposits. A larger distance to the metal source may be another possible explanation.

The following genetic aspects of the copper deposits in the Fore-Sudetic Monocline, Bolesławiec and Spremberg-Weißwasser are important:

- The occurrence of rich copper mineralisations on both sides of the Eger Lineament does not exceed 60–80 km, indicating that a large fluid system was active in the Early Triassic. This is also indicated by a heat flow anomaly.
- Ore controlling factors are large NW-SE striking fault systems, especially where intersected by major NE-SW fault zones.
- The fluids were dominated by Cu, but also contained Au and PGE. The precious metals are not concentrated within the copper mineralisation.
- The most intense copper mineralisation in the Fore-Sudetic Monocline and in the North-Sudetic Trough is surrounded by a huge area of oxidisation (Rote Fäule) of about $12,000 \text{ km}^2$ size between Berlin and Lubin.
- The hydrothermal vein type copper deposits of Miedzanka in Southwest Poland, Ludwigsdorf near Görlitz (Germany) and others hosted in the adjacent crystalline blocks in the south,

may be coeval with the copper deposits in the lower Zechstein sediments. However, this is still an open question.

One other important parameter controlling the copper accumulation is the occurrence of thick impermeable layers of anhydrite and salt in the hanging wall. For example, in the North-Sudetic Trough, in the area between Spremberg and Weißwasser a very clear relationship exists between the thickness of the Staßfurth Cyclothem and the occurrence/distribution of copper mineralisations. The thickness of the Staßfurth Formation must be at least 20 m in order to host copper ore. Thick units of the Werra Cyclothem, $>150 \text{ m}$, increase the potential for economic copper deposit.

7.5 Geochemical Zoning

An oxidised (hematitic) facies at the base of the Zechstein, the so-called Rote Fäule, seems to control the copper distribution. The copper mineralisation occurs proximal to the Rote Fäule facies while lead and zinc are found more distal to this front. Most distal, outside of the zinc mineralization, a pyrite zone occurs (see Kopp et al. 2008 and Oszczepalski 1999).

This general geochemical zoning in the copper deposits at the Zechstein basis has been already described very early. Rentzsch and Langer (1963) as well as Rentzsch (1964) reported that these observations, made in Central Germany (Mansfeld-Sangerhausen copper deposit), were applicable to the Spremberg-Weißwasser region. This typical zoning can be further extended to the whole North-Sudetic Trough and to the Fore-Sudetic Monocline and can be defined both laterally and vertically.

This zoning model of Kopp et al. (2008) was applied by Hartsch (2012) for the Weißwasser region in Lusatia. However, review and assessment of old exploration and new drilling data as well as laboratory assays revealed a more complex system for the Weißwasser area where the Rote Fäule facies may occur above and below the

Cu zones. This may be explained by large scale lateral migration of the metal bearing brines.

Geochemical work on precious metals carried out in Poland (e.g. Kucha 1981; Piestrzyński and Pieczonka 1997; Piestrzyński and Wodzicki 2000; Piestrzyński et al. 2002; Pieczonka et al. 2008; Oszczepalski and Speczik 2011; Oszczepalski et al. 2011) and in Germany (e.g. Hammer et al. 1990; Borg et al. 2005; Hartsch 2012; Fiedler and Borg 2012, Walther 2012) confirmed the presence of gold at the base of the Zechstein in association with platinum and palladium. The gold grade may exceed 1 g/t, while the PGE grades are lower.

The studies by Hartsch (2012) performed in the Weißwasser area showed that the gold always occurs in the transition zone between the copper zone and the Rote Fäule, which was described by Pieczonka et al. (2008) for the Fore-Sudetic Monocline. However, Hartsch (2012) described for the first time precious metals not only below, but also above the copper zone. In addition, Hartsch (2012) reported that the highest gold concentrations occur, when the copper grades are below 0.01 % Cu. Copper and gold thus show a negative correlation. A high gold content is associated with increased platinum and palladium concentrations in the Weißwasser area. According to Hartsch (2012) the precious metals form a separate geochemical zone. Implementing all these new facts in a specified model for Weißwasser the geochemical zoning can be described as presented in Fig. 7.5. Considering the geochemical results reported by Borg et al. (2012) for the Kupferschiefer deposits of Spremberg, the conclusion must be drawn that only the lower half of the model of Fig. 7.5 is applicable to Spremberg although it is located immediately adjacent to Weißwasser. Thus Weißwasser seems to represent a special case where the highest copper concentrations occur around the lead zone. Within the copper shale (T1) and in the overlying Zechstein Marl (Ca1m) silver correlates very well with the copper and can reach maximum values of >400 g/t, while the underlying Grauliegend sandstone is characterised by very low silver grades (normally <10 g/t)

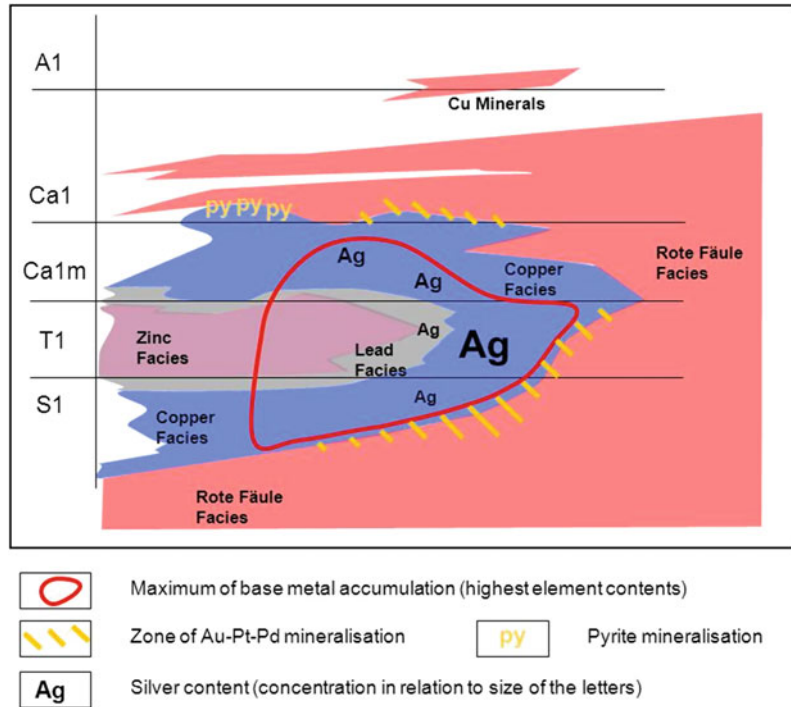
and not correlated with the copper mineralisation. At Weißwasser the lead zone may contain silver in slightly increased concentrations, 5–20 g/t, only very close to the interface with the copper zone within the Kupferschiefer. Hence, two horizontal copper ore horizons can be developed at some places, separated from each other by lead and zinc mineralisations.

At Weißwasser the gold zone can contain >1 g/t Au, when above or below a mineable copper mineralisation with average grades of >1 % Cu. Generally, high copper and high gold grades never occur together in the same strata, because of the different redox potential of these metals. In general the conditions are comparable with the occurrence of gold at the same stratigraphic level in Poland (Pieczonka et al. 2008 and Oszczepalski et al. 2011). As an economic consequence separate gold production is not feasible in the present underground mines.

Vertical zoning of copper vary significantly. Anomalous concentrations, >0.1 % Cu, can be observed over several tens of metres, comprising an interval from the Weissliegend/Grauliegend beds through copper shale, Zechstein Marl up to the Zechstein Limestone/Dolomite. The minable interval with average grades of 1–2 % Cu is much thinner and the average thickness in the North-Sudetic Trough and the Fore-Sudetic Monocline varies between 0.4 and 26 m, with an average of 3.4 m (Kopp et al. 2008).

In Weißwasser traces of disseminated chalcopyrite and galena were identified in the Main Dolomite (Ca2) in one of the boreholes drilled by KGHM in 2011. The dolomite layer with an extreme thickness of 70 m occurred here above 54 m of anhydrite. This observation suggests that the base metal mineralisation is younger than 254 Ma, which is the age of the host rock. Elevated copper contents of up to >0.1 % Cu were detected in the same area in Lower Carboniferous schists, which occurs immediately below the Kupferschiefer in KGHM borehole 103. The copper shale in this borehole contained a zinc zone. Conglomeratic sandstones of the Rotliegend and the Lower Carboniferous schists also contain anomalous precious metal contents. The mineralised rocks

Fig. 7.5 Geochemical model for the vertical succession of mineralisations at the base of the Zechstein, specified for the Weißwasser area. *S1*—Grauliegend/Weissliegend, *T1*—Kupferschiefer, *Ca1m*—Zechstein Marl, *Ca1*—Zechstein Limestone/Dolomite, *A1*—Werra Anhydrite



show typical bluish-grey or greenish-grey alteration, which follow fracture zones indicating a post-sedimentary hydrothermal event.

The lateral geochemical zoning in the copper-bearing series at the base of the Zechstein of Poland and East Germany constitutes a large elliptic area dominated in the western part by Rote Fäule and in the eastern part by copper (Fig. 7.6). Between Potsdam and Wrocław this large geochemical anomaly correlates excellently with the outline of the Silesian High Bouguer gravity anomaly reported by Królikowski (2006). It is situated between the East-European Platform in the NE and the Lusatian and Iżera-Karkonosze blocks in the SW. According to Rentsch and Franzke (1997a) this area as well as the Rote Fäule area in Mecklenburg (North Germany, see Fig. 7.7), represent block segments with relatively elevated areas of the Variscan basement and their Permian molasse cover.

For the North-German Rote Fäule area (at the coast of the Baltic Sea, see Fig. 7.7), Runge (2002) interpreted geophysical data as an indication for a hidden body of mafic rocks at depth

(see above). The shape of this Rote Fäule area follows the NW extension of the Szczecin-Mogilno-Miechów low gravimetric anomaly according to Królikowski (2006). Rentsch and Franzke (1997a) could not explain why this area is not associated with copper mineralisation, although Cu-enriched tholeiites occur in deep drill holes. They assumed that the heat flow was too low and could not drive effective circulation of metal bearing brines. However, larger fluid systems with oxidising brines should have existed as the Rote Fäule is distributed over an area of about 3000 km². The difference compared to the North-Sudetic Trough and Fore-Sudetic Monocline area is the position of the Mohorovičić-Discontinuity, which in the north is much deeper at 34–36 km displaying a linear depression, which can be followed towards WNW across Denmark to the North Sea.

The ore zones shows a close relation to the known fault systems and therefore indicates that more zones may exist. They outline an elliptical area including Potsdam in the northwest and Wrocław in the southeast. Within this large

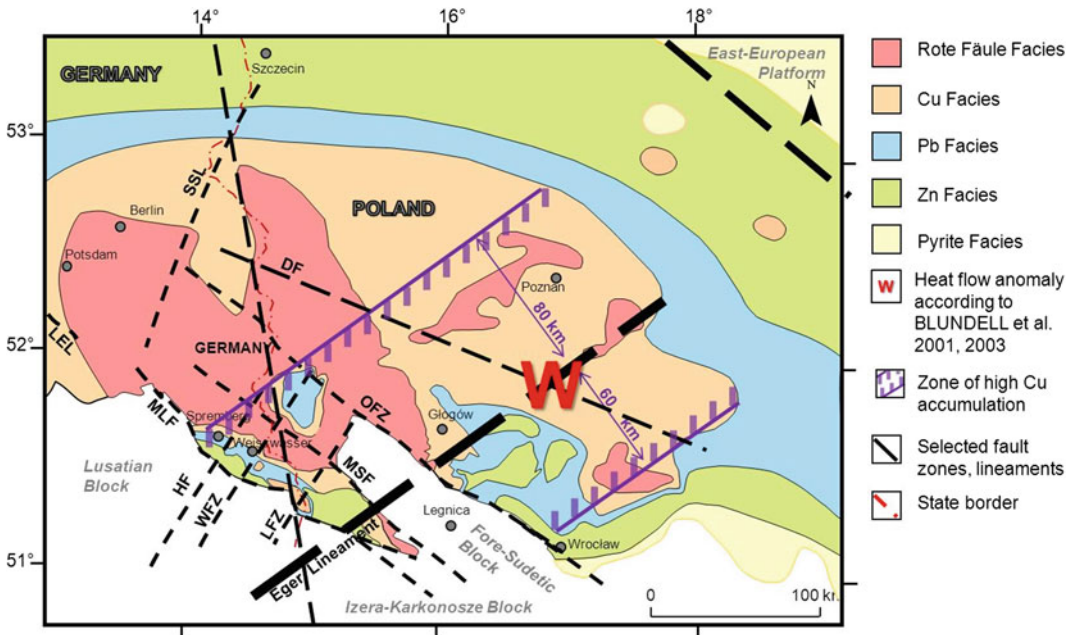


Fig. 7.6 Lateral geochemical zoning at the base of the Zechstein (after Oszczepalski and Rydzewski 1997; Rentsch and Franzke 1997a) and with the zone of high copper accumulation at the base of the Zechstein. LEL—Lower Elbe Lineament; SSL—Schwedt-Szczecin

Lineament; MLF—Main Lusatian Fault; MSF—Marginal Sudetic Fault; OFZ—Odra Fault Zone; DF—Dolsk Fault; HF—Hoyerswerda Fault; WFZ—Weißwasser Fault Zone; LFZ—Löbau Fault Zone

metalogenic province Rote Fäule and copper zones are dominating. This is different to the western parts of the Central European Copper Belt (Rentsch 1981). From Aderstedt-Bernburg through Mansfeld-Sangerhausen to the Rhön and the Spessart Mountains large areas of zinc and lead mineralization, around some small patches of Rote Fäule and copper mineralization, define the mineralisation style at the base of the Zechstein (Rentsch and Franzke 1997a). The amount of copper in this area is estimated at only 1 % of what is found in SW Poland and eastern Germany. This substantial difference speaks against further utilisation of the term “Central European Copper Belt”.

In the NE part of the Zechstein Sea the Trans-European Suture (Tornquist-Teisseyre Line) cuts the boundary between the zinc and the pyrite zones. To the NE the pyrite zone prevails according to Oszczepalski (1999), see Fig. 7.8, while the zinc and lead zones are parallel to the Odra Fault zone and the marginal Sudetic

Fault/Warta-Osiecznica Fault. This underlines that these structures have a very strong influence on the distribution of the base metals.

7.6 Distribution of Copper

In 2011 Oszczepalski and Speczik published a map regarding the potential copper resources in the deeper parts of the Fore-Sudetic Monocline. Kopp et al. (2008) and Hartsch (2012) suggested that base metal potential exists west of the North Sudetic Trough, in Lusatia (at Spremberg and Weißwasser). Compiling all this information, a SW-NE striking copper zone of 200 km length can be outlined on both sides of the Eger Lineament and its northeastern extension. The zone has a width of about 140 km (see Fig. 7.6). All known significant copper occurrences and deposits at the base of the Zechstein in Central Europe with a surface density of $>60 \text{ kg/m}^2$ of

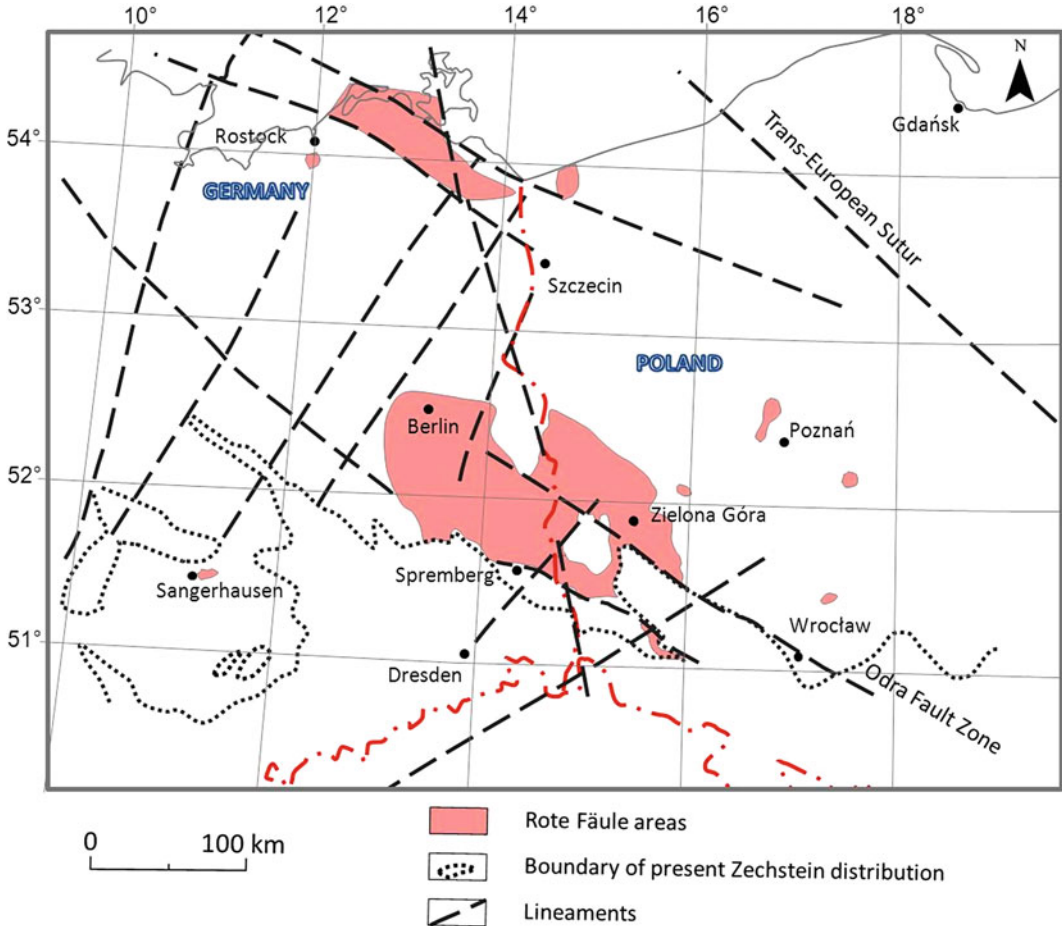


Fig. 7.7 Distribution of Rote Fäule areas in Central Europe (after Rentzsch and Franzke 1997a and Oszczepalski 1999)

Cu are located within this zone. Considering all the areas with a copper surface density $>40 \text{ kg/m}^2$ Cu as presented on map of Oszczepalski and Speczik (2011) an elliptic area with high copper accumulation can be outlined in the Fore-Sudetic Monocline, with the Early Triassic heat flow anomaly of Blundell et al. (2003) in its centre. This anomaly is located at the intersection of the Eger Lineament and the WNW-ESE striking Dolsk Fault connecting two areas with significantly increased helium contents (of mantle origin), reported by Blundell et al. (2001) for one area NNE of Wrocław and by Hoth et al. (1993) for an area east of Berlin.

The copper mineralisation in the North-Sudetic Trough is located outside the elliptic

structure (see Fig. 7.9), and this could be explained by the fact that at the intersection of the Eger Lineament with a NNW striking fault zone near the city of Zittau a heat anomaly existed, responsible for the copper occurrences/deposits in the North-Sudetic Trough. The southern section of this large NNW striking fault zone is indicated by a succession of local faults and Tertiary basalt volcanism. This structure may continue towards north towards the Rügen Island in the Baltic Sea (Kramer, 1994), see Fig. 7.9. The central section of this fault zone overlapping with the Żary Pericline and the helium anomaly east of Berlin of Hoth et al. (1993). The crescent-shaped zone with the copper occurrences/deposits in the North-Sudetic Trough comprises the localities of

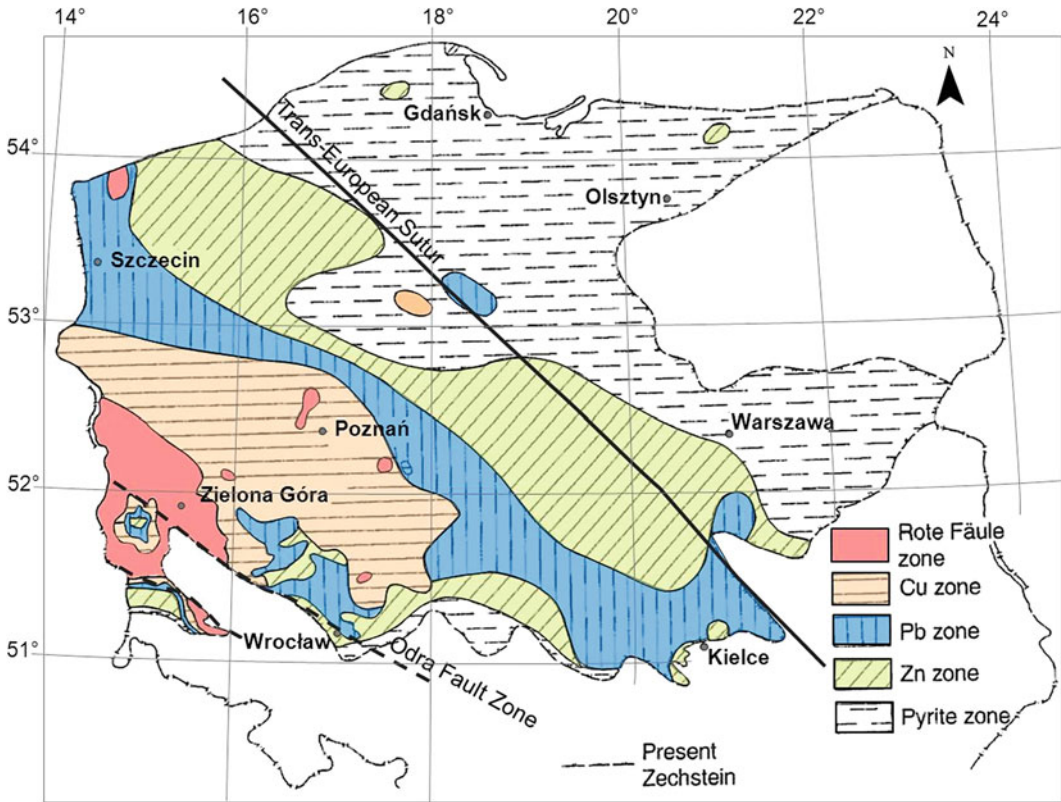


Fig. 7.8 Metal zoning in the Kupferschiefer ores in Poland (after Oszczepalski 1999). Abbreviations: see Fig. 7.6

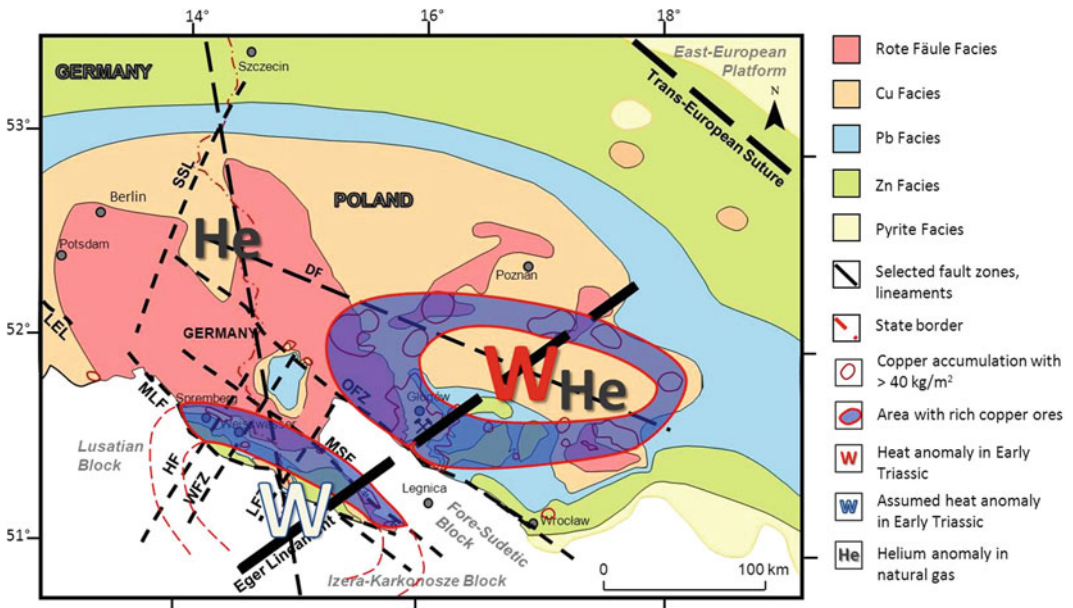


Fig. 7.9 Relationship between copper mineralisations at the base of the Zechstein and regional geological structures

Spremberg, Weißwasser, Nowiny, Wartowice and the former Lena mine near Złotoryja. It is bordered towards southwest by the the Lusatian and Izera-Karkonosze blocks.

The copper accumulations in Poland are surrounded by areas of the oxidised facies (Rote Fäule). This can be explained by migrating metal bearing brines that were spreading radially around the thermal hot spot and thus moving the copper zone outwards or/and already existing oxidised zones acted as geochemical barriers and provided the prerequisite for copper accumulation.

The geochemical zoning described in Fig. 7.5 for the Weißwasser region, seems to match with this situation. The observations made do not only support a multi-stage copper mineralizing event at the base of the Zechstein (e.g. Rentzsch and Franzke 1997b; Pieczonka et al. 2008; Kopp et al. 2008), but also imply that these processes might be much more complex than previously assumed.

7.7 Conclusions

The genesis of base and precious metal accumulation and zoning at the base of the Zechstein are the same in the Fore-Sudetic Monocline and in the North-Sudetic Trough.

Following the discussion of Pieczonka et al. (2008) regarding the importance of the Odra Fault Zone as an ore-controlling factor for the copper deposits in the Fore-Sudetic Monocline, the suggestion can be made that the Warta-Osiecznica Fault and its extension towards NW (Fig. 7.1) had a similar role for the North-Sudetic Trough. Fault systems with other directions, affecting the mineralisation, are also probable. This is obvious in western Poland where the NE margin of the large Rote Fäule area (see Fig. 7.6), forms an almost straight line over a distance of approximately 200 km. The WNW-ESE striking faults (blue in Fig. 7.1), may have been important for emplacement of the mineralisations at the base of the Zechstein. They are part of a lineament trending from Cracow in the SE to Hamburg in the NW. There are other large base metal deposits, geographically related to this lineament, that

underline that this structure had an important metallogenic function not only during the Early Triassic, but also over a much longer geological period. The big porphyry Mo-Cu-W deposit at Myszków near Cracow formed in connection with the intrusion of a predominantly granodioritic pluton of Late Carboniferous age (Strzelecki Metals 2010) and the Zn-Pb-Ag MVT deposits in the Olkusz-Rokitno area near Cracow, represent other younger mineralisation styles of probably late Jurassic age (Slowey 2010).

The 200 km long copper zone to both sides of the NE extension of the Eger Lineament has the highest potential for copper deposits at the base of the Zechstein (Figs. 7.6 and 7.9). It is related to the Odra Fault Zone and the Dolsk Fault. Oszczepalski and Speczik (2011) estimate that within this area approximately 250–300 Mt Cu and 200,000–300,000 t Ag exist.

At Weißwasser the copper mineralisation seems to belong to a separate hydrothermal cycle in the very Early Triassic. Because of the unique association of the base metals with gold, platinum and palladium and a vertical distribution reaching up to the Main Dolomite (Ca₂). Hence, it is not necessarily related to one of the Post-Variscan hydrothermal processes, which developed during the rifting of Pangaea 220 Ma ago (Seifert et al. 2001) or younger events as in Central Europe (Borg et al. 2012).

Acknowledgment The author would like to thank KGHM Kupfer AG (Weißwasser) very much for making new geological data available, which were an essential prerequisite for the studies performed. The scientific discussion with and contributions of other colleagues involved in the ProMine Project gave much motivation and input. Many thanks especially to Prof. Jean-Jacques Royer and Pablo Mejía-Herrera (both from Université de Lorraine, Vandoeuvre-Lès-Nancy, France), and to Peggy Hielscher from the Technical University Bergakademie Freiberg, Germany.

References

- Blundell, D.J., Alderton, D.H.M., Karmkowski, P.H., and Oszczepalski, S., Stroetmann-Heinen, V. and Kucha, H., 2001. A new genetic model for the copper mineralisation of the Polish Kupferschiefer. Proc.

- Joint 6th Biennial SGA-SEG Meeting on Mineral deposits at the beginning of the 21st Century, Kraków, Poland, 26-29 August 2001; 215–218
- Blundell, D.J., Karnkowski, P.H., Alderton, D.H.M., Oszczepalski, S., and Kucha, H., 2003. Copper mineralization of the Polish Kupferschiefer: A proposed basement fault-fracture system of fluid flow. *Economic Geology*; 98, vol.7: 1487–1495
- Borg, G., Fritzscher, M. and Ehling, B., 2005. Metal content and spatial distribution of Au and PGE in the Kupferschiefer of the Mansfeld/Sangerhausen mining district, Germany. Proc. 8th Biennial SGA Meeting Beijing, China, 18-21 August 2005
- Borg, G., Piestrzyński, A., Bachmann G.H., Püttmann, W., WALTHER, S. and Fiedler, M., 2012. An overview of the European Kupferschiefer deposits. SEG Special Publication 16, 455-486
- Cymerman, Z., 2010. Tectonic map of the Sudetes and the Fore-Sudetic Block 1:200 000. PIG Panstwowy Instytut Geologiczny, Warszawa, 2nd edition
- Dèzes, P. and Ziegler, P.A., 2010. Map of the European Moho. EUCOR URGENT – Upper Rhine Graben Evolution & Neotectonics. University Basel
- Fiedler, M. and Borg, G., 2012. Nobel metals and selected trace elements of the Kupferschiefer-type mineralization of the former Mansfeld district. Proc. SDGG, GeoHannover 80
- Franz, R., Dette, K., Rusitzka, D., Richter, G., Gerasch, A., Rentzsch, J. and Siegert, C., 1967. Ergebnisbericht mit Massenberechnung über die geologische Erkundung auf Kupferschiefer im Raum Spremberg – Weißwasser/Bez. Cottbus vom 01.11.1958 bis Oktober 1964, unpublished. - VEB Geologische Erkundung Süd, Freiberg 1967. (Unpublished report)
- Hammer, J., Junge, F., Rösler, H.J., Niese, S., Gleisberg, B. and Stiehl, G., 1990. Element and isotope geochemical investigations of the Kupferschiefer in the vicinity of "Rote Fäule", indicating copper mineralization (Sangerhausen basin, G.D.R.). *Chemical Geology* 85 3-4: 345–360
- Hartsch, J., 2012. About Genetic Aspects of the Copper Mineralisation at the Zechstein Basis in the Weißwasser Region / Lusatia. In: Proc. II International Copper Mining Congress / II Międzynarodowa Konferencja Górnictwa Rud Miedzi 2012, Lubin/Poland
- Haslam, H.W., 1982. The Marle Slate (Kupferschiefer) in the Southern North Sea Basin. Report No. 52 Inst. Geol. Sci., London
- Hielscher, P. and J. Hartsch, J., 2010. 3D Modelling of the Kupferschiefer area in Poland and Germany. Presentation on the Malta Workshop of the ProMine research project, EC 7th Frame Programme, CP-ProMine FP7-NMP-2008-LARGE-2
- Henning, D., Kühne, R., Neuber, S., Seeliger, M., Seidel, B., Schmidt, M. and Lange, H., 1974. Ergebnisbericht über die Erkundung der Kupferlagerstätte Spremberg-Graustein 1970-74. VEB Geologische Forschung und Erkundung Halle/Saale, Betriebsteil Freiberg, (unpublished report)
- Hoth, K., Rusbült, J., Zagora, K., Beer, K. and Hartmann, O., 1993. Die tiefen *Bohrungen* im Zentralabschnitt der Mitteleuro- päischen *Senke* - Eine Dokumentation für den Zeitabschnitt. 1962 – 1990. Schriftenr. Geowiss., Berlin Verl. Geowiss 2
- Kopp, J. and Bankwitz, P., 2003. The European Crystalline Zone (ECZ) – a Summary (German). *Z. geol. Wiss.*, Berlin 31-3: 179–196
- Kopp, J., Simon, A. and Göthel, M., 2006. The copper deposit Spremberg-Graustein in South Brandenburg. *Brandenburg. geowiss. Beitr.*, Kleinmachnow 13-172: 117–132
- Kopp, J., Herrmann, S., Höding, Th., Simon, A. and Ullrich, B., 2008. The Copper-Silver Deposit Spremberg-Graustein (Lusatia, F.R. Germany) – Enrichment of non-ferrous metals at the Zechstein base between Spremberg and Weißwasser (German). *Z. geol. Wiss.*, Berlin 36-1: 75–114
- Kramer, W., 1994. Phanerozoic magmatic indications in the NW-part of the Tornquist-Teisseyre zone and "Tornquist-Fan". *Z. geol. Wiss.* Berlin 22-1/2, 129–137
- Królikowski, C., 2006. Crustal-scale complexity of the contact zone between the Palaeozoic Platform and the East European Craton in the NW Poland. *Geological Quarterly* 50 (1): 33–42
- Kucha, H., 1981. Precious metal, alloys and organic matter in the Zechstein copper deposits, Poland. *TMPM Tschermaks Mineralogische und Petrographische Mitteilungen* 28: 1–16
- Kuzmin, M.I., Yarmolyuk, V.V., Kravchinsky, V.A., 2010. Phanerozoic hot spot traces and paleogeographic reconstructions of the Siberian continent based on interaction with the African large low shear velocity province. In: *Earth-Science Reviews* 102 (2010) 29–59
- Oszczepalski, S. and Rydzewski, A., 1997. Map of the distribution of metals within the Zechstein copper-bearing series in Poland. PIG Panstwowy Instytut Geologiczny, Warszawa
- Oszczepalski, S., 1999. Origin of the Kupferschiefer polymetallic mineralization in Poland. *Mineralium Deposita* 34, 599–613
- Oszczepalski, S. and Speczik, S., 2011. Prospectivity analysis of the Polish Kupferschiefer – ne insight. Proc. SGA 11th Biennial Meeting, Antofagasta, Chile
- Oszczepalski, S., Speczik, S. and Wojcechowski, A., 2011. Gold mineralization in the Kupferschiefer oxidized series of the North Sudetic trough, SW Poland. *Gold in Poland*, AM Monograph No. 2, 153–168
- Piesterzyński, A. and Pieczonka, J., 1997. Gold and PGE on an oxide-reducing interface in Lower Zechstein sediments of the Fore-Sudetic Monocline, SW Poland. In: Papunen H. (ed.) *Mineral deposits: Research and exploration where do they meet?* In: Proc. IVth SGA Meeting, Turku, Finland. Balkema/Rotterdam: 99–102
- Piesterzyński, A. and Wodzicki, A., 2000. Origin of the gold deposit in the Polkowice-West Mine. -

- Lubin-Sierszowice Mining District, Poland. *Mineralium Deposita* 35:1: 37–47
- Piastowski, A., Pieczonka, J. and A. Głuszek, A., 2002. Redbed-type gold mineralisation, Kupferschiefer, south-west Poland. *Mineralium Deposita* 37:5: 512–528
- Pieczonka, J., Piastowski, A., Mucha, J., Głuszek, A., Kotarba, M and Więclaw, D., 2008. The Red-bed-type precious metal deposit in the Sierszowice-Polkowice copper mining district, SW Poland. *Annales Geologorum Poloniae* 78:3: 151–280
- Rentzsch, J. and Langer, M., 1963. Fazielle Probleme des Kupferschiefers von Spremberg-Weißwasser. *Z. angew. Geol.*, Berlin, 9:10: 507–513
- Rentzsch, J., 1964. Der Kenntnisstand über die Metall- und Erzmineralverteilung im Kupferschiefer. *Z. angew. Geol.*, Berlin, 10:6: 281–287
- Rentzsch, J., 1981. Mineralogical-geochemical prospecting methods in the Central-European Copper Belt. *Erzmetall*, Weinheim, 34, 492–495
- Rentzsch, J. and Franzke, H.J., 1997a. Regional Tectonic Control of the Kupferschiefer Mineralization in Central Europe. *Z. geol. Wiss.*, Berlin 25:1/1: 121–139
- Rentzsch, J. and Franzke, H.J., 1997b. Die laterale Verbreitung der Erzmineralassoziationen im deutschen Kupferschiefer. *Z. geol. Wiss.*, Berlin 25:1/1: 141–149
- Runge, W. (ed.) 2002. *Chronik der WISMUT*. WISMUT GmbH, Chemnitz
- Schmidt, A.P., Hartog, F.A., B.J.H. van Os, B.J.H. and Schuiling, R.D., 2000. Production of ²¹⁰Pb from a Slochteren Sandstone gas reservoir. *Applied Geochemistry* 15, 1317–1329
- Seifert, Th., Niederschlag, E., Pernicka, E. and Fiedler, F., 2001. Lead isotope pilot study from ore deposits in the Erzgebirge, Germany, and surrounded areas by multiple-collector inductively coupled plasma mass spectrometer (MC-ICP-MS). In: Piastowski, A. et al. (eds.): *Mineral deposits at the beginning of the 21st century*. Balkema, Rotterdam, 1095–1098
- Slowey, E. 2010. Rokitno & Zawiercie Zinc-Lead Projects Poland. 43-101 Technical Report. RATH-DOWNEY RESOURCES LIMITED, Dublin
- Strzelecki Metals Limited, 2010: Project Links – Myskow Geology. <http://www.strzeleckimetals.com.au/index.php?page=myskow-geology>. 10.12.2010
- Walther, S., 2012. Occurrence of precious metals in the German Kupferschiefer. – <http://www.petrology.de/research/kupferschiefer1/?lang=en>; Martin-Luther-Universität Halle-Wittenberg 24.05.2012

4D Geomodelling A Tool for Exploration—The Kupferschiefer in The Lubin Region, Poland

8

P. Mejia, J.J. Royer, J.G. Fraboulet and A. Zielińska

Abstract

The Polish Kupferschiefer, with sediment-hosted polymetallic (Cu, Ag, Au, PGE) deposits, is one of the most important sources for copper and silver in the world. Within the framework of the ProMine project, the Lubin region (southwestern Poland), was selected for modelling the geological formations in 3 dimensions and 4 dimensions in order to better understand the distribution of the Cu-Ag mineralization, and possibly to define new potentials. The restoration—decompaction methodology available in gOcad, coupled with PetroMode 1D, were used to reconstruct the temperatures, pressures, hydraulic fracturing favourable conditions, and oil and gas maturation during the burying history of the Lubin Kupferschiefer, Southwestern Poland basin. Conditions for hydraulic fracturing were identified for the base of the Zechstein shales, during an inversion phase at the Late Cretaceous-Early Palaeocene. This Late Cretaceous up lift yields the conditions for hydrothermal recirculation of mineralizing brines explaining the location of Cu (Cu-Fe) sulphides ores in the area. The Zechstein evaporite series played a role of impermeable cover confining the hydrothermal fluids in the lower Zechstein series. The 4D restoring-decompacting modelling allows for reconstructing the burial, deformation and natural hydro-fracturing history of intra-basin sediment-hosted ore deposits. In the Lubin region, the obtained results show a good agreement between the spatial hydro-fracturing index and the emplacement of the Cu (Cu-Fe) sulphides exploited today.

P. Mejia · J.J. Royer (✉) · J.G. Fraboulet
Université de Lorraine, CNRS-ENSG,
Vandoeuvre-Lès-Nancy, France
e-mail: royer@gocad.org

A. Zielińska
Cuprum Research and Development Centre,
KGHM, Wrocław, Poland

8.1 Introduction

The Polish sediment-hosted Kupferschiefer deposits are world-class polymetallic deposits. They extends across north-central Europe from north-westernmost Belorussia to Northern

Ireland, along an east-westerly belt of more than 1500 km (Vaughan et al. 1989). Today this world class ore belt, exploited in the south-western of Poland by KGHM Polska Miedź S.A. (Lubin, Sieroszowice- Polkowice, and Rudna and Głogów-Głęboki-Przemysłowy mines), is one of the main sources of Cu and Ag in the world¹ ($\sim 2\%$ Cu and ~ 2 Oz/t Ag in over 1 Gt bearing metals ore²). Lead, zinc, gold, PGE, and some critical raw materials, such as rhenium, have also economic importance (KGHM 2011). The copper production of Poland represents half of the total copper production in Europe (or a quarter of the total European copper consumption).

This work focuses on the Kupferschiefer formation in an area surrounding the Lubin mining district. Research active today in restoration focuses mostly on oil and gas and little literature refers to mineral resources exploration. A reconstruction of the formation history of the Lubin district was performed using a 4D restoration approach in order to better understand the ore potential. A 3D model of the district has been built using surfaces to create the different main layers. The kine 3D plug-in available in gOcad was then used to restore the different layers in their primary depositional position accounting for compaction and fracturing. This reconstruction promotes understanding of the major mineralization phases and remobilization. The mineralization of the Kupferschiefer is mainly related to redistribution of sedimentary deposited metals by hydrothermal fluid circulation that was favoured by hydraulic fracturing of the host rocks. Therefore, it is important to date the hydraulic fracturing for understanding the physical and chemical conditions involved in the mineralization processes. This work includes 4D restoration models for evaluating the favourable mechanical conditions, which could have lead to the hydro fracturing of the host rocks during the inversion stage, which took place at the Late Cretaceous-Early Palaeocene. Each layer has

been restored accounting for decompaction. A hydro-fracturing index was evaluated to estimate the fracture distribution. The objective of this work is also to transfer restoration methodologies developed in oil and gas to mineral exploration for sediment hosted mineralization systems.

8.2 Geological Setting of the Kupferschiefer

The sedimentary formation of Kupferschiefer (literally copper shale) is situated in northern Europe over more than 600,000 km² (Blundell et al. 2003). The formation of the Kupferschiefer is related to the eustatic variations of the Zechstein Sea at the end of Permian. It is composed of a thin (<1 m) shale layer containing in average about 7 % organic matter, situated between the Lower Permian terrestrial/volcanic sediments (Rotliegend and Weissliegendes) and the Upper Permian Zechstein marine sediments (Jowett 1986; Oszczepalski 1999; Blundell et al. 2003; Gouin 2008; Borg et al. 2012; Hartsch 2015) (Figs. 8.1 and 8.2).

8.2.1 Geodynamic of the Kupferschiefer Basin

In many parts of Poland, as well as in other parts of northern Europe, uplift related to tectonic inversion during Late Cretaceous to Early Palaeocene time caused erosion of hundreds to thousands of meters of Cretaceous sediments (Mazur et al. 2005; Scheck-Wenderoth and Lamarche 2005; Resak et al. 2008; Narkiewicz et al. 2010). For the Lubin region the uplift has been estimated to at least 1000 m (Stephenson et al. 2003) resulting in erosion of Triassic to Cretaceous rocks. The pre-Cenozoic rocks were tilted 3–6° to the northeast, probably during the Alpine orogeny (Oszczepalski 1999). This structural basin evolution favoured the creation and the reactivation of fractures that probably played a major role in the mineralization episodes.

¹The Poland production, estimated at 571,000 t Cu and 1260 t Ag (KGHM 2011) is ranked at the 10th and 3rd world positions for copper and silver, respectively.

²Values for Fore-Sudetic monocline mined ore since 1949, remaining proven and indicated reserves are estimated at 1.7 Gt of ore representing over 33.8 Mt of Cu metal (Borg et al. 2012).

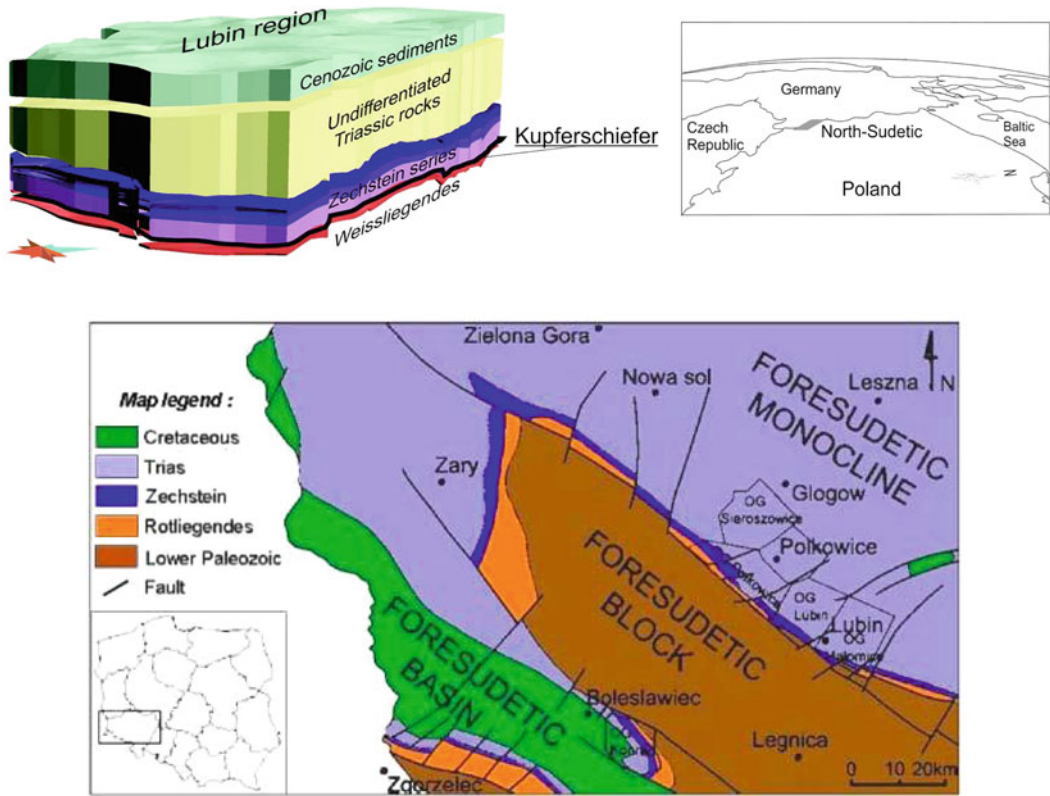
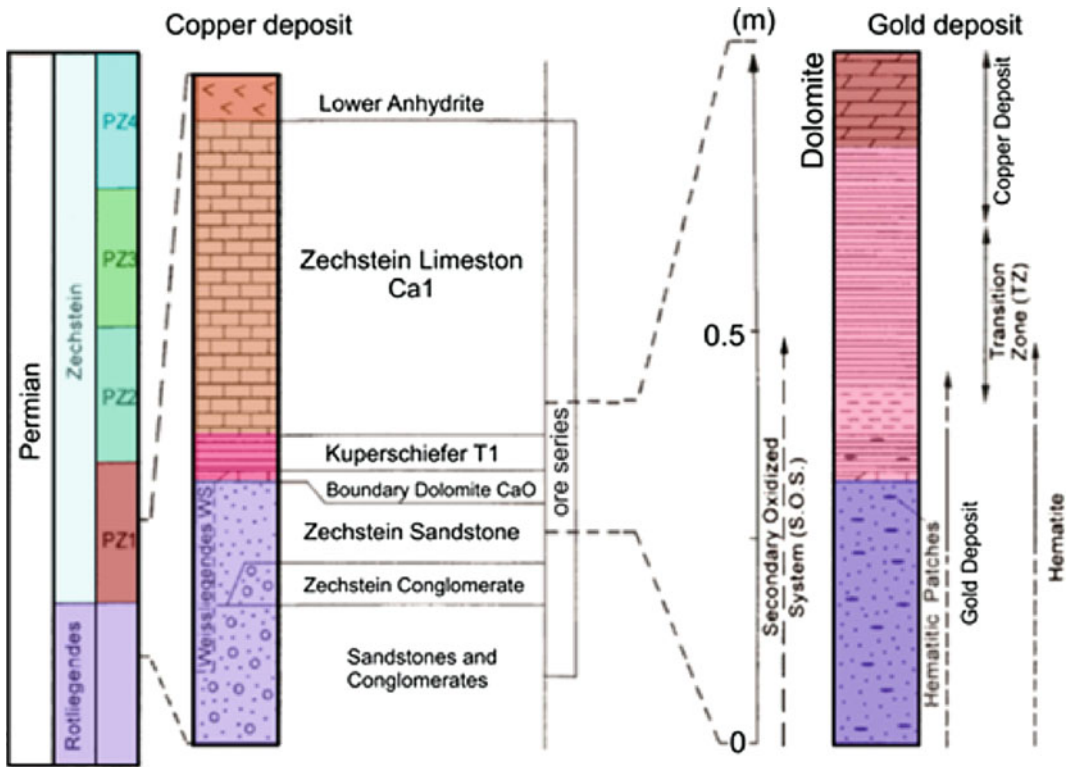


Fig. 8.1 Upper left illustration 3D model of the Lubin region, Poland. Bottom 2D geological map of the Lubin region and mining district exploited by KGHM (www.kghm.com)

8.2.2 A Complex Multistage Multi-stage Metallogenic Model

Three main mineralized sulphide levels can be identified occurring both as disseminated coarse copper sulphides and veinlets: (i) a boundary dolomite (lower) level, (ii) a bituminous black shale (middle) level, and (iii) a dolomite black shale (upper) level (Fig. 8.3). The polymetallic Kupferschiefer ore in the Lubin region contains main minerals such as chalcocite, bornite, chalcopyrite, covellite, digenite, pyrite, galena, sphalerite, tennantite, native silver, stromeyerite, cobaltite and castaingite. Also other Cu, Ag, Fe, Ni, Co, Mo, Hg, Bi, Pt and Pd sulphides, arsenides, diarsenides, sulphosalts, thiosulphates, arsenates, and noble metals and alloys containing Au, Ag, Hg and Pb (Piestrzyński et al. 2002) occur. In the Lubin region, shale T1 contains the

highest Cu, Ag grades with typical arithmetic average grade of 3.9 % Cu and 150 ppm Ag, respectively ($n = 250$), median grades are 2.9 % Cu and 110 ppm Ag, respectively. The grades are highly variable with coefficient of variation ρ close to one ($\rho = \sigma/m$ with σ standard deviation, m arithmetic mean). Carbonate layers have lower grades at 0.16 % Cu and 19.5 ppm Ag, but with a higher coefficient of variation, 2–3 (average calculated with sample number n over 1000 for Ag and 5500 for Cu). The Cu-Ag stratabound mineralization is related to the reduced part of sediment pile, while the Au-PGE stratabound mineralization is limited to the oxidized zone including Cu, Co, Ni, Bi, Ag, (probably controlled by oxydo-reduction fronts), while As vein-type mineralization cross cuts all the formations (Pieczonka and Piestrzyński 2011a, b). This superposition of diagenetic and hydrothermal events (Vaughan et al. 1989; Speczik 1995;



(After Oszczepalski, 1999 and Piestrzyński et al., 2002)

Fig. 8.2 Stratigraphic column of the Lubin region, Poland after Oszczepalski (1999), and Piestrzyński et al. (2002). The mineralization occurs at the basement/cover interface in the Zechstein formation. Copper is

concentrated in dolomite and in the *upper part* of the black shales series, while gold and PGE are located in the FZ at the base

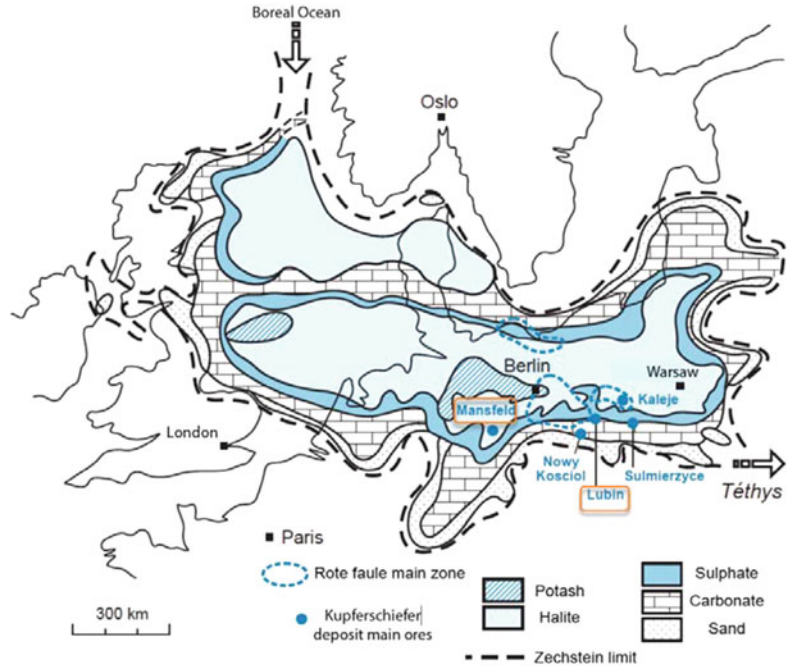
Wagner et al. 2010; Pieczonka and Piestrzyński 2011a, b) makes it difficult to build a simple metallogenic model explaining all the mineralization phases observed in Kupferschiefer.

8.2.2.1 Metallogenic Model

Many controversial opinions have been expressed regarding the genetic models of the Kupferschiefer mineralization (Oszczepalski 1999). Several mineralization stages (Wodzicki and Piestrzyński 1994; Speczik 1995) can be observed: (i) a first syn-sedimentary to early diagenetic bacterial pyrite mineralization phase substantiated by the presence of framboidal pyrites, followed by (ii) a replacement phase and

the main formation of Cu (or Cu-Fe) sulphides related to hydrothermal fluids and, (iii) a final hydrothermal stage during which Au, other precious metals and significant quantities of Cu were remobilized (Piestrzyński and Wodzicki 2000; Gouin 2008; Pieczonka et al. 2008; Hartsch, this volume). According to Oszczepalski (1999), the remobilisation of the sulphides would result from the mixing of upward and lateral diagenetic oxidizing chloride brines, and reduced hydrothermal fluids expelled from an up to 2 km-thick pile of Carboniferous sediments. The pre-Permian and the Rotliegendes volcanic rocks are assumed to have provided the source rocks, leached metals being transported as cuprous

Fig. 8.3 Maximal transgression of the Zechstein sea (Jébrak and Marcoux 2008)



chloride complexes by the oxidizing warm brines (Oszczepalski 1999).

8.2.2.2 Role of Fractures

Fracturing of host rocks is one of the main factors that control the distribution of metals in the Kupferschiefer (Jowett 1986, 1992; Jowett et al. 1987). Ore deposit related fractures have channelled hydrothermal fluids, enhancing the metal migration, and were therefore important for the formation of the mineralization. They were important for the replacement of early bacterial pyrite, and made space for precipitating the ore sulphides. Several fracture types with various orientations exist in the Kupferschiefer formation, and therefore it is difficult to decipher their effective role in the ore-deposit history. Some of these fractures are related to the regional up-lift that affected northern Europe during the Late Cretaceous-Early Palaeocene (Mazur et al. 2005; Resak et al. 2008; Narkiewicz et al. 2010). This major tectonic event produced favourable conditions for hydrofracturing of the mineralized rocks (Oszczepalski 1999).

8.3 Introducing 4D Modelling and Restoration Techniques

Understanding the history of sedimentary basins is of paramount importance for reconstructing oil and gas related fluid migration, but also in mineral exploration for identifying brine pathways. The process which reconstructs the initial geometry of a geological structure is called “restoration”. Restoration focuses on the evolution through time of 3D geological structures. It aims at returning a geological structure to its original pre-deformation geometry with respect to its deformation history (Mallet 2002). In case of sedimentary basins, restoration is the reconstruction of the initial geometry of the horizons. As restoration accounts for 3D geometry and time, it is sometimes referred as 4D modelling.

Restoration methods have been successfully applied to basin analysis for understanding deformation mechanisms (Moretti 2008), fracture forecasting (Macé et al. 2005), or validating

structural models (Titeux 2009). Different restoration tools in gOcad have been developed: (i) the Kine3D-(1, 2, 3) toolkit and workflow developed by the IFP and commercialized by Paradigm (Moretti et al. 2006; Moretti 2008); (ii) the 3D restoration toolkit based on mechanical approach (see Muron 2005; or Kine3D-3).

8.3.1 Basin Analysis and Compaction Effects

Basin analysis involves reconstruction of syn-sedimentary conditions such as sedimentary cycles, erosion, sea level variation, and climate change. The analysis also takes into account tectonic events that have imprinted these primary features. The volume or/and the shape of lithological sequences change under the load of overlying units, regional stress, hydrogeological changes and also due to geomechanical rock properties. Understanding basin formation involves the reconstruction of these events through time, in particular the shape and volume changes, which require the estimation of the thickness of sequences which have disappeared during erosion. The last part of the reconstruction is particularly difficult and requires many assumptions.

Even in the absence of a regional tectonic event, the weight of the overlying sediments is sufficient to deform the underlying layers at depth, during the burying phase, a mechanism known as compaction. The compaction will affect the successive layers differently depending on the hydraulic parameters, the nature and the composition of sediments, and the thickness of the overlying rocks. Compaction magnitude due to vertical loading may differ at two locations within the same layer.

8.3.2 Restoring Sedimentation History

Different stress configurations of multi-tectonic events can produce a similar arrangement of the observed deformed sedimentary layers. Thus, it

is necessary to estimate the uncertainty attached to each possible modelled solution (Caumon 2010). Restoration is reconstruction of the initial geometry of horizons into their depositional state. It requires the removal of the tectonic deformation and the compaction effects due to the weight of the upper layers (Durand Riard et al. 2010). The restoration can be used to validate a geological model especially in presence of faults, to reduce the uncertainties in complex layer areas (Fig. 8.4). It can also be used to estimate deformation and stress directions responsible for deformations, to predict failures and fractures, to infer paleo-geometries and even to test the consistency of the original data (Groshong 2006; Moretti 2008; Durand Riard et al. 2011). Restoration is not restricted to the geometry of the geological structures but also includes coherency between stresses and times at which deformation occur. A number of commercial tools are available for restoring geo-models. They are shortly discussed below.

8.3.3 Restoration Toolkits

Structural restoration tools are available in several commercial 3D-modelling computer programs such as 3DMove from Midland Valley (2012), a software for 3D palinspastic restoration; Igeoss, a structural geology software from Schlumberger; and gOcad with the plug-in KINE3D, a restoration method developed by IFP and Paradigm based on a mixed approach linking geometry and geomechanics (Moretti 2008). These restoration tools work with 1D (curves), 2D (vertical cross-sections or surface models) and 3D geological objects (meshed solid, usually tetrahedra or rigid blocks). The geometric methods concern geological horizons and allow restoration of fold and fault horizons (sometimes referred as 2.5D restoration) (Gratier et al. 1991; Rouby et al. 2000; Dunbar and Cook 2003). Most of the commercial softwares include geometry-based methods such as cross-section balancing assuming various tectonic contexts (preservation of length, flexural slip, simple shear, fault bend folding, detachment folding,

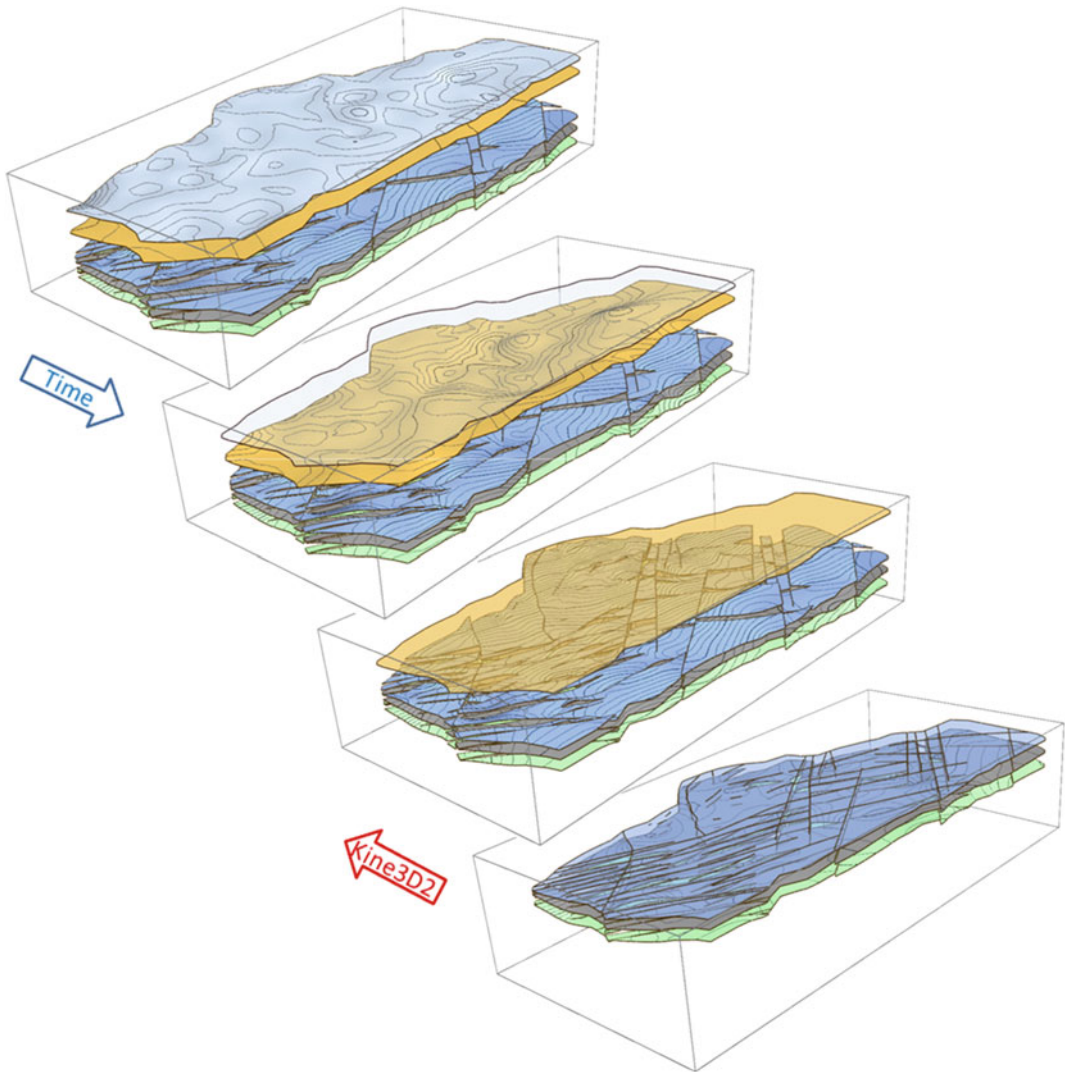


Fig. 8.4 A Kine 3D-2 reconstruction of the burial history of the Kupferschiefer deposits in the Lubin region (after Mejia et al. 2012, Mejia and Royer 2012)

etc.). In addition, some others also include geomechanical restoration (Moretti 2008). More recent methods assume volume-balanced restoration (also named 3D restoration) reproducing heterogeneous mechanical behaviour of a volume rock including different rock types (Muron 2005; Maerten and Maerten 2006; Moretti 2008; Guzowski et al. 2009). Although 3D restored models probably provide more accurate 4D models, because they consider strain and stress in 3D (De Santi et al. 2002; Muron 2005; Maerten and Maerten 2006; Moretti et al. 2006; Moretti

2008; Durand Riard et al. 2010), they, however, include limitations especially in the mesh generation which is required to represent the 3D objects. Mesh generation is often time-consuming and requires a very large number of elements when interpreting fine-scale structural features, especially in structurally complex areas. This limitation has been addressed by Durand Riard et al. (2010) using an implicit scalar field $f(x)$, $x = \{x, y, z\}$ to represent chronostratigraphic horizons. Within this context, the geomechanical restoration can be performed on a coarser mesh

conforming only to faults. In the presence of unconformities, several scalar fields may be used, which also helps in estimating the volume of eroded material (Caumon 2010). Mesh generation issues remain an active research area, especially in structurally complex areas (Pellerin et al. 2012). Except for the recent work by Durand Riard et al. (2010), most of the above approaches do not take into account the compaction.

8.3.4 Advantages and Limitations of 2.5D Restoration

Different hypotheses explaining the geological evolution of an area can be tested with restoration techniques. Volume restoration techniques are better because they give a more realistic representation of the rock behaviour. Thus, the explicit surface representation method followed by a simplified 2.5D kinematic restoration method remains a good alternative. In addition, most 2.5D restoring tools based on an explicit surface representation do not presently account for compaction effects and mechanical rock properties, but focus mainly on geometric criteria. Volume variations between restored and restored-decompact models are not negligible (Durand Riard et al. 2011; Poblet and Stuart 1995). However, classical 2.5D restoration methods generally neglect to estimate that volume reduction due to compaction.

Even if tectonic events are recorded in the deformed sedimentary layers, reconstruction of original depositional conditions is sometimes very difficult especially in the case of multi-tectonic phases. Solutions to reconstruct a previous state of structural configuration are not necessarily unique as only the final state is known. However, instead of being a limitation of the methodology, restoration can provide several possible solutions to deformation reconstructions to explain the final observed state, offering the interpreter various hypotheses on the deformation history to be validated in the studied area.

8.4 Sequential Restoration Using the gOcad KINE3D-2

Several restoration methods are implemented in the gOcad KINE3D-2 Plug-in including mainly *simple shearing*, *flexural slip*, and *unfaulting*.

8.4.1 Simple Shearing

In the simple-shear context, 3D models are restored assuming an infinite number of closely spaced, parallel planar slices that are free to slip on each other with no length or thickness changes parallel or perpendicular to the slip planes. Simple shearing produces cylindrical folds with axes parallel to the shear planes, having a geometry very close to class 2, that characterize incompetent rocks (salt, shale, sandstones). The shearing can be oriented in any direction of space, along the depositional planes, oblique or perpendicular to it. Simple shear preserves distances in the shear direction, but lengths, layer thicknesses and areas are not necessarily preserved (Moretti et al. 2007). Simple shear oblique to bedding is a kinematic model that causes bed length and bed thickness changes. Thicknesses would be preserved with pure shearing (flattening or bucking) and thus resulting in parallel folds. The method works sequentially from the younger to the older depositional surfaces. When the simple shearing is applied, a reference horizon at a given position is assumed to be the initial deposition surface. This implies vertical or oblique differential displacements of elementary blocks of a vertical cross section (Verral 1981) (see Fig. 8.5). The simple shear method can be used for restoring a pile of sedimentary horizons modelled as triangular surfaces sequentially. Simple shear mainly affects poorly compacted material and incompetent rocks (Verral 1981).

8.4.2 Flexural Slip

Flexural slip is the usual deformation mechanism for rigid layered sediments. Deformation occurs

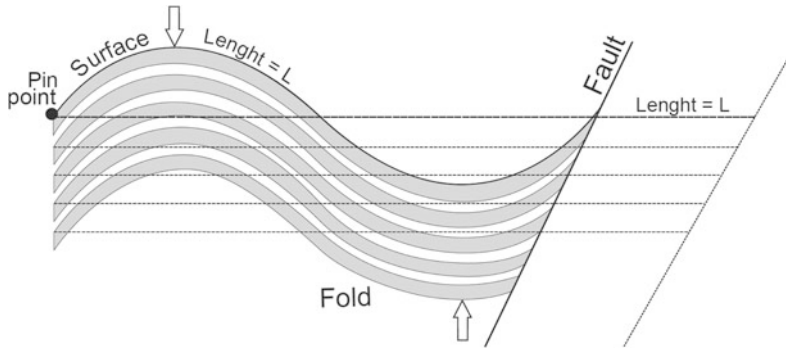


Fig. 8.5 Simple-shear is produced by slip on closely spaced, parallel planes with no length or thickness changes parallel or perpendicular to the slip planes. These structures are restored as if they were built up by an

infinite number of planar slices. Simple shear preserves distances in the shear direction, but lengths, layer thicknesses and areas may change

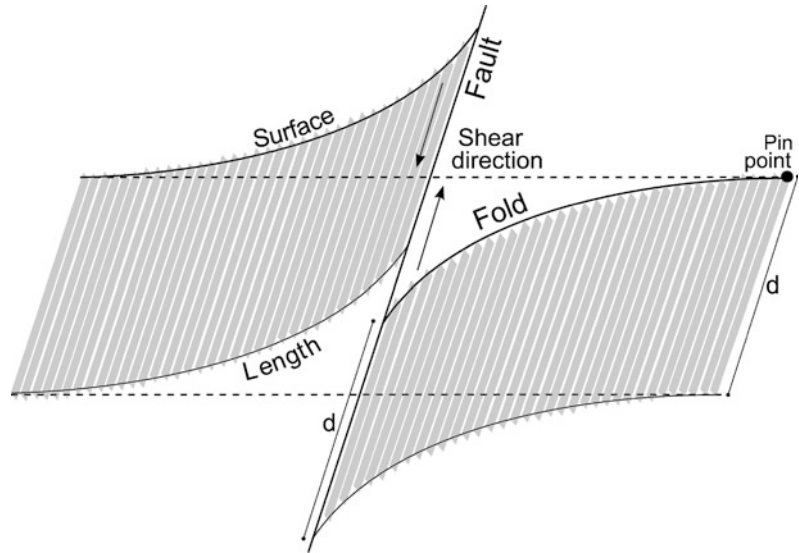
along surfaces parallel to the beds which often correspond to small-scale mechanical discontinuities (Galera et al. 2003). It involves slip along bedding planes or along surfaces of foliation keeping individual strata thickness constant (unless otherwise specified) and the resultant folds are parallel. If a layer was isopach (i.e. with a constant thickness) after the depositional and compaction phase, it remains isopach during and after the deformation. Flexural slip occurs in case of several intercalated layers of highly contrasting competence where interlayer slip is taken up by deformation in the incompetent layers. The result is a class IC fold. If the thickness varies laterally, the preservation of bed thickness and bed length may lead to area changes (Moretti 2008). When restoring using flexural slip, it is necessary to impose the displacement of at least one located pin point on the boundary or at any location in the model (see Fig. 8.6).

8.4.3 Implementation and Discussion

In the Lubin region, the areas of most sediment layers were preserved during folding and faulting that occurred either during the depositional process or during major regional deformation phases of the basin (the Alpine orogeny being the latest). Therefore, the flexural slip multiple-surface restoration available in the Kine3D-2 workflow was

applied on the studied area instead of simple shearing that may lead to significant volume change. It operates by flattening the top horizon and consequently deforming the underlying layers. Each restored layer is then removed and the process is reiterated with the remaining deeper horizons (i.e. back-stripping procedure). With this approach, removing the overlying top layer decreases the total vertical loading and subsequently would modify the compaction state of the underlying layers (see below). During restoration, some inconsistencies are often pointed out, such as hole in faulted surfaces, unrealistic folding of the surface border, and surface cross-overs (underlying horizon crossing upper horizon at depth). They are due to unrealistic nearby horizon shapes, fault behaviour or ill-estimated thickness variations. So in practice, restoring a model is an iterative process, which imposes eventually the reconstruction of the initial surface model to correct these inconsistencies due to unconstrained surface extrapolation in under sampled regions of the initial model. This procedure was applied to the Zechstein formation in order to obtain a realistic faulted model which was coherent regarding the relationship between the faults and the deformed layers. It is achieved by manually modifying the initial surface shape in extrapolation zones, respecting all data about wells and faults and by modifying their continuity (suppression or addition of potential faults in non sampled areas, forcing continuity,

Fig. 8.6 Flexural slip involves slip along bedding planes or along surfaces of foliation keeping individual strata thickness constant. Flexural slip preserves lengths, thicknesses and areas (and consequently volumes of sediment)



modifying the position in some unrecognized zones, etc.). These corrections are applied prior to making any new restoration procedures. Despite the fact that a high degree of uncertainty remains in unrecognized zones or under sampled areas, the final model seems more robust because it is more coherent in terms of compatible deformations.

8.4.4 Decompacting a Sediment Stack

Compaction occurs when a sedimentary layer causes the volume and thickness of the underlying sediments to decrease by porosity reduction and water expel. Reconstructing the initial layer volumes throughout the burying and sedimentation cycles is called decompaction. The decompaction step aims at removing the loading effect of the overlying sedimentary sequence, which had compacted and expelled water from the underlying buried sediments. Commonly, the compaction influences the pile as a vertical movement of the horizons and with a negative layer volume change depending on the rock type. The decompaction can be calculated from the sediment layer properties (initial porosity, and porosity depth factor), the depth of the reference

layer, its current restored position, and thickness of the bedrock. The first decompaction models were proposed by Athy (1930) and then enhanced by several authors (see Durand Riard et al. (2011) for a complete review). The so-called isostatic approaches assume that the reduction in volume of sediments is due to the reduction of the porosity against depth according to the following exponential law:

$$\Phi = \Phi_0 e^{-cz} \quad (8.1)$$

where ϕ is the porosity at any depth z , ϕ_0 is the porosity at the depositional time and c an internal coefficient depending on the rock type (or *porosity depth factor*). The initial porosity ϕ_0 refers to a non consolidated sediment (i.e. a mixture of water and particles), and can reach very high values compared to normal consolidated sediments (see Table 8.1 and Sclater and Christie 1980). The isostatic approach assumes that the load-response compaction rate is constant through time and similar to the vertical solid volume (no erosion). The methodology described by Sclater and Christie (1980) was used in this work. It gives the governing equation, which quantifies the upward movement of the stratigraphic horizons as follows (see Fig. 8.7 for explanation):

Table 8.1 Rock properties used in this work for different stratigraphic layers of the Polish Zechstein series in the area of the Lubin mine [after Scheck-Wenderotha and Lamarche (2005) and Resak et al. (2008)]

Rock type	Stratigraphic units ¹	Thickness (m)	ϕ_0 Initial porosity ⁴ (%)	c Porosity depth factor (10^{-4} m^{-1})	T —tensile ³ strength (in MPa)
Clastic	<i>Quaternary (Q)</i>	44	0.51	6.2	3.5
	Tertiary (TR)	262	0.51	6.2	3.5
	Upper cretaceous	411	0.48	5.0	–
	Lower cretaceous	823	0.48	6.1	–
	Upper jurassic	188	0.51	5.2	–
	Middle jurassic	140	0.62	19.4	–
	Lower jurassic	110	0.35	5.0	–
	Norian-rhaetian	318	0.48	4.4	–
Evaporitic	Schilfsandstein				
	Upper gypsum beds ²	108	0.06	0.3	–
	Lower gypsum beds	34	0.06	0.3	–
Clastic	Lower Keuper	1100	0.70	8.3	8.8
	Muschelkalk	450	0.53	5.6	8.8
	Upper buntsandstein	450	0.62	19.4	3.6
	<i>Middle buntsandstein</i>	200	0.35	5.0	3.6
	<i>Lower buntsandstein</i>	200	0.62	19.4	3.6
Evaporitic	Triassic (T)	37	0.06	0.03	–
	<i>Cyclothem aller (PZA)</i>	43	0.06	0.03	6.9
	<i>Cyclothem leine (PZ3)</i>	64	0.06	0.03	6.1
	<i>Cyclothem stassfurt (PZ2)</i>	16	0.06	0.03	6.0
	<i>Cyclothem stassfurt (PZ1)</i>	204	0.06	0.03	6.2
Clastic	Rotliegend white sandstone (PCB)	18	0.51	6.2	0.8
	Rotliegend red sandstone (PCC)	–	0.51	6.2	0.8

Layers in italic are not eroded nearby the Lubin mine

¹Rock density assumed nearly at $\rho = 2670 \text{ kg m}^{-3}$ for each layer; ²this layer has been eroded during the 221–214 Ma time interval, while the other layers have been eroded after the deposit of the Upper Cretaceous from 66 to 59 Ma;

³Average tensile strength computed for each layer from values reported by Pytel (2003) from the mining district; ⁴The initial porosity ϕ_0 refers to a non consolidated sediment (i.e. a mixture of water and particles), and can reach very high values compared to normal consolidated sediments

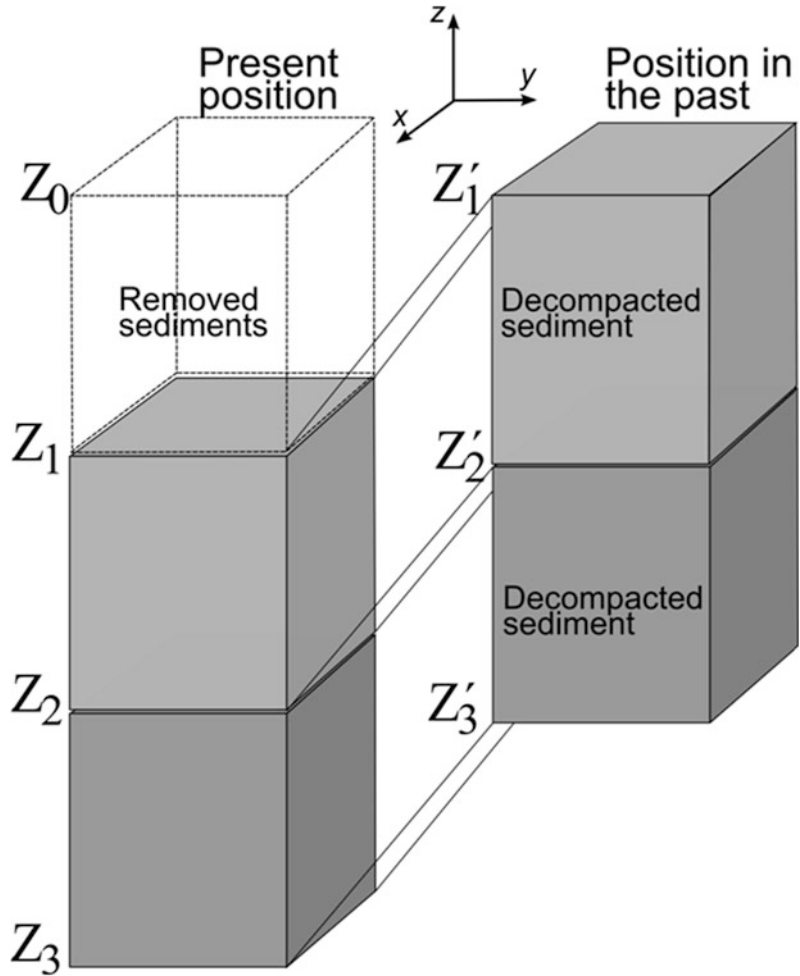
$$\begin{aligned}
 z'_2 - z'_1 &= z_2 - z - \frac{\Phi_0}{c} (e^{-cz_1} - e^{-cz_2}) \\
 &\quad + \frac{\Phi_0}{c} (e^{-cz'_1} - e^{-cz'_2}) \\
 \delta z &= z'_2 - z'_1 \quad (8.2)
 \end{aligned}$$

where z_1 (resp. z_2) is the known depth of the top (resp. base) surface of the current layer (l) before decompaction, z'_1 (resp. z'_2) the unknown depth of l of the top (resp. base) surface after decompaction, ϕ_0 the initial porosity of sediments or surface

porosity (in %), c the porosity depth factor (in m^{-1}) of overlying sediments, and δz the thickness variation due to the decompaction.

Equation (8.2) is valid for the given reference layer l . However, as rock types vary from one layer to the other, layer properties (z , ϕ_0 , c , δz) will be labelled i (i.e. z_i , $\phi_0(i)$, c_i , δz_i) in the following. For a given restoration step, the decompaction is estimated sequentially for each underlying layer i from top to bottom. This decompaction estimation is performed

Fig. 8.7 Schematic view illustrating the sediment thickness variations before and after compaction. Z_1 is the sedimentation level of the first layer before burying (assumed here to be sea level), while Z_1 is the depth after burying; Z_2, Z_3 depths of the successive underlying layers before burying layer Z_1 (resp. Z_2, Z_3 , after burying Z_1) (after Sclater and Christie 1980)



for every underlying layer, each time the upper layer is removed and the base of the removed layer located at the top of the sequence is restored (see Fig. 8.8). For a given layer l , the total thickness variation is the sum of the δ_{lz_j} , where δ_{lz_j} is the variation due to the decompaction of l at step j . The cumulative thickness compaction Δ_l^i of a given layer l restored between decompaction step 1 and i is given by:

$$\Delta_l^i = \sum_{j=0}^i \delta_{lz_j} \quad (8.3)$$

To better visualize the compaction effect, the cumulative thickness compaction against time (or decompaction steps i) is plotted. Usually this type of graph characterizes the rock type layer. It is possible to estimate the cumulative layer volume

variations ΔV_l^i from their cumulative thickness variations Δ_l^i if the area S_l of layer surfaces are kept constant during the deformation:

$$\Delta V_l^i = \Delta_l^i S_l \quad (8.4)$$

Plot of ΔV_l^i against time can characterize the rock mechanical properties of a given layer during burying. An example is given in Fig. 8.9. The decompaction effect was included into the classical geometric restoration workflow used in Kine3D-2 through a GoPy plug-in (Antoine and Caumon 2008). The method involves two steps: (i) a 2.5D restoration algorithm used to flatten a reference horizon; (ii) a surface decompaction routine which estimates the correct layer thicknesses in the sedimentary pile accounting for the release loading.

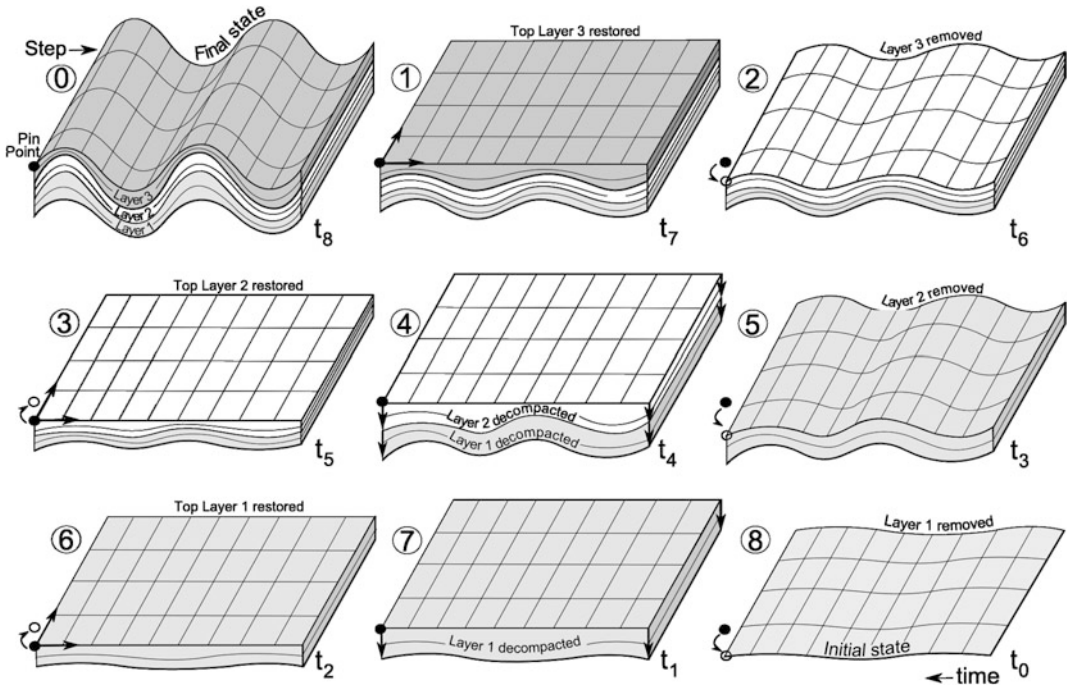


Fig. 8.8 Cartoon illustrating the different steps involved in the decompaction-restoring algorithm: (1) the top of the first layer is restored in its original depositional state (here flattened) from the initial present model (0); (2) the first layer is removed; (3) the top of the second layer is restored (flattened) and the pile moved to the reference sea-level → ○; (4) the layers of the sedimentary pile are

decompacted iteratively using the Scatler’s equation (Eq. 8.2); (5) the process is reiterated from step (2), the second layer is removed; (6) the third layer top is flattened and the pile moved to the reference sea-level as in step (3); (7) the layers of the pile are decompacted as in step (4); (8) the process is then reiterated with the last layer

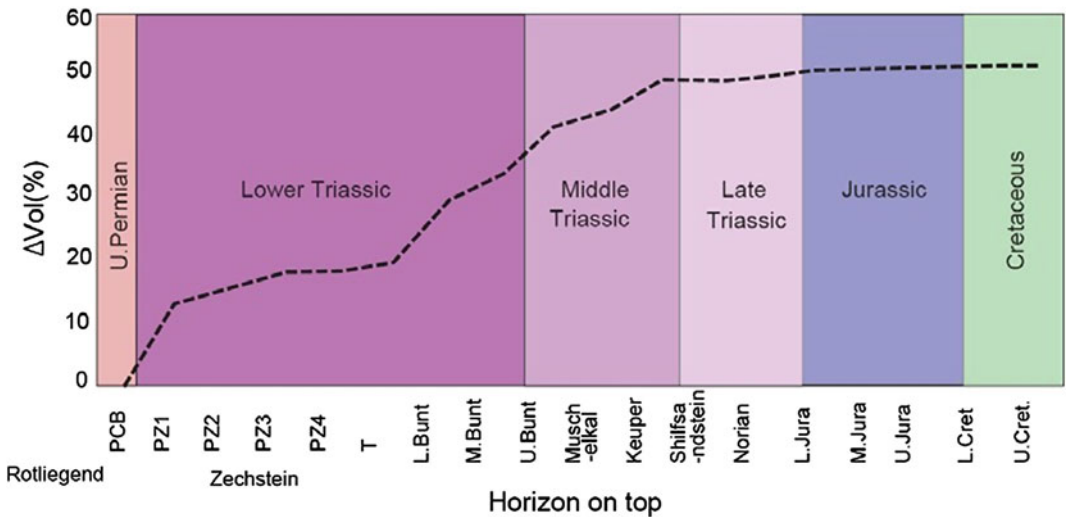


Fig. 8.9 Example of volume variation (in %) through time during decompaction. The studied layer is formed by clastic sediments (PCB) overlain by PZ1 to Upper

Cretaceous series (Kupferschiefer, Lubin region, Poland), see Table 8.1 (after Fraboulet 2012)

8.4.5 Materials Behaviour

Equation (8.2) requests the knowledge of the initial porosity $\phi_0(l)$ and the porosity depth factor c_l for each layer l together with their variations throughout times. Table 8.1 reports values for the porosity and the porosity depth factor of some common rocks found in the Kupferschiefer formation nearby the Lubin copper mine (Poland).

During decompaction the materials with sufficiently high natural porosity can change volume according to Eq. (8.2) depending on the thickness variation. By contrast, the volume variation of some other layers such as evaporitic rocks does not vary during the decompaction because their natural porosity is very low. It is therefore considered that the layer thickness remains constant throughout the restoration-decompaction process. However, the layers of clastic sediments, which are confined by evaporitic layers may or may not vary in volume depending on their ability to dewater throughout the sedimentary load history. It is assumed that the fluids are confined by the evaporitic rocks and remain hydraulically isolated from the hydraulic system of the sediment cover above the evaporitic rocks. Therefore their volumes remain almost constant. In the case of a tectonic inversion the fluid can flow upwards by fault reactivation and a strong pressure gradient, or laterally following the layering until it reach vertical conduits (faults, basin margins).

8.5 Hydraulic Fracturing and Kupferschiefer Mineralization

During a tectonic inversion and uplifting the overlying layers are removed by erosion, then the pore pressure changes and may lead to natural hydraulic fracturing. This process has been invoked to explain metal re-mobilization.

8.5.1 Processes Involved in the Mineralization of the Kupferschiefer

One of the factors involved in the formation of the Kupferschiefer ore in the Lubin region is the presence of fractures that concentrate metals in sulphides (Blundell et al. 2003, Jowett et al. 1987; Gouin 2008). Hydraulic fracturing necessary to transport and enrich deposits in base metals has been suggested in several papers (Jowett et al. 1987; Jowett 1992). However, to establish the time and geologic conditions for hydraulic fracturing related to the Kupferschiefer ore emplacement is not easy. One of the main drawbacks is the difficulty to date the mineralizing event. Several workers suggest different ages (from early Triassic to Cenozoic) for the Kupferschiefer mineralization, resulting in contradictory models for explaining the ore formation regarding physical and chemical constrains. However, the recent publication by Symons et al. (2011) on the Sangerhausen district (Germany), suggests two possible mineralization episodes of 149 ± 3 and 53 ± 3 Ma from paleo-magnetic data of the ore formation. The older age defines a Late Jurassic extensional tectonic event that formed the nearby North German Basin, and also reactivated the Variscan basement faults and extended them up through the overlying strata. Meanwhile, hydrothermal basement fluids ascended through the overlying Rotliegendes and Weissliegendes layers and faults, and formed epigenetic mineralization in the Kupferschiefer shale (Symons et al. 2011). The younger age is not discussed in the light of a geological event related to mineralization. In this work, it is presumed that the younger age reported by Symons et al. (2011), 53 ± 3 Ma, corresponds to a period of tectonic inversion which occurred in northern Europe, and which led to the erosion of several hundred meters of the Triassic to Cretaceous sedimentary formations. This tectonic inversion allowed fluid pressure increase and possibly

triggered hydraulic fracturing required for the transport of mineralizing fluids, remobilization of elements and reorganization/redeposition of sulphides.

8.5.2 Hydro Fracturing

According to Cosgrove (1995), the common condition for tensile failure [cf. Royer (2012)] by hydraulic fracturing along any plane is that the fluid pressure (P_f) must be equal to or greater than the sum of the tensile strength of the rock (T) normal to that plane and the normal stress (σ_n):

$$P_f \geq T + \sigma_n \quad (8.5)$$

Thus, hydraulic fracturing can occur either by increasing the fluid pressure P_f , or reducing the tensile strength T of the rock (e.g. alteration), or decreasing the normal stress σ_n . During subsidence, the normal stress σ_n will increase like the fluid pressure due to the weight of sediments, while the tensile strength remains more or less constant, but increasing with time by expelling fluids and cementation of the rock. In this case, the only way to get a fluid overpressure is to increase the fluid pressure P_f on the left side of (Eq. 8.5). This is the idea suggested by Jowett et al. (1987) who invoked an aqua-thermal pressuring mechanism due to the generation of water, CO_2 and CH_4 from the coal material inter-bedded in the Carboniferous rocks below the Kupferschiefer (Jowett 1992). The Zechstein formation is known as a reservoir rock in many places in Europe. Another way to reach hydro-fracturing overpressure is to reduce the normal stress σ_n magnitude in Eq. (8.5) maintaining steady fluid pressure at the same time (usually the rock tensile strength remains more or less constant, or increases during burying). For a sufficient decreasing in σ_n , due to erosion of the over-lying series, favourable hydraulic fracturing conditions may be reached. This situation might occur during a tectonic inversion event. During the subsidence phase of a basin, the normal stress increases continuously and the fluid pressure

remains between lithostatic and hydrostatic pressure. On the contrary, during an uplift event, the normal stress decreases and the fluid pressure decreases if it can re-equilibrate under hydrostatic conditions. However, in the case of the Kupferschiefer, the fluids are trapped and sealed below the evaporitic rocks of the Zechstein series, and are not able to re-equilibrate through a normal dewatering mechanism. The internal pressure P_f will exceed the tensile strength T of the rock and the normal stress σ_n leading to hydro-fracturing (see Fig. 8.7). σ_n corresponds to the lithostatic pressure (the minimum stress value during the tectonic inversion) or the pressure imposed on the sediments by the weight of the overburden at the depth (z). Consequently, the condition for the tensile failure by hydraulic fracturing can be expressed as a function of depth as:

$$P_f \geq T + g \int_0^z \rho(z) dz \quad (8.6)$$

where (g) is the gravity and (ρ) the bulk density of the overlying materials. This dependency of the depth in the hydraulic fracturing conditions (Eq. 8.6) must also account for the compaction effect (see above).

8.5.3 Hydro Fracturing Index

Equation (8.5) can be turned into a more practical form introducing the hydro-fracturing index (HF) defined as:

$$HF = P_f - (T + \sigma_n) \quad (8.7)$$

where P_f is the fluid pressure, T the rock tensile strength, σ_n the normal stress equal to the lithostatic pressure according to Eq. (8.6). Positive fracturing index values ($HF \geq 0$) defines regions where hydraulic fracturing might occur, the fracturing probability being proportional to HF , while negative fracturing index ($HF < 0$) values indicate zones where the rock is preserved from hydraulic fracturing. Fracture mode and

orientation can be predicted according to the Mohr-Coulomb or Griffith's theory, depending on many factors such as the rock type (its cohesion, tensile strength, Poisson's ratio), the depth, the regional stress, and the possible pre-existing fractures, which can be reactivated during hydraulic fracturing (Royer 2012).

8.6 Application to the Kupferschiefer

8.6.1 Restoring-Decompaction of the Kupferschiefer

A 3D restoring-decompacting procedure was performed on the Kupferschiefer series of the Lubin region from Permian to present time (Figs. 8.10 and 8.11).

The lithostatic, hydrostatic and fluid pressures are calculated as a function of depth. The tensile strength of each layer is obtained from the values

reported by Pytel (2003) (see Table 8.1). Rock properties and pressure values are assigned to the cell centre of a regular stratigraphic grid fitting the structural model (cell size $200 \times 200 \times 10$ m). The hydraulic factor HF was calculated at the centre of each cell according to Eqs. (8.7) and (8.6).

Figure 8.12 shows the hydraulic index HF calculated in each layers during restoration in colour. Mineralized zones are located at the interface between negatives (dark blue) and positive (light blue to grey) hydraulic index HF within the Zechstein cyclotherms up to the salt layer. The calculated hydraulic index shows that the post Zechstein rocks are more fractured than the rocks below. The reasons for this is that the effective pressure of fluids trapped in the sediment reach the limit of rupture of the rock during up-lifting causing the fracturing of the surrounding rocks. However, as no major impermeable layers confined the fluids expelled during the fracturing, the fluids dispersed in the upper permeable layers. Therefore, the overlying rocks are not potential targets.

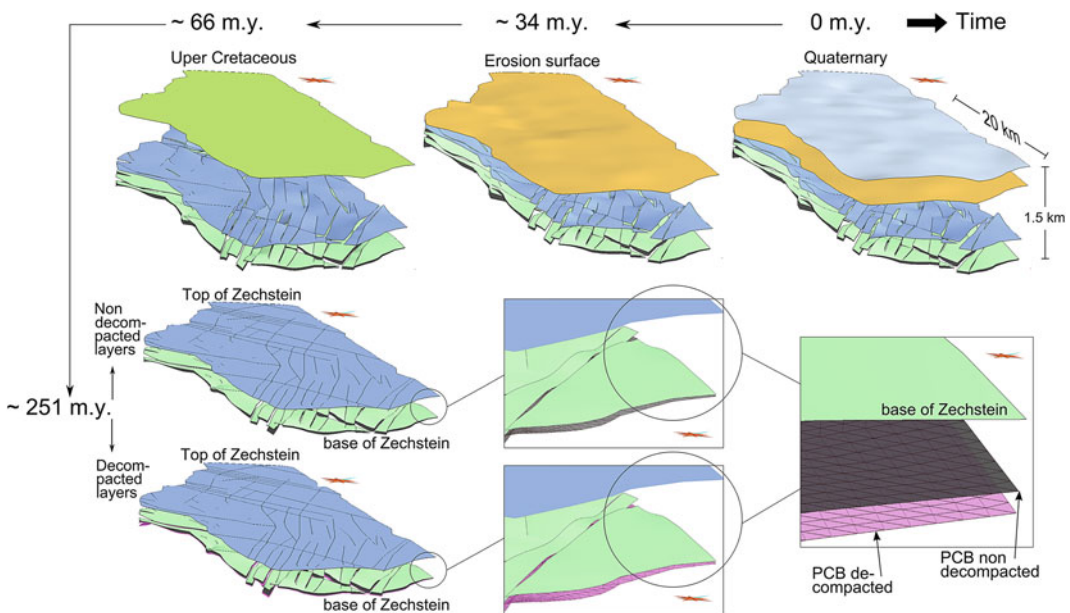


Fig. 8.10 3D restoring models of the Lubin region showing the restored layer with the compaction effect both taken and not taken into account (decompacted and non-decompacted surfaces) in the Triassic. The PCB layer represents the *Upper part* of the Rotliegend formation and

also the location of the Kupferschiefer deposits. The thickness variation of the Zechstein series is zero because they are mainly composed of evaporitic rocks and hence the porosity remains almost constant ($5 \times$ vertical exaggeration)

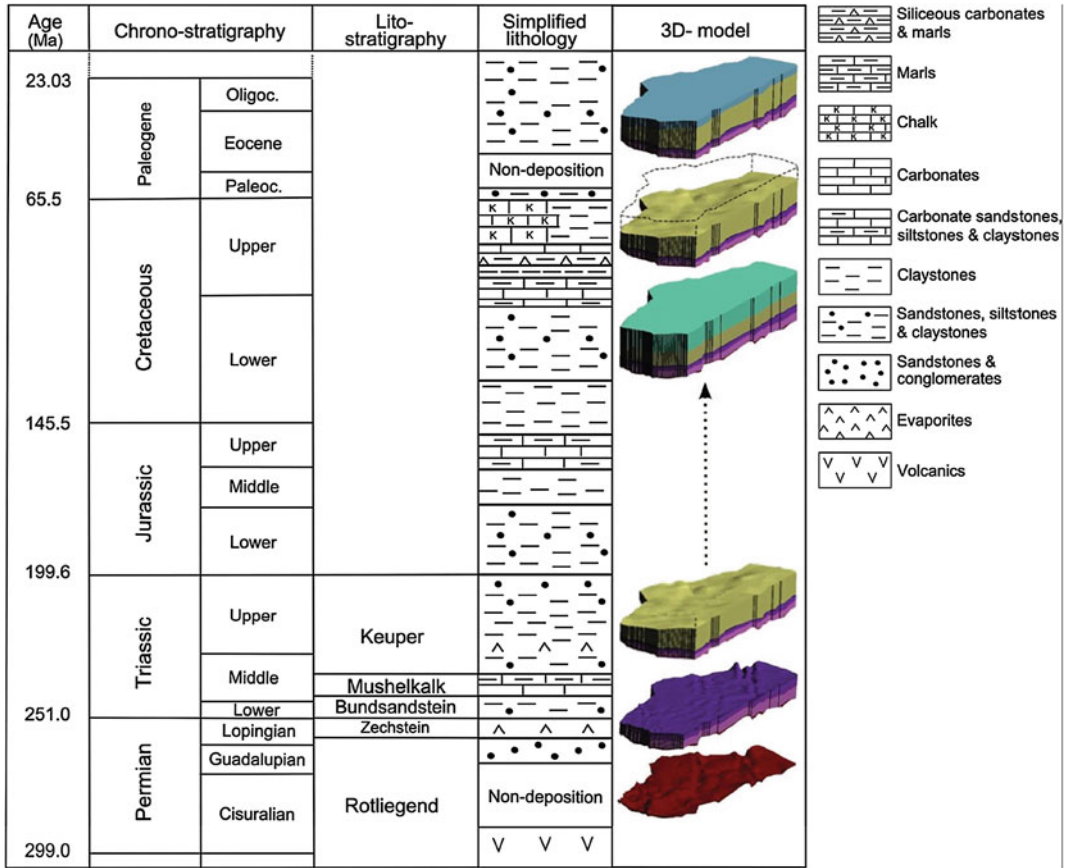


Fig. 8.11 3D sedimentary block diagrams of the Lubin region, Poland, evolving through the geological time. From Mid Permian to Upper Jurassic/Early Cretaceous, the basin subsided down to a depth estimated at about 2700 m (T_{max} between 120 and 130° C based on the vitrinite reflectance ($R_r = 0.80$ to 0.85 %) of organic matter contained in the black shale have been reported by Barker and Pawlewicz

(1994) and Gouin (2008). During the Upper Cretaceous to Early Paleocene, an uplift phase eroded more than 2000 m of sediments. This inversion phase is thought to be related to the Alpine orogeny. During the uplift, trapped fluids reached over-pressure producing hydro-fracturing and circulation of hydrothermal fluids which redistributed the mineralization. Column modified from Resak et al. (2008)

Within the Zechstein formations, the positive values of the hydraulic factor HF shows that fracturing may have occurred during up-lift in the Rotliegend and in the sedimentary rocks overlying the Zechstein series, while no fracturing occurred in the Zechstein series (HF being negative). This is in agreement with the observation that mineralization occurs and spreads out close to the cover/basement interface. The overlying Triassic and Cretaceous rocks are not considered as potential targets because the fluids are confined to areas close to the basement because of the impermeable Zechstein series evaporitic cover

(Fig. 8.12). Figure 8.13 shows the relationship between the HF index and the copper content of the Kupferschiefer and Rotliegend (Weissliegend) formations. The copper cumulative distribution in the mineralized layers correlates with the fracture zones created during the Last Cretaceous to Early Palaeocene uplift. Furthermore, Fig. 8.13 shows the relationship between the hydraulic factor (HF) and the high copper grades contained in the ore bearing series. The copper content rises abruptly when HF is positive. It is difficult to establish a predictive correlation model between the copper grade and the hydraulic

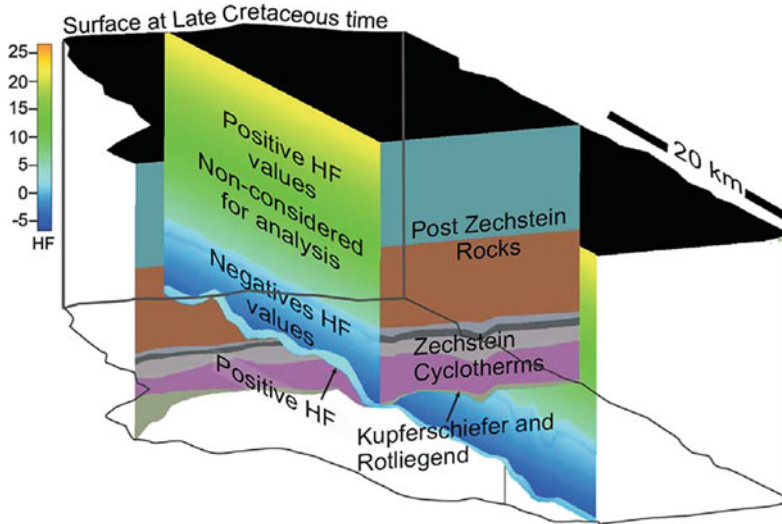


Fig. 8.12 Stratigraphical grid representing the Lubin 3D model at Late Cretaceous to Early Paleocene time. The high HF index calculated according to layers depth and tensile strength defines possible hydro-fracturing

zones favourable for re-circulation of metal rich brines located under the sealing Zechstein salt layer. 5 × vertical exaggeration

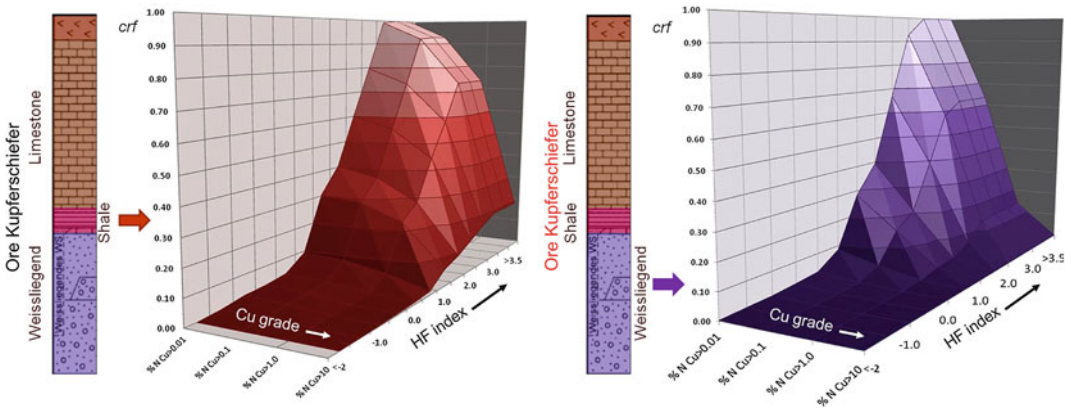


Fig. 8.13 Relationship between the copper content and the hydraulic factor (HF). The copper content rises abruptly when HF is positive (i.e. in hydro fractured areas). No mineralization occurs in unfractured rock (negative HF), the copper grade is zero. Mineralization is found in hydro-fractured rocks (positive HF), but the copper grade is not necessarily high. No clear correlation is observed between high HF and the high-grade copper

values in the Kupferschiefer and Rotliegend (Weissliegend) formations, indicating that hydro-fracturing is a pre-requisite, but not the only factor controlling the mineralization. The copper grade is mostly controlled by the local redox conditions of the fractured medium through which the mineralized solution flows. The vertical axis is the cumulative distribution function of copper (crf)

factor. This is probably due to the fact that the copper content distribution is related to the rock type (footwall Rotliegend-Weissliegend and black shales) and concentrates in reduced zones enriched in organic matter, while the fracturing

occurs everywhere. Therefore, the hydraulic factor indicates the favourable permeable zones for finding copper, but other factors such as the presence of organic matter are necessary for high copper concentration. This indicates the efficiency

of the organic matter present in the black shales for precipitating the Cu (Cu-Fe) sulphides, or the positive role of the primary pyrite in the black shales. The latter is replaced by the Cu (Cu-Fe) sulphides during the hydrothermal remobilization of metals where the iron contained in pyrite is possibly dissolved and precipitated in magnetite or pyrrhotite (Symons et al. 2011).

These spatial correlation indirectly confirm the major role of the evaporitic series in the remobilization of metals. Evaporitic rocks prevent the fluids to be expelled up to the surface and therefore force them to re-circulate and accumulate metals in the bottom layers. Results from this hydro fracturing model indicate that the favourable zones for mineralization are located just below the evaporite Zechstein series, where the Kupferschiefer and the other ore-series are enriched in base and precious metals. The hydro fracturing index estimated from the failure conditions induced by over-pressured trapped fluids seems to correlate with the mineralized zones. This result is in agreement with the Early Palaeocene to Late Cretaceous ages of the mineralization as suggested by Symons et al. (2011). These structural attributes can be used as a regional exploration guide together with other predictors based on the maturation of the organic matter (when available), such as the hydrogen (HI) and oxidation (OI) indexes deduced from Rock Eval analyses (Więclaw et al. 2007; Pieczonka and Piestrzyński 2011a, b). The HI decreases in mineralized zones due to the consumption of hydrocarbon during the thermochemical sulphate reduction (TSR), a mechanism evoked to explain the enrichment in base metals and copper during diagenesis (Gouin 2008). The oxidation (OI) index shows the nature of the organic matter: waxy organic matter (OM) (type I), algal OM (type II) or vascular plant OM (type III) (Espitalié et al. 1985). The origin of the organic matter contained in the Kupferschiefer back shale is algal to continental type (type II or III) similar to the OM of the Zechstein carbonates (Gouin 2008). The OM associated with the Pb-Zn mineralization is typically close to type II, revealing an alteration process under oxidation

induced by the Rote Fäule (Bechtel et al. 2002). Geochemical features based on the OM are very efficient in delimitating potential mineralized zones from barren areas, and in explaining metal zoning. To use these criteria it is necessary to sample and analyze on a local scale. Geometrical structural attributes such as those discussed above, result from a restoration process on a more regional scale and can be applied prior to drilling for locating potential permeable areas.

8.6.2 Analysis of Pressure During the Basin History

Virtual wells were performed in the 4D geomodel for studying the pressure evolution through time during the basin evolution using PetroMod 10-1D. Assumed thicknesses and properties of present and eroded layers are given in Table 8.1. Results reported in Fig. 8.14, suggest the existence of two main overpressure periods in the Lubin region: (i) the Upper Jurassic—Lower Cretaceous subsidence and (ii) the Upper Cretaceous-Early Palaeocene uplift inversion.

During the subsidence, the pore pressure in the evaporitic series reaches the lithostatic pressure creating some fractures around 2.400 m below the Schilfsandstein lower gypsum series, and a few thousand meters below the Zechstein series. During the tectonic inversion at 53 ± 3 Ma, the pore pressure in the evaporitic series reaches the lithostatic pressure creating some fractures around 600 m below the Schilfsandstein lower gypsum series and around 2500 m below the Zechstein series, possibly with a reactivation of pre-existing fractures (Fraboulet 2012). At these periods, fracturing and fluid recirculation might have occurred (see Figs. 8.11 and 8.14). These results are in agreement with previous dating by Symons et al. (2011) who suggested the same ages for the Kupferschiefer mineralization in Germany corroborating the assumption that the mineralization has both a diagenetic and an epigenetic origin.

The restoration-decompaction and hydraulic factor index methodology developed for the

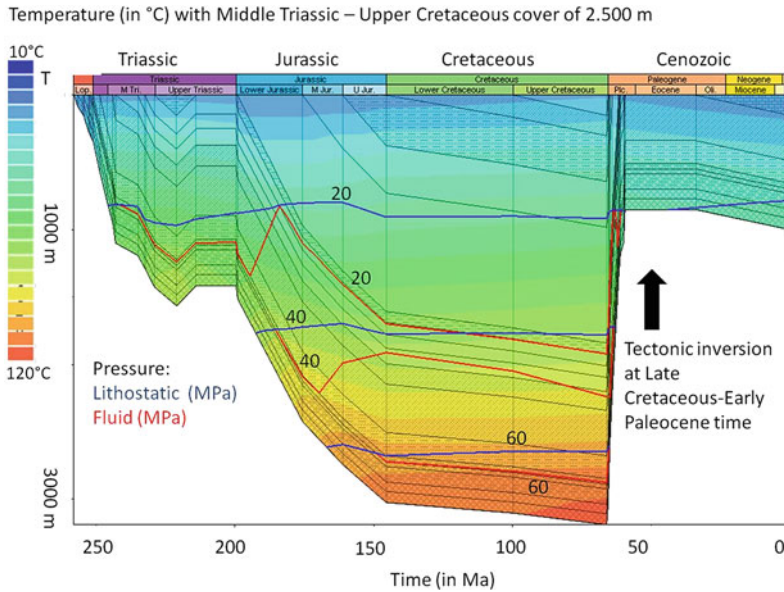


Fig. 8.14 Reconstruction of pressure conditions through time using PetroMod 10-1D. Lithostatic and fluid pressure (MPa), and temperature against time of deposition on a virtual well located close to the Lubin mine. Notice that hydraulic fracturing is caused by the expansion of fluids

trapped in the sediments during the uplift (not during burial) in Early Paleogene, because the pressure is no longer compensated by the overlying sediments (after Mejia et al. 2012)

Lubin mining region, was applied on the entire Foresudetic Polish Basin. Several virtual wells were formed on the regional 3D geomodel to estimate the pressure conditions using PetroMod 10-1D. These punctual overpressure values were then interpolated in each cell of the regional 3D geomodel. Results are shown in Fig. 8.15. Overpressure iso-surfaces are represented for 20 MPa (light-blue) and 40 MPa (Blue), respectively. They indicate where the hydraulic fracturing might have occurred during the up-lift which began during the Alpine orogeny in the Early Paleogene. Prospective map and reserves established (red circle) by Oszczepalski and Speczik (2011) correspond roughly with the potential hydraulic fracturing zone and overpressures.

8.7 Discussions

Results given by the 4D modelling approach seem to be coherent with mineralization processes evoked from explaining the Kupferschiefer ore

deposits, making this approach an exploration tool to investigate potential formation that were affected by the same fracturing-hydrothermal processes. This approach has been used with success to relate prospective maps based on drilling data with over-pressured 3D models. In detail, it can be noted that hydraulic fracturing conditions were also reached in the upper layers located below the Schilfsandstein lower gypsum, probably the Keuper horizon, which have similar lithology (clastic sand and shale) as those encountered in the PCB Zechstein layer. Two periods of possible hydrothermal circulation linked with hydro-fracturing can be observed: the first during the Middle Jurassic to Lower Cretaceous when subsidence increased, and the second during the Upper Cretaceous to Early Palaeocene uplift and inversion. If correct, this indicates that Keuper layers could have hosted hydrothermal cells and consequently possible metal remobilization.

The results stress the important role of the evaporite series in the mineralization process by confining fluids and preventing them to escape up to the surface. From this hydro-fracturing

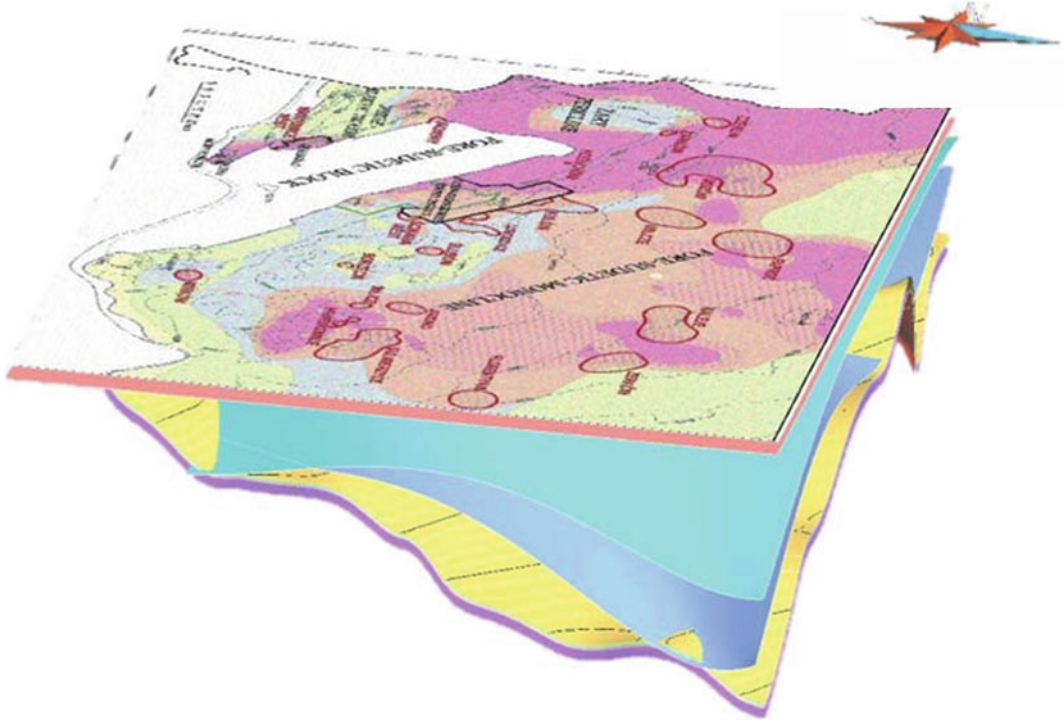


Fig. 8.15 3D Reconstruction of over-pressure conditions using PetroMod. Overpressure iso-surfaces are shown for 20 MPa (*light-blue*) and 40 MPa (*Blue*) ($15 \times$ vertical exaggeration). Hydraulic fracturing occurred in layers located under the 40 MPa iso-pressure surface, especially in the Zechstein series (*violet*). The prospectivity map of

Polish Kupferschiefer by Oszczepalski and Speczik (2011) is draped on top of the 3D geomodel. The prospective areas, in red, coincide with over-pressured zones defined in the 4D restoration, making 4D investigations a prospective tool for identifying potential mineralization (after Fraboulet 2012)

model, favourable zones of mineralization can be located just below the impermeable evaporite series, which have prevented metal-rich fluids to circulate in the Zechstein series (such as the Schilfsandstein and the Zechstein series). However, it is obvious that the most favourable zones are distal to major regional faults that could stop the circulation of fluids, or connect them to upper level. In this context, the evaporite series behave as a perfect cover, confining fluids at depth like for oil and gas. They also confine strain and stress during subsidence or uplift to the lower level.

It can be noted that the sediment hosted copper deposit of the Copper Belt in DRC and Zambia, present very similar geological features as those of the Kupferschiefer. Similar tectonic phases, subsidence followed by regional uplift, have been reported (Hitzman et al. 2005; Brown 2011).

The metal precipitation is related to a hydraulic fracturing episode. Moreover, traces of hydrocarbon have also been found in the Copper Belt in DRC.

This association of “diagenetic sedimentary” copper deposits with evaporite series is classical. Aitken et al. (1981), Gourlay (2005) and Hartsch (pers. comm., 2013) reported similar settings for the Late Proterozoic Coates Lake copper deposits, classified as a sediment-hosted stratiform copper deposits. The deposit is located in the Mackenzie Mountains Supergroup (Western Territories, Canada). The mineralization is inter-bedded in a transition zone between a lower red, green, and maroon coloured near continental clastic sequence overlain by a copper rich carbonate copper. The Rapitan Group made of turbiditic, siliceous red siltstones unconformably overlies the lower mineralized series. The copper

occurrences are hosted by carbonate-evaporite beds, each composed of dolosiltite, dololutite, dolostone, gypsum and anhydrite capped by a crypt-algal laminated carbonate bed. Other classic examples of SCD's include White Pine in Michigan, the Dzhezkazgan area in Kazakhstan, the Lisbon Valley, Utah, the Graviisk area of Russia and possibly the Revett Formation of the Belt Supergroup in western Montana and Idaho (Gourlay 2005; Pieczonka et al. 2007). This long list of copper deposits with similar geological setting as those encountered in the Polish Kupferschiefer, demonstrates the great potential of the integrated quantitative approach and conceptual modelling advocated in this work.

Similar ore forming mechanisms might have occurred in the upper Keuper below the Schilfsandstein evaporitic series linked to a hydraulic fracturing phase both during the subsidence and the tectonic inversion. Further studies could benefit from new data obtained by drilling north east of Lubin, to support or discard the suggested existence of an upper mineralization. Moreover, new geological data such as occurrences of faults and folds could be beneficial for the precision of the model. More generally, this genetic model with large evaporate series, black shales containing abundant organic matter and iron could be tested with exploration for new sediment hosted copper deposits.

8.8 Conclusions

This work summarizes some important ideas and results related to decompacting sediments, restoring sedimentary series and predicting hydro-fracturing index during tectonic events. 3D models coupled to 4D restoration have been applied for restoring the Polish Kupferschiefer sedimentary series. The results of this numerical 3D and 4D modelling show that the natural hydro fracturing occurred during the Upper Cretaceous to Early Palaeocene uplift, favouring recirculation of mineralizing fluids.

The important role of the Zechstein evaporitic series in the mineralization process has been

proven. This series behaved as an impermeable screen preventing the fluid from being expelled, forcing hydraulic fracturing in the lower levels. Two periods of hydraulic fracturing linked to metal accumulation have been identified: (i) a first episode during the Upper Jurassic to Lower Cretaceous subsidence, the second during the Upper Cretaceous to Early Palaeocene linked to metal remobilization. The remobilization of the mineralization implies both diagenetic and epigenetic mineralization.

It has been shown, based on the Kupferschiefer series, that 3D reconstruction and restoration techniques (4D) can be used as a prognostic exploration tool for sediment-hosted deposits. It provides useful structural attributes (in this case the hydraulic-factor) that can help to better understand the current distribution of metals in the ore-deposit. In this way, it was possible to define exploration targets from the correlation of copper content and the hydro-fracturing index in the 3D model for the Lubin region, and possibly elsewhere in the world within similar geological settings.

Acknowledgments The authors would like to express their thanks for the support to the gOcad consortium, the Centre National de Recherche Scientifique CNRS-CRPG, and the Université de Lorraine. This work was performed within the framework of the "Investissements d'avenir" Labex RESSOURCES21 (ANR-10-LABX-21) and partially financed by the ProMine FP7 NMP European Research Project grant agreement no 228559.

References

- Aitken, J.D., Ruelle J.D. and Cook D.G. (1981) - Copper mineralization near an intra- Rapitan unconformity, Nite copper prospect, Mackenzie Mountains, Northwest Territories, Canada: Discussion, *Can. J. Earth Sci.*, 18, 410-413.
- Antoine C. and Caumon G. (2008) - Rapid algorithm prototyping in Gocad using Python plugin. 28th Gocad Meet. Proc., Nancy, France, Gocad Research Group. 4p.
- Athy L. (1930) - Density, porosity, and compaction of sedimentary rocks. *American Ass. of Petroleum Geologists Bulletin*, 14, 1-24.
- Barker C.E. and Pawlewicz M.J., (1994). Calculation of vitrinite reflectance from thermal histories and peak temperatures. In *ACS Symposium Series 570*,

- Vitrinite Reflectance as a Maturity Parameter, Applications and Limitations. Mukhopadhyay P. K. & Dow W.G. Eds. Chapter 14, 216-229.
- Bechtel A., Gratzner R., Püttmann W. and Oszczepalski S. (2002). Geochemical characteristics across the oxic/anoxic interface (Rote Fäule front) within the Kupferschiefer of the Lubin-Sieroszowice mining district (SW Poland). *Chemical Geology*, 185, 9-31.
- Blundell, D.J., Karnkowski, P.H., Alderton, D.H.M., Oszczepalski, S., and Kucha, H. (2003). Copper mineralization of the Polish Kupferschiefer: a proposed basement fault-fracture system of fluid flow. *Economic Geology* 98, 1487 - 1495.
- Borg G., Piestrzyński, A., Bachmann, G.H., Püttmann W., Walther S., and Fiedler, M. (2012) - An Overview of the European Kupferschiefer Deposits. *Soc. of Economic Geologists, Inc. Special Pub. 16*, 455 - 486.
- Brown A.C. (2011) - Adding geochemical rigor to the general basin-scale genetic model for sediment-hosted stratiform copper mineralization, 11th SGA Biennial Meeting, Antofagasta, 3p.
- Caumon G. (2010) - Towards Stochastic Time-Varying Geological Modeling. *Mathematical Geosciences*, 42 (5): 555–569
- Cosgrove J. W. (1995) - The expression of hydraulic fracturing in rocks and sediments. In Ameen, M.S. (ed.) *Fractography: fracture topography as a tool in fracture mechanics and stress analysis*, Geological Society Special Publication No. 92, 187–196.
- De Santi M., Campos J., and Martha L. (2002) - A finite element approach for geological section reconstruction. In 22th Gocad Meeting Proc., Nancy, France, Gocad Research Group.
- Dunbar J. and Cook R. (2003) - Palinspastic reconstruction of structure maps: an automated finite element approach with heterogeneous strain. *Journal of Structural Geology*, 26:1021–1036.
- Durand Riard P., Caumon G., and Muron P. (2010) - Balanced restoration of geological volumes with relaxed meshing constraints. *Computers & Geosciences*, 36, 441–452.
- Durand Riard P., Salles L., Ford M., Caumon G., and Pellerin J. (2011) - Understanding the evolution of syndimentary faults: coupling decompaction and 3D sequential restoration. *Marine and Petroleum Geology*, 28(8): 1530–1539.
- Espitalié J., Deroo G. et Marquis F. (1985) - La pyrolyse Rock-Eval et ses applications. *Deuxième Partie. Revue de l'IFP*, 40, 755-785.
- Fraboulet J. G. (2012) - 3D modeling of Kupferschiefer, Poland. MSc, Specialty: Engineering and Management of Mineral Raw Materials, Université de Lorraine, Nancy, France, 37p.
- Galera C., Bennis C., Moretti I., and Mallet J.L. (2003) - Construction of coherent 3D geological blocks. *Computers & Geosciences*, 29, 971–984.
- Gratier J.-P., Guillier B., Delorme A., and Odonne F. (1991) - Restoration and balance of a folded and faulted surface by best-fitting of finite elements: principle and applications. *Journal of Structural Geology*, 13(1): 111–115.
- Gouin, J. (2008) - Mode de genèse et valorisation des minerais de type black shales: cas du Kupferschiefer (Pologne) et des schistes noirs de Talvivaara (Finlande). PhD. Thesis Report. Université d'Orléans.
- Gourlay A.W. (2005) - On the Coates Lake copper deposit Nahanni Mining District, Western Northwest Territories, for Lumina Resources Corp. Technical report, Vancouver, B.C., 38p.
- Groshong R. (2006) - 3-D Structural Geology: A Practical Guide to Quantitative Surface and Subsurface Map Interpretation. Springer, Heidelberg. 400p.
- Guzofski C., Mueller J., Shaw J., Muron P., Medwedeff D., Bilotti F., and Rivero C. (2009) - Insights into the mechanisms of fault-related folding provided by volumetric structural restorations using spatially varying mechanical constraints. *AAPG Bulletin*, 93, 479-502.
- Hartsch J. (2015) - New Aspects of Copper Deposits at the Base of the Zechstein in Central Europe. (this book), 23p.
- Hitzman, M., Kirkham R., Broughton, D., Thorson, J., Selley, D., (2005) - The sediment –hosted stratiform copper ore system. *Soc. of Economic Geologist, Inc. Economic Geology 100th Anniversary Vol.*, 609–642.
- Jébrak M. and Marcoux E. (2008) - *Géologie des ressources minérales. Ressources naturelles et Faune*, Québec, ed., Québec: MRNF, 667p.
- Jowett, E.C. (1986) - Genesis of Kupferschiefer Cu-Ag deposits by convective flow of Rotliegendes brines during Triassic rifting. *Economic Geology* 81, 1823–1837.
- Jowett, E.C. (1992). Role of organics and methane in sulphide ore formation, exemplified by Kupferschiefer Cu–Ag deposits, Poland. *Chemical Geology* 99, 51–63.
- Jowett, E.C., Pearce, G.W., and Rydzewski, A. (1987). A Mid-Triassic Paleo- magnetic Age of the Kupferschiefer Mineralization in Poland, Based on a Revised Apparent Polar Wander Path for Europe and Russia. *J. Geophys. Res.* 92, 581–598.
- KGHM (2011). Annual Report 2011. <http://www.kghm.pl>.
- Macé L., Muron P., and Mallet J.-L. (2005) - Integration of Fracture Data into 3D Geomechanical Modeling to Enhance Fractured Reservoirs Characterization. In SPE Annual Conference and Exhibition, Dallas, Texas, U.S.A., 9p.
- Mallet J.-L. (2002) - *Geomodeling. Applied Geostatistics*. Oxford University Press, New York, NY, 624 p.
- Maerten L. and Maerten F. (2006) - Chronologic modeling of faulted and fractured reservoirs using geomechanically based restoration: Technique and industry applications. *AAPG Bulletin*, 90(8), 1201–1226,
- Mazur, S., Scheck-Wenderoth, M., and Krzywiac, P. (2005). Different modes of the Late Cretaceous–Early Tertiary inversion in the North German and Polish basins. *Int. Journal of Earth Sciences* 94, 782–798.
- Mejia P., Royer J.J. and A. Zielińska (2012) - Late Cretaceous-Early Paleocene up- lift inversion in

- northern Europe: implications for the Kupferschiefer ore deposit in the Lubin-Sieroszowice Mining District, Poland. ProMine Workshop on Mineral Resources Potential Maps, Nancy, March, France, 8p.
- Mejia P. and Royer J.J. (2012) - Explicit Surface Restoring-Decompacting Procedure to Estimate the Hydraulic Fracturing: Case of the Kupferschiefer in the Lubin Region, Poland. 32th Gocad Meeting, Nancy, France, September, 19p.
- Midland Valley (2012) – Vendor of 3D Move. <http://www.mve.com/software/move>
- Moretti I. (2008) Working in complex areas: New restoration workflow based on quality control, 2D and 3D restorations. *Marine and Petroleum Geology*, 25, 205-218.
- Moretti I., Lepage F., and Guiton M. (2006) - KINE3D: a New 3D Restoration Method Based on a Mixed Approach Linking Geometry and Geomechanics. *Oil & Gas Science and Technology Rev. IFP*, 61(2), 277–289.
- Moretti I., Delos V., Letouzey J., Otero A., and Calvo J. C. (2007) - The Use of Surface Restoration in Foothills Exploration: Theory and Application to the Sub- Andean Zone of Bolivia. In O. Lacombe, F. Roure, J. Lav, and J. Vergs, ed., *Thrust Belts and Foreland Basins, Frontiers in Earth Sciences*, Springer Berlin Heidelberg 149–162.
- Muron P. (2005) - Méthodes numériques 3-D de restauration des structures géologiques faillées. PhD thesis, INPL, Nancy.
- Narkiewicz, M., Resak, M., Littke, R., and Marynowski, L. (2010). New constraints on the Middle Palaeozoic to Cenozoic burial and thermal history of the Holy Cross Mts. (Central Poland): results from numerical modelling. *Geologica Acta* 8, 189–205.
- Oszczepalski, S. (1999) - Origin of the Kupferschiefer polymetallic mineralization in Poland. *Mineralium Deposita* 34, 599–613.
- Oszczepalski, S. and Speczik S. (2011) - Prospectivity analysis of the Polish Kupferschiefer - New insights, in 11th biennial meeting “Let’s talk ore deposit”, Antofagasta, Chile. 295 – 297.
- Pellerin J., Lévy B., and Caumon G. (2012) - Conformal hybrid meshing of structural models. 32nd gOcad Meeting Report, LIAD, Nancy, France.
- Pieczonka J., Piestrzyński A., Lutyński P., (2007). Comparison between stratabound Copper-Silver mineralization of Mitu formation, Peru, and Polish Kupferschiefer Deposit. In: *Digging Deeper, Proc. 9th Biennial SGA Meeting, Dublin 2007*, C.J. Andrew et.al. (eds), 241-244.
- Pieczonka, J., Piestrzyński, A., Mucha, J., Głuszek, A., Kotarba, M and Więclaw D. (2008) - The Red-bed-type precious metal deposit in the Sieroszowice-Polkowice copper mining district, SW Poland. In: *Annales Geologorum Poloniae* 78(3): 151–280.
- Pieczonka J., Piestrzyński A., (2011a) - Mineral zonation in the Lubin-Sieroszowice mining district, Kupferschiefer-type deposit, SW Poland. In: *Let’s Talk Ore Deposits*, Bara F. et al eds, *Proceedings of the 11th Biennial SGA Meeting, Antofagasta*, 1, 43-45.
- Pieczonka, J. and Piestrzyński, A. (2011b) - Gold and other precious metals in copper deposit, Lubin-Sieroszowice district, SW Poland. In: *Gold in Poland*, A. Kozłowski and S. Mikulski eds, MSC of the PAS, UW Warsaw and PGI Warsaw: 135-152.
- Piesterzyński, A., and Wodzicki, A. (2000). Origin of the gold deposit in the Polkowice- West Mine, Lubin-Sieroszowice Mining District, Poland. *Mineralium Deposita* 35, 37–47.
- Piesterzyński, A., Pieczonka, J., and Głuszek, A. (2002). Redbed-type gold mineralisation, Kupferschiefer, south-west Poland. *Mineralium Deposita* 37, 512–528.
- Poblet J. and Stuart H. (1995) - Reverse modeling of detachment folds; application to the Pico del Aguila anticline in the South Central Pyrenees (Spain). *Journal of Structural Geology*, 17(12), 1707–1724.
- Pytel W. (2003) - Rock mass-mine workings interaction model for polish copper mine conditions. *Int. Journal of Rock Mechanics and Mining Sciences*, 40, 497–526.
- Resak, M., Narkiewicz, M., and Littke, R. (2008). New basin modelling results from the Polish part of the Central European Basin system: implications for the Late Cretaceous–Early Paleogene structural inversion. *Int. Journal of Earth Sciences* 97, 955–972.
- Rouby D., Xiao H., and Suppe J. (2000) - 3-D restoration of complexly folded and faulted surfaces using multiple unfolding mechanisms. *AAPG Bulletin*, 84(6), 805–829.
- Royer J.-J. (2012) - Hydraulic fracturing in homogeneous media, 32th Meeting, Gocad Research Group, Nancy, France, 20p.
- Slater J. and Christie P. (1980) - Continental stretching: an explanation of the Post- Mid-Cretaceous subsidence of the Central North Sea basin. *Journal of Geophysical Research*, 85(5), 3711–3739.
- Scheck-Wenderoth, M., and Lamarche, J. (2005). Crustal memory and basin evolution in the Central European Basin System—new insights from a 3D structural model. *Tectonophysics* 397, 143–165.
- Speczik, S. (1995) - Restauation et incertitudes structurales: changement d’échelles des propriétés mécaniques et gestion de la tectonique salifère. PhD Thesis, INPL, Nancy.
- Speczik, S. (1995) - Restauation et incertitudes structurales: changement d’échelles des propriétés mécaniques et gestion de la tectonique salifère. PhD Thesis, INPL, Nancy.
- Stephenson, R.A., Narkiewicz, M., Dadlez, R., van Wees, J.-D., and Andriessen, P. (2003). Tectonic subsidence modelling of the Polish Basin in the light of new data on crustal structure and magnitude of inversion. *Sedimentary Geology* 156, 59–70.
- Symons D., Kawasaki K., Walther S., and Borg G. (2011) - Paleomagnetism of the Cu-Zn-Pb-bearing Kupferschiefer black shale (Upper Permian) at Sangerhausen, Germany. *Mineralium Deposita*, 46(2), 137–152.
- Titeux M.-O. (2009) - Restauation et incertitudes structurales: changement d’échelles des propriétés mécaniques et gestion de la tectonique salifère. PhD Thesis, INPL, Nancy.

- Verral P. (1981) - Structural interpretation with application to North Sea problems. In Course note no. 3 Joint Association for Petroleum Exploration courses (UK).
- Vaughan, D.J., Sweeney, M.A., Friedrich, G., Diedel, R., and Haranczyk, C. (1989). The Kupferschiefer; an overview with an appraisal of the different types of mineralization. *Economic Geology* 84, 1003–1027
- Wagner, T., Okrusch, M., Weyer, S., Lorenz, J., Lahaye, Y., Taubald, H., and Schmitt, R. (2010). The role of the Kupferschiefer in the formation of hydrothermal base metal mineralization in the Spessart ore district, Germany: insight from detailed sulfur isotope studies. *Mineralium Deposita* 45, 217-239.
- Więclaw D., Pieczonka J., Kotarba M.J., Piestrzyński A., (2007). Geochemical characteristics of organic matter and its relation to ore mineralization in Kupferschiefer, Lubin-Sierszowice deposit, SW Poland. In: *Digging Deeper, Proceedings of the ninth Biennial SGA Meeting, Dublin 2007*, C.J. Andrew et.al. (eds), 225-228.
- Wodzicki A. and Piestrzyński A., 1994: An ore genetic model for the Lubin-Sierszowice mining district, Poland. *Mineralium Deposita* 29(1), 30-43.

Part IV

**The Iberian Pyrite Belt and Ossa Morena
Zone**

Introduction and Geological Setting of the Iberian Pyrite Belt

9

C. Inverno, A. Díez-Montes, C. Rosa, J. García-Crespo, J. Matos, J.L. García-Lobón, J. Carvalho, F. Bellido, J.M. Castello-Branco, C. Ayala, M.J. Batista, F. Rubio, I. Granado, F. Tornos, J.T. Oliveira, C. Rey, Vítor Araújo, T. Sánchez-García, Z. Pereira, P. Represas, A.R. Solá and P. Sousa

Abstract

The 250 × 20–70 km Iberian Pyrite Belt (IPB) is a Variscan metallogenic province in SW Portugal and Spain hosting the largest concentration of massive sulphide deposits worldwide. The lowermost stratigraphic unit is the early Givetian to late Famennian-Strunian (base unknown) Phyllite-Quartzite Group (PQG), with shales, quartz-sandstones, quartzwacke siltstones, minor conglomerate and limestones at the top. The PQG is overlain by the Volcanic Sedimentary Complex (VSC), of late Famennian to mid-late Viséan age, with a lower part of mafic volcanic rocks, rhyolites, dacites and dark shales, hosting VHMS deposits on top (many times capped by a jasper/chert layer), and an upper part, with dark, purple and other shales and volcanogenic/volcaniclastic rocks, carrying Mn oxide deposits. The VSC is covered by the thousands of meters thick Baixo Alentejo Flysch Group of late Viséan to Moscovian age. The VSC

C. Inverno (✉) · J. Carvalho · M.J. Batista
I. Granado · J.T. Oliveira · P. Represas · A.R. Solá
Laboratório Nacional de Energia e Geologia
(LNEG), Estrada Portela—Zambujal, Apartado
7586, 2610-999 Alfragide, Portugal
e-mail: carlos.inverno@lneg.pt

A. Díez-Montes · J. García-Crespo · J.L. García-Lobón
F. Bellido · C. Ayala · F. Rubio · C. Rey
T. Sánchez-García
Instituto Geológico y Minero de España (IGME),
C/ Ríos Rosas, 23, 28003 Madrid, Spain

C. Rosa
Empresa de Desenvolvimento Mineiro SA (EDM),
Rua Sampaio e Pina 1 3 DTO, 1070-248 Lisboa,
Portugal

J. Matos · P. Sousa
LNEG, Rua Frei Amador Arrais, 39 r/c, Apartado
104, 7801-902 Beja, Portugal

J.M. Castello-Branco
Geology and Geotechnics Consultores Lda., Rua
Cunha Júnior, 41b Sala 1.6, 4250-186 Porto,
Portugal

C. Ayala
Institute of Earth Sciences Jaume Almera (CSIC),
C/ Lluís Solé i Sabarís, s/n, 08028 Barcelona, Spain

F. Tornos
CSIC-INTA, Ctra. Ajalvir, km 4, 28850 Torrejón de
Ardoz, Spain

V. Araújo
Rua Sub-carreira, 575, 4815-517 Vizela, Portugal

Z. Pereira
LNEG, Rua da Amieira, Apartado 1089, 4466-901
S. Mamede Infesta, Portugal

comprises a bimodal submarine volcanic succession, with VHMS deposits spatially associated to dacites and rhyolites corresponding to effusive/explosive lava-cryptodome-pumice cone volcanoes. The lava/domes consist of coherent lithofacies surrounded by clast-rotated hyaloclastite breccia and minor autobreccia, with massive VHMS ore at the top of the felsic effusive units and stockworks in the autoclastic and pyroclastic breccias. The eastern IPB rocks are intruded by the voluminous Sierra Norte Batholith (tonalite-trondhjemite-granodiorite, TTG series). Felsic volcanic rocks (dacite to high-silica rhyolite) predominating over basalts and dolerites, belong to the calc-alkaline series and plot mostly in the within-plate field in tectonic discriminative diagrams. Several periods of volcanism, from 384 to 359 Ma are recognized. Dacites and rhyolites exhibit Nd and Sr enrichment, typical of a crustal signature, and their overall geochemistry suggests generation by fractionation/partial melting of amphibolites at low pressure. Trace elemental modelling of the basic rocks, involving tholeiitic lavas and alkaline basaltic lavas and dolerites, points to mixing between E- and N-MORB and assimilation of crustal material. Variscan NW-SE/W-E-trending and SW- or S-verging folds (with NE- or N-dipping planar cleavage) and thrusts, occur in west-central and eastern IPB, respectively. In late to post-Variscan time strike-slip oblique faults formed, either N-S to NNW-SSE or NE-SW to ENE-WSW, dextral or sinistral (both extensional), respectively. The first set hosts late Variscan Cu-Pb-Ba veins and Mesozoic(?) dolerite dykes. IPB contains over 90 VHMS deposits, estimated before erosion at >1700 Million tonnes (Mt), with 14.6 Mt Cu, 34.9 Mt Zn, 13.0 Mt Pb, 46,100 t Ag, 880 t Au and many other metals, particularly Sn. Eight of these are giant (≥ 100 Mt) VHMS deposits, namely Rio Tinto, Tharsis, Aznalcóllar-Los Frailes, Masa Valverde, Sotiel-Migollas and La Zarza (Spain) and Neves Corvo and Aljustrel (Portugal). The VHMS deposits are of the felsic-siliclastic type and mostly of the Zn-Pb-Cu and Zn-Cu-Pb metal content types. The deposits range in thickness from 1 m to tens of meters (plus increase from tectonic stacking) and up to a few kilometers in extension, and many are underlain by large stockwork zones. Their age is either Strunian (palynological age) in the southern IPB or mostly Tournaisian in the northern IPB. The major massive ore minerals are pyrite, sphalerite, chalcopyrite, galena (and cassiterite at Neves Corvo), also present with dominant quartz-chlorite-sericite-carbonate in the stockwork ore. Sericite and chlorite were also formed from additional alteration in the hanging wall rocks. Metal zonation in most VHMS deposits consists of a Cu-rich stockwork and base of the massive ore, with Zn-Pb massive ore above and extending laterally. S-, O-, H- and C-isotope data indicate that ore-forming fluids contain predominant or exclusive modified seawater. A magmatic fluid contribution to the dominant seawater has been proposed for some deposits. The deposits are exhalative or formed by shallow subsurface replacement of either muds/shales or coherent felsic volcanic rocks.

9.1 Geologic Setting

The metallogenic province known as the Iberian Pyrite Belt (IPB), in southwestern Portugal and Spain, is one of the domains of the South Portuguese Zone in the Iberian Massif (Oliveira 1990; Fig. 9.1). It is a 250 km long and 20–70 km wide belt, bounded to the north by the Pulo do Lobo Domain (PLD) and overlain by the Baixo Alentejo Flysch Group (BAFG) also designated as Culm. The South Portuguese Zone (SPZ) constitutes the southernmost paleogeographic and paleotectonic unit of the European Variscan orogen.

The PLD, tectonically structured as a Variscan antiform (Pereira et al. 2006), is a succession of highly sheared phyllites intercalated with MORB type basalts in the lower part (Pulo do Lobo Formation), which grades into the south to the overlying highly deformed sandstone dominated Atalaia Formation. The age of these units is not well constrained, the Pulo do Lobo Formation, based on U-Pb zircon ages (Braid et al. 2011) is suggested to be middle-late(?) Silurian to middle Devonian in age. These units are overlain in both limbs of the antiform by a flyschoid sequence

which age ranges from the upper Frasnian to the upper Famennian (Pereira et al. 2006, 2008). Various tectonic interpretations have been suggested for the PLD: (i) an accretionary prism in close association with a subduction zone dipping to the north below the Ossa-Morena Zone as a consequence of the Rheic Ocean closure (Munhá et al. 1986a; Quesada et al. 1994; Pereira et al. 2006; Ribeiro et al. 2007); (ii) an independent terrane (Ribeiro et al. 1990); (iii) an escaped crustal block that resulted from the Iberia indentation with Laurussia, responsible for the generation of the Ibero-Armorican arc (Braid et al. 2011) and, finally, (iv) the infilling of a deep extensional basin between the SW border of the Ossa Morena Zone and the Iberian Pyrite Belt (Pereira et al. 2012a).

The IPB is one of the most outstanding ore provinces of the world. It represents the largest crustal anomaly in sulphur (Laznicka 1999) and arguably hosts the largest concentration of volcanogenic massive sulphide deposits worldwide, including several world-class and giant deposits such as Río Tinto in Spain and Neves Corvo in Portugal (Tornos 2006). Mining in the IPB is documented from 4000 BC and the exploitation

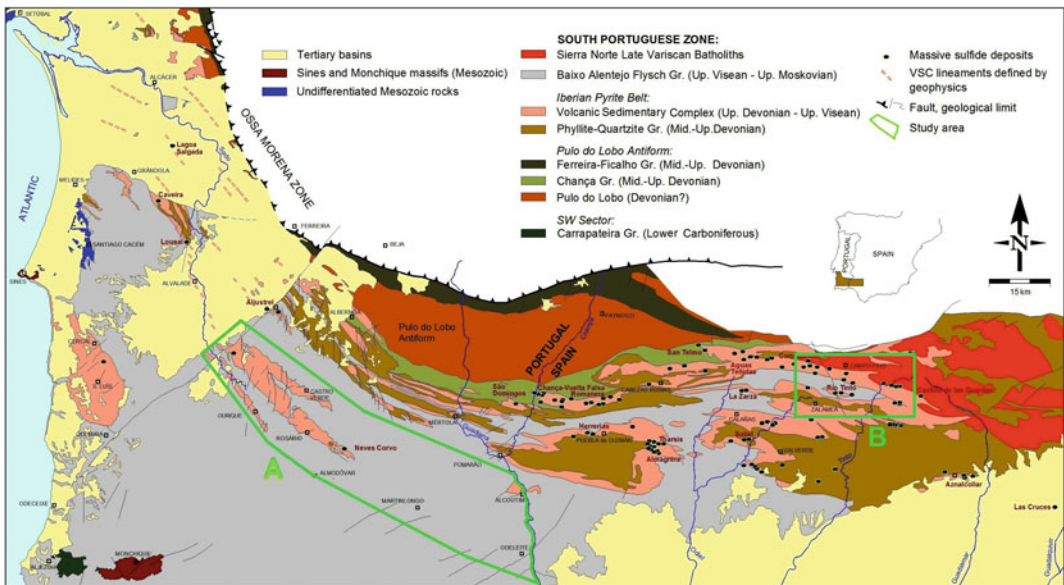


Fig. 9.1 Regional geology of the South Portuguese Zone, including the Iberian Pyrite Belt and associated VHMS deposits and showing location of the Neves Corvo (A) and Río Tinto (B) project areas

has been oriented to the extraction of precious (Au, Ag) and base (Cu, Zn, Pb) metals and pyrite.

The IPB is composed of three major lithostratigraphic units, the Phyllite Quartzite Group (PQG), the Volcanic Sedimentary Complex (VSC), which is the focus of the present work, and the Baixo Alentejo Flysch Group (BAFG) (Schermerhorn 1971; Oliveira 1983). General syntheses on the IPB include those of Strauss et al. (1977), Routhier et al. (1980), IGME (1982), Barriga (1990), Sáez et al. (1996), Leistel et al. (1998), Carvalho et al. (1999), Junta de Andalucía (1999), Tornos et al. (2000), Tornos (2006). Other general studies deal with stratigraphy (Oliveira 1990; Pereira et al. 2007), volcanism (Munhá 1983; Mitjavila et al. 1997; Thiéblemont et al. 1998), structure and regional metamorphism (e.g., Munhá 1990; Silva et al. 1990; Quesada 1998) or the facies architecture of the volcano-sedimentary complex (Soriano and Martí 1999; Junta de Andalucía 1999; Rosa 2007).

The Baixo Alentejo Flysch Group well exposed in SW Iberia, represents the infill of a foreland basin, which was developed following a compressive Variscan tectonic inversion that occurred during the upper Visean and lasted until the upper Moscovian (Oliveira et al. 1979; Silva et al. 1990; Pereira et al. 2008). The sandy/shale turbidites that filled the foreland basin had their multiple sources in the SW border of the Ossa Morena Zone, in the IPB and in the Avalonia plate (Jorge et al. 2012).

9.2 Stratigraphy

The lowermost lithostratigraphic unit in IPB is the Phyllite-Quartzite Group (PQG), underlying the Volcanic Sedimentary Complex (VSC). The PQG is largely dominated by dark shales in which there are interbedded packets of quartz-sandstones, quartzwacke siltstones, rare conglomerates and carbonate lenses and nodules at the top. The quartz-sandstone beds are predominantly massive or show less frequent parallel lamination, large scale cross bedding and graded bedding. The siltstones are thin-bedded and

current ripples are common. The quartzwackes are massive or show rare graded bedding.

In the northern branch of the IPB (Oliveira 1990) the PQG lithologies are organized in allochthonous tectonic sheets and the sandstones are frequently disrupted in lenses, blocks and pebbles of variable size, which make sedimentological studies difficult. This disruption is mainly caused by tectonism but, at least in part, was formed by large debris flows (Oliveira 1990; Moreno et al. 1995). Detailed palynostratigraphic studies of drill-holes and sections, complemented by regional geological studies, from the northern branch of IPB, indicate that the age of PQG unit spans from the upper Famennian to the upper Strunian (Upper Devonian). Furthermore, it confirms that here the PQG tectonically overlies the VSC sequence.

In the southern branch of the IPB the PQG lithologies are associated with antiformal structures. In spite of the tectonic deformation, the PQG lithologies appear organized in a very thick megasequence (up to 2000 m thick), in which the quartz-rich sandstones are more abundant at its upper part. The age of the PQG, based on detailed palynostratigraphic data, ranges from the lower Givetian of middle Devonian (Junta de Andalucía 1999; Pereira et al. 2008, 2009), in the WNW region of the IPB, Frasnian (Rodríguez et al. 2002; López et al. 2004), to the late Famennian and Strunian of the Upper Devonian in the entire IPB (Junta de Andalucía 1999; Rodríguez et al. 2002; Pereira et al. 2008). Palynomorph assemblages include well to moderately preserved acritarchs and prasinophytes, substantiating a shallow marine depositional environment for these rocks (Junta de Andalucía 1999; Pereira et al. 2008). Sedimentological studies in the Virgen de la Peña region (Moreno and Sáez 1990) and at Berrocal (Jorge et al. 2007) prove that the PQG sediments were deposited in shallow water marine platform environments, confirming palynologic data.

A particular characteristic of this south branch is the occurrence of a decametric thick lithological unit composed of dark shales with intercalations of limestone lenses and nodules at the top of the PQG megasequence. The limestones

display excellent faunas of conodonts of late Famennian age (Boogaard 1963; Boogaard and Schermerhorn 1980, 1981).

The stratigraphically overlying VSC is dominated by shales and thin-bedded siltstones, and minor volcanogenic sedimentary rocks. The latter sedimentary units encompass dominant felsic volcanic rocks (rhyolites, rhyodacites and dacites), mafic volcanic rocks (basalts and dolerites), either in the foot- or hanging wall of the volcanogenic massive sulphide (VHMS) deposits, and minor andesites. The felsic rocks occur dominantly as lava/dome complexes, associated with minor pyroclastic flows and intrusions (Martí Molist et al. 1994; Soriano and Martí 1999; Junta de Andalucía 1999; Rosa et al. 2010a). The massive sulphide ore deposits and related hydrothermal systems, when present, usually occur at the top of felsic volcanic rocks in close association with black shales and may have a relatively thin layer of jasper/carbonates commonly at the top (Leca et al. 1983; Barriga and Kerrich 1984; Carvalho et al. 1999). Most of the black mudstones that enclose the massive sulphide ores are of late Strunian age (e.g., Neves Corvo, Lousal, Caveira, Montinho, Aznalcóllar and Tharsis) based on their palynomorph assemblages (Pereira et al. 1996, 2008, 2012b; González et al. 2002; Oliveira et al. 2004; Matos et al. 2011).

A notable characteristic of this complex is the occurrence of a decametric thick level of purple, green and grey shales at its upper part. This level occurs throughout the IPB at the same stratigraphic position, which is an excellent marker for lateral correlation and mapping purposes. Palynostratigraphic data allowed dating the VSC at late Famennian to mid late Viséan (Oliveira et al. 2004, 2005; Pereira et al. 2007). Several chronostratigraphic gaps were identified in the Portuguese part of the IPB succession, the most important being the absence of Tournaisian sedimentary rocks, e.g. in the Neves-Corvo area (Oliveira et al. 2004). The occurrence of marine fossils (mainly prasino-phytes algae and conodonts of early late Viséan age) in the VSC indicates that it formed in a submarine setting. The VSC thickness is variable across the basin and reaches 1300 m in the

proximity of volcanic centres. In many regions of the IPB, the VSC has been divided into several lithostratigraphic units. The dating of all these units across the IPB is a fundamental step towards a regional stratigraphic correlation and consequently better understanding of the IPB basin development. This approach is essential for massive sulphide ore exploration.

The eastern IPB rocks are intruded by large volumes of subvolcanic-plutonic rocks of the Sierra Norte Batholith (SNB) (Simancas 1983; De la Rosa 1992). The SNB includes three types of geochemical associations, mafic rocks (gabbrodiorite) with ultramafic cumulates, subvolcanic TTG intrusions, tonalite, trondhjemite and granodiorite (Schütz et al. 1987; Halsall 1989; Díez-Montes and Bellido-Mulas 2008; Díez-Montes et al. 2011) with an age range of 335–355 Ma (Dunning et al. 2002; Barrie et al. 2002; Gladney et al. 2014, in press), and aluminopotassic granitoid plutons that intruded the TTG group (Díez-Montes and Bellido-Mulas 2008). There is common evidence of mingling between the TTG and the mafic rocks.

U–Pb dating of zircons has been carried out in several places in the IPB (Nesbitt et al. 1999; Barrie et al. 2002; Dunning et al. 2002; Rosa et al. 2009; Valenzuela et al. 2011). The age determinations were predominantly made of felsic rocks (rhyolites and rhyodacites). More recently, new data was obtained for felsic rocks of the Neves Corvo-Rosário Antiform, Portugal, and five episodes of volcanism were recognized, from 359 to 384 Ma. This means that in these regions high heat flow was maintained for ~30 Ma and may have been responsible for the generation and maintenance of hydrothermal convective cells that contributed to the genesis of the massive sulphide ores (Oliveira et al. 2013). However, a better age constraint of the lithological sequences is still needed.

The VSC was formed as a consequence of a Famennian to mid-late Viséan extensional tectonic regime that disrupted the siliciclastic platform in extensional graben-type basins (Oliveira 1990) related to continent (South Portuguese Zone)-continent (Ossa Morena Zone) oblique collision (Silva et al. 1990; Quesada 1998;

Tornos et al. 2005). From a paleogeographic point of view it has been suggested that the PQG and the VSC were situated at the eastern margin of the Avalonia plate (Oliveira and Quesada 1998; Ribeiro et al. 2007) or that they have affinities with the Meguma terrane (Braid et al. 2011) before their integration in the Variscan Chain following the Rheic Ocean closure and culmination of the amalgamation of the Pangea supercontinent by the collision between Gondwana and Laurussia during the late Palaeozoic.

9.3 Physical Volcanology

The Volcanic Sedimentary Complex (VSC) of the IPB comprises a bimodal volcanic submarine succession that together with accompanying sedimentary rocks hosts one of the largest concentrations of massive sulphide deposits in the earth's crust. The massive sulphide deposits are considered to be spatially associated to felsic (dacitic to rhyolitic) volcanic units (Routhier et al. 1980; Barriga 1990; Barriga et al. 1997), black shales (Barriga et al. 1997; Tornos 2006), or both (Barriga et al. 1997; Sáez et al. 1999; Relvas 2000; Tornos 2006). The volcanic rocks are only approximately 25 % of the stratigraphic record of the VSC, the remaining 75 % are mainly mudstone.

Studies of the volcanic facies architecture of the VSC in several areas of the IPB interpreted the felsic volcanic centres as constructed by a combination of effusive and explosive volcanic units and high-level intrusions (e.g., Martí Molist et al. 1994; Soriano and Martí 1999; Boulter 1993, 1996; Donaire et al. 2002; Rosa et al. 2008; Valenzuela et al. 2011). Recently, a regional study of the volcanic and sedimentary facies architecture in SW Iberia pointed out that the felsic volcanic centres correspond to "lava-cryptodome-pumice cone volcanoes" (Junta de Andalucía 1999; Rosa et al. 2010a). These volcanoes have formed in submarine setting at variable water depth and can be up to 8 km laterally and 800 m thick (Rosa et al. 2010a).

The volcanic centres consist of a variety of lithofacies that correspond to felsic lavas and domes, pyroclastic units and intrusions; and minor mafic lavas, locally showing pillows, and intrusions. The felsic lavas/domes are dominant and can occur at several stratigraphic levels. The pyroclastic units are mostly lava/dome derived and less voluminous than the lava/domes. The intrusions are minor and occur as cryptodomes, partly extrusive cryptodomes and sills. The architecture of the felsic centres throughout the IPB comprises different combinations and proportions of these units (Rosa et al. 2010a).

The lava/domes typically consist of thin intervals of coherent lithofacies that are surrounded by very thick intervals of in situ and clast-rotated hyaloclastite breccia and minor autobreccia. The coherent lithofacies are characterized by microcrystalline groundmass textures and may also show spherulites and lithophysae. The hyaloclastite breccias typically comprise angular clasts with planar and curvilinear margins and abundant perlite fractures in the groundmass. These breccias are abundant throughout the VSC and indicate that the felsic effusive units had glassy groundmasses that underwent significant quenching in contact with water. Units of bedded hyaloclastite derived from the clastic components of the lava/domes occur on top of and laterally from the lava/domes (Rosa et al. 2011).

The cryptodomes and partly extrusive cryptodomes, contrary to the lava/domes, consist of thick intervals of coherent facies and thin margins of hyaloclastite and autobreccia. The partly extrusive cryptodomes may have small aprons of redeposited hyaloclastite. The pyroclastic units display mainly fiamme, interpreted to have been pumice clasts, crystal fragments and sedimentary and dense volcanic clasts (Rosa et al. 2010a). The pyroclastic deposits can occur as thin units with limited lateral extent overlying the lava/domes, or as relatively thick units with several kilometres of extension, indicating that explosive eruptions produced a significant volume of felsic rocks.

The VSC also comprises well-defined beds of volcanogenic sandstones and breccias, locally

showing graded bedding and load casts. These units occur laterally or above the volcanic centres and their bedded nature indicate that they were deposited from water-supported gravity currents (Rosa et al. 2011). The composition is consistent with a source from the clastic volcanic components of the lava/domes and pyroclastic units (Rosa et al. 2010a).

Some massive sulphide ore deposits occur on top of the felsic effusive units (e.g. Neves Corvo, Aljustrel, São Domingos and Lousal; Rosa et al. 2008, 2010a, b), and the mineralizing hydrothermal alteration stockworks are hosted and deeply rooted in these units. These spatial associations suggest that the ore-forming hydrothermal activity occurred at the late stages of effusive volcanic events, and that also a strong genetic relationship between the ore-forming processes and the volcanic activity exists. Within the volcanic centres, the stockworks were emplaced preferentially in the breccia zones (autoclastic and pyroclastic) due to their low permeability, which favoured the circulation of hydrothermal fluids.

9.4 Geochemistry of Volcanic Rocks

Volcanism of the Volcanic Sedimentary Complex (VSC) is mainly bimodal, with a predominance of felsic (dacitic to rhyolitic volcanites) over basic rocks (basalts and dolerites). Although subordinate on a regional scale, andesitic lavas also occur (Munhá 1983; Mitjavila et al. 1997; Díez-Montes et al. 1999).

Felsic rocks range from dacite to high-Si rhyolites and belong to a calc-alkaline series. Rhyolites (and Sierra Norte Batholith leucogranites) show similar REE patterns displaying moderate LREE enrichment, pronounced negative Eu anomalies, and relatively flat to slightly HREE enrichment (Munhá 1983; Díez-Montes and Bellido-Mulas 2008). Dacites (and tonalites) are enriched in Al_2O_3 , TiO_2 , and P_2O_5 and display smaller negative Eu-anomalies relative to most rhyolites (e.g., Munhá 1983). On primitive

mantle-normalized spider plots for trace elements, all the intermediate-felsic rocks show similar patterns, with negative anomalies in Nb, Th and Ti (Díez-Montes and Bellido-Mulas 2008). As a group, they define a low-Al TTG and high-HREE series (Arth et al. 1978), broadly equivalent to the FII dacite-rhyolite group of Leshner et al. (1986), Hart et al. (2004). These series are commonly related to massive sulphide deposits.

Dacites and rhyolites exhibit an enriched crustal signature based on the Nd and Sr isotopic systematics, consistent with derivation from an older crust (Mitjavila et al. 1997). The zircon inheritance provides direct evidence for older (Proterozoic to Ordovician) detrital components in their source rocks (Barrie et al. 2002; Rosa et al. 2009). The diversity of chemical and Sr–Nd isotopic composition of rhyolites, dacites and minor andesites can mainly be explained either by differences in composition of the source rocks or by different degrees of partial melting of upper crust (e.g., Mitjavila et al. 1997). Andesites have been interpreted as formed due to contamination (mixing) between basaltic magmas and upper-crust material (Mitjavila et al. 1997). The geochemical characteristics of felsic magmatism suggest that they were generated by fractionation/partial melting of amphibolites at low pressures, involving plagioclase and pyroxene in the petrogenetic process without involvement of garnet, and with a significant contamination of crustal material (Díez-Montes and Bellido-Mulas 2008).

The geochemical similarities between the volcanic rocks of the VSC and the TTG plutonic rocks of the SNB (Schütz et al. 1987; Thiéblemont et al. 1998; Díez-Montes and Bellido-Mulas 2008; Díez-Montes et al. 2011), as well as the available U–Pb geochronology data (Barrie et al. 2002; Dunning et al. 2002; Valenzuela et al. 2011) suggest that the Volcano-Sedimentary Complex was approximately coeval and cogenetic with the TTG plutonic rocks of the Sierra Norte Batholith.

Based on geochemical characteristics of rocks and minerals, two main types of mafic rocks are distinguished: (1) tholeiitic lavas, which crop out across the whole IPB; and (2) alkaline lavas and

dolerites which are similar to recent within-plate basalts, and restricted to the western and southern parts of the IPB. According to Munhá (1983) alkaline basalts are restricted to the upper part of the volcanic sequence, in the Portuguese sector, while in the Spanish sector there is no evidence of a temporal evolution from tholeiitic to alkaline basalts (e.g., Mitjavila et al. 1997).

The tholeiitic lavas show a wide range of geochemical characteristics, medium La/Nb (1–2) and Y/Nb (2–7) compositions, similar to recent continental tholeiites, whereas higher ratios of La/Nb (>2) and Y/Nb (>6) have some affinities to arc-related basalts (Munhá 1983; Thiéblemont et al. 1998). Alkaline-affinity basalts show higher TiO₂, P₂O₅, and LREE and lower Y/Nb ratio. The lavas with andesitic compositions are spatially and temporally associated with tholeiitic basic lavas and fall into the field of normal calc-alkaline series rocks (K₂O < 2.5 wt %; e.g. Munhá 1983).

Although closely associated, the felsic and mafic volcanic rocks originated and evolved independently. No lithological transitions occur, the volcanic centres are distinct, and available geochemical and isotopic data refute any relationship by pure fractional crystallization between basalts, andesites and felsic rocks (e.g., Munhá 1983; Mitjavila et al. 1997). The mafic rocks were formed due to partial melting of the asthenospheric mantle, whereas the felsic volcanism derived from crustal anatexis, possibly promoted by heat supplied by rising mafic magmas (Munhá 1983; Mitjavila et al. 1997; Thiéblemont et al. 1998), at low- to medium-pressures and steep geothermal gradients. This makes the IPB different from the massive sulphide-bearing volcanic arc-related series and settings (Leistel et al. 1998).

Petrogenetic modelling of trace elements of the various basalts precludes an evolution solely by fractional crystallization and the variable compositions can be explained by a single mixing model between E- and N-MORB and assimilation of crustal material (Mitjavila et al. 1997). However, the mixing model between E- and N-MORB used to explain the origin of the most

primitive basaltic rocks does not discriminate between the origin of both tholeiitic and alkaline affinities in the same magmatic context (Mitjavila et al. 1997). The existence of tholeiitic and alkaline rocks may be explained by different degrees of partial melting of a peridotitic mantle (Mitjavila et al. 1997), but according to Munhá (1983) at least two different mantle sources are required to explain the compositional differences.

Overall, the bimodal nature, with continental tholeiites and the alkaline character of some lavas, with only minor amounts of intermediate rocks, points to a consensual extensional tectonic setting for the genesis of VSC (e.g., Munhá 1983; Mitjavila et al. 1997; Thiéblemont et al. 1998; Rosa et al. 2006). However, there are different opinions regarding the regional significance of this extensional tectonic setting.

9.5 Structural and Tectonic Evolution

The IPB is interpreted to correspond to basins generated by the oblique collision of the South Portuguese Zone and the autochthonous Iberian terranes (north Gondwana), during the Devonian-Carboniferous (Silva et al. 1990; Quesada 1991; Oliveira et al. 2004; Tornos et al. 2005). This transtensive tectonic regime triggered volcanism that formed the felsic and mafic volcanic rocks that occur in the IPB, and the geothermal gradients that permitted the hydrothermal activity responsible for the IPB massive sulphide deposits. The change to a transpressive regime was responsible for the Variscan deformation (Upper Devonian to Carboniferous) that disrupts the IPB stratigraphy, corresponding to a thin-skinned foreland fold and thrust belt (Silva et al. 1990; Quesada 1998), confirmed by deep seismic reflection studies (Simancas et al. 2003). The IPB structure e.g. in the Central Domain of South Portuguese Zone (Fig. 9.1; Mantero et al. 2007), is characterized by northwest-southeast trending folds verging towards southwest (with axial plane cleavage steeply dipping to NE) and thrusts in the western part of the IPB, and east-west

trending folds verging towards south (with cleavage dipping to N) and thrusts in the central and eastern IPB.

Late- to post-Variscan faulting is expressed as oblique strike-slip faults. N-S to NNW-ESE-striking, dextral/extensional faults, conjugate NE-SW to ENE-WSW-striking, sinistral/extensional faults, such as the Messejana Fault (with 4 km of displacement and down-drop of the NW block), and additional E-W-striking, commonly sinistral faults (Ribeiro 1984; Schermerhorn et al. 1987; Oliveira and Araújo 1992; Liñán 1994; Quesada 1996, 1998; Leitão 1997) are the main features. Cu, Pb and Ba mineralized quartz/carbonate veins typically infill some of these faults, particularly the NE-SW to ENE-WSW-striking faults, and Mesozoic (?) microgabbro and lamprophyre dykes were later emplaced within the same fault set in the Portuguese part of IPB (Oliveira and Araújo 1992).

9.6 Mineral Deposits

9.6.1 General

The IPB contains about 90 volcanogenic massive sulphide (VHMS) deposits, estimated before erosion at over 1700 Mt containing 14.6 Mt Cu, 34.9 Mt Zn, 13.0 Mt Pb, 46,100 t Ag, 880 t Au and significant amounts of other metals, in particular Sn (Leistel et al. 1998). About 20 % of the total amount has been mined and 10–15 % was lost to erosion. The belt includes eight giant VHMS deposits, >100 Mt: Rio Tinto, Tharsis, Aznalcóllar-Los Frailes, Masa Valverde, Sotiel-Migollas and La Zarza in Spain and Neves Corvo and Aljustrel in Portugal. Three of these are supergiants (>200 Mt): Río Tinto (500 Mt), Neves Corvo (>300 Mt) and Aljustrel (>200 Mt). Additional world-class VHMS deposits (>30 Mt) are Concepción, La Romanera, Aguas Teñidas Este and Las Cruces in Spain, and Lousal and S. Domingos in Portugal. The average grade of all VHMS deposits in the IPB is 45 % S, 40 % Fe, 1.3 % Cu, 2.0 % Zn, 0.7 % Pb, 26 g/t Ag and

0.5 g/t Au (Carvalho et al. 1999). Hundreds of Mn occurrences and small deposits are also related to the felsic volcanism, the most significant being Solo Viejo in Spain (Carvalho et al. 1976, 1999; Barriga et al. 1997; Leistel et al. 1998; Tornos et al. 2000; Relvas et al. 2002, 2006a; Matos et al. 2006; Tornos 2006).

The massive sulphide deposits range in thickness from 1 m to tens of metres and up to a few kilometres in extension. Many of the major deposits display several clustered lenses (2–7 in the giant deposits). Furthermore, tectonic stacking significantly increased the thickness of massive ore bodies in some deposits. Despite thrusting, most of the massive sulphides ore piles are underlain by, or imbricated with large stockwork or stringer zones, made up of sulphide-bearing, mm-thick stringers to dm-thick veins (Carvalho 1979; Leistel et al. 1998).

Several classifications have been applied to these deposits. They are divided into stratiform polymetallic massive sulphide bodies, mostly pyritic (35–51 % S or 66–96 % pyrite equivalent), semi-massive to disseminated polymetallic pyrite bodies (“safrão”), with <35 % S and stockwork ores (5–25 % S or 10–25 % pyrite equivalent) in the footwall, well developed in Rio Tinto, Aznalcóllar, La Zarza, Concepción, Aljustrel (Feitais) and Neves Corvo (Strauss et al. 1977; Carvalho et al. 1999). The IPB deposits are also included in the felsic-siliciclastic type of Barrie and Hannington (1999). Based on Large’s (1992) metal content classification most of these VHMS deposits are Zn–Pb–Cu or Zn–Cu–Pb types (including the giant deposits), with a few Cu and Cu–Pb types, and possibly still a few others belonging to the Zn–Pb type (Tornos et al. 2000). The zones with high Zn–Pb or Cu are currently the main mining targets.

Depending on their tectonic position, these VHMS deposits can be classified as autochthonous (rooted or proximal), transitional or allochthonous (redeposited or distal), with most deposits having stockwork included in the autochthonous and transitional sub-types, while some ore bodies in the Lousal, Sotiel and Tharsis deposits, without stockwork or hydrothermal

alteration are considered as allochthonous (Carvalho 1979; Barriga et al. 1997; Carvalho et al. 1999).

Based on the dominant geologic setting, Tornos (2006) classified these deposits as:

- (a) *shale-related massive sulphide deposits*, in which the massive sulphides are clustered in isolated VSC outcrops and in direct relationship to black shales volumetrically important in the VSC pile, either directly above the contact of the PQG and the VSC or above dacitic domes. These deposits are usually large, stratabound and pyrite rich, showing characteristic sedimentary features and sometimes displaying a typical siderite-pyrite ore. These deposits, many of them dated as Strunian (Pereira et al. 2008; González 2005), are located in the southern IPB and include Las Cruces, Aznalcóllar-Los Frailes, Valverde, Sotiel-Migollas, Tharsis and Neves Corvo;
- (b) *felsic volcanic-hosted massive sulphide deposits*, with minor or absent shale, with the stockwork rooted in felsic volcanic domes, many of which of early Tournaisian age, either hosted in the dome pumice- and glass-rich volcanoclastic rocks or in the dome carapace. They occur in the northern IPB and are exemplified by Río Tinto (Filón Norte), Concepción, Aguas Teñidas Este, La Zarza and Aljustrel.

Re–Os and Rb–Sr isotopic ages for sulphide and tin ores from Neves Corvo indicate formation ages of 358 ± 29 and 347 ± 25 Ma respectively (Munhá et al. 2005; Relvas et al. 2001). Based on Re–Os isotopes for the Tharsis and Río Tinto ores the obtained formation ages, also with considerable errors, were 353 ± 44 and 346 ± 26 Ma respectively (Mathur et al. 1999). As stated above, a late Strunian palynological age was obtained for the shales enclosing the massive sulphide ore in Neves Corvo, Lousal, Caveira, Montinho, Aznalcóllar and Tharsis.

9.6.2 Mineralogy

The four major minerals in massive ore are dominant fine- to medium-grained pyrite (commonly recrystallized), sphalerite, chalcopyrite and galena (also cassiterite at Neves Corvo). These minerals are also present in stockwork ore together with a quartz-chlorite-sericite-carbonate assemblage, but in different proportions. Many of the deposits exhibit common clastic textures, mostly sedimentary, but in places of tectonic origin, involving pyrite and other minerals within the massive sulphide ore pile. Accessory minerals in both ore types are tetrahedrite-tennantite, bournonite, arsenopyrite and pyrrhotite. The numerous trace minerals include magnetite (can be accessory) and electrum (Yamamoto et al. 1993; Gaspar 1996; Leistel et al. 1998; Carvalho et al. 1999). Not only sphalerite with chalcopyrite disease, but also Bi and Co sulphosalts and sulphides occur in the stockwork ore and at the base of the massive sulphide interacting with it (Marcoux et al. 1996). Tin sulphides (stannite, kesterite, mawsonite and stannoidite) occur in both massive and stockwork ores as trace minerals but are common in Neves Corvo, especially in Sn and Cu–Sn ores (Gaspar and Pinto 1991; Gaspar 2002).

9.6.3 Geochemistry

The classical VHMS zonation is present in several VHMS deposits in IPB, with Cu-rich stockwork and base of massive ore, and Zn–Pb massive ore above and extending laterally. Au is more enriched in stockwork and distal parts of the orebodies, whereas Ag is mostly associated with massive Zn–Pb ore (Leistel et al. 1998; Carvalho et al. 1999). Common chalcopyrite disease textures in sphalerite and Bi, Co, Te, Se and Cu minerals in both stockwork and basal part of the massive ore interacting with it apparently reflect late-stage copper enrichment from high-temperature Cu-bearing fluids (Marcoux et al. 1996).

S-isotope values of -35 to $+12$ per mil have been reported for pyrite and other sulphide minerals, ranging from more negative values in massive ore to more positive in stockwork ore, and indicating a predominance of reduced seawater sulphur (as do values up to 28 ‰ in barite), but with involvement of bacteriogenic sulphur particularly in samples with more negative values (Mitsuno et al. 1988; Barriga 1990; Yamamoto et al. 1993; Velasco et al. 1998; Inverno et al. 2008; Tornos et al. 2008). $\delta^{18}\text{O}$ and δD values for the hydrothermal fluids responsible for the ore formation are 0 to $+7$ per mil and -10 to $+15$ per mil, respectively, indicating seawater derivation with minor contribution from magmatic or metamorphic reservoirs (Barriga and Kerrich 1984; Munhá et al. 1986b; Barriga et al. 1997; Inverno et al. 2008). The $\delta^{13}\text{C}$ values of carbonates from massive and stockwork ores (-14.3 to -5.0 ‰) indicate a $\delta^{13}\text{C}_{\text{fluid}}$ of -15.9 to -6.6 per mil for the Aljustrel and Tharsis deposits. Coupled with O-isotope values from these carbonates, this suggests that carbonate was derived from mixing of seawater with a hot hydrothermal fluid and/or methane from degradation of organic matter, with the last to explain the lowest values (Inverno et al. 2008; Tornos et al. 2008).

The lead isotope composition (Marcoux 1998) is very similar for massive ores, the stockwork ores and for the volcanic host rocks throughout the belt, indicating that Pb in the ores and volcanic rocks was derived from the same continental crust. Only Neves Corvo displays a highly radiogenic ($^{208}\text{Pb}/^{204}\text{Pb} > 18.4$ in cassiterite) stanniferous ore, implying a more complex ore-forming process with metals derived from the basement, volcanic rocks or a magmatic source of lead (Barriga et al. 1997; Carvalho et al. 1999; Tornos et al. 2000; Relvas et al. 2001). Reported $^{87}\text{Sr}/^{86}\text{Sr}$ ratios in barite from Feitais (Aljustrel) hanging wall rocks and from the massive ore (0.708836–0.709063), from hydrothermal minerals at Tharsis (0.707301–0.722085), and from various Neves Corvo ore types (0.710881–0.713556), are all more radiogenic than late Strunian seawater (0.7080–0.7085) and than felsic volcanic rocks in the IPB in Spain (Mitjavila et al. 1997). This suggests that

ore-forming fluids in Feitais resulted from mixing of seawater with a crustal fluid (Inverno et al. 2008), only the latter fluid type would explain the high radiogenic values from Neves Corvo, particularly the tin ores (Relvas et al. 2001). The two sources explain both the low and the high values in Tharsis, the latter suggesting equilibration with either the PQG or an unknown underlying basement (Tornos and Spiro 1999; Tornos 2006).

9.6.4 Hydrothermal Alteration

A low-temperature regional seawater dominant alteration in the basalts and rhyolites, converted into “spilites” and “quartz keratophyres”, respectively (Munhá 1990), was overprinted by higher temperature ore-zone hydrothermal alteration, both in the foot- and hanging wall, pre-dating regional metamorphism. The footwall alteration consists of an internal stockwork zone with chlorite-quartz-sulphides (-carbonates), surrounded by an intermediate, peripheral stockwork zone with sericite-quartz-sulphides (-carbonates). In some deposits (e.g. Gavião, Aljustrel) these are surrounded by a distal, ultraperipheral stockwork zone with quartz-sericite—Na-sericite-chlorite-sulphide, with an overall removal of alkalis from the internal zone, fixing of K (+Ba) in the intermediate zone, and addition of Na in the outer zone (Barriga et al. 1997; Tornos et al. 1998, 2000; Carvalho et al. 1999; Relvas et al. 2011). Pyrophyllite, indicative of advanced argillic alteration in the internal zone, may be present in a few deposits (e.g., Lagoa Salgada) (Relvas et al. 1994; Oliveira et al. 1998; Matos et al. 2000; de Oliveira et al. 2011). When hosted in shales, the hydrothermal alteration related to stockworks is restricted to the chloritic type (Tornos et al. 1998, 2000).

Hanging wall alteration of many VHMS deposits in the IPB affects volcanic rocks, when present, cherts and jaspers, and pelitic sedimentary rocks. Volcanic rocks are altered to sericitic- or chloritic-dominated pyrite-bearing rocks while jaspers turn into cherts above the ore zone due to hematite reduction to magnetite and formation of chlorite+carbonate+pyrite and Mn silicates,

carbonates and oxides. As to pelitic sedimentary rocks, they commonly but not always, come to be veined with significant chlorite (Mn-rich), sericite, carbonate, barite and sulphide (Barriga and Fyfe 1988; Carvalho et al. 1999; Tornos et al. 2000; Inverno et al. 2008).

9.6.5 Metallogenesis

It is generally accepted that the IPB massive sulphides precipitated at or near the sea floor, from a dominant hydrothermal seawater fluid, as substantiated by O- and H-isotope data (Munhá et al. 1986b). However, it is disputed whether seafloor replacement occurred. Tornos et al. (2000) suggested the existence of deposits formed on the sea floor with minor footwall replacement (e.g., Río Tinto, Planes-San Antonio), deposits formed by shallow seafloor replacement of black muds (e.g., Aznalcóllar), and deposition by replacement (>50 m depth?) of reactive volcanic rocks related to stockworks, as is the case in many deposits in the northern IPB. Sáez et al. (1999) went further and proposed that most IPB massive sulphide deposits formed by seafloor replacement of black muds. Barriga and Fyfe (1988), Barriga (1990) proposed that Aljustrel massive sulphide deposits, particularly Feitais, formed by shallow seafloor replacement of volcanic and sedimentary rocks beneath a jasper cap that inhibited oxidation and dispersion of sulphides.

Currently, there are two models for the origin of VHMS mineralization in the IPB. In one, a magmatic fluid contribution to the hydrothermal dominant seawater depositional fluid has been suggested. High grade Au ores at La Zarza (Strauss and Beck 1990), pyrophyllite at Lagoa Salgada stockwork, suggesting advanced argillic alteration akin to high sulphidation deposits, and Sn ores and Cu-rich complex ores at Neves Corvo, where zone refining occurs and Bi–Co–Te–Se–Cu minerals are present in stockwork and base of massive ore, are all suggestive of a magmatic-hydrothermal contribution at least in a few of the VHMS deposits in IPB (Relvas et al. 1994; Carvalho et al. 1999). O-, H- and C-isotope data

from Neves Corvo are consistent, for the highest temperature fluids, with the involvement of a non-seawater fluid, possibly magmatic-hydrothermal fluids exsolved from a hypothetical granitic pluton emplaced at depth (Relvas et al. 2006b). However, despite the fact that melt inclusions in quartz phenocrysts in the IPB felsic volcanic rocks suggest possible Sn-rich granites at depth (Huston et al. 2011), the felsic (dacitic to rhyolitic) sub-volcanic sills occurring in several areas intruded after the formation of the VHMS deposits, contradicting Boulter's (1996) hypothesis that the intrusions triggered massive sulphide formation. Additionally, basaltic subvolcanic sills predate massive sulphides in Rio Tinto and Tharsis (Tornos et al. 1998, 2000), although in Aznalcóllar they occur beneath the massive sulphide deposits and therefore a link was suggested between mafic volcanism and VHMS deposits as possible in Aznalcóllar (Almodóvar et al. 1998; Sáez et al. 1999). In fact, in other VHMS belts there are massive sulphide deposits interpreted as formed by magmatic-hydrothermal fluids derived from subvolcanic felsic igneous complexes accompanied by mafic-ultramafic rocks (Galley 2003; Díez-Montes and Bellido-Mulas 2008). An alternative to the magmatic contribution to the hydrothermal seawater fluid could be metamorphic or crustal fluids (Sánchez-España et al. 2003; Moura 2005).

The second model is mainly based on the isotope geochemistry and geology of the deposits of the southern part of the belt. Here, the radiogenic isotope values and the lack of evidence of magmatic-hydrothermal fluids led Tornos (2006) to propose that the fluids were derived from the PQG or the underlying basement during the extension and high heat flow, which promoted faster diagenesis and dewatering of the siliciclastic sediments. The model implies the separation of fluids with intermediate salinities, rich in metals, but carrying little reduced sulphur, which were rising through the crust until they mixed with reduced seawater (Tornos and Heinrich 2008).

Additionally, deposition of the massive sulphides in a brine pool and not in a Kuroko-type mound has been proposed for several VHMS

deposits in the IPB, mostly from the southern branch, in part due to the morphology of the orebodies and to the presence of high-saline ore-forming fluids (Tornos et al. 1998; Solomon et al. 2002, 2004). This has been suggested for San Miguel, San Telmo, Aguas Teñidas and Río Tinto (Sánchez-España et al. 2003), Masa Valverde (Toscano et al. 1997), Tharsis (Tornos and Spiro 1999; Tornos et al. 2008), Aznalcóllar and Los Frailes (Almodóvar et al. 1998) and Feitais-Aljustrel (Inverno et al. 2008).

References

- Almodóvar, G.R., Saéz, R., Pons, J.M., Maestre, A., Toscano, M., Pascual, E. 1998. Geology and genesis of the Aznalcóllar massive sulphide deposits, Iberian Pyrite Belt, Spain. *Mineralium Deposita*, 33: 111-136.
- Arth, J.G., Barker, F., Peterman, Z.E., Friedman, I. 1978. Geochemistry of the gabbro-diorite-tonalite-trondhjemite suite of southwest Finland and its implications for the origin of tonalitic and trondhjemitic magmas. *Journal of Petrology*, 19 (2): 289-316.
- Barrie, C.T., Amelin, Y., Pascual, E. 2002. U-Pb geochronology of VMS mineralisation in the Iberian Pyrite Belt. *Mineralium Deposita*, 37: 684-703.
- Barrie, C.T., Hannington, M.D., 1999. Introduction: Classification of VMS deposits based on host rock composition. *Reviews in Economic Geology*, 8: 1-12.
- Barriga, F.J.A.S. 1990. Metallogenesis in the Iberian Pyrite Belt. In: Dallmeyer, R.D., Martínez García, E., (eds.). *Pre-Mesozoic Geology of Iberia*. Berlin, Springer-Verlag, p. 369-379.
- Barriga, F.J.A.S., Fyfe, W.S. 1988. Giant pyritic base-metal deposits: The example of Feitais (Aljustrel, Portugal). *Chemical Geology*, 69: 331-343.
- Barriga, F.J.A.S., Kerrich, R. 1984. Extreme ^{18}O -enriched volcanics and ^{18}O -evolved marine water, Aljustrel, Iberian Pyrite Belt: Transition from high to low Rayleigh number convective regimes. *Geochimica et Cosmochimica Acta*, 48: 1021-1031.
- Barriga, F.J.A.S., Carvalho, D., Ribeiro, A. 1997. Introduction to the Iberian Pyrite Belt. In: Barriga, F.J.A.S., Carvalho, D. (eds.). *Geology and VMS deposits of the Iberian Pyrite Belt*. Society of Economic Geologists Neves Corvo Field Conference, Guidebook Series, 27: 1-20.
- Boogaard, M. V. 1963. Conodonts of upper Devonian and lower Carboniferous age from southern Portugal. *Geol. Mijnbouw*, 42 (8): 248-259.
- Boogaard, M. V., Schermerhorn, L.J.G. 1980. Conodont faunas from Portugal and southwestern Spain. Part 4- A Famennian conodont fauna near Nerva (Río Tinto). *Scrip. Geol.*, 56: 1-14.
- Boogaard, M. V., Schermerhorn, L.J.G. 1981. Conodont faunas from Portugal and southwestern Spain. Part 6- A lower Famennian conodont fauna at Monte Formo da Cal (South Portugal). *Scrip. Geol.*, 63, 1-16.
- Boulter, C.A. 1993. High-level peperitic sills at Río Tinto, Spain: Implications for stratigraphy and mineralization. *Transactions Inst. Mining Metallurgy (Section B: Applied Earth Science)*, 10: B30-B38.
- Boulter, C.A. 1996. Extensional tectonics and magmatism as drivers of convection leading to Iberian massive sulphide deposits? *Journal of the Geological Society*, 153: 181-184.
- Braid, J.A., Murphy, J.B., Quesada, C., Mortensen, J. 2011. Tectonic escape of a crustal fragment during the closure of the Rheic Ocean: U-Pb detrital zircon data from the Late Paleozoic Pulo do Lobo and South Portuguese zones, southern Iberia. *Journal of the Geological Society*, 168: 383-392.
- Carvalho, D. 1979. Geologia, metalogenia e metodologia da investigação de sulfuretos polimetálicos do Sul de Portugal. *Comunicações Serviços Geológicos Portugal*, 65: 169-191 (in Portuguese; abstract in English).
- Carvalho, D., Conde, L., Enrile, J.H., Oliveira, V., Schermerhorn, L.J.G.S. 1976. Livro-guia das excursões geológicas na Faixa Piritosa Ibérica, na III Reunião do Sudoeste no Maciço Hespérico da Península Ibérica. *Comunicações Serviços Geológicos Portugal*, 60: 271-315 (in Portuguese).
- Carvalho, D., Barriga, F.J.A.S., Munhá, J. 1999. Bimodal siliciclastic systems: the case of the Iberian Pyrite Belt. *Reviews in Economic Geology*, 8: 375-408.
- De La Rosa, J.D. 1992. *Petrologia de las rocas básicas y granitoides del Batolito de la Sierra Norte de Sevilla. Zona Surportuguesa. Macizo Ibérico*. Unpublished Doctoral Thesis, Univ. of Sevilla, 312 pp.
- de Oliveira, D.P.S., Matos, J.X., Rosa, C.J.P., Rosa, D.R. N., Figueiredo, M.O., Silva, T.P., Guimarães, F., Carvalho, J.R.S., Pinto, A.M.M., Relvas, J.R.M.S., Reiser, F.K.M. 2011. The Lagoa Salgada orebody, Iberian Pyrite Belt, Portugal: Geology, distribution, mineralogy and geochemistry of Indium. *Economic Geology*, 106: 1111-1128.
- Díez-Montes, A., Bellido-Mulas, F. 2008. Magmatismo TTG y Al-K en la Zona Surportuguesa. Relaciones entre plutonismo y vulcanismo. VII Congreso Geológico de España. Las Palmas de Gran Canaria (España). *Geo-Temas*, 10: 1449-1452.
- Díez-Montes, A., Matas, J., Leyva, F., Martín Parra, L.M. 1999. Mapa geológico a escala 1:50.000, Hoja 939-III (Minas del Castillo de las Guardas). In: Donaire, M. and Almarza, J. (eds.). *Investigación geológica y cartografía básica en la Faja Piritica y áreas aledañas*. Junta de Andalucía & Instituto Geológico y Minero de España. Available on line: <http://www.juntadeandalucia.es/innovacioncienciayempresa/sigma/paginas/productos/fpi.jsp>.
- Díez-Montes, A., Bellido, F., Sánchez García, T. 2011. TTG and Al-K magmatism in the South Portuguese Zone. Relations between plutonism and volcanism.

- Seventh Hutton Symposium on Granites and Related Rocks*. Ávila (Spain). Abstract Book, p. 47.
- Donaire, T., Sáez, R., Pascual, E. 2002. Rhyolitic globular peperites from the Aznalcóllar mining district (Iberian Pyrite Belt, Spain): physical and chemical controls. *Journal of Volcanology and Geothermal Research*, 114: 119-128.
- Dunning, G.R., Díez-Montes, A., Matas, J., Martín Parra, L.M., Almarza, J., Donaire, M. 2002. Geocronología U/Pb del volcanismo ácido y granitoides de la Faja Piritica Ibérica (Zona Surportuguesa). *Geogaceta*: 32: 127-130
- Galley, A.G. 2003. Composite synvolcanic intrusions associated with Precambrian VMS-related hydrothermal systems. *Mineralium Deposita*, 38: 443-473.
- Gaspar, O.C., 1996. Microscopia e petrologia de minérios aplicadas à gênese, exploração e mineralurgia dos sulfuretos maciços dos jazigos de Aljustrel e Neves-Corvo. *Estudos, Notas e Trabalhos, Instituto Geológico e Mineiro*, 38: 3-195 (in Portuguese; extended abstract in English).
- Gaspar, O.C. 2002. Mineralogy and sulfide mineral chemistry of the Neves-Corvo ores, Portugal: Insight into their genesis. *Canadian Mineralogist*, 40: 611-636.
- Gaspar, O., Pinto, A. 1991. The ore textures of the Neves-Corvo volcanogenic massive sulphides and their implications for ore beneficiation. *Mineralogical Magazine*, 55: 417-422.
- Gladney et al., 2014 (in press). The Gil Marquez pluton, Southern Iberia: Magmatism during continental amalgamation of Pangea. *International Journal of Earth Sciences*.
- González, F. 2005. *Las pizarras negras del límite Devónico/Carbonífero de la Faja Piritica Ibérica (SO de España)*. Estudio bioestratigráfico e implicaciones sobre la paleogeografía de la cuenca y el origen de las mineralizaciones de sulfuros. Ph.D. Thesis, Huelva, 200 p.
- González, F., Moreno, C., Sáez, R., Clayton, J. 2002. Ore genesis age of the Tharsis Mining District, Iberian Pyrite Belt: a palynological approach. *Journal of the Geological Society*, 159, 229-232.
- Halsall, C.E. 1989. *The relationship between intrusive magmatism, volcanism and massive sulphide mineralisation at Rio Tinto, Spain*. Unpublished Doctoral Thesis, Univ. of London, 298 pp.
- Hart, T.R., Gibson, H.L., Leshner, C.M. 2004. Trace element geochemistry and petrogenesis of felsic volcanic rocks associated with volcanogenic massive Cu-Zn-Pb sulfide deposits. *Economic Geology*, 99: 1003-1013.
- Huston, D.L., Relvas, J.M.R.S., Gemmill, J.B., Driberg, S. 2011. The role of granites in volcanic-hosted ore-forming systems: an assessment of magmatic-hydrothermal contributions. *Mineralium Deposita*, 46: 473-507.
- IGME. 1982. *Síntesis Geológica de la Faja Piritica del SO de España*. IGME, Madrid. 106 pp.
- Inverno, C.M.C., Solomon, M., Barton, M.D., Foden, J. 2008. The Cu-stockwork and massive sulfide ore of the Feitais volcanic-hosted massive sulfide deposit, Iberian Pyrite Belt, Portugal: A mineralogical, fluid inclusion, and isotopic investigation. *Economic Geology*, 103: 241-267.
- Jorge, R., Fernandes, P., Pereira, Z., Oliveira, J.T. 2007. A late Famennian age storm-dominated succession at Berrocal, Iberian Pyrite Belt-Spain. In: Z. Pereira, J. T., Oliveira, R. Wicander (eds.), *CIMP Lisbon 07-Joint Meeting of Spores /Pollen and Acritarch Sub-commissions*. Abstracts, 83-87.
- Jorge R.C.G.S, Fernandes, J.P., Rodrigues, B., Pereira Z., Oliveira J.T. 2012. Geochemistry and provenance of the Carboniferous Baixo Alentejo Flysch Group, South Portuguese Zone. *Sedimentary Geology*, (2013), <http://dx.doi.org/10.1016/j.sedgeo.2012.12.005>.
- Junta de Andalucía, 1999. Project: *Investigación geológica y cartografía básica en la Faja Piritica y áreas aledañas*. Junta de Andalucía & Instituto Geológico y Minero de España. Available on line: <http://www.juntadeandalucia.es/innovacioncienciayempresa/sigma/paginas/productos/fpi.jsp>.
- Large, R.R. 1992. Australian volcanic-hosted massive sulfide deposits: Features, styles, and genetic models. *Economic Geology*, 87: 471-510.
- Laznicka, P. 1999. Quantitative relationships among giant deposits of metals. *Economic Geology*, 94: 455-473.
- Leca, X., Ribeiro, A., Oliveira, J.T., Silva, J.B., Albouy, L., Carvalho, D., Merino, F., 1983. Cadre Géologique des Mineralisations de Neves Corvo (Baixo Alentejo, Portugal). Lithostratigraphie, Paléogéographie et Tectonique. *Mémoire Bureau de Recherches Géologiques et Minières*, 121, 80 pp.
- Leistel, J.M., Marcoux, E., Thiéblemont, D., Quesada, C., Sánchez, A., Almodóvar, G.R., Pascual, E., Sáez, R. 1998. The volcanic-hosted massive sulphide deposits of the Iberian Pyrite Belt. *Mineralium Deposita*, 33: 2-30.
- Leitão, J. 1997. Geology of the Aljustrel massive sulfide deposits. *Society of Economic Geologists Field Trip Guidebook Series*, 27: 82-97.
- Leshner, C.M., Goodwin, A.M., Campbell, I.H., Gorton, M.P. 1986. Trace-element geochemistry of ore-associated and barren, felsic metavolcanic rocks in the Superior province, Canada. *Canadian Journal of Earth Sciences*, 23: 222-237.
- Liñán, C. 1994. *Mapa Geológico de la Península Ibérica, Baleares y Canarias*, escala 1:1,000,000: Madrid, Instituto Tecnológico Geominero de España.
- López, M.J., Moreno, C., González, F., Dino, R., Antonioli, L. 2004. Palinostrotigrafía del Grupo Pizarroso-Cuartzítico del Sector más oriental de la Faja Piritica Ibérica, SO de España. *Revista Española de Micropaleontología*, 36 (2): 279-304.
- Mantero, E.M., García Navarro, E., Alonso-Chaves, F.M., Martín Parra, L.M., Matas, J., Azor, J. 2007. La Zona Sudportuguesa: propuesta para la división de un

- bloque continental en dominios. *Geogaceta*, 43: 27-30.
- Marcoux, E. 1998. Lead isotope systematics of the giant massive sulfide deposits in the Iberian Pyrite Belt. *Mineralium Deposita*, 33: 45-58.
- Marcoux, E., Moëlo, Y., Leistel, J.M. 1996. Bismuth and cobalt minerals as indicators of stringer zones to massive sulphide deposits, Iberian Pyrite Belt. *Mineralium Deposita*, 31: 1-26.
- Martí Molist, J., Mitjavila de Balanzó, J., Soriano Clemente, C., Viladevall Solé, M. 1994. Proyecto de investigación Fundació Bosch i Gimpera-ITGE sobre la reconstrucción paleogeográfica y volcanológica de la Faja Pirítica del SW de España. IGME, Unpublished open-file report, code: 25072, 51 p.
- Mathur, R., Ruiz, J., Tornos, F. 1999. Ages and sources of the ore at Tharsis and Rio Tinto, Iberian Pyrite Belt, from Re-Os isotopes. *Mineralium Deposita*, 34: 790-793.
- Matos, J.X., Pereira, Z., Oliveira, V., Oliveira, J.T. 2006. The geological setting of the São Domingos pyrite orebody, Iberian Pyrite Belt. *VII Congresso Nacional Geologia, Estremoz, Univ. Évora, Portugal*, 283-286.
- Matos, J.X., Barriga, F.J.A.S., Oliveira, V.M.J., Relvas, J. M.R.S., Conceição, P. 2000. The structure and hydrothermal alteration of the Lagoa Salgada orebody (Iberian Pyrite Belt – Sado Tertiary Basin). *Volcanic Environments and Massive Sulfide Deposits – SEG-CODES International Conference Abstracts Volume-, Tasmania, Australia*, 119-121.
- Matos, J., Pereira, Z., Rosa, C., Rosa, D. N., Oliveira, J. T., Relvas, J., 2011. A key time frame for VMS deposit exploration in the Iberian Pyrite belt. *SGA 2011, 11th Biennial Meeting, Antofagasta, Chile*, 790-792.
- Mitjavila, J., Martí, J., Soriano, C. 1997. Magmatic evolution and tectonic setting of Iberian Pyrite Belt volcanism. *Journal of Petrology*, 38: 727-755.
- Mitsuno, C., Nakamura, T., Kanehira, K., Sugita, M., Kase, K., Thadeu, D., Carvalho, D., Arribas, A. 1988. *Geological studies of the "Iberian Pyrite Belt" – with special reference to its genetic correlation of the Yanahara ore deposit and others in the inner zone of south-west Japan..* University Okayma, Japan, 300 p.
- Moreno, C., Sáez, R., 1990. Sedimentación marina somera en el Devónico del Anticlinorio de Puebla de Guzman, Faja Pirítica Ibérica. *Geogaceta*, 8: 62-65.
- Moreno, C., Sierra, S., Sáez, R., 1995. Mega-debris flows en el transito Devónico-Carbonífero de la Faja Pirítica Ibérica. *Geogaceta*, 17: 9-11.
- Moura, A. 2005. Fluids from the Neves Corvo massive sulphide ores, Iberian Pyrite Belt, Portugal. *Chemical Geology*, 223 (1-3), 153-169.
- Munhá, J. 1983. Hercynian magmatism in the Iberian Pyrite Belt. In: Sousa, M.J.L., Oliveira, J.T. (eds.). *The Carboniferous of Portugal*. Memória Serviços Geológicos Portugal, 29: 39-81.
- Munhá, J. 1990. Metamorphic evolution o the South Portuguese/ Pulo do Lobo Zone. In: Dallmeyer, R.D., Martínez García, E. (eds.). *Pre-Mesozoic Geology of Iberia*. Berlin, Springer-Verlag, p. 363-368.
- Munhá, J., Oliveira, J.T., Ribeiro, A., Quesada, C., Kerrich, R. 1986a. Beja-Acebuches Ophiolite and geodynamic significance. *Maleo*, 2 (13): 31.
- Munhá, J., Barriga, F.J.A.S., Kerrich, R. 1986b. High ¹⁸O ore-forming fluids in volcanic-hosted base metal massive sulfide deposits: Geologic, ¹⁸O/¹⁶O, and D/H evidence from the Iberian Pyrite Belt, Crandon, Wisconsin, and Blue Hill, Maine. *Economic Geology*, 81: 530-552.
- Munhá, J., Relvas, J.M.R.S., Barriga, F.J.A.S., Conceição, P., Jorge, R.C.G.S., Mathur, R., Ruiz, J., Tassinari, C.C.G. 2005. Os isotopes systematics in the Iberian pyrite belt. In: Mao, J., Bierlein, F.P., (eds.). *Mineral deposit research: Meeting the global challenge*, v. 1, Proceedings of the 8th Biennial SGA Meeting, Beijing, China, August 2005: Berlin, Germany, Springer-Verlag, p.: 663-666.
- Nesbitt, R.W., Pascual, E., Fenning, C.M., Toscano, M., Sáez, R., Almodóvar, R.G. 1999. U-Pb dating of stockwork zircons from the eastern Iberian Pyrite Belt. *Journal of the Geological Society London*, 156: 7-10.
- Oliveira, J. T. 1983. The marine Carboniferous of South Portugal: a stratigraphic and sedimentologic approach. In: Sousa, M., Oliveira, J.T. (eds.). *The Carboniferous of Portugal*. Memória dos Serviços Geológicos de Portugal, 29: 3-37.
- Oliveira, J.T. 1990. Stratigraphy and syn-sedimentary tectonism in the South Portuguese Zone. In: Dallmeyer, R.D., Martínez García, E. (eds.). *Pre-Mesozoic Geology of Iberia*. Springer, Berlin, 334-347.
- Oliveira, J.T., Araújo, A. 1992. Paleozóico-Tectónica tardi e pós-Varisca, in: Oliveira, J.T. (coord.), *Notícia Explicativa da Folha 8, Carta Geológica de Portugal, escala 1:200,000: Lisboa, Serviços Geológicos de Portugal*, p. 49-50 (in Portuguese).
- Oliveira, J. T., Quesada, C. 1998. A comparison of stratigraphy, structure and paleogeography of the South Portuguese Zone and Southwest England, European Variscides. Annual Conference of the Ussher Society, *Geoscience in South-west England*, 141-150.
- Oliveira, J.T., Horn, M., Paproth, E. 1979. Preliminary note on the stratigraphy of the Baixo Alentejo Flysch Group, Carboniferous of Southern Portugal and on the paleogeographic development, compared to corresponding units in Northwestern Germany. *Comunicações Serviços Geológicos Portugal*, 65: 151-168.
- Oliveira, J. T., Carvalho, P., Pereira, Z., Pacheco, N., Korn, D. 2004. Stratigraphy of the tectonically imbricated lithological succession of the Neves-Corvo mine region, Iberian Pyrite belt. Implications for the regional basin dynamics. *Mineralium Deposita*, 34: 422-436.
- Oliveira, J.T., Rosa, C.J.P., Rosa, D.R.N., Pereira, Z., Matos, J.X., Inverno, C.M.C., Andersen, T. 2013. Geology of the Neves-Corvo antiform, Iberian Pyrite Belt, Portugal: new insights from physical

- volcanology, palynostratigraphy and isotope geochronology studies. *Mineralium Deposita*, 48:749-766.
- Oliveira, V., Matos, J.X., Bengala, M., Silva, N., Sousa, P. e Torres, L. 1998. Geology and geophysics as successful tools in the discovery of the Lagoa Salgada orebody (Sado Tertiary Basin - Iberian Pyrite Belt), Grândola, Portugal. *Mineralium Deposita*, 33: 170-187.
- Pereira, M.F., Chichorro, M., Johnston, S.T., Gutiérrez-Alonso, G., Silva, J.B., Linnemann, U., Hofmann, M., Drost, K., 2012a. The missing Rheic Ocean magmatic arcs: provenance analysis of Late Paleozoic sedimentary clastic rocks of SW Iberia. *Gondwana Research*, 22 (3-4): 882-891.
- Pereira, Z., Sáez, R., Pons, J., Oliveira, J., Moreno, C. 1996. Edad devónica (Struniense) de las mineralizaciones de Aznalcóllar, Faja Pirítica Ibérica, en base a palinología. *Geogaceta*, 20 (7): 1609-1612.
- Pereira, Z., Fernandes, P., Oliveira, J. T., 2006. Palinostratigrafia do Domínio do Pulo do Lobo, Zona Sul Portuguesa. *Comunicações Geológicas, INETI*, 93: 23-38.
- Pereira, Z., Matos, J., Fernandes, P., Oliveira, J.T. 2007. Devonian and Carboniferous palynostratigraphy of the South Portuguese Zone, Portugal - An overview. *Comunicações Geológicas*, 94: 53-79.
- Pereira, Z., Matos, J., Fernandes, P. Oliveira J.T. 2008. Palynostratigraphy and Systematic Palynology of the Devonian and Carboniferous Successions of the South Portuguese Zone, Portugal. Memória N° 34 do INETI, 1-176.
- Pereira, Z., Matos, J., Fernandes, P., Oliveira, J.T. 2009. A new Lower Givetian age Miospores of the Phyllite Quartzite Group (S. Francisco da Serra Anticlinal, Iberian Pyrite Belt, Portugal). In: *Abstracts CIMPF-ARO'09*. Fernandes, P., Pereira, Z., Oliveira, J.T., Clayton, C & Wicander, R. (eds.), p. 75-78.
- Pereira, Z., Matos, J., Rosa, C., Oliveira, J.T. 2012b. Palynostratigraphic importance of the Strunian in the Iberian Pyrite Belt. Joint Meeting of the 45th Annual Meeting of American Association Stratigraphic Palynology (AASP) - The Palynological Society and Meeting of Internacional Commission of Paleozoic Microflora (Cimp), Lexington, KY, USA, Abstract Book, 42-43.
- Quesada, C. 1991. Geological constraints on the Paleozoic tectonic evolution of tectonostratigraphic terranes in the Iberian Massif. *Tectonophysics*, 185: 225-245.
- Quesada, C. 1996. Estructura del sector español de la Faja Pirítica: implicaciones para la exploración de yacimientos. *Boletín Geológico y Minero*, 107 (3-4): 265-278.
- Quesada, C. 1998. A reappraisal of the structure of the Spanish segment of the Iberian Pyrite Belt. *Mineralium Deposita*, 33: 31-44.
- Quesada, C., Fonseca, P. E., Munhá, J., Oliveira, J.T., Ribeiro, A. 1994. The Beja-Acebuches Ophiolite (Southern Iberia Variscan Fold Belt): Geological characterization and significance. *Boletín Geológico y Minero*, 105: 3-49.
- Relvas, J.M.R.S. 2000. *Geology and metallogenesis at the Neves Corvo deposit, Portugal*. Ph.D. Dissertation, University of Lisbon, 319 p.
- Relvas, J.M.R.S., Barriga, F.J.A.S., Bernardino, F.B.C.P., Oliveira, V.M.S., Matos, J.X. 1994. Ore zone hydrothermal alteration in drill hole IGM-LS1, at Lagoa Salgada, Grândola, Portugal: A first report on pyrophyllite in a central stockwork. *Boletín Sociedad Española Mineralogía*, 17-1: 157-158.
- Relvas, J.M.R.S., Tassinari, C.C.G., Munhá, J., Barriga, F.J.A.S. 2001. Multiple sources for ore-forming fluids in the Neves Corvo VHMS deposit of the Iberian Pyrite Belt (Portugal): strontium, neodymium and lead isotope evidence. *Mineralium Deposita*, 36: 416-427.
- Relvas, J.M.R.S., Barriga, F.J.A.S., Pinto, A., Ferreira, A., Pacheco, N., Noiva, P., Barriga, G., Baptista, R., Carvalho, D., Oliveira, V., Munhá, J., Hutchinson, R. W. 2002. The Neves-Corvo deposit, Iberian Pyrite Belt, Portugal: Impacts and future, 25 years after the discovery. *Society of Economic Geology Special Publication*, 9: 155-176.
- Relvas, J.M.R.S., Barriga, F.J.A.S., Ferreira, A., Noiva, P. C., Pacheco, N., Barriga, G. 2006a. Hydrothermal alteration and mineralization in the Neves-Corvo volcanic-hosted massive sulfide deposit, Portugal: I. Geology, mineralogy, and geochemistry. *Economic Geology*, 101: 791-804.
- Relvas, J.M.R.S., Barriga, F.J.A.S., Longstaffe, F. J. 2006b. Hydrothermal alteration and mineralization in the Neves-Corvo volcanic-hosted massive sulfide deposit, Portugal: II. Oxygen, hydrogen, and carbon isotopes. *Economic Geology*, 101: 753-790.
- Relvas, J.M.R.S., Barriga, F.A.S., Carvalho, J.R.S., Pinto, A.M.M., Matos, J.X., Rosa, C.J.P., Pereira, Z. 2011. Structure, stratigraphy and hydrothermal alteration at the Gavião orebodies, Aljustrel: reconstruction of a dismembered ore-forming system at the Iberian Pyrite Belt and implications for exploration. *11th Biennial SGA Meeting*, Antofagasta, Chile, 772-774.
- Ribeiro, A. 1984. Paleozóico – Tectónica. In: Oliveira, J. T. (coord.), Notícia explicativa da Folha 7, Carta Geológica de Portugal, escala 1:200,000. Lisboa, Serviços Geológicos de Portugal, p. 28-30 (in Portuguese).
- Ribeiro, A., Quesada, C., Dallmeyer, R.D. 1990. Geodynamic evolution of the Iberian Pyrite Belt. In: Dallmeyer, R.D., Martínez García, E. (eds.). *Pre-Mesozoic Geology of Iberia*. Springer, Berlin, 339-409.
- Ribeiro, A., Munhá, J., Dias, R., Mateus, A., Pereira, E., Ribeiro, L., Fonseca, P., Araújo, A., Oliveira, J. T., Romão, J., Chaminé, H., Coke, C., Pedro, J. 2007. Geodynamic evolution of the SW Europe Variscides. *Tectonics*, Dec. 2007, 26(6), TC6009, <http://dx.doi.org/10.1029/2006TC002958> (24 p.)
- Rodríguez, R.M., Díez-Montes, A., Leyva, F., Matas, J., Almarza, J., Donaire, M. 2002. Datación palinoestratigráfica del volcanismo en la sección de la Ribera del Jarama (Faja Pirítica Ibérica, Zona Surportuguesa). *Geogaceta*, 32: 247-250.

- Rosa, C.J.P. 2007. Facies architecture of the Volcanic Sedimentary Complex of the Iberian Pyrite Belt, Portugal and Spain. PhD thesis, University of Tasmania, 357 p.
- Rosa, D., Inverno, C., Oliveira, V., Rosa, C., 2006. Geochemistry and geothermometry of volcanic rocks from Serra Branca, Iberian Pyrite Belt, Portugal. *Gondwana Research*, 10: 328–339.
- Rosa, C.J.P., McPhie, J., Relvas, J., Pereira, Z., Oliveira, T., Pacheco, N. 2008. Volcanic setting of the giant Neves Corvo massive sulfide deposit, Iberian Pyrite Belt, Portugal. *Mineralium Deposita*, 43: 449–466.
- Rosa, C., McPhie, J., Relvas, J., 2009. The Felsic Volcanic Centres of Neves Corvo and Lousal Massive Sulfide Deposits in the Iberian Pyrite Belt. In: Williams, P.J. et al. (eds.), 10th Biennial SGA Meeting. Smart Science for Exploration and Mining, Townsville, Australia, Economic Geology Reserch Unit, James Cook University, vol. 1, 484–486.
- Rosa, C.J.P., McPhie, J., Relvas, J. 2010a. Type of volcanoes hosting the massive sulfide deposits of the Iberian Pyrite Belt. *Journal Volcanology Geothermal Research*, 194: 107–126.
- Rosa, C., Rosa, D., Matos, J., Relvas, J. 2010b. The volcanic-sedimentary sequence of the Lousal deposit, Iberian Pyrite Belt (Portugal). *Geophysical Research Abstracts*, EGU General Assembly, Vol. 12, EGU2010- 11000.
- Rosa C, McPhie J, Relvas J, (2011) Sediment-matrix igneous breccias at the top contacts of felsic units in the IPB: implications for VHMS exploration. 11th SGA Biennial Meeting: Let's Talk Ore Deposits. Antofagasta, Chile. s2.6.5, 754–756.
- Routhier, P., Aye, F., Boyer, C., Lécolle, M., Molière, P., Picot, P., Roger, G. 1980. *Le ceinture sud-ibérique à amas sulfurés dans sa partie espagnole médiane*. Mémoire du BRGM 94, 265 pp.
- Sáez, R., Almodóvar, G.R., Pascual, E. 1996. Geological constraints on massive sulphide genesis in the Iberian Pyrite Belt. *Ore Geology Reviews*, 11: 429–451.
- Sáez, R., Pascual, E., Toscano, M., Almodóvar, G.R. 1999. The Iberian type of volcano-sedimentary massive sulphide deposits. *Mineralium Deposita*, 34: 549–570.
- Sánchez-España, J., Velasco, F., Boyce, A.J., Fallick, A. E. 2003. Source and evolution of ore-forming hydrothermal fluids in the northern Iberian Pyrite Belt massive sulphide deposits (SW Spain): evidence from fluid inclusions and stable isotopes. *Mineralium Deposita*, 38: 519–537.
- Schermerhorn, L.J.G., 1971. An outline stratigraphy of the Iberian Pyrite Belt. *Boletín Geológico y Minero*, 82 (3/4): 239–268.
- Schermerhorn, L.J.G., Zbyszewski, G., Veiga Ferreira, O., 1987, Notícia Explicativa da Folha 42-D (Aljustrel), Carta Geológica de Portugal, escala 1:50,000: Lisboa, Serviços Geológicos de Portugal, 55 p. (in Portuguese).
- Schütz, W., Ebner, J., Meyer, K.D. 1987. Trondhjemites, tonalites and diorites in the South Portuguese Zone and their relations to the vulcanites and mineral deposits of the Iberian Pyrite Belt. *Geologische Rundschau*, 76 (1): 201–212.
- Silva, J.B., Oliveira, J.T., Ribeiro, A. 1990. South Portuguese Zone. Part VI. Structural outline. In: Dallmeyer, R.D., Martínez García, E. (eds.). *Pre-Mesozoic Geology of Iberia*. Springer, Berlin, 348–362.
- Simancas, J.F. 1983. *Geología de la extremidad oriental de la Zona Sudportuguesa*. Unpublished Doctoral Thesis, Univ. Granada, España, 439 pp.
- Simancas, J.F., Carbonell, R., González Lodeiro, F., Pérez Estaún, A., Juhlin, C., Ayarza, P., Kashubin, A., Azor, A., Martínez Poyatos, D., Almodóvar, G.R., Pascual, E., R. Sáez, R., Expósito, I. 2003. Crustal structure of the transpressional Variscan orogen of SW Iberia: SW Iberia deep seismic reflection profile (IBERSEIS). *Tectonics*, 22 (6), 1062, 1–11 – 1–19.
- Solomon, M., Tornos, F., Gaspar, O.C. 2002. A possible explanation for many of the unusual features of the massive sulfide deposits of the Iberian Pyrite Belt. *Geology*, 30: 87–90.
- Solomon, M., Tornos, F., Large, R.R., Badham, J.N.P., Both, R.A., Khin Zaw. 2004. Zn-Pb-Cu volcanic-hosted massive sulfide deposits: Criteria for distinguishing brine pool- from black smoker-type sulfide deposition. *Ore Geology Reviews*, 25: 259–283.
- Soriano C, Martí, J. 1999. Facies Analysis of Volcano-Sedimentary Successions Hosting Massive Sulfide Deposits in the Iberian Pyrite Belt, Spain. *Economic Geology*, 94: 867–882.
- Strauss, G.K., Madel, J., Fernández Alonso, F. 1977. Exploration practice for strata-bound volcanogenic sulphide deposits in the Spanish-Portuguese Pyrite Belt: Geology, geophysics, and geochemistry. In: Klemm, D.D., Schneider, H.J. (eds.). *Time and strata-bound ore deposits*. Berlin, Springer-Verlag, p. 55–93.
- Strauss, G.K., Beck, J.S. 1990. Gold mineralizations in the SW Iberian Pyrite Belt. *Mineralium Deposita*, 25: 237–245.
- Thiéblemont, D., Pascual, E., Stein, G. 1998. Magmatism in the Iberian Pyrite Belt: petrological constraints on a metallogenetic model. *Mineralium Deposita*, 33: 98–110.
- Tornos, F. 2006. Environment of formation and styles of volcanogenic massive sulfides: The Iberian Pyrite Belt. *Ore Geology Reviews*, 28: 259–307.
- Tornos, F., Heinrich, C.A. 2008. Shale basins, sulfur-deficient ore brines, and the formation of exhalative base metal deposits. *Chemical Geology*, 247: 195–207.
- Tornos, F., Spiro, B. 1999. The genesis of the shale-hosted massive sulphides in the Iberian Pyrite Belt. In: Stanley, C.J. et al. (eds.). *Mineral deposits: Processes to processing*. Rotterdam, Balkema, p. 605–608.
- Tornos, F., González-Clavijo, E., Spiro, B.F. 1998. The Filón Norte orebody (Tharsis, Iberian Pyrite Belt): a proximal low-temperature shale-hosted massive sulphide in a thin-skinned tectonic belt. *Mineralium Deposita*, 33: 150–169.
- Tornos, F., Barriga, F., Marcoux, E., Pascual, E., Pons, J. M., Relvas, J., Velasco, F. 2000. The Iberian Pyrite Belt, in Large, R., Blundell, D. (eds.). *Database on global VMS districts: CODES-GEODE*, p. 19–52.

- Tornos, F., Casquet, C., Relvas, J.M.R.S. 2005. Transpressional tectonics, lower crust decoupling and intrusion of deep mafic sills: a model for the unusual metallogenesis of SW Iberia. *Ore Geology Reviews*, 27: 133-163.
- Tornos, F., Solomon, M., Conde, C., Spiro, B. F. 2008. Formation of the Tharsis massive sulfide deposit, Iberian Pyrite Belt: Geological, lithogeochemical, and stable isotope evidence for deposition in a brine pool. *Economic Geology*, 103: 185-214.
- Toscano, M., Sáez, R., Almodóvar, G.R. 1997. Multi-scale fluid evolution in the Masa Valverde (Iberian Pyrite Belt): Evidence from fluid inclusions. [abs.]: Society of Economic Geologists Neves Corvo Field Conference, Abstracts and Program, p. 101.
- Valenzuela, A., Donaire, T., Pin, C., Toscano, M., Hamilton, M., Pascual, E. 2011. Geochemistry and U-Pb Dating of felsic volcanic rocks in the Río Tinto-Nerva unit, Iberian Pyrite Belt, Spain: crustal thinning, progressive crustal melting and massive sulphide genesis. *Journal of the Geological Society*, 168: 717-731.
- Velasco, F., Sánchez-España, J., Boyce, A.J., Fallick, A. E., Sáez, R., Almodóvar, G.R. 1998. A new sulphur isotopic study of some Iberian Pyrite Belt deposits: evidence of a textural control on sulphur isotope composition. *Mineralium Deposita*, 34: 4-18.
- Yamamoto, M., Kase, K., Carvalho, D., Nakamura, T., Mitsuno, C. 1993. Ore mineralogy and sulfur isotopes of the volcanogenic massive sulfide deposits in the Iberian Pyrite Belt. *Resource Geology Special Issue*, 15: 67-80.

Alejandro Díez-Montes, Jesús García-Crespo,
Concepción Ayala, José Luis García-Lobón,
Teresa Sánchez-García, Carmen Rey-Moral, Félix Bellido,
Félix Rubio, J.F. Mediato and Fernando Tornos

Abstract

The *Río Tinto* project area is located in the South Portuguese Zone, in the eastern part of the Iberian Pyrite Belt. The Iberian Pyrite Belt (IPB) is one of the world's best-known ore provinces hosting volcanogenic massive sulphide deposit, formed in the latest Famennian (ca. 360 Ma) and subsequently folded and metamorphosed during the Variscan orogeny (330–300 Ma). The study area is located in the *Río Tinto* syncline, with Carboniferous metasediments (Culm) in its core. The volcanic sedimentary complex (VSC) is overthrust in the central part of the syncline forming the *Río Tinto* anticline outcrop (an antiformal stack). The aim of this work was to construct a 3D geological model of the *Río Tinto* mine area. To achieve this data compilation has been done including new geological mapping and structural interpretations, petrological and petrophysical sampling, drill hole logging, and geophysical data interpretation (gravimetric, magnetic and radiometric data). Complex surfaces were constructed using large data sets analysed by suitable geometrical techniques. The obtained 3D model shows the relationships between several lithologies, tectonic surfaces and mineralization zones, and is an example of reconstruction of complex geological units within the Iberian Pyrite Belt. In addition, in the *Río Tinto* area it was possible to derive a predictive model defining four areas of high ore potential based on detailed geological field work, fracture analyses and geophysical studies related to the possible presence of massive sulphides and stockwork zones.

A. Díez-Montes (✉)
IGME, C/ Azafranal, 48, 1^oB, 37001 Salamanca,
Spain
e-mail: al.diez@igme.es

J. García-Crespo · C. Ayala · J.L. García-Lobón ·
T. Sánchez-García · C. Rey-Moral · F. Bellido ·
F. Rubio · J.F. Mediato
IGME, C/ Ríos Rosas, 23, 28003 Madrid, Spain

C. Ayala
IGME, Institute of Earth Sciences Jaume Almera
(CSIC), C/ Lluís Solé i Sabarís, s/n, 08028
Barcelona, Spain

F. Tornos
CSIC-INTA, Ctra. Ajalvir, 28850 Torrejón de
Ardoz, Spain

10.1 Local Geological Setting

The *Río Tinto* area is located in the eastern part of the SPZ (see Chap. 9, Fig. 9.1, Zone B). During the ProMine Project a new geological map (1:10000 scale, Fig. 10.1) was produced and new structural data were collected in the field using structural measurement stations. Petrography, litho-geochemistry, microstructural analyses and petrophysical measurements were carried out. New geophysical data have also been acquired during the project.

The *Río Tinto* mine is located in the *Río Tinto* syncline where the core is made up of Carboniferous metasediments (Culm) (Navarro Vázquez and Ramírez Copeiro del Villar 1982), but this syncline is not simple, in its central part volcanic rocks of the VSC outcrop through a thrust, which formed the *Río Tinto* anticline (an antiformal stack, González-Clavijo and Díez-Montes 2010). The deformed stratigraphic succession in the *Río Tinto* area includes Upper Devonian to Lower Carboniferous age rocks, and where the regional mapping has identified a relatively simple stratigraphic sequence, this comprises three major lithostratigraphic units (Schermerhörn 1971): 1) phyllite quartzite group (PQG), 2) the volcanic sedimentary complex (VSC) and 3) a Carboniferous sequence (Culm flysch) which are all described in the previous chapter (Part A). To build the 3D model of the *Río Tinto* anticline, the lithostratigraphic units represented in Fig. 10.1 have been simplified as reflected in the legend of Fig. 10.2, as follows.

- (i) The PQG outcrops to the south of the *Río Tinto* village. At the top of the PQG and in contact with the base of the CVS (basalts) there is a level of black shales of Strunian age (Rodríguez et al. 2002). In the “*Corta Atalaya*” (Figs. 10.1 and 10.2a) conglomerates with a black colour shaly matrix exist. They contain cobbles of slate, quartzite and massive sulphides. This conglomerate may be correlated with other conglomerates described elsewhere in the SPZ, near the top of the PQG and mark the

onset of instability of the basin, predating the development of the volcanism in the SPZ.

- (ii) The VSC is stratigraphically overlying the PQG. This unit is a mainly submarine succession dominated by felsic and mafic volcanic rocks, which are interbedded with mudstones and volcanoclastic sediments. The VSC has been dated at Late Fammenian to Late Visean (Oliveira 1990; Rodríguez et al. 2002; Barrie et al. 2002; Dunning et al. 2002; Rosa et al. 2009; Valenzuela et al. 2011). The volcanic lithostratigraphic units used to build the 3D model of the *Río Tinto* area are from bottom to top: basalts (VS1), felsic rocks (massive rhyolite-dacite, volcanic breccias, epiclastic) (VS2) and finally the purple slates (VS3) and the transition series (VS4). VS3 and VS4 represent the only stratigraphic marker for mapping in the SPZ. In places it was not possible to differentiate VS3 and VS4, and they have been combined into a single unit (see cross-section in Fig. 10.2b).
- (iii) Stratigraphically overlying the VSC, there is a sedimentary sequence, the Culm flysch. This is the uppermost unit in the entire SPZ and consists of shale, litharenite and a rare conglomerate with turbiditic features. The Culm ranges in age from Late Visean to Late Moscovian and is interpreted to represent a synorogenic flysch related to the Variscan tectonic event.

The Iberian Massif was deformed mainly by the Variscan Orogeny. The tectonic evolution of the SPZ shows the characteristic features of a foreland fold-thrust belt dominated by thin-skinned tectonics (Silva et al. 1990; González-Clavijo et al. 1994; Quesada 1998). This tectonic deformation has been confirmed by deep-seismic reflection profiling (Simancas et al. 2003). Three major tectonic domains, younging towards north, have been established in the southern Portuguese zone based on stratigraphic, lithologic, structural and metamorphic criteria. The *Río Tinto* area is located within the northern domain of the Iberian

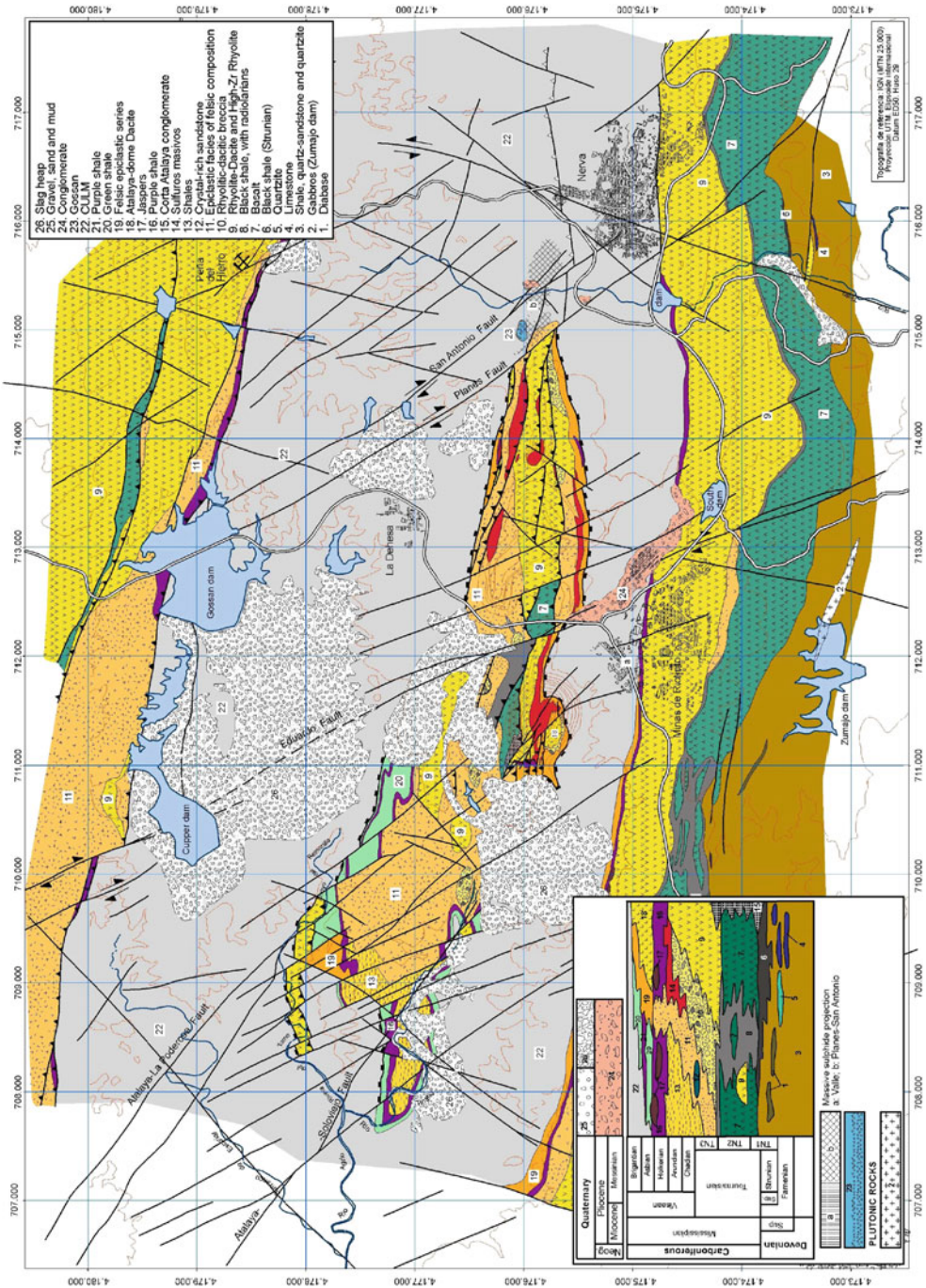


Fig. 10.1 Geological map of the Río Tinto area

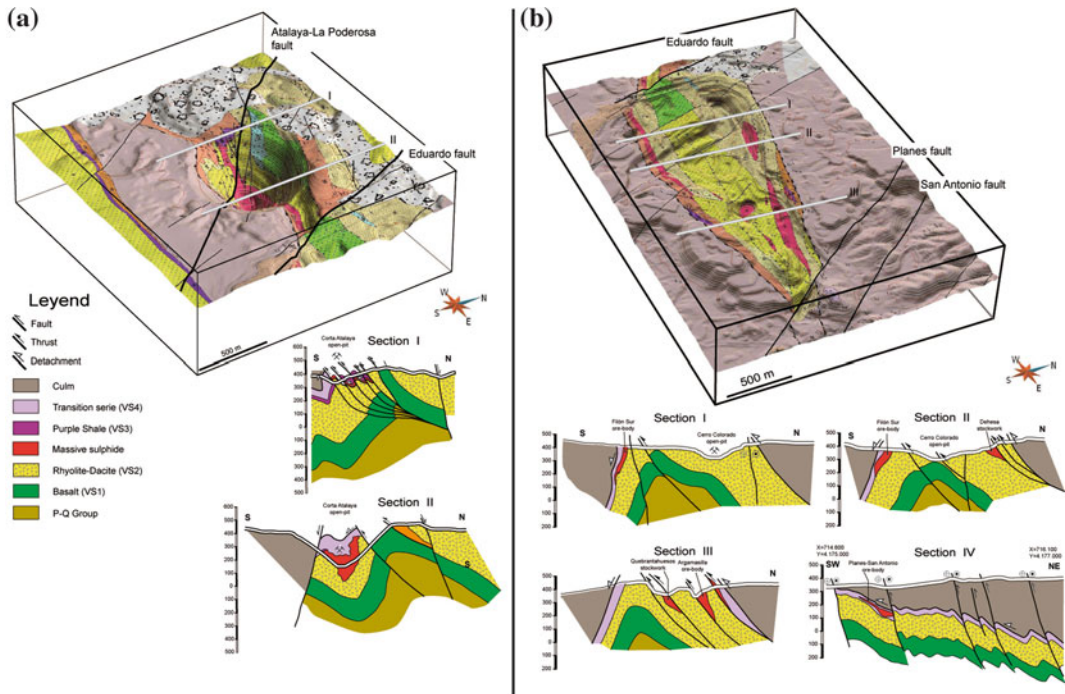


Fig. 10.2 a 3D geological map of “Corta Atalaya” open-pit and two examples of the geological cross-sections for building the 3D model of this zone. Simplified legend used to build the 3D model of *Río*

Tinto. b 3D geological map of the “Cerro Colorado” open-pit and four examples of the geological cross-sections for building the 3D model of this zone

Pyrite Belt (Quesada 1998), characterized by intense deformation, which decreases towards the southwest. Overall, the structural development of the SPZ is characterized by south-westward vergent folding and thrust displacement.

In this area, the first episode of the Variscan deformation generated a S to SSW vergent, thin-skinned fold and thrust belt that propagated southwards. The structure proposed for the *Río Tinto* area mainly consists of southward-vergent folds with sub-horizontal axes oriented N90°E to N120°E. In general, due to cogenetic thrusting, only the normal limbs of the folds are preserved, whilst the short reverse limbs are rarely recognized in this area. Near *Río Tinto*, in the central part of the synclinal structure an antiform with volcanic rocks crop out (Mellado et al. 2006; González-Clavijo and Díez-Montes 2010). It has been interpreted as an anti-formal stack of thrust sheets (Quesada 1998; González-Clavijo and Díez-Montes 2010), the core of which is mainly formed by mafic and felsic volcanic rocks

showing hydrothermal alteration and stockwork type mineralization. The geometry of the km-scale anti-formal stack system and the lateral variations of the fold axes are shown in Fig. 10.2.

In the *Río Tinto* area an extensional detachment at the contact between the volcanic rocks and the Culm is an important tectonic structure (González-Clavijo and Díez-Montes 2010, Fig. 2). This detachment was already proposed by Quesada (1998) for the entire IPB. The detachment is not only situated at the base of the Culm, but also in the upper part of the VSC, affecting the purple shale and the top of the massive sulphide ores where mylonites and ultramylonites formed. This detachment seems to occur mainly in the areas where there are large massive sulphide ore bodies, and it has also been described in other areas of the IPB, e.g. in the *Valverde* Deposit (Castroviejo et al. 2011).

This detachment is interrupted by ductile thrusts (Fig. 10.2a, Sect. 10.1). In these thrusts, the stockwork is parallel to the main foliation.

The detachment and the ductile thrusts are interrupted by another set of E-W thrusts with a brittle-ductile character.

The youngest deformation is a system of conjugate faults with NW-SE dextral and NE-SW sinistral kinematics. In the *Río Tinto* area there is a predominance of NW-SE faults. *Atalaya-La Poderosa*, *Eduardo*, *Planes* and *San Antonio* are examples of faults of this type (Fig. 10.1).

10.2 Dataset and Methods Used to Build the 3D Models

Traditionally, geological maps have been the main tool to represent geological features and the relationships between lithologies. They are often accompanied by cross sections to help to understand how rocks and structures behave in the subsurface.

Today, 3D technologies provide new tools which make the representation and the understanding of the geology easier. Most geologic maps, are available in GIS formats and the use of tools to analyse the data linked to them is widespread. Recently, new software has been developed, allowing the management of 3D data, making it easier to interpret geological structures.

To accomplish the modelling objectives of this study, two software programs have been used. ArcGIS has been employed for extracting data from layers loaded in a geodatabase format, used to construct the geological maps. After field work, these maps were reviewed and recompiled, in terms of stratigraphic and structural evolution. gOcad was used for the 3D modelling to extract the data from ArcGis (i.e. geological borders, faults etc.) and combined with 3D data such as drillings, dip points, and geological cross-sections this was the baseis for the 3D modelling. Furthermore, integrating structural geology and petrology, was made with gOcad, in order to define geological relationships between different rock types and mineralization zones.

The input data used in this study were the reference topographic map (as DEM of 100×100 m, basic datum of all the 3D features), the updated geological map, structural data, petrological, petrophysical and geophysical data (including interpretations and models) and borehole data (source data of Fig. 10.3a). The first step concerned the creation of a geological database, which contains all the information needed for 3D modelling. Six main typologies of geometric features and related attributes were exported from the ArcGIS-geodatabase:

1. Topographic data as points from a digital elevation model.
2. 2D linear features from geological maps (stratigraphic and intrusion contacts, fold axial traces, faults, foliations, etc.): a geological map with stratigraphic, tectonic and intrusion boundaries, linear features as 2D polylines.
3. 2D polygonal features of outcropping units, and 2D geological cross-sections.
4. Petrological and petrophysical data from laboratory determination of physical properties (density, magnetic susceptibility) from surface rocks in the studied area.
5. Geophysical data and interpretations.
6. Data from drill holes and old maps, vertical sections, and horizontal level plans of ore bodies.

All these data were the source of the initial geological model. The processing of the data generated new layers of information, step by step (Fig. 10.3b):

- 3D geological maps and cross-sections: building of a set of 3D parallel geological cross-sections across the analysed structures and intrusions constitutes the first basic step.
- 3D point sets: these correspond mainly to borehole intersects of top/bottom boundaries of selected units, and 3D layers of dip points and structural measurements, needed for surface interpolation.
- Petrological, petrophysical samples and radiometric measurements.

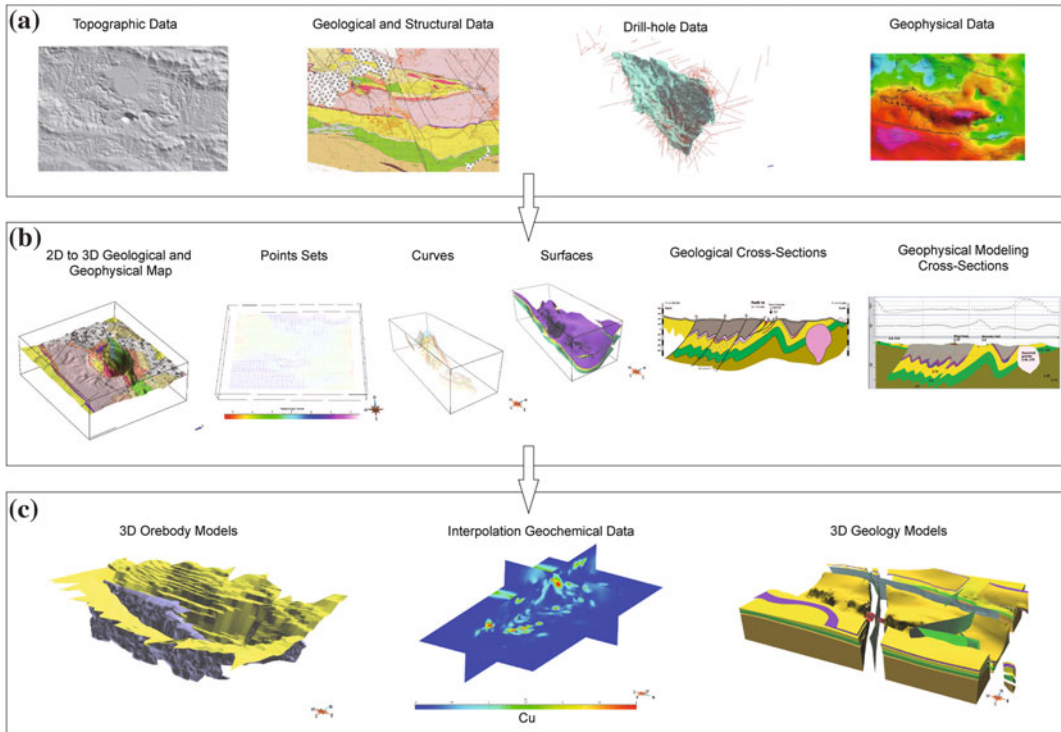


Fig. 10.3 Schematic flow-chart for 3D modelling through data integration between source data, GIS and gOcad. **a** Source data, **b** processed data, **c** final results

- 3D geological cross-sections built previously adjusted to fit geophysical data.
- All these layers were processed within gOcad with appropriate interpolators to generate 3D layers of curves and surfaces, and the final voxets model (Fig. 10.3c).

Existing geophysical data was complemented with new acquired gravity and natural gamma ray data. These data were first interpreted qualitatively, and then by geophysical inversion.

Geophysical modelling defines the correlation between a model of the subsurface and the geophysical data acquired, usually at the surface. Potential field data the variations that occur in the earth's gravitational and magnetic fields, allows for a crude subsurface 3D modelling.

The final 3D geological models were obtained from geological cross-sections that were adjusted to fit potential field data. After calculating the gravimetric responses from the initial geological model a review of the initial deep structural cross-sections was done (see below).

10.3 3D Modelling Results

10.3.1 Initial 2D Geological Model

In the geological 3D modelling of the *Río Tinto* area several data sets were involved. The mining company (EMED-Tarthessus) provided part of the information and additional data were acquired from new surveys.

Topographic data

For the *Río Tinto* area, the EMED Tarthessus Company provided an updated survey made in 2010. This covered the area next to the site with mining interest. New data of a larger surrounding area were also included. The Cartographic Institute of *Andalucía* (ICA) constructed maps at 1:10 000 scale.

The topographic data processing included several steps, beginning with the conversion from CAD to GIS format. For the transformation

the FME software was used, creating a transformer for filtering elements and extracting only the topography curves and points. Further coordinate transformation was necessary to project data from WGS84 to ED50 Zone 29.

Once in GIS format, lines and points were transformed to a grid using the “Topo to Raster” tool in ArcGis. The cell size was established to 10 m. Then, this grid was converted into a grid of points, ready to use in gOcad. Finally, the meshes were imported and a topographic surface was built in gOcad.

Geological data

One of the first tasks in the project was to establish a new geological map of the area at 1:10,000 scale. At the same time, 44 cross sections were drawn from the map interpretation, as a guide for further modelling, especially for the *Río Tinto* anticline. The map was digitized and coded for GIS, using ArcGis software.

The geological map in ArcGIS format contains linear features such as stratigraphic boundaries, faults and structural measurements that can be imported directly into gOcad and projected onto the topographic surface. Lines were then coded, separating different features, in order to create model surfaces.

The cross sections were imported to gOcad for 3D vectorization. The lines drawn on paper sections were digitized and coded geologically.

Subsurface mine data

During the active life of a mine abundant documentation is generated. This information includes detailed subsurface mapping. Such documents are useful for delineating the 3D geology at depth.

In the *Río Tinto* area maps and sections mining and ground surveys are available from which valuable information has been extracted allowing the reconstruction of historical ore bodies. The mine levels plans have been especially helpful. They contain survey data, grades, lithological interpretations and information on the presence of sulphide ore. When available, sections have been incorporated.

In the *Río Tinto* area there are nine mine sites, currently abandoned. The traditional method for mapping involved the use of a local grid system for each mine site or group of mine sites. Thus, a reference system for *Filón Sur*, for *San Dionisio* and another for *San Antonio* exists. To geo-reference cartographic documents, a transformation has been necessary. The transformation parameters were obtained from measured points with a precision of $\pm 5-7$ m. The digitalization was done on the transformed documents. Sometimes this transformation involved translation, or translation and rotation to fit the data to a common mesh. Then, the transformation to UTM ED50 Zone 29 was carried out.

Drill hole data

In the *Río Tinto* area, data from about 6700 drill holes were available. The majority was only location data without any other valuable information. Filtering of relevant information led to 2658 drill holes with significant data. They contained as a minimum the deviation data of the hole and, in most cases, geochemical data.

The data were imported into gOcad, after having structured the information in comma delimited files.

Geophysical Data

In the *Río Tinto* area, information contained in geophysical and petro-physical databases of IGME, and from other companies that worked in the area, have been used. IGME data are available in the SIGECO Geophysical Databases (on line, IGME, 2012). 234 samples were collected for a petrophysical study. In the petrophysical study, density and magnetic susceptibility have been used. Moreover, natural gamma radiometric characteristics of some igneous and metasedimentary rocks and ores were included.

10.3.2 Geophysical Surveys. 2.5D Modelling

Geophysical data represent the physical properties of the earth's subsurface. Geophysical modelling fits a model of the subsurface to the

Table 1 Geophysical and petrophysical data of the *Río Tinto* area

Data	New acquisition	Compilation	
Gravimetric	327 points	SIGECO: 4504 points;	Regional gravity (1976 points) Detailed gravity (2528 points)
		Riomin: 401 points	
		Atlantic Copper: 2199 points	
		ADARO: 316 points	
Magnetic	-	Grids from flights 1996–97	
Radiometric	-	Grids from flights 1996–97	
Petrophysic	67 samples	167 samples (Plata and Navas 1996)	

geophysical data. The 2.5D potential field models described in this section are based on the cross sections built from geological data and the observed gravity and magnetic data. Original geological cross sections were adjusted by forward modelling, mainly changing the geometry of the different geological bodies based on the constraint of the physical properties measured in the laboratory from rock samples.

In the *Río Tinto* area, the available geophysical and petrophysical available data used for the modelling are (Table 10.1): (1) Magnetic and natural gamma ray radiometric surveys from the IGME Database (SIGECO geophysical database, online). These include the magnetic and radiometric airborne survey data of the Iberian Pyrite Belt and surrounding areas from 1996–97 (Bates and García-Lobón 1998), (2) A new gravity survey carried out in the southern part of the study area, where no gravity data were available. 327 stations were measured using a Scintrex CG5 gravity meter. Bouguer anomaly was calculated taking into account measurements from previous surveys (Table 10.1), using the GRS67 geodetic system and with a density reduction of 2.60 g/cm^3 . From the Bouguer anomaly, a suitable residual gravity anomaly was obtained (Sánchez-García et al. 2015, open-file geophysical report).

Residual Bouguer anomaly map

The residual Bouguer anomaly map (Fig. 10.4a) shows the density distribution of the metasedimentary and metavolcanic succession. Gravity minima occur in the north and are related to low

density black slates and greywackes of the Culm facies (Carboniferous-Viséan; C in Fig. 10.4), also outcropping in the southwest corner of the area. Intermediate to high anomaly values in the middle part correspond to outcropping acidic VSC rocks (VS2, in Fig. 10.4) suggesting sub-cropping of high density rocks (of the *Río Tinto* ore body and VS1 basalts). The gravity maxima in the south coincide with high density CVS rocks (outcropping basaltic wedge, VS1), which extends to the south under Devonian slates, lime stones and quartzites (PQG).

The *Río Tinto* mine is situated in the centre of the map, which depicts a more than 4 mGal positive anomaly coinciding with outcropping rhyolites, breccias and acid epiclastic rocks (VS2) and minor VS1 basalts and massive sulphides (O). It is worth noting that the character of the anomaly that extends under the Culm cover from the *Río Tinto* antiformal core both to the N-NE (as two intense lobes) and to the S-SE (as an intermediate positive area) suggests the likely occurrence of massive sulphides at an unknown depth. Two geological cross sections have been modelled to unravel the structure and mining potential of these areas (P9 and P14 in Fig. 10.4a).

Reduced to the pole magnetic map

The reduced to the pole (RTP) aeromagnetic map of the *Río Tinto* region (Fig. 10.4b) is a portion of the airborne geophysical study over the Spanish part of the Iberian Pyrite Belt and the southern areas of the OMZ (Ossa-Morena Zone)

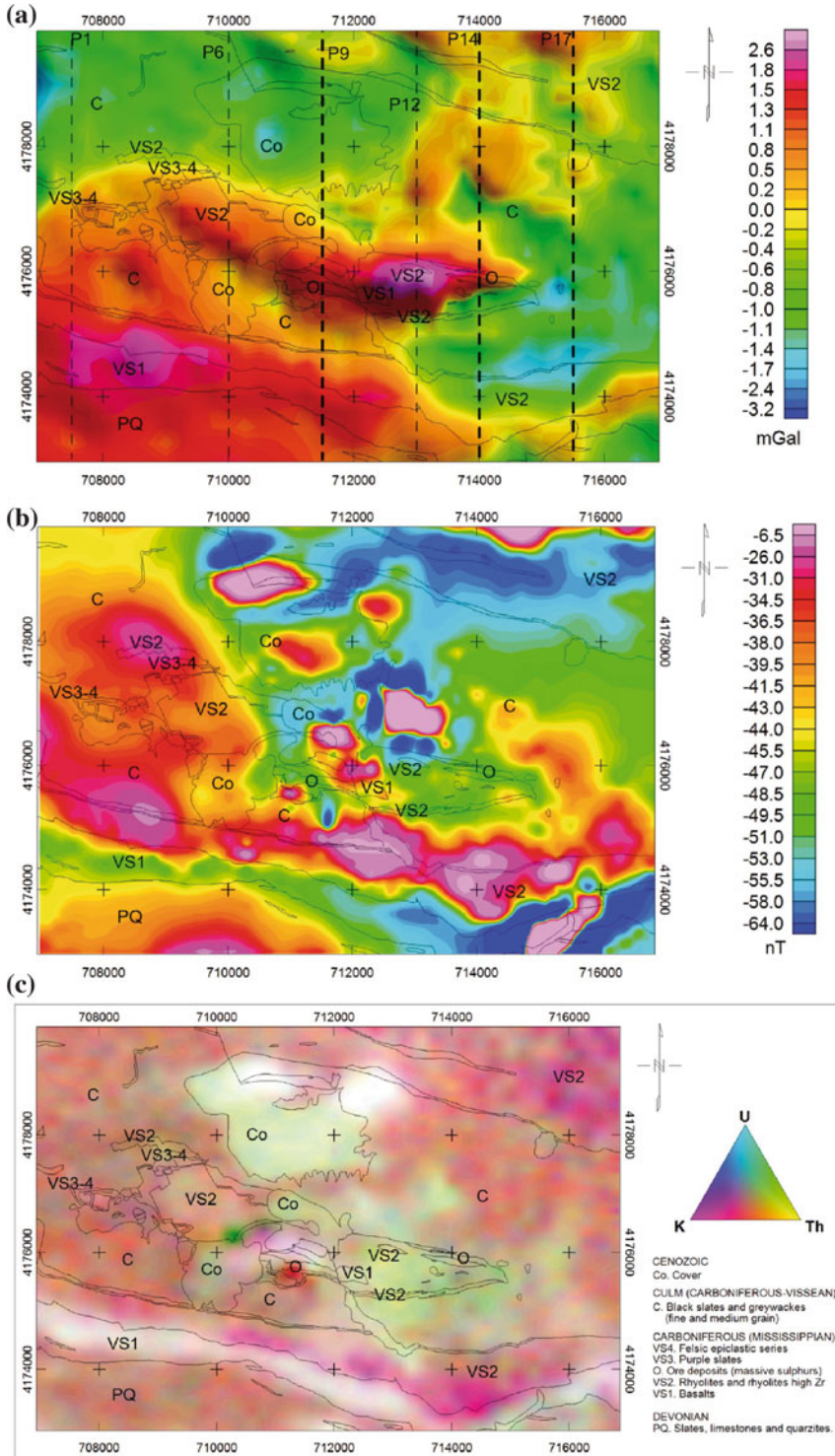


Fig. 10.4 a Residual Bouguer Anomaly Map of the Rio Tinto area. P-9 and P-14 are gravity-modelled profiles, included in this report, representative of this area. b Reduced to the Pole Magnetic Map of the Rio Tinto area. c Radiometric Anomaly Ternary Map

carried out 1996–1997 with a line spacing of 250 m, at an altitude of 80 m. A magnetometer, Geometrics G-822, with a sensibility of 0.01 nT, a natural gamma spectrometer, Exploranium 830, and a differential GPS as navigational system were used. An IGRF correction of 43,245 nT was removed.

Based on the anomaly pattern the RTP map can be divided into two main zones (Fig. 10.4b):

1. Low intensity areas, with values below -45 nT are located in the northern segment of the map, the low magnetic values are a consequence of the low magnetite (also low density) contents of the Culm facies rocks (black slates and greywackes), and rhyolites, breccias and acid epiclastics of VS2. A few areas of high magnetic intensity are visible within the low area of the central-northern section of the studied area. The most remarkable is the one located in the west, related to outcropping jasper enriched, purple slates, (VS3-4; jaspers are the likely source of these magnetic signatures).
2. An E–W high intensity area, >-45 nT, occurs in the south of the map over the Mississippian VS2 unit. As the rhyolites, breccias, tuffs and felsic epiclastics of this unit are composed of mainly paramagnetic materials (see petrophysical results), VS1 basalts must be present at depth, as seen in the gravity residual map. Combining the information provided by both maps, a smooth basaltic VS1 antiform (Fig. 10.4b and related to geological cross sections) is predicted in the south, its northern limb being covered by felsic VS1, and its southern limb by the PQG.

Some shorter and medium wavelength magnetic anomalies over the *Río Tinto* antiform are related to shallower bodies whose geological features are unclear. Some of the maxima appear over the Cenozoic cover and the Culm, and may be anthropogenic in origin (*Río Tinto* mine installations and facilities, etc.). The *Río Tinto* ore body itself, like most deposits of the Iberian Pyrite Belt, contains neither magnetite nor pyrrhotite and does not produce magnetic anomalies.

Ternary map

Airborne radiometric methods measure the radiometric element content in the uppermost part of the crust and can be used as a useful tool for exploration.

The majority of the map area (Fig. 10.4c) is made up of high K+Th signatures (red colours). Mafic rocks in the south (VS1) are perfectly mapped by a white band indicating their extremely low radiometric-element content. The sites with high concentrations in Th+U are located over the cover of mine dumps (Co) and the mining sites.

Correlation between the outcropping geology and radioactive elements (K, Th and U) in Ternary maps is difficult. The area is highly disturbed by the anthropogenic activities due to the intensive mining causing large areas of tailings and rock dumps. Nevertheless some sites are of interest for exploration based on high concentration of K+Th (red colour, O) and high concentration of Th+U (green colour, to the northwest of the previous one, O).

The petrophysical character of *Río Tinto* rocks

Petrophysical properties (density and magnetic susceptibility) from 234 surface rock samples, collected in the *Río Tinto* area, were measured in the laboratory. Petrophysical data constitute a fundamental constraint to interpret the potential field data and to build a regional 2.5 D potential field model along selected transects. The samples include the main outcropping geological units targeted in the modelling.

Laboratory measurements of density have been made on hammer-cut samples (0.3–0.6 kg) by weighing them in air and water (Archimedes principle). These samples come from 2 kg of rock collected in the field. From each of these samples, powder (2 mm grid pass) is obtained and magnetic susceptibility determined in a kappabridge instrument; the mass of the powder is measured, and the values are converted to mass susceptibility values, then corrected by the density of the sample to obtain volume susceptibility.

In order to assess the physical property variation within the geological age domains, samples

have been grouped in a pseudo-log (Fig. 10.5). Volcano-sedimentary felsic rocks display low densities, in general below 2.65 g/cm^3 . They comprise 2.38 g/cm^3 values of green slates (Fig. 10.5) to 2.65 g/cm^3 densities (rhyolites, dacites, breccias, tuffs and felsic epiclastics of VS2). The rest of the felsic rocks are made up of VSC epiclastics characterized by a heterogeneous mixture of purple slates, slates, felsic tuffs, etc. (VS3-4). They all have density values below 2.63 g/cm^3 (with average density of 2.61 g/cm^3). In contrast, ore deposits represent the densest group in the area, with an average density of 4.3 g/cm^3 . The mafic rocks such as basalts, diabases, dolerites, andesites and trachyandesites (VS1 black slates and basalts) represent a group of dense rocks (averaging 2.80 g/cm^3) which display gravity maxima in the south of the area and around the *Río Tinto* mining area. Apart from the green slates in the CVS, the least dense major units of the study zone are represented by the slates, quartzites and greywackes of the P-Q group and Culm facies (average density of 2.60 g/cm^3 and 2.41 g/cm^3 , respectively).

Paramagnetic rocks (also low density rocks) coincide with the Culm facies and rhyolites, breccias and felsic epiclastic metasedimentary units of VS2–VS4. There are only a few strong ferromagnetic rocks among the samples, which correspond to mafic VS1 volcanites (a couple of basalts in Fig. 10.5). Some jaspers can be also ferromagnetic (Plata and Navas 1996), but these have not been recorded in the samples used. Ore-body samples are completely paramagnetic.

10.3.3 2.5D Gravity and Magnetic Modelling

In the study area, eight N-S cross-sections, approximately perpendicular to the strike of the gravity data, were extracted from the starting 3D gOcad model previously built from the available information as described above. The profiles cross the main geological features and were selected in order to constrain the structures by 2.5 D gravity modelling. For this task we have used the GM-SYS software (by Geosoft), extending the models far

enough at both ends of the profiles in order to avoid edge effects. The reduced to the pole magnetic field has been modelled with an IGRF of 43,407 nT, $I = 90^\circ$, $D = 0^\circ$ and taking into account that all the magnetic field is induced (i.e., no remanence). Calculations of the gravity and magnetic model response are based on the methods of Talwani et al. (1959) and Talwani and Heirtzler (1964), and the algorithms described in Won and Bevis (1987). In this study, we present the most representative cross-sections of the lithologies in the area (see profiles 9 and 14 in Fig. 10.4a).

Densities and magnetic susceptibilities have been obtained from the petrophysical data. As the main uncertainties are the geometry of the bodies, for the densities we have used the average in the majority of the cases, (see Table 10.2) or a value within the range of uncertainty ($\pm 0.05 \text{ mGal}$). For the magnetic susceptibilities we have used values within the range of the measured values (Table 10.2).

In profile 9 (Fig. 10.6), the gravity data are characterized by a subtle N-S gradient from -0.5 to 1 mGal with a succession of maxima and minima of different amplitudes and wavelengths. The first minima, about 0.7 mGal in amplitude and extending over a Culm outcrop has been assumed to be mainly due to its thickness, although a small increase in the PQG density is needed in order to improve the fitting of the anomaly in this area. In the neighbouring thrusts (c. 2570 and 4000 m horizontal distance) the volcanic suite, mainly VS2 and VS1, crops out, and a certain alteration of the outcropping rocks is needed in order to fit the observed anomalies. The relative maximum centred on the *Atalaya* open-pit, about 1 mGal in amplitude, is primarily explained by the mineralization. As the mineralization is small compared to the grid spacing of the gravity data (0.5 km), it is not possible to model it with its real density, even limiting its lateral extension to 500 m . The transition to the following minimum is a locally steep gradient that has been modelled assuming a thin layer of massive sulphides with a density of 3.8 g/cm^3 . The aforementioned minimum is centred in an outcrop of VS2–VS3. It has been very difficult to adjust and finally we have settled on decreasing

IPB_Litology Groups

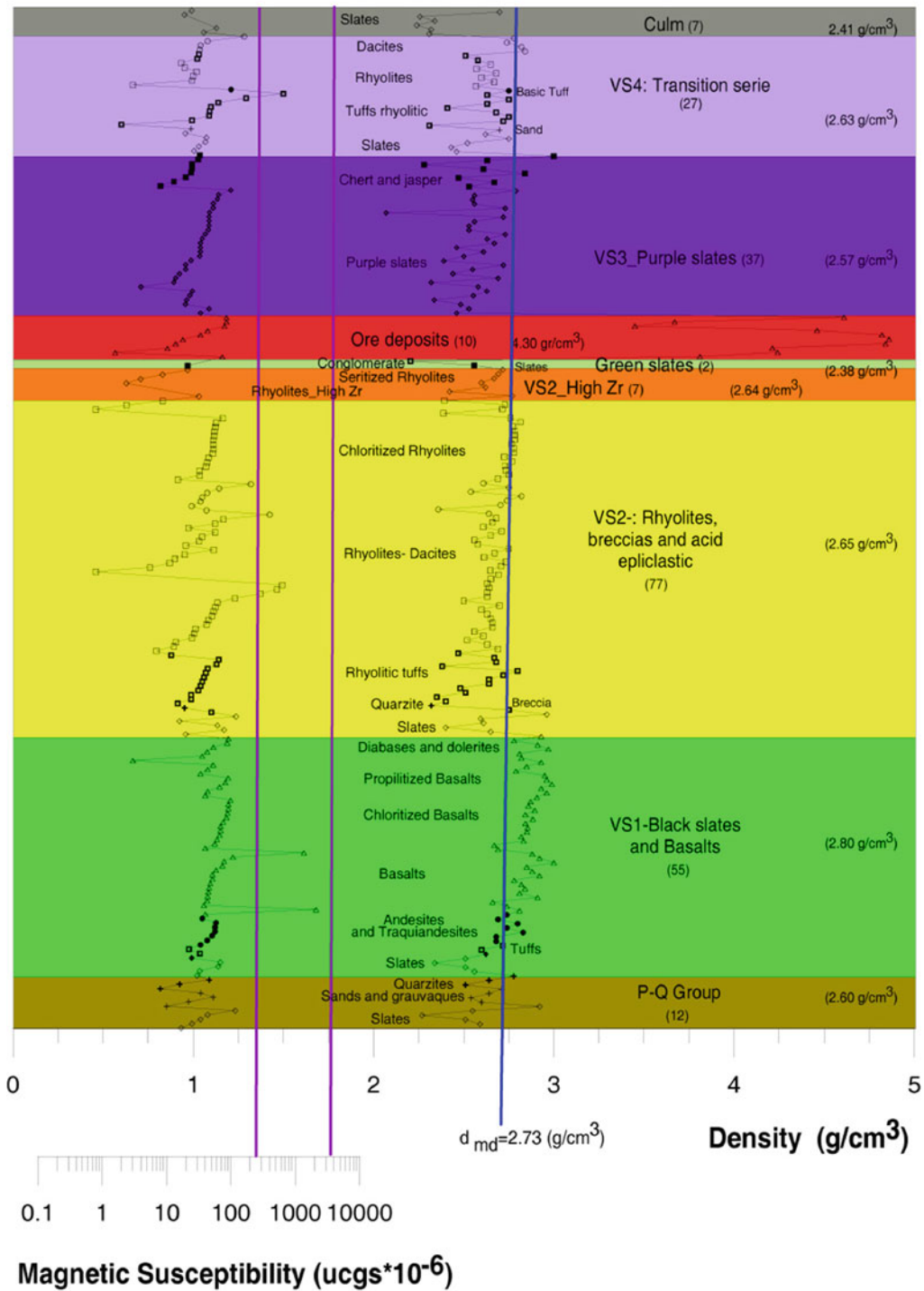


Fig. 10.5 Pseudo-log of density (blue line to the right) and magnetic susceptibility (purple line to the left) of the 234 samples. Samples are sorted by groups in different colours, and according to lithology, represented by different symbols within each group. Number in parentheses shows the number of samples of each group, whilst the other displays average density (g/cm³). The blue bar represents average

density of the whole sample. The two purple bars over the magnetic susceptibility scale represent ferromagnetism limits: samples on the left side are paramagnetic (susceptibility $k < 250 \times 10^{-6}$ ucgs); samples between both bars are weak to moderate ferromagnetic ($0.1 < \% \text{Fe}_3\text{O}_4 < 1$), and on the right side second bar samples are ferromagnetic ($k > 2500 \times 10^{-6}$ ucgs; $\% \text{Fe}_3\text{O}_4 > 1 \%$)

Table 2 Measured versus modelled geophysical properties in a model of Figs. 10.9 and 10.10

Lithology	Petrophysics		Modelling Profile P9		Modelling Profile P14	
	Avg. Density d (g/cm ³)	Range Susceptibility k (*10 ⁻⁶ ucs)	Density d (g/cm ³)	Susceptibility k (*10 ⁻⁶ ucs)	Density d (g/cm ³)	Susceptibility k (*10 ⁻⁶ ucs)
Culm	2.41 (2.54)	0–60	2.41–2.54	0–130	2,54	0
VS4	2,63	0–650	2,63	0	/	/
VS3	2,57	4–100	2.57 (2.30)	0	2.57 (2.20)	0
VS2	2,65	0–32	2.40–2.65 (2.30)	0	2.50–2.75 (2.00)	0–20
VS1	2,80	3–2000	2.55–2.80	0–3700	2.80–2.90	0–510
PQ	2,60	10–120	2.55–2.67	0	2.58–2.74	0
Assumed Massive Sulphides	n/a	n/a	3,8	0	3,8	0–2400
Mineralisations	4,30	2–86	2,75	80	3	0
Assumed Granite	n/a	n/a	/	/	2,58	270
Epiclastic	n/a	n/a	2,57	150	/	/
Black shales with radiolaries	n/a	n/a	2,52	70	/	/

the density of the VS2 and VS1 by 0.1 mGal, which is still within the range of measured densities. In the southernmost end of the model, the anomaly is adjusted by slightly increasing the density within the PQG.

Along profile 14 (Fig. 10.7), whose long wavelength component is almost constant at c. 0 mGal, the gravity anomaly shows a prominent central maximum of c. 1 mGal that can be associated with the combined effect of the mineralization (red body) and the VS2-VS1 anticline. East and west of this relative maximum, there is a set of maxima and minima of smaller amplitude (less than 0.7 mGal). In order to fit these anomalies, we included three relevant features, deduced from the modelling, which were not present in the initial geological model: firstly, the occurrence of massive sulphides (blue bodies), modelled as thin layers located between VS2 and VS3, secondly, the stockwork made up of an interconnected network of sulphide veinlets within PQG, VS1 and VS2 rocks that increases the density of those lithologies, located between faults, and thirdly the presence of granites towards the southern end of the profile, which had been already predicted in previous studies (e.g. Díez-Montes and Bellido-Mulas 2008, Díez-Montes et al.2011).

The SW magnetic maximum has been modelled as a more magnetic rock within the VS1; the prominent maximum towards the end of the profile has been modelled assuming a slightly ferromagnetic granitoid and some magnetization within the VS1. In the assumed massive sulphides, magnetic susceptibility varies between 0 and 2400 ucs.

10.3.4 The Final 3D Model

After importing the data concerning lithological contacts from the geological map, they have to be projected onto the topographic surface. This surface has been previously created from the point grid generated in ArcGIS by direct triangulation. To reflect the variation in slope, the contact curves have been densified before the projection. The codification of the lines is maintained as the import of the shape format, used for the translation between GIS and gOcad, maintains the fields used for the map making it easy to filter the different types of curves. Manual editing is then necessary to classify the curves as the top level of each lithology.

For the cross-sections, the digitized curves have been classified in the same way as the

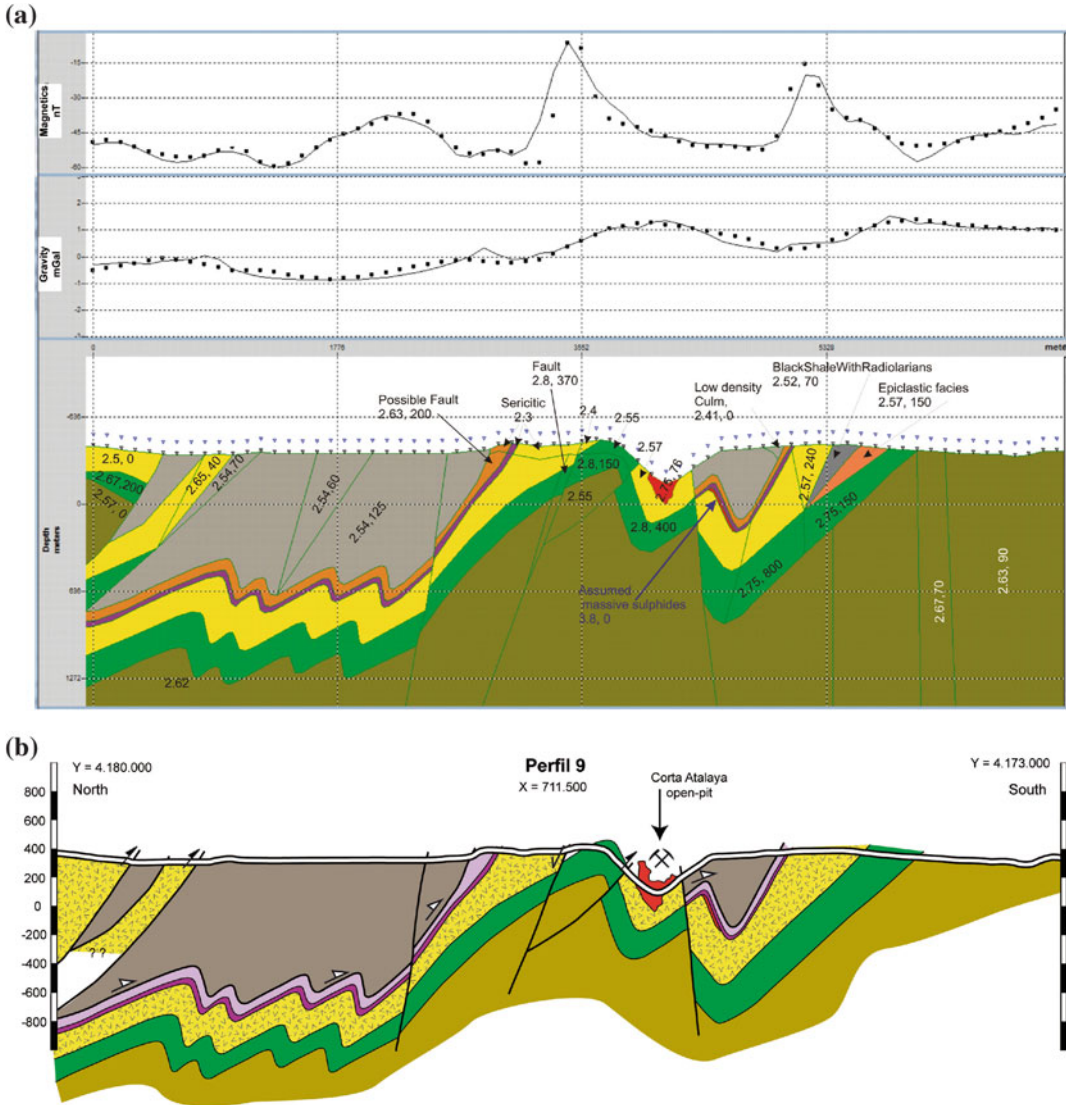


Fig. 10.6 Profile 9. **a** Cross-section model fitted to gravity and magnetic anomalies. Note the adjustment between measured (*dotted line*) and calculated (*solid line*) responses (magnetic above, gravimetric below). **b**: Geological cross-section. (densities in g/cm^3). Red- assumed massive sulphides with a density of $3.8 g/cm^3$. RMS of

the gravity anomaly differences between observed and calculated is $0.18 mGal$. 2.54, 125 = first number, density in g/cm^3 ; second number, magnetic susceptibility in cgs. Coordinates: UTM projection, Hayford ellipsoid. Longitudes referred to Greenwich Meridian. European Datum-1950

contacts of the geological map. Thus, each surface can be generated from a set of lines from horizontal and vertical planes, if possible. As a limit for the model, a box, or Voxet, enclosing both kinds of curves has been created.

The surfaces or horizons have been generated as medium planes of each set of curves for each

top level and then each surface has been shaped up using the D.S.I. (Discrete Smooth Interpolator), respecting the contact curves. To achieve this, the constraints to these curves must be established. To obtain a suitable surface, a succession of interpolations and triangle densifications has been carried out. Local editing has been

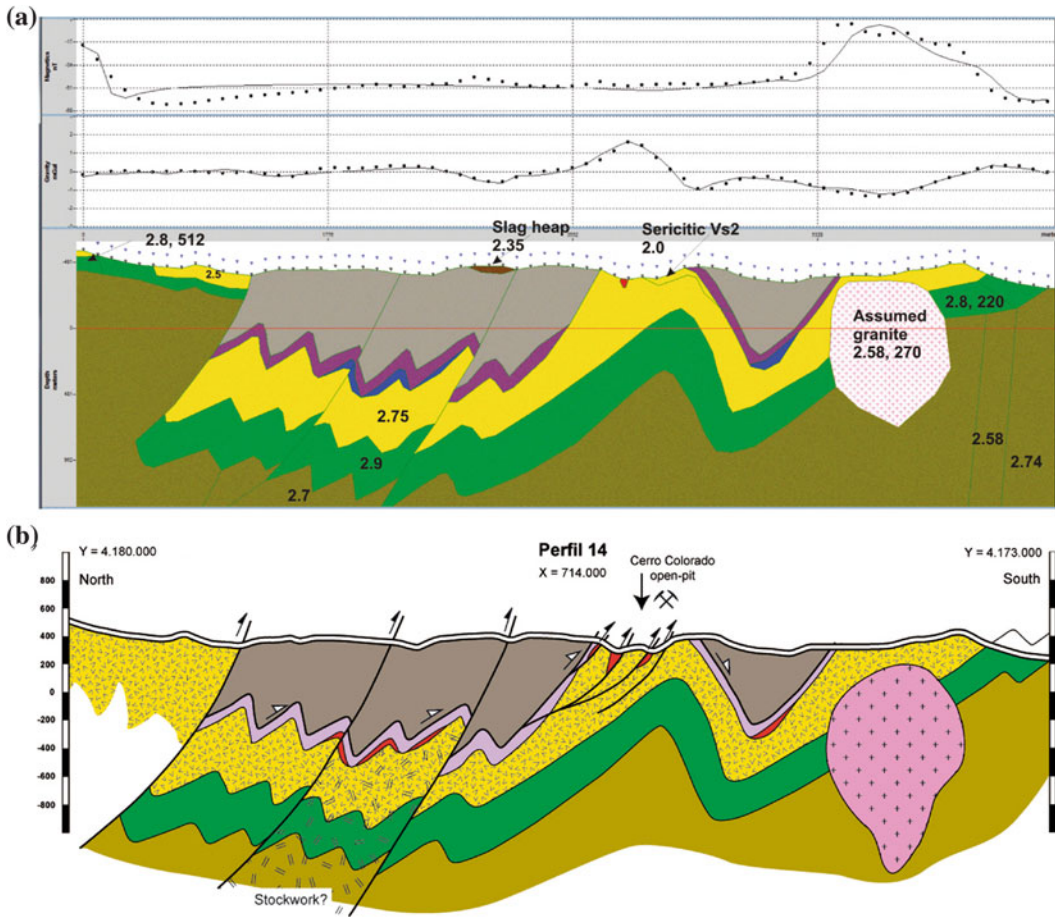


Fig. 10.7 Profile 14. **a** Cross-section model fitted to gravity and magnetic anomalies. Note the adjustment between measured (*dotted line*) and calculated (*solid line*) responses (magnetic above, gravimetric below). **b** Geological cross-section. (densities in g/cm^3). *Blue* assumed massive sulphides with a density of $3.8 \text{ g}/\text{cm}^3$; *Small red body* mineralization with a density of $3.0 \text{ g}/\text{cm}^3$. RMS of

the gravity anomaly differences between observed and calculated is 0.13 mGal and of the magnetic anomalies is 7 nT . 2.8, 512 = first number, density in g/cm^3 ; second number, magnetic susceptibility in cgs. Coordinates: UTM projection, Hayford ellipsoid. Longitudes referred to Greenwich Meridian. European Datum-1950

necessary where some conflict has been detected, especially in reverse fault zones.

The faults system displays a complex pattern making the fault distribution hard to model. Therefore, amongst all the existing faults, only the most relevant have been modelled. They have been created in a similar way as the horizons, taking fault traces from the map and fault interpretations from the cross-sections. Once again, modelling using medium planes seems the best way to create these surfaces.

Intersections between fault surfaces have been made so that they respect the temporal

relationships of the fault blocks and the lithological units. Surfaces are cut and their borders are linked to other surfaces or surfaces borders by means of constraints. Such constraints are borders on surfaces or vector fault links. At the same time the constraints from curves and free borders are respected.

After modelling of the faults, horizons have been cut by faults and constraints in faults borders have been established in order to recreate the fault movement. The horizons are thus defined by up to four types of constraints: 1) control points, 2) borders on straight lines, 3) borders on surfaces

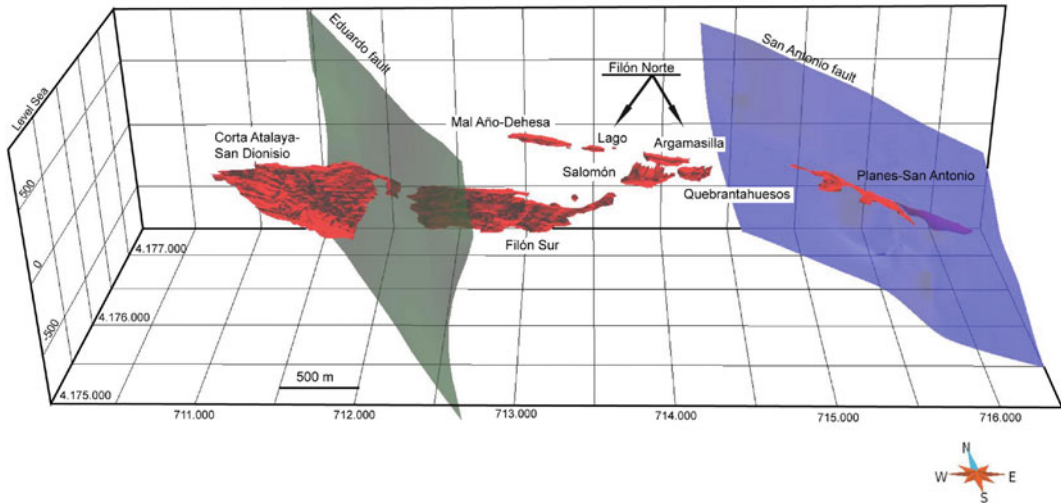


Fig. 10.8 Visualisation of the massive sulphide ore-body of *Río Tinto* from gOcad

and 4) vector links on borders and, where necessary, nodes have been blocked by control nodes.

The massive sulphide bodies are represented by mainly closed surfaces with a different geometry. They are generally well known if they have been mined and a great deal of data are available from drillings and large scale level maps. The surfaces are thus constructed by triangulating between the outlines of two consecutive outlines among the level plans, so that a series of triangulated bands is obtained. Constraints can be set to the outlines and later interpolations lead to a smoother surface that can be adjusted to other data, such as sections or drillings. In this way it has been possible to reconstruct the shape of the massive sulphide ore-body from drill-hole data and maps of mine workings.

Following this process, we have been able to obtain a precise morphology of the massive sulphides that form the large ore-body of *Río Tinto* (Fig. 10.8). All massive sulphide ore-bodies have been exploited by open-pit mining, except the *Planes-San Antonio* body that was exploited by underground mining. ‘*Corta Atalaya-San Dionisio*’, ‘*Filón Norte*’, ‘*Filón Sur*’ and ‘*Planes-San Antonio*’ are massive sulphide ore-bodies, whilst ‘*Mal Año-Dehesa*’, ‘*Salomón*’ and ‘*Quebrantahuesos*’ are intense stockwork ores, which in places even replace the rock almost entirely.

The gOcad software allows the making of models according to a grid in order to make interpolations on the basis of some properties. Several simulations have been performed to see if the variations in content of some elements are related to the geological structures in the study area.

In gOcad, two types of cell distribution can be used: Voxet and SGrid. The latter (Stratigraphic GRID) has been chosen, taking into account the bending of the anticline of *Río Tinto*. The SGrid is a compound of 79, 692, 500 cells and it has been built from a Voxet of $5 \times 5 \times 1$ meters that has been deformed to adjust to the volume defined by the volcano-sedimentary sequences. The method of interpolation used is the Discrete Smooth Interpolator. As a result, the simulation of the distribution of the elements adapts to the general structure.

The grades of the elements are held as properties in the well objects in the gOcad and are transferred to the cells prior to the interpolation.

Analytical contents of several elements of economic interest were available among the data provided by the EMED Tartessus Company: Cu, S, Pb, Ag, Zn and As. The simulation shows the interpolation of the copper distribution in the Cerro Colorado open-pit. The correlation between the high grade zones and the ore-bodies

is clear. The broad spread of the grades in the area is due to the stockwork and the chloritic alteration present in the central part of the anticlinal. The original data, taken from drilling campaigns previous to the open-pit exploitation, have been useful to reconstruct the original copper distribution, as the upper part of the structure is not present today.

Once the surfaces have been created and adjusted, a model can be constructed. The creation of a 3D model in gOcad involves the use of a number of regions in which the model is divided. Given the local nature of the model, a simplified column has been used, leaving eight major units, and the surfaces for these units have been created. To avoid excessive complexity when creating the 3D model for the east zone, five major units have been modelled, the PQG, basalts (VS1), rhyolites-dacites (VS2), massive sulphide, purple shales (VS3) and transition series (VS4) (see legend of Fig. 10.2).

The 3D model obtained shows the general structure in the area, a wide syncline with an anticline in the middle (Fig. 10.9a). The Culm formation can be found structurally on top. The contact with the VSC is defined by an extensional detachment, cutting through some parts of the underlying units (footwall ramp). In order to make the model easier to understand, neither this layer model, nor the eroded upper part is shown in the model, so that observation of the folding at the central part and how it affects the sulphides is enhanced. The massive sulphide ore-bodies are also shown, revealing their geometric relationships with the felsic volcanism and how they have been affected by the tectonics.

The 3D reconstruction of the *Río Tinto* ore-bodies and their relationships with the thrust and faults has greatly improved the understanding of this complex structure (Fig. 10.9b). 3D modelling takes into consideration the strong lateral variations of the tectonic structures and the thickness of each volcanic unit. Folded surfaces have been finally constructed in gOcad using cross-sections, fold axes and surface stratigraphic boundaries as constraints.

10.4 Potential Resources Assessment

The predictive model is based on the following assumptions:

1. There are two styles of volcanogenic massive sulphide mineralization in the Iberian Pyrite Belt and they are located in different positions within the sequence. The first includes dominantly exhalative shale-hosted deposits of probable late Strunian age located at or near the PQ Group—volcano sedimentary complex contact. This style of mineralization is located in the southern IPB and includes some major deposits such as *Las Cruces*, *Aznalcóllar-Los Frailes*, *Sotiel-Migollas*, *Masa Valverde*, *Tharsis* and *Neves Corvo* (Chap. 9, Fig. 9.1). The second style of mineralization includes the deposits located in the northern part of the IPB; they are usually hosted by glassy/pumice-rich domes of dacite-rhyolite composition of early Tournaisian age. The most significant deposits are *San Telmo*, *Aguas Teñidas*, *Concepción* and *San Platón* (Chap. 9, Fig. 9.1). Both *Río Tinto* and *La Zarza* belong to this group, but display a shale-hosted exhalative zone above a volcanic-hosted replacive one. Both styles of mineralization contain an underlying stockwork.
2. The estimated total tonnage of the already discovered ore (including both the stockwork and the massive sulphides) is ca. 852 Mt in the southern zone and 1085 Mt in the northern zone.
3. Thus, there are two major ore-bearing horizons: The shale and volcanic rocks near the PQ Group-VS Complex contact in the southern zone and the hanging wall of a dacite-rhyolite unit in the northern zone. These two metallotects are reasonably well explored and it is unlikely that there are undiscovered masses at depths, more than 800 m above the ore deposits or 200 m away from them. For modelling purposes, unknown new deposits should be at depths of >600 m.

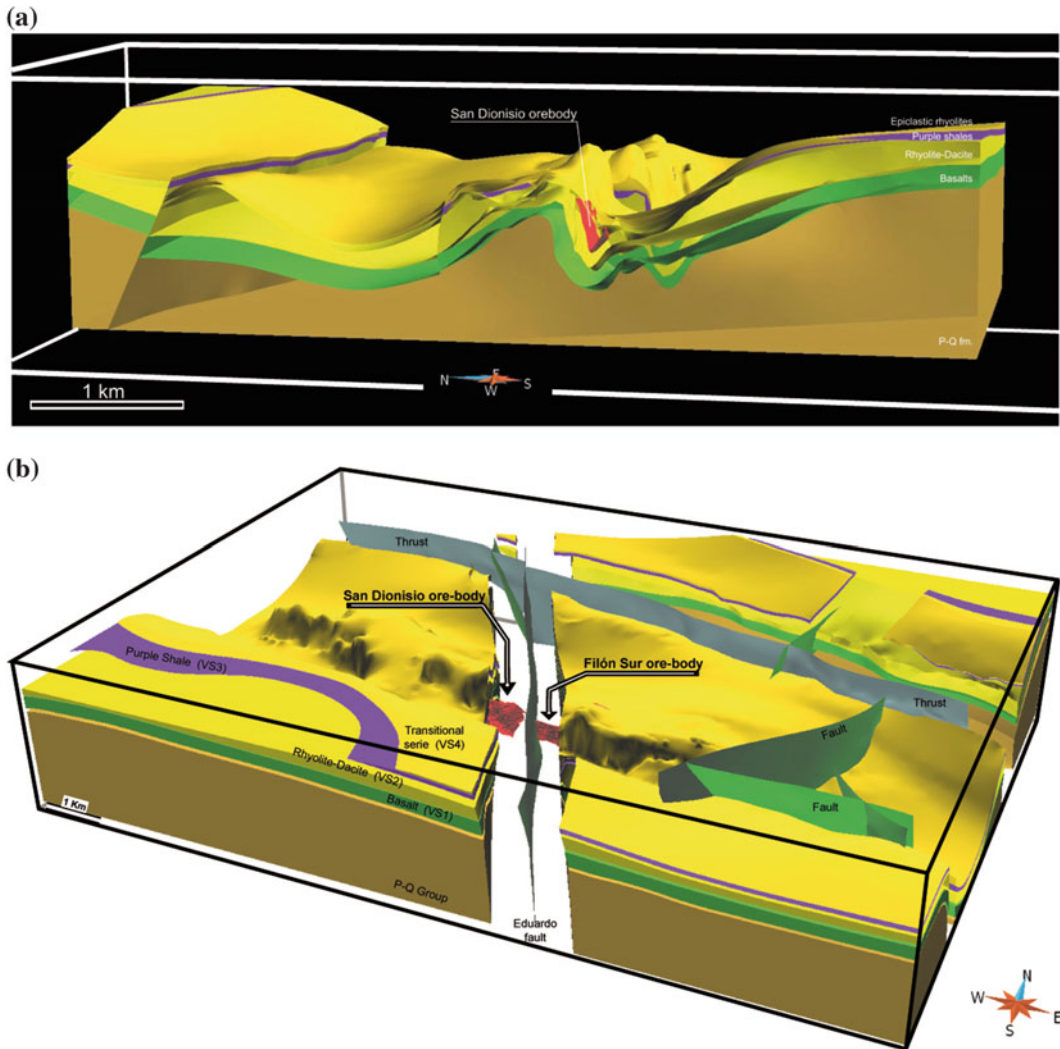


Fig. 10.9 **a** 3D surface of the *Río Tinto* structure in a N-S section. **b** Visualisation of the 3D model of *Río Tinto*

4. The final assumption is that deposits located at depths near 1000–1200 m can be mined if grades and tonnages are viable.

If these assumptions hold true, then the amount of undiscovered massive sulphides is ca. 1.7 Gt in the southern part and 2.1 Gt in the northern part. These estimations include both massive sulphides and stockwork zones.

More specifically in the *Río Tinto* area, we have been able to detect two areas of great interest from gravimetry studies (Fig. 10.10, zones A and B) due to the possible presence of

massive sulphides and stockwork zones, as we can see in profile 14 (Fig. 10.7). It has been necessary to insert these masses of sulphides into the stratigraphic column to be able to correlate the gravimetric curves.

We have also identified two other possible areas of prospective interest from the detailed geological field work (Fig. 10.10, zones C and D). These areas are associated with two faults that link the *Atalaya-San Dionisio* massive sulphide ore body with the *La Poderosa* and *Solviejo* mines located to the NW.

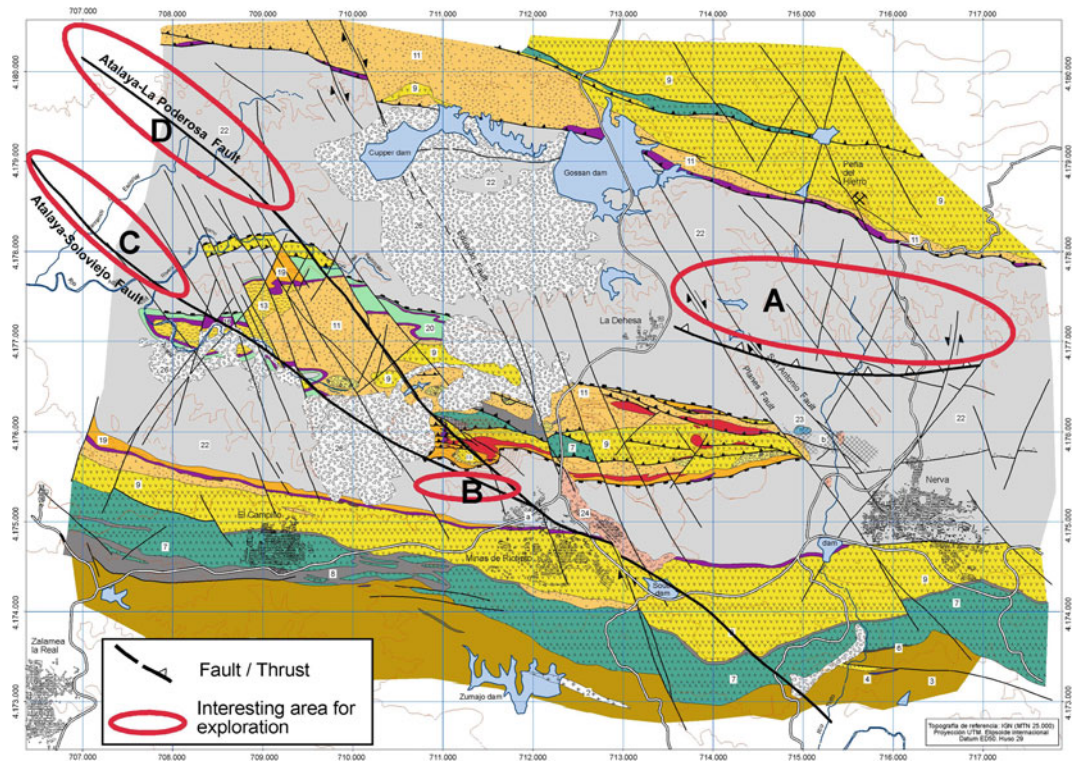


Fig. 10.10 Potential prospective areas next to *Río Tinto* mining district (Legend as Fig. 10.1)

Some areas may be of interest for future mineral exploration. With a combination of geological potential, magnetic and gravity anomalies, together with results in the ternary map, the areas outlined in the Fig. 10.10 are considered to be potential sites for future mineral exploration.

10.5 Summary and Conclusions

In order to validate the 3D model, a gravimetric inversion was made and the results have been used to feed the model. To generate a consistent 3D model, all surfaces must have a precise fit at the intersections and have a geological meaning. Geological attributes are assigned and the stratigraphic column is created, which is related to geological objects and defines relationships and types of contacts between units.

The detailed map of the *Río Tinto* anticline reveals the complex tectonic evolution of this zone. We have been able to identify the detachment which is located at the contact between the CVS and the Culm. This detachment is folded and cut by ductile thrust and then by out of sequence thrust. The detachment and thrusts can produce a tectonic stacking. This tectonic stacking can either contribute to add or reduce the tonnage of a VHMS deposit.

The 2.5D modelling results indicated that a further revision of the initial geological model would be necessary:

- The relative residual Bouguer minimum located to the SW requires the presence of buried granite without having to draw unrealistic geometries to the volcanosedimentary sequences or unlikely low densities for the PQ. This granite was already postulated by Díez-Montes and Bellido-Mulas (2008).

- To fit some of the profiles it was required to increase the density of the PQ, VS1 and VS2 beneath the central part of the northern out-cropping Culm facies, which have been assumed to host massive sulphides and stockwork and to be located within a thrust that was not previously identified.
- Some of the small amplitude relative maxima have been adjusted by assuming the presence of massive sulphides between the VS2 and VS3. Again this is required in order to preserve the consistency between geometries and physical properties and avoid unrealistic scenarios.

As a general conclusion, 3D modelling has proved to be a powerful tool. It provides the geologist with a way to represent complex surfaces from several sources of data. In this study, data from geologic maps, cross sections, drillings, gravimetry and field surveying have been used.

Acknowledgments This study has been partly funded by the ProMine project “Nano-particle products from new mineral resources in Europe”, in the VIII Framework Programme for research. We gratefully acknowledge the EMED-TARTESSUS Company, and especially Nikos Adamides and Angelo Farci, for facilitating access to the *Río Tinto* mine. We gratefully acknowledge the positive comments by the reviewer Cecilio Quesada which have improved the paper. Thanks also go to A.L. Tate for revising the English text.

References

- Barrie, C.T., Amelin, Y., Pascual, E. 2002. U-Pb Geochronology of VMS mineralization in the Iberian Pyrite Belt. *Mineralium Deposita*, 37, 684-703.
- Bates, M., García Lobón, J.L. 1998. Exploration of Pyrite Belt and surrounding areas concerning aeromagnetic and radiometric data. IGME documentary Report (SID N°. 40464. Madrid). Available on line: http://www.igme.es/internet/sistemas_infor/Sid.htm
- Castroviejo, R., Quesada, C., Soler, M. 2011. Post-depositional tectonic modification of VMS deposits in Iberia and its economic significance. *Mineralium Deposita*, DOI: [10.1007/s00126-010-0306-7](https://doi.org/10.1007/s00126-010-0306-7).
- Díez Montes, A. y Bellido Mulas, F. 2008. Magmatismos TTG y Al-K en la Zona Surportuguesa. Relaciones entre plutonismo y vulcanismo. *Geo-Temas*, 10, 1449-1452.
- Díez-Montes, A., Bellido, F., Sánchez García, T. 2011. TTG and Al-K magmatism in the South Portuguese Zone. Relations between plutonism and volcanism. *Seventh Hutton Symposium on Granites and Related Rocks*. Ávila (Spain). Abstracts Book, p. 47.
- Dunning, G.R., Díez Montes, A., Matas, J., Martín Parra, L.M., Almarza, J., Donaire, M. 2002. Geocronología U/Pb del volcanismo ácido y granitoides de la Faja Piritica Ibérica (Zona Surportuguesa). *Geogaceta*, 32, 127-130.
- González-Clavijo, E.J., Oswin, W.M., Ferrer, A., Fernández Gianotti, J. 1994. Esquema estructural de un sector de la Zona Surportuguesa al este de las minas de *Río Tinto*. *Boletín Geológico y Minero de España*, 105-3, 225-235.
- González-Clavijo, E.J. and Díez-Montes, A. 2010. Propuesta de estructura geológica para el depósito gigante de sulfuros masivos volcanogénicos de *Río Tinto*, Faja Piritica Ibérica. *Geogaceta*, 48, 203-206.
- Mellado, D., González Clavijo, E.J., Tornos, F., Conde, C. 2006. Geología y estructura de la Mina de *Río Tinto* (Faja Piritica Ibérica, España). *Geogaceta*, 40, 231-234.
- Navarro Vázquez, D. and Ramírez Copeiro del Villar, J. 1982. Mapa y Memoria de la Hoja n° 938 (Nerva). 2ª serie del Mapa Geológico Nacional a escala 1:50.000 (MAGNA). Instituto Geológico y Minero de España, Madrid, pp 1-68.
- Oliveira, J.T. 1990. South Portuguese Zone: Introduction. Stratigraphy and synsedimentary tectonism. In: Dallmeyer, R.D. & Martínez García, E. (eds.). *Pre-Mesozoic Geology of Iberia*. Springer, Berlin, 333-347.
- Plata, J.L., Navas, J. 1996. *Proyecto integrado de estudio Geológico y Metalogenético de la Faja Piritica. Geofísica. Parte II: Caracterización petrofísica de unidades y edición digital de Cartografía Geofísica*. IGME internal report SID 40454.
- Quesada, C. 1998. A reappraisal of the structure of the spanish segment of the Iberian Pyrite Belt. *Mineralium Deposita*, 33, 31-44.
- Rodríguez, R.M., Díez-Montes, A., Leyva, F., Matas, J., Almarza, J., Donaire, M. 2002. Datación palinoestratigráfica del volcanismo en la sección de la Ribera del Jarama (Faja Piritica Ibérica, Zona Surportuguesa). *Geogaceta*, 32, 247-250.
- Rosa, D.R.N., Finch, A.A., Andersen, T., C. M. C. Inverno, C.M.C. 2009. U-Pb geochronology and Hf isotope ratios of magmatic zircons from the Iberian Pyrite Belt. *Miner. Petrol.*, 95, 47-69
- Sánchez-García, T.; Ayala Galán, C.; Díez-Montes, A.; García Lobón, Rey Moral, C.; J.L.; García Crespo J.; Bellido Mulas, F.; Rubio, F.M.; Tornos, F. 2015. Characterization of the Riotinto geological, structure (Huelva, Iberian Pyrite Belt) from gravity and magnetic data (PROMINE project). Serie de informes técnicos. IGME, Madrid, pp 1-114.
- Schermerhorn, L.J.G. 1971. An outline of the stratigraphy of the Iberian Pyrite Belt. *Boletín Geológico y Minero de España*, 82, 239-268.

- Silva, J.B., Oliveira, J.T., Ribeiro, A. 1990. Part VI: South Portuguese Zone. 3: Structural Outline. In: Dallmeyer, R.D. and Martínez García, E. (eds.). *Pre-Mesozoic Geology of Iberia*. Springer-Verlag Berlin Heidelberg, 348-362.
- Simancas, J.F., Carbonell, R., González Lodeiro, F., Pérez Estaún, A., Juhlin, C., Ayarza, P., Kashubin, A., Azor, A., Martínez Poyatos, D., Almodóvar, G.R., Pascual, E., R. Sáez, R., Expósito, I. 2003. Crustal structure of the transpressional Variscan orogen of SW Iberia: SW Iberia deep seismic reflection profile (IBERSEIS). *Tectonics*, 22 (6), 1062, doi: [10.1029/2002TC001479](https://doi.org/10.1029/2002TC001479).
- Talwani, M., Heirtzler, J. R. 1964. Computation of magnetic anomalies caused by two dimensional bodies of arbitrary shape. In: Parks, G. A. (Ed.), *Computers in the mineral industries, Part 1*. Stanford University Publications, Geological Sciences, 9, 464-480.
- Talwani, M., Worzel, J. L., Landisman, M. 1959. Rapid gravity computations for two dimensional bodies with application to the Mendocino submarine fracture zone. *Journal of Geophysical Research*, 64, 49-59.
- Valenzuela, A., Donaire, T., Pin, C., Toscano, M., Hamilton, M.A., Pascual, E. 2011. Geochemistry and U–Pb dating of felsic volcanic rocks in the Riotinto-Nerva unit, Iberian Pyrite Belt, Spain: crustal thinning, progressive crustal melting and massive sulphide genesis. *Journal of the Geological Society, London*, 168, 717-731.
- Won, I.J., Bevis, M. 1987. Computing the gravitational and magnetic anomalies due to a polygon: Algorithms and Fortran subroutines. *Geophysics*, 52, 232-238.

C. Inverno, C. Rosa, J. Matos, J. Carvalho,
J.M. Castello-Branco, M.J. Batista, I. Granado,
J.T. Oliveira, V. Araújo, Z. Pereira, P. Represas,
A.R. Solá and P. Sousa

Abstract

3D, 4D and predictive geological modelling, including all known geoscientific data, were applied to the 100 × 25 km large Neves Corvo project area located in the Portuguese part of the Iberian Pyrite Belt. The lowermost unit in the area is the Givetian to Famennian-Strunian Phyllite-Quartzite Group (PQG), which is overlain by three SE-plunging volcanic axes with the Strunian to Visean Volcanic Sedimentary Complex (VSC), hosting in its lower sequence the Neves Corvo VHMS giant deposit. The VSC is covered with mid late Visean and Serpukhovian to Bashkirian flysch rocks [Mértola and Mira formations of the Baixo Alentejo Flysch Group (BAFG), respectively]. Six NE-SW deep 2D reflection seismic profiles acquired by LNEG between Neves Corvo mine and the Spanish border (60 km to the SE) during the ProMine project, allowed to extend a 3D-model of the Neves Corvo main thrust (that brings VSC rocks onto Mértola Fm. very close to VHMS ores) throughout the eastern part of the area. NE-SW to ENE-WSW (sinistral) and N-S to NNW-SSE (dextral) late Variscan strike-slip oblique faults (a few >5 km deep) displaced all former geological units and structures, as shown by the 3D models. In late Variscan time, small vein-type Cu (and other metals) deposits were emplaced along them.

C. Inverno (✉) · J. Carvalho · M.J. Batista
I. Granado · J.T. Oliveira · P. Represas · A.R. Solá
Laboratório Nacional de Energia e Geologia
(LNEG), Estrada Portela—Zambujal, Apartado
7586, 2610-999 Alfragide, Portugal
e-mail: carlos.inverno@lneg.pt

C. Rosa
Empresa de Desenvolvimento Mineiro SA (EDM),
Rua Sampaio e Pina 1 3 DTO, 1070-248 Lisboa,
Portugal

J. Matos · P. Sousa
LNEG, Rua Frei Amador Arrais, 39 r/c, Apartado
104, 7801-902 Beja, Portugal

J.M. Castello-Branco
Geology and Geotechnics Consultores Lda., Rua
Cunha Júnior, 41b Sala 1.6, 4250-186 Porto,
Portugal

V. Araújo
Rua Sub-carreira, 575, 4815-517 Vizela, Portugal

Z. Pereira
LNEG, Rua da Amieira, Apartado 1089, 4466-901
S. Mamede Infesta, Portugal

The 4D model enabled to establish a clear age sequence of mineralization types, inferring also that VHMS mineralization may possibly exist at depth between the Neves Corvo mine and the Alcoutim sector (near the Spanish border). The 3D predictive model, constructed exclusively for the restricted area of the Neves Corvo mine, pinpoints, both through the 3D-density (from gravity inversion) and the % Cu-drill hole-based block diagrams, not only the known Neves Corvo orebodies, but also other possible extensions. The regional extension of the Neves Corvo model increases significantly the overall exploration potential of the whole IPB region in this study.

11.1 Introduction

In the geographic area covered by this project four main antiformal structures encompassing the Iberian Pyrite Belt succession are recognized: Castro Verde-Casével, Neves Corvo-Rosário, Ourique and Alcoutim (Fig. 11.1). In all these antiforms the rock exposure is largely dominated by the Volcanic Sedimentary Complex (VSC) lithologies and the underlying Phyllite-

Quartzite Group (PQG) is only exposed in the Lançadoiras region, 1 km NW of Neves Corvo mine. The Pyrite Belt succession is stratigraphically overlain by the Mértola Formation (Fm) turbidites of the Baixo Alentejo Flysch Group but tectonic imbrications among this formation and the other Pyrite Belt lithostratigraphic units may occur. Distinct turbidites of the same flysch group make up the Mira Fm that covers Mértola Fm rocks at the southeasternmost end of the project area.

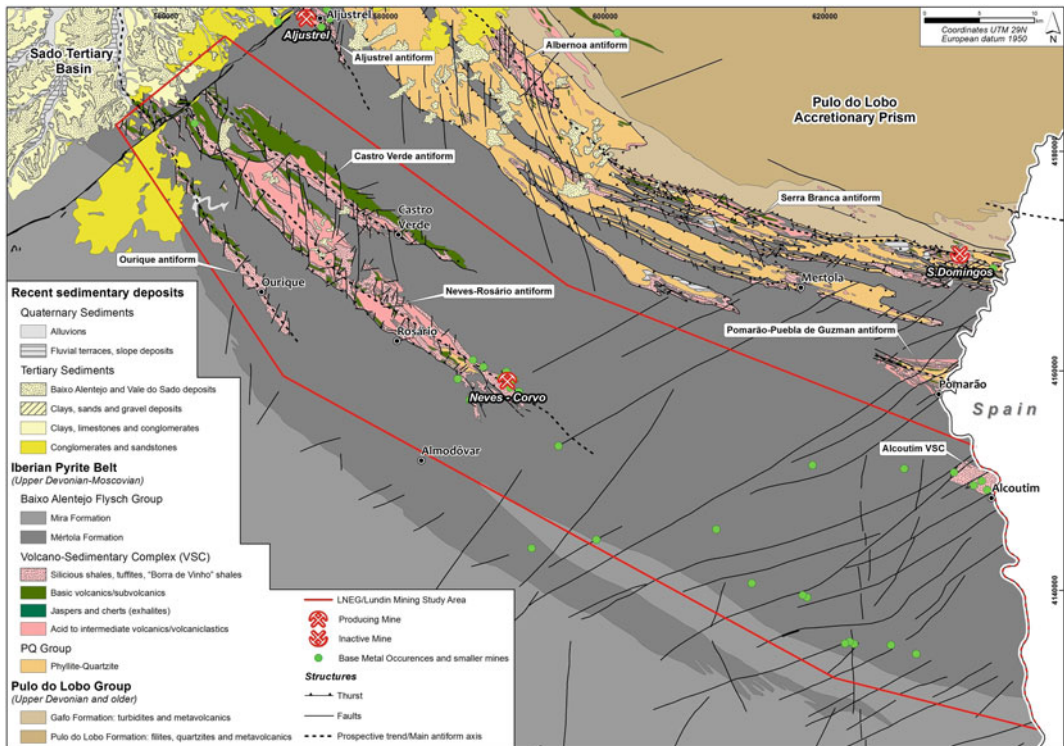


Fig. 11.1 Regional geology map of the Neves Corvo project area (modified from Lundin Mining 2012)

The existing geological knowledge of these antiforms is very different from one another: while the Neves Corvo mine area at the SE termination of the Neves Corvo—Rosário antiform has been studied in detail, the knowledge of the remaining areas is still limited. As such, we will briefly describe the geology of these remaining areas of the antiforms and will later describe the Neves Corvo mine region.

The stratigraphy of all the antiforms is composed of three main groups of lithologies, all belonging to the VSC: felsic volcanic rocks (V α), mafic volcanic rocks (V β) and dark shales and fine volcanogenic sedimentary rocks (XV) in which the volcanic rocks are interbedded.

The felsic volcanic rocks are dominant in the Neves Corvo—Rosário antiform where they form the outcropping core of this tectonic structure. Rhyolites, rhyodacites and felsic volcaniclastics represent the dominant rock types. The same types of volcanic rocks occur in the Castro Verde—Casével antiform but are absent in the Ourique antiform.

The mafic volcanic rocks comprise mostly basalts and dolerites and tend to occupy a stratigraphic position high in the VSC succession. Pillow lavas and hyaloclastites are common. Rare limestone lenses at the top of these volcanics contain conodonts of late Viséan age (Oliveira 1983).

The XV lithologies comprise dark and black shales, thin-bedded siltstones, siliceous shales and fine volcanogenic sediments and purple shales. Siliceous, manganese oxides, phosphate and siderite nodules can be found dispersed in all these shales. The XV lithotypes are dominant in the Alcoutim antiform and represent an important proportion in the Ourique antiform.

The Mértola Formation consists of classic turbidites characterized by packages of greywacke beds of variable thickness and grain size alternating with bands of shales and siltstones. The greywacke beds show the typical sedimentary structures that are common in deep water gravity clastic sedimentation (turbidites s. l.). The thickness given by exposed sections and drill cores is variable, depending on the tectonic blocks, and may reach 1500 m. Fossils of *Posidonia becheri*, ammonoids and palynomorphs indicate a late Viséan age

(Oliveira 1983; Korn 1997; Oliveira et al. 2004). This unit outcrops in about 70 % of the project area and the investigation of the sector situated between the Neves Corvo mine and the Portuguese/Spanish border is one of the main goals in the present project. The Mira Fm, outcropping in the vicinity of the border, is 1000–2500 m thick and made up of fine-grained greywackes, siltstones and shales of Serpukhovian age (several species of the Order Goniatitida; Oliveira and Wagner-Gentis 1983).

All the stratigraphic units are affected by NW-trending folds and associated cleavage dipping 60–70° towards NE. Folds styles vary from isoclinal in the VSC and PQG units to asymmetrical folds with long normal limbs and short reverse limbs in the Mértola and Mira formations and all show vergence towards SW. The VSC may exhibit an earlier cleavage, also NW-trending, not as penetrative as the main cleavage. Thrust faults parallel to the main cleavage may occur, a few extending continuously throughout the project area, as well as late near-vertical faults grouped in two main families, NW-SE, dextral and NE-SW, sinistral.

Metamorphism in the Pyrite Belt units is syn- to late-orogenic and characterized by the prehnite-pumpellyite—lower greenschist facies (Munhá 1983a, b). The volcanic rocks and the rocks hosting the massive sulphides ores are also affected by a pre-orogenic hydrothermal metamorphism underlined by the development of calcite, sericite and chlorite (Munhá 1990). The Mértola and Mira formations turbidites are metamorphosed in the prehnite-pumpellyite/zeolite and zeolite facies, respectively (Munhá 1983a).

Mapping carried out in the larger Neves Corvo mine region (Leca et al. 1983) complemented by logging of dozens of drill cores by mine geologists, palynostratigraphic research (Oliveira et al. 1997; Pereira et al. 2003; Oliveira et al. 2004) and recent research on the SE part of the Neves Corvo-Rosário antiform (Rosa et al. 2008; Oliveira et al. 2013) identified the regional stratigraphic sequence described below.

The Phyllite-Quartzite Group is represented by the dark shales with siliceous lenses and nodules of the Barrancão member, which are overlain by shales, siltstones and quartz-

sandstones of the Phyllite-Quartzite Formation. The unit's thickness as a whole is in excess of 100 m (base not seen). Palynomorphs indicate a late Famennian age for the Barrancão member and a Strunian (latest Famennian) age for the Phyllite-Quartzite Fm (Oliveira et al. 2004, 2006, 2013; Pereira et al. 2008). At the Monte Forno da Cal farm and at depth, the top of the Phyllite-Quartzite Group is overlain by a tens of meters thick shale band with interbedded limestone lenses and nodules. The latter yielded conodonts of upper Famennian age (Boogaard and Schermerhorn 1981).

The VSC has been divided into two main sequences that appear separated by a stratigraphic gap marked by the absence of Tournaisian sedimentary rocks (Oliveira et al. 2004). The Lower VSC sequence is composed of rhyolites, rhyodacites, volcanoclastic sedimentary rocks, basalts and dolerite sills. Its thickness varies depending on the distribution of the volcanic facies and may reach 500 m. Shales interbedded in these volcanic rocks yielded palynomorphs of Strunian age (Oliveira et al. 2004; Pereira et al. 2008). The massive sulphides occur at the top of the felsic volcanic rocks usually associated with black shales. Deep in the mine area, this lower sequence is unconformably overlain by greywackes and shales of the Mértola Fm (Mt2) which thickness is variable, from a few meters to several tens of meters, depending on the sea floor paleotopography. Fossils of ammonoids and palynomorphs show that these turbidites are of upper Viséan age (Oliveira et al. 2004; Pereira et al. 2008). The time gap between these turbidites and the underlying VSC rocks has been related to submarine erosion that removed the Tournaisian sediments (palynomorph reworked assemblages are found in the overlying younger units; Oliveira et al. 2004).

The Upper VSC sequence is composed of the Grandãos Fm (dark shales with phosphate nodules, cherts and fine volcanogenic sedimentary rocks), "Borra de Vinho" purple shales Fm and Godinho Fm (shales, siliceous shales and felsic volcanoclastic rocks), 300 m thick altogether. In the Neves Corvo mine, this lithostratigraphic succession has been dated as lower upper Viséan, based on palynomorphs (Oliveira et al. 2004). At depth in the mine area, drill cores have shown

that gray siliceous and black shales rich in phosphate nodules (Graça Formation) occur below the Godinho Fm. This unit has locally intercalations of felsic volcanic rocks. The black shales contain palynomorphs of lower Viséan age (Oliveira et al. 2004). The recently mapped—150 m thick—Ribeira de Cobres Fm (Oliveira et al. 2013), with shales, siltstones and fine volcanoclastic rocks, may represent a lateral facies variation of the Graça Fm. Above the Godinho Fm dark shales and thin-bedded greywackes of the Brancanes Formation that make the transition to the Mértola Fm flysch turbidites (Mt1) occur. Both units have an upper Viséan age given by palynomorphs and ammonoids (Oliveira et al. 2004).

The thrust of Upper VSC/Mt2 flysch rocks is particularly relevant as a tectonic marker at the Neves Corvo mine site, since it is very close to massive sulphide ore and serves in the area as a guide to Neves Corvo VHMS ore position.

Recent U–Pb dating of zircons recovered from felsic rocks in the SE region of the Neves Corvo-Rosario antiform indicated five episodes of felsic volcanism at 384, 373, 365, 359 and 354 Ma respectively (Oliveira et al. 2013). This indicates that a high heat flow was operative for 30 Ma and may have had an important role in the formation of convective cells that lead to the genesis of the massive sulphides.

Correlations from drill cores in the mine area show that mostly the Upper VSC sequence, but in many places the Lower VSC sequence as well, is stacked in tectonic sheets that were transported over the lower Mértola Fm turbidites (Mt2) (Fig. 4 in Oliveira et al. 2004) during the Variscan orogeny. This structural arrangement proved to be of fundamental importance for the interpretation of the deep seismic profiles that were performed in this project between the Neves Corvo mine and the Spanish border.

11.2 Methodology

The modelling of the Neves Corvo project area was done using geological data from surface and exploration drill holes, and seismic, gravity,

magnetic and electromagnetic data. This information was compiled from pre-existing data available at LNEG and from Lundin Mining, complemented with new data acquired during the PROMINE project to fill data gaps. The pre-existing data were acquired by LNEG in regional surveys, and by exploration companies that had exploration licenses relative to parts of the project area. All geological and geophysical information have been compiled throughout time and homogenised at LNEG, which is an essential procedure to integrate data from different sources and therefore draw the interpretations required to model the project area. Nevertheless, and given the large geographic extent of the Neves Corvo project area, the type of information available and its detail was quite variable. Surface geological information was available for the whole region. However, geological information at depth was difficult to obtain since exploration drill holes occur in clusters (concentrated over geophysical anomalies) and have a variable distribution. Additionally, the distribution of different geophysical surveys and methods is also variable, and mainly conditioned by the surface geology, implying that the project area turned out not to be entirely surveyed by one single method. Therefore, and according to the extent and variability of the available data, the modelling of the project area was done in three phases.

The NW sector of the project area was modelled by surface geological maps, geological log analyses of relatively shallow (up to 1000 m) drill holes, and TEM, gravity, magnetic and radiometric data. The modelling of the central part of the area, that concerns Neves Corvo mine and surroundings, was based on geological logs from deep (up to 1900 m) drill holes, surface and underground geology from the mine, combined with detailed seismic, gravity and TEM data. The SE sector (including Alcoutim) of the project area was mainly modelled by seismic data acquired under the Promine project, combined with TEM data and geological logs from few relatively deep (up to 1300 m) drill holes. The integration of the wide, variable and extensive information available was made using gOcad and GIS software. The models for the near Neves

Corvo mine area were produced by Lundin Mining that currently exploits the massive sulphide deposits of Neves Corvo and were included in gOcad as well. The scarcity of geological and geophysical data for the area between Neves Corvo mine and Alcoutim (SE sector of the project area) and the great depth of the top of the VSC complex were the motivation to conduct a seismic reflection survey in this area. Seismic reflection data are an essential tool to obtain structural and physical properties information of the subsurface at great depth. It has long been employed to study tectonic and sedimentary evolution of sedimentary basins, where impedance contrast is generally strong enough to allow imaging of the subsurface based on reflections. In the last decades, due to the advances in electronics such as 24 bit A/D converters and processing techniques, the seismic reflection method has gained a dramatic increase in the number of applications to hard-rock exploration (e.g. Kim et al. 1994; Radzevicius and Pavlis 1999; Eaton 2003). The mining industry is one of the fields where the seismic reflection method has shown great utility to complement the more generally applied gravimetric, magnetic, electrical and electromagnetic methods in VSC.

Metallic ore deposits such as the VHMS deposits of the IPB are commonly associated with high-angle structures, strong deformation and metamorphism, which prevented in past the use of seismic methods to locate them. Recent developments in migration algorithms and the surge of new methods which increased coverage and signal to noise ratio in poor reflectivity areas, such as the common reflection surface (CRS) method or 3D seismics (e.g. Hubral 1999; Cordsen et al. 2000), have changed the scenario. The seismic reflection method has now the capability of providing important structural information that coupled with the potential methods used in mineral exploration can become an important asset. Both 3D and 2D seismic methods have provided successful case histories in the mining industry. In the Portuguese mainland, the first seismic reflection profiles acquired for this purpose in Alentejo by Compagnie Générale de Géophysique (CGG) were supported

by Somincor in 1991 and 1996. The results were not conclusive and they were soon forgotten. Not much after the last CGG survey, the first deep seismic reflection profile started in the Spanish part of the IPB, close to the Portuguese border (e.g. Simancas et al. 2003; Carbonell et al. 2004). In Portugal, useful results were obtained using seismic reflection and gravimetric modelling for shallow massive sulphides exploration, under a relatively thin Tertiary cover that occurs in the NW part of the IPB (Oliveira et al. 1998; Carvalho et al. 2011). Due to the superior resolution and depth penetration the seismic reflection method was the most suited for the purpose of geological modelling of the IPB. The mechanical soundings generally do not exceed 2–3 km, while potential-field data give information at various wavelengths that are originated at different depths. Short wavelengths are usually attributed to shallow sources in the upper crust while long wavelength anomalies originate at greater depth. Gravimetric data has been useful to locate massive ore bodies at depths above 1 km. Aeromagnetic data has been less useful to locate sulphide deposits since these are associated with felsic volcanic rocks (that have lower magnetic susceptibilities than mafic volcanic rocks) and due to the greater sensitivity of the magnetic field to lithological changes when compared with the gravimetric field. Electrical and electromagnetic methods often applied in the area are useful to locate ore bodies also up to 1–2 km depth, but they do not provide accurate structural information such as the location of major thrust planes and faults.

Therefore, six 2D seismic profiles striking approximately SW-NE, perpendicular to the main geological structures, and totalling 82 km were planned and carried out by LNEG for the Neves Corvo mine—Alcoutim sector (see Sect. 11.3.2). Due to the depth penetration required (4–5 km), the seismic equipment available at LNEG was not adequate for this purpose and it was necessary to rent equipment from a large geophysical services company. Prospectiuni company (Romania) was already working in Portugal and had wireless seismic equipment that allowed greater flexibility in data acquisition. Villages, roads, small rivers could be easily crossed and the initial design of the profiles could

be followed more closely. The system used was the state of the art cable-less Sercel 428, E-Unite Full with 480 active channels, six in-line geophones per channel, a channel spacing of 25 m and a source interval of 50 m, resulting in 120 full fold data. The source used was provided by three synchronised ION AHV-IV vibroseis trucks of 28.5 tons each. A linear up sweep 16 s long with a frequency varying between 10 to 90 Hz was used to allow recording information from shallow and deeper reflections. Two or three vibrations per vibration point were carried out. Finally, SG 10 Hz receivers were employed to record the seismic wave field, which was sampled at 2 ms rate during six seconds.

Several processing sequences were attempted for each profile. A standard processing sequence with Pre-Stack Time Migration (PSTM) and post-stack migration, and a second processing sequence with the common-reflection surface method (CRS; Mann et al. 1999) also coupled with PSTM and post-stack migration. All processing sequences included geometry introduction (crooked line geometry for lines 3, 4, 5 and 6), trace editing, first break and bottom muting, refraction statics computations (weathering zone velocity of 1 km/s and replacement velocity of 4–5 km/s) and conversion to flat datum, FK filter, spherical divergence correction, spiking deconvolution (zero phase with 240 ms operator length), bandpass frequency filtering (8–12–70–80 Hz), automatic gain control (AGC, 500 ms window length), two iterations of velocity analysis and residual statics calculations and, finally, the normal moveout (NMO) correction.

From this point the standard and PSTM processing sequences diverged. The CDP gathers were either stacked and post-stack F-X deconvolution and AGC applied, or/and prepared for PSTM. In the first case, Steep Dip Explicit Finite Difference Time Migration was applied to the stacked sections, while in the second the CDP gathers were prepared for PSTM. A 2D Kirchoff time migration algorithm with an aperture of 3–5 km was applied to the gathers. To conclude the processing sequence, CDP stacking and some post-stack filtering was applied. The CRS processing sequence was identical to the previous one until the

pre-PSTM gathers and before NMO correction, after which FX-deconvolution, creation of CRS gathers and stacking were carried out. From this point onwards, the standard and PSTM sequences were applied to the CRS gathers.

Migration was essential to image appropriately these profiles due to the steep dips present. The CRS stacked sections resulted in a clear improvement of the signal to noise ratio. PSTM sections show a better coherency of the reflectors and a clear improvement in the conflicting dips affecting all profiles that resulted from the 3D nature of the geological structures but some artefacts were introduced anyhow in the stacked sections. For the final interpretation, it was an advantage to have both processing sequences and non-migrated stacks.

The seismic reflectors observed in the seismic profiles were interpreted and correlated with the geology, based on the geological information obtained from exploration drill holes located close to the profiles and also from the knowledge of the regional geology. The integration of all data sets was georeferenced and integrated in gOcad, which was a complex task, due to the distinct investigation depths. Gravimetric, aeromagnetic, radiometric and TEM data were also used to interpret each profile, to aid the study of lateral variations of VS units, locate igneous structures (e.g. several dykes associated with late Variscan faults) and the interpretation of deeper units. Information from the Iberseis profiles (Simancas et al. 2003; Carbonell et al. 2004) was used for this. When all the profiles were interpreted, we checked the consistency of the interpretation with gravimetric and aeromagnetic data that covered almost all the study area.

11.3 3D Modelling of Project Area

11.3.1 Area in and Around Neves Corvo Mine

A detailed drill hole-based 3D geological model covering the total extent of Neves Corvo VHMS

deposit (see Fig. 11.2) and its immediate NW and SE along strike extensions was developed by Lundin Mining within the scope of their exploration activities in the IPB Portuguese sector. Geophysical data were also used in the modelling. 2D and 3D seismic reflection profiles indicated the location of several thrusts, faults, and possible lithological contacts and in places the presence of some massive sulphide orebodies (e.g., Lombador and Semblana; Fig. 11.3). TEM and gravity data were also extensively acquired to locate the presence of VHMS deposits. Together with geological outcrop and drill hole data, the geophysical dataset provided valuable information between drill holes and, in particular, seismic data with its greater depth penetration allowed modelling up to several kilometers.

The main objective was to define exploration vectors for targeting by modelling the spatial distribution of specific “marker-horizons” of the known stratigraphic sequence in order to outline trends and favourable areas where lateral and down dip extensions of the prospective ore horizon might potentially occur.

Detailed 3D modelling was done using Gemcom software, version 6.4. The model covered an area of approximately 68 km², on which a total of 4165 combined underground (from the Neves Corvo mine) and surface drill holes have been considered. Interpretation was made along parallel 50–250-m laterally spaced NE-SW oriented sections, where nearly 3000 drill hole intersects have been selected to model the horizons by creating best-fit surfaces. A total of three horizons were modelled, namely the lower contacts of the turbiditic upper Mértola Fm., the VSC *Xistos Verdes e Violetas* Fm. (“Borra de Vinho” green and purple shales), as well as the top of the PQG (Figs. 11.5, 11.6 and 11.7). The Neves Corvo massive sulphide lenses, Neves, Corvo, Graça, Zambujal and Lombador, and the new Semblana orebody were integrated in the model (data from Lundin Mining/ Somincor and AGC companies). The Neves Corvo mine geological sequence (Oliveira et al. 2006; Relvas et al. 2006a; Pereira et al. 2008) was also used as the reference model applied to the project area.

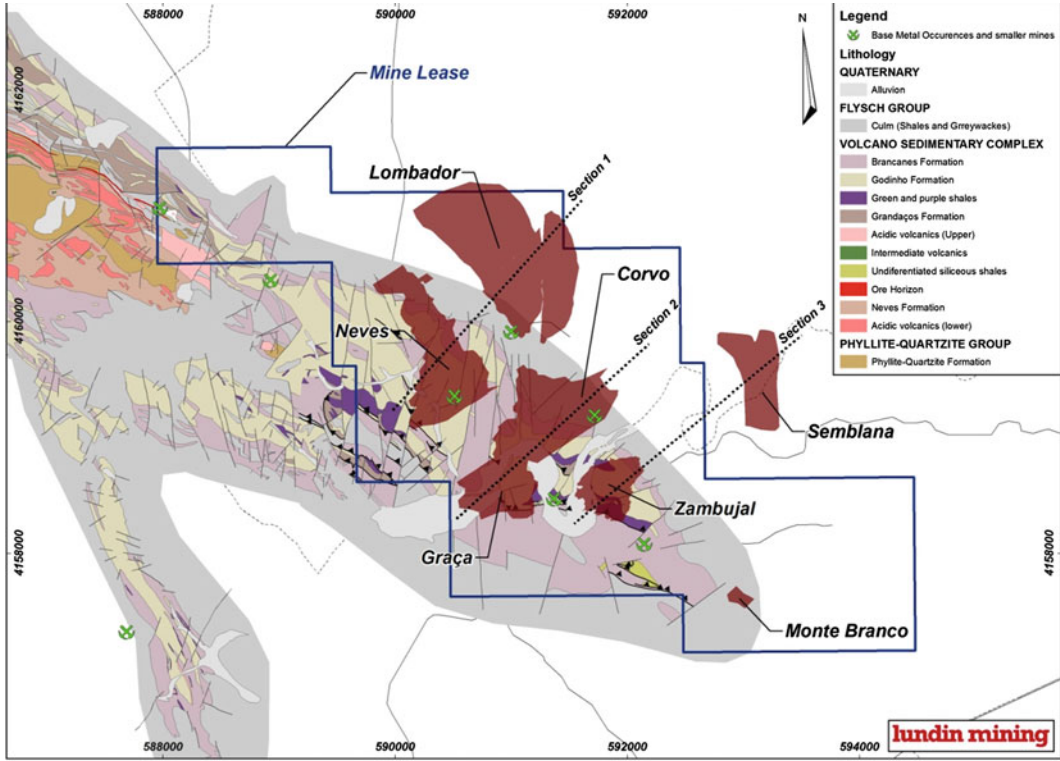
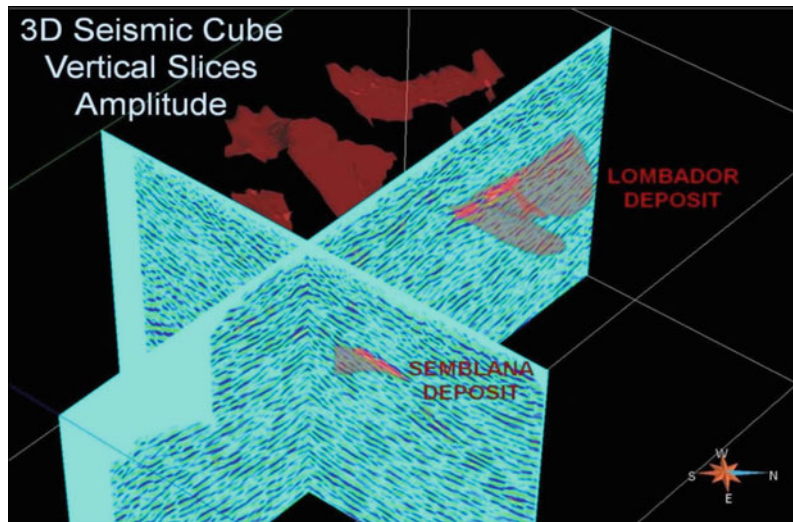


Fig. 11.2 Geological map of the Neves-Corvo antiform with the projection of vertical sections along the ore-bodies used for the geological modelling displayed

(see Figs. 11.5, 11.6 and 11.7). The newly discovered Semblana and Monte Branco orebodies are also included (from Lundin Mining map 2012)

Fig. 11.3 3D seismic cube —vertical slices showing location of Semblana and Lombador reflectors with the Neves Corvo ore bodies



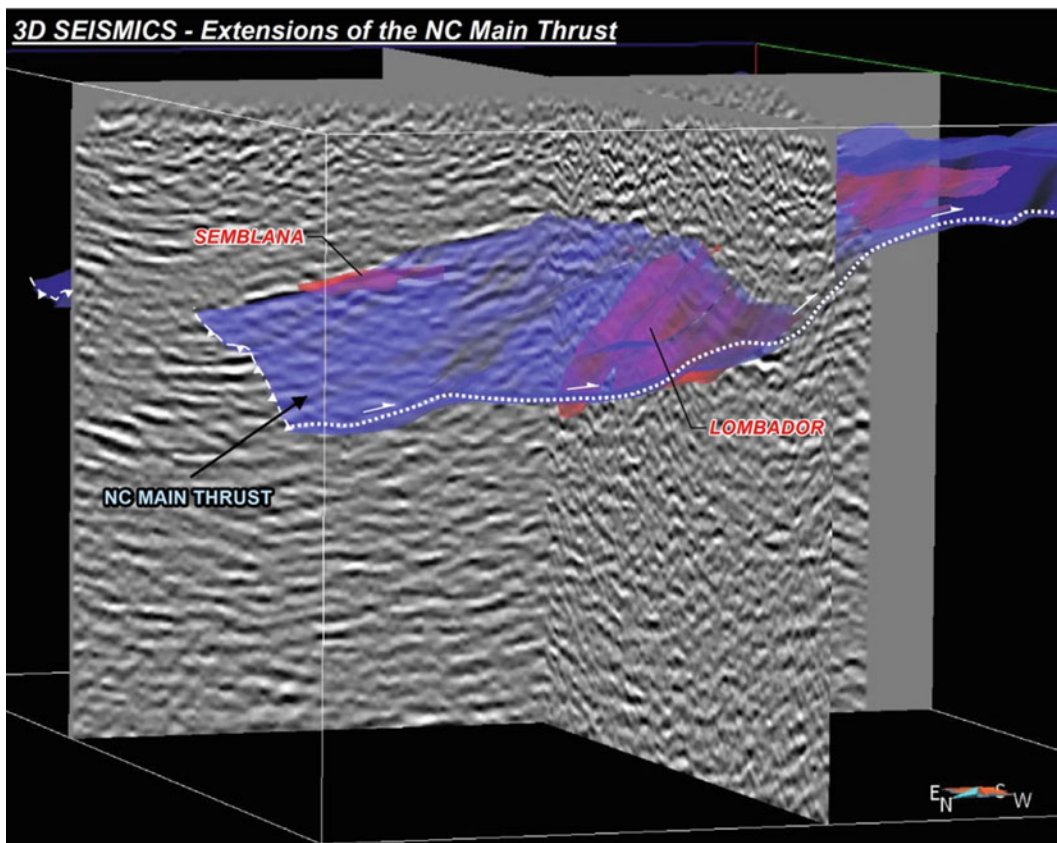


Fig. 11.4 3D view of TEM sections and gravity excess mass isoshells in the Neves Corvo Mine area with the projection of the ore bodies

Based on geologic outcrop, drill hole and some geophysical (TEM, gravity and magnetics) data, LNEG extended the Lundin Mining 3D model, more centered on Neves Corvo mine and surroundings, to a zone some 7 km to the NW, but still within this central area of the project. The modelling of this extension was done in a more simplified way, with the exclusion of the horizon of top of the “Borra de Vinho” green and purple shales Fm. of VSC. The same horizon was not considered for the modelling of the SE and NW sectors (see Sects. 11.3.2 and 11.3.3) either.

In addition to the stratigraphic focus of the model, structural aspects were also considered by modelling the Neves Corvo Main Thrust (Figs. 11.4, 11.5, 11.6 and 11.7; Oliveira et al. 2004; Relvas et al. 2006a), a complex

deformational shear corridor developed on top of the massive sulphides that splits an allochthonous block from an underlying prospective parautochthonous sequence (see Sect. 11.1). This major structural panel is interpreted as having played a key role on the mechanical/geometrical controls of the mineralization and on the concentration of the copper-rich ore shoots and therefore providing important exploration guidance on the definition of drill targets for new discoveries. It is important to emphasize that the combined use of these geological and geophysical exploration tools in the interpretation process was critical in delineation of the target area that led to the discovery of the new Semblana and Monte Branco massive sulphide deposits (Lundin Mining 2010, 2012).

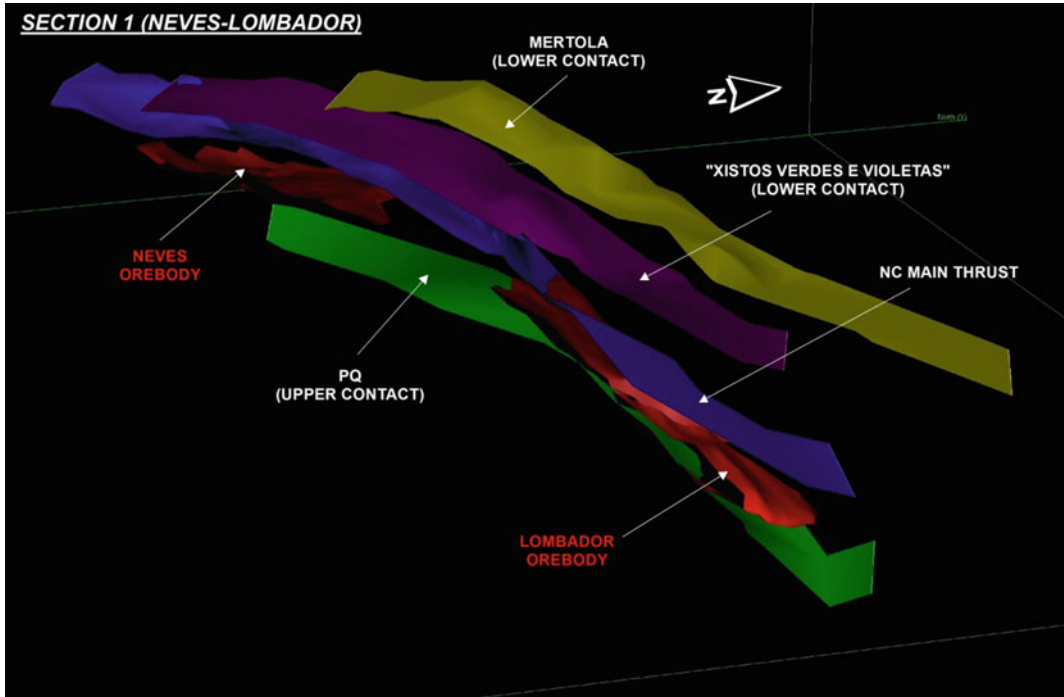


Fig. 11.5 Section-1 (see position in Fig. 11.2) along Neves-Lombador ore bodies showing the modelled surfaces using drill-hole intersections

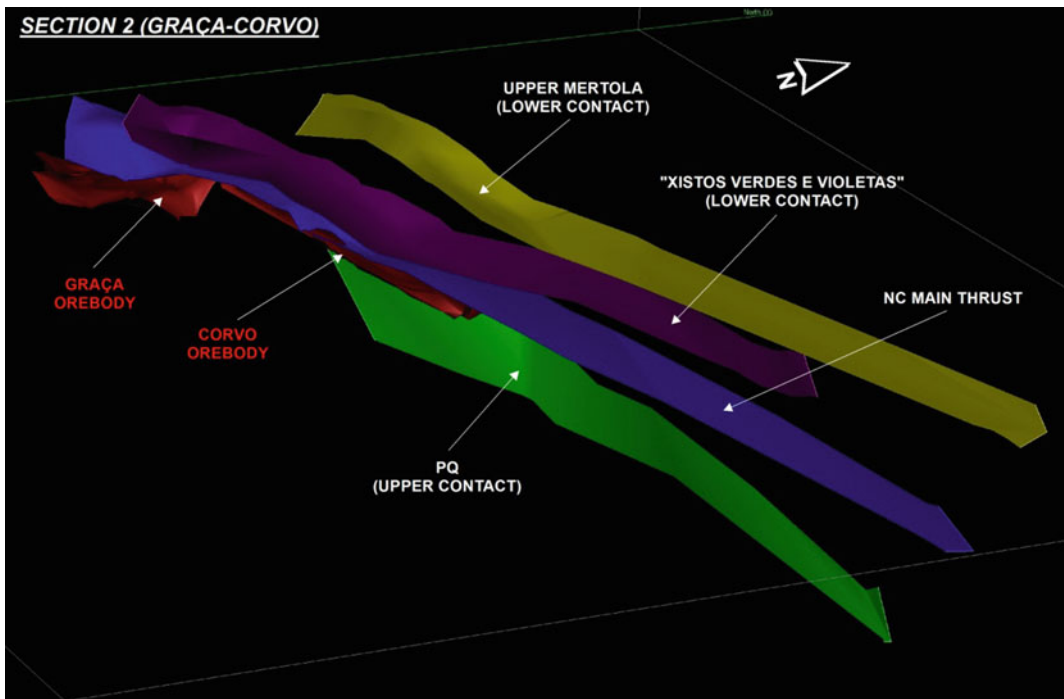


Fig. 11.6 Section-2 (see position in Fig. 11.2) along Graça-Corvo ore bodies showing the modelled surfaces using drill-hole intersections

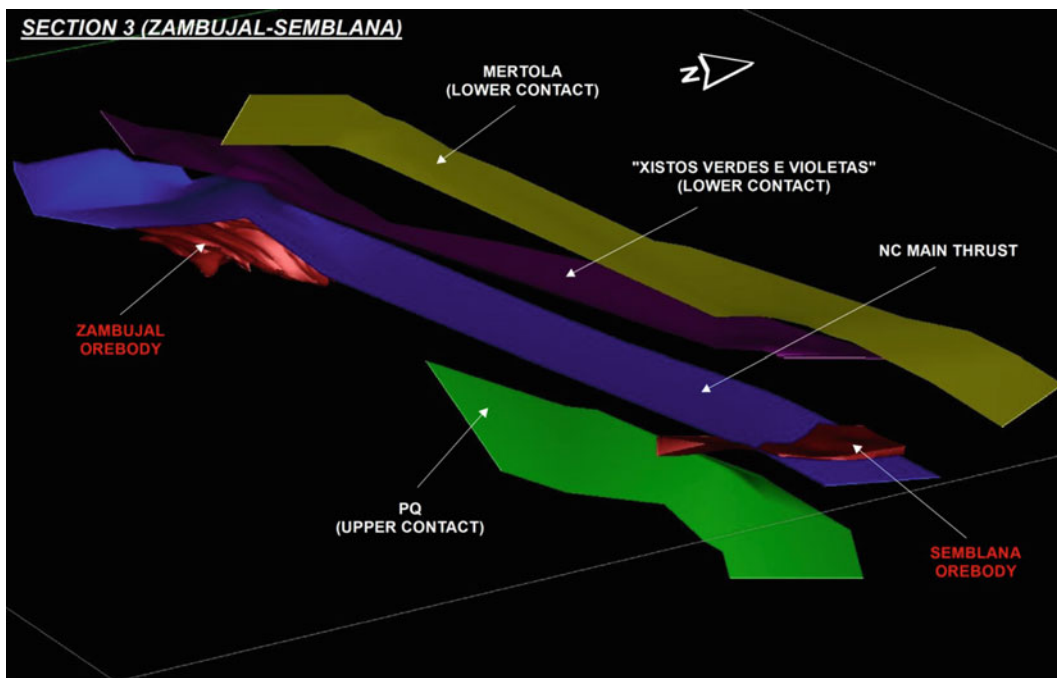


Fig. 11.7 Section-3 (see position in Fig. 11.2) along Zambujal-Semblana ore bodies showing the modelled surfaces using drill-hole intersections

11.3.2 SE Sector (Including Alcutim)

In this sector the modelling was based mostly on 2D seismic reflection data acquired under the scope of the Promine project (see above). The six SW-NE seismic profiles (Fig. 11.8) were interpreted taking into consideration the information from exploration drill holes, outcrop data at various scales and other geophysical data. The latter include aeromagnetic and radiometric (natural gamma-ray) data from surveys flown at an altitude of 90 m, gravimetric and magnetic data obtained by exploration companies, and also some TEM profiles. The gravimetric and magnetic data have been integrated and homogenised at LNEG. Additionally, seismic reflection data acquired in 1991 and 1996 by CGG for Somincor was also taken into consideration, as well as unpublished data from very recent 3D and 2D seismic reflection surveys carried out by Lundin Mining in the Neves Corvo mine area. The geological data used to model this area were

compiled from LNEG published national geological maps and ongoing surveys, and from unpublished maps and cross-sections done by exploration companies, including Billinton and Lundin Mining, that have worked in the area. All data were georeferenced and integrated in gOcad.

The seismic reflection survey penetrated to a greater depth than any of the geophysical potential field methods or mechanical soundings. In the profiles closer to the Neves Corvo mine (profiles 1 and 2), clear reflections were obtained from depths up to 4 to 5 km, while in the profiles located further SE (profiles 3, 4, 5 and 6) information was obtained from up to 10 km depth. After processing, it became evident that a good part of the stronger reflectivity patterns detected in each stacked section has a structural imprint that is stronger than the more subtle reflectivity variation of the lithological changes.

It was concluded that the extension of the Neves Corvo volcanic axis below the flysch sedimentary rocks, known from former drill

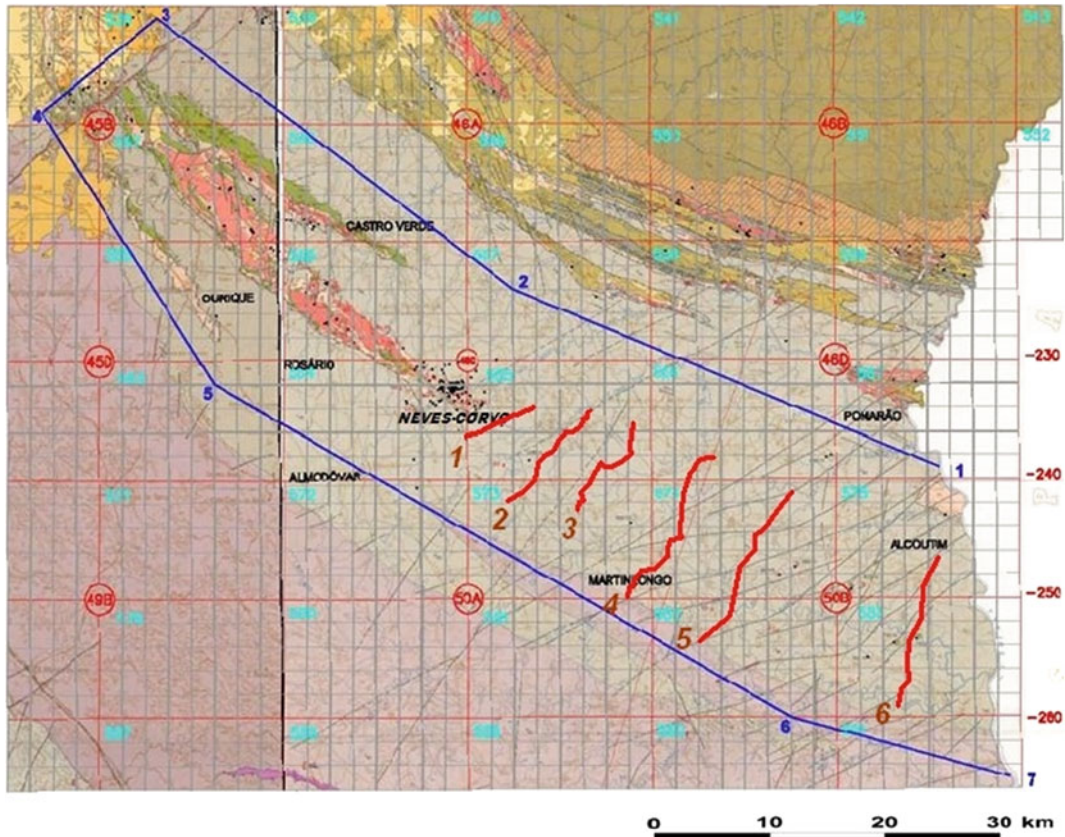


Fig. 11.8 Neves Corvo project area with location of the six 2D deep seismic reflection SW-NE profiles carried out by LNEG in the SE sector, between Neves Corvo mine and the Spanish border

holes, towards the SE, is consistently supported by all datasets. The contacts between PQG, VSC and the Mértola and Mira formations were identified in the seismic sections and confirmed in the drill holes. The Neves Corvo main thrust, identified in the Neves Corvo mine occurring almost adjacent to the VHMS ores, and dividing the sequence in an allochthonous block and a parautochthonous block (Figs. 11.9 and 11.10), also extends to the SE at least up to the Spanish border. In the Neves Corvo mine, immediately above the massive sulphide orebodies, sedimentary rock intervals with variable thickness and lateral extent can occur locally. They are made up of shales and greywackes of the Mértola Formation, which is therefore named there as “Mértola 2” to distinguish it from the Mértola Formation closer to surface. In the Alcoutim area

a similar sequence consisting of rocks from the Mértola Formation at surface, followed at depth successively by VSC units, the Neves Corvo main thrust, a thin interval of Mértola Formation and VSC rocks was also identified, both in drill holes and in the seismic profiles, correlating very well with the general sequence identified at the mine.

All these surfaces were connected from one seismic section into another to define a 3D model (Figs. 11.11 and 11.12). We also note a good consistency between the interpretation of the Promine seismic profiles and the Somincor seismic profiles located further north. Taken together, they show the culminations of a pre-PQG unknown basement (Figs. 11.9 and 11.10), never drilled to date, along the Neves Corvo main thrust in agreement with the variations shown by

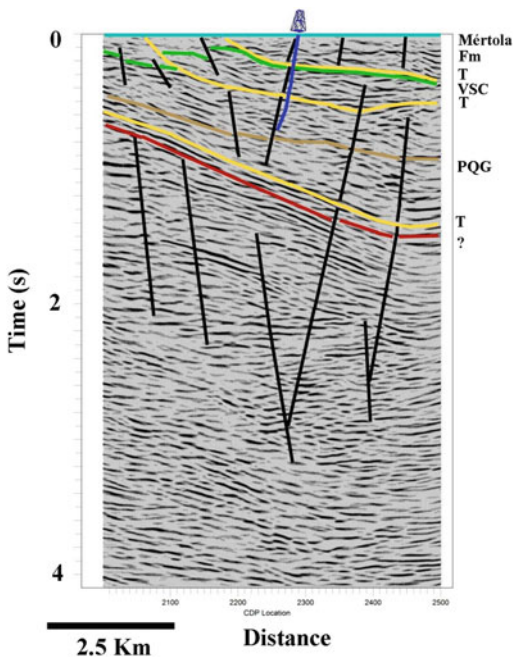
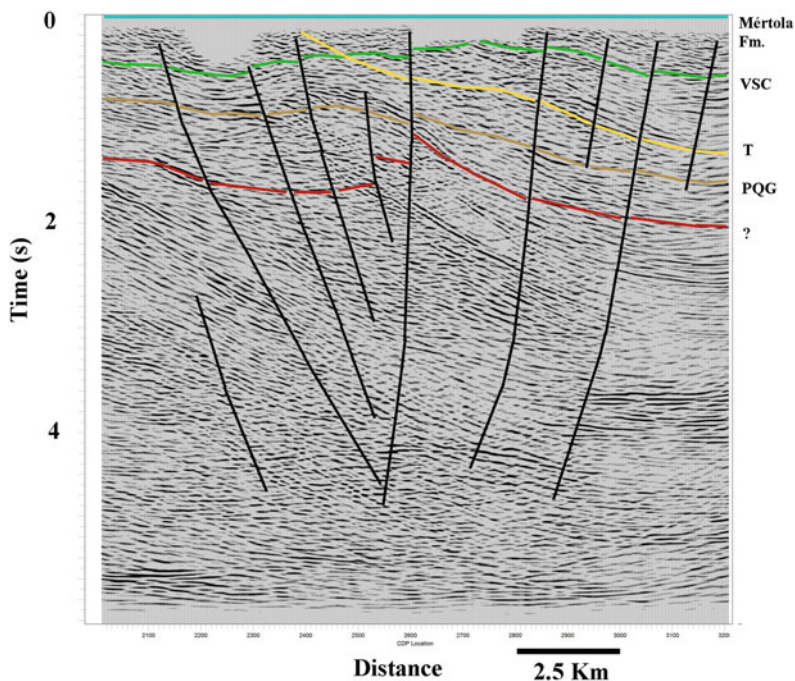


Fig. 11.9 Geological interpretation of 2D seismic reflection SW-NE profile 1 in the SE sector. Top of VSC (green), top of PQG (brown), T-thrust to SW (yellow), late Variscan faults (black), and unknown pre-basement surface (red); drill hole (blue). The Neves Corvo main thrust is the intermediate thrust

potential field data. This basement was detected underneath the PQG in all six seismic sections. Late Variscan faults were also incorporated into the model. They displace the contacts between the PQG, VSC and the Mértola and Mira formations as well as the previous Variscan thrust faults. The late Variscan faults are extensional, strike-slip oblique, vertical to near-vertical faults that trend NE-SW, N-S and NNW-SSE (Figs. 11.11 and 11.12). The seismic data show that the principal faults are deeply rooted, being traceable down to 10 km depth (Fig. 11.10). The VSC that crops out in the Alcoutim area is interpreted to be at surface due to vertical movements along some of these fault planes, forming a horst type structure. According to the seismic and drill-hole geological data, the Neves Corvo main thrust was brought closer to surface in the Alcoutim area (where it is ≈ 1000 m deep) by the movements along the late Variscan faults. It is also noteworthy that these faults host Cu (and Pb) sulphide veins with carbonates and barite mineralisations that were exploited in the 19th century (e.g. Barrigão, Ferrarias, Alcaria Queimada, Furnazinhas; Reiser et al. 2011; Matos et al. 2003) (see Fig. 11.24).

Fig. 11.10 Geological interpretation of 2D seismic reflection SW-NE profile 5 in the SE sector that includes the Neves Corvo main thrust. Symbols and patterns as in Fig. 11.9



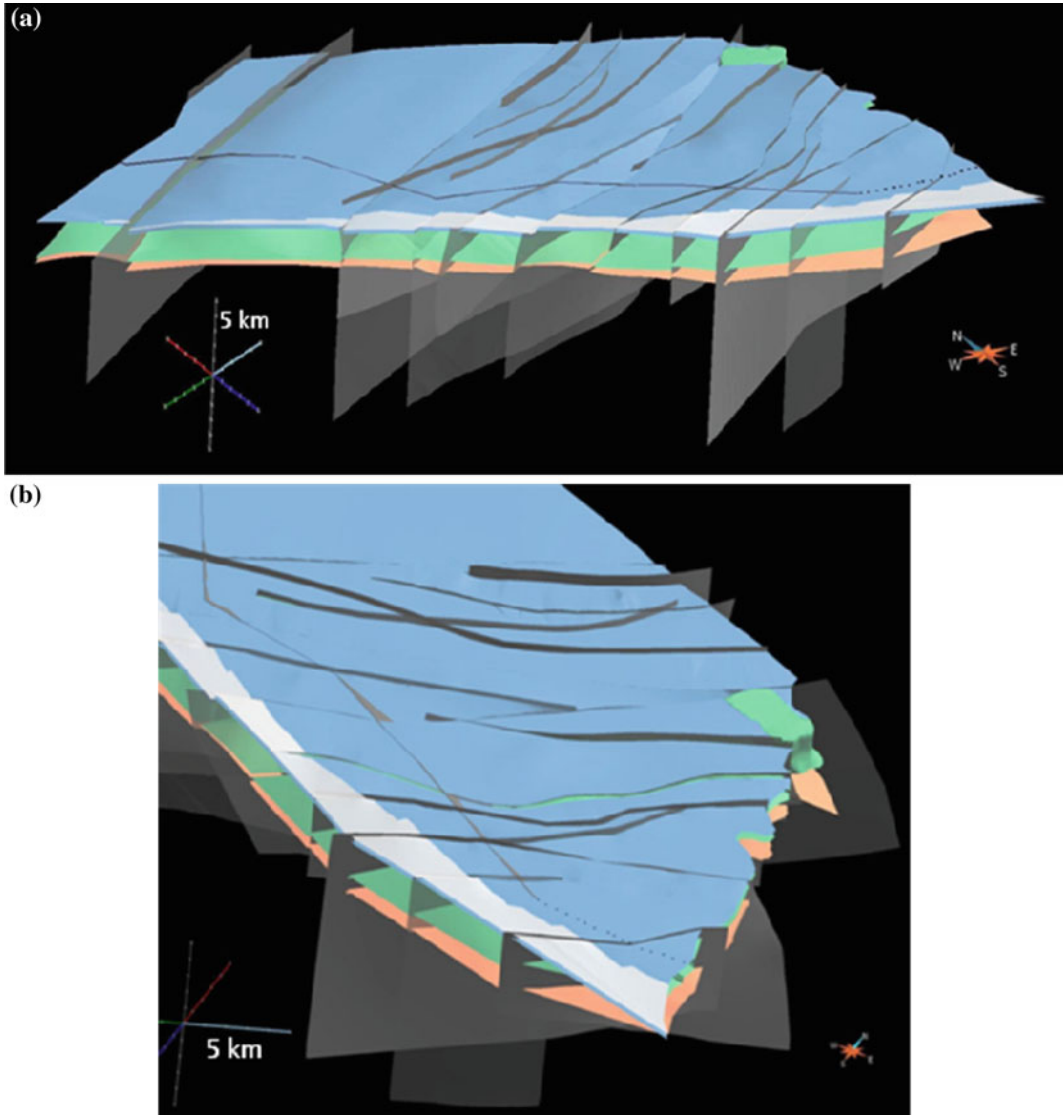


Fig. 11.11 3D (geological) model (a and b) of the entire SE area (above) and detail (below), containing tops of PQG (orange), VSC (green), Mértola (blue) and Mira

(white) formations, and also exhibiting the longitudinal trace of the Neves Corvo main thrust (black-grey) and late Variscan faults (grey). Each cross arm is 5 km long

Connecting the area surrounding Neves Corvo mine and the SE area, and removing the upper Mértola and Mira flysch formations, a 3D model such as that of Fig. 11.13 is obtained, with a continuous Neves Corvo main thrust all along from west of the mine (west of the model) to the Spanish border, and the Late Variscan faults. If in

the same common area, the flysch rocks and VSC (except VHMS ores) are removed, a 3D model only containing PQG, Neves Corvo deposits above it and the Neves Corvo main thrust shows (viewed from the west) how close VHMS ores are to this thrust (Fig. 11.14) and therefore its regional significance for VHMS exploration.

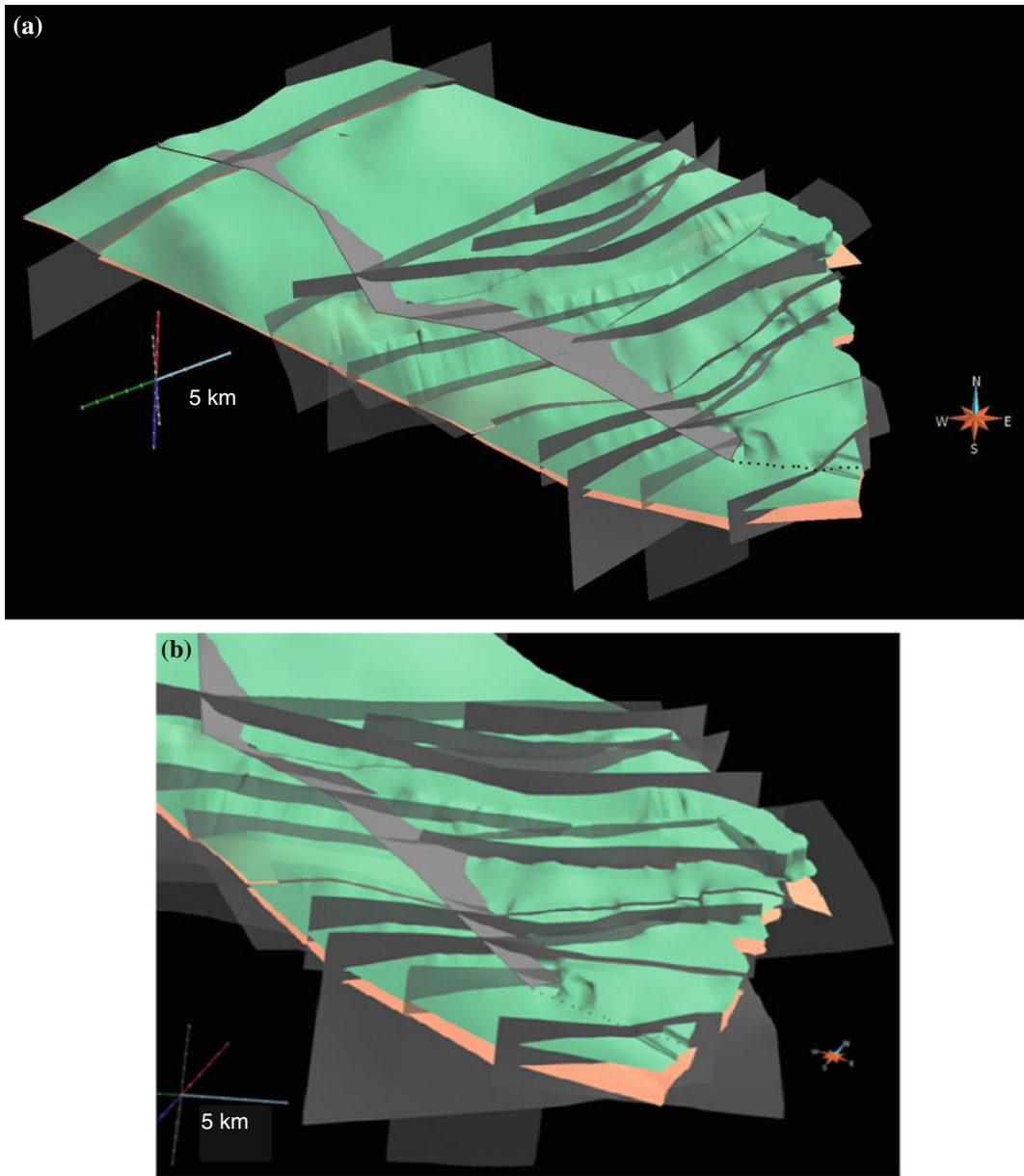


Fig. 11.12 Identical to Fig. 11.11, but with the 3D model (a and b) obtained after removal of the Mértola and Mira Flysch formations to better display the extension and

attitude of the Neves Corvo main thrust and late Variscan faults. Symbols and patterns as in Fig. 11.11. Each cross arm is 5 km long

11.3.3 The NW Sector

The NW sector corresponds to the sector between the Neves Corvo Mine and the NW end of the project area. The area is characterized by the presence of the VSC rocks in the Castro

Verde, Rosário and Ourique (from NE to SW) antiform structures (Fig. 11.1; Oliveira et al. 2006). The VSC units are formed by sedimentary rocks and felsic and mafic volcanic rocks. The IPB rocks are affected by significant late Variscan strike-slip oblique faults striking

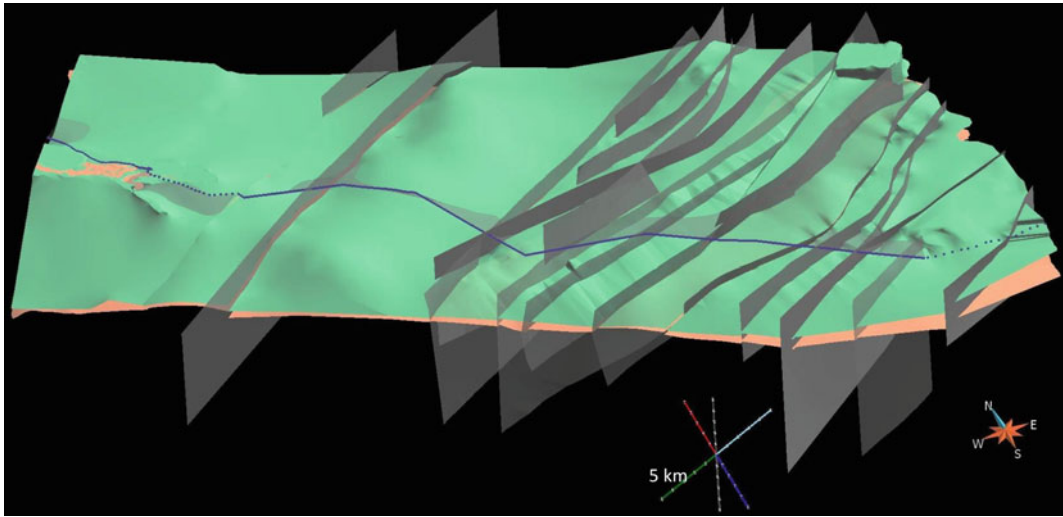


Fig. 11.13 3D model of joint Neves Corvo mine and the SE areas, after removal of the Mértola and Mira formations, displaying tops of PQG and VSC, Neves

Corvo main thrust (in *blue*) and late Variscan faults. Symbols and patterns as in Fig. 11.11. Each cross arm is 5 km long

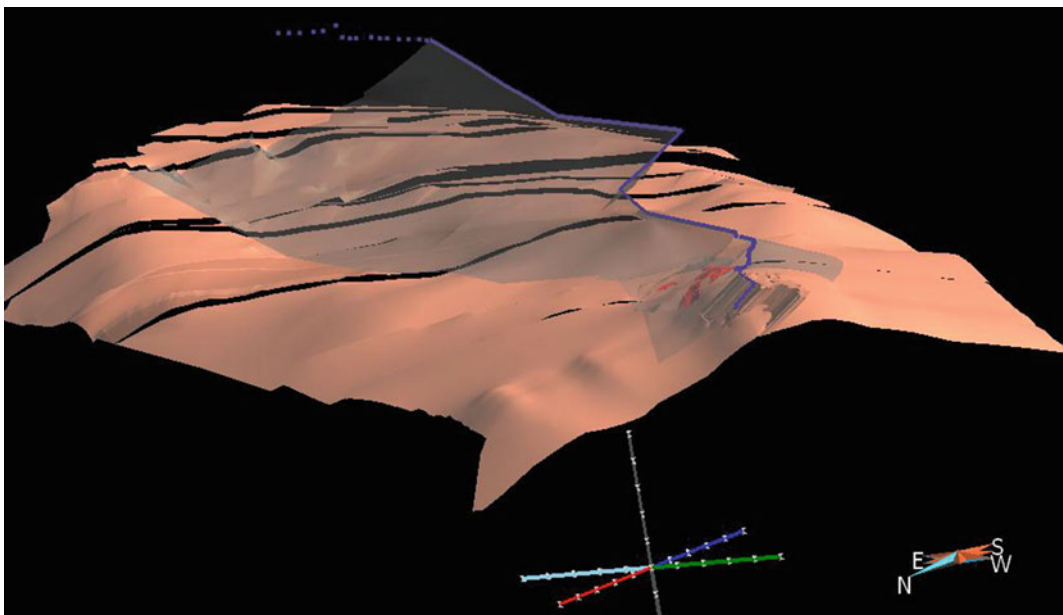


Fig. 11.14 3D model of same joint Neves Corvo mine and the SE areas, after removal of the Mértola and Mira formations, VSC (except VHMS ores) and late Variscan faults, to show, in a view from west, the top of PQG

(*orange*), Neves Corvo VHMS ores (*red*) above, close to the Neves Corvo main thrust (*blue*). Each cross arm is 5 km long

NE-SW (sinistral) and N-S (dextral) (Figs. 11.15 and 11.16). The Messejana fault (Figs. 11.1, 11.15, 11.16 and 11.17), in the NW end of this sector, is the most significant of the former

group. This is a near-vertical, NE-SW-striking fault, that shows sinistral movement, displacing the Variscan structures for approximately 4 km (Schermerhorn et al. 1987; Leitão 1997), and

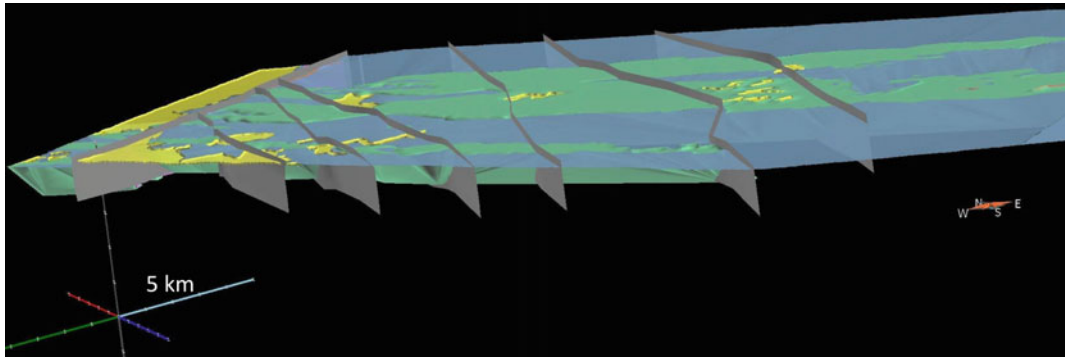


Fig. 11.15 3D model of the entire NW area showing part of PQG (*orange*) in the eastern end, VSC (*green*), Mértola Fm. (*blue*) and Cenozoic cover (*yellow*). Also NW-SE

and NE-SW faults where the Messejana fault is the westernmost fault (*grey*). Each cross arm is 5 km long

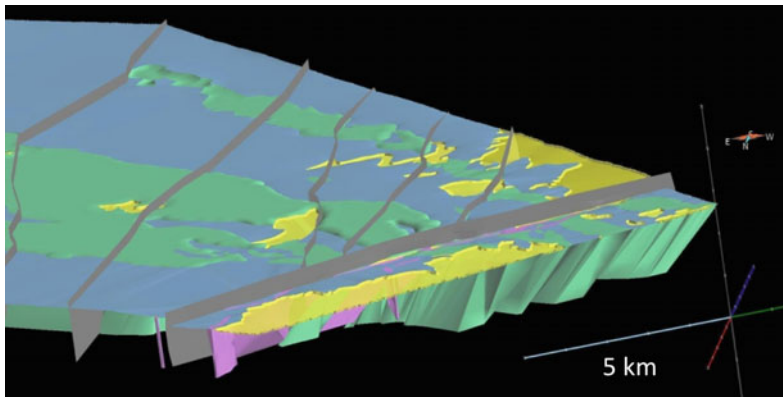


Fig. 11.16 3D model of the western part of the NW area (view from west), using same symbols and patterns as in Fig. 11.15. The prominent NE-SW Messejana fault,

accommodating a Jurassic dolerite dyke (*violet*) and with more developed Cenozoic cover deposits on the western fault block, is displayed. Each cross arm is 5 km long

also a downthrow of the NW fault block. Cenozoic sedimentary rocks are present in that block of the Messejana fault, forming part of the Sado-Alvalade Cenozoic basin (Schermerhorn et al. 1987; Oliveira et al. 2006). In the SE block minor Cenozoic overburden occurs and its distribution is controlled by late Variscan faults.

Located NE of Panóias, the small Montinho massive sulphide deposit crops out, rather close to the Messejana fault. The sulphides were exploited down to 50 m depth in the 1950s by Mines d'Aljustrel (Matos and Rosa 2001). The Montinho mineralization consists of a stockwork hosted by black shales of Strunian age (Zélia Pereira 2013, personal communication). This age and recent exploration drill holes suggest that the

PQG occurs at depth in the Montinho sector. In fact, the PQG also crops out near the Rosário village in the Promine area. Additionally, small syngenetic Mn mineralisations are hosted by VSC units in this NW sector. The 3D modelling of the NW area allows a better understanding of the VSC antiforms, which are complex and dominated by tectonic imbrication. This model is supported by geophysical EM data showing VSC black shale units gently dipping to NE. Drill hole data confirms the SW vergence of the structures also defined by large extension of the NE anti-form limbs and minor development of the SW limbs. Figure 11.18 shows a 3D model of this NW area together with the other two areas. The 3D model in Fig. 11.19 correlates surface and

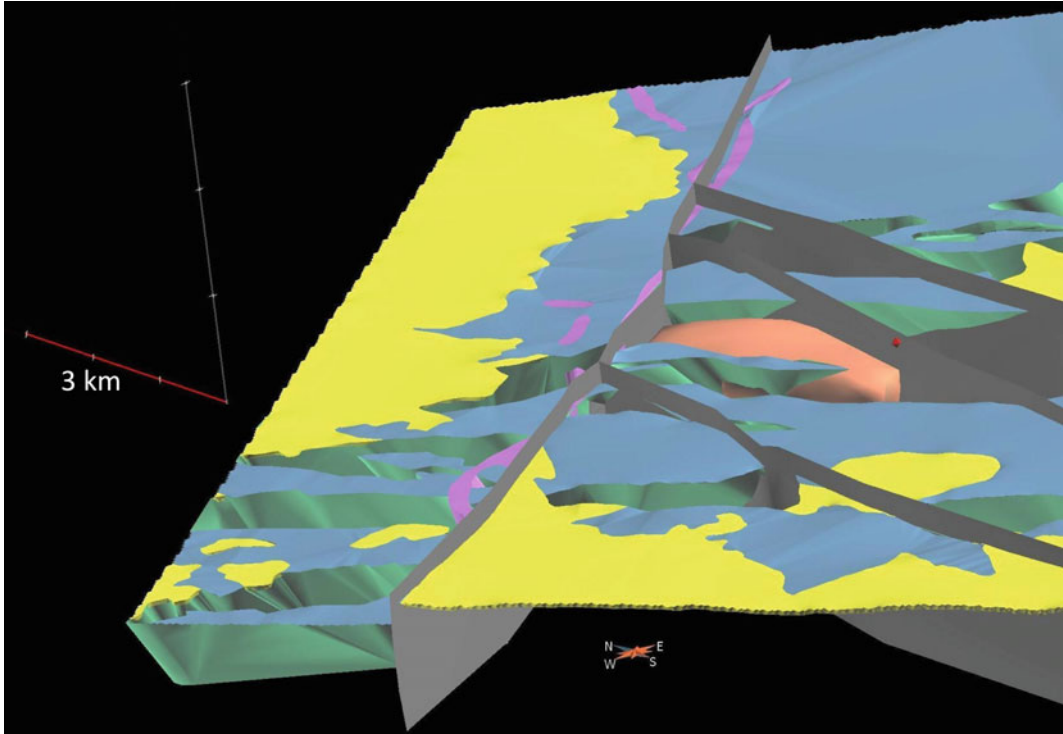


Fig. 11.17 Unroofed PQG (*orange*) at depth, VSC, Mértola Fm. and Cenozoic cover. Late Variscan faults, both NW-SE- and particularly the NE-SW striking Messejana fault accommodating a dolerite dyke are

displayed. The small VSC-hosted Montinho VHMS deposit is shown (*red dot*). Symbols and patterns as in Fig. 11.16. Each cross arm is 3 km long

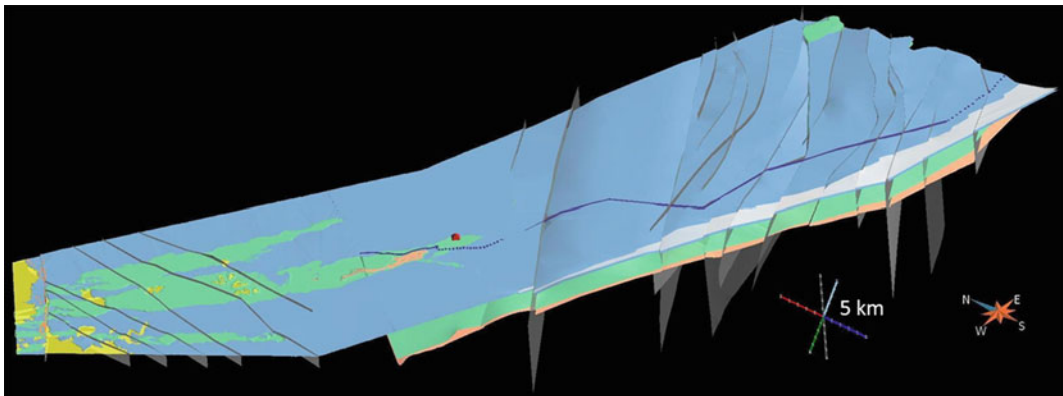


Fig. 11.18 3D model of the entire Neves Corvo area, showing tops of PQG, VSC, Mértola Fm. and Mira Fm. Neves Corvo mine shown as *red/blue dot*. Also, the

Neves Corvo main thrust (longitudinal blue line along the area) and late Variscan faults are displayed. Symbols and patterns as in Fig. 11.11. Each cross arm is 5 km long

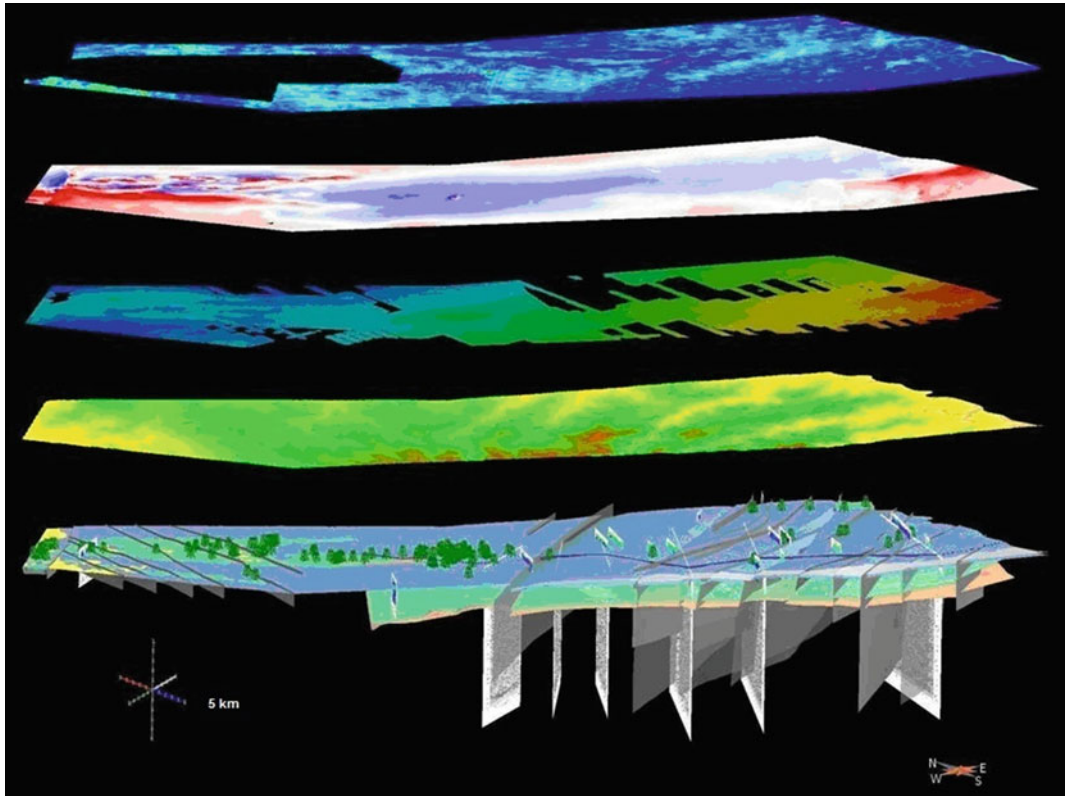


Fig. 11.19 3D geological-structural model of the Neves Corvo area, using the same symbols and patterns as in Fig. 11.18, but also including the drill holes used (*dark green*) and the six new 2D seismic reflection sections.

Detached layers, from bottom to top, of the digital terrain model, gravity (terrain), magnetics TMI, and radiometric maps for the entire area also used for the 3D model. Each cross arm is 5 km long

subsurface (drill holes) geology and structure with the six new 2D seismic reflection sections and with a digital terrain model as well as gravimetric, magnetic and radiometric data of the whole area used for this model.

11.4 4D Modelling of Project Area

The 3D models obtained for the project area form the basis for reconstruction of the sequence of geological events from the time of deposition of the oldest geological unit occurring in the area until the present state. The main geological events recognized in the area were considered (e.g. massive sulphide formation, Variscan deformation, late Variscan faulting, among other

events) and a tight control of their ages was done where possible, in order to define the correct sequence of the main geological events. The age of the main sedimentary units of the IPB was already known in some regions of the project area. This knowledge is more comprehensive for the Neves Corvo mine where the age of the sedimentary units that occur beneath, above and intercalated in the massive sulphide pile helps to constrain the age of the mineralization (Oliveira et al. 2004). However, the amount of available data and its detail along the lithostratigraphic column varies significantly from location to location of the project area, and in fact for the majority of the project area there are no data. In order to increase the knowledge about some locations within the project area, new analyses of sedimentary rocks were performed. Regarding

the volcanic rocks that constitute a significant part of the VSC, few absolute ages from zircon were available and only a few others were obtained during the project. The age of the late Variscan faults and of the mineralizations that they contain is more dubious, since there are no data available regarding the time of their formation. However, the field relations of these structures with the enclosing geological units and with structures are informative enough to confidently place their formation in relative time.

The sequence of the most relevant geological events considered in the comprehensive interpretation of the geological evolution of the Neves Corvo Project area started with the deposition of the sedimentary units that constitute the PQ Group. These rocks formed in a shallow marine platform (Oliveira et al. 1986) and constitute the substrate for the VSC. The top of the PQ Group has a Strunian age ($\sim 362\text{--}360$ Ma; Pereira et al. 2008) (Fig. 11.20) and at least in some locations of the IPB, during the Strunian the depositional setting was relatively deep, in anoxic conditions (Oliveira et al. 2004). It was also during the Strunian that the volcanism that sourced the lower volcanic sequence of VSC developed (Pereira et al. 2008; Matos et al. 2011). Detailed lithofacies mapping indicates that several

submarine felsic volcanic centres formed in the basin (Fig. 11.21). It was also during the late Strunian that hydrothermal activity, close to the felsic volcanic centres, occurred and led to the formation of the giant Neves Corvo massive sulphide deposits, and of the smaller Algaré and Montinho massive sulphide deposits. It is noteworthy that the mineralizing events of these three massive sulphide deposits have a similar age, and that this is the time for the formation of several other massive sulphide mineralizations in the IPB (Matos et al. 2011). The volcanic activity and deposition of volcanogenic sediments of the VSC occurred throughout the IPB until the Viséan, $\sim 339\text{--}346$ Ma, during which the widespread and abundant syngenetic Mn mineralizations formed in this part of the IPB (Fig. 11.22). A syn-orogenic flysch sequence occurs above the VSC rocks, represented by the Mértola and Mira Formations. All these rocks were deformed during the Variscan orogeny into a thin-skinned foreland fold and thrust belt (Silva et al. 1990; Quesada 1998) and a consequence of this deformation was the folding and faulting of the IPB rocks, including the mineral deposits and the formation of the Neves Corvo main thrust (Fig. 11.23) that was recognised to the SE of the mine, towards the Alcoutim area. Several late

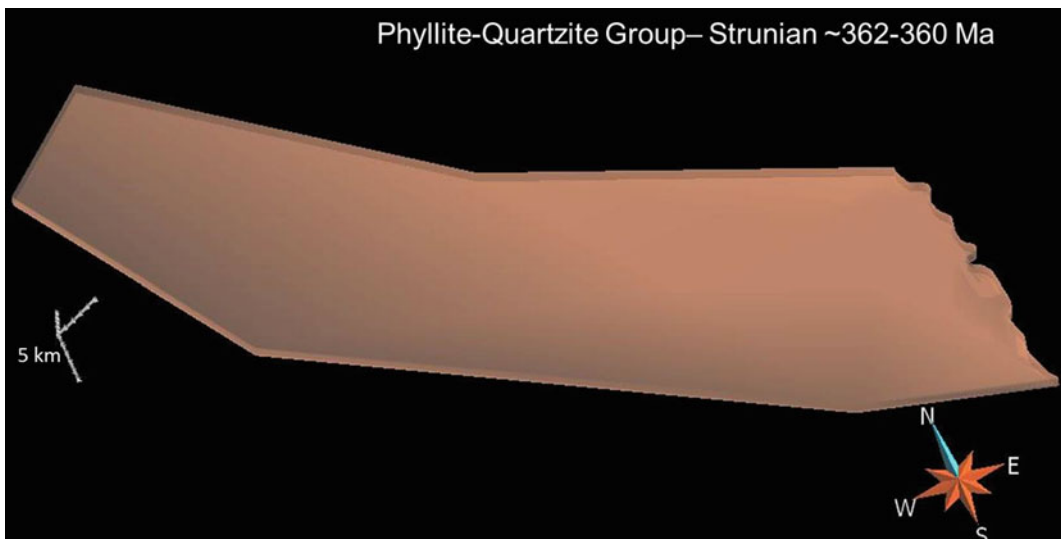


Fig. 11.20 4D model sequence: Phyllite-Quartzite Group in Strunian time ($\approx 362\text{--}360$ Ma)

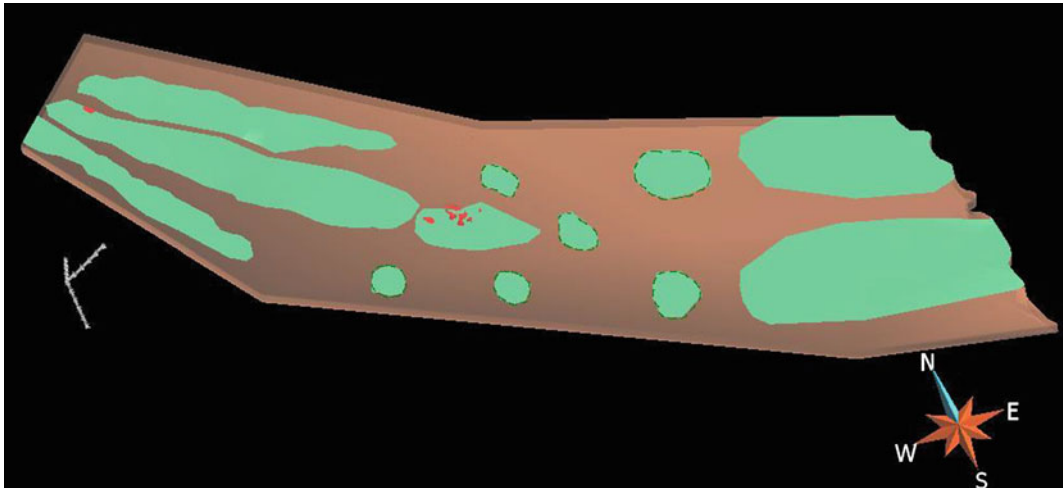


Fig. 11.21 4D model sequence: Volcanic Sedimentary Complex, including deposition of VHMS mineralization, in Strunian time (≈362–360 Ma)

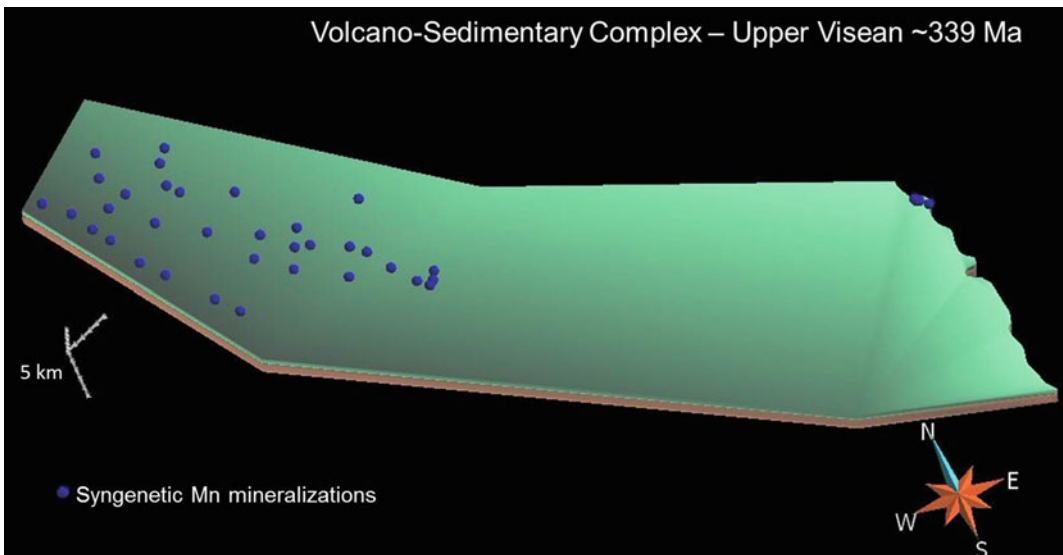


Fig. 11.22 4D model sequence: Volcanic Sedimentary Complex, including deposition of syngenetic Mn mineralization, in Visean time (≈346–339 Ma)

Variscan faults developed subsequently and disrupted the geological structures previously formed. These strike-slip oblique faults were identified throughout the Neves Corvo project area striking NE-SW to ENE-WSW (sinistral) and N-S to NNW-SSE (dextral), and are

particularly conspicuous in the Alcoutim area (Fig. 11.24). These faults can host late Variscan (Cu and Pb) sulphide mineralisations (Fig. 11.24), clearly defining a NW-SE trend to the SE of Neves Corvo mine. NW of the Neves Corvo project area (Fig. 11.24), the

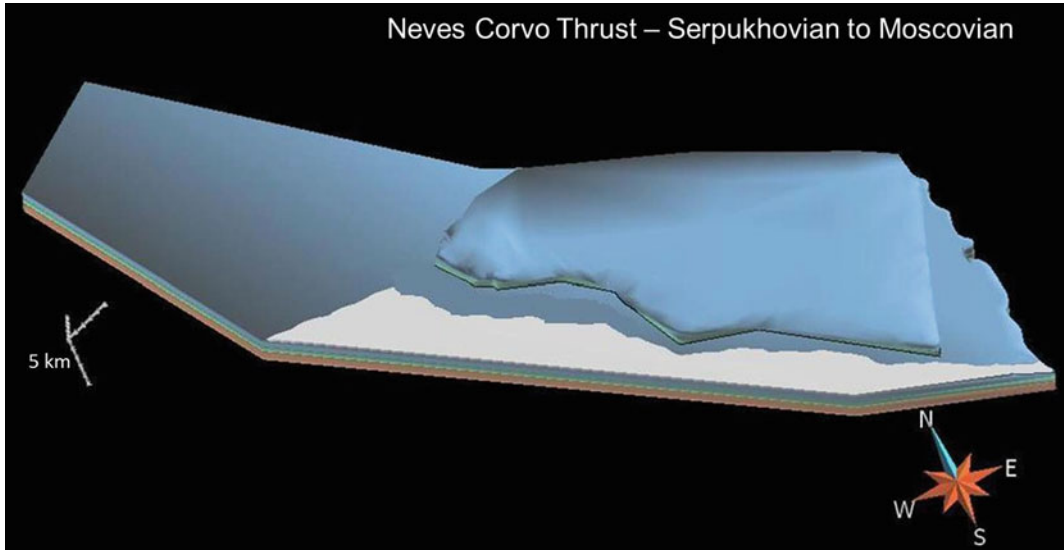


Fig. 11.23 4D model sequence: development of Neves Corvo main thrust in Serpukhovian to Moscovian time (≈ 320 Ma)

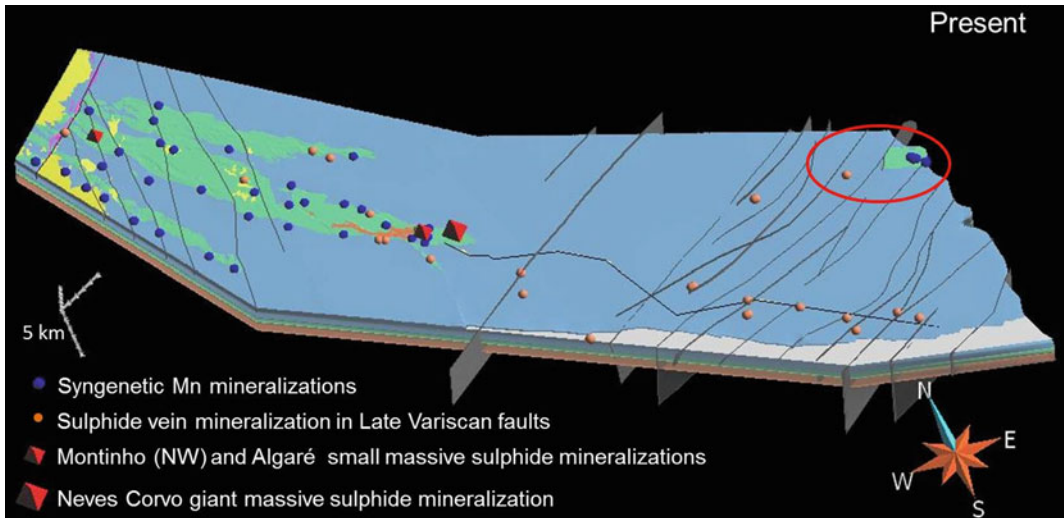


Fig. 11.24 4D model sequence: Status at Present time, exhibiting PQG, VSC and its VHMS mineralization, Mértola and Mira flysch formations, Neves Corvo main

thrust, late Variscan faults with late Variscan vein-type (Cu, etc.) sulphide mineralization and/or Jurassic dolerite dykes, and Cenozoic cover

occurrence of the Messejana fault that extends for approximately 500 km in the Iberian peninsula, hosting dolerite intrusions of Jurassic age, is also noteworthy. Cenozoic

sedimentary units included in the southern region of the Sado Alvalade Cenozoic Basin occur in grabens close to the Messejana fault (Fig. 11.1).

11.5 Predictive Modelling of Project Area and Exploration Significance

11.5.1 Regional Exploration and Predictive 2D Modelling

After a criterion-based attempt to find the most appropriate data available from different sources, a predictive model has been produced for the study area. A 2D GIS integrated project was produced combining the most significant exploration data from the Rosário-Neves Corvo anticline, Ourique and Castro Verde anticlines and the Alcoutim/Odeleite region (Oliveira et al. 2006). Those data include soil geochemistry, magnetic data as its first vertical derivative, residual gravity data, and geological mapping (1/200,000 scale, Sheets 7 and 8 maps; Oliveira et al. 1984, 1992), including structural features such as major NW-SE thrusts and N-S, NE-SW and E-W Late Variscan strike-slip oblique faults. The regional trend of key tectonic structures such as the main Neves Corvo thrust (Leca et al. 1983; Relvas et al. 2006a; Oliveira et al. 2006; Pereira et al. 2008) was introduced in the predictive model, considering its exploration potential. The most important structural features are at least partially related with base metal mineralization, including volcanogenic massive sulphides such as Neves Corvo, Algaré and Montinho (Carvalho 1982; Barriga and Carvalho 1983; Oliveira et al. 1984, 1992; Carvalho et al. 1999) and Late Variscan vein-type deposits such as Ferrarias (Matos et al. 2003), Cortes Pereiras (Mateus et al. 2006) and Barrigão (Reiser et al. 2011). Studies of fluid inclusions in quartz, stibnite, and barite as well as sulphur isotopic compositions from Late Variscan vein-type base metal deposits reveal different sources of sulphur and deposition conditions of the mineralizations (Germann et al. 2003); different sources for the hydrothermal depositional fluids were also proposed by Relvas et al. (2006b) for the Neves Corvo deposit based on O-, H- and C-isotope studies. The volume/tonnage of Cu in some VHMS deposits

is significant, especially in Neves Corvo, the most Cu-rich IPB deposit (Relvas et al. 2006a). The massive sulphide deposits are associated to the VSC key exploration unit. Their stockworks are commonly hosted in VSC rocks, but also in the underlying Phyllite-Quartzite sedimentary unit rocks. The Late Variscan mineralized veins occur in the Flysch barren units (e.g. Mértola Formation of the Baixo Alentejo Flysch Group; Oliveira et al. 2006) and in the VSC units.

The surface geology was not considered for the predictive 2D modelling, with the exception of structural features, because the VSC is covered to a very significant part of the project area by a thick turbiditic sequence (Mértola and Mira formations). The lower weight that, in this case, would be given to this flysch-covered area could induce underestimation of the overall exploration potential, neglecting the influence of the VSC that is known to occur at depth. The distance from the occurrences of both volcanogenic and vein-type mineralization to either the Late Variscan faults or the main Neves Corvo thrust were calculated using the Near Distance tool in ArcGIS, originating a GIS variable. The “Two Conditions” settings were used during the processing, one where no distance restriction was imposed and the other where a 1500 m maximum distance was imposed. The geophysical data were combined using the available exploration information. The gravity and magnetic data were plotted to analyse the positive anomalies, which favour higher predictivity. In this respect, the highest predictive rate is given if gravity and magnetic positive anomalies are coincident when the two methods are combined. This is why the values higher than the 90th percentile of both methods added have the higher weight, and the respective areas were defined using GIS and the domains allocated as “area favourable by geophysics”.

The main Neves Corvo thrust and the Late Variscan faults were buffered by an area 300 m wide, centered in the thrust/fault and those areas were also integrated in the predictive map. This restriction does not take into account that mineralized faults may not be mineralized in all its extension, but only where certain decompression

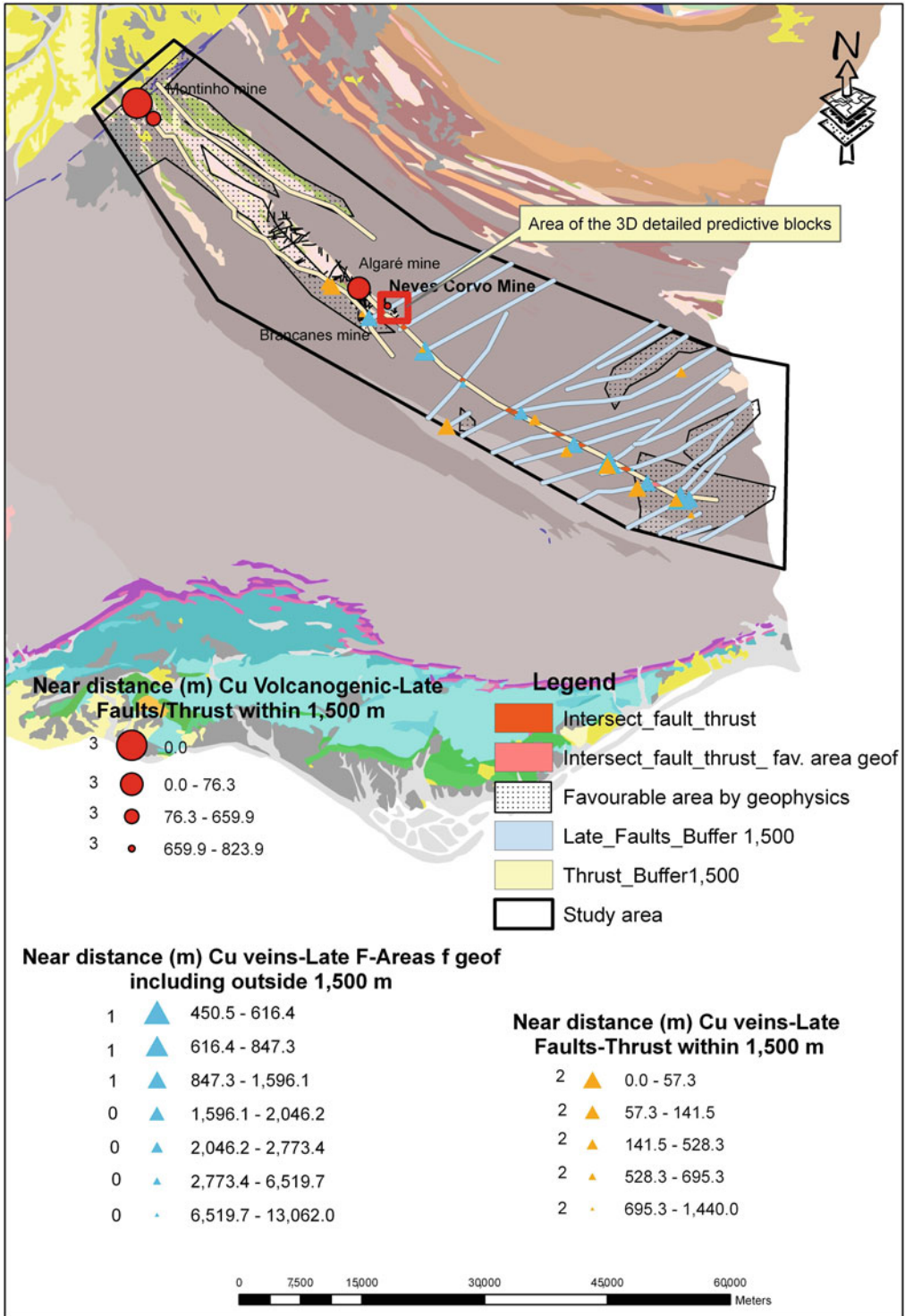


Fig. 11.25 2D predictive map of the study area. The Neves Corvo deposits were excluded to display the potential of the remaining area

conditions occurred and with that type of faulting present locally in the host rock. The intersection areas among “areas favourable by geophysics”, Late Variscan faults and Neves Corvo thrust were also integrated in the predictive map, and are referred to as “intersection” below. The near distance (within 1500 m) from the volcanogenic deposits and the intersection of the previous referred to areas and thrust/faults were calculated and given the higher predictability rate. The near distance (within 1500 m) between the Late Variscan vein type deposits plus the area favoured by geophysics, thrust and faults, were determined and given a median rate. The near distance (including outside the 1500 m) between the Late Variscan vein-type deposits and the favourable areas given by geophysics, thrusts and faults, was determined and given the lower rate. Table 11.1 shows the variables used in calculation of the predictive map, Table 11.2 shows the weight criteria that defined the predictive area of focus for the exploration of Cu.

Geochemistry was used to trace the natural pathfinders, with Cu taken as the main commodity mined in Neves Corvo and the most important commodity in the historical mining of the region, characterized by small Cu vein exploitations in the 19th century down to 200 m depth and by modern massive sulphide exploitation down to 900 m depth at the Neves Corvo

mine (Somincor mining project, with production since 1987).

The deficient spatial distribution of the geochemical data at the scale of the study area precluded its use for the 2D predictive modelling. However, because of its great exploration significance, it is taken in consideration in the final decision. Therefore, with the available information from different geochemical campaigns that were performed in the NW-SE Neves Corvo-Rosário volcanic axis/structure, a factorial analysis with varimax rotation was applied and the Kaiser (1960) criteria used. Table 11.3 shows the results and the variation in the superficial pathfinders (Cu and related elements) along that volcanic axis/structure from the Montinho area, extending to the SE into the Garronchal, Zambujeira and finally into the Neves Corvo area. The results are strongly dependent on the chemical elements analysed, which restricts greatly any possible conclusions that can be drawn.

Based on the available information the Neves Corvo thrust and the alignment of the outcropping axis/structure at the surface, are the most important guides for mineral exploration in the study area. The highly predictive areas for VHMS deposits were coincident with this alignment. A special conclusion is the fact that the extension of the Neves Corvo thrust, obtained in the 3D modelling and applied in the predictive

Table 11.1 Selected variables for predictive modelling

Methods	Conditions
Favourable area given by geophysics Gravimetry+magnetics Gravimetry-magnetics	From above 90 % positive when adding and negative when subtracting
Late Variscan faults	Buffer 1500 m
Thrusts	Buffer 1500 m
Nearest distance from volcanogenic deposits and intersection of thrusts and Late Variscan faults	Within 1500 m distance
Nearest distance from vein type deposits and intersection of thrusts and Late Variscan faults	Within 1500 m distance
Nearest distance from vein type deposits and intersection of thrusts and Late Variscan faults and favourable area given by geophysics	Within the 1500 m distance
Nearest distance from vein type deposits and intersection of thrusts and Late Variscan faults and favourable area given by geophysics	Outside the 1500 m range

Table 11.2 Predictive weights

Methods		Weight
Nearest distance from volcanogenic deposits and intersection of thrusts and Late Variscan faults	Within 1500 m distance	3
Nearest distance from vein type deposits and intersection of thrusts and Late Variscan faults	Within 1500 m distance	2
Nearest distance from vein type deposits and intersection of thrusts and Late Variscan faults and favourable area given by geophysics	Within the 1500 m distance	1
Nearest distance from vein type deposits and intersection of thrusts and Late Variscan faults and favourable area given by geophysics	Outside the 1500 m range	0

3 the higher weight; 2 medium weight, 1 lower weight, 0 no influence in predictivity

Table 11.3 Factorial analysis of PC extraction and representation of the Cu probable pathfinders in the area, considering the elements used in the calculation

Area (% variance explained in the 1st 2 axis)	Total elements used in PCA	Correlated with the occurrence of Cu (>0.7) and PC extraction using Kaiser (1960) criteria
Moitinhos (62 %)	As, Ba, Co, Cr, Cu, Fe, Mg, Mn, Ni, P, Pb, Rb, S, Sc, V, Zn	(Axis 2) As, Cu , Pb, Zn
Garrochal (54 %)	Cu, Pb, Zn, Ni, Co, As, Fe, Mn, Ba, Cr, V, Al, Sr, Nb, Sc	(Axis 1) Cu , Ni, Co, Fe, Mn, V, Al
Zambujeira (64 %)	Cu, Pb, Zn, Ni, Co, As, Fe, Mn, Ba, Cr, V, Al, Nb	(Axis 1) Cu , Zn, Ni, As, Fe, Cr, Al
Neves Corvo (samples from 1998) (60 %)	Cu, Pb, Zn, Ni, Co, Mn, Fe, As, V, Ca, P, Cr, Mg, Ba, Ti, Al, Na, Sn, Nb, Sc	(Axis 2) Cu , Pb, Zn, As, Sn
Neves Corvo area before start of mine production (archived samples from the 70s analysed recently) (56 %)	Cu, Pb, Zn, Ni, Co, Mn, Fe, As, V, Cr, Mg, Ba, Ti, Nb	(Axis 2) Cu , Pb, Zn, Co

maps, coincides spatially with the main alignment of the Cu mineralizations identified by the authors as vein-type late Variscan mineralisations. Also, the intersection of the Neves Corvo thrust and the late Variscan faults is sometimes not far from these mineral occurrences. Sulphide remobilization during late Variscan deformation must be properly understood, considering the mineral dispersion from a giant sulphide deposit (Neves Corvo) or from other possible hidden VHMS ores. These results, combined in the 2D predictive map, seem to be of great exploration importance (Fig. 11.25).

11.5.2 3D Predictive Modelling of Neves Corvo Mine Area

The previously produced 2D predictive map needs further developments at depth. Because most of the area is covered by the thick flysch of the Mértola Fm., it is appropriate to go over the data location and information available relative to VSC below that formation. The exploration drill hole data show a variable distribution of the VSC, controlled by late Variscan faults and regional folds. Because different formations have different densities and the massive sulphides

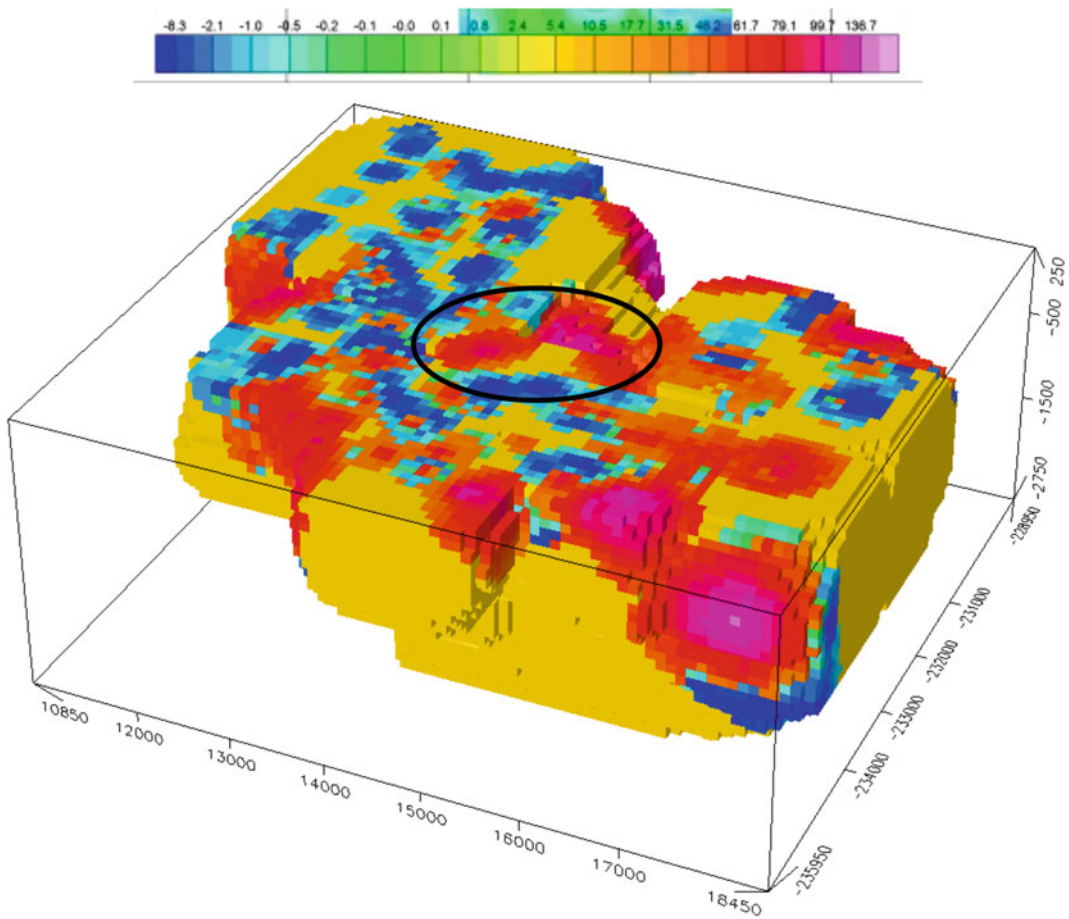


Fig. 11.26 3D densities from gravity inversion in the Neves Corvo mine area

usually have higher density than the host rocks, densities at depth were investigated relative to a restricted area around the Neves Corvo mine. A 3D density model was calculated by applying an inversion methodology (Camacho et al. 2002) to the gravity data. The gravity dataset allowed a resolution grid of 100 m, given that this was the average distance between data points. The voxel of the calculated densities produced using 3D kriging is shown in Fig. 11.26.

The geochemical information was compiled from previous exploration campaigns that included soil geochemistry surveys and drill hole rock geochemical analysis. The information was selected using only drill holes where Cu results were reported in weight %. A 3D grid was built and, also at this stage, several drill holes were

discarded due to the distance of interpolation. The 3D voxel is composed by cubic cells whose values were determined using linear interpolation between the values of the eight voxel points, which form the corners of the cube. The size of the edges of the cubes is 50 m to obtain a continuous image. The resulting calculation indicates a trend of Cu open in both sides. This trend and its extensions were considered the highest level of predictive VHMS volume (Fig. 11.27). Even though the geochemistry and density models were calculated using very different approaches, it can be observed that the places where high density and high Cu concentration coincide are places where the predictability values are considered to be the highest. This corresponds to one of the known massive sulphide

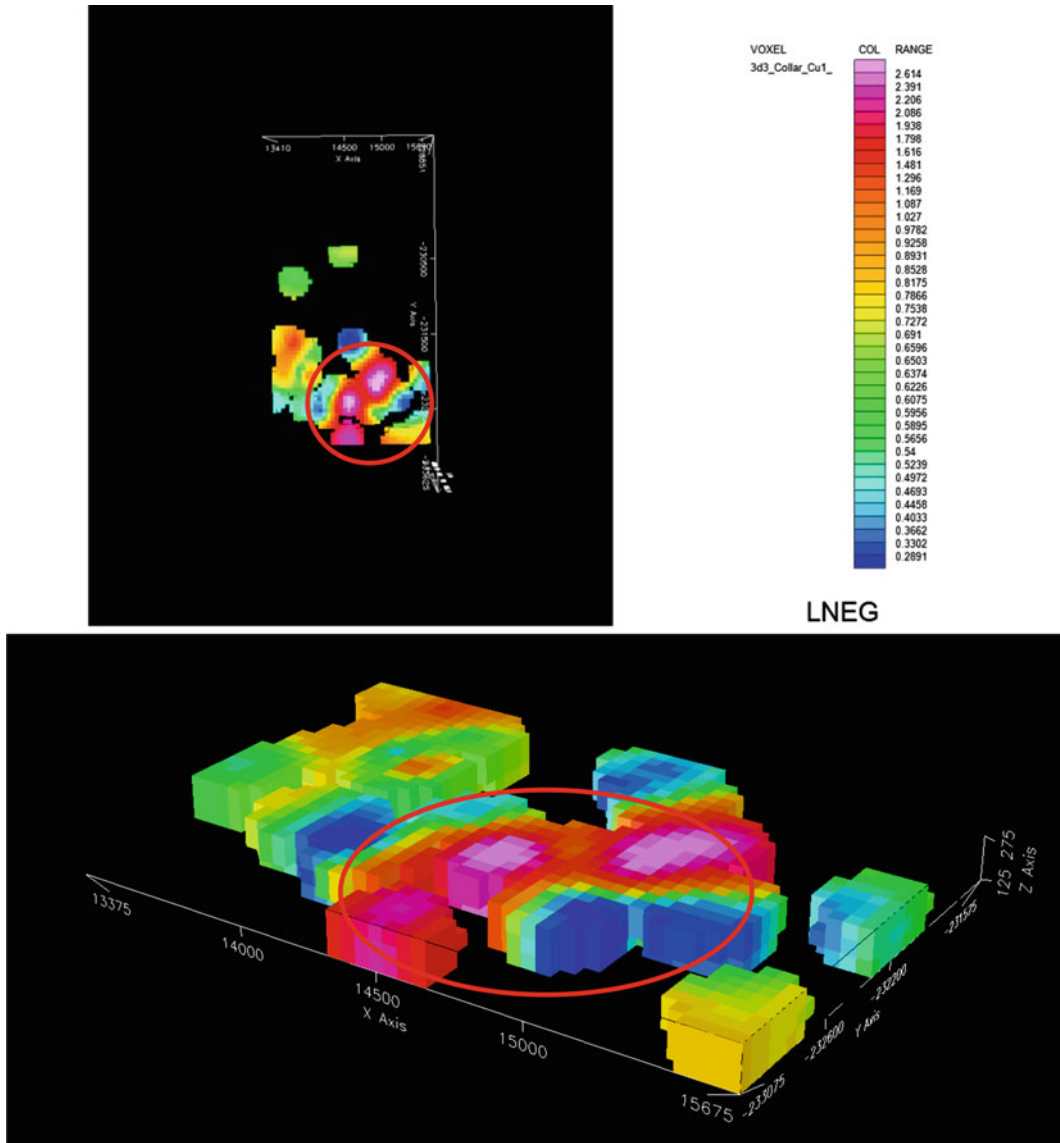


Fig. 11.27 3D Cu (%) in drill holes from the Neves Corvo mine area

orebodies of Neves Corvo mining site. Therefore, the other anomalies, observed further away in Fig. 11.26 are worth being investigated in the Neves Corvo mine area. Furthermore, it would be relevant to consider if gravity inversion modelling should be applied in the rest of the area where this kind of information is available.

11.6 Summary and Conclusions

The use of 3D, 4D and predictive geological modelling for the Neves Corvo 100 × 25 km project area enabled to correlate its geological,

stratigraphical, geochronological, structural, mineral deposit, geophysical, geochemical and other characteristics. Half of the area, the western part, is known to contain the Givetian to Famennian-Strunian Phyllite-Quartzite Group (PQG), overlain, along the three volcanic axes, by the Strunian to Visean Volcanic Sedimentary Complex (VSC), hosting in its lower sequence the Neves Corvo VHMS giant deposit and the Montinho and Algaré small VHMS deposits. Additionally, an inlier of VSC outcrops in Alcoutim, adjacent to the Spanish border in the eastern end of the project area. The remaining area is covered by Visean and Serpukhovian to Moscovian flysch rocks [Mértola and Mira formations of the Baixo Alentejo Flysch Group (BAFG), respectively]. The three volcanic axes that plunge to the SE are known to extend at depth under the BAFG sedimentary rocks in the eastern part of the area, where they were modelled in 3D as well.

A particularly relevant feature of the area is the NW-SE (dipping to NE) Neves Corvo main thrust bringing VSC rocks on top of the Mértola Fm., extremely close to Neves Corvo VHMS ores. This main thrust serves in Neves Corvo mine area as an exploration guide to VHMS ore. The use of six NE-SW very deep 2D reflection seismic profiles carried out by LNEG during this project, between the Neves Corvo mine and the Spanish border, 60 km to the SE, allowed to extend and 3D-model of the Neves Corvo main thrust throughout all the eastern part of the area.

Late Variscan faults displaced all former geological units and Variscan structures, including thrusts, as shown by the 3D models. They are strike-slip oblique faults, mostly striking NE-SW to ENE-WSW (sinistral) and N-S to NNW-SSE (dextral). In some cases the seismic sections show deep development (>5 km depth) of these fault zones. Also in late Variscan time, small vein-type Cu (and other metals) deposits and occurrences, abundant in the eastern part of the area, were emplaced along these faults, also used during the Middle Jurassic to locally accommodate intrusions of dolerite dykes, particularly along the prominent NW-SE sinistral Messejana fault in the northwesternmost end of the area.

The 4D model enabled to establish a clear age succession, important for the succeeding mineralization types, namely Strunian VHMS mineralization in VSC lower sequence, Visean Mn mineralization in VSC upper sequence and late Variscan vein-type Cu-sulphide mineralization associated with late Variscan faults. Particularly important was the constraint of the Neves Corvo main thrust to a Serpukhovian to Moscovian age (Fig. 11.23). The 4D model also shows that in Strunian time the lower sequence of the VSC (the sequence hosting VHMS mineralization) may possibly exist at depth (dashed lines in Fig. 11.22) in between the Neves Corvo mine and Alcoutim.

The parameters used for the predictive modelling that took into account (1) the position of Neves Corvo main thrust in the central and eastern areas, (2) the position of VHMS deposits and vein-type Cu deposits in close proximity to this thrust and to Late Variscan faults in the latter case and (3) the proximity of gravimetric and magnetic anomalies. All point out, in the 2D predictive model, that the vicinity of this thrust between Neves Corvo mine and the Spanish border is an extremely important target for volcanic-hosted massive sulphide deposit exploration. Also relevant for this purpose may be the Alcoutim area, with above-mentioned vein-type Cu occurrences, and where the Neves Corvo main thrust, which is very deep farther away, is closer to the surface (≈ 1000 m deep) due to late Variscan faults. Furthermore, the thrust consists of the characteristic VSC/thin flysch sequence at depth, as in the Neves Corvo mine. The 3D predictive model, exclusively done for the Neves Corvo mine area, pinpoints, both through the 3D-density (from gravity inversion) and the % Cu drill hole-based block-diagrams, the known Neves Corvo orebodies, including the newly discovered deposits, but also other possible extensions.

The regional extension of the Neves Corvo model increases significantly the exploration potential of this part of the IPB. The ProMine LNEG/AGC-Lundin Mining team work improved the geological knowledge of the Portuguese IPB sector, showing new possibilities for VHMS deposits discoveries.

Acknowledgments The authors thank LNEG and Lundin Mining for supporting this study and allowing the publication of its results. Augusto Filipe (LNEG) is thanked for improving and editing several figures.

References

- Barriga, F., Carvalho, D., 1983. Carboniferous volcanogenic sulphide mineralizations in south Portugal (Iberian Pyrite Belt). *Memórias dos Serviços Geológicos de Portugal* v. 29, pp. 99–113.
- Boogaard, M.V., Schermerhorn, L.J.G., 1981. Conodont faunas from Portugal and Southwestern Spain, Part 6-A Lower Famennian faunas at Monte Forno da Cal (South Portugal). *Scripta Geologica*, 63,1–16.
- Camacho, A.G., Montesinos, F.G., Vieira, R., 2002. A 3-D gravity inversion tool based on exploration of model possibilities. *Computers & Geosciences*, 28, 191–204.
- Carbonell, R., Simancas, F., Juhlin, C., Pous, J., Pérez-Estaún, A., González-Lodeiro, F., Muñoz, G., Heise, W., Ayarza, P., 2004. Geophysical evidence of a mantle derived intrusion in SW Iberia. *Geophysical Research Letters* 31, L11601.
- Carvalho, D., 1982. New paths to massive sulphide exploration in the Iberian Pyrite Belt. *Comunicações Serviços Geológicos Portugal*, 68 (2), 149–162
- Carvalho D, Barriga F J A S, Munhá J., 1999. Bimodal-siliciclastic systems—the case of the Iberian Pyrite Belt. In: Barrie, C.T., Hannington, M.D. (eds.), *Volcanic-Associated Massive Sulphide Deposits: Processes and Examples in Modern and Ancient Settings*, Reviews Economic Geology, 8, 375–408.
- Carvalho, J., Sousa, P., Matos, J., Pinto, C., 2011. Ore prospecting in the Iberian Pyrite Belt using seismic and potential-field data. *Journal of Geophysics and Engineering* 8 (2), 142–153.
- Cordson, A., Galbraith, M., Peirce, J., 2000. Planning Land 3-D Seismic Surveys. SEG Geophysical Development Series No. 9, Tulsa, Oklahoma (OK), USA, 204 p
- Eaton, David W., 2003. Hardrock Seismic Exploration. SEG Geophysical Development Series N° 10, Tulsa, OK, USA, 270 p.
- Germann, K., Luders V., Banks, D.A., Simon K., Hoefs, J., 2003. Late Hercynian polymetallic vein-type base-metal mineralization in the Iberian Pyrite Belt: fluid-inclusion and stable-isotope geochemistry (S–O–H–Cl). *Mineralium Deposita*, 38: 953–967.
- Hubral, P. (ed.), 1999. Macro model independent seismic reflection imaging. *Journal of Applied Geophysics*, 42 (3-4) – Special issue on Karlsruhe Workshop on macro model independent seismic reflection imaging.
- Kaiser, H. F., 1960. The application of electronic computers to factor analysis. *Educational and Psychological Measurement*, 20, 141–151.
- Kim, J. S., Moon, W. M., Lodha, G., Serzu, M., Soonavvala, N., 1994. Imaging of reflection seismic energy for mapping shallow fracture zones in crystalline rocks, *Geophysics*, 59, 753–765.
- Korn, D., 1997. The Palaeozoic ammonoids of the South Portuguese Zone. *Memórias do Instituto Geológico e Mineiro*, 33, 131 p.
- Leca, X; Ribeiro, A; Oliveira, T.; Brandão Silva, J.; Albouy, P.; Carvalho, P.; Merino, H., 1983. Cadre Géologique des Mineralisations de Neves Corvo, Baixo-Alentejo, Portugal, Litostratigraphie, Paléogéographie et Tectonique”: *Mémoire du Bureau de Recherches Géologiques et Minières*, Orléans, n° 121, 79 p.
- Leitão, J., 1997. Geology of the Aljustrel massive sulphide deposits, in Barriga, F.J.A.S., Carvalho, D., eds., *Geology and VMS deposits of the Iberian Pyrite Belt: Society of Economic Geologists Field Trip Guidebook Series*, v. 27, p. 82–97.
- Lundin Mining, 2010. Management’s discussion and analysis for the year ended December 31, 2010 – Lundin Mining Press Release, www.lundinmining.com
- Lundin Mining, 2012. Third Quarter 2012 Exploration Update press release, <http://www.lundinmining.com/ExplorationUpdate.asp?ReportID=555171>.
- Mann, J., Hubral, P., Hocht, G., Jaeger, R., Mueller, T., 1999. Applications of the common-reflection-surface stack; in 69th Annual International Meeting of the Society of Exploration Geophysicists, 1829–1832.
- Mateus, A. Munhá, J., András, P., Matos, J.X., 2006. Geoquímica isotópica do chumbo em mineralizações hidrotermais antimoníferas do Sul de Portugal. VII Congresso Nacional de Geologia. Universidade de Évora, Livro de Resumos, v. 3, p. 1039–1042.
- Matos, J.X., Rosa, C., 2001. Diagnóstico Preliminar de Minas Abandonadas – Área Sul. Relatório Interno, Instituto Geológico e Mineiro, 276 pp (in Portuguese).
- Matos, J. X., Martins, L. P., Rosa, C., 2003. Parque Mineiro da Cova dos Mouros - IGM contribute for the sustainable development of the mining park. IGME, *Cuadernos del Museo Geominero*, n° 2, 487–494.
- Matos, J., Pereira, Z., Rosa, C., Rosa, D. N., Oliveira, J. T., Relvas, J., 2011. A key time frame for VMS deposit exploration in the Iberian Pyrite belt. SGA 2011, 11th Biennial Meeting, Antofagasta, Chile, 790–792.
- Munhá J., 1983a. Low grade regional metamorphism in the Iberian Pyrite Belt: *Comunicações Serviços Geológicos de Portugal*, 69,3-35.
- Munhá J., 1983b. Hercynian magmatism in the Iberian Pyrite Belt. In: Sousa M J L, Oliveira JT. (eds.), *The Carboniferous of Portugal, Memórias Serviços Geológicos Portugal* 29: 39–81.
- Munhá, J., 1990. Metamorphic evolution of the South Portuguese/Pulo do Lobo Zone. In: Dallmeyer, R.D., Martinez-Garcia, E. (eds.), *Pre-Mesozoic geology of Iberia*. Berlin, Springer-Verlag, 363–368.
- Oliveira, JT., 1983. The marine Carboniferous of South Portugal: a stratigraphic and sedimentological approach. In: Sousa M J L, Oliveira JT (eds), *The*

- Carboniferous of Portugal, *Memórias Serviços Geológicos Portugal* 29, 3–37.
- Oliveira, J.T., Wagner-Genthis, C., 1983, The Mértola and Mira formations boundary between Doguedo and Almada do Ouro, marine Carboniferous of South Portugal. In: Lemos de Souda, M.J. (ed.), Contributions to the Carboniferous Geology and Palaeontology of the Iberian Península. Porto, Univ. Porto – Faculdade de Ciências, 1–39.
- Oliveira, J. T., Monteiro, J. H., Zbyszewski G., Manuppella, G., Oliveira V., 1984. Carta Geológica de Portugal, 1/200 000, Folha 7 and Notícia Explicativa. Lisboa, Serviços Geológicos de Portugal (in Portuguese).
- Oliveira, J.T., Garcia-Alcaide, J., Liñan, E., Truyols, J., 1986. The Famennian of the Iberian Peninsula. *An. Soc. Géologique Belgique*, 109, 159–174.
- Oliveira, J. T., Oliveira, V., Manuppella, G., Zbyszewski G., Monteiro, J. H., 1992. Carta Geológica de Portugal, 1/200 000, Folha 8 and Notícia Explicativa. Lisboa, Serviços Geológicos de Portugal (in Portuguese).
- Oliveira, JT, Pacheco, N, Carvalho, P, Ferreira, A., 1997. The Neves Corvo Mine and the Paleozoic Geology of Southwest Portugal. In: F JAS Barriga and D. Carvalho, eds : Geology and VMS Deposits of the Iberian Pyrite belt. SEG Neves Corvo Field Conference, 1997, Field trip # 1. Guidebook Series Volume 27. Society of Economic Geologists, p. 21–71.
- Oliveira, V., Matos, J.X., Bengala, M., Silva, N., Sousa, P e Torres, L., 1998. Geology and Geophysics as Successful Tools in the Discovery of the Lagoa Salgada Orebody (Sado Tertiary Basin - Iberian Pyrite Belt), Grândola, Portugal. *Mineralium Deposita*, 33: 170–187.
- Oliveira JT, Pereira Z, Carvalho P, Pacheco N, Korn D., 2004. Stratigraphy of the tectonically imbricated lithological succession of the Neves Corvo mine area, IPB, Portugal. *Mineralium. Deposita* 39, 422–436.
- Oliveira JT, Relvas JMRS, Pereira Z, Matos JX, Rosa CJ, Rosa D, Munhá J, Jorge R, Pinto A., 2006. O Complexo vulcano-sedimentar da Faixa Piritosa: estratigrafia, vulcanismo, mineralizações associadas e evolução tectono-estratigráfica no contexto da zona Sul-Portuguesa: In Dias R, Araújo A, Terrinha P, Kulberg JC (eds) Geologia de Portugal no contexto da Ibéria: VII Cong. Nac. Geologia, Universidade de Évora, Portugal: 207–244.
- Oliveira JT, Rosa C, Pereira Z, Rosa D, Matos J, Inverno C, Andersen T., 2013. Geology of the Rosário - Neves Corvo antiform, Iberian Pyrite Belt, Portugal: new insights from physical volcanology, palynostratigraphy and isotope geochronology studies. *Mineralium Deposita*, 48, 749–766.
- Pereira Z, Pacheco N, Oliveira JT., 2003. A case of applied palynology: dating the lithological succession of the Neves-Corvo Mine, Iberian Pyrite Belt, Portugal. In: Wong TE (ed) Proceedings of the XVth International Congress on Carboniferous and Permian Stratigraphy. R. D. Academy Arts and Sciences, Utrecht, The Netherlands, pp 345–354.
- Pereira Z, Matos J X, Fernandes P, Oliveira J T, 2008. Palynostratigraphy and systematic palynology of the Devonian and Carboniferous successions of the South Portuguese Zone, Portugal. *Memórias Geológicas do INETI*, 34, 181 p.
- Pereira, Z., Matos, J., Fernandes, P., Jorge, R., Oliveira. J. T., 2009. A new Lower Givetian age Miospores of the Phyllite Quartzite Group (S. Francisco da Serra Anticline, Iberian Pyrite Belt, Portugal). In: Abstracts Cimpfaro'09. Fernandes, P., Pereira, Z., Oliveira, J.T., Clayton, C & Wicander, R. (eds), pp. 75–78.
- Quesada, C., 1998. A reappraisal of the structure of the Spanish segment of the Iberian Pyrite Belt. *Mineralium Deposita*, 33: 31–44.
- Radzevicius, S. J., Pavlis, G. L., 1999. High-frequency reflections in granite? Delineation of the weathering front in granodiorite at Piñon Flat, California, *Geophysics*, 64, 1828–1835.
- Reiser, F. K. M., Rosa, D.R. N., Pinto, Á.M. M., Carvalho, J.R. S., Matos, J'X., Guimarães, F.M. G., Alves, L.C. and de Oliveira, D. P. S., 2011. Mineralogy and geochemistry of tin- and germanium-bearing copper ore, Barrigão re-mobilized vein deposit, Iberian Pyrite Belt, Portugal, *International Geology Review*, 53 (10), 1212–1238.
- Relvas, J.M.R.S., Barriga, F.J.A.S., Ferreira, A., Noiva, P. C., Pacheco, N., Barriga, G., 2006a. Hydrothermal alteration and mineralization in the Neves-Corvo volcanic-hosted massive sulphide deposit, Portugal: I. Geology, mineralogy, and geochemistry. *Economic Geology*, 101: 791–804.
- Relvas, J.M.R.S., Barriga, F.J.A.S., Longstaffe, F.J., 2006b. Hydrothermal alteration and mineralization in the Neves-Corvo volcanic-hosted massive sulphide deposit, Portugal: II. Oxygen, hydrogen, and carbon isotopes. *Economic Geology*, 101: 753–790.
- Rosa C, McPhie J, Relvas J, Pereira Z, Oliveira T, Pacheco N., 2008. Facies analyses and volcanic setting of the giant Neves Corvo massive sulphide deposit, Iberian Pyrite Belt, Portugal. *Mineralium Deposita*, 43: 449–466.
- Schermerhorn, L.J.G., Zbyszewski, G., Veiga Ferreira, O., 1987. Notícia Explicativa da Folha 42-D (Aljustrel), Carta Geológica de Portugal, escala 1:50,000: Lisboa, Serviços Geológicos de Portugal, 55 p. (in Portuguese).
- Silva, J.B., Oliveira, J.T., Ribeiro, A., 1990. South Portuguese Zone. Part VI. Structural outline. In: Dallmeyer, R.D., Martínez García, E. (eds.). Pre-Mesozoic Geology of Iberia. Springer, Berlin, 348–362.
- Simancas, J.F., Carbonell, R., González Lodeiro, F., Pérez Estaún, A., Juhlin, C., Ayarza, P., Kashubin, A., Azor, A., Martínez Poyatos, D., Almodóvar, G.R., Pascual, E., R. Sáez, R., Expósito, I., 2003. Crustal structure of the transpressional Variscan orogen of SW Iberia: SW Iberia deep seismic reflection profile (IBERSEIS). *Tectonics*, 22 (6), TC1062, 1–11—1–19

Modelling of the Cala area (Ossa-Morena Zone)

12

Teresa Sánchez-García, Félix Bellido, José Mediato,
Jose Luis García-Lobón, Jesús García-Crespo,
Concepción Ayala, Carmen Rey-Moral, Félix Rubio,
Alejandro Díez-Montes, Santiago Martín-Alfageme,
Fernando Tornos and César Martínez

Abstract

The *Cala* project area is a region ca. 400 km² in size that comprises several mines and prospects hosted by Palaeozoic rocks. The Cala area is located in the southern segment of the Iberian Massif that forms the pre-Mesozoic basement in most of the Iberian Peninsula and constitutes the westernmost extent of the European Variscan orogeny. More precisely, it is situated in the south-western limb of the *Monesterio* Antiform, within the *Ossa-Morena Zone* (OMZ), which exposes a complex geological evolution. The current structure of the OMZ is mainly due to the Variscan orogeny. This study is focused on Variscan plutons that were emplaced into Late Proterozoic and Paleozoic sediments. Igneous and metamorphic activity of the Variscan Orogeny led to the formation of various types of mineralization. Two of these are studied in this paper: the iron oxide replacement and skarn in the Cala mine and the Ni-(Cu-PGE) deposit in the Aguablanca mafic to ultramafic intrusion. The aim of this work is to build three 3D geological models: one at regional scale (Cala regional model) and two at local scale (Cala mine and Aguablanca deposit). To achieve this we have improved the previous geological mapping and carried out two regional gravity surveys and one detailed survey in the neighborhood of Cala mine. Moreover, in order to study the Aguablanca deposit the geological information supplied by Lundin Mining was very useful. The use of geophysical data provide a tool to check the final models. Fully honoring the geological data and starting cross-sections, best processing practices, model properties based on petrophysical data,

T. Sánchez-García (✉) · F. Bellido · J. Mediato ·
J.L. García-Lobón · J. García-Crespo · C. Ayala ·
C. Rey-Moral · F. Rubio · A. Díez-Montes ·
S. Martín-Alfageme
IGME, C/Ríos Rosas, 23, 28003 Madrid, Spain
e-mail: t.sanchez@igme.es

C. Ayala
IGME, Now visiting at ICTJA-CSIC, C/Lluís Solé i
Sabaris, s/n, 08028 Barcelona, Spain

F. Tornos
CAB (INTA-CSIC), Crta. Ajalvir km. 4, 28850
Torrejón de Ardoz, Spain

C. Martínez
Departamento de Geología, Mina “Aguablanca”,
06260 Monesterio Badajoz, Spain

and the use of a profile mesh providing a great number of intersections where profile consistencies are proven in a 3D environment was the working scheme. The final 3D geological models give a new insight into the Cala and Aguablanca Variscan plutons concerning depth geometry, volume of mineralization and geological environment, not previously known. The regional model provides the geological context of the complex geological evolution that took place in the southern segment of the Iberian Massif. Furthermore, a predictive model has been constructed, including three areas of high potential for mineralization, based on geophysical studies. In addition occurrences of magnetite deposits related to replacement or skarn formation and possible uranium enrichment would be expected based on the predictive models.

12.1 Regional and Local Geological Setting

The *Cala* project area is approximately 400 km² large with several mines and prospects hosted by Palaeozoic rocks. It is located in the southern segment of the Iberian Massif that forms the pre-Mesozoic basement in most of the Iberian Peninsula and constitutes the westernmost extent of the European Variscan orogen (Fig. 12.1a). More precisely, it is situated in the south-western limb of the *Monesterio* antiform, within the *Ossa-Morena* Zone (OMZ in Fig. 12.1b), one of the major tectonic units of the Iberian Massif (Julivert et al. 1974). It is limited to the north by the Iberian central zone (CIZ), and to the south by the southern Portuguese zone (SPZ). The precise limits are under discussion in the geological literature (Quesada 1990a, b, 1997; Quesada et al. 1991; Dallmeyer and Martínez García 1990; San José et al. 2004) and beyond the aim of this paper.

The *Ossa-Morena* Zone exposes a polyphase and poly-orogenic geological record with a complex history. It represents a continental magmatic arc accreted to the Iberian Autochthon during the Late Proterozoic-Early Cambrian Cadomian Orogeny (Quesada 1990a, b, 2006). A subsequent Cambrian-Early Ordovician rifting event is recorded in OMZ, which was accompanied by intrusion and eruption of large volumes of igneous rocks (Quesada 1991; Sánchez-García et al. 2003, 2008, 2010). This rifting episode was followed by a passive margin development in Ordovician-Devonian times.

Finally, the Variscan Orogeny culminated the evolution of this zone in late Palaeozoic times (Quesada 1991, 1992; Quesada et al. 1991; Eguluz et al. 2000; Pereira and Quesada 2006; Sánchez-García et al. 2003, 2008; Nance et al. 2010, among other authors).

The general stratigraphy exposed in this area includes a Neoproterozoic and Paleozoic basement with meta-sedimentary and meta-volcanic successions which are intruded by a variety of plutonic rocks of different ages.

The current structure of the area is mainly due to the Variscan orogeny, which in this area is characterized by transpressional tectonics, with the development of large sinistral strike-slip faults into sigmoidal shaped blocks. This thick-skinned tectonic regime led to lateral juxtaposition of units that were originally separated from one another (Quesada 2006). In addition, according to this author, variable transpressional uplift or erosion and/or subsidence of the different blocks during their Variscan displacement and deformation resulted in the present juxtaposition of different crustal levels across the strike-slip faults.

The *Monesterio* Antiform is a large structure (>200 km long), which consists of a Late Proterozoic, mainly crystalline core, flanked by well-developed Early Cambrian rift sequences. Throughout this structure, a suite of Variscan plutons was emplaced, and one of the plutonic units of this suite is the *Santa Olalla de Cala* Plutonic Complex (SOC), which includes the *Santa Olalla Massif* (SOM) and the *Aguablanca* (Agb), *Cala* (Cg), *Teuler* (Tg) and *Helechoso* (Hg) plutons (Fig. 12.1c).

The OMZ hosts abundant ore deposits associated with different orogenic cycles. Some volcanic-hosted massive sulphides and some minor porphyry copper-like mineralisation related to the Cadomian Orogeny exist. Mainly, iron oxide stratabound deposits related to bimodal volcanic activity of Cambrian-Ordovician Rift can be found (Dupont 1979; Tornos et al. 2004). Exhalative-sedimentary barite is hosted in marbles and volcano-sedimentary rocks of the Loma del Aire Fm. of Lower Cambrian age, which was recently dated (Sánchez-García et al. 2014).

Igneous and metamorphic activity of the Variscan Orogeny led to the formation of various types of mineralization (Tornos et al. 2004). Mineralization processes related to the Variscan orogeny are highly diverse and are conditioned by the transpressional character of the orogen and by their magmatic and tectonothermal evolution. Among the Variscan mineral deposits, base metal bearing veins related with granitic plutons, iron oxide mineralization skarn and related replacement deposits can be found. Other types of mineralizations are small massive sulphide deposits associated with igneous rocks, magmatic mineralization of magnetite and Cu-Ni, and veins and peri-plutonic replacements of W and Sn, and hydrothermal veins with Au, Pb, Zn, U and barite.

The Variscan metallogenic complexity of the OMZ is related to the geodynamic evolution of this area from an active continental arc regime to another of collisional character after amalgamation with the SPZ (Tornos et al. 2004).

The main ore deposits in the studied area correspond to iron rich mineralization associated with skarn zones produced by the emplacement of Variscan plutons in metasediments of the Lower Cambrian Detrital-Carbonate Formation, Ni-(Cu-PGE) magmatic mineralizations hosted by Variscan mafic and ultramafic plutonic rocks, and quartz-ankerite veins with Cu (Au-Bi), hosted by Variscan tonalites, and Neoproterozoic and Lower Cambrian metasediments and meta-volcanic rocks (IGME 1975a, b; Vázquez et al. 1980; Vázquez 1983; IGME 1980; Tornos et al. 2004; Piña 2006; Carriedo and Tornos 2010).

In order to carry out 3D modelling, nine plutonic units have been considered, which correspond to some associations of the cartographic units distinguished. (1) Pre-Variscan granites; (2) *Santa Olalla Massif* in the strict sense (SOM), which includes four units, (3) the *Aguablanca* (Agb) pluton, (4) *Cala* (Cg), (5) *Teuler* (Tg), (6) *Helechoso* (Hg) plutons (Fig. 12.1c). Except for the group of Pre-Variscan granites, the rest are considered as a single set of rocks constituting the so-called *Santa Olalla de Cala* plutonic complex (SOC, henceforth).

The meta-sedimentary units have been grouped and reduced to only 4 for the creation of a 3D model. From the bottom to the top they are: (1) the *Serie Negra* Formation; (2) the Cambrian metasediments and volcanics; (3) the Lower Cambrian Carbonate Detrital Group (DCG), separated because it is a good reference level in the area; (4) other Paleozoic metasediments.

All the descriptions of the units will refer to the geological legend shown in Fig. 12.1.

Within this geological context, we have developed the following models:

- (A) A regional 3D model covering the entire *Cala* area (Fig. 12.1c) that illustrates the geology at depth surrounding the two outstanding ore-bodies of the Spanish OMZ: *Aguablanca* (Ni-Cu), and *Cala* (Fe-Cu). The purpose for building this model was to establish a structural framework encompassing the host rocks of both ore-deposits, which in turn will contribute to a better understanding of ore genesis and emplacement, and ore predictivity.
- (B) A local 3D model of the *Cala* Fe-Cu mineralization (Fig. 12.1c). The purpose for model building was to improve the geometrical knowledge and estimation of reserves of the ore body (poorly determined at depths below 400 m), testing inexpensive geophysical methods not used previously.
- (C) A local 3D model of the *Aguablanca* ore deposit (Ni-Cu).

12.2 Dataset and Methods Used to Build the 3D Model

Nowadays, most of the cartography, including geologic maps, is available in GIS formats and the use of tools to analyse the data linked to them are widespread. Recently, new software has been developed, allowing the management of 3D data, and facilitating the interpretation of geological structures. Thus, the use of both technologies enables new interpretations and the reconstruction of geological bodies in the subsurface.

To accomplish the modelling objectives of the study cases presented here, two software programs were used, ArcGIS for extracting data from previous layers loaded in geodatabase format, which were used to compound the geological maps. After adequate field work, these maps were reviewed and recompiled, both in stratigraphic and structural terms. gOcad was the 3D modelling software then used to load the data from ArcGIS (i.e., geological contacts, faults) and 3D data such as drillings, dip points, and geological cross-sections. A modelling study, integrating results from structural geology and petrology, was performed with gOcad in order to decipher geometrical and geological relationships between different rocks and mineralization zones.

The input data used in this study were the topographic reference map (as DEM of 100×100 m, basic datum of all the 3D features), reviewed geological maps, structural data and samples for petrological and petrophysical characterization, geophysical data with corresponding interpretations and models, and borehole data (source data of Fig. 12.2a). The first step concerns the creation of a geological database which includes all the information needed for 3D modelling. Six main typologies of geometric features and related attributes are exported from an ArcGIS-geodatabase:

1. Topographic data: topographic data as points from a digital elevation model.
2. 2D linear features from geological maps (stratigraphic and intrusion boundaries, fold

axial traces, faults, foliations, etc.): a geological map with stratigraphic, tectonic and intrusion boundaries, linear features such as 2D polylines, etc.

3. 2D polygonal features of outcropping units and 2D geological cross-sections.
4. Petrological and petrophysical samples for laboratory determination of properties (densities, magnetic susceptibilities) from some surface rocks of the studied area, and in situ natural gamma ray measurements.
5. Geophysical data and interpretations.
6. Data from drill holes and old maps, vertical sections, and horizontal slices of ore bodies in some cases.

All these data are the source of the starting geological model. The processing of previous data generates new layers of information, step by step (Fig. 12.2):

- 3D geological maps and cross-sections. Building of a set of 3D parallel geological cross-sections across the analysed structures and intrusions constitutes the first basic step.
- 3D point sets. These correspond mainly to borehole intersects of top/bottom limits of selected units, and to 3D layers of dip points and structural measurements, needed for surface interpolation.
- Petrological, petrophysical samples and radiometric measurements.
- Previously built 3D geological cross-sections are adjusted to fit geophysical anomalies.

All these layers are processed within gOcad with adequate interpolators to generate 3D layers of curves and surfaces, and finally voxets of the modelled bodies (Fig. 12.2).

As subsurface information is scarce in the *Cala* area (i.e., only a few drill holes are available, and no seismic deep reflection profile has been recorded to date), we proceeded to recompile and reinterpret old geophysical data from the *Cala* area (gravity, magnetic and radiometric data) available at SIGECO (IGME, Databases, on line, 2014) and other studies such as those of

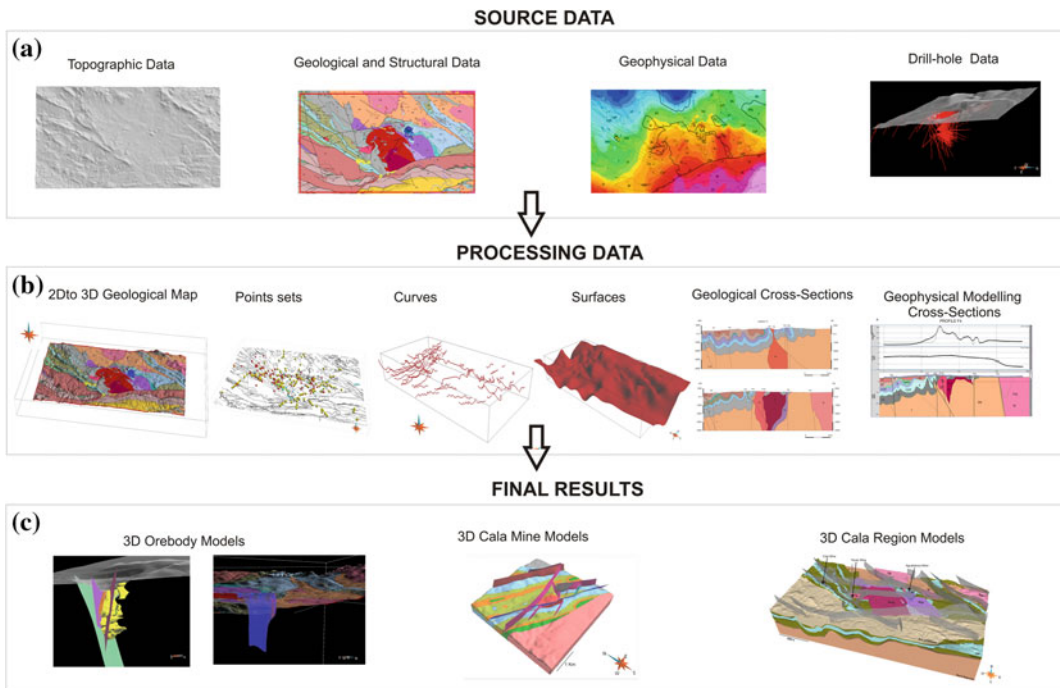


Fig. 12.2 Schematic flow-chart for 3D modelling through data integration between GIS and gOcad

Romeo (2006), Romeo et al. (2008). Existing geophysical coverage was complemented with new acquired data. Although these were non-seismic surveys, they were sufficiently precise to solve the problem faced. New geophysical surveys consisted of a gravity and natural gamma ray data.

These surveys were interpreted qualitatively first, and then by geophysical inversion. Geophysical modelling defines the correlation between a model of the subsurface and the geophysical data acquired, usually, on the surface. Working with potential fields, the subsurface geology is investigated, taking into account the variations that occur in the earth's gravitational and magnetic fields due to the density and magnetic susceptibility distribution at depth. The final 3D geological models were obtained mainly from geological cross-sections that were adjusted to fit potential field anomalies. After calculating the gravimetric responses from the starting geological model (direct problem), we proceeded to review structural cross sections and new sections were built with the support of the geophysical

models. Differences between the original and modelled cross-sections are sometimes significant, as described below.

12.3 3D Modelling Results

As previously mentioned, we present three models: a regional 3D model, a local 3D model of the *Cala* mine area and a local 3D model of the *Aguablanca* ore deposit.

12.3.1 3D the *Cala* Regional Model

12.3.1.1 Initial 2D Geological Model

The starting point geological map is a modified version after the Geological map compilation of the *Ossa-Morena* Zone in Spain (Quesada and Sánchez-García 2002, Fig. 12.1). The modifications were required because the representation of

Table 12.1 Summary of the samples used in the project

	Petrography		Chemical analysis	Petrophysics		Natural gamma
	New	Compiled		New	Compiled	
Regional <i>Cala</i>	276	137	96	180	234	221
<i>Cala</i> mine	32	–	6	–	–	–
<i>Aguablanca</i>	120	–	120	–	–	–
<i>Total</i>	565		222	414		221

Table 12.2 Geophysical and petrophysical data of the *Cala* area

Data	New acquisition	Compilation
Gravimetric	852 points: 490 in the regional survey, 362 detailed	920 points: 315 regional, 605 detailed Romeo et al. (2006a, b, 2008), SIGECO geophysical database, online (2014), Bates and García Lobón (1998)
Magnetic	–	Grids from flights 1996–97, SIGECO geophysical database, online (2014)
Radiometric	–	Grids from flights 1996–97, SIGECO geophysical database, online (2014)
Petrophysics	180 samples	234 samples: García-Lobón et al. (2006)

the geological data in the original maps showed some deficiencies in the lithostratigraphic and structural control to allow a good 3D model and its construction. Thus, it became necessary to review the mapping of stratigraphic units, plutons and fractures, before the modelling of an area of about 406 km² (29 km × 14 km) that includes the *Santa Olalla de Cala* plutonic complex (SOC) and the *Aguablanca*, *Cala* and *Teuler* mines.

Previous samples of the MAGNA (Spanish National Geological Map) databases have been petrographically studied (SIGECO IGME, Databases, on line, 2014). New samples were collected and new geochemical analyses (XRF and ICP-MS) were made (see Table 12.1). As a result, in the new map, several plutonic facies have been identified within the *Santa Olalla de Cala Massif* (in s.s. SOM), and relationships between them have been established. New mapping has also highlighted the relationship between the fault sets, emphasizing the importance of a N70–90°E sinistral shear set. This has led to greater consistency when constructing the 3D geological model.

The information contained in geophysical and petrophysical databases of IGME has been used (Sect. 12.3.1.2, Table 12.2). Data are available in

SIGECO (IGME, Databases, on line, 2014). 180 new samples have been collected for a petrophysical study. We have also used 234 other samples from previous projects (García-Lobón et al. 2006). In the petrophysical study parameters commonly measured, such as density and magnetic susceptibility have been determined. Moreover, natural gamma radiometric characteristics of some igneous and metasedimentary rocks and ores are also included (221 measurements). The radiometric data have been acquired in an in situ radiometric survey carried out with a hand spectrometer. Regional gravity and magnetic considerations of Sánchez-Jiménez (2003) have also been taken into account in this study.

In the study area 20 geological cross-sections have been constructed across the main geological structures, 17 of them with a SW-NE orientation and 2 in an E-W direction (Fig. 12.1). These sections were carefully constructed taking into account the surface geology and radiometric maps. Whenever the information was available, depth estimations from the literature were considered. Stratigraphic columns with estimated thicknesses are mainly from the MAGNA cartography, and a first approach to granitoid pluton thicknesses are from Romeo (2006), Romeo et al. (2006a, b,

2008), who estimated a maximum depth of around 4000 m for the *Santa Olalla* Massif.

In this area the main structures have resulted from the Variscan orogeny, although in the NW, outside the study area, pre-Variscan relict structures can be recognized. One of the main Variscan structures is the *Monesterio* antiform. The study area is located on the southern limb of this antiform, in the footwall of the *Monesterio* thrust. There, the sequence has a right way-up stratigraphic arrangement. Some examples of built cross-sections are provided in Figs. 12.4 and 12.5 (profiles T7 and T5 of Fig. 12.1: starting point geological profile at the bottom, and the profile based on geophysical fit at the top).

The metasedimentary succession form a series of SW-verging, NW-SE synclines and anticlines, which are cut by plutons such as the *Cala* granite (Cg, unit 24), the *Teuler* granite (Tg, unit 23) and the *Santa Olalla* tonalitic Massif (SOM, units 17–21; Fig. 12.1).

Modelled lithologies

For the regional model of the *Cala* area, 30 units have been distinguished in the geological map: 15 are metasedimentary and 15 plutonic. The metasedimentary units have been grouped and reduced for 3D model construction purposes, from bottom to top: (i) *Serie Negra* (SN, unit 1); (ii) Lowermost Cambrian, which unconformably overlies *Serie Negra*; (iii) Lower Cambrian Carbonate-detrital formation (CDF), which overlies the Lowermost Cambrian and has been identified as the host of major mineralizations; and (iv), the rest of the Palaeozoic rocks overlying the CDF. Only 8 plutonic units have been considered for the purposes of the 3D modelling: Units 16, 17, (18 + 19), (20 + 21), 22, 23, 24, (26 + 27 + 28) (Fig. 12.1; see legend for a summary description).

The *Serie Negra* Formation (SN, unit 1)

The oldest unit in the OMZ is the *Serie Negra* Formation that appears in the north and southeast

of the studied area (Fig. 12.1). It consists of alternating graphite-rich slates and meta-greywacke with interbedded black quartzites (cherts), metabasites and felsic metavolcanic rocks. The *Serie Negra* is affected by polyphase penetrative deformation and a low metamorphic grade (greenschist facies) in the study area. The age considered for this unit is Ediacaran (Schäfer 1990; Ochsner 1993; Chichorro et al. 2008; Linnemann et al. 2008; Pereira et al. 2008, 2012a; Ordóñez 1998). The thickness assigned for this series range between 3000 and 4000 m, although this value is imprecise because the bottom is not exposed.

The Cambrian sequence

Within the Cambrian sequence four groups can be distinguished from bottom to top (see Fig. 12.1): (i) lower detrital fm. (LDF and LF); (ii) carbonate-detrital fm. (CDF); (iii) upper detrital fm. (UDF) and (iv) main rift-related volcanic rocks (MRV) according to Sánchez-García et al. 2003, 2008, 2010).

In order to carry out 3D modelling, all the Cambrian sequence has been considered as a whole, but the carbonate-detrital formation (unit 4, CDF) has been separated as it hosts the skarn mineralization in the study area (*Cala* and *Teuler* mines). The thickness considered for this assemblage ranges from 3700 to 2600 m.

The Carbonate-Detrital Formation (CDF, unit 4)

This unit is a marker horizon throughout the OMZ. In this area several belts trending NW-SE are folded and cut by faults and intruded by igneous rocks [i.e. *Cala* granite, *Aguablanca* stock, *Santa Olalla Massif* (SOM)]. These intrusive belts have produced a low grade of metamorphism into CDF, except in the periphery of the *Santa Olalla Massif* and the *Aguablanca* stock, where it may reach the pyroxene hornfels facies. This unit has yielded Lower Cambrian fossils (e.g. Liñán et al. 2002, 2004; Perejón et al. 2004). The estimated thickness of this formation

is 500–700 m. A group of skarn rocks are also identified as CDF because they originally derived from the same protolith as the rest of CDF rocks (Unit 5, skarn outcrops are labelled Sk in Fig. 12.1 and in the profiles). They include diopside and garnet bearing calc-silicate rocks and are in places not possible to represent at the scale of this study. They appear in the *Cala*, *Teuler* and *Aguablanca* mines and west of the *Santa Olalla Massif* (SOM), in the *Sierra Cerrada*. The thickness of this unit varies widely.

Ore Deposits

The main mineral deposits in the study area were exploited in the *Aguablanca*, *Cala* and *Teuler* mines. In the *Cala* mine the mineralization is hosted in a calcium skarn and it is composed of layers and irregular masses of magnetite separated by skarn zones between the meta-limestone and meta-dolomite layers of the CDF. The ore corresponds mainly to magnetite with minor pyrite and chalcopyrite. This deposit is located at the contact with the *Cala* granite (Cg, unit 24) that appears to be thrust on top of the deposit and the CDF rocks. In the *Cala* mine anastomosing and irregular dykes of granodiorite porphyry, occur within the skarn and the ore deposit (Carriedo and Tornos 2010).

The *Teuler* ore deposits occur at the southern and western contacts of the granite massif with the same name (Tg, unit 23) and is associated with the formation of a magnesium skarn within horizons in shales (CDF, unit 4). The mineralization mainly corresponds to magnetite, with minor pyrite and chalcopyrite. In an IGME report (1975b) the presence of uranium salts in this mine was identified and chemical analyses in the present study confirm a high uranium content.

The *Aguablanca* mineralization is completely different and consists of a large magmatic Ni-Cu deposit with minor platinum group elements hosted in pyroxenites, gabbro and gabbro-diorites (Agb, units 26, 27 and 28). The ore body forms a breccia pipe about 500 m in length, 60–100 m wide and more than 700 m deep, which dips about 70°S (Tornos et al. 1999). The ore

consists mainly of pyrrhotite, chalcopyrite and pentlandite.

The post-Cambrian units (Palaeozoic)

The remaining Palaeozoic units (unit 8–15 in Fig. 12.1) have been grouped together for the 3D modelling, but we will refer to them individually in the gravimetric study and the geophysical interpretation of the profiles modelled. They include the *Barrancos*, *Cubito* and *Terena* formations. The total thickness for these units varies between 1100 and 1400 m.

The *Cubito Fm.* consists of phyllites and schists with minor amounts of intercalated metabasites. They show a pervasive foliation and a main feature is the abundance of quartz segregations, sometimes with chlorite. The latter distinguishes them from the *Barrancos* slates. The *Barrancos Fm.* (Delgado 1908) is made up of a monotonous succession of greenish gray shales, which may be locally purple, with interbedded metabasites. The *Terena Fm.* is a detrital sequence that includes sandstones, greywackes and slates. A detailed description of these formations can be seen in the papers of e.g. Apalategui et al. (1990), Apalategui and Sánchez-Carretero (1991), Robardet and Gutiérrez-Marco (1990, 2004), Robardet et al. (1998), San José et al. (2004), Quesada (2006), Piçarra et al. (2011).

The igneous rocks

Five different types of plutons were studied in the *Cala* region. Their petrophysical characteristics are briefly described below (see Table 12.3). The maximum thickness considered for the plutonic units is 4000 m (cf. Romeo 2006; Romeo et al. 2006a, 2008).

The pre-variscan granites (Unit 16)

This unit includes three different plutons: The *Castillo* granite (Ctg.), the *Don Rufino* granite (Rg) and the *Sierra Padrona* granite (SPg) that

Table 12.3 Measured versus modelled geophysical properties in a model of Figs. 12.4 and 12.5

Sampled units	Density d (g/cm ³)	Susceptibility k (*10 ⁶ ucgs)	Modelling: profile-T7		Modelling: profile-T5	
	Avg	Main ferromagnetic mode	d	k	d	k
SNegra Fm (SN,1)	2.61	–	2.61–2.67		2.62–2.68	0–500
LF (2)	2.56	~ 1500	2.56		2.56	0–1000
LDF (3)	2.62	–			2.62–2.65	0–100
CDF (4)	2.73	–	2.73		2.73	0–200
CDF-Skarn (5)	3.06	>2500				
UDF (6)	2.58	>2500	2.58		2.58	0
MRV (7)	2.80	5	2.8			
CUBITO Fm (EC) (8)	2.63	~ 1000			2.8	0–100
Barrancos Fm (BF) (9)	2.67	–	2.65–2.70		2.65–2.75	0
Terena Fm (TF) (12)	2.56	–	2.56		2.56	0
ORE DEPOSITS (O)	3.71	~ 15,000	2.9	25,000		
Castillo pluton (Ctg.16)	2.60				2.65	0
SOM/Migmatitic (Mg, 17)	2.65	~ 2500			2.64	1
SOM/Canteras(TC.18) + Comun (TCF, 19)	2.74				2.74	0–200
Som/Sultana (St.20) + Dioritoides(D.21)	2.75				2.75	0
SOC/Teuler pluton (tg.23)	2.63	~ 1000				
SOC/Cala pluton (Cg.24)	2.66		2.66	100		
SOC/Aguablanca Stock (Agb,26,27,28)	3.05				2.95	100

intrude into the *Serie Negra* formation. The *Castillo* granite (CTg), in the northern part of the studied area, produced a contact metamorphic aureole in the host rocks. The granites are in places deformed and transformed into banded gneisses. The main lithology is alkaline biotite-amphibole granite, interpreted to have been formed in response to the rifting event that affected the OMZ in the Cambrian (e.g. Quesada 1991; Sánchez-García et al. 2003, 2008, 2010). It is the oldest of the plutons studied in this project, dated as Cambrian at 502 ± 5 Ma (Montero et al. 2000). The *Don Rufino* granite (Rg) outcrops north of the *El Real de la Jara* village. It is a fine-grained biotite granodiorite, with frequent mega-enclaves derived from the immediate host rocks. Mafic and aplitic dykes cut across this pluton, which is not dated. The *Sierra Padrona* granite (SPg) outcrops in the NE part of the study area. It is a white and

pink coloured biotite granite varying between fine and very fine grained, and is not yet dated.

The Santa Olalla plutonic complex (SOC)

As noted above this complex consists of the *Cala* and *Teuler* plutons, the *Santa Olalla Massif* itself (SOM), the gabbroic *Aguablanca* stock and the *Helechoso* pluton.

The *Helechoso* granite, also called the *Garrote* pluton by Romeo (2006) (Unit 22 in Fig. 12.1, Hg) is a small drop-shaped granitic stock with an outcrop area somewhat less than 1 km². Its composition varies between quartz syenite and granite, it is pink coloured and fine to very fine-grained, with ductile relationships between the different facies. It is intrusive into the LF (unit 2 in Fig. 12.1) and the

Detrital-Carbonate Fm (CDF, 4, in Fig. 12.1). The age is 339 ± 3 Ma (Romeo 2006) and according to this author it displays an intrusive contact with the *Aguablanca* gabbro-norites in a drill core.

The *Teuler* pluton is located about 5 km northwest of the town of *Santa Olalla de Cala*. It outcrops to the west of the *Santa Olalla Massif* (SOM), and it is emplaced within the LF volcano-sedimentary succession (Unit 2). It is exposed over a length of about 2 km and a width of 1 km, elongated in an E-W direction. It consists of grey to pink, inequigranular, fine to medium grained biotite granite. A magnesium skarn with associated magnetite mineralization is visible in the host rocks. Age data by Salman (2004) using the Kober method on zircon yielded an age of 348 ± 4 Ma. Subsequently, Romeo et al. (2006b) reported an age of 338 ± 2 Ma using the U-Pb (TIMS) zircon method from a muscovite-bearing biotite granite.

The *Cala* granite is a small stock with a lenticular shape (700×300 m). It is located southwest of the town of *Cala* and consists of grey to pink, inequigranular and fine to medium grained biotite granite. The contact between the granite and the mineralized skarn rocks is a brittle thrust ($N145^\circ E/50^\circ$ –NE). The granite contains magnetite skarn enclaves. It is dated by TIMS U-Pb on zircon as Lowermost Carboniferous at 342 ± 4.2 Ma (Carriedo and Tornos 2010).

Santa Olalla Massif (SOM) plutonic massif intrudes Proterozoic metasedimentary rocks of the LF volcanic sedimentary succession (unit 2). Towards the SE, the *Santa Olalla* pluton is limited by Devonian-Carboniferous slates through a faulted contact (*Zufre* Fault, Fig. 12.1). This massif has been dated as Visean at 341 ± 3 Ma by Romeo et al. (2006b). This massif produced contact metamorphism and skarn alteration in the surrounding rocks. Six phases have been distinguished in this plutonic massif (“*Canteras*” granodiorite-tonalite, TC, 18; “*Común*” tonalites, *Sultana* diorites, TCf, 19; Migmatites, Mg, 17; Dioritoids, D, 21 and leucogranitoids Lg, 25), although for 3D modelling they are grouped into three facies as described below.

The migmatitic granitoids (Mg, 17) include migmatites, migmatitic granites and

leucogranites rocks. The occurrences of these granitoids is restricted to the eastern zone of the SOM pluton. They are exposed in a triangular area with a main axis trending approximately in $N135^\circ E$, with a dimension of approximately 4 km and 1.8 km at its widest point and just 130 m at its narrowest NW end. These granitoids are relatively poor in mafic minerals, medium to fine grained, heterogeneous and variably foliated, with locally a gneissic-migmatitic appearance. They display a “ductile looking” contact with the granitoids of the *Común* phase (TCf) and mingling between them is observed locally.

The *Común* and *Canteras* phases (Units 19 and 18, respectively) mainly consist of biotite-amphibole tonalites and biotite granodiorites, respectively. Their contacts are transitional and the main difference is the coarser grain-size of the *Canteras* phase and the presence of amphibole in the *Común* phase. These phases constitute the main body of the massif. The predominant rock types in the *Común* phase (TCf) are biotite-amphibole tonalites. It is in most places heterogranular, xenomorphic, and sometimes slightly deformed, defining a magmatic foliation. The predominant rock types in the *Canteras* phase (TC) are biotite tonalites and granodiorites. They are hypidiomorphic heterogranular, coarse grained, and in places display a magmatic foliation.

The composition of the *Sultana* (St, 20) phase varies between tonalite and quartzdiorite (Unit 20). It locally displays mingling relationships with both migmatitic granites (Mg) and the *Aguablanca* gabbros (Agb). These phases outcrop NW of the main SOM as an isolate body forming an irregular belt in the NE margin that widens towards the SE. It intruded into the LF (2) and *Serie Negra* (SN, unit1) in the NW and into the LDF and DCF limestones in the east. Romeo et al. (2006b) dated this phase at 341 ± 3 Ma (U-Pb TIMS on zircon).

The *Aguablanca* stock (Agb, units 26, 27 and 28) is located in the north-central part of the *Santa Olalla Massif* (SOM), surrounded mainly by granitoid rocks of the SOM in its southern part. The stock is mapped as Units 26, 27 and 28 in Fig. 12.1. It is a small sub-circular pluton

(with a diameter of 1.27 km), composed of phlogopite-rich gabbros and pyroxenites, southward passing over to diorites and quartz-diorites. In the map three different phases are distinguished, leucogabbros, melanogabbros and dioritoids, but they are considered as a single entity base on their petrophysical character. This small intrusive body with a mafic and locally ultramafic character, consists of a discontinuous outer halo of pyroxene rich gabbroic rocks, an intermediate zone of hornblende and biotite gabbro-norites (leucogabbros) and a core of diorites and biotite-amphibole quartz-diorites with clinopyroxene (melanogabbros and dioritoids). This intrusion displays major endo-skarns along its northern edge, due to interaction with Lower Cambrian marbles. In the northern half of the *Aguablanca* stock a pipe of magmatic breccias with a significant mineralization of Ni and Cu occurs. These igneous breccias are partially cemented by pyrrhotite, pentlandite and chalcocopyrite that according to Casquet et al. (1999, 2001) were formed from the separation and injection of an immiscible sulphide phase. This mineralization includes minor amounts of Co, Pt, Pd and Au (Ortega et al. 1999). Where the *Aguablanca* gabbro-norites and SOC granitoids display mingling textures (Romeo et al. 2006b) zircons from the felsic rocks using the (TIMS) U-Pb method, yield an age of 341 ± 1.5 Ma. This age is considered to represents the age of crystallization of both rock types.

12.3.1.2 Geophysical Surveys. 2.5 D Geophysical Modelling

Geophysical modelling defines the correlation between a model of the subsurface and the geophysical data acquired, usually, on the surface. The 2.5D potential field models described in this section are based on the cross-sections built from geological data and the measured gravity and magnetic data. Original geological cross-sections were adjusted by geophysical forward modelling, changing mainly the geometry of the different geological bodies with the constraints imposed by the physical properties measured in the laboratory from rock samples. Once the differences between observed and calculated anomalies were

adequate, the modelled cross-sections were “loaded” into the gOcad software in order to build up the 3D model. In the *Cala* area, the available geophysical and petrophysical data used for the modelling are shown in Table 12.2.

Two new gravimetric surveys were carried out in the study area. One of regional character in order to complete the regional coverage of Romeo (2006) of Santa Olalla de *Cala* area (490 measurements with a sampling density of 3 points/km²), and another, more local, with a total of 362 measurements (50 stations/km²) focused at the *Mina de Cala*. The Bouguer anomaly was calculated taking into account measurements from previous surveys of Romeo (2006), Romeo et al. (2008), using the GRS67 geodetic system and with a density reduction of 2.60 g/cm³, see García-Lobón et al. (2014) open-file geophysical report.

A strong regional NW-SE gravity trend, originated in deep crustal sources, was subtracted from the Bouguer anomaly to obtain suitable residual gravity anomalies (García-Lobón et al. (2014) open-file geophysical report on the *Cala* area). In fact, the residual Bouguer anomaly map (Fig. 12.3a) is still characterized by a NW-SE trend reaching positive values in the south-eastern part of the studied area. Considering the residual Bouguer anomaly intensity, two areas can be clearly identified:

1. To the north, minimum residual values (<0 mGal) outline the Neoproterozoic *Serie Negra* succession, the Cambrian detrital formations (sandstones and slates) and the pre-Variscan granitoids (*Castillo* and *Sierra Padrona*). Within this gravity minimum, the Carbonate-Detrital Formation (CDF) displays mixed low-intermediate responses, not easily limited by the gravity field. In the same way, responses from Silurian and Devonian metasediments are masked by the regional gradient in the map.
2. A southern zone, with positive anomalies (0 to +9 mGal) is represented by the gravity maximum over the *Santa Olalla Massif* (SOM). This is a complex anomaly that includes two north trending alignments

originating at the Zufre fault, and following the tonalitic phase of the SOM and the Sultana pluton and the dioritic phase of the SOM respectively. Between these two maxima a gravity minimum outlines the less dense migmatitic granites of the SOM (Mg).

Some other short wavelength anomalies are:

- The *Aguablanca* gabbroic stock (Agb), hosting the Ni-Cu deposit, is correlated with a remarkable maximum (2 mGal), shifted slightly northward in the map (Fig. 12.3a) compared to the stock shown in the geological map. A short wavelength maximum also occurs over the *Cala* mine.
- The *Teuler* biotitic monzogranite (Tg) corresponds to a maximum, suggesting that denser mafic rocks should exist beneath. Moreover, the gravity image suggests that these rocks could be related to mafic SOC rocks. In fact, in this area some mafic rocks have been described.
- South of the Zufre fault the highest values of residual gravity correlate with the post-Cambrian sequence (*Terena*, *Barrancos* and *Cubito* formations).

All these anomalies are related to the mafic volcanics belonging to the post-Cambrian sequence.

The reduced to the pole aeromagnetic map of the *Cala* region (Fig. 12.3b) is part of the airborne geophysical survey of the Spanish Pyrite Belt and southern areas of OMZ that was carried out 1996–1997 (García-Lobón et al. 2006). The survey was carried out with a line spacing of 250 m and an altitude clearance of 80 m with an airborne magnetometer (Geometrics G-822) with a sensibility of 0.01 nT and using a differential GPS as navigational system. The data were processed with a medium IGRF correction of 43,245 nT. In contrast to the residual Bouguer anomaly map, high magnetic areas mainly coincide with the northern zone of negative gravity anomalies, whilst low magnetic areas broadly correspond to the southern gravity zone, with

positive residual Bouguer anomalies. Positive magnetic and gravimetric anomalies only coincide in the surroundings of the SOM, and over the mineralizations.

The maximum magnetic anomaly trends NW-SE where low density-paramagnetic metasedimentary rocks (LDF, UDF and LF) containing Lower Cambrian volcanic rocks occur. These ferromagnetic volcanic belts are the most probable cause of the magnetic signature of these northern formations. Some remarkable short wavelength anomalies also occur in peripheral areas of the SOM where a number of strong magnetic anomalies appear. In the western area, north of the *Teuler* granite, skarn rocks (Sk) correspond with several of the highest intensity anomalies (+550 nT) of the entire region.

The intrusive bodies of the *Santa Olalla Massif* (SOM), with the exception of the migmatitic phase, are characterized by low magnetic values corresponding to tonalites of the *Canteras* phase and medium-grained and heterogranular granodiorites of the *Común* phase. *Sultana* and dioritic phase of the *Santa Olalla Massif* do not show up as magnetic anomalies. Similarly, the *Aguablanca* gabbro-dioritic massif only produces intermediate intensity anomalies along its northern border. In the southern formations, low magnetic areas mainly correspond to paramagnetic rocks, such as greywacke and slate, of the *Terena* and *Barrancos* Fms (post-Cambrian sequence).

South of the Zufre fault (ZF) high magnetic areas caused by mafic rocks occur, within the TF, BF and EC (*El Cubito*) (sequences post-Cambrian). The *Cala* biotitic granite (Cg) delineates a wider anomaly than the ore deposits of the *Cala* mine.

In summary, granitoids display medium to low magnetic values, with the exception of the migmatitic SOM phases, which are mappable by their magnetic signature, and the *Cala* biotitic granite and the *Teuler* biotitic monzogranite. These latter anomalies, however, are not due to granitic rocks, but produced by magnetite-rich ferromagnetic skarns that affect these granitic plutons.

The radiometric ternary map provides a tool for mapping areas of mining interest.

The *Cala* area ternary map (Fig. 12.3c) displays the following main characteristics: (1) Low radioactivity in the *Serie Negra* (SN) represented by white colours; (2) The pre-Variscan *Castillo* (CTg) and *Sierra Padrona* (SPg) granitoids are rich in radioactive elements (K + U and Th + U signatures); (3) The *Cala* biotitic granite (Cg) displays high U contents, and (4) Coarse-grained tonalites and medium-grained and heterogranular granitoids (TC, *Canteras* phase) of the *Santa Olalla Massif* are rich in Th + U. Uranium anomalies occur in the *Cala* and *Teuler* mine areas. These anomalies have been checked on the ground by means of in situ natural gamma ray measurements. The U anomalies constitute a good indicator of possible extensions at depth of the known mineralized areas.

In order to interpret the available potential field data and to build 2.5 D potential field models along selected transects, 414 surface rock samples have been collected in the *Cala* area for petrophysical measurements. Laboratory measurements provide density and magnetic susceptibility. The samples include the main outcropping geological units targeted in the modelling. Laboratory density measurements have been made on hammer-cut samples (0.3–0.6 kg) by weighing them in air and water (Archimedes principle). These samples come from 2 kg of rock collected in the field. From each of these samples, powder (2 mm grid pass) was obtained and magnetic susceptibility determined in a kappabridge instrument. The mass of the powder was measured, and the values were converted to mass susceptibility values, then corrected by the density of the sample to obtain volume susceptibility. The less dense rocks, with values between 2.50 and 2.61 g/cm³, of the *Cala* area correspond to metasedimentary rocks (slates, limestones, greywackes, etc., labelled as SN, LDF and UDF in Fig. 12.1) They are also a clearly paramagnetic. The set of granitic samples displays no clear correlation between density and magnetic susceptibility. They show a wide range of susceptibility values (from paramagnetic to ferromagnetic), and a homogeneous density (around 2.73 g/cm³). This fact is clearly reflected in the potential field maps (Fig. 12.3a, b). In

general the main geophysical anomalies in the *Cala* region correspond to mafic volcanic and skarn rocks (those related to larger ore bodies are denser and more ferromagnetic), as indicated in a regional study of the Monesterio antiform (García-Lobón et al. 2006). Geophysical maps outline the SOC and are in good agreement with the petrophysical data.

In the study area, 20 geological cross-sections were constructed, 18 oriented SW-NE, perpendicular to the main structural direction, and 2 with an E-W orientation (Fig. 12.1c). The 2.5D quantitative interpretation of the residual Bouguer anomaly and the reduced to pole total magnetic field was carried out along nine selected profiles (8 approximately perpendicular to the strike of the anomalies, and one with an E-W orientation, see location in Fig. 12.1c) that are representative of the main structures crossed by the geological sections. For this purpose we have used the latest GM-SYS software (by Geosoft). The reduced to the pole magnetic field has been modelled with an IGRF of 43,245 nT, I = 90°, D = 0°, and assuming that all the magnetic field is induced (i.e. no remanence). The models extend far enough at both ends of the profiles in order to avoid edge effects. Calculations of the gravity and magnetic model response are based on the methods of Talwani et al. (1959) and Talwani and Heirtzler (1964) and the algorithms described in Won and Bevis (1987).

The objectives were to refine the geometry of the different formations, to delimit the depth and geometry of the granitoid bodies and to have an image of the distribution of physical properties in the study area. The modelled profiles were the starting point to build a 3D model that was inverted in order to obtain the best fit geometry, and density and susceptibility distribution in the study area.

Densities and magnetic susceptibilities were obtained from the petrophysical data (Table 12.3). Since the main uncertainties are the geometry of the bodies, we have used its average for the densities in the majority of cases (see Table 12.3) or a value within the range of uncertainty (± 0.05 mGal). For the magnetic susceptibilities, given the significant variations

within the various lithologies, we have used values within the minimum and maximum ranges for each lithology (Table 12.3).

The colour code and numbers are the same as the ones in the geological map. In the anomaly panels in all the figures, points correspond to the observed residual Bouguer and reduced to pole magnetic data and the thin black line is the response of the model. The green lines dividing the formations correspond to either faults or lateral changes of the physical properties. The images show the modelled profile with the geological section underneath for comparison. All the models have been extended far enough to

avoid edge effects. Please note that the images of the profiles are scale 1:1. Since the profiles have different lengths, the depths might vary from image to image.

Profile T7 (Fig. 12.4)

The stratigraphic succession represented in the cross-section includes the oldest OMZ rocks at its base, *Serie Negra* (SN, unit 1). Cambrian formations (LF, CDF, UDF and MRV) lie unconformably on top of the SN, and overlying the Cambrian, also unconformably, Ordovician

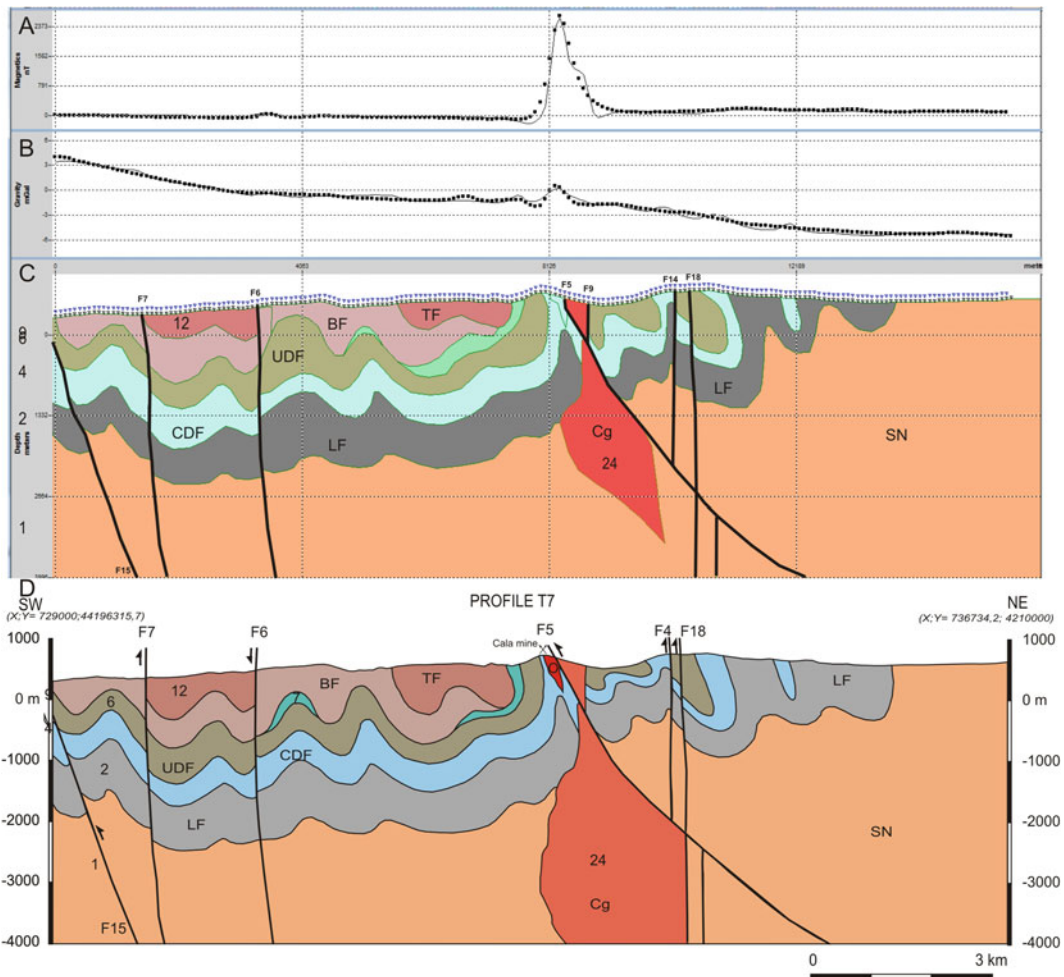


Fig. 12.4 Profile T7. *Top* Fitted to gravity and magnetic anomalies cross-section model. Note the adjustment between measured (*dotted line*) and calculated (*solid*

line) responses (magnetic above, gravimetric below). *Bottom* Original geological cross-section

detrital rocks of the *Barrancos Fm* (BF, unit 9, post-Cambrian sequence) occur. The youngest metasedimentary rocks are represented by detrital *Terena* formation (TF, unit 12, post-Cambrian sequence) of Devonian-Lower Carboniferous age. The Variscan granitic stock of *Cala* intrudes in all these metasedimentary succession. In the contact zone of the granitic rocks with the carbonate-detrital formation (CDF) iron skarn mineralization (magnetite) is exposed in the *Cala* mine outcrops. South of the *Cala* mine the sequence is folded with subvertical axial planes, while to the north the axial planes show a gentler south vergence. Most of the faults in the profile correspond to the group of N110–120°E faults dipping >70°. This family of faults is affected by the F5 fault (N120°E) that produces thrusting of the *Cala* granite (Cg, unit 24) onto the skarn and the CDF. The northern end of the *Cala* massif is affected by the F9 fault (N70–80°E) and displaces the N110–120°E group of faults. In the fitted geophysical model (top of Fig. 12.9), the *Cala* granite pluton has been reduced in size and depth with respect to the original shape, its bottom situated approximately 3400 m instead of around 4000 m. The changes in the thickness of the metasedimentary sequence required to adjust the gravity anomaly have been very small (in the range of 200 m). The most relevant change is the thickening of the CDF sequence in order to adjust the steep gradient from the F6 fault towards the SW end of the profile. It is noteworthy that the magnetic anomaly remains practically flat at about 0–150 nT except for a prominent central maximum of around 2500 nT in amplitude. The susceptibility value of $25,000 \times 10^{-6}$ SI that has been assigned to the outcropping mineralised CDF-skarn was needed to adjust the maximum in the magnetic anomaly, which could be due to the proximity of magnetite rich bodies. RMS of the gravity anomalies is 0.28 mGal and 94 nT for the magnetic anomalies.

Profile T5 (Fig. 12.5)

This profile is parallel to profile T7 and is situated close to the *Aguablanca* mine.

Regarding the Palaeozoic metamorphic rocks, it should be emphasized that in this profile *El Cubito* schists (EC, unit 8, post-Cambrian sequence) also appear. At the northern end, detrital rocks of the Lower Cambrian succession (LDF, unit 3) crop out. With respect to Variscan plutonic bodies, the migmatitic granite phase (Mg, unit 17) and the tonalites-quartzdiorites *Sultana* phase (St, unit 20) of the *Santa Olalla Massif*, and the *Aguablanca* gabbros (Agb, units 26, 27 and 28) appear in this profile. Cambrian granites are represented by the *Don Rufino* pluton (Rg, unit 16). The styles of folding and faulting are similar to what is observed in the profile T7, with the exception of the *Zufre* fault (F12). This major fault has a main sinistral tear component and produced uplift of the northern block, causing mechanical juxtaposition of Palaeozoic rocks with granitoids of the *Santa Olalla Massif* (SOM) that intruded into the *Serie Negra* (SN, unit 1). In the adjusted model to fit the gravity data (consistently with the other profiles), the most important change made was a dramatic reduction of the thicknesses of all the Variscan intrusive bodies. The SOM shows three peak-shaped roots, which reach about 1000 m in depth. The northernmost peak possibly corresponds to sheared feeder conduits of the *Santa Olalla Massif* (SOM) and the *Aguablanca* stock (Agb). The other two maximum depth points (roots) may also correspond to feeder conduits, although in the southernmost end, next to the *Zufre* fault (F12). The modelled feature may be due to tectonic thickening produced by such a fault. The geometry of the *Don Rufino* pluton (Rg, unit 16) has also been greatly thinned. The *Aguablanca* stock, which gives the highest amplitude gravity maximum in the profile, has been modelled as a body that extends 2000 m into the direction parallel to the strike. The modelled *Aguablanca* stock is not as massive as it is known to be due to the fact that our starting gravity data is a 250 m grid that comes from a regional gravity survey (spacing approximately 1 point/km²), and this relatively large cell size can produce a smoothing effect on the anomaly peak. At the SW part of the profile, from F24, there is a change in gravimetric gradient with a broad

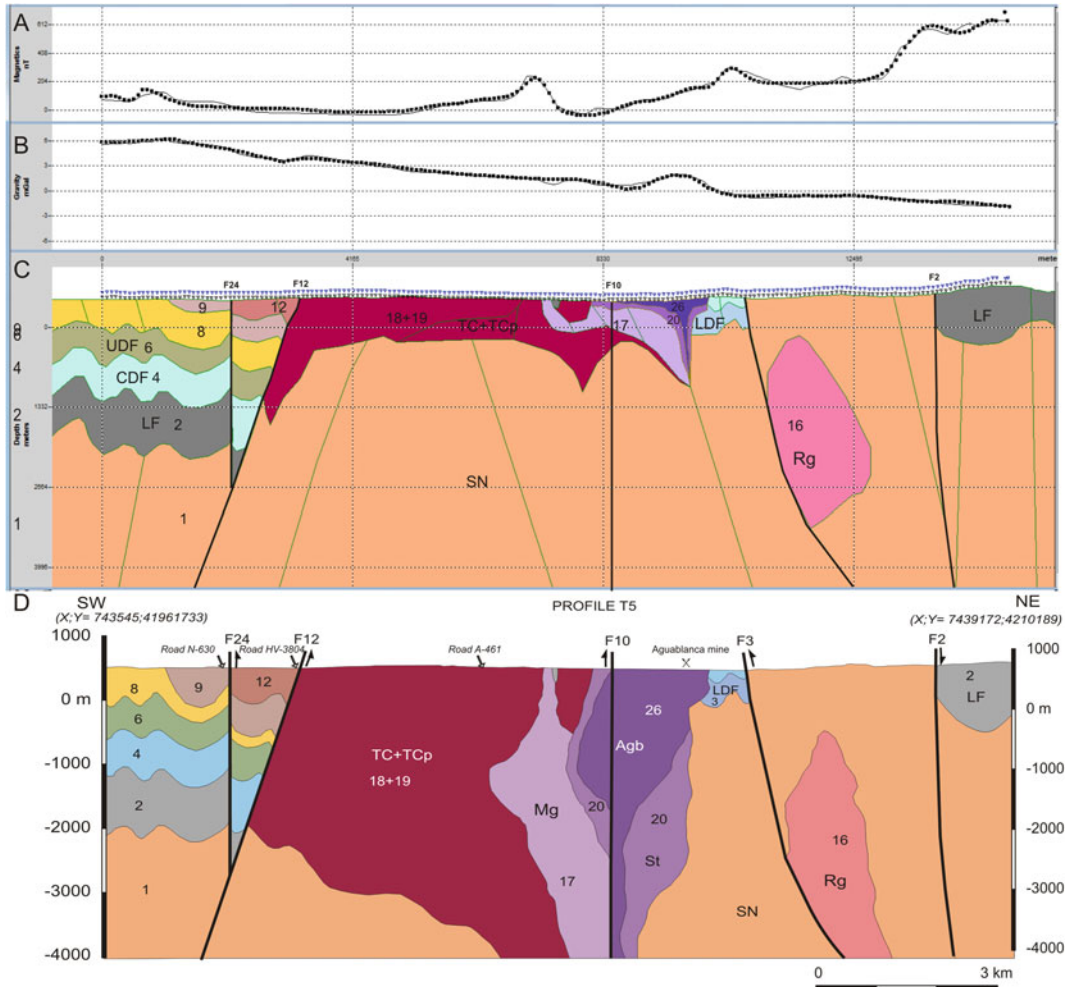


Fig. 12.5 Profile T5 *Top* Fitted to gravity and magnetic anomalies cross-section model. Note the adjustment between measured (*dotted line*) and calculated (*solid line*) responses (magnetic above, gravimetric below). *Bottom* Original geological cross-section

relative maximum of small amplitude that is due to changes in thickness within the folded metasedimentary sequences.

The magnetic profile displays five peaks with different intensities, and shows a strong increasing trend of the magnetic anomaly from the middle part to the NE end. The southernmost peak is located over exposures of the ‘El Cubito’ mafic schists (EC, 8) and the central peak corresponds to the migmatite granites of the SCM (Mg, 17). The other maxima are located over exposures of the Cambrian Lower Detrital

Formation (LDF). Root mean square (RMS) of the gravity anomalies is 0.23 mGal and 28 nT for the magnetic anomalies.

12.3.1.3 The Final 3D Model

Given the regional nature of the model, a simplified column has been used (Fig. 12.1c), leaving five major lithostratigraphic units. 3D surfaces for the limits of these units have been built. Eight intrusive bodies have also been modelled. Two of them are related to ore bodies (Cala and Aguablanca deposits) that have also

been constructed in 3D. The sedimentary units have been grouped into four main facies, taking the CDF unit as a reference level.

When creating surfaces, the temporal order of the succession has been taken into account. First, 3D plutons, which cut the metasedimentary series, were built, and next, the surfaces of stratigraphic horizons. The traces of the faults have also been digitized, taking into account the cross-cutting relations among them and with other surfaces.

When constructing the plutons, two important aspects have been considered. The temporal relationship amongst them which influences the order in which the work of 3D reconstruction has been carried out. First, the youngest bodies, which cut through the oldest, were constructed. The problem faced here is that the intrusions are almost coeval, i.e. the age difference found by radiometric dating is small. The age relationship had to be determined in the field. Thus, the order followed for the construction of the intrusive bodies, from younger to older, was as follows: *Teuler* granite (Tg, 23), *Helechoso* granite (Hg, 22), *Aguablanca* stock (26, 27 and 28), *Santa Olalla Massif* (17, 18, 19, 20 and 21), *Cala* granite (24), and finally, *Castillo* granite (CTg, 16). Among the units that make up the *Santa Olalla Massif* three intrusive episodes have been established, although they are all roughly the same age. First, we have modelled the migmatitic granites (Mg, 17), then the *Común* and *Canteras* phases (18 and 19), and finally, the *Sultana* and *Dioritoid* phases (20 and 21). Given the complex geometry the plutons, a very careful editing had to be done. First, a 3D surface defined between each two adjacent geological cross-sections was constructed, then the 3D pieces were joined into a single surface, then the adjustment of the surface with the outcropping contact line map was made and, finally, the intersection with the topographic surface was taken into account. When a body is also cut by another pluton, it was set by the constraints.

Comparing the 3D original model from the starting geological cross-sections (Figs. 12.4 and 12.5), and the geophysical fitted model of Fig. 12.6, several important facts can be pointed out:

- No significant changes in the thickness or the geometry of the metasedimentary units, between the starting point and the final models, are observed.
- A significant reduction of the volume of the plutons has been applied, as a result of mass deficiency/excess determined by the geophysical inverted anomalies.
- The thickness and geometry of the plutons have been modified in more detail. They change from a cup or inverted drop shaped geometry, to a more irregular, laccolithic geometry, with different rooting zones. One of them, in the southern part, can be associated with drag along the *Zufre* fault.

12.3.2 The Cala Mine 3D Model

12.3.2.1 Initial 2D geological model

The *Cala* mine was one of the largest iron producing mines in Spain during the 20th century. It is located in the southern limb of the *Monesterio* antiform (Fig. 12.1), within a mega structure whose axial trace trends NW-SE, next to an oval granitic stock, approximately 800 × 400 m in size (*Cala* granite). The *Cala* granite is limited by an intrusive contact with the Cambrian Upper Detrital Formation (UDF) and a NW-SE thrust, through which it is situated on top of the mineralized zone.

The starting point to construct the initial geological model is the *Ossa-Morena* geological map (Quesada and Sánchez-García 2002, Fig. 12.1). This map has been revised at a 1:15,000 scale to improve the location of the geological contacts and by adding structural data. Additional information includes a revision of the available geological mapping of the open pit mine (Carriedo et al. 2007; Carriedo and Tornos 2010) and old mining reports (IGME 1975a, b), which contain 24 cross-sections of the mineralized zone, data from 45 shallow boreholes, drilled from the surface and from the galleries, and also two maps of the deep mine galleries. The information contained in the papers by Carriedo et al. (2006, 2009) has also been taken into account. With all

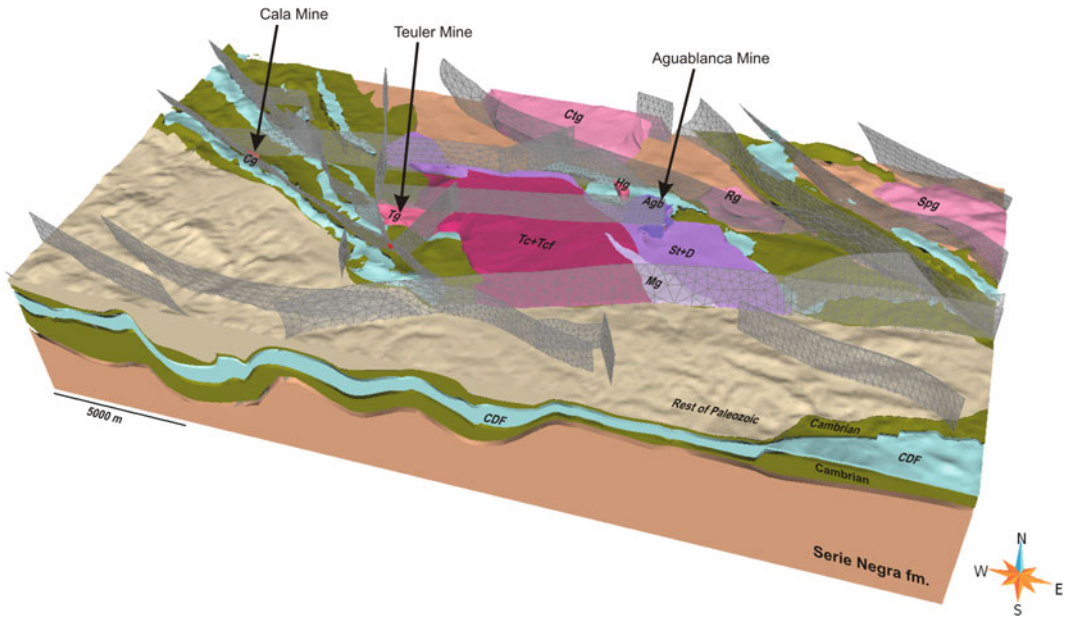


Fig. 12.6 Regional *Cala* 3D model

this information, a total of 14 geological cross-sections were constructed (see Fig. 12.7 for location): 12 (SW-NE) are perpendicular to the main structures, and five cross the mineralization. The other two profiles have NNW-SSE and WSW-ENE orientations. The purpose was to provide additional information to build a more detailed geometry of the mineralized area.

For the modelling, the lithological units of the geological map (Fig. 12.7) have been simplified by grouping them according to their structural equivalence. From the base to the top:

- (i) at the bottom of the Cambrian stratigraphic succession the LF formation appears, with a thicknesses of 1500–1800 m. It crops out NE of the *Cala* mine.
- (ii) The Carbonate Detrital Formation (CDF) lies on top of LF and hosts the mineralization; it is folded into a tight asymmetric anticline, faulted at its northern border. This fault thrusts the *Cala* granitic stock and shales of the UDF (unit 4) on top of the mineralization. Its thickness is about 300 m, almost constant throughout the area.

- (iii) The Upper Detrital formation has been divided into two sequences. The first one (UDF1), is composed of three subunits: unit 3 (arkoses, greywackes and shales), unit 4 (shales) and unit 5 (alternating sandstones and shales). This succession presents a thickness of approximately 500 m. The second sequence (UDF2- unit 6) overlies UDF1 and is composed of shales and sandstones with a maximum thickness of 150 m.
- (iv) The main rift volcanic sequence (MRV) is the uppermost Cambrian unit in the area where it reaches thicknesses up to 150 m towards the western part of the area.
- (v) The *Terena* Fm, Devonian-Carboniferous in age, lies unconformably on top of the Cambrian formations. To the SW the unconformity erodes the upper Cambrian units, situated on top of the CDF southeast of the mine.

The host rocks to the ore bodies intruded the skarn rocks and show a wedge-like geometry, thinning in depth. From the geological mapping and borehole data it has been deduced that the

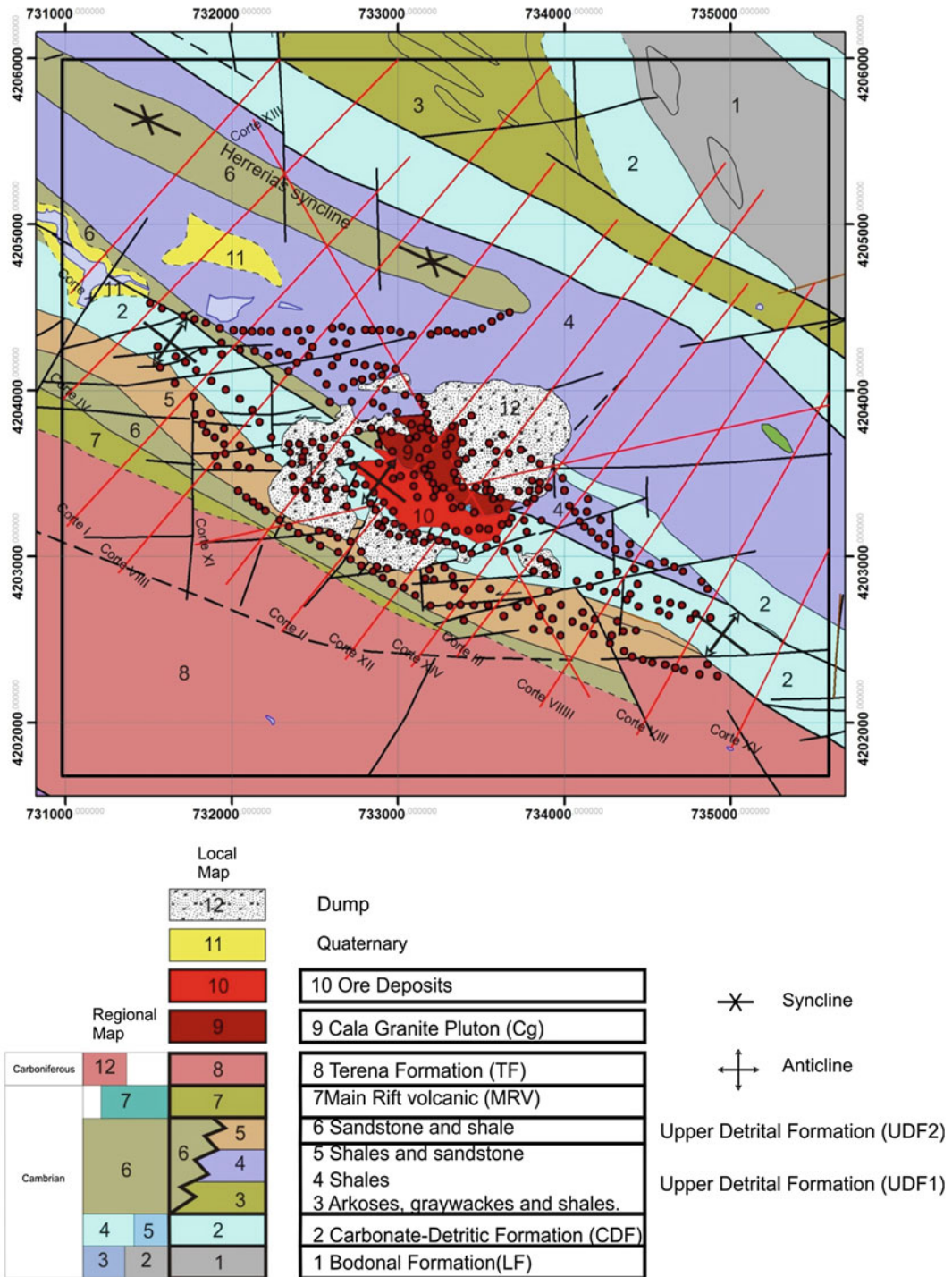


Fig. 12.7 Geological map with the location of the geological cross-sections used to build up the model (in red). Red dots Location of the gravimetric measurements. Black rectangle modelled area

structure of the ore bodies towards the north has the same dip as the CDF, 65–70° (Fig. 12.7), becoming thinner with depth, at least up to 400 m, the deepest level of the present open-pit. The boreholes do not crosscut the mineralization entirely, thus opening up the possibility that it continues at depth. The *Cala* granite (Cg) is a biotite granite. At present, its exposure at surface is mainly buried beneath a slag heap. As mentioned above, at its southern border the *Cala* granite was thrust onto the mineralization. This thrust has a 130°N strike and dips 60–70°NE. The base of the granite before the modelling was unknown. The slag heaps has not been included in the model because their thicknesses are assumed to be irrelevant for the modelling.

12.3.2.2 3D potential fields modelling

A local gravimetric survey was carried out in the study area, with a total of 362 measurements (50 stations/km²) focused on the *Cala* mine. The Bouguer anomaly was calculated using the GRS67 geodetic system with a density reduction of 2.60 g/cm³. For the topographic correction, a 25 m DEM was used to calculate the near topographic correction up to a distance of 4470 m (Hammer sector I) and a 100 m DEM for the far topographic correction, from 4470 to 21,945 m (Hammer sectors J to M). Those DEM came from the Spanish *Instituto Geográfico Nacional* (IGN). A residual Bouguer anomaly was obtained using the Zengh method, which is suitable for modelling the first km of the crust.

The residual Bouguer anomaly map shows amplitudes between –2.79 and 2.92 mgal (Fig. 12.8a). The central part of the map displays a prominent maximum that corresponds to the skarn zone and the mineralization at the *Cala* mine. Two relative minima located to the N and S, next to the mine, can be associated to the slag heaps. We do not have enough information to model them, so this is likely to generate some errors in the calculated anomaly. A conspicuous minimum to the NW can be correlated with a small dam and another slag heap. Overall, there is a NW-SE positive gradient, truncated in

places. These sites coincide with the presence of faults oriented between N70 and 90°E.

Once the starting point model was built up, we calculated its gravimetric response by forward modelling (Fig. 12.8b). For this purpose we have used the Geomodeller software. The patterns of the calculated anomalies are very close to the observed, so we proceeded with the inversion after small changes in the starting point model.

Densities for the different lithologies (Table 12.4) are the same as the ones from the petrophysics used in the 2.5 D regional calculations, the only exception being the mineralized zone and the skarn, where a value of 3.06 g/cm³ has been used, instead of the 3.48 g/cm³ obtained from the samples, in order to maintain the calculated central maximum with a similar amplitude to the one observed. The calculated residual anomaly presents values ranging between –3 and 3.08 mGal. The main difference from the observed residual is the absence of the NW-SE positive gradient and the strong positive anomalies due to the CDF and MRV units.

Once the observed and calculated anomalies had a similar pattern, we proceeded to the stochastic inversion, with 1 million iterations, allowing small variations in the densities (since they come from somewhat altered rock samples) and allowing more variation in the lithostratigraphic interfaces. The RMS varied from 0.97 mGal at the beginning of the calculations to 0.27 mGal at the last iteration.

The calculated residual anomaly from the inversion is shown in Fig. 12.8c. The range of the anomalies is from –2.24 to 3.48 mGal. The pattern of these anomalies (direction, intensity and range) is very similar to the ones observed. The mineralization is well delimited by the central maximum and the shape of the positive NW-SE gradient together with the NE-SW small breaks that correspond to faults similar to the one depicted in the observed residual Bouguer anomaly (Fig. 12.8a).

The density variations resulting from the inversion show that the average variation is very small, 0.02 g/cm³ with a SD of 0.1 g/cm³. In the mineralization zone, the density after the

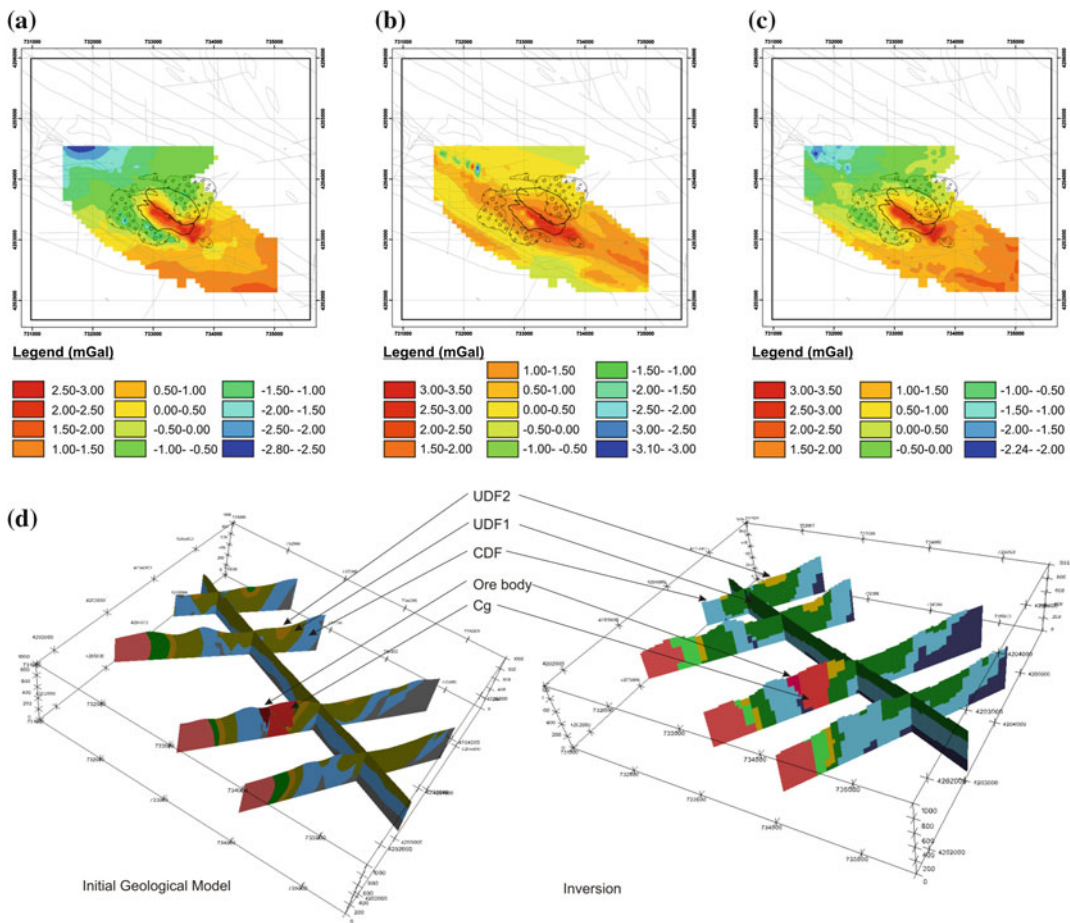


Fig. 12.8 a Observed residual Bouguer anomaly. b Calculated residual Bouguer anomaly from forward modelling. c Calculated residual anomaly from the inversion. d Model obtained from the inversion

Table 12.4 Starting point geophysical properties of the 3D Cala Mine model

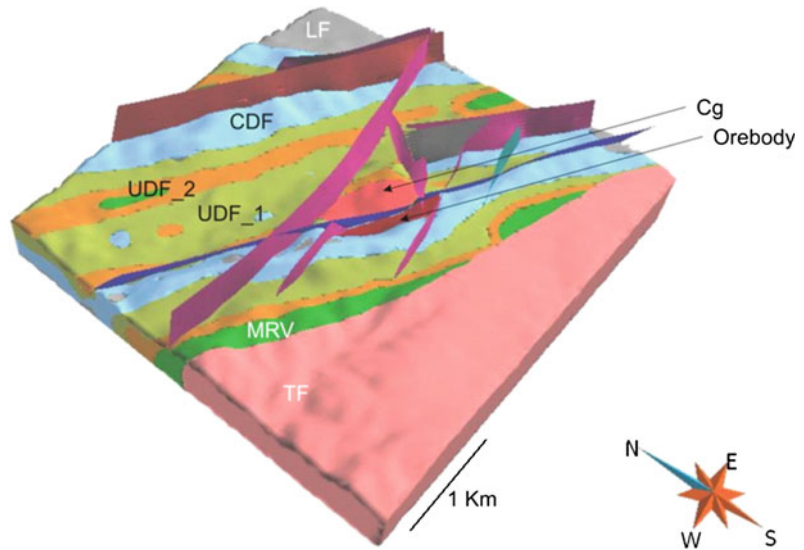
	Density (g/cm ³)
Sampled units	avg
LF	2.56
CDF	2.73
UDF1	2.58
UDF2	2.58
MRV	2.80
CDF_Skam-Orebody	3.06
Terena Fm (TF)	2.56
Cala pluton (Cg)	2.66

inversion increased by 0.4 g/cm³, resulting in a calculated density for the ore bodies of 3.48 g/cm³, which is closer to that obtained from the samples in the laboratory. The densities of the granite, CDF and MRV formations increased by 0.1 g/cm³, whereas the density of the UDF rocks decreased by 0.2 g/cm³. In the SE area, the results show a general density increase in the UDF and CDF formations between 0.1 and 0.3 g/cm³, in agreement with the hypothesis of the existence of denser rocks in this area.

12.3.2.3 The final 3D model

The geological model obtained from the inversion (Fig. 12.9) shows large similarities with the

Fig. 12.9 3D gOcad geological model of the *Cala* mine



starting point model. To the NW, the MRV completely disappears within unit 4 (UDF). The thickness of UDF2 decreases, whereas the thickness of UDF1 increases and the CDF units appear to be deeper. The bottom of the mineralization is at around 200 m in the central and SO zones, whereas to the NW it becomes shallower than in the starting point model.

The final 3D model is characterized by two fold structures, the *Herrerías* syncline with its axis in the UDF, and an anticline with its axis along the exposed CDF to the south of the mine (Fig. 12.7). Both are slightly verging south, with their southern limbs near vertical or overturned. Within the *Herrerías* syncline small tight folds can be distinguished.

Two sets of faults were included in the starting point model and are compatible with the geological structure obtained from the inversion. The oldest faults, striking 120–130°N are crosscut by sinistral 70–80°N faults. The latter faults also have an important vertical component that progressively uplifts the SW blocks, thus the *Herrerías* syncline tends to be tighter at the surface and the CDF Fm crops out in the smaller synclines. These geometries fit the relative maximum of the Bouguer anomaly in the area.

The modelled ore body reaches a depth of up to 400 m, in agreement with previous studies (e.g.

IGME 1975a) and dips 70°N. Its contact with the *Cala* granite on the surface is a thrust, but probably with very little displacement given the abrupt change in the residual anomaly and the data from the shallow boreholes (IGME 1975a). Even though the slag heaps have not been included in the modelling, the results of the inversion are good, with an RMS of 0.27 mGal (about 5 % of the total amplitude of the residual Bouguer anomaly).

The volume of unit 9 (skarn and ore body) calculated from the final model is about 43 Mm³. Using the density obtained from the inversion, 3.48 g/cm³ as a reference, the approximate weight of this unit is 150 Mt. From this quantity, 75–60 Mt corresponds to the ore body. These values are in the range proposed by Tornos et al. (2004) who estimated a minimum resource of 90 Mt @ 39 % Fe and 0.27 % Cu, and by Carriedo et al. (2009) who suggested 60 Mt @ 39 % Fe and 0.27 % Cu.

The geometry obtained from the 3D inversion shows that the ore body is affected by two sets of faults, therefore occurrence of mineralization north of the 80–90° directed faults, although located at a greater depth, can be expected. The increase in density of the CDF and the UDF1 towards the SE, where the residual Bouguer anomaly displays relative maxima, suggests the possible existence of hidden deposits. The most

probable location of these deposits would be next to the sinistral faults associated to this fault set. The *Cala* mine inversion model confirms that the *Cala* granitic stock must be shallower than in the proposed regional model (see Section *Cala* Region).

12.3.3 The Aguablanca Ore Deposit

12.3.3.1 Initial 2D geological model

The *Aguablanca* stock is a small intrusion associated with the Variscan *Santa Olalla de Cala* Plutonic Complex, as described above. This stock consists of three main lithological units: (1) A mafic group, composed of pyroxenites, gabbros and gabbro-diorites, (2) an intermediate group, containing diorites, tonalites and quartz-diorites, and (3) a vertical pipe, including Ni-Cu sulphide-rich mafic magmatic breccias.

The Ni-Cu-Fe sulphides are concentrated in a funnel-like magmatic breccia body situated near the northern boundary of the *Aguablanca* stock. Within the breccia, the mineralization is concentrated in sub-vertical ore bodies (Piña 2006; Piña et al. 2010).

The breccia consists of fine to coarse fragments of ultramafic rocks, gabbros and gabbro-diorites and host rocks of variable size, supported by a gabbro-diorite matrix, although in the core of the breccia pipe, the fragments are supported by a sulphide matrix (mineralized breccia). The main ore minerals are pyrrhotite, chalcopyrite and pentlandite.

In this model the input data have been provided by Lundin Mining. The data provided were: DEM (1 × 1 m) in the area of the mine (5.4 km²), a detailed legend of the mine's geological map, level maps (horizontal slices) and profiles (cross-sections), see Fig. 12.10a, and geological survey data and drill holes and core samples, see Fig. 12.10b. Fifteen level maps (slices) at different depths and fifteen N-S profiles have been included in the model. The absence of data from deep boreholes outside the mine area should be noted.

12.3.3.2 The final 3D model

Although three different intrusive phases have been distinguished in the geological map (leucogabbros, melanogabbros and dioritoids), they have been considered as a single entity for the 3D modelling due to their similar petrophysical properties.

This study only includes the regional gravimetric and magnetic data. With this information, the different types of mineralization were grouped to determine the overall geometry of the deposit (Fig. 12.10c), distinguishing two main ore bodies, a small one located to the north and a larger with more complex geometry located to the south. The resulting 3D modelling of the ore body within the *Aguablanca* pluton is shown in Fig. 12.10d, e. Roughly a pipe-like structure can be seen, although it displays an irregular shape. The breccia body extends from the surface to more than 600 m depth, and is about 250–300 m wide and 600 m long in section. These dimensions are not well-defined owing to a lack of detailed geophysical surveys or drillholes to confirm the depth of the mineralized bodies.

The geometry of the resulting model is consistent with the geometry of the detailed model of the *Aguablanca* stock developed by Romeo (2006), Romeo et al. (2006a, 2008). However, the geometry of the mineralized bodies obtained in the model appears not to be controlled by any dominant fault direction at the level of emplacement.

12.3.4 4D Modelling of the Project Area

The ore deposits modelled in this work are related to igneous activity during the Variscan orogeny. Two types have been studied; (1) Iron oxide skarn and replacement mineralization produced by intrusives in the *Cala* mine and (2) Ni-(Cu-PGE) magmatic mineralization hosted by mafic and ultra-mafic intrusions in the *Aguablanca* mine.

Based on the existing geochronological data and geological relationships observed the oldest intrusion is the *Cala* granite dated at 342 ± 4.2 Ma (Carriedo and Tornos 2010), see

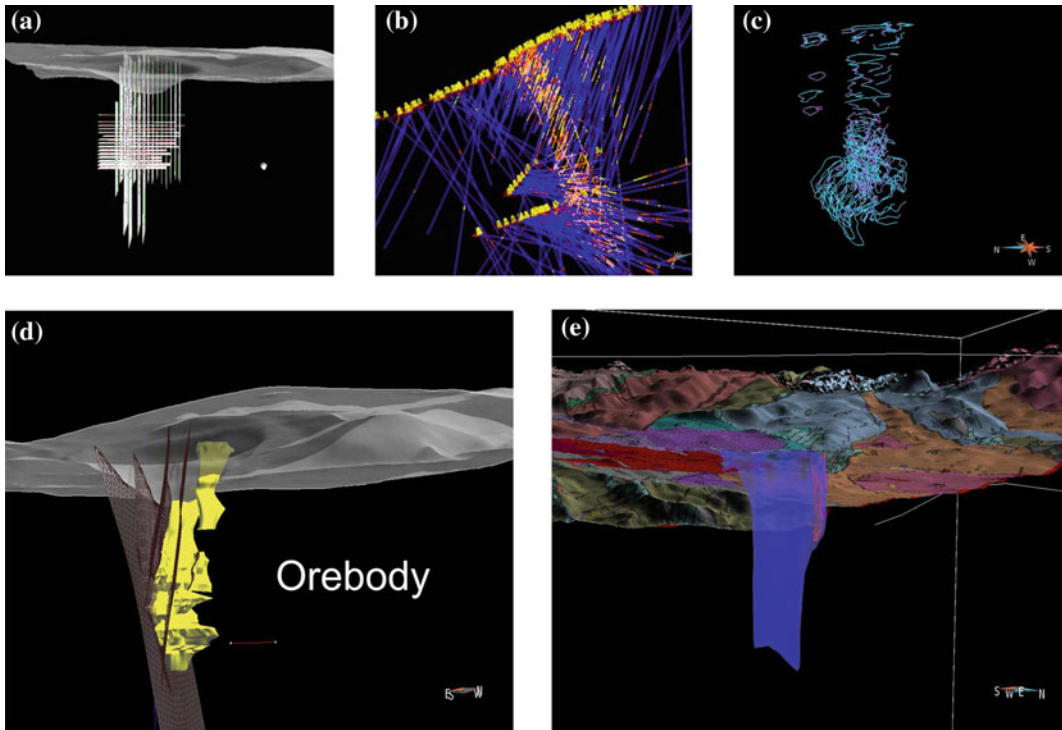


Fig. 12.10 **a** Profiles and levels supplied by Lundin Mining for the *Aguablanca* ore deposit. **b** Whole of drill-holes showing the mineralized sections, highlighted in red and yellow colours, it's possible to guess the ore body

shape. **c** Contour curves of the ore body generated in gOcad. **d** 3D model of the *Aguablanca* ore body. **e** Ore body within the *Aguablanca* stock

Fig. 12.11b. It was emplaced almost simultaneously with the 341 ± 3 Ma *Santa Olalla de Cala* (SOM) and 341 ± 2 Ma *Aguablanca* massifs (Romeo et al. 2006b, see Fig. 12.11c, d). This is consistent with the observed field relationships between the two intrusions. The next intrusive event corresponds to the emplacement of the *Teuler* granite at 339 ± 3 Ma (Romeo et al. 2006b), see Fig. 12.11e, and the final event was the intrusion of the *Helechoso* stock at 338 ± 4 Ma (Romeo et al. 2006b), see Fig. 12.11f and Table 12.5). It is evident that the intrusions were emplaced over a relatively short time range.

Although other ages are reported (see Table 12.5), we use these ages since they are more consistent with observed field relationships.

The *Santa Olalla de Cala* plutonic complex (SOC) as a whole is cut by a set of tardi-Variscan faults, of which the most important in the study area, is the *Zufre* fault. The *Zufre* fault is a

normal fault with a sinistral shear component that moved the northern block up, along with the *Aguablanca* mineralization.

Taking into account the interpretation of a strong seismic reflector (the so-called Iberian Reflector Body) by Simancas et al. (2003, 2004), the origin of the *Aguablanca* stock was interpreted by Tornos et al. (2006) as derived from a large mafic-ultramafic sill that intruded into the lower/middle crust in the OMZ during the Variscan orogeny. The development and emplacement of this large sill in the lower/middle crust, is considered to have occurred during a metamorphic event reaching sillimanite facies, probably related to subduction of a mid-ocean ridge beneath the OMZ. This ridge subduction would produce an increased heat-flow in the upper plate, eventually leading to the partial melting of the lithospheric mantle and the production of high-Mg magmas with boninite affinities, such as the *Aguablanca* stock.

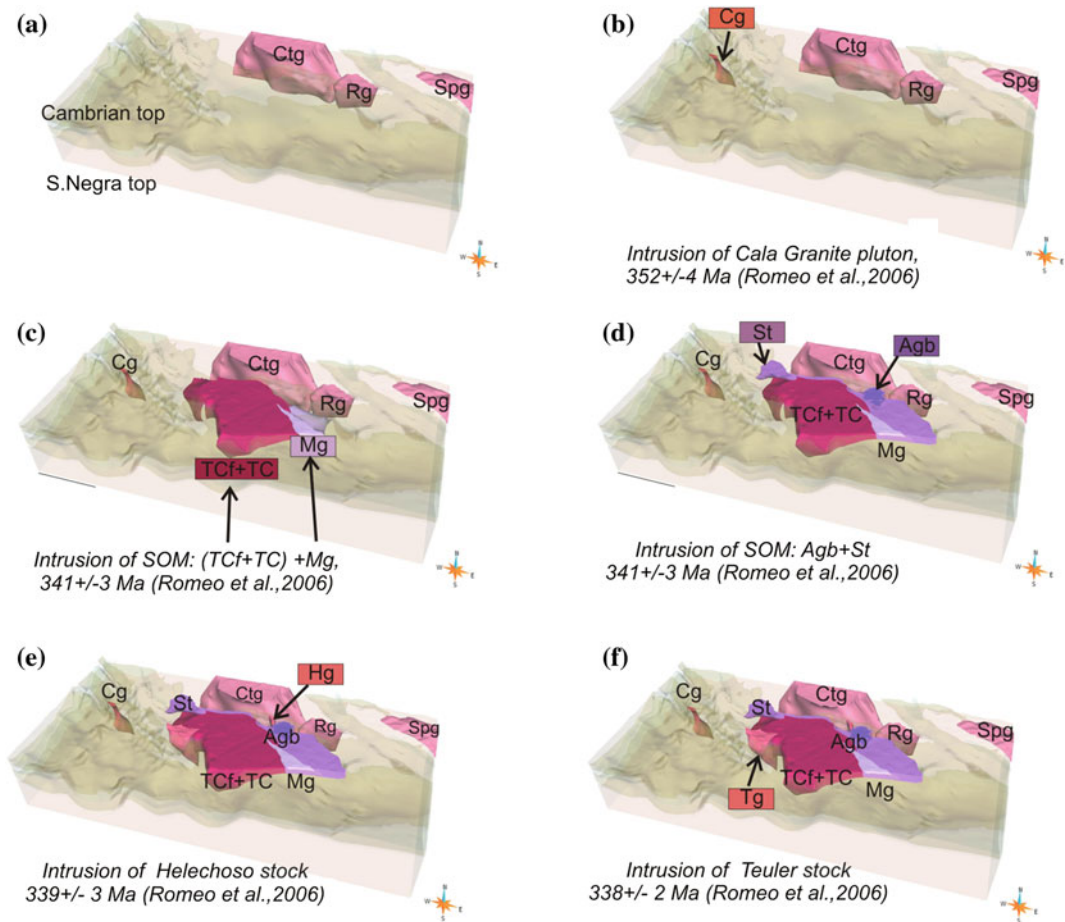


Fig. 12.11 4D evolution of the plutonic intrusions in Cala. Modelled plutons are represented with the same colours as in the geological map of Fig. 12.1

Table 12.5 Summary of published ages in the studied area

Pluton	SOM	Aguablanca	Helechos	Teuler	Cala	Granodiorite porphyry Cala mine
Romeo et al. (2006b), Romeo (2006)	341 \pm 3 TIMS,Zr	341 \pm 2 TIMS, Zr	338 \pm 4 TIMS,Zr	339 \pm 3 TIMS, Zr	352 \pm 4 TIMS,Zr	
Ordoñez-Casado et al. (2009)	347 \pm 3.4 SHRIMP, Zr	344 \pm 2.1 SHRIMP,Zr	–	–	–	
Spiering et al. (2005)	–	344 \pm 1.1 SHRIMP,Zr	–	–	–	
Carriedo and Tornos (2010)	–	–	–	–	342.2 \pm 4.2 SHRIMP,Zr	338 \pm 0.4 SHRIMP,Zr
Tornos et al. (2006)	–	338–334 Ma ^{40}Ar – ^{39}Ar , phlogopites	–	–	–	

12.4 Potential Resources Assessment

The *Ossa-Morena* Zone (OMZ) contains the largest number and widest variety of ore deposits and showings in the entire Iberian Massif. Their formation took place during two successive orogenic cycles (Cadomian and Variscan) and was linked to both rifting, stable platform and orogenic stages. Only those formed after the Cadomian orogeny are considered here, since no examples of the latter occur in the study area.

The most important mineral deposits related to inter orogenic stages mainly correspond to stratabound iron-oxide mineralizations associated with bimodal Cambrian rifting magmatism. The mineralization processes related to the Variscan orogeny were highly diverse and were conditioned by the transpressional deformation character of this part of the orogen and by its magmatic and tectono-thermal evolution. Among the Variscan mineral deposits, base metal bearing veins related with granitic plutons can be found. There are also iron oxide mineralizations related to skarns and replacement processes. Small massive sulphide deposits associated with igneous rocks are also present.

The main ore deposits in the studied area correspond to:

- (i) iron-rich deposits associated with skarn zones produced by the emplacement of Variscan plutons in metasediments of the Lower Cambrian Detrital-Carbonate Formation.
- (ii) Ni-(Cu-PGE), magmatic deposits hosted by Variscan mafic and ultramafic plutonic rocks.
- (iii) quartz-ankerite veins with Cu (Au-Bi), hosted by Variscan tonalites and Neoproterozoic and Lower Cambrian metasediments and metavolcanic rocks. This group of generally very small deposits has not been studied in the project.

The *Cala* ore deposits

The first group of deposits is represented in this area by the *Cala* and *Teuler* mines. The *Cala* mine is located close to the fault contact of a small granitic stock (*Cala* stock) with Cambrian carbonate rocks and skarn rocks developed at the contact. The iron mineralization occurs as two sub-vertical lenses, one in a garnet skarn, and other near the contact with the granites (Vázquez 1983; IGME 1975a, 1980). These lenses probably occupy dilatation structures associated with the main fault, and the ore consists of magnetite intergrown with actinolite and late pyrite and chalcopyrite (Tornos et al. 2004). According to data from Tornos et al. (2004), the Au content in copper concentrates is about 4 g/t, and major faults are regarded as conduits for fluids that caused the mineralization. Carriedo and Tornos (2010) suggested that the *Cala* ore deposit corresponds to a IOCG type mineralization.

Although the origin of the *Cala* mine skarn is not clear, the *Cala* granite pluton includes some magnetite skarn enclaves, so the *Cala* granite pluton is excluded as the cause of the skarn. Carriedo and Tornos (2010) interpreted the *Cala* mine skarn as produced by the intrusion of granodiorite porphyries, dated at 338 ± 0.4 Ma, which appear as small bodies in the mineralized zone. However, the age is younger than the age for the *Cala* granite, so these porphyries may not be related to the origin of the skarn.

Ore reserves of the *Cala* mine were estimated based on several sections, interpolating and extrapolating data provided by the Río Tinto Patiño and Andévalo Mining societies from the mineralized zones and other mineralized bodies.

Proven reserves are 22.96 Mt, probable reserves are 25.4 Mt and possible reserves are estimated at 13.3 Mt. The total mineral reserves thus amount to 61.7 Mt, with an average grade of 39 % Fe and 0.27 % Cu (IGME 1975a). These figures are lower than those provided by Carriedo and Tornos (2010), which provided a reserve estimation of about 90 Mt with 39 % Fe and 0.5 % Cu.

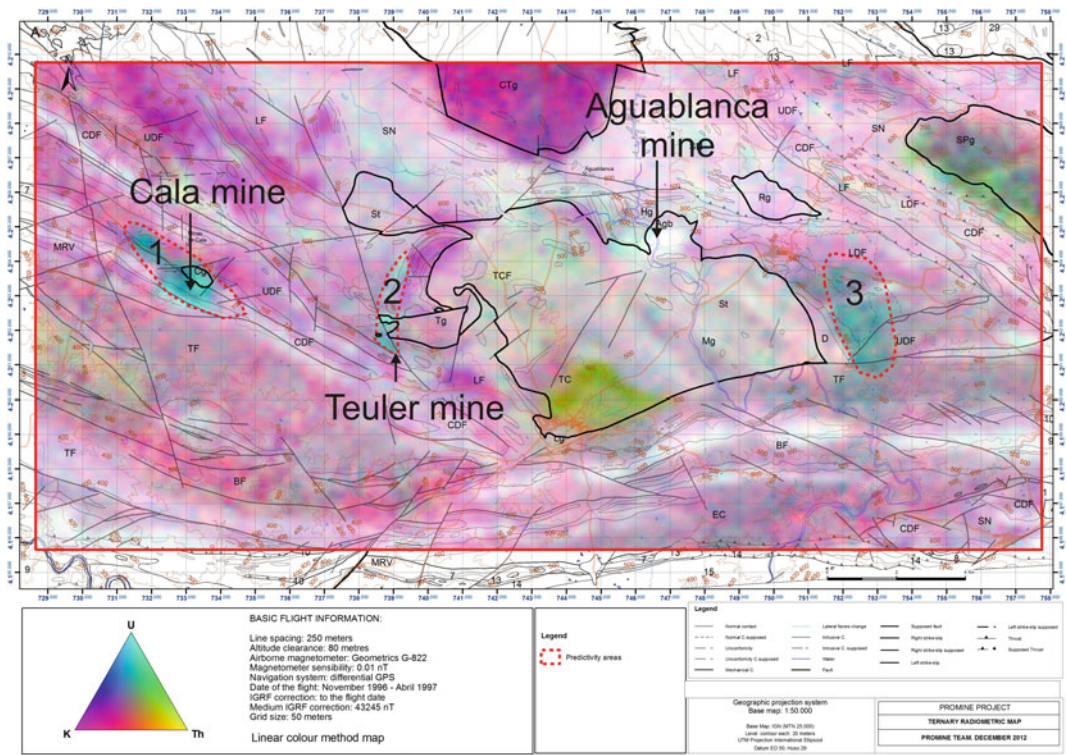


Fig. 12.12 Airborne radiometric ternary map of the Cala area (1996–97 flight). The three prospective areas are shown (dotted red figures)

The Aguablanca ore deposit

The Aguablanca Ni-Cu-(PGE) magmatic deposit is hosted by the Aguablanca stock. The proven and probable reserves are estimated at 15.7 Mt, grading 0.66 % Ni, 0.46 % Cu, 0.47 g/t PGE, and 0.13 g/t Au (Piña 2006). According to current data from the company operating the mine (Lundin Mining) the reserves are 6.0 Mt @ 0.6 % Ni, 0.5 % Cu.

The Aguablanca mineralization was discovered in 1993 by Presur-Atlantic Copper during a regional geochemical exploration program. This ore deposit was acquired by Río Narcea Gold Mines Ltd. in 2001 and is now owned by the Lundin Mining Company.

Three possible areas of mineral potential have been identified from studies for this project (Fig. 12.12). These areas have been determined by analysing the geophysical and geological data from the project, based on the presence of

U anomalies around the Teuler and Cala mines (areas 1 and 2 in Fig. 12.12) and in the eastern study zone (area 3 in Fig. 12.12). These anomalies have been checked and confirmed with in situ radiometric measurements, and clearly indicate possible extensions of the mineralized zones. They are possibly caused by hydrothermal activity associated with the intrusion processes.

Area 1 in Fig. 12.12, is trending in a N120°E direction extending ESE of the Cala Mine, and could contain mineralization associated with skarn zones not outcropping or hidden by tectonic structures such as the fault responsible for thrusting the Cala stock on top of the mineralization.

Area 2 in Fig. 12.12 is composed of metamorphic rocks that are strongly affected by contact metamorphism and there are several outcrops of skarn rocks to which positive gravimetric and magnetic anomalies are associated. These may be linked to the existence of magnetite and

sulphides. The area with the highest potential is located north of the *Teuler* mine.

Area 3 in Fig. 12.12 displays significant positive magnetic and uranium anomalies linked to the outcrops of siliciclastic rocks of the Detrital Lower Series (LDF) located near the eastern contact of the main pluton of *Santa Olalla de Cala*. All these U anomalies coincide with positive gravimetric and magnetic anomalies.

In all of three areas the potential for magnetite deposits related to replacement or skarn processes, and possible uranium enrichment is high.

12.5 Summary and Conclusions

A full revision of the geology of the *Cala* area has been carried out. Changes mainly affect the Cambrian units, which have been reviewed and described in terms of their stratigraphic and structural features. The geology and structure of the *Santa Olalla de Cala* intrusive complex and its environment has also been reviewed, and a new map of the complex is now available taking into account geophysical interpretation of potential field and radiometric surveys.

For 3D modelling we have followed a method based on an adequate selection of the surfaces to model (stratigraphic limits, faults and intrusions), and an exhaustive analysis and processing of the reviewed geological data within the gOcad environment, where surfaces are built by interpolation of the 3D data. This approach has demonstrated the usefulness of this type of software in the definition of the geometry of geological bodies.

An outstanding step of our methodological approach is the adjustment of geological cross-sections to fit potential field anomalies. Adequate processing of gravity data to obtain residual anomalies plays an important role because it greatly affects the outcome of the modelling. In our study, the intrusive bodies and geological cross-sections differ greatly from previous studies in the area (Romeo et al. 2006a, b, 2008). The

differences involve a major change in the volume and geometry at depth of the *Santa Olalla* Complex (SOC), showing a drastic decrease in the overall thickness of the body relative to the pre-existing model. New potential root zones have been identified within the massif. Conversely, major changes in the thickness and geometries initially proposed in the geological cross-sections were not required for adjustment of gravimetric and magnetic responses in the case of the metasedimentary successions.

It is worth pointing out that our work has fulfilled the most demanding rules of geophysical modelling: fully honouring the geological data and starting cross-sections, best processing practices, model properties based on petrophysical measurements and analysis, and the use of a profile mesh of adequate density with different directions providing a great number of intersections where profile consistencies are proven in a 3D environment.

The *Cala* Regional Model

No significant changes in the thickness or in the geometry of the metasedimentary units between the initial and the final models have been observed. The update of the surface geology induced significant changes in the overall obtained model geometry. New lithological units have been distinguished, which display different geophysical responses influencing the accuracy of the model as a whole. For example, migmatitic granites and the *Canteras* intrusive phase that have been differentiated within the SOC for the first time have a clear response on gravimetric, magnetic and radiometric maps. It has been shown that the effects of contact metamorphism induce significant changes in the magnetic properties of the materials involved. The 3D modelling of the studied area has revealed a tabular geometry of the *Santa Olalla Massif* with three possible root zones. One of them is located in the south and related to the *Zufre* fault, while the others are located in the northern boundary of the massif. These root zones may correspond to feeder zones of either the *Aguablanca* stock, that

displays a pipe-shaped architecture (Romeo et al. 2006a, 2008), or the *Santa Olalla Massif* itself.

The Cala mine

Even though the slag heaps have not been included in the modelling, the results of the inversion are good, with a RMS of 0.27 mGal (about 5 % of the total amplitude of the residual Bouguer anomaly). The volume of unit 9 (skarn and ore body) calculated from the final 3D model is about 43 Mm³. Using the density obtained from the inversion, 3.48 g/cm³ as a reference, the approximate weight for this unit is 150 Mt. From this quantity 60–75 Mt corresponds to the ore body. These values are in the range proposed by Tornos et al. (2004), who estimated a minimum resource of 90 Mt @ 39 % Fe and 0.27 % Cu and Carriedo et al. (2009) who reported 60 Mt @ 39 % Fe and 0.27 % Cu. The geometry obtained from the 3D gravity inversion shows that the ore body is affected by two sets of faults, and mineralization north of the 80°–90° striking faults could be expected, although located at a greater depth. The increase in density of the CDF and the UDF1 towards the SE, where the residual Bouguer anomaly displays relative maxima, suggests the possible occurrence of mineralization in this area as well. The most probable location would be next to the sinistral faults. The 3D local *Cala* Mine model locates the top of the *Cala* granitic stock closer to the surface than the regional model.

The Aguablanca ore-body model

The geometry of the resulting model is consistent with the geometry of detailed model of the Aguablanca stock developed by Romeo (2006), Romeo et al. (2006a, 2008). However, the geometry of the ore bodies obtained in the model appears not to be conditioned by any dominant fault direction at the level of emplacement.

As a general conclusion, 3D modelling has proved to be a powerful tool for the definition of shapes and volumes of complex ore bodies, which is useful for the evaluation work and

exploration of mineral deposits. As far as the predictivity of mineral resources (i.e. Fe) and processes of mineralization is concerned, the common assumption that deposits are related to major intrusions or shear zones and faults is currently under debate. One of the outputs of the project, after a detailed petrochemical analysis of different types of mineralizations, is that they show significant differences of composition (i.e. U contents). This fact establish a generic rule: Prospectivity areas are those close to igneous intrusions, or skarn zones affected by contact metamorphism, and displaying positive gravity and magnetic anomalies, in conjunction with high U signatures. Unfortunately, the intensity of anomalies is not a reliable indicator of the amount of reserves of unexplored ore bodies. As zones of high prospectivity for Fe (Cu) three areas have been identified: (1) one located to the north of *Teuler* massif and to the NW of the *Santa Olalla Massif*, (2) one is the extension towards the SE of the *Cala* mine, and (3) a third is located to the east of the town of El Real de la Jara.

Acknowledgments This study has been partly funded by the ProMine project “*Nano-particle products from new mineral resources in Europe*”, within the VIII Framework Programme for research (NMP-2008-4.0-5, contract 228559) and IGME (project N° 72.5.00.16.00). We thank the mining companies, Lundin and Presur for providing information and access to the mines. We gratefully acknowledge the positive comments by the reviewer Cecilio Quesada which have improved the paper. Thanks also go to A.L. Tate for revising the English text.

References

- Apalategui, O., Contreras, F., Eguiluz, L. 1990. Mapa Geológico de España a escala 1:50.000. Hoja 918 (Santa Olalla del Cala). I.G.M.E., Mapa geológico y memoria, pp 1-65.
- Apalategui, O., Sánchez-Carretero, R. (1991). Síntesis y correlación de unidades en el borde meridional de la Zona de Ossa-Morena (ZOM): Implicaciones geológicas. Bol. Geol. Min., 102, 339-347.
- Bates, M., García Lobón, J.L. 1998: Exploración aeromagnética y radiométrica de la Faja Pirítica y zonas limítrofes. Fondo documental del IGME Informe 40464. Madrid. http://www.igme.es/internet/sistemas_infor/Sid.htm
- Carriedo J., Tornos R., Velasco F., Terrón A. 2006: Mineralizaciones de magnetita asociadas a skarns y

- bandas de cizalla: La mina de *Cala* (Huelva). *Geogaceta*, 40, 235-238.
- Carriedo, J., Tornos, F., Velasco, F., Stein, H. 2007. Complex structural and hydrothermal evolution of the *Cala* magnetite deposit, SW Iberia – an IOCG deposit? In: Andrews et al. (eds.) *Digging Deeper*. Irish Association for Economic Geology, Dublin, v2, 1351-1354.
- Carriedo J., Chiaradia M., Tornos F. 2009. Extracción secuencial del Pb como método de datación directa de mineralizaciones: La Mina de *Cala* (Huelva). *Macla*, 9, 63-64.
- Carriedo, J., Tornos, F. 2010. The iron oxide, copper-gold belt of the *Ossa-Morena* Zone, southwest Iberia: implications for IOCG genetic models. In: Porter, T. M., (ed), *Hydrothermal Iron Oxide Copper-Gold and Related Deposits: A Global Perspective*, v.4.- *Advances in the Understanding of IOCG Deposits*; PGC Publishing, 441-460.
- Casquet, C., Eguiluz, L., Galindo, C., Tornos, F., Velasco, F. 1999. The *Aguablanca* Cu-Ni (PGE) intraplutonic ore deposit (Extremadura, Spain). Isotope (Sr, Nd, S) constraints on the source and evolution of magmas and sulfides. *Geogaceta*, 24, 71-74.
- Casquet, C., Galindo, C., Tornos, F., Velasco, F., Canales, A. 2001. The *Aguablanca* Cu-Ni ore deposit (Extremadura, Spain), a case of synorogenic orthomagmatic mineralization: age and isotope composition of magmas (Sr, Nd) and ore (S). *Ore Geology Reviews*, 18, 237-250.
- Chichorro, M., Pereira, M.F., Díaz-Azpiroz, M., Williams, I.S., Fernández, C., Pin, Ch., Silva, J.B., 2008. Cambrian ensialic rift-related magmatism in the *Ossa-Morena* zoe (Évora-Aracena metamorphic belt, SW Iberian Massif): Sm-Nd isotopes and SHRIMP zircon U-Th-Pb geochronology. *Tectonophysics*, 461, 91–113.
- Dallmeyer, R.D., Martínez García, E. 1990. Pre-Mesozoic geology of Iberia. *Springer-Verlag*, pp 1–410.
- Delgado, J.F.N. 1908. *Système Silurique du Portugal. Étude de stratigraphie paléontologique*. Mémoires de la Commission du Service Géologique du Portugal, Lisboa, pp 1- 245.
- Dupont, R., 1979. *Cadre géologique et métallogénèse des gisements de fer du sud de la province de Badajoz (Sierra Morena occidentale-Espagne)*. PhD Thesis, Institut National Polytechnique de Lorraine, France, pp 1-497.
- Eguiluz, L., Gil Ibaguchi, I., Abalos, B., Apraiz, A. 2000. Superposed Hercynian and Cadomian orogenic cycles in the *Ossa-Morena* zone and related areas of the Iberian Massif. *Geological Society of America Bulletin*, T112 (9), 1398-1413.
- García Lobón, J.L., Rey-Moral, C., Ayala, C. 2006. Comprehensive petrophysics of rocks from the Monesterio Antiform (*Ossa Morena* Zone, SW Spain). *Journal of Applied Geophysics* 59, 190– 204.
- García Lobón, J.L., Rubio, F.M.; Rey Moral, C.; Sánchez García, T.; Ayala Galán, C.; Mediato Arribas, J.; García Crespo J.; Bellido Mulas, F.; Martín Alfageme, S.; Martínez, C.; Tornos, F. 2014. Characterization of the Santa Olalla de *Cala* and *Cala* mine geological structures (Badajoz and Huelva, *Ossa Morena*, SW Spain) from gravity and magnetic data. *Serie de informes técnicos*. IGME, Madrid, pp 1-143.
- IGME, 1975a. Investigación de magnetitas en el área de *Cala* (Huelva). Programa sectorial de investigación de minerales de hierro. Reserva del S.O. de la península. Plan Nacional de Investigación Minera. Informe interno IGME, pp 1-80.
- IGME, 1975b. Investigación de magnetita en el área de *Teuler* (Huelva). Programa sectorial de investigación de minerales de hierro. Reserva del S.O. de la península. Plan Nacional de Investigación Minera. Informe interno IGME, pp 1-44.
- IGME, 1980. Depósitos minerales de España, Plan Nacional de Investigación Minera. Informe interno IGME, pp 1-75.
- Julivert, M., Fontboté, J.M., Ribeiro, A., Conde, L.N., 1974. Mapa Tectónico de la Península Ibérica, Baleares y Canarias. Instituto Geológico y Minero de España, pp 1-101.
- Linnemann, U., Pereira, M.F., Jeffries, T., Drost, K., Gerdes, A., 2008. Cadomian Orogeny and the opening of the Rheic Ocean: new insights in the diachrony of geotectonic processes constrained by LA-ICP-MS U-Pb zircon dating (*Ossa-Morena* and Saxo- Thuringian Zones, Iberian and Bohemian Massifs). *Tectonophysics* 461, 21–43.
- Liñán, E., Gozalo, R., Palacios, T., Gámez-Vintaned, J.A., Ugidos, J.M., Mayoral, E. 2002. Cambrian. In: Gibbons, W., Moreno, T. (eds.) *The Geology of Spain*. Geological Society, London, 17-29.
- Liñán, E., Perejón, A., Gozalo, R., Moreno-Eiris, E., & Oliveira, J.T. 2004. The Cambrian system in Iberia. *IGME, Cuadernos del Museo Geominero*, 3, 1-63.
- Montero, P., Salman, K., Bea, F., Azor, A., Expósito, L., González Lodeiro, F. Martínez-Poyatos, D., Simancas, J.F. 2000. New data on the geochronology of the *Ossa-Morena* zone, Iberian Massif. In: *Variscan-Appalachian dynamics: the building of the Upper Paleozoic basement*. *Basement Tectonic*, 15, A Coruña, Abstracts, 136-138.
- Nance, R.D., Gutiérrez-Alonso, G., Keppie, J.D., Linnemann, U., Murphy, J.B., Quesada, C., Strachan, R.A., Woodcock, N.H. 2010. Evolution of the Rheic Ocean. *Gondwana Research*, 17, 194-222.
- Ochsner, A. 1993. U-Pb Geochronology of the Upper Proterozoic–Lower Paleozoic geodynamic evolution in the *Ossa Morena* Zone (SW Iberia): Constraints on the timing of the Cadomian Orogeny. Ph. D. Thesis. Geology, Swiss Federal Institute of Technology Zurich, ETH, pp 1–249
- Ordóñez, B. 1998. Geochronological studies of the Pre-Mesozoic basement of the Iberian Massif: The *Ossa Morena* Zone and the Allochthonous Complexes within the Central Iberian Zone. Ph. D. Thesis. Geology, Swiss Federal Institute of Technology Zurich, ETH, pp 1–207.
- Ordoñez-Casado, B., Martín-Izard, A., García-Nieto, J. 2009. SHRIMP-zircon U-Pb dating of the Ni-Cu-

- PGE mineralized Aguablanca gabbro and Santa Olalla granodiorite: confirmation of an Early Carboniferous metallogenic epoch in the Variscan Massif of the Iberian Peninsula. *Ore Geology Reviews*, 34, 343-353.
- Ortega, L., Moreno, T., Lunar, R., Prichard, H., Sierra, J., Bomati, O., Fisher, P., García Palomero, F. 1999. Minerales del grupo del platino y fases asociadas en el depósito de Ni-Cu-EGP de *Aguablanca*, SO España. *Geogaceta*, 25, 155-158.
- Pereira, M.F., Quesada, C. 2006. Ediacaran to Viséan crustal growth processes in the Ossa Morena Zone (SW Iberia). *Publicaciones del Instituto Geológico y Minero de España*, Madrid, pp 1-120.
- Pereira, M.F., Chichorro, M., Williams, I.S., Silva, J.B., 2008. Zircon U-Pb geochronology of paragneisses and biotite granites from the SW Iberia Massif (Portugal): evidence for a paleogeographic link between the Ossa-Morena Ediacaran basins and the West African craton. In: Ennih, N., Liégeois, J.P. (Eds.), *The Boundaries of the West African Craton*. *Geol. Soc.*, 297. *Spec. Publ.*, London, 385-408.
- Pereira, M.F., Linnemann, U., Hofmann, M., Chichorro, M., Solá, A.R., Medina, J., Silva, J.B., 2012a. The provenance of Late Ediacaran and Early Ordovician siliciclastic rocks in the Southwest Central Iberian Zone: constraints from detrital zircon data on northern Gondwana margin evolution during the late Neoproterozoic. *Precamb. Res.* 192, 166-189.
- Prejón, A., Liñán, E., Quesada, C. 2004. Evolución paleozoica, Cambrico. En: *Geología de España* (J.A. Vera, Ed.), SGE-IGME, Madrid, 166-169.
- Piña, R., 2006. El yacimiento de Ni-Cu-EGP de Aguablanca (Badajoz): Caracterización y modelización metalogenética [Ph.D. thesis]: Universidad Complutense de Madrid, pp 1-254.
- Piña, R., Romeo, I., Ortega, L., Lunar, R., Capote, R., Gervilla, F., Tejero, R., Quesada, C. 2010. Origin and emplacement of the Aguablanca magmatic Ni-Cu-(PGE) sulfide deposit, SW Iberia: A multidisciplinary approach. *GSA Bulletin*, 122, 5/6, 915-925.
- Piçarra, J., Pereira, Z., Gutiérrez-Marco, J.C. 2011. Ordovician graptolites and acritarchs from the Barancos region (Ossa-Morena Zone, South Portugal). In: J.C. Gutiérrez-Marco, I. Rábano and D. García-Bellido (eds.), *Ordovician of the World*. Cuadernos del Museo Geominero, 14. Instituto Geológico y Minero de España, Madrid, 429-439.
- Quesada, C., 1990a. Precambrian terranes in the Iberian Variscan Foldbelt. In: Strachan, R.A., Taylor, G.K. (Eds.), *Avalonian and Cadomian Geology of the North Atlantic*. Blackie, New York, 109-133.
- Quesada, C., 1990b. Precambrian successions in SW Iberia: their relationship to "Cadomian" orogenic events. In: D'Lemos, R.S., Strachan, R.A., Topley, C. G. (Eds.), *The Cadomian Orogeny*. *Geol. Soc.*, 51. *Spec Publ.*, London, 353-362.
- Quesada, C. 1991. Geological constraints on the Paleozoic tectonic evolution of tectonostratigraphic terranes in the Iberian Massif. *Tectonophysics*, 185: 225-245.
- Quesada, C. 1992. Evolución tectónica del Macizo Ibérico: Una historia de crecimiento por acreencia sucesiva de terrenos durante el Proterozoico superior y el Paleozoico. In: Gutiérrez Marco, J.C., Saavedra, J., Rábano, I. (eds.), *Paleozoico inferior de Ibero-América*. University of Extremadura, Mérida, 173-190.
- Quesada, C., 1997. Evolución geodinámica de la Zona de Ossa-Morena durante el ciclo Cadomiense. In: Araújo, A., Pereira, M.F. (Eds.), *Estudios sobre a geología da Zona de Ossa-Morena (Maciço Ibérico)*. Universidade de Évora, 205-230.
- Quesada, C., 2006. The Ossa-Morena zone of the Iberian Massif: a tectonostratigraphic approach to its evolution. *Z. Deuts. Gesell. Geowiss.* 157, 585-595.
- Quesada, C., Bellido, F., Dallmeyer, R.D., Gil Ibarguchi, J.I., Oliveira, J.T., Pérez Estaún, A., Ribeiro, A., Robardet, M., Silva, J.B. 1991. Terranes within the Iberian Massif: correlations with West African sequences. In: Dallmeyer, R.D., Lecorché, J. P. (eds.), *The West African orogens and Circum-Atlantic correlations*. Springer-Verlag, Berlin, 267-294.
- Quesada, C., Sánchez-García, T. 2002. Cartografía geológica continua de la Zona Ossa-Morena, Escala 1:50.000. Instituto Geológico y Minero de España.
- Robardet, M., Gutiérrez-Marco, J. C. (1990): Ossa-Morena Zone, Stratigraphy, Passive Margin Phase (Ordovician - Silurian - Devonian). In: R. D. Dallmeyer, E. Martínez García (eds.) *Pre-Mesozoic Geology of Iberia*, Springer-Verlag, Berlin, 267-272.
- Robardet, M. and Gutiérrez-Marco, J.C. 2004. The Ordovician, Silurian and Devonian sedimentary rocks of the Ossa-Morena Zone (SW Iberian Peninsula, Spain). *Journal of Iberian Geology*, 30, 73-92.
- Robardet, M., Piçarra, J.M., Štorch, P., Gutiérrez-Marco, J.C. and Sarmiento, G.N. 1998. Ordovician and Silurian stratigraphy and faunas (graptolites and conodonts) in the Ossa Morena Zone of the SW Iberian Peninsula (Portugal and Spain). *ITGE, Temas Geológico-Mineros*, 23, 289-318.
- Romeo, I. 2006. Estudio estructural, gravimétrico y geocronológico del Complejo ígneo de *Santa Olalla* (SO de la península Ibérica): Marco tectónico del Yacimiento de Ni-Cu-(EGP) de *Aguablanca*. Thesis. Univ. Complutense de Madrid, pp 1-248.
- Romeo, I., Capote, R., Tejero, R., Lunar, R., Quesada, C. 2006a. Magma emplacement in transpression: the *Santa Olalla* Igneous Complex (Ossa-Morena Zone, SW Iberia). *Journal of Structural Geology* 28, 1821-1834.
- Romeo, I., Lunar, R., Capote, R., Quesada, C., Dunning, G.R., Piña, R., Ortega, L. 2006b. U-Pb age constraints on Variscan magmatism and Ni-Cu-PGE metallogeny in the Ossa-Morena Zone (SW Iberia) *Journal of the Geological Society*, London, 163/ 5, 837-846.
- Romeo, I., Tejero, R., Capote, R., Lunar, R. 2008. 3D gravity modelling of the *Aguablanca* Stock, tectonic control and emplacement of a Variscan gabbro-norite

- bearing a Ni-Cu-PGE ore, SW Iberia. *Geological Magazine*, 145, 3, 345-359.
- Schäfer, H.J., 1990. Geochronological investigations in the Ossa Morena Zone, SW Spain. Ph. D. Thesis. Geology, Swiss Federal Institute of Technology Zurich, ETH, pp 1-153.
- Salman, K. 2004. The timing of the Cadomian and Variscan cycles in the Ossa Morena Zone, SW Iberia: granitic magmatism from subduction to extension. *Journal Iberian Geology*, 30, 119-132.
- Sánchez-García, T., Bellido, F., Quesada, C. 2003. Geodynamic setting and geochemical signatures of Cambrian-Ordovician rift-related igneous rocks (*Ossa-Morena Zone*, SW Iberia). *Tectonophysics*, 365, 233-255.
- Sánchez-García, T., Quesada, C., Bellido, F., Dunning, G., González de Tanago, J. 2008. Two-step magma flooding of the upper crust during rifting: The Early Paleozoic of the *Ossa-Morena Zone* (SW Iberia). *Tectonophysics*, 461, 72-90.
- Sánchez-García, T., Bellido, F., Pereira, M.F., Chichorro, M., Quesada, C., Pin, C., Silva, J.B., 2010. Rift-related volcanism predating the birth of the Rheic Ocean (*Ossa-Morena zone*, SW Iberia). *Gondwana Res.* 17, 392-407.
- Sánchez-García, T., Quesada, C., Bellido, F. Dunning, G. R., Pin, Ch., Moreno-Eiris, E., Perejón, A., 2014. Age and correlation of the Loma del Aire Unit, *Ossa-Morena Zone*, SW Iberia. *Gondwana 15*, Conference abstracts, 157.
- Sánchez-Jiménez, N. 2003. Estructura gravimétrica y magnética de la corteza del suroeste peninsular (Zona Surportuguesa y Zona de *Ossa-Morena*). Unpublished Ph.D. Thesis, Complutense University of Madrid., pp 1-243.
- San José, M.a.A. de, Herranz, P., Pieren, A.P. 2004. A review of the *Ossa-Morena Zone* and its limits. Implications for the definition of the Lusitan-Marianic Zone. *Journal of Iberian Geology*, 30, 7-22.
- SIGECO. Geological Information System, Geophysical database [on line] 2014. IGME. Editor: J. Navas. Available in: <http://cuarzo.igme.es/sigeco/default.htm>.
- Simancas, J.F., Carbonell, R., González Lodeiro, F., Pérez Estaún, A., Juhlin, C., Ayarza, P., Kashubin, A., Azor, A., Martínez Poyatos, D., Almodóvar, G.R., Pascual, E., R. Sáez, R., Expósito, I. 2003. Crustal structure of the transpressional Variscan orogen of SW Iberia: SW Iberia deep seismic reflection profile (IBERSEIS). *Tectonics*, 22, 1962-1974.
- Simancas, J.F., Carbonell, R., González Lodeiro, F., Pérez Estaún, A., Juhlin, C., Ayarza, P., Azor, A., Martínez Poyatos, D., Almodóvar, G.R., Pascual, E., Sáez, R., Kashubin, A., Alonso, F., Álvarez Marrón, J., Bohoyo, F., Castillo, S., Donaire, T., Expósito, I., Flecha, I., Galadí, E., Galindo Zaldívar, J., González, F., González Cuadra, P., Macías, I., Martí, D., Martín, A., Martín Parra, L.M., Nieto, J.M., Palm, H., Ruano, P., Ruiz, M., Toscano, M. 2004. The Seismic Crustal Structure of the *Ossa-Morena Zone* and its geological interpretation. *Journal of Iberian Geology*, 30, 133-142.
- Spiering, E.D., Rodríguez Pevida, L., Castelo, J.M., García Nieto, J., Martínez, C. 2005. *Aguablanca* : a new nickel mine in a potential new Ni/Cu and IOCG belt of southern Spain and Portugal. *Proceedings Geological Society Nevada. Symposium 2005*.
- Talwani, M., Heirtzler, J. R. 1964. Computation of magnetic anomalies caused by two dimensional bodies of arbitrary shape. In Parks, G. A. (Ed.), *Computers in the mineral industries, Part 1: Stanford University Publications, Geological Sciences* 9, 464-480.
- Talwani, M., Worzel, J. L., Landisman, M. 1959. Rapid gravity computations for two dimensional bodies with application to the Mendocino submarine fracture zone: *Journal of Geophysical Research* 64, 49-59.
- Tornos, F., Casquet, C., Galindo, C., Canales, A., Velasco, F. 1999. The genesis of the Variscan ultramafic-hosted magmatic Cu-Ni deposit of *Aguablanca*, SW Spain. In: Stanley et al. (eds), *Mineral deposits: processes to processing*. Balkema, Rotterdam, 795-798.
- Tornos, F., Galindo, C., Casquet, C., Rodríguez Pevida, L., Martínez, C., Martínez, E., Velasco, F., Iriondo, I. 2006. The *Aguablanca* Ni-(Cu) sulfide deposit, SW Spain: geologic and geochemical controls and the relationship with a midcrustal layered mafic complex. *Mineralium Deposita*, 41, 737-769.
- Tornos F, Inverno C, Casquet C, Mateus A, Ortiz G, Oliveira V. 2004. The metallogenic evolution of the *Ossa Morena Zone*. *J. Iber. Geol* 30,143-180.
- Vázquez, F. 1983. Depósitos minerales de España, *Temas geológico mineros*, IGME, Servicio de Publicaciones. pp 1-154.
- Vázquez, F., Arteaga, R., Schermerhorn, J.J. 1980. Depósitos minerales del SO de la Península Ibérica. *Boletín Geológico y Minero*, 91-2, 293-342.
- Won, I.J. , Bevis, M. 1987. Computing the gravitational and magnetic anomalies due to a polygon: Algorithms and Fortran subroutines: *Geophysics* 52, 232-238.

Part V
The Hellenic Belt

N. Arvanitidis, C. Michael, C. Christidis, G. Perantonis,
V. Bakalis and D. Ballas

Abstract

The updating of the Greek mineral deposit database and the available geological, geophysical and geochemical layers were used to construct 3- and 4-dimensional models of the most important Greek deposit groups that are located in Hellenic belt. Combining the different thematic layers of the GIS, different predictive maps were produced for specific types of ore deposits and specific commodities. The 3 and 4D geological models were produced for major epithermal gold deposits in the Rhodope zone (Perama and Aghios Demetrios) and the main sulphide mineral deposits (Olympias, Madem Lakkos/Mavres Petres and Skouries) in the Serbomacedonian zone, northern Greece. The 3D models were constructed in three different scales; deposit, semi-regional and regional. The 4D models demonstrate the main stages of the development of epithermal gold and polymetallic replacement deposits. The 3D models were built in gOcad and Gemcom Gems and the 4D models were built in gOcad and Midland Valleys MOVE.

13.1 Introduction

The geology of Greece is favourable and shows good potential for mineral resources. Among the non-energy metallic minerals, base and precious metals, in particular zinc, lead, copper, gold, and

silver are becoming an increasingly important and rapidly growing target for the mining industry. In the north-eastern part of Greece, where most of the potential resources and feasible deposits are hosted, polymetallic gold deposits occur in a wide range of genetic types, comprising magmatic porphyry copper type deposits, hypothermal/mesothermal manto-type polymetallic sulphides and epithermal gold systems (Arvanitidis 2010).

The use of 3D geomodelling has an increasingly important role in integrating and analyzing geoscientific information to make it easier to present and understand, and to develop more

N. Arvanitidis (✉) · C. Michael · C. Christidis
Greek Institute of Geology and Mineral Exploration,
Athens, Greece
e-mail: nikolaos.arvanitidis@sgu.se

G. Perantonis · V. Bakalis · D. Ballas
Hellas Gold S.A., Stratonis, Greece

efficient exploration tools. It opens up the possibility to co-interpret the available information and to compare heterogeneous data within a modelling platform. This multidisciplinary approach allows the comparison between the relationships and probably genetic links between faults, lithologies, alteration zones, metal distribution patterns, and ranges in grades, as well as geochemical and geophysical anomalies. The use of 3D modelling tools highlights the widening gap between hardcopy maps (2D) and interactive multimedia environments for communicating geoscientific information and concepts.

In the Greek study areas, the 3D models not only contribute to ore feasibility evaluation, which is a key factor in the mining industry, but also enables better understanding of the mineralizing processes that led to the ore formation, and assists in the exploration of new deposits as well as the expansion of known mining areas and mineral belts.

The 3D models are very useful tools for improving the knowledge of the ore deposition and conduct an efficient and successful mineral exploration for locating deep-seated mineralization. Given the multi-disciplinarity of the existing data and the advanced IT capabilities it is realistic to further develop 3D into 4D models when the time parameter is combined and added. This will make the exploration more sustainable by determine additional potential areas and discover new exploitable deposits with the same or different resource characteristics.

The following districts have been studied (Fig. 13.1):

- (a) Eastern Chalkidiki peninsula in northern Greece hosting polymetallic replacement deposits (Olympias, Madem Lakkos, Mavres Petres) and porphyry copper deposit (Skouries)
- (b) Western Thrace hosting epithermal gold deposits (Perama and Aghios Demetrios deposits)

The following geomodels have been constructed:

- Deposit scale 3D geomodels of Olympias, Mavres Petres, Skouries, Piavitsa, Perama Hill, Aghios Demetrios
- Semi-regional scale 3D geomodels of the North-Eastern Chalkidiki peninsula and Western Thrace districts
- A regional scale model of the Hellenic-Balkan belt

13.2 Geological Setting

13.2.1 The Hellenic-Balkan Belt

The Hellenic-Balkan metallogenic belt was formed along the southern margin of the Eurasian plate during Mesozoic-Cenozoic time. Modern structural data indicate that the Rhodope and Serbo-Macedonian massifs (Jones et al. 1992; Dinter and Royden 1993) are products of Alpine convergence between Africa and Europe during Cretaceous to Tertiary time, which led to the formation of a metamorphic core complex and silicic to intermediate magmatism (Burchfiel 1980; Ivanov 1989; Burg et al. 1990, 1995, 1996; Jones et al. 1992; Ricou et al. 1998; Lips et al. 2000).

In the Rhodope massif the Alpine convergence resulted in a north-dipping subduction zone, which gave rise to Late Cretaceous calc-alkaline magmatism with related porphyry Cu-Au and high sulphidation epithermal Au-Cu mineralization in the Srednogorie zone in Bulgaria (Moritz et al. 2003; Von Quadt et al. 2003). During the Tertiary, plate convergence moved southward. Throughout the Rhodope massif, the latest stages of extension are indicated by the development of late Eocene to Oligocene sedimentary basins followed up by late Eocene to Oligocene—early Miocene calc-alkaline to shoshonitic volcanic-plutonic suites. The resulting arc extends across the Greek-Bulgarian border hosting epithermal gold systems of high exploration and exploitation potential. The deposits were formed during the post-collisional orogenic collapse and related crustal extension (Marchev et al. 2005).

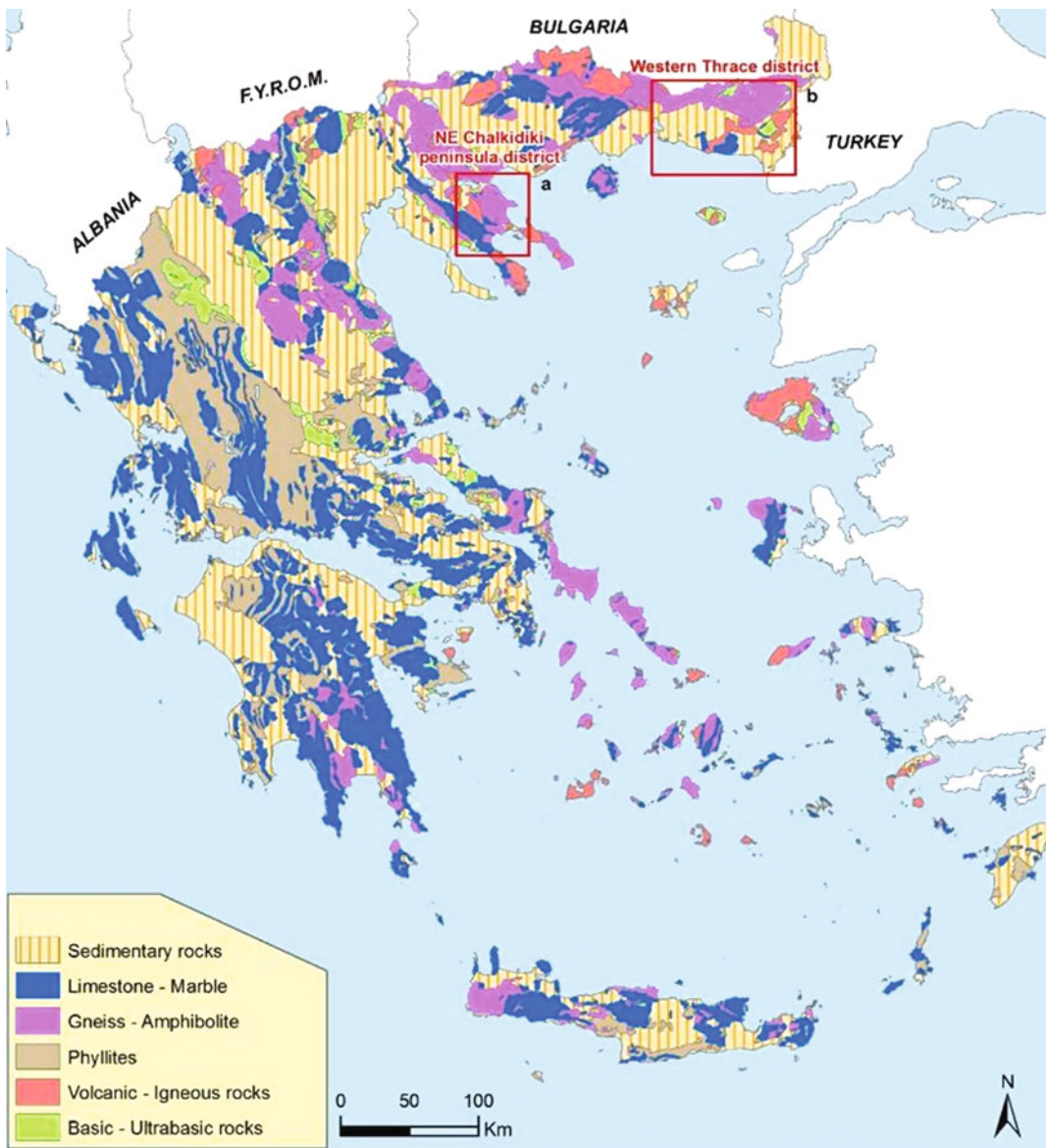


Fig. 13.1 The study area of **a** the Eastern Chalkidiki peninsula and **b** the Western Thrace region

13.2.2 Eastern Chalkidiki Peninsula (Serbomacedonian Zone)

The Serbomacedonian zone consists of gneisses, mica schists, amphibolites and marbles that are part of two major lithostratigraphic units of Paleozoic age, known as the Kerdylia and

Vertiskos formations (Fig. 13.2). The Olympias, Madem Lakkos and Mavres Petres manto-type polymetallic sulphide deposits belong geotectonically to the Kerdylia formation whereas the Skouries porphyry copper-gold deposit is part of the Vertiskos formation.

The Kerdylia formation to the east comprises biotite gneiss interbedded with hornblende

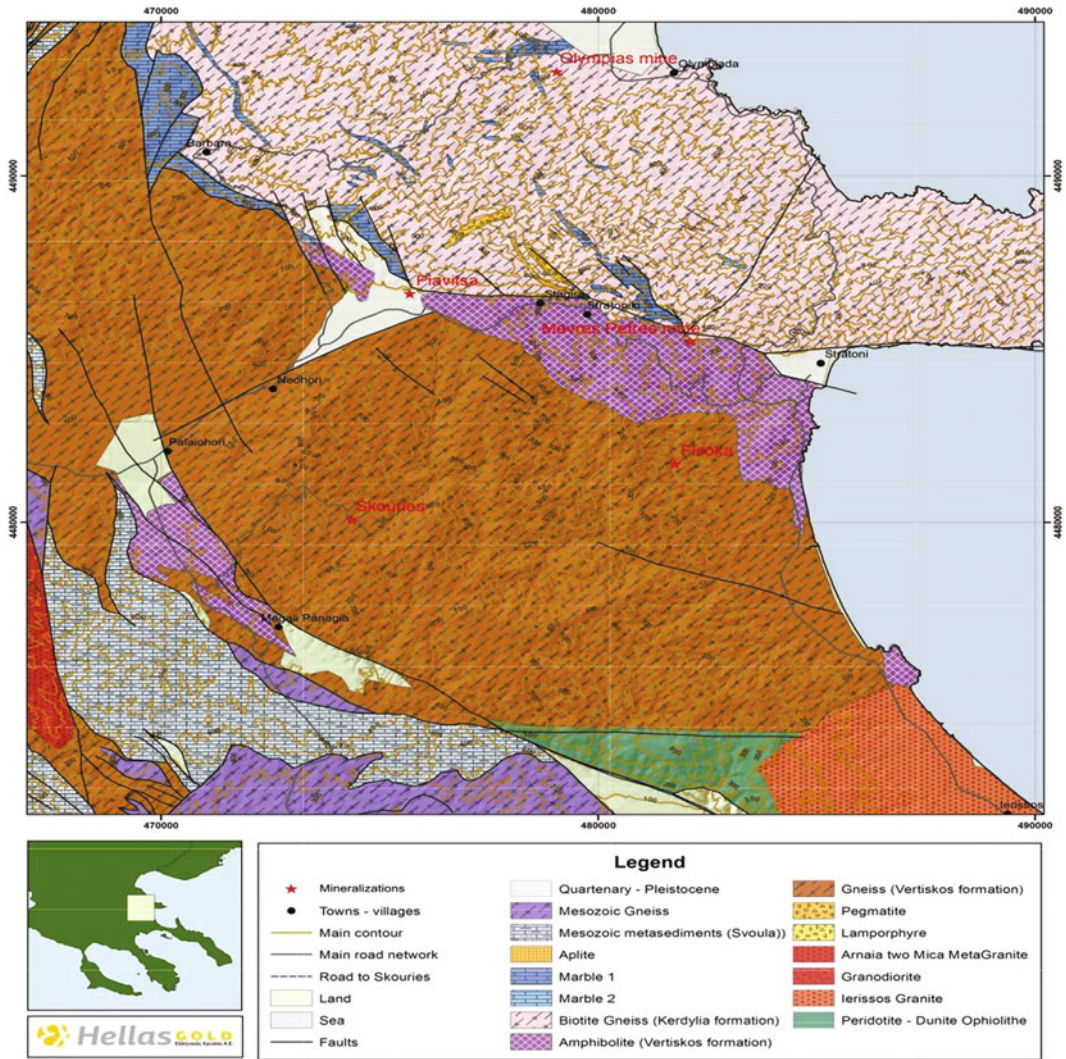


Fig. 13.2 Geological map of Eastern Chalkidiki peninsula

gneiss, amphibolite and marble, probably derived from an original volcano-sedimentary sequence (Kockel et al. 1971).

The Vertiskos formation to the west overlying the Kerdyllia formation consists mainly of two-mica gneiss, in places containing garnet-, tourmaline- and sillimanite-bearing quartz-feldspar gneiss and ortho-amphibolite. Metamorphosed mafic and ultramafic rocks occur frequently near the contact with the Kerdyllia formation. Rare marbles are considered to be tectonically emplaced slices of Mesozoic carbonate rocks (Arvanitidis 1993). The contact between the Kerdyllia and Vertiskos

formations is partly gradational, but largely deformed and displaced by the major Stratoni-Varvara fault zone.

13.2.3 Western Thrace (Rhodope Zone)

The Rhodope zone in Thrace comprises complex metamorphic rocks of inferred Paleozoic age, such as gneisses and amphibolites, structurally overlain by lower grade metamorphic sequences belonging to the Mesozoic Circum-Rhodope zone. This

zone consists of metasedimentary and meta-volcanosedimentary series (Pomoni-Papaioannou and Papadopoulos 1986). The underlying metasedimentary series comprises carbonate rocks (calc-schist, marble, dolomitic marble) and the overlying meta-volcanosedimentary series consists predominantly of greenschists (chlorite-epidote-talc-actinolite bearing). The Circum Rhodope zone has been folded, metamorphosed and thrust onto Rhodope metamorphic basement during Alpine orogenesis in late Cretaceous time.

The epithermal gold deposits in the Thrace region are related to the post-collisional extension during late Eocene–Oligocene. A number of structurally controlled rift-basins along the southern and eastern margins of the Rhodope zone were formed during this crustal extension. The basins are characterized by deposition of Early Eocene sediments (molasses, limestones) followed by late-Eocene–early Oligocene volcanosedimentary series with calc-alkaline to

shoshonitic volcanic rocks (Innocenti et al. 1980; Fytikas et al. 1980) (Fig. 13.3). The Saint Demetrios and Perama Hill deposits are related to Oligocene volcanic arc magmatism. This arc extends across the Greek-Bulgarian border hosting epithermal systems of high exploration and exploitation potential.

13.3 Datasets and Methods Used to Build the 3D Models

Local, semi-regional and regional scale of 3D and 4D models were constructed for the majority of the above mentioned deposit types and areas and new metallogenic interpretations and exploration potential were defined. The models constructed combining geology, structural setting, stratigraphy, tectonic evolution, ore bodies

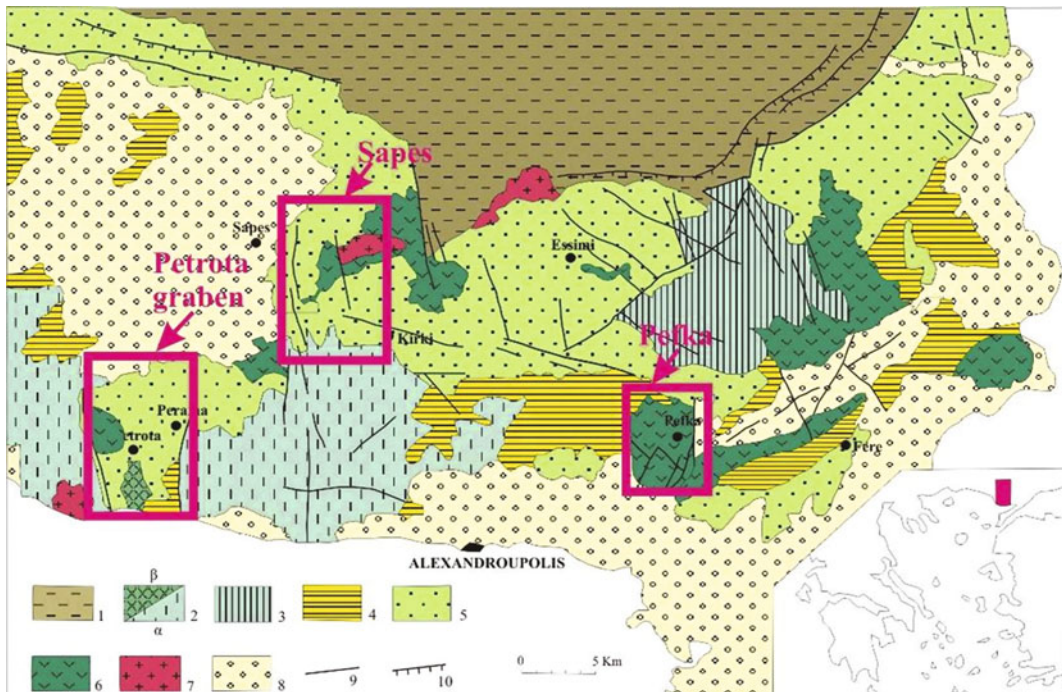


Fig. 13.3 Geological sketch map of Western Thrace (Papadopoulos P. modified by Michael C.). 1 Rhodopian basement, 2 Circum-Rhodope zone—Makri unit (upper Triassic—upper Jurassic age), α . Phyllite series, β . Mafic rocks (gabbro-diorites), 3 Circum-Rhodope zone—Melia

unit (Lower Cretaceous—upper Cretaceous age), Flysch—ophiolite, 4 Eocene sedimentary deposits, 5 Eocene—Oligocene volcano-sedimentary deposits, 6 Oligocene volcanics, 7 Oligocene intrusive rocks, 8 Neogene and Quaternary sediments, 9 Faults, 10 Overthrust

geometry, alteration zones, ore grades and the genetic links between the spatially related porphyry and manto systems. Also, the construction was based on airborne geophysics, along with further interpretations for across border regional exploration potential.

Information and data used for 3D modelling included:

- Aeromagnetic data
- Semi-regional strategic geochemical surveys
- Geological and structural data
- Geological cross sections
- Soil geochemical data
- Ground geophysical surveys
- Down-hole surveys and drill hole logs providing information on
 - Wallrock lithology and geochemistry
 - Alteration zones
 - Metal distribution (drill hole mineralization intersections)
 - Structural data

13.4 3D Models

13.4.1 The Olympias Manto-Type Polymetallic Deposit (Deposit Scale Model)

The Olympias deposit is a polymetallic (Pb, Zn, Ag, Au) massive sulphide replacement ore body hosted by Kerdyllia marbles. The depositional mechanism and structural setting of the ore bodies are genetically related to fault-controlled mineralizing fluids ascending and interacting with reactive carbonate rocks interbedded within crystalline basement of the Kerdyllia formation (Fig. 13.3; Kalogeropoulos et al. 1989).

Two main deposits have been identified, the West and East deposits. The West deposit is the largest and is approximately 250 m wide and plunges along strike 1200 m to the southeast. Its thickness varies between 5 and 15 m. Previous operators left behind gold-rich pockets, as well as additional resources. The East deposit lies

approximately 150 m east of the West deposit and has an average width of 75 m and an average thickness of 7 m.

The 3D model created shows the structure of the deposit and the fault-controlled setting of the ore-bodies, as well as the stratabound replacement mantos at the contact and inside the marbles (Figs. 13.4 and 13.5). A deeper-seated extension of the west ore body is indicated and makes a potential target to further underground surveys and exploration drilling.

13.4.2 Madem Lakkos and Mavres Petres Polymetallic Replacement Deposits (Deposit Scale Model)

Madem Lakkos and Mavres Petres are, like Olympias massive stratabound replacement deposits hosted by Kerdyllia formation marbles and developed along cross-cutting fault zones. The geological setting comprises also the major Stratoni-Varvara thrust fault bringing the Kerdyllia marble interbedded, biotite gneiss and Vertiskos amphibolite in contact tectonically. The E-W trending Stratoni-Varvara fault also displays a semi-regional control on the extension of the polymetallic mineralization and the location of the Madem Lakkos, Mavres Petres, Piavitsa and Varvara ore deposits (Fig. 13.2).

The Mavres Petres ore body was modelled in 3D (Fig. 13.6a), with respect to intersecting fault zones (Fig. 13.7), the overall geological setting (Fig. 13.6b), the geology (Fig. 13.8) and the distribution of metal grades (Fig. 13.9).

During the creation of the model, a considerable amount of knowledge concerning the mineralized area and the ore body was obtained. Some unknown N-S-striking and cross-cutting fault structures were interpreted, but further investigations are required to determine their metallogenetic implications. This could be a target for 4D modelling, in order to outline the geological evolution of all deformation stages, focusing on the interrelations between the E-W trending Stratoni-Varvara fault and the

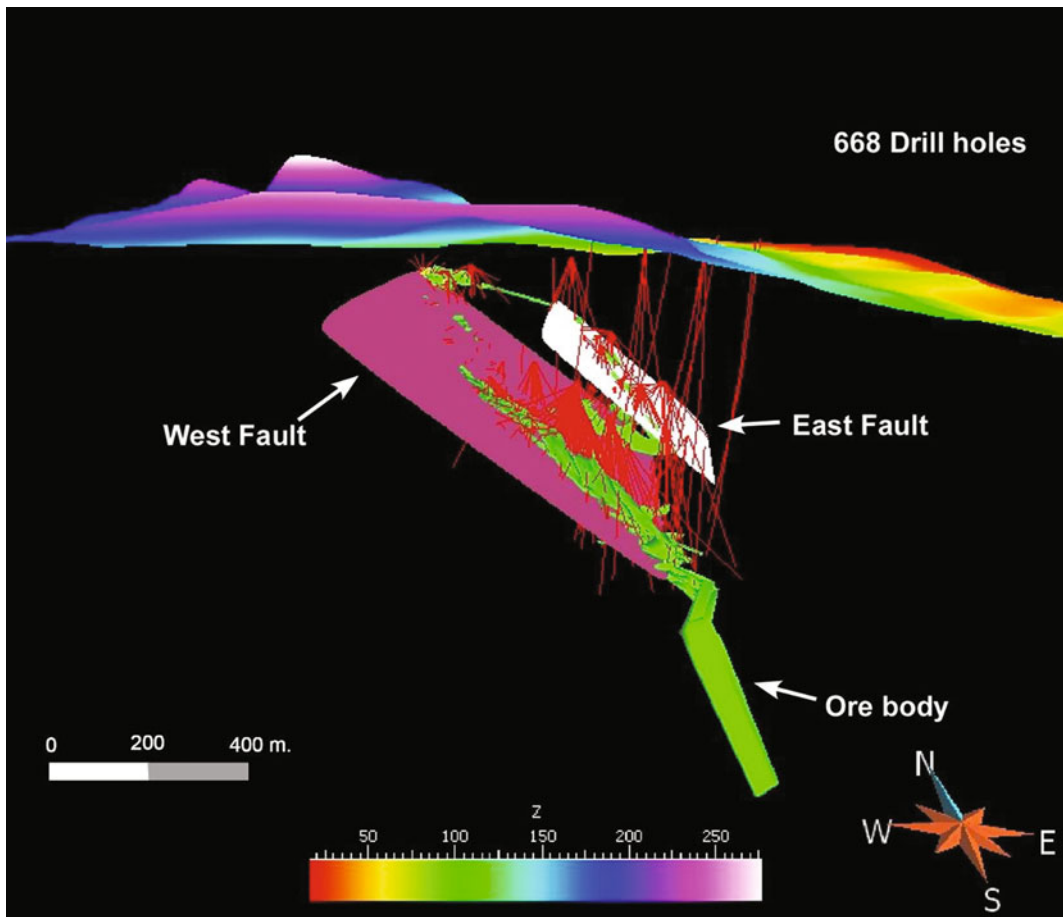


Fig. 13.4 3D visualization of the Olympias ore deposit (Screenshot from gOcad). Z elevation

cross-cutting S-N faults, and their relationships with mineralization. The preliminary model displayed in Fig. 13.7 is a first step to meet these objectives (Adeline 2010).

There are 3 deformation stages: (1) The upper Paleozoic orogenic period. Radiocarbon dating indicates an Erkyanian age at 300 Ma. During this deformation isoclinal folds, with fold axis striking and dipping to the north were formed, (2) The Alpine orogeny between Upper Jurassic and Lower Cretaceous formed a second phase of folding that created sub-isoclinal folds and (3) Upper Cretaceous and Oligocene imbrications, local and large scale thrusts, as well as geological inversion.

The in situ reserve estimation of the Mavres Petres ore provided a 3D mining model as a useful tool for improving the knowledge of the area. Sampling and analysis were extended in three dimensions with 45 m horizontal and 10 m vertical intervals. More than 50 % of the grades vary at a small scale with a high nugget effect (Fig. 13.9). Grades are log-normally distributed leading to direct proportional effects (variability depends on metal content) (Adeline 2010). Therefore variable on grades production should be expected. The in situ reserves using kriging shows that the Mavres Petres deposit contains more than 1 Mt of mineable ore with 5.5 % Pb, 5.4 % Zn and 180 ppm Ag.

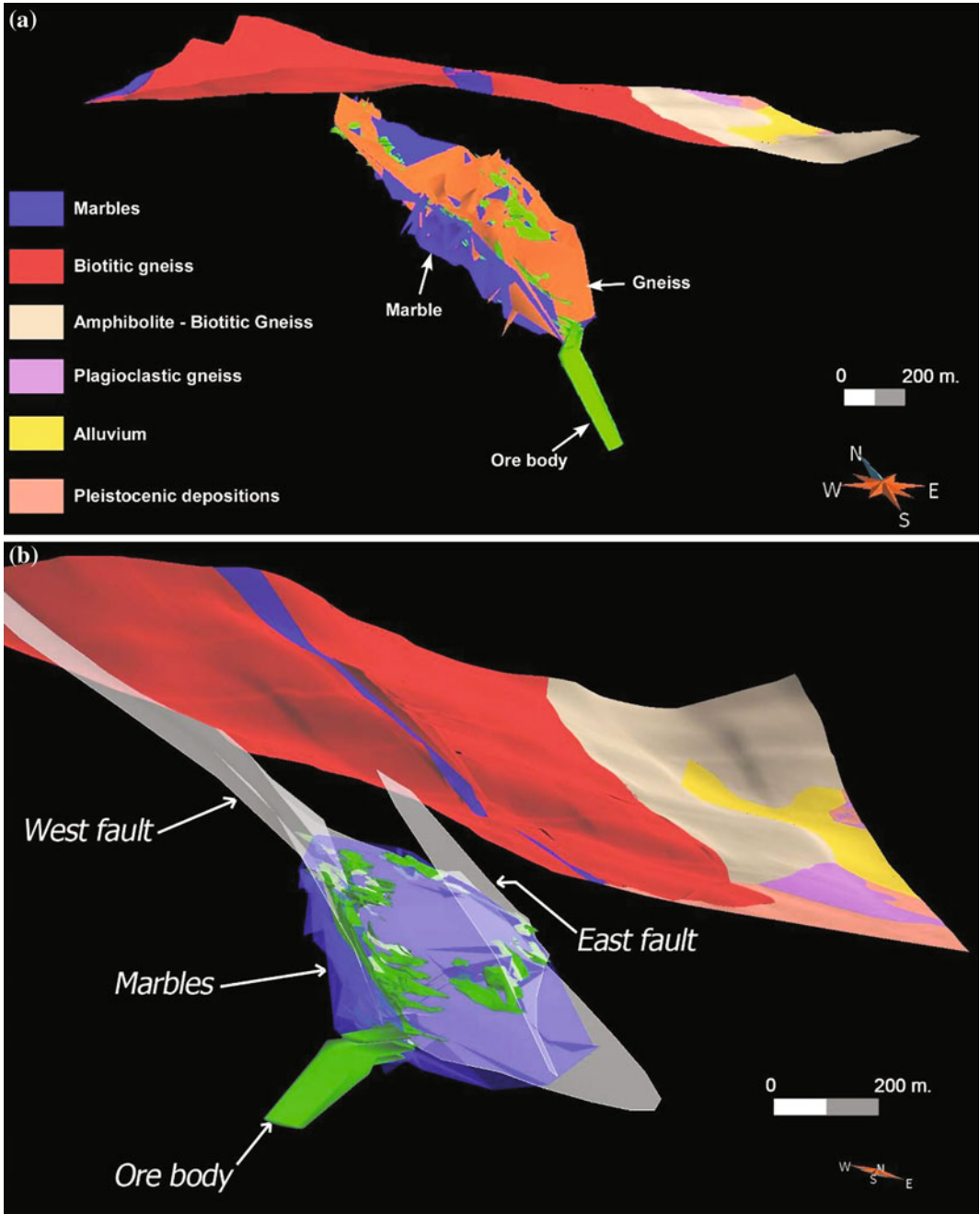


Fig. 13.5 **a** 3D lithological map of Olympias ore deposit, **b** Stratabound replacement mantos mineralization on the contact and inside the marbles (Screenshot from gOcad)

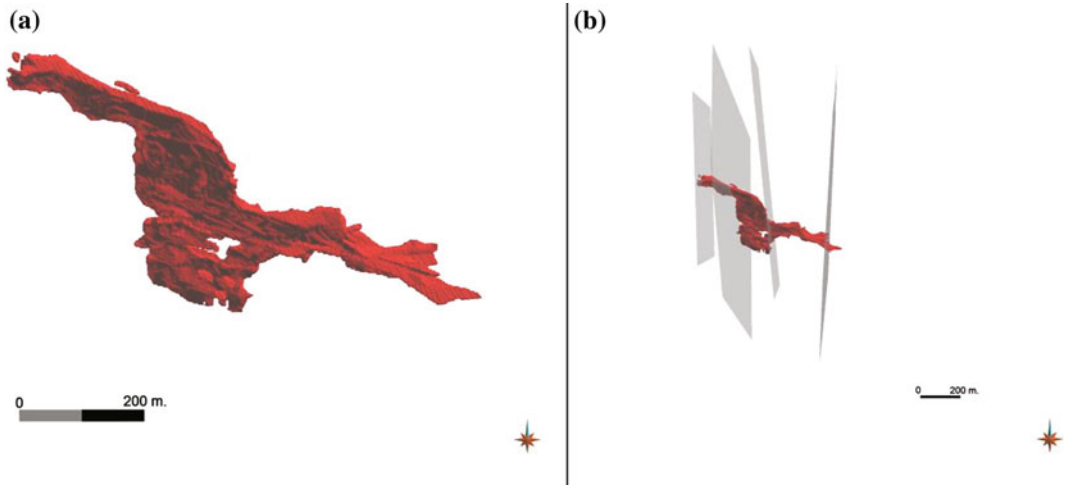


Fig. 13.6 a 3D model of the Mavres Petres deposit, b 3D model showing four sub vertical faults observed also during underground mapping (Screenshot from gOcad)

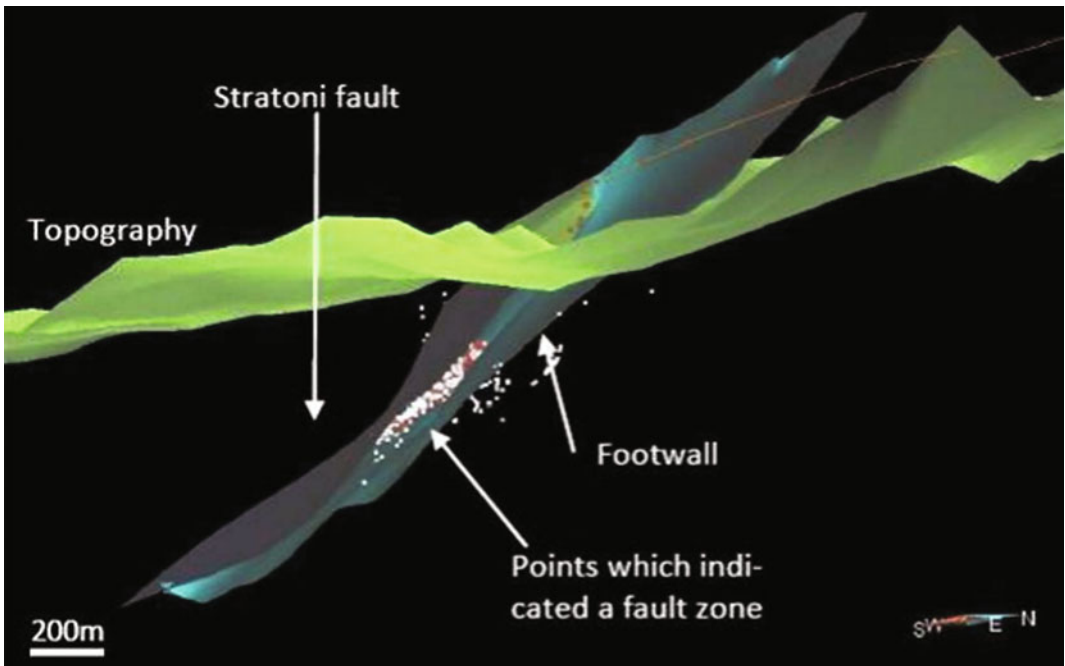


Fig. 13.7 The Stratoni-Varvara fault depth extension and cross-cutting fault structures indicated by white dots corresponding to observations and descriptions of mylonite, breccia and kaolin zones in the available drillcores (Screenshot from gOcad)

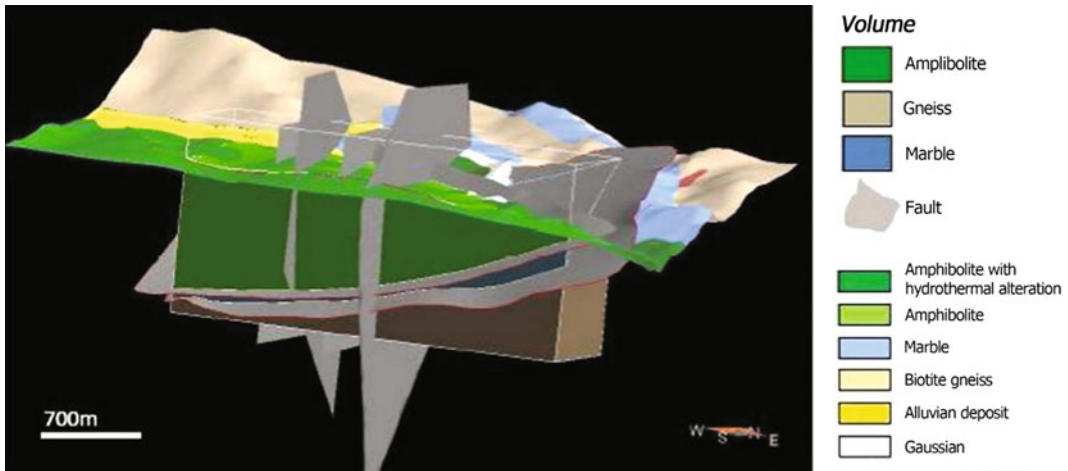


Fig. 13.8 Final 3D model of the Mavres Petres mining area (Screenshot from gOcad)

13.4.3 Skouries Porphyry Copper-Gold Deposit (Deposit Scale Model)

The Skouries ore deposit is part of the NW trending Serbomacedonian porphyry copper belt (Serbomacedonian zone) extending through FYROM to Serbia and Romania. The Skouries porphyry intrusion consists of a series of rhyodacitic, dioritic to andesitic dykes and stocks emplaced into Vertiskos amphibolitic basement rocks in association with ultrabasic lithologies. It forms a pipe-like, mineralized subvolcanic body with surface dimensions of 180 m N-S and 200 m E-W and a vertical extent of at least 700 m (Frei 1992, 1995; Tarkian 1991; Eliopoulos and Economou-Eliopoulou 1991).

Based on existing data and the work carried out by Adeline (2010), it was possible to identify and map the major brittle deformation structures, such as faults and related fracture zones. And interpreting digital topography data to model and locate main lineaments controlling and defining the porphyry intrusive corridor (Fig. 13.10). Three main directions of faulting were identified, N15°, N35° and N325° (Fig. 13.11).

The total estimated resources are 191.2 Mt at 0.82 g/t Au and 0.55 wt% Cu, equivalent to 5.03 Moz Au and 1.043 Mt Cu. Current reserves are estimated at 129.5 Mt, at 0.89 g/t Au and

0.56 wt% Cu, corresponding to 3.71 Moz Au and 725,000 t Cu.

Further 3D modelling includes integrating and interpreting the three fault sets identified with respect to drillcore information on composition and age of porphyry dykes. Existing geostatistical data could also be used for 3D modelling to delineate metal distribution and the exploitation/mining plan of the ore. Also, the Skouries 3D models are efficient explorations tools to target and locate new potential porphyry copper-gold mineralizations in the area.

13.4.4 Semi-regional 3D Modelling Across North-Eastern Chalkidiki

The deposit scale 3D models were integrated with the regional scale geological information to provide semi-regional 3D models of the metallogeny. For the region of North-Eastern Chalkidiki peninsula the previously presented deposit scale 3D models were evaluated with regional geological, structural and geophysical data. The construction of the 3D geological map was further corroborated by 15 geological cross-sections, for better understanding the 3rd dimension (Fig. 13.12).

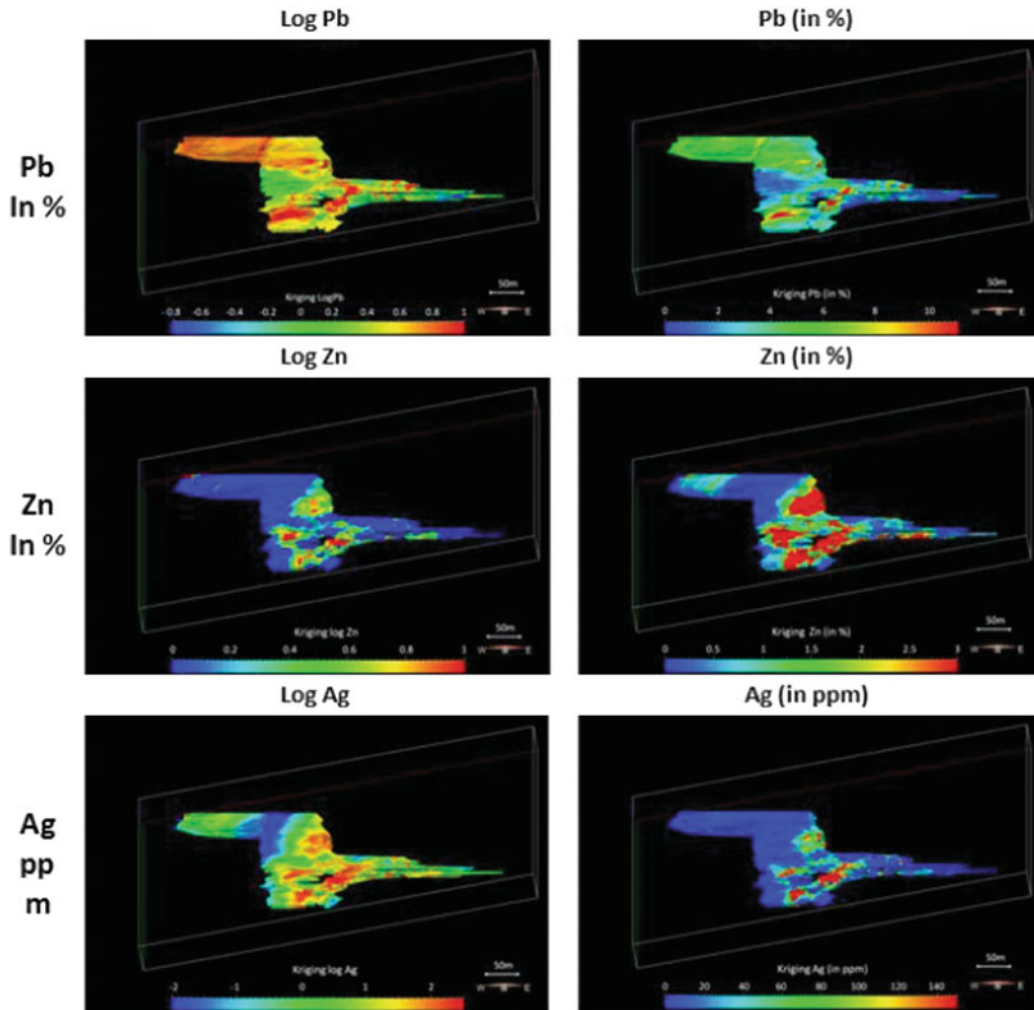


Fig. 13.9 Kriging metal contents at Mavres Petres. *On the left*, logarithmic kriging maps of grades, *on the right* normal values. Both log and normal metal content maps show a strong correlation between Ag, Zn and Pb. Highest grades seem to be concentrated along a NE direction in the main part of the ore body limited by the F2 and

F3 N-S faults. The grades are smaller in the uppermost west part of the ore body, especially along the F2 N-S fault. This part is also less sampled than the rest of the ore body (especially the central part) leading to less variability in the map (Screenshot from gOcad)

By integrating structural, geological and the geophysical data it was possible to model the intrusive bodies and the basement rocks of the area in 3D. In this respect, Fig. 13.13 shows the semi-regional geological setting of the Vertiskos and Kedyllia formations, composing the Paleozoic Serbomacedonian zone, in tectonic contact with the Mesozoic Circum Rhodope Belt.

13.4.5 Perama Hill Epithermal Gold Deposit (Deposit Scale Model)

The Perama Hill epithermal gold deposit is located in the eastern part of the Petrota graben (Fig. 13.3) consisting of subaqueous pyroxene andesitic flows, debris-flows and hyaloclastites, resting on turbiditic series (Lescuyer et al. 2003).

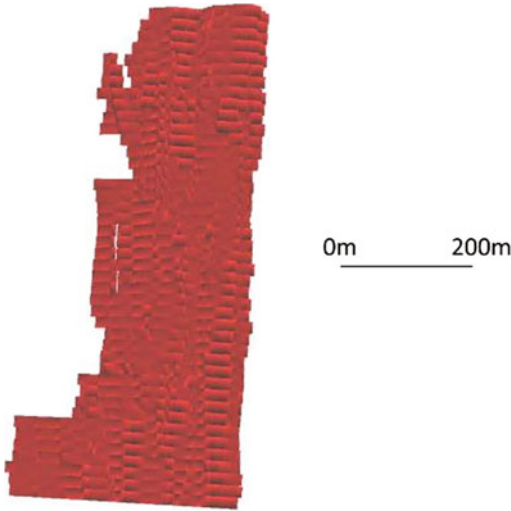


Fig. 13.10 Skouries orebody (Screenshot from gOcad)

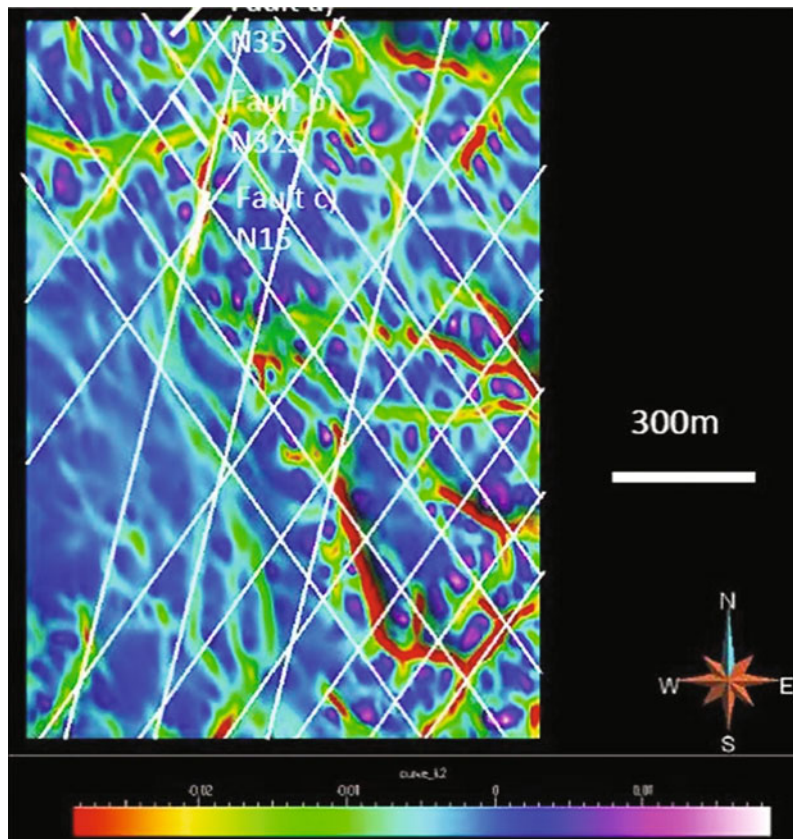
The Perama sandstones, which host the gold mineralization, are coeval with subaerial felsic eruption in the western part of the graben

constituting pyroclastic flows, accretionary lapilli tuff, quartz porphyry domes and dacite flows (Lescuyer et al. 2003). The metamorphic basement close to the deposit is part of the Circum Rhodope zone (Mesozoic age) and consists of greenschists and calcschists. Silicified fracture zones and hydrothermal breccias occur at the contact between Mesozoic greenschists-calcschists and Perama sandstones. Silicification and advanced argillic alteration (kaolinite-illite) are the main alteration styles of the epithermal gold mineralization in Perama Hill (Fig. 13.14).

From the 3D modelling the following conclusions can be drawn:

- The mineralizing hydrothermal system was structurally controlled (Figs. 13.15 and 13.16)
- The normal fault situated between the Mesozoic basement and the Tertiary Petrota graben was possibly the channel way of the mineralizing hydrothermal fluids (Figs. 13.15 and 13.16)

Fig. 13.11 Three main faulting directions of N35° E, N 35°W and N15°E identified at Skouries (Screenshot from gOcad)



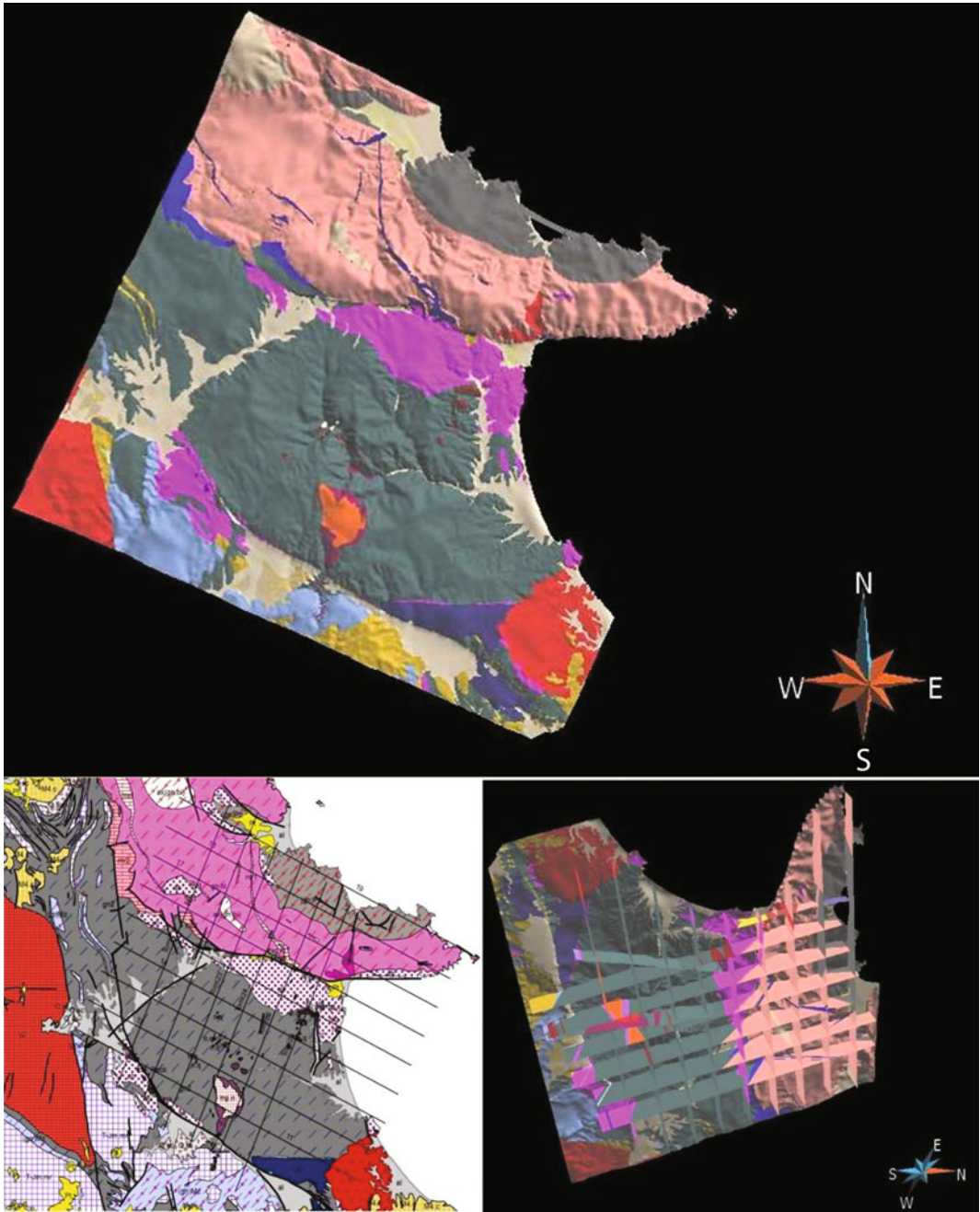


Fig. 13.12 3D geological map and 15 geological sections provided lithostratigraphic and structural information across the study area of North-Eastern Chalkidiki (Screenshot from gOcad)

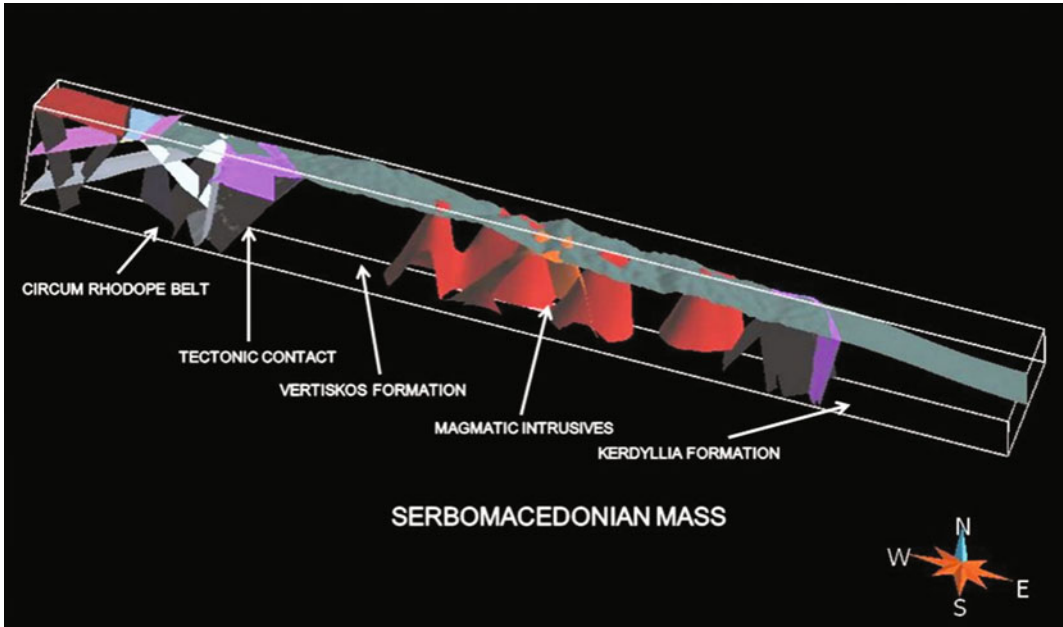


Fig. 13.13 3D geological cross section through Serbomacedonian zone (Screenshot from gOcad)

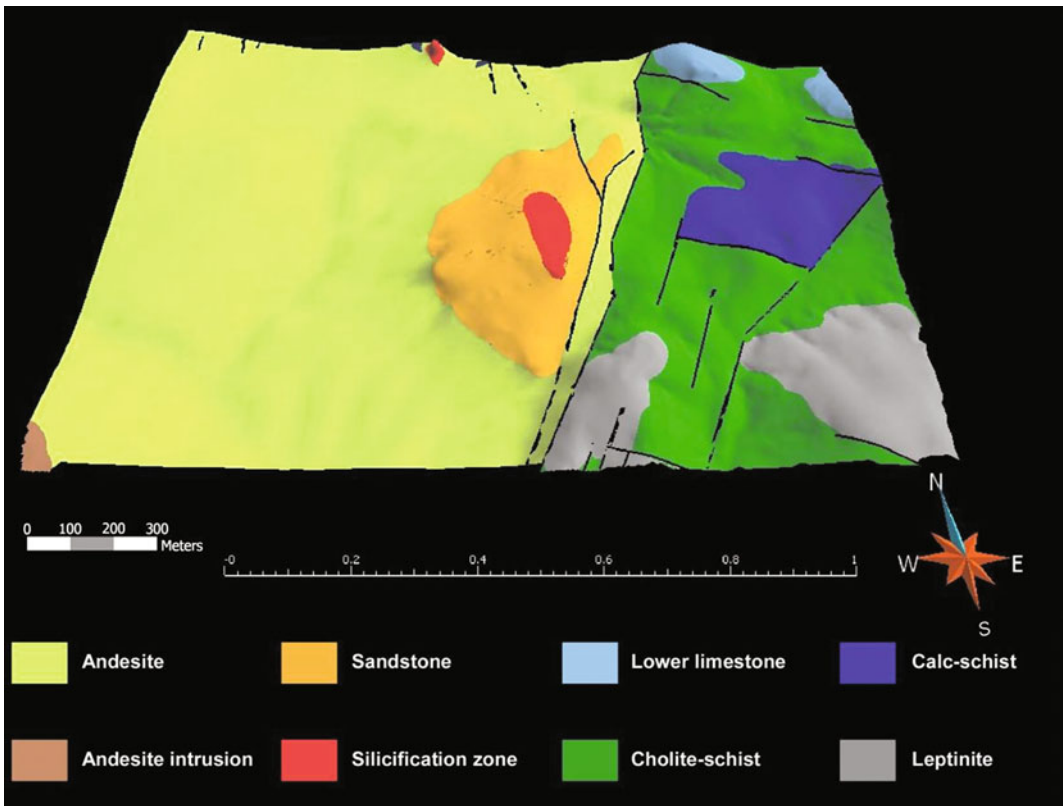


Fig. 13.14 3D local geology of the Perama Hill area showing the extension of silicification (Screenshot from gOcad)

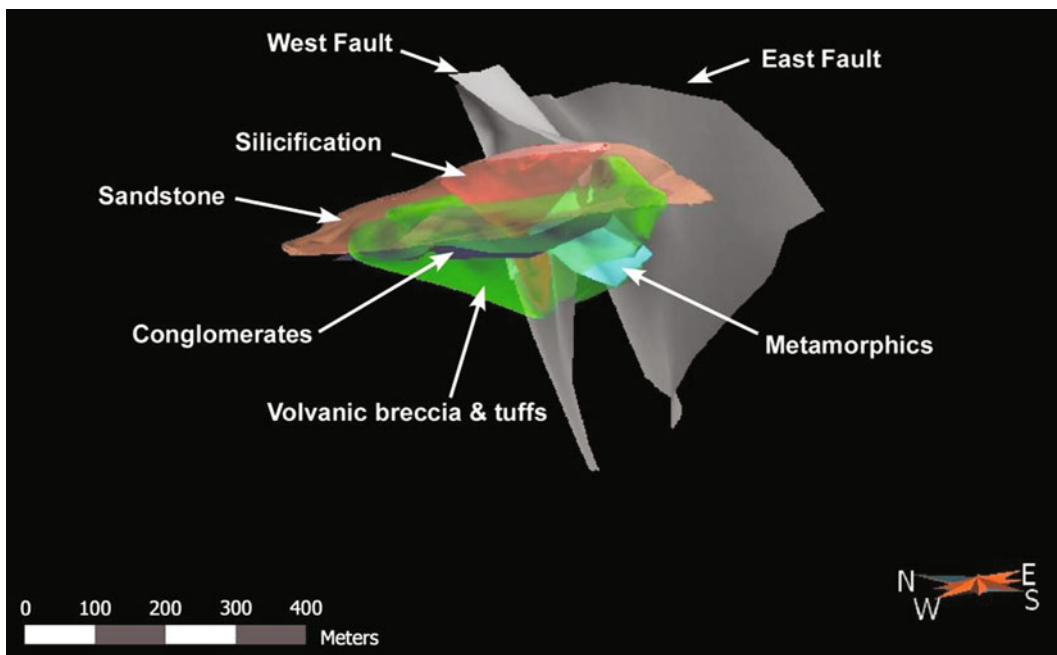


Fig. 13.15 Major faults at the contact of Petrota graben and metamorphic basement rocks in the Perama Hill area (Screenshot from gOcad)

- The permeable sandstones favoured fluids migration and deposition of gold.
- The deposit is characterized by a vertical metal zonation. The main part of the base metals sulphide mineralization is hosted by volcanic breccias and tuffs at depth.
- Silicification (hydrothermal eruption vent breccias) (Fig. 13.17)
- Advanced argillic alteration (subzones of alunite, diaspore, argillic alteration and pyrophyllite)
- Propylitic alteration
- Potassic alteration (southern part of the Tertiary basin)

13.4.6 Aghios Demetrios Epithermal Gold Deposit (Deposit Scale Model)

The geological setting comprises strongly altered andesitic agglomerates, tuffs, lavas and volcanic breccias. The paragenetic distribution of the mineral assemblages distinguishes four main and two overlapping alteration zones in the area (Michael 1988, 1993, 1995; Michael et al. 1989, 1995; Velinov et al. 1999). The main alteration zones are:

The overlapping alteration zones are:

- Sericitic alteration (Aghios Demetrios deposit)
- Adularia-rich alteration (southern part of the Tertiary basin)

The hydrothermal eruption vent breccias are the favourable structural setting for the gold mineralization in the Aghios Demetrios deposit.

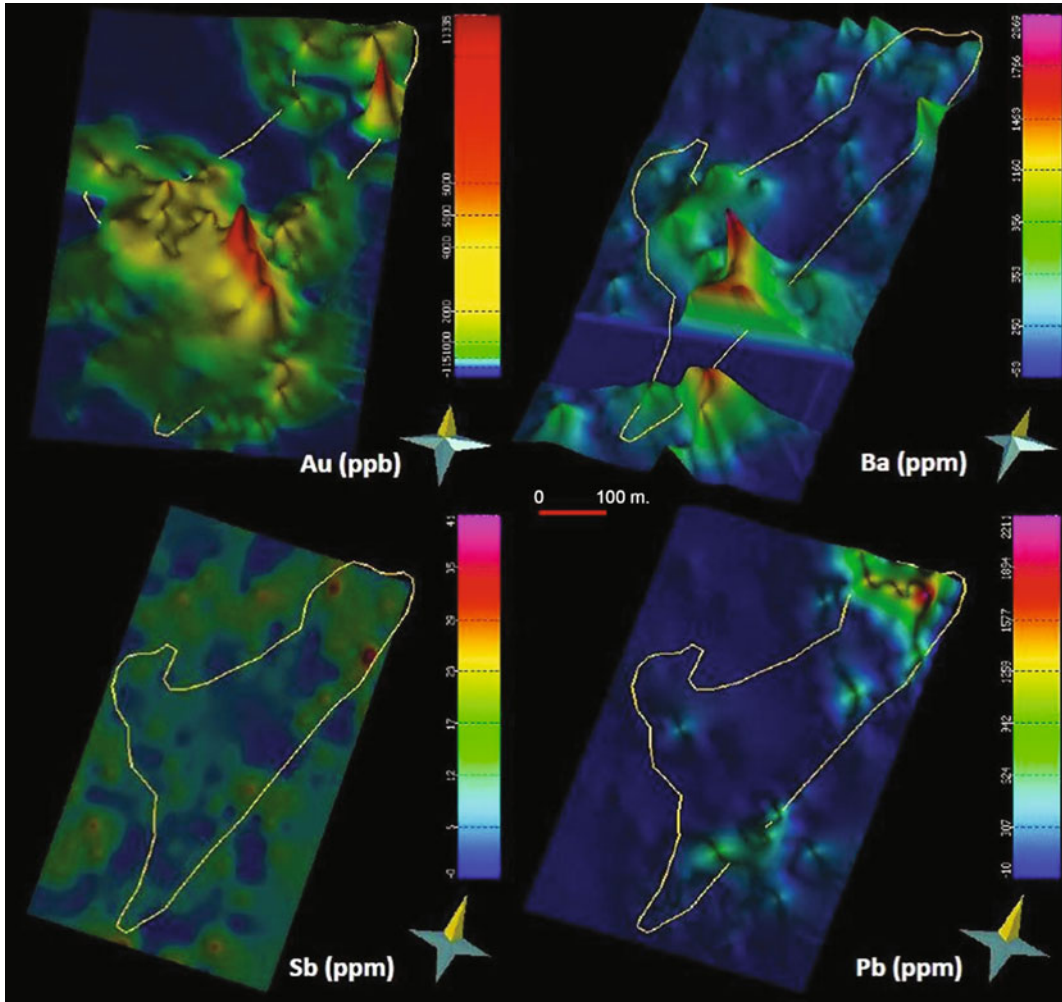


Fig. 13.16 3D soil geochemical anomalies of Au, Ba, Sb and Pb from Perama Hill in relation to the mineralization (Screenshot from MOVE)

The younger north-eastern faults caused displacement of the wall rocks.

Based on 3D modelling of the two epithermal deposits the following can be concluded:

- The ore forms a flat lying body trending NW and dipping 5–10° towards NNE (Fig. 13.18).
- The NNE part of the area is of high potential for gold exploration.
- The ore body is approximately 550 m long and 100–160 m wide (Fig. 13.18).
- A NE trending fault zone intersects and separates the ore body (Figs. 13.17 and 13.18).

This fault zone has also caused displacement of the wall rock alteration zones.

- Gold mineralization is mainly associated with hydrothermal eruption vent breccias.
- Base metals mineralization is developed at deeper levels (Fig. 13.18).
- The deposit is characterized by a vertical zonal pattern of metals and alteration zones.
- The hydrothermal eruption vent breccias (siliceous zone) are very important as host rocks.
- Advanced argillic alteration is widespread. It can be divided in subzones of alunite, silica with diasporite, argillic/sericite and pyrophyllite.

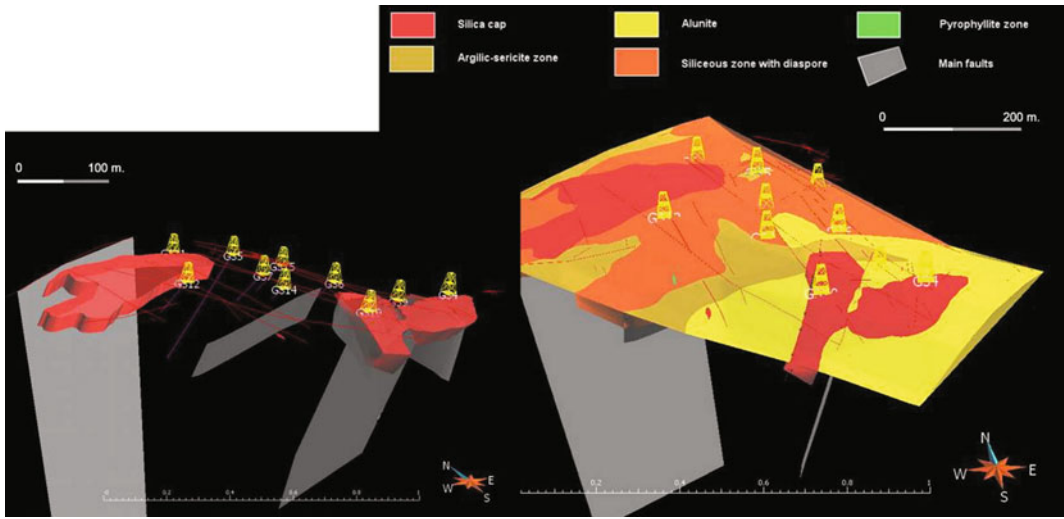


Fig. 13.17 Hydrothermal alteration zones and main faults in the Aghios Demetrios epithermal gold deposit (Screenshot from gOcad)

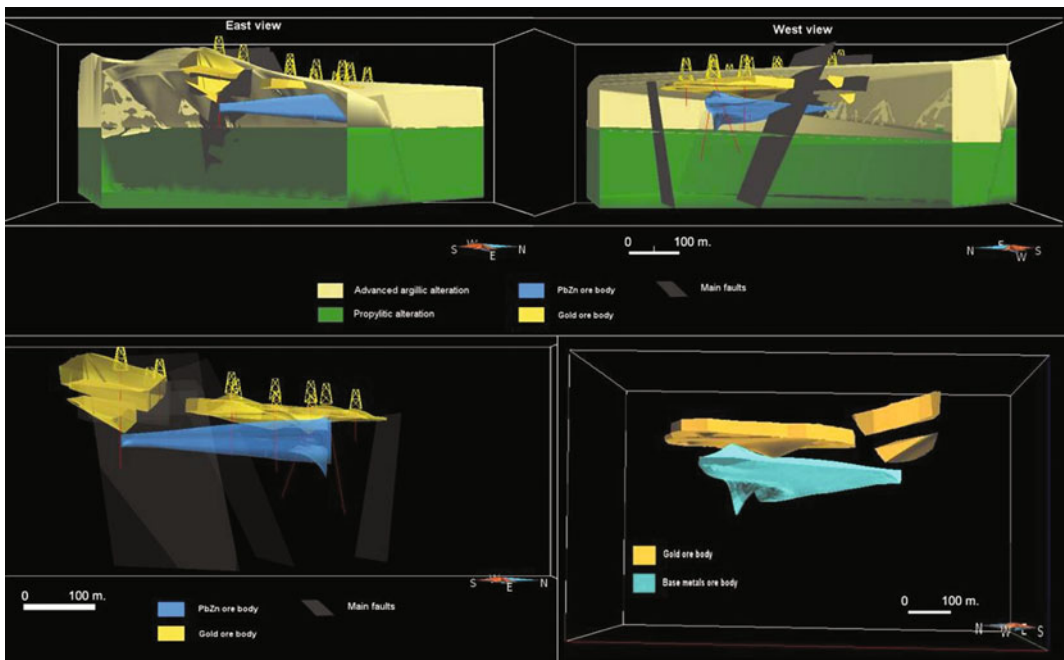


Fig. 13.18 Upper figure Cross sections through the Aghios Demetrios Au mineralization and related alteration zones. Lower figures Structural setting of the Aghios Demetrios gold and base metal ore bodies (Screenshot from gOcad)

- The mineralizing hydrothermal system was structurally controlled and related to deep structures (Fig. 13.19).

13.4.7 Semi-regional 3D Modelling Across the Thracian Epithermal Gold Deposits

A geological reconstruction of the area in semi-regional scale was established using cross sections (Fig. 13.20), aeromagnetic data (Fig. 13.21), rift basin structures (Fig. 13.22) and the 3D models developed at deposit scale. Fifteen

geological cross sections were set up across the Petrota and Sappes-Kirki Tertiary basins (Fig. 13.20). An extensive N-S structure, about 7.5 km long, at the western part of Sappes-Kirki Tertiary basin is considered to represent a fissure vent system (Fig. 13.22).

13.4.8 Regional 3D Model of the Carpatho-Balkan Belt

The Carpathian-Balkan metallogenetic belt was formed along the southern margin of the Eurasian plate during Mesozoic-Cenozoic time.

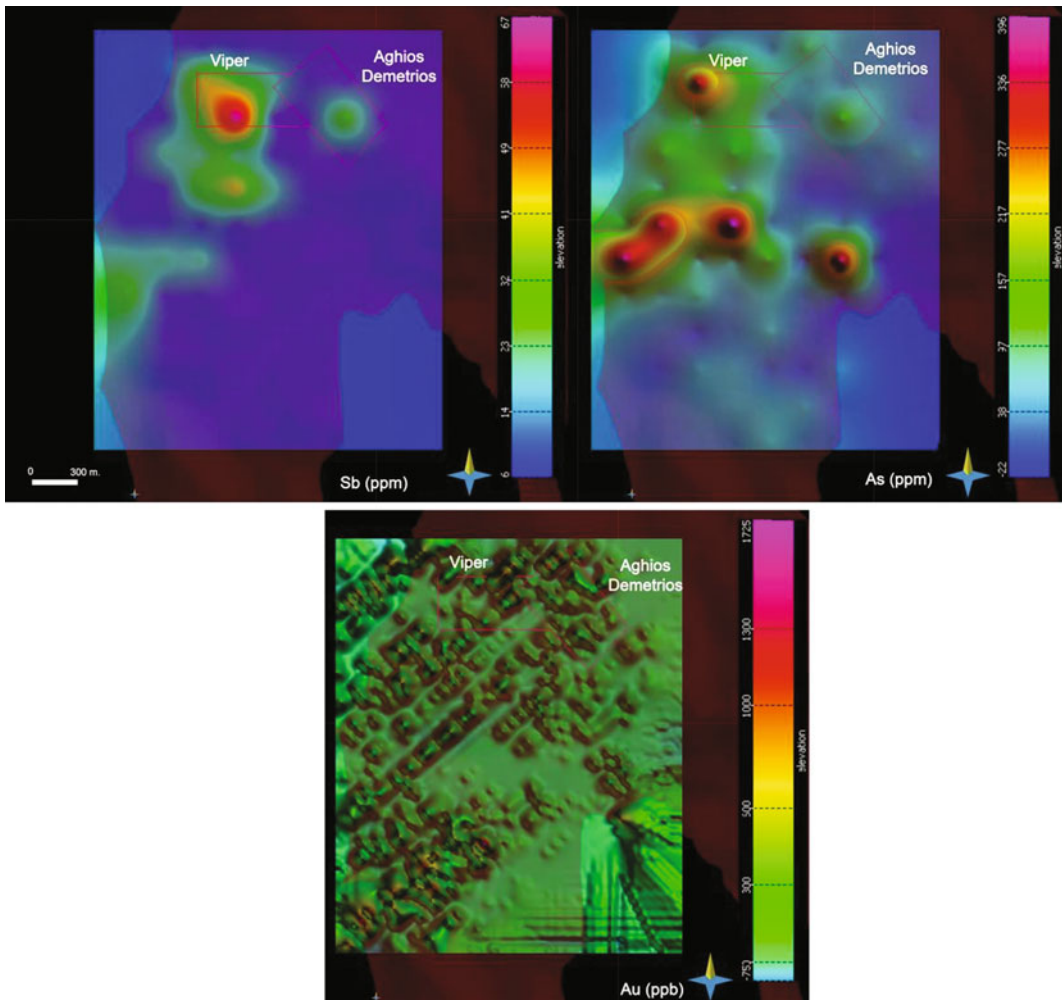


Fig. 13.19 Soil geochemical anomalies of Au, As and Sb related to deep faults controlling the location of mineralization (Screenshot from MOVE)

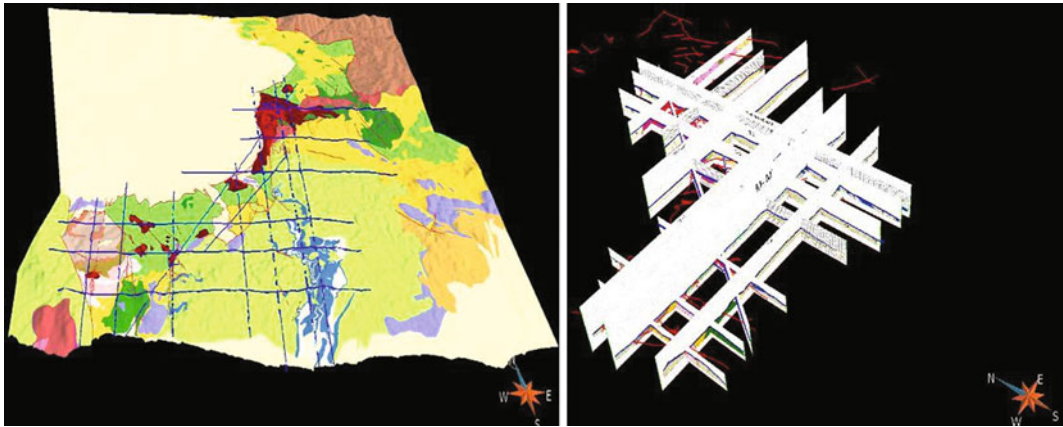


Fig. 13.20 3D geological map and fifteen (15) geological sections across the epithermal gold deposits in Thrace (Screenshot from gOcad)

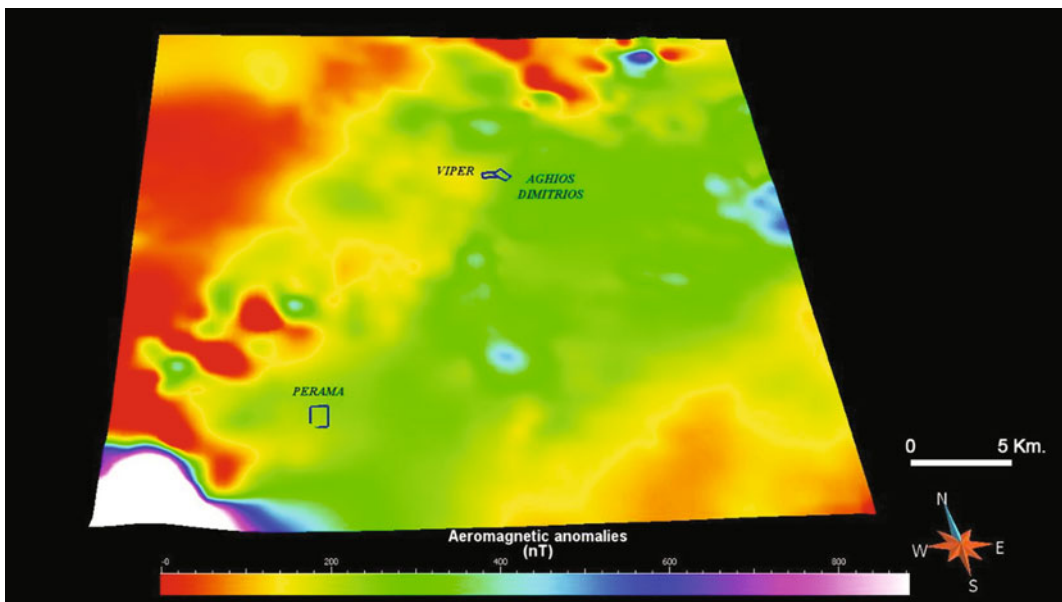


Fig. 13.21 Aeromagnetic data over Perama Hill and Aghios Demetrios epithermal gold deposits in Thrace (Screenshot from gOcad)

A regional 3D model was created for the southernmost part of the Carpathian-Balkan belt. Three metallogenetic zones were modelled in the Hellenic-Balkan belt (Fig. 13.23): (1) The Sredna Gora metallogenetic zone with porphyry copper and epithermal gold deposits related to late Cretaceous magmatic activity, (2) the Rhodope

metallogenetic zone with epithermal gold deposits and porphyry copper molybdenum deposits related to Tertiary magmatic activity and (3) the Serbomacedonian metallogenetic zone with porphyry copper—gold and mantle Pb-Zn-Ag-Au deposits related to Tertiary magmatic activity.

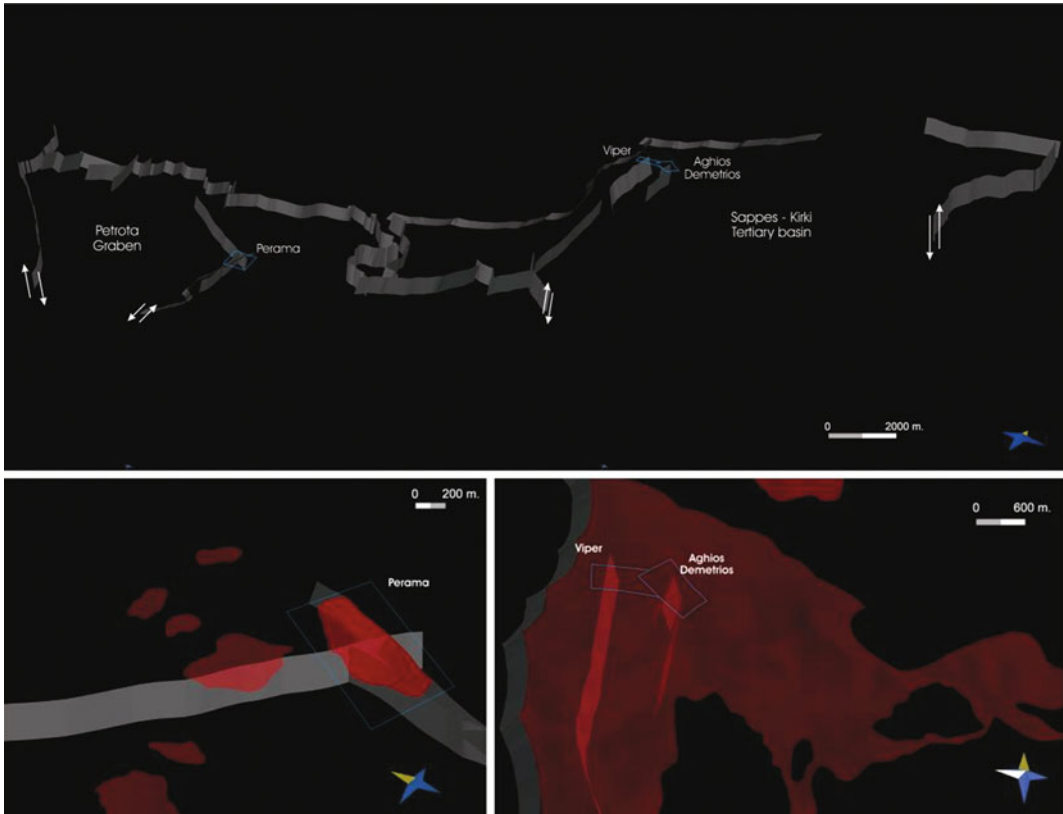


Fig. 13.22 *Upper illustration* Fault structures in the Thrace region forming the rift-basins of Petra and Sappes-Kirki. *Lower illustrations* Fault structures controlling the location of the Perama (P) and Aghios

Demetrios (AD) deposits. The N-NE and N-S striking faults are deep structures forming regional scale rift-basins (Petra graben and Sappes-Kirki Tertiary basins) (Screenshot from MOVE)

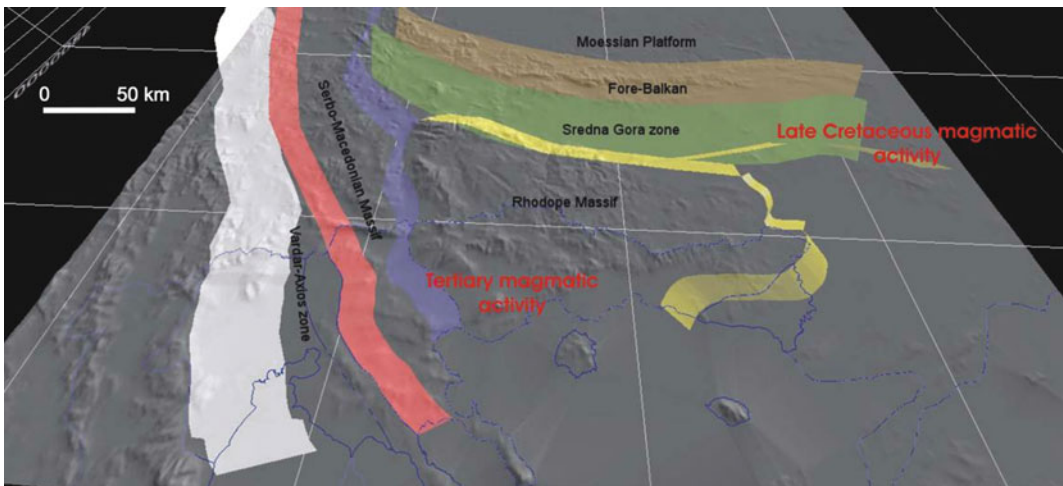


Fig. 13.23 Regional 3D model of Hellenic-Balkan geotectonic units. This model demonstrates the tectono-magmatic evolution of the Hellenic-Balkan geotectonic units from upper Cretaceous to Neogene (Screenshot from MOVE)

13.5 Conceptual 4D Modelling and Related Exploration Implications

13.5.1 Epithermal Au Deposits in Tertiary Basins of Western Thrace

Combining the information obtained from the 3D local and semi-regional scale models with background geological data and geochronology, a conceptual 4D model for the metallogenetic evolution of Western Thrace was constructed by means of foreword modelling. The 3D models were created using the gOcad software and the 4D model using the MOVE software from Midlands Valley.

For the construction of the 4D model showing the epithermal metallogenetic evolution in western Thrace the following sources of information were used (Fig. 13.24):

- Geology from the Rhodope zone
- Main tectonic and structural characteristics
- Geochronology

- Magmatic activity (volcanic and emplacement of granitoids and shallow porphyry intrusives)
- Fluid inclusion data
- Stable isotopes geochemistry

Along the southern and eastern margins of the Rhodope zone, major volcanosedimentary rift-basins were formed with coeval granitoid intrusions and porphyry stocks during late Eocene-Oligocene. Acid sulphate fluids ascended from the magmatic source (granitoid intrusives and porphyry stocks) causing acid leaching, creation of silica supersaturation solutions and precipitation of massive chalcedonic silica (impermeable horizon) at the base of water table. Convecting fluids were trapped beneath the impermeable horizon and a hot overpressured aquifer formed. The increased pressure led to hydrothermal explosion with formation of hydrothermal breccias and precipitation of gold and base metals (Michael 1988, 1993, 1995, 2005). The hydrothermal breccia constituted a favorable site for gold deposition. Gold mineralization was mainly

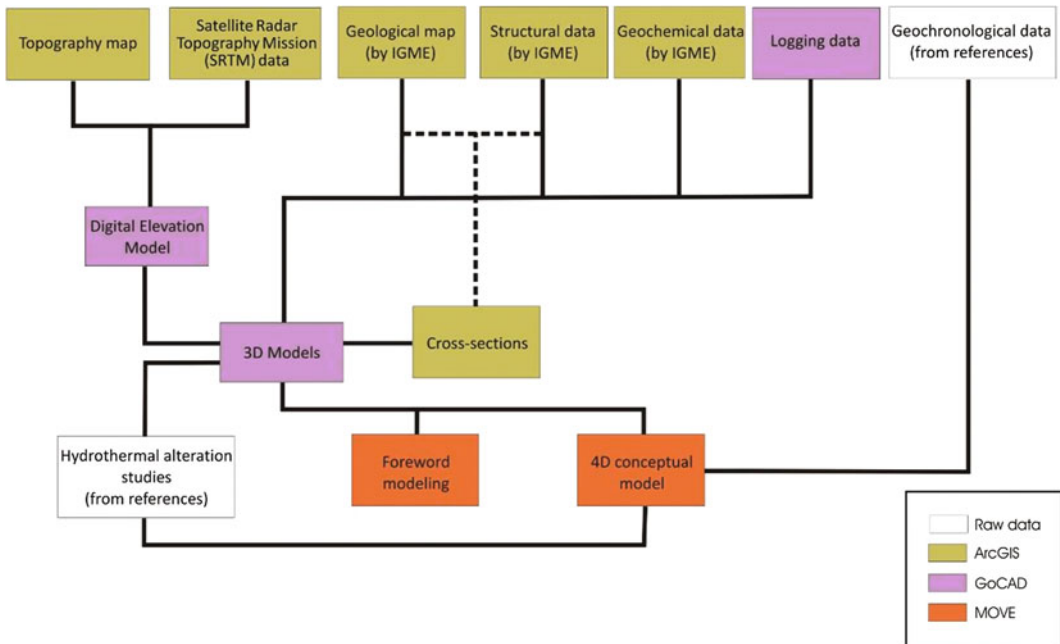


Fig. 13.24 Work flow for the construction of 3D and 4D models

associated with hydrothermal eruption vent breccias and fissure vent systems (Bridges et al. 1998; Border et al. 1999; Andrew et al. 2001). The 4D models can be very useful tools for improving the knowledge of the ore deposition and can be used for mineral exploration in order to determine new potential areas.

13.5.2 Polymetallic Manto and Porphyry Type Systems of Eastern Chalkidiki Peninsula

The information used to analyze the geological evolution in order to construct the 4D model of Eastern Chalkidiki peninsula included: (1) Geochronology of formations, (2) main structural data, (3) geology of the Kerdyllia and Vertiskos formations and (4) hydrothermal alteration, fluid inclusion and stable isotope data.

The orientation/dip analysis shows that the Kerdyllia and Vertiskos formations, which constitute the Serbomacedonian zone, have experienced many deformation phases, but the main stress orientation is NNE. The first major tectonic movement probably took place before the Palaeozoic. Geochronological data indicate an age of 300 Ma (Mountrakis 1985). The second tectonic event is related to the Alpine orogenesis. This tectonic event formed the main Stratonifault, which constitutes the tectonic contact between the Kerdyllia and Vertiskos formations. In early stages this fault behaved as a reverse fault, but during the Tertiary it behaved as a normal fault. During the Tertiary the final magmatic event formed intrusions that generated hydrothermal fluids which followed existing faults and fracturing systems. The Stratonifault granodiorite is part of this event and the related hydrothermal activity resulted in fault and stratabound controlled base metal sulphide deposition. During the Miocene, syenitic porphyry stocks and dykes intruded into the Vertiskos metamorphic basement to form stockwork copper—gold mineralization.

The 4D models were incorporated into local exploration as they proved significant for

identifying new potential mineralization. All information was synthesized using the Move Software from Midland Valley in order to create the conceptual 4D model. In the model the Kerdyllia and Vertiskos formations were constructed as simple planes at the very first steps of the 4D model. They were then only in contact with the plane of the Stratonifault. The movements that occurred during the orogenesis were modelled using information from dip orientation and geochronology. Modelling the orientation of these features involved the original main orientation derived from the above analysis. Each different frame output from the Move software was exported to Microsoft Powerpoint in order to create the animation mpeg. Screenshots are shown in Fig. 13.25.

13.6 Potential Resources Assessment

Predictive modelling based on 3D/4D models can also be subdivided into deposit scale, local scale, semi-regional scale and regional scale. Below some case studies for each scale are presented.

13.6.1 Deposit Scale

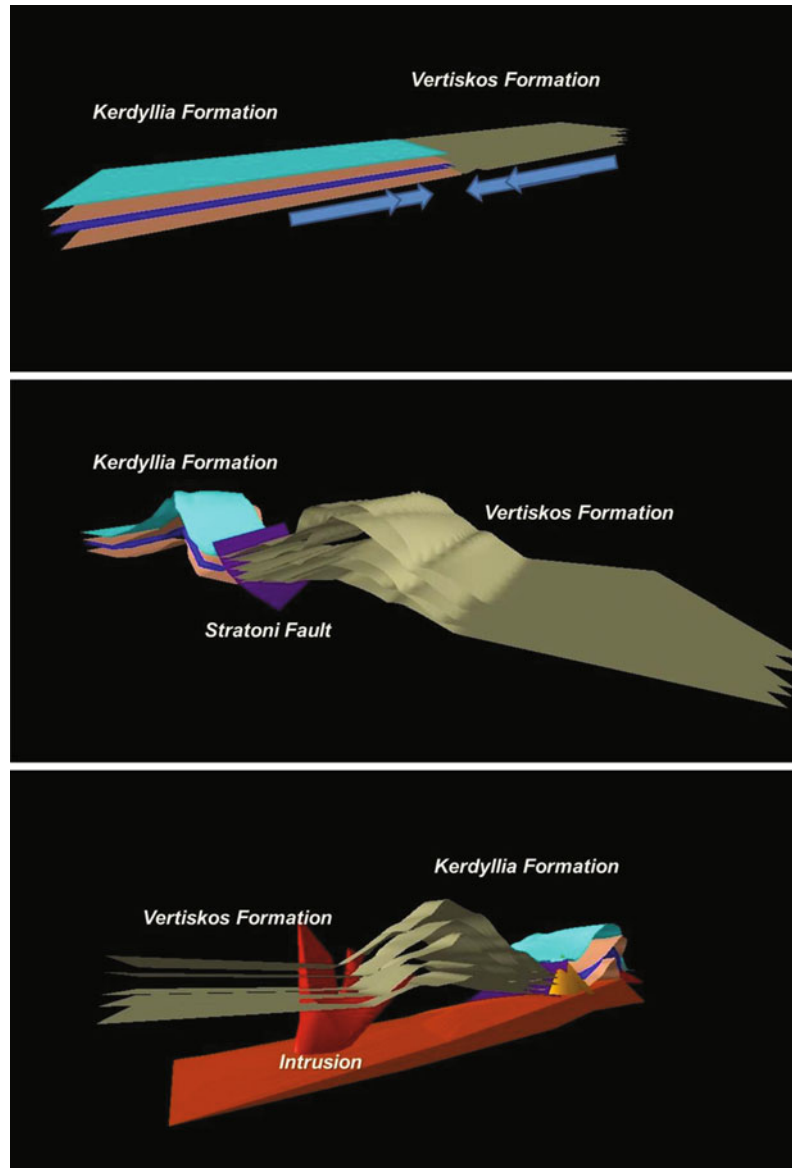
13.6.1.1 Aghios Demetrios Epithermal Au Deposit

Based on the 3D model of Aghios Demetrios, it is indicated that the ore body is dipping N-NE and the NNE part of the area shows considerable potential for the extension of the ore body (Fig. 13.26). The vertical zonal pattern of the ore metals and alteration zones distribution can be used as exploration tool for other districts and the hydrothermal eruption vent breccia is a favourable structural setting for the gold mineralization.

13.6.1.2 Olympias Manto Polymetallic Deposit

The structures of the east and west ore bodies are related to respective fault zones and an

Fig. 13.25 Screenshots from the 4D model that depict the main stages of the development of polymetallic replacement deposits of the Eastern Chalkidiki peninsula (Screenshot from MOVE)



indication for potential of deeper seated extension of the mineralization is clearly shown (Fig. 13.27). This could be a guide for further exploration.

13.6.1.3 Mavres Petres Polymetallic Replacement Deposit

Based on the 3D model of the Mavres Petres deposit the orebody is crosscut by several faults

that are almost vertical. These faults seem to have a very significant role on the shape and morphology of the mineralization. During previous exploration projects the eastern lower part of the orebody was investigated without any success. The next target for exploration is the possible extension of the lower western part of the orebody (Fig. 13.28). An exploration campaign recently discovered a small mineralization west of the western vertical fault.

Fig. 13.26 Potential area to further exploration indicated by the 3D model of the Aghios Demetrios deposit (Screenshot from gOcad)

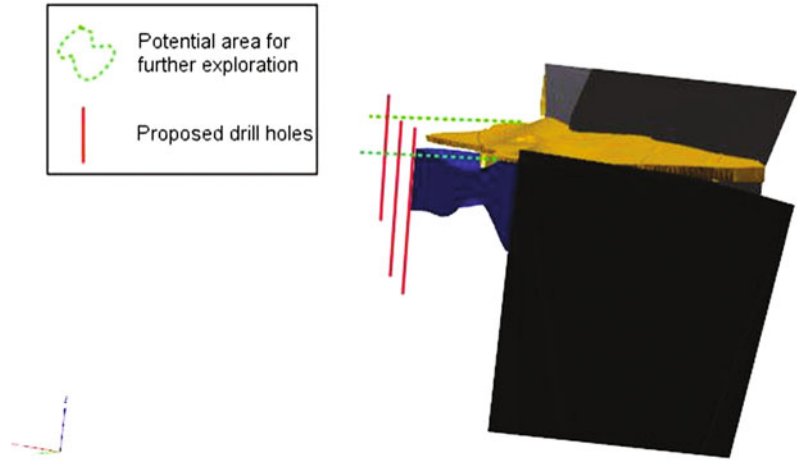


Fig. 13.27 SW extension at depth of the mineralization at Olympias (Screenshot from gOcad)

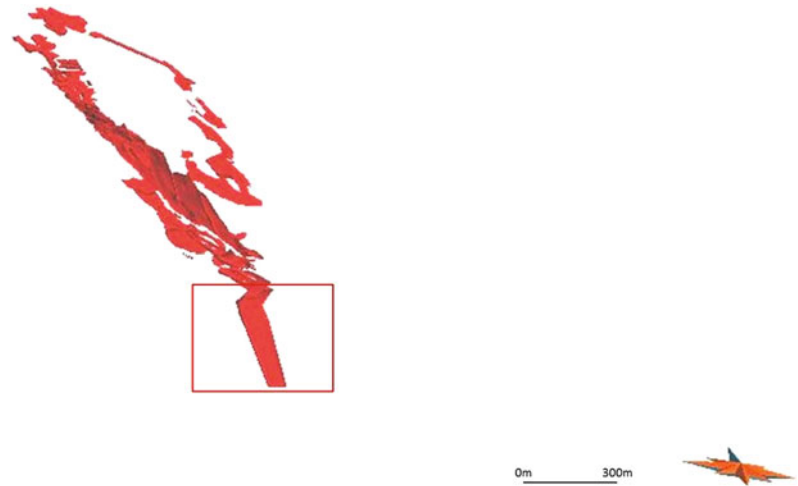
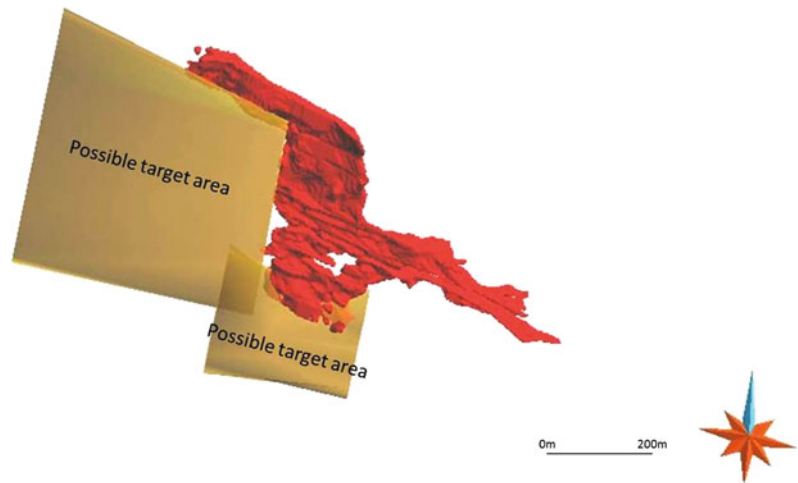


Fig. 13.28 West extension of the mineralization at Mavres Petres (Screenshot from gOcad)



13.6.1.4 Piavitsa Polymetallic Replacement Deposit

The Piavitsa area is a potential target for polymetallic mineralization similar to Mavres Petres. A drilling exploration program started by Hellas Gold S.A in 2012, and the results of the first drillholes carried out were used to construct a preliminary geologic model of the deposit (Fig. 13.29). Like in Mavres Petres the ore body follows the geometry of the fault, and is located above the marbles and below the amphibolite.

13.6.2 Local Scale

13.6.2.1 Western Thrace

The Tertiary Petrotta graben and the epithermal gold deposits of Perama Hill and Aghios Demetrios in the Sappes-Kirki basin, have been studied at a local scale. Generally the epithermal gold systems are widespread, showing the same

alteration characteristic as the Perama and Aghios Demetrios epithermal gold deposits. The Perama and Aghios Demetrios deposits have the following common features:

- Coincident with low magnetic anomalies
- Closely associated with graben structures or big structures close to steep faults.
- Located on the margins of the volcanosedimentary basins.

Based on the knowledge derived from the deposit scale 3D models, the areas of Odontoto, Mavrokorifi and Kommaros are potential targets to further exploration (Fig. 13.30). They all show favorable structural settings for epithermal Au mineralizations. The similarities with the Perama Hill epithermal Au deposit are: the graben faults and intense fracturing and the presence of the same alteration zones. The structural contact (graben fault) between Mesozoic rocks and

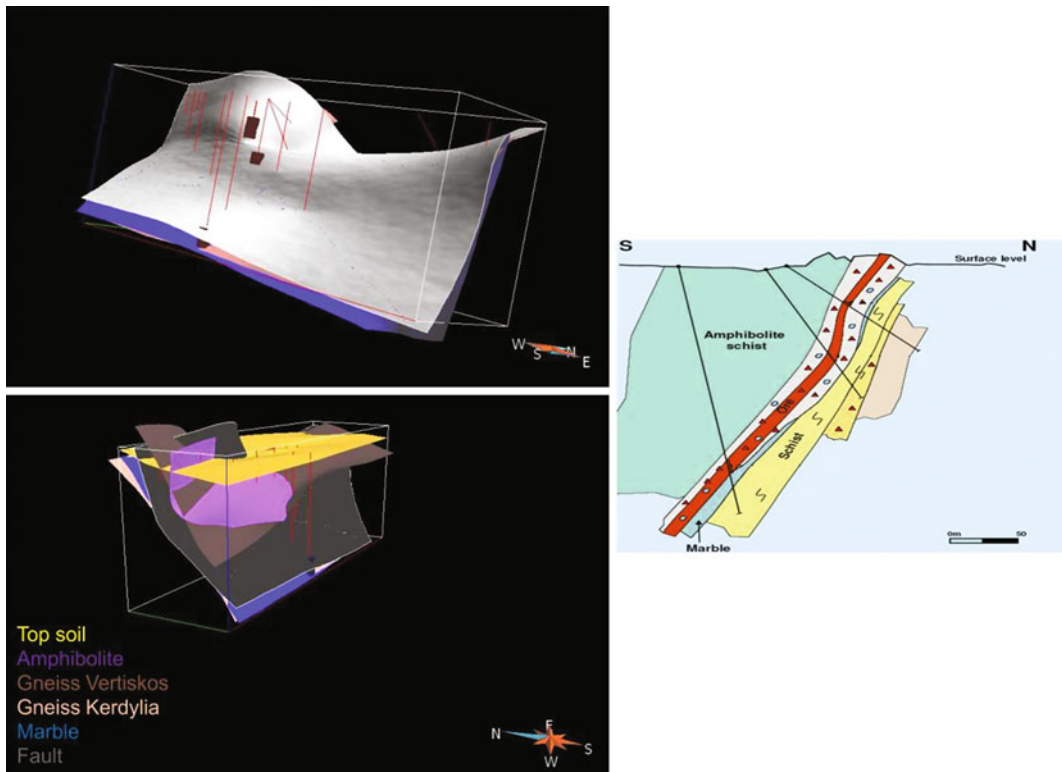
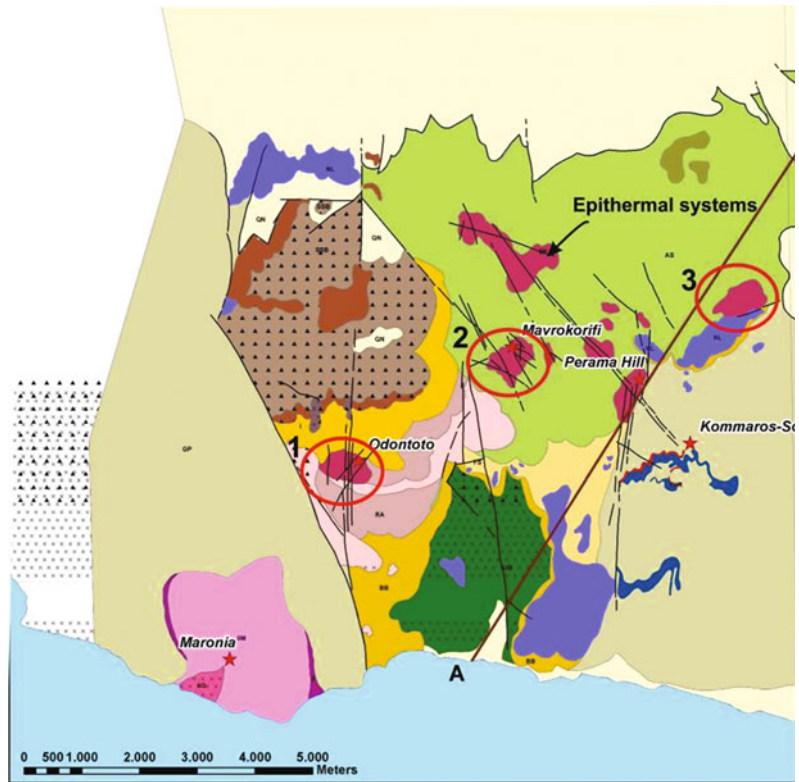


Fig. 13.29 Preliminary geologic model of SW Piavitsa, with indications of mineralization (*red*) (Screenshot from gOcad)

Fig. 13.30 New exploration targets in Petrota graben (Created with ArcMap)



Tertiary rocks seems to have been the channel way of the hydrothermal fluids.

Three areas with favorable structural settings for epithermal Au mineralization can be outlined in the Sappes-Kirki basin (Fig. 13.31). The common characteristics with Aghios Demetrios epithermal Au deposit are: (1) the presence of hydrothermal eruption vent breccias, (2) the presence of similar alteration zones, (3) the fact that they coincide with low magnetic anomalies similar to Aghios Demetrios and (4) a major N-S structure, about 7.5 km long, at the western part of the area is considered to mark a fissure vent system for the entire region. The soil geochemical anomalies of Sb and As delineate this big structure (cf. Figure 13.19).

13.6.2.2 NE Chalkidiki

From the local and semi-regional scales model of NE Chalkidiki, and also to the information acquired from the deposit scale modelling, some structures with good potential for mineralization were identified in the NE Chalkidiki region. A

similar geologic environment to the Mavres Petres deposit is found a few km to the west in the area of Piavitsa, including the same Stratonii granodioritic intrusion, the same main fault structures as well as indications of replacement of marble, which could result in polymetallic mineralization. Earlier the area was exploited for supergene Mn. The area is currently under exploration and a preliminary 3D model can be seen in Sect. 13.6.1.4.

The NE-SW trending corridor of intrusions, hosting the economic Skouries deposit, well explored and studied through airborne geophysics and drilling, also shows potential for deposits similar to Skouries in the areas Fisoka and Tsikara (Fig. 13.32).

13.6.3 Semi-regional Scale

Based on the knowledge obtained from deposit and semi-regional scale 3D models, the Melitena—Kaloticho Tertiary, Pefka and Virini



Siliceous zone ("silica cap"- hydrothermal breccia) & silica alunite zone.

Fig. 13.31 New exploration targets in the Sappes-Kirki Tertiary basin

—Pessani volcanosedimentary Tertiary basins with epithermal style alteration zones can be selected as new exploration targets (Fig. 13.33).

The common characteristics of these basins are (1) the presence of hydrothermal eruption vent breccias, (2) the presence of similar alteration zones, (3) granitoid and porphyry stocks and (4) low grade porphyry Cu-Mo occurrences hosted by granitoid stocks found in the Sappes/Konos and Melitena epithermal systems.

13.6.4 Regional Scale

Using existing and new geological data from Greece, a multi-layer Geographic Information System was created (Arvanitidis et al. 2012a, b). The system includes databases on mineral deposits, and anthropogenic/mining and metallurgical residues along with relevant geological, structural, geochemical, geophysical layers and other information from a diverse range of sources. Based on the database information, maps of Mineral Commodities, Genetic types, Metallogenetic districts and "Hot" metallic commodities for Greece were created (one example is shown in Fig. 13.34).

In regional scale three metallogenetic zones of the Hellenic-Balkan belt were modelled (Fig. 13.35):

- The Sredna Gora metallogenetic zone with porphyry copper and epithermal gold deposits related to late Cretaceous magmatic activity (Fig. 13.36).
- The Rhodope metallogenetic zone with epithermal gold deposits and porphyry copper

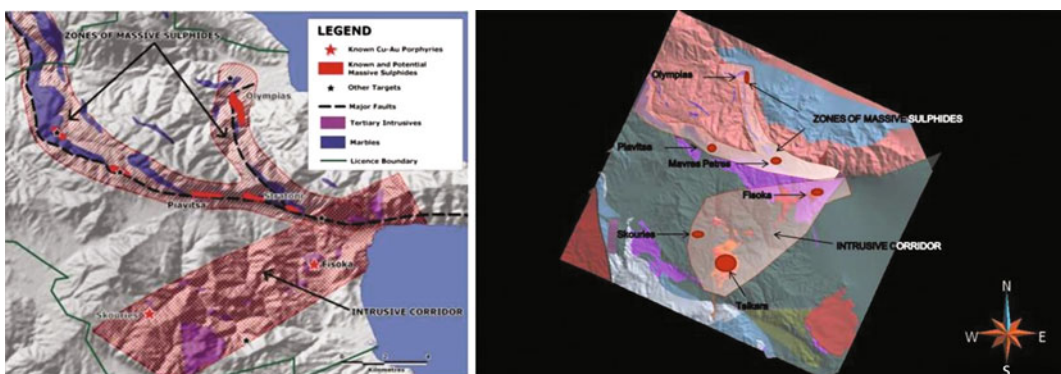


Fig. 13.32 Potential mineralization targets in NE Chalkidiki peninsula

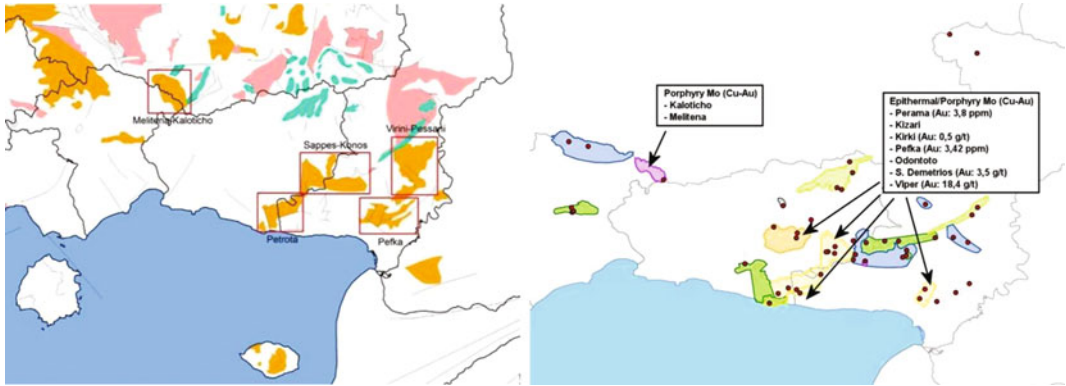


Fig. 13.33 New Tertiary basin targets with exploration potential in western Thrace

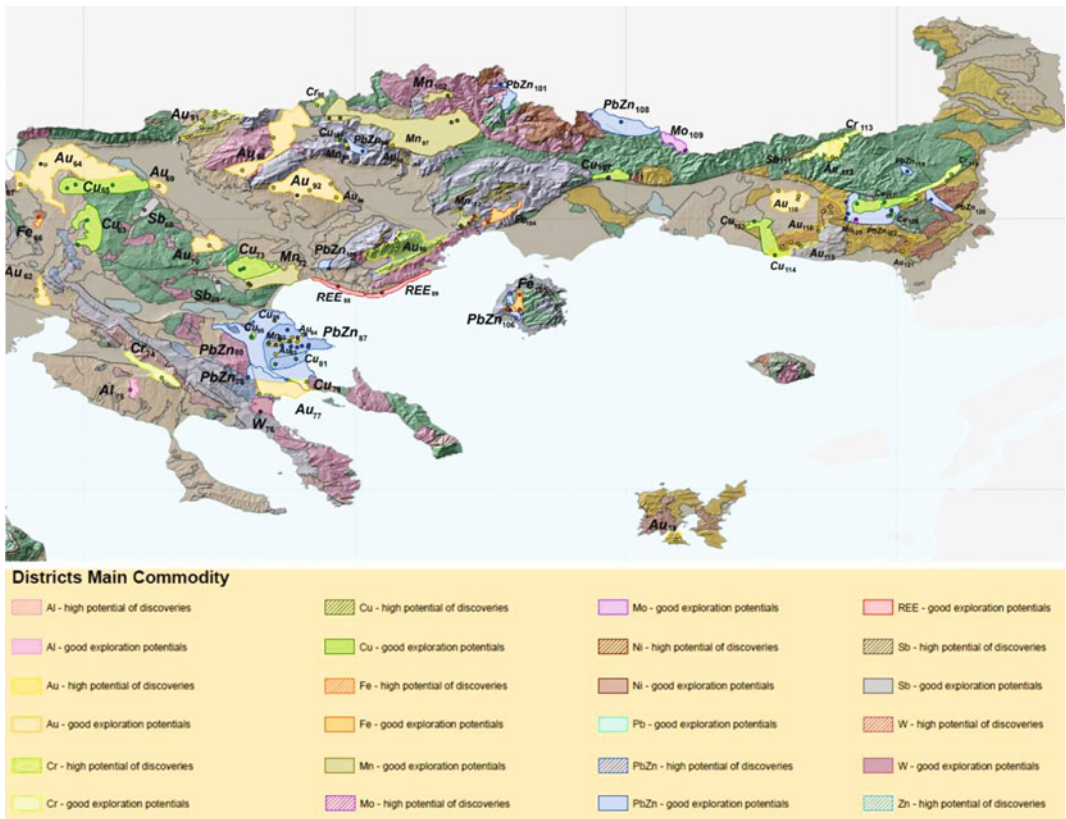


Fig. 13.34 Metallogenic districts and mineral commodities in Northern Greece

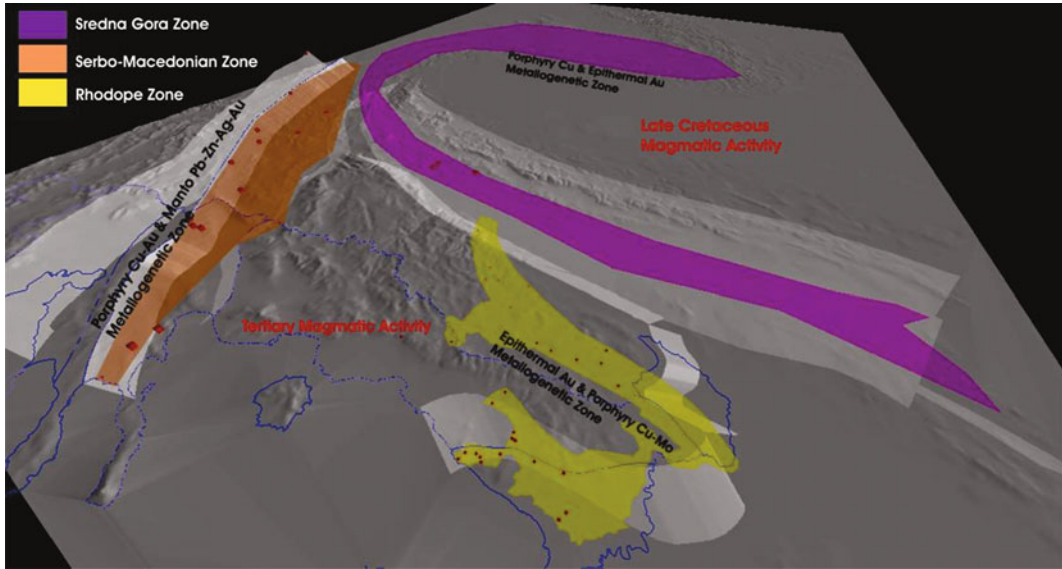


Fig. 13.35 Predictive regional model of Southern Carpathian-Balkan belt (Screenshot from MOVE)

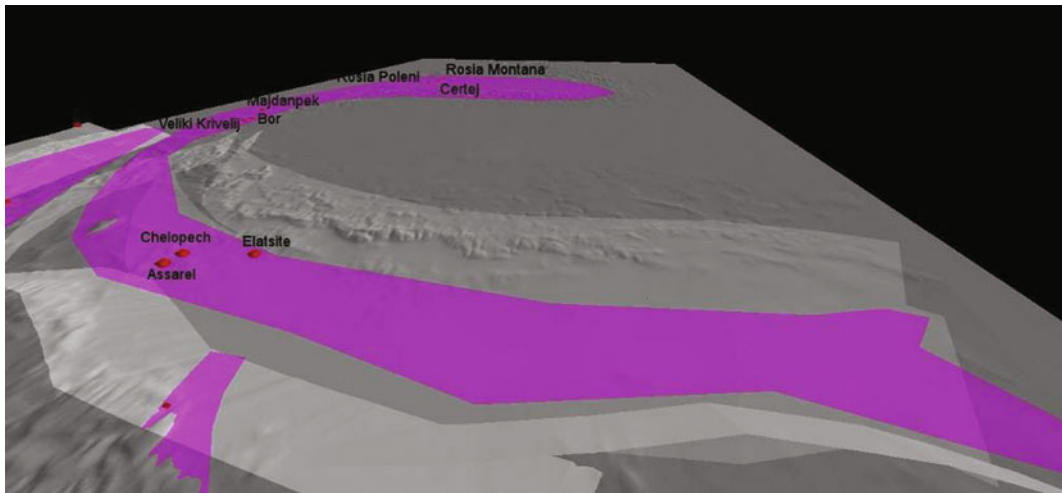


Fig. 13.36 Sredna Gora metallogenetic zone (Screenshot from MOVE)

molybdenum deposits related to Tertiary magmatic activity (Fig. 13.37).

- The Serbomacedonian metallogenetic zone with porphyry copper—gold deposits and manto Pb-Zn-Ag-Au deposits related to Tertiary magmatic activity (Fig. 13.38).

Using 3D models, metallogenetic data and known mineral districts in Rhodope zone across

the Greek–Bulgarian border a prospective province for epithermal gold and copper-molybdenum deposits was identified (Fig. 13.37).

The epithermal gold deposits developed at the structural contact (graben structures) between the Tertiary rocks and the metamorphic basement. Hydrothermal breccia is a favourable site for gold deposition. Gold mineralization is mainly related to hydrothermal eruption vent breccias

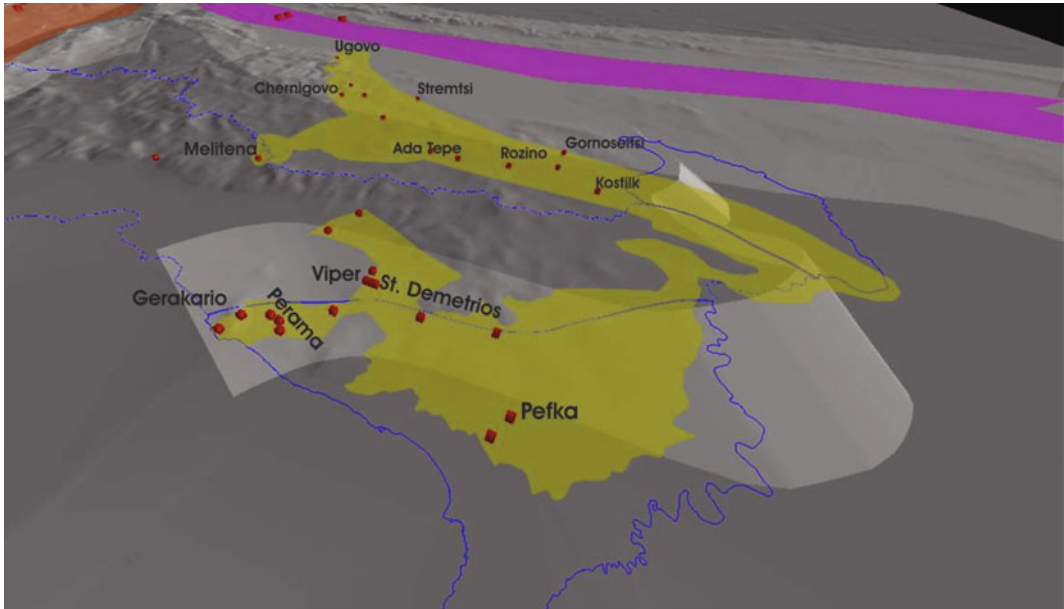


Fig. 13.37 3D model that depicts the epithermal mineralization prospective province in Rhodope zone (Screenshot from MOVE)

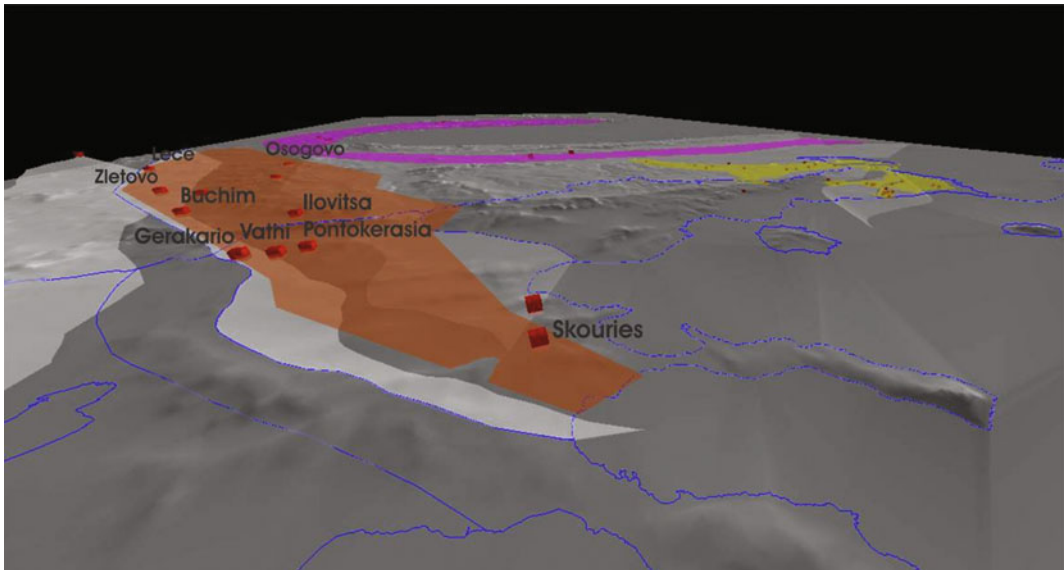


Fig. 13.38 3D model that depicts the prospective porphyry Cu province in the Serbomacedonian zone (Screenshot from MOVE)

and fissure vent systems. Other less favorable sites of epithermal gold deposition are volcanic rocks of intermediate composition, sedimentary rocks, shoshonitic rocks and felsic volcanic and metamorphic rocks.

There is a potential for new discoveries of high-sulphidation epithermal systems in Greece and low-sulphidation gold deposits in Bulgaria as well as a potential for porphyry Cu-Mo in Greece. The Cu-Mo occurrences and associated

potassium alteration found in many areas, indicate that the porphyry copper deposits are also a prospective target.

It is suggested that the hydrothermal systems are generated by igneous activity as indicated by the spatial relationship between granitoids and epithermal systems (Fig. 13.37). Sulphur isotopes indicate that the fluids were predominantly magmatic (values $\sim 0\%$). Using metallogenetic data from the ProMine databases, a prospective province for potential deposits of epithermal gold, porphyry copper-gold and replacement base metals is identified in northern Greece (Fig. 13.38).

Using the density estimation method on ProMine database and geological information (D. Singer pers. com.) for northern Greece it can be concluded: based on one well-explored deposit (e.g. Skouries) in the tract, that there is a 90 % probability that there are ≥ 3 undiscovered deposits, a 50 % probability that there are ≥ 6 and 10 % probability that there are ≥ 12 undiscovered porphyry copper deposits in the region. With two well explored deposits known, the number of undiscovered polymetallic deposits as estimated by the density equation, are 2, 6, 16 at the 90, 50, and 10 % probability respectively.

13.7 Summary and Conclusions

The Mavres Petres mine 3D model reveal a series of parallel faults, parallel to the main Stratonivarvara fault. The 3D model can be used as a reliable tool for exploration of new ore potential areas at depth and along the westward extension of the main fault structure, in the area of Piavitsa. In the semi-regional scale 3D modelling of NE Chalkidiki peninsula, the relationship between faults and intrusions became obvious. In general the 3D model of the Aghios Demetrios deposit defines the geometry and orientation of the ore body, the metal distribution, the role of later faults in displacing the ore body and verification of the reserves of the deposit. In the Perama Hill epithermal gold deposit, the 3D model defines the evolution of mineralization zones, as well as

the structural and lithological control on ore deposition.

A geological reconstruction of the epithermal deposits in the Thrace region, at semi-regional scale, shows that N-NE and N-S trending structures seems to have been the conduits for hydrothermal fluids and the fissure vent systems. These faults correspond to deep structures that formed the rift/graben Tertiary basins.

In summary:

- 3D model technology has an increasingly important role in integrating and analyzing of geoscientific information for constructing more detailed and understandable exploration models.
- Using all the available information has allowed to integrate and compare heterogeneous sources of data in the same 3D models.
- Different information can be combined to better understand the relationship between faults, lithology, alteration zones, metal zoning and the sites of highest potential for mineralization.
- In general the 3D models are very useful tool for improving the knowledge of the ore deposition and for conducting a successful mineral exploration program.
- 3D models helps the development of a 4D model (including geological time) in order to realize and visualize the geological evolution and the ore deposition.

References

- Adeline P., 2010. 3D Geomodeling of the Mavres Petres (Pb-Zn-Ag) and Skouries (Cu-Au) mineralizations, Straton (Greece). MSc thesis in INPL-NNancy.
- Andrew S., Constantinides D., 2001. The Sappes gold project-Bulletin of the Geological Society of Greece. Vol.34, 3, 1073-1080. Proceedings of the 9th International Congress, Athens, September 2001.
- Arvanitidis N., 2010. New metallogenetic concepts and sustainability perspectives for non-energy metallic minerals in Greece - 12th International Congress Of The Geological Society Of Greece Bulletin Of The Geological Society Of Greece Volume XLIII. No 5. 2010.

- Arvanitidis N.D., Michael C., Christidis C., Cassard D., Perantonis G., Bertrand G., Kaja J., Ballas D. Bakalis V., 2012a. GIS-based datasets of mineral deposits and man-made resources as valuable exploration tools for discovering potential ore deposits in Greece. 7th EUREGEO- Bologna 2012.
- Arvanitidis N.D., Michael C., Perantonis G., Bakalis V., Ballas D., Christidis C., 2012b. Using 3D/4D modeling tools in exploration of gold-polymetallic potential areas in Greece. 7th EUREGEO- Bologna 2012.
- Arvanitidis, N., 1993. Regional ore geologic studies setting controls and distribution of Metallic ore deposit types in the Serbo-Macedonian and Western Rhodope zone. I.G.M.E. technical report.
- Border A.J.M., Constantinides D.C., Michael C., 1999. Discovery and evaluation of the Sappes gold deposits, North-eastern Greece. In: New generation Gold Mines 99. Conference proceedings, 22-23 November, Perth, Western Australia.
- Bridges P.S., Gordon M.J., Michael C., Abatzioglou M., 1998. Gold mineralization at Sappes, northern Greece. In: Europe's Major gold Deposits, Irish Association for Econ. Geol., Abstract volume, IAEG, c/o Geological Survey of Ireland. 95-107.
- Burchfiel, B.C., 1980. Eastern European Alpine system and the Carpathian orocline as an example of collision tectonics. *Tectonophysics* 63, 31– 61.
- Burg, J.P., Ivanov, Z., Ricou, L.E., Dimor, D., Klain, L., 1990. Implications of shear-sense criteria for the tectonic evolution of the Central Rhodope Massif, southern Bulgaria. *Geology* 18, 451– 454.
- Burg, J.-P., Ricou, L.-E., Ivanov, Z., Godfriaux, I., Dimov, D., Klain, L., 1996. Syn-metamorphic nappe complex in the Rhodope Massif. Structure and kinematics. *Terra Nova* 8, 6 – 15.
- Burg, J-P., Godfriaux, I., Ricou, L.E., 1995. Extension of the Mesozoic Rhodope thrust units in the Vertiskos–Kerdyllion Massifs (northern Greece). *Comptes Rendus de l'Academie des Science Paris* 320, Se'rie Ila, 889– 896.
- Dinter, D.A., Royden, L., 1993. Late Cenozoic extension in northeastern Greece: Strimon valley detachment and Rhodope metamorphic core complex. *Geology* 21, 45–48.
- Eliopoulos D, Economou-Eliopoulos M, 1991. Platinum-Group Element and Gold Contents in the Skouries Porphyry Copper Deposit, Chalkidiki Peninsula, Northern Greece. *Economic Geology* 86, 740–749.
- Frei R., 1992. Isotope (Pb, Rb - Sr, S, O, C, U- Pb) geochemical investigation on Tertiaryintrusive and related mineralizations in the Serbomacedonian Pb-Zn, Sb + Cu_ Mo metallogenetic province in N. Greece - Ph D Thesis. Swiss Federal Institute of Technology (ETH) Zurich, Switzerland. 231 pp.
- Frei R., 1995. Evolution of Mineralizing Fluid in the porphyry copper system of the Skouries deposit, Northeast Chalkidiki (Greece) - Evidence from combined Pb-Sr and stable isotope data *EconomicGeology*, vol 90, 1995, pp 746-762 Kalogeropoulos, S. I., Economou, G.S.
- Fytikas M. ; Giuliani O. ; Innocenti F. ; Manetti P. ; Mazzuoli R. ; Peccerillo A. ; Villari, 1980. Neogene volcanism of the northern and central Aegean region. *Ann.Geol.Pays Hell.* 30(1) 1980.
- Innocenti F.; Kolios N.; Manneti P.; Mazzuoli R.; Peccerillo A.; Rita F.; Villari L.; 1980. The geology and geodynamic significance of Tertiary orogenic volcanism in Northeastern Greece. *Bull. Vol no 1, 47* (1), 25–37
- Ivanov, Z., 1989. Structure and tectonic evolution of the central parts of the Rhodope Massif. In: Ivanov, Z. (Ed.), Guide to excursion E3, XIV Congress of the Carpathian–Balkan Geological Association. Publishing House bG. DimitrovQ Yambol, Sofia, pp. 53– 91 (in Russian).
- Jones, C.E., Tarney, J., Baker, J.H., Gerouki, F., 1992. Tertiary granitoids of Rhodope, northern Greece: magmatism related to extensional collapse of the Hellenic orogen? *Tectonophysics* 210, 295– 314.
- Kalogeropoulos S I Kiliias S P Bitzios D C., 1989. Genesis of the Olympias Carbonate-hosted Pb-Zn(Au, Ag) Sulfide ore deposit, eastern Chalkidiki Peninsula, northern Greece - *Econ. Geol vS4 pp 1210-1234*
- Kockel F., Mollat H., Walter H.W., 1971. Geologie des Serbo-Mazedonischen Massive und seines mesozoischen Racmens (Nord-Grecheland). *Geol. Jb.*, 89; 529-551.
- Lescuyer, J. L. , Bailly, D., Cassard, A. L. W. Lips & Piantone, P. Mc. Alister, M. 2003. Sediment - hosted gold in south - eastern Europe : the epithermal deposit of Perama, Thrace, Greece. *Mineral Exploration and Sustainable Development et. al. (eds)*.
- Lips, A.L.W., White, S.H., Wijbrans, J.R., 2000. Middle–Late Alpine thermotectonic evolution of the southern Rhodope Massif, Greece. *Geodinamica Acta* 13, 281–292.
- Marchev, P., Jelev, D., Hasson, S., 2005. Ada Tepe sedimentaryhosted, low-sulphidation epithermal Au deposit, SE Bulgaria. *Ore Geology Reviews* 27, 92–93 (this volume).
- Michael C. 1993. Geology and Geochemistry of the epithermal gold deposit in Konos area. Xanthi. IGME. 1-75 (In Greek).
- Michael C., 1988. Epithermal gold mineralization at Konos area, Rhodope county, Xanthi. IGME (In Greek), p.1-23.
- Michael C., 1995. Conceptual model of Konos epithermal system. *Geol. Soc. Greece, sp. Publ.* 4/2.
- Michael C., 2005. Mineralogical and Geochemical characteristics of Sappes epithermal system in western Thrace (Northern Greece). *Comptes rendus de l'Academie Bulgare des Sciences*, vol. 58, N6. *Geologie, cites metalliferes*.
- Michael C., Arvanitidis N., Papavasileiou K., Iliadis A., Christidis C., 2012. Orogenic mineralizations – a new exploration target for gold-polymetallic ore deposits in Greece. 34th International Geological Conference (IGC), Australia 2012.
- Michael C., Papadopoulos P., Evangelou E., Marantos I., 1989. Epithermal gold mineralization at Konos area. In: 2nd Hellenic-Bulgarian symposium on the

- Geological and Physicogeographical problems of the massif. Abstract volume. Arist. Univ. of Thes., Sch of Geol., Greece.
- Michael C., Perdikatsis V., Dimou E., Marantos I., 1995. Hydrothermal alteration and ore deposition in epithermal precious metal deposit of Agios Demetrios, Konos area, Northern Greece. *Geol. Soc. Greece, sp. Publ.*, 4/2.
- Moritz, R., Jacquat, S., Chambefort, I., Fontignie, D., Petrunov, R., Georgieva, S., von Quadt, A., 2003. Controls on ore formation at the high-sulphidation Au–Cu Chelopech deposit, Bulgaria: evidence from infrared fluid inclusion microthermometry of enargite and isotope systematics of barite. In: Eliopoulos, D., et al., (Eds.), *Mineral Exploration and Sustainable Development*. Millpress, Rotterdam, pp. 1209–1212.
- Mountrakis D., 1985. “Geology of Greece”, University Studio Press, Thessaloniki
- Pomoni-Papaoiannou F., Papadopoulos P., 1986. Dolomitization of carbonate rocks of metasedimentary series of Makri unit, Southeast Rhodope. *Bulletin Of The Geological Society Of Greece*. 1988, XX/2, p. 429-447.
- Ricou, L.-E., Burg, J.-P., Godfriaux, I., Ivanov, Z., 1998. Rhodope and Vardar: the metamorphic and the olistostromic paired belts related to the Cretaceous subduction under Europe. *Geodinamica Acta* 11, 1 –25.
- Tarkian M., Eliopoulos D.G., and Economou EM., 1991. Mineralogy of precious metals in the Skouries porphyry copper deposit northern Greece. -N, *Jb. Minier. Ath, Monatshefte* 1991.(12), p 529-537.
- Velinov I., Kunov A., Petrounov R., Michael C., 1999. Mineralogy and zoning of hydrothermal alterations with examples from Bulgaria, Greece and Turkey. *Metallogenesis of Bulgaria, International symposium, 22-24 Nov. 1999, Sofia*.
- von Quadt, A., Peytcheva, I., Cvetkovic, V., 2003. Geochronology, geochemistry and isotope tracing of the Cretaceous magmatism of east-Serbia and Panagyurishte District (Bulgaria) as part of the Apuseni–Timok–Srednogorie metallogenic belt in eastern Europe. In: Eliopoulos, D., et al., (Eds.), *Mineral Exploration and Sustainable Development*. Millpress, Rotterdam, pp. 407– 410.